

1. Report No.		2. Government Accession No.		3. Recipient's Catalog No.	
4. Title and Subtitle MEASUREMENT-BASED PERFORMANCE EVALUATION OF A SEGMENTAL CONCRETE BRIDGE				5. Report Date September 1998 <i>Revised May 1999</i>	
				6. Performing Organization Code	
7. Author(s) Rodney T. Davis, M. Keith Thompson, Bryan A. Wood, John E. Breen, and Michael E. Kreger				8. Performing Organization Report No. Research Report 1404-3F	
9. Performing Organization Name and Address Center for Transportation Research The University of Texas at Austin 3208 Red River, Suite 200 Austin, TX 78705-2650				10. Work Unit No. (TRAIS)	
				11. Contract or Grant No. Research Study 0-1404	
12. Sponsoring Agency Name and Address Texas Department of Transportation Research and Technology Transfer Office P.O. Box 5080 Austin, TX 78763-5080				13. Type of Report and Period Covered Research Report (9/96-8/97)	
				14. Sponsoring Agency Code	
15. Supplementary Notes Project conducted in cooperation with the U.S. Department of Transportation					
16. Abstract Construction of around 10km of the US 183 elevated highway in Austin, Texas, using precast segmental post-tensioned construction provided a unique opportunity to investigate many aspects of segmental bridge technology. The project included balanced cantilever erection, span-by-span erection and some cast-in-place transitions. Some of the piers were also made with precast box sections. A detailed instrumentation study was carried out to determine post-tensioning force losses, thermal gradients and their effects, live load response, behavior of local zones such as diaphragms p-t anchorages and blisters and diffusion of post-tensioning forces, as well as evaluation of the degree of continuity obtained with the semicontinuous details utilized. The measurement results are presented and evaluated. Recommendations are made for improvement in bridge design specifications and construction practices.					
17. Key Words Field measurements, precast concrete piers, segmental bridges, bridge instrumentation, thermal gradients, live load tests, strut-and-tie models, local zones, post-tensioning, losses, external tendons, cantilever erection.			18. Distribution Statement No restrictions. This document is available to the public through the National Technical Information Service, Springfield, Virginia 22161.		
19. Security Classif. (of report) Unclassified		20. Security Classif. (of this page) Unclassified		21. No. of pages 422	22. Price

MEASUREMENT-BASED PERFORMANCE EVALUATION OF A SEGMENTAL CONCRETE BRIDGE

by

***RODNEY T. DAVIS, M. KEITH THOMPSON, BRYANA A. WOOD,
JOHN E. BREEN, AND MICHAEL E. KREGER***

Research Report No. *1404-3F*

Research Project *0-1404*

"Instrumentation of Precast Segmental Box Girder Bridges on US 183 in Austin"

conducted for the

Texas Department of Transportation

in cooperation with the

US Department of Transportation
Federal Highway Administration

by the

CENTER FOR TRANSPORTATION RESEARCH
BUREAU OF ENGINEERING RESEARCH
THE UNIVERSITY OF TEXAS AT AUSTIN

October 5, 1998

Revised May 21, 1999

This report was prepared in cooperation with the Texas Department of Transportation and the US Department of Transportation, Federal Highway Administration.

DISCLAIMERS

The contents of this report reflect the views of the authors, who are responsible for the facts and the accuracy of the data presented herein. The contents do not necessarily reflect the official views or policies of the Federal Highway Administration or the Texas Department of Transportation. This report does not constitute a standard, specification, or regulation.

There was no invention or discovery conceived or first actually reduced to practice in the course of or under this contract, including any art, method, process, machine, manufacture, design or composition of matter, or any new and useful improvement thereof, or any variety of plant which is or may be patentable under the patent laws of the United States of America or any foreign country.

NOT INTENDED FOR CONSTRUCTION,
BIDDING, OR PERMIT PURPOSES

John E. Breen, P.E. (Texas PE# 18479)

Michael E. Kreger (Texas PE# 65541)

Research Supervisor

ACKNOWLEDGMENTS

The research studies reported herein involved a complex instrumentation program of an ongoing major bridge project. The report is based on The University of Texas dissertation of Rodney Davis (Ref. 57). In addition, the authors are indebted to a number of other graduate students who assisted on the project, particularly Keith Thompson, Val Andres, Wade Bonzon and Bryan Wood. The overall project was greatly helped by the interest and cooperation of Tom Rummel of the Design Division, who was the TxDOT Project Director. He played an invaluable role in providing background information and in liaison with the casting yard and site operations. The TxDOT inspectors, the TxDOT District construction engineers and the two splendid contractors, Martin K. Eby Construction and Flatiron Structures Company provided substantial assistance to the project. We are most appreciative of their interest and in their willing cooperation in scheduling, communicating and putting up with interlopers on their time-critical project.

*Research performed in cooperation with the Texas Department of Transportation and the
U.S. Department of Transportation, Federal Highway Administration.*

TABLE OF CONTENTS

CHAPTER 1: INTRODUCTION	1
1.1 THE US 183 STUDY	1
1.2 PURPOSE FOR THE STUDY	5
1.2.1 Structural Performance and Safety.....	5
1.2.2 Constructibility Problems.....	5
1.2.3 Initial Cost of Future Bridges.....	6
1.2.4 Maintenance Problems.....	6
1.3 PROJECT OBJECTIVES.....	6
1.3.1 Identify and Study Major Design Uncertainties	6
1.3.2 Instrument and Test Structural Elements	6
1.3.3 Interpret Measurements.....	6
1.3.4 Make Recommendations to TxDOT and FHWA	6
1.4 STRUCTURAL ELEMENTS UNDER STUDY	7
1.4.1 Mainlane Pier.....	12
1.4.2 Mainlane Girder	15
1.4.3 Ramp P Girder	23
1.4.4 Large Ramp Pier	27
1.4.5 Transition and Modified Spans	37
1.5 TOPICS STUDIED ON THE US 183 SEGMENTAL PROJECT.....	39
1.5.1 Friction losses in post-tensioning tendons.....	39
1.5.2 Thermal gradients and their effects	40
1.5.3 Strut-and-tie design regions	40
1.5.4 Stress distributions in box girders	41
1.5.5 Behavior of semicontinuous multiple-span units.....	42
1.6 SCOPE AND CHAPTER ORGANIZATION.....	42
CHAPTER 2: INSTRUMENTATION PROGRAM	45
2.1 GENERAL APPROACH TO MEASUREMENTS.....	45
2.2 INSTRUMENTATION	46
2.2.1 Strain Gauges	46
2.2.2 Thermocouples.....	52
2.2.3 Linear Potentiometers	53
2.2.4 Pressure Transducers.....	53
2.2.5 Load Cells	54
2.2.6 Data Acquisition System.....	54
2.2.7 Demec Extensometer	61
2.2.8 Deflection Measurements.....	62
2.2.9 Tiltmeter	64
2.2.10 Epoxy Sleeve System.....	64
2.3 INSTRUMENT LOCATIONS.....	66
2.3.1 Mainlane Pier	66
2.3.2 Three-Span Mainlane Box Girder Unit	69
2.3.3 Segmental Large Ramp Pier.....	74
2.3.4 Five-Span Ramp Box Girder Unit.....	81
2.3.5 Multiple-Celled Box Girder Units.....	88

2.4	MATERIAL PROPERTY TESTS	90
CHAPTER 3: PRESTRESSING FORCE LOSSES IN POST-TENSIONING TENDONS		97
3.1	PROBLEM DESCRIPTION AND TECHNICAL BACKGROUND.....	97
3.2	LITERATURE REVIEW AND FIELD EXPERIENCE.....	100
3.2.1	Friction Losses	100
3.2.2	Elastic Shortening Losses.....	105
3.2.3	Creep and Shrinkage	106
3.3	INSTRUMENTATION PROGRAM	107
3.3.1	Bench Test	107
3.3.2	Mainlane Girder Tests.....	109
3.3.3	Ramp Girder Tests	115
3.3.4	Large Ramp Pier Tests.....	119
3.4	DISCUSSION OF RESULTS.....	122
3.4.1	Friction Losses	122
3.4.2	Elastic Shortening	126
3.5	CONCLUSIONS	127
CHAPTER 4: THERMAL GRADIENTS AND THEIR EFFECTS		129
4.1	PROBLEM DESCRIPTION AND TECHNICAL BACKGROUND.....	129
4.1.1	Superstructure Behavior and Analysis Techniques	129
4.1.2	Substructure Behavior and Analysis Techniques	138
4.2	PREVIOUSLY MEASURED GRADIENTS AND DESIGN GRADIENTS.....	141
4.2.1	Hoffman, McClure and West [32].....	141
4.2.2	Hirst and Dilger [33].....	142
4.2.3	Shui [34]	142
4.2.4	Priestley [35].....	142
4.2.5	Roberts, Breen, Kreger [7].....	143
4.2.6	Arockiasamy and Reddy [36].....	143
4.2.7	Pentas, Avent, Gopu, and Rebello [37]	144
4.2.8	Potgieter and Gamble [38]	145
4.2.9	NCHRP 276 [39].....	145
4.2.10	AASHTO LRFD [9]	147
4.3	DATA COLLECTION AND ANALYSIS	148
4.3.1	Ramp P Superstructure.....	148
4.3.2	Mainlane Superstructure	165
4.3.3	Large Ramp Pier P16	180
4.3.4	Mainlane Pier D6.....	200
4.4	DISCUSSION OF RESULTS.....	206
4.4.1	Superstructure Thermal Gradients for Longitudinal Analysis.....	207
4.4.2	Superstructure Thermal Gradients for Transverse Design	211
4.4.3	Pier Gradients.....	214
4.5	CONCLUSIONS	217
4.5.1	Superstructure Gradients for Longitudinal Design.....	217
4.5.2	Thermal Gradients for Transverse Design	218
4.5.3	Thermal Gradients for the Design of Piers.....	218
CHAPTER 5: LOAD RESPONSE OF BOX GIRDERS		219
5.1	INTRODUCTION	219

5.2	PROBLEM AND TECHNICAL BACKGROUND.....	219
5.2.1	Structural Response of Box Girders to Dead Load and Live Load	219
5.2.2	Diffusion of Post-Tensioning Forces.....	221
5.2.3	Behavior of Multiple-Cell Box Girders.....	222
5.3	TYPICAL SOLUTIONS, DESIGN CODE METHODS, AND PREVIOUS MEASUREMENTS	224
5.3.1	Analysis of Box Girder Structures	224
5.3.2	Design Code Methods of Analysis	227
5.3.3	Previous Measurements	232
5.4	DATA COLLECTION, ANALYSIS AND RESULTS.....	232
5.4.1	Mainlane Girder	233
5.4.2	Ramp P Girder	254
5.4.3	Two-Cell Girder–Unit C15, L2.....	270
5.4.4	Three-Cell Girder – Unit C13	278
5.4.5	Large Ramp Pier	286
5.5	DISCUSSION OF RESULTS.....	290
5.5.1	Diffusion of Post-Tensioning	290
5.5.2	Response to Dead Loads and Live Loads.....	291
5.5.3	Behavior of Multiple-Cell Box Girders.....	291
5.6	CONCLUSIONS	293
5.6.1	Temporary Post-Tensioning for Epoxying Segments.....	293
5.6.2	Diffusion of Post-Tensioning Forces.....	293
5.6.3	Girder Response to Dead Loads and Live Loads	293
5.6.4	Performance of Multiple-Cell Girders under Live Load	294
5.6.5	Performance of the Segmental Pier under Bending.....	294
CHAPTER 6: BEHAVIOR OF DISCONTINUITY (OR D-) ZONES		295
6.1	PROBLEM AND TECHNICAL BACKGROUND.....	295
6.2	PREVIOUS STUDIES	300
6.3	DATA COLLECTION, ANALYSIS, AND DISCUSSION OF RESULTS	304
6.3.1	Mainlane Pier	304
6.3.2	Mainlane Deviator Segment.....	310
6.3.3	Mainlane Anchor Segment.....	316
6.3.4	Large Ramp Pier Capital.....	326
6.3.5	Ramp Interior Anchor Segment	330
6.3.6	Ramp Deviator Segment	336
6.3.7	Ramp Anchorage Blister Segment	343
6.4	RECOMMENDATIONS AND CONCLUSIONS	349
6.4.1	Pier Capitals	349
6.4.2	Deviators	349
6.4.3	Pier Segments.....	350
6.4.4	Anchorage Blister	351
CHAPTER 7: BEHAVIOR OF A SEMI-CONTINUOUS UNIT		353
7.1	INTRODUCTION	353
7.2	PROBLEM AND TECHNICAL BACKGROUND.....	357
7.3	PREVIOUS STUDIES	359
7.4	DATA COLLECTION AND ANALYSIS.....	360
7.4.1	Live-Load Tests	361

7.4.2	Temperature Gradient Effects	374
7.5	CONCLUSIONS AND RECOMMENDATIONS	377
7.5.1	Construction Procedures	378
7.5.2	Cast-in-Place Joint Behavior under Live Loads and Thermal Loads	378
CHAPTER 8: SUMMARY, RECOMMENDATIONS AND CONCLUSIONS		379
8.1	PROJECT SUMMARY	379
8.2	GENERAL CONCLUSIONS	379
8.2.1	Post-Tensioning Losses.....	379
8.2.2	Thermal Gradients	380
8.2.3	Load Response of Box Girders	380
8.2.4	Behavior of D-Zones.....	380
8.2.5	Cast-in-Place Joint Behavior.....	380
8.3	SPECIFIC CONCLUSIONS AND RECOMMENDATIONS	380
8.3.1	Post-Tensioning Losses.....	380
8.3.2	Thermal Gradients	382
8.3.3	Load Response of Box Girders	384
8.3.4	Behavior of D-Zones.....	386
8.3.5	Cast-in-Place Joint Behavior.....	387
8.4	OBSERVATIONS ON CONSTRUCTIBILITY AND DESIGN.....	388
8.4.1	Mainlane Y-Pier.....	388
8.4.2	Mainlane Girder.....	389
8.4.3	Segmental Pier P16.....	389
8.4.4	Ramp P Constructed in Balanced Cantilever	390
8.4.5	Transition Spans.....	391
8.4.6	Modified Spans	392
8.5	RECOMMENDATIONS FOR FUTURE STUDIES	392
8.5.1	Instrumentation	392
8.5.2	Future Research Topics.....	393
APPENDIX.....		395
REFERENCES.....		397

LIST OF FIGURES

Figure 1.1	Location map	1
Figure 1.2	Span-by-span construction.....	2
Figure 1.3	Mainlane structure	3
Figure 1.4	The San Antonio Y	4
Figure 1.5	US 183 North Ramp P constructed in balanced cantilever	4
Figure 1.6	The AASHTO Segmental Guide Specification [8]	7
Figure 1.7	Mainlane superstructure section	8
Figure 1.8	Ramp superstructure section.....	9
Figure 1.9	Cast-in-place transition spans	10
Figure 1.10	Pier types	10
Figure 1.11	Project precasting plant	11
Figure 1.12	Casting machines	11
Figure 1.13	Mainlane pier	12
Figure 1.14	Mainlane pier elevation	13
Figure 1.15	Mainlane pier details.....	14
Figure 1.16	Construction of mainlane pier capital	15
Figure 1.17	Mainlane girder.....	16
Figure 1.18	Construction of a mainlane girder.....	17
Figure 1.19	Construction of a cast-in-place deck joint.....	17
Figure 1.20	Cross section and elevation–Span D5.....	18
Figure 1.21	Casting machine.....	19
Figure 1.22	Casting machine details	19
Figure 1.23	Geometry control of the casting machine	20
Figure 1.24	Transporting segments.....	20
Figure 1.25	Locating segments on the erection trusses	21
Figure 1.26	Epoxying segments	22
Figure 1.27	Stressing a pair of mainlane girder external tendons	23
Figure 1.28	Plan of US 183 at IH 35.....	24
Figure 1.29	Construction sequence of Ramp P	25
Figure 1.30	End view of balanced cantilever ramp under construction	26
Figure 1.31	Ramp P anchor segment dimensions.....	26
Figure 1.32	Ramp P typical segment dimensions.....	27
Figure 1.33	Typical large ramp pier: elevation view.....	28
Figure 1.34	Typical sections: large ramp pier	29

Figure 1.35	Pier segment casting machine	30
Figure 1.36	Typical segment-per-day casting sequence	31
Figure 1.37	Placement of outer pier segment form	32
Figure 1.38	Casting bed with steel support frame for formwork.....	33
Figure 1.39	Hydraulic jacks used to align the bulkhead pier segment	33
Figure 1.40	U-shaped tendon ducts located in pier foundation	34
Figure 1.41	Steel support frame for first precast segment.....	35
Figure 1.42	Cast-in-place base forming a rigid moment connection between base segment PC16-1 and foundation.....	36
Figure 1.43	Hydraulic ram stressing temporary post-tensioning bars	37
Figure 1.44	Plan and section of transition Unit C13	38
Figure 1.45	Plan and section of modified Unit C15-L2	39
Figure 1.46	External tendon layouts for the US 183 box girders	39
Figure 1.47	Structural response to thermal gradients.....	40
Figure 1.48	Strut-and-tie model for diffusion of a point load	41
Figure 1.49	Diffusion of post-tensioning forces.....	41
Figure 1.50	Construction of a cast-in-place continuity joint	42
Figure 2.1	Gauge installation	45
Figure 2.2	Vibrating concrete near instrumentation.....	46
Figure 2.3	Electronic strain gauge.....	47
Figure 2.4	Wheatstone bridge circuit	47
Figure 2.5	"S" series gauges installed on rebar	48
Figure 2.6	"S" series gauges installed on prestressing tendon.....	48
Figure 2.7	"S" series gauges installed on structural pipe	49
Figure 2.8	"C" series gauge construction	49
Figure 2.9	C-gauge tested against the Demec extensometer	50
Figure 2.10	C-gauge calibration.....	51
Figure 2.11	Installation of C-gauges	52
Figure 2.12	Thermocouple circuit.....	52
Figure 2.13	Installation of a thermocouple	53
Figure 2.14	Linear potentiometer schematic	53
Figure 2.15	Pressure transducer schematic	54
Figure 2.16	Load cell schematic	54
Figure 2.17	Data acquisition systems used on the project.....	55
Figure 2.18	Wiring the AM416 Multiplexer to the 21X Datalogger.....	56
Figure 2.19	Wiring diagram for 350Ω strain gauges including the Wheatstone circuit	57

Figure 2.20	Concrete specimen and 21X datalogger temperatures recorded during temperature effects test	58
Figure 2.21	C-gauge output recorded during temperature effects test.....	58
Figure 2.22	Wiring diagram for thermocouples	59
Figure 2.23	Wiring diagram for linear potentiometers.....	60
Figure 2.24	Wiring diagram for pressure transducers and load cells	61
Figure 2.25	The Demec extensometer.....	62
Figure 2.26	Demec extensometer schematic	62
Figure 2.27	Piano wire deflection measuring system schematic	63
Figure 2.28	Taking deflection measurements.....	63
Figure 2.29	GPS deflection measurement equipment	64
Figure 2.30	Tiltmeter gauge mounting plate	64
Figure 2.31	Epoxy sleeve strain measurement system	65
Figure 2.32	Epoxy sleeves tested during the bench test	66
Figure 2.33	Elevation of Y-pier with gauge locations.....	67
Figure 2.34	Y-pier sections showing gauge locations	68
Figure 2.35	Plan view of Y-pier showing gauge locations.....	69
Figure 2.36	Elevation of mainlane girder D5 with deflection measurement locations	70
Figure 2.37	Tendon gauge locations for mainlane girder D5	70
Figure 2.38	Strain gauge locations for segment D5-9	71
Figure 2.39	Thermocouple locations for segment D5-9.....	71
Figure 2.40	Longitudinal strain gauge locations for segment D5-16	72
Figure 2.41	Strain gauge locations for deviator segment D5-12	72
Figure 2.42	Strain gauge locations for anchor segment D5-16	73
Figure 2.43	Linear potentiometer locations at pier D6.....	74
Figure 2.44	Strain gauge locations for the cast-in-place joint over pier D6.....	74
Figure 2.45	Elevation of large ramp pier P16 with segment identification	75
Figure 2.46	Segment PC16-1 sections with gauge locations.....	76
Figure 2.47	Segment PC16-5 sections with gauge locations.....	76
Figure 2.48	Segment PC16-7 sections with gauge locations.....	77
Figure 2.49	Segment PC16-8 top C-gauge locations	78
Figure 2.50	Segment PC16-8 bottom C-gauge locations	79
Figure 2.51	Segment PC16-8 S-gauge locations on rebar.....	80
Figure 2.52	Segment PC16-8 S-gauge locations on tie-down bars	81
Figure 2.53	Elevation of Ramp P, span P16, with segment identification	82
Figure 2.54	Ramp P tendon gauge locations.....	82
Figure 2.55	Anchor segment P16-1A section with gauge locations	83

Figure 2.56	Segment P16-2 sections with gauge locations	83
Figure 2.57	Deviator segment P16-10 sections with gauge locations	84
Figure 2.58	Segment P16-17 sections with strain gauge locations.....	85
Figure 2.59	Segment P16-17 section with thermocouple locations.....	86
Figure 2.60	Deviator segment P16 section with S-gauge locations on rebar	87
Figure 2.61	Segment P16-4 anchorage blister strain gauge locations	88
Figure 2.62	Plan and section of transition spans showing instrumentation locations.....	89
Figure 2.63	Plan and section of modified spans showing instrumentation locations.....	90
Figure 2.64	Concrete modulus of elasticity test specimen	91
Figure 2.65	Modulus of elasticity test results for mainlane pier D6.....	91
Figure 2.66	Modulus of elasticity test results for mainlane superstructure Unit D2	92
Figure 2.67	Modulus of elasticity test results for large ramp pier P16.....	92
Figure 2.68	Modulus of elasticity test results for Ramp P superstructure	93
Figure 2.69	Concrete compressive strengths for mainlane D	94
Figure 3.1	Friction loss model	98
Figure 3.2	Prestress force loss from creep and shrinkage	99
Figure 3.3	Mainlane girder tendons	100
Figure 3.4	Ramp P girder tendons.....	100
Figure 3.5	Results from previous friction tests.....	102
Figure 3.6	Bench test	108
Figure 3.7	Instrumentation calibration from bench test.....	109
Figure 3.8	Mainlane girder D5 tendon profiles–elevation	110
Figure 3.9	Mainlane girder D5 tendon profiles–end view.....	110
Figure 3.10	Ramp P tendon geometry–elevation	115
Figure 3.11	Ramp P tendon geometry–end view	116
Figure 3.12	Strain change in ramp tendons over time	119
Figure 3.13	Pier P16 elevation and tendon profiles	120
Figure 3.14	Sequence of final post-tensioning of pier P16 tendons	121
Figure 3.15	Selected axial strains in segment PC16-1 during pier post-tensioning, north-south axis locations.....	122
Figure 4.1	Climatic influences on superstructure thermal gradients	130
Figure 4.2	The effects of cross-section shape on thermal gradient shape	131
Figure 4.3	Components of a nonlinear thermal gradient	131
Figure 4.4	Effect of linear thermal gradient components on a statically determinate span	132
Figure 4.5	Effect of linear thermal gradient components on a statically indeterminate bridge structure.....	133
Figure 4.6	Calculation of self-equilibrating stresses from a nonlinear thermal gradient when plane sections remain plane.....	134

Figure 4.7	Thermal gradient that varies across the width and depth of a cross section.....	135
Figure 4.8	Transverse analysis for thermal gradients.....	136
Figure 4.9	Girder response to an applied positive thermal gradient when warping occurs.....	137
Figure 4.10	Girder response to an applied positive thermal gradient when warping occurs.....	138
Figure 4.11	Response of a single column to a thermal gradient.....	139
Figure 4.12	Response of a single-column bridge pier to a thermal gradient.....	139
Figure 4.13	Response of a multiple column bridge pier to a thermal gradient.....	140
Figure 4.14	Response of solid column to thermal gradients.....	140
Figure 4.15	Thermal gradient orientations at different times of the day.....	141
Figure 4.16	Thermocouple locations and maximum recorded thermal gradients for the Hoffman, McClure and West study [32].....	142
Figure 4.17	Thermocouple layout for the San Antonio Y study by Roberts [7].....	143
Figure 4.18	Temperature distributions through the depth of the section for the US 190 Atchafalaya River Bridge study by Pentas et al. [37].....	144
Figure 4.19	Proposed maximum solar radiation zones by Imbsen, et al. [39].....	145
Figure 4.20	Recommended positive vertical temperature gradient by Imbsen, et al. [39].....	146
Figure 4.21	Recommended negative vertical temperature gradient by Imbsen, et al [39].....	147
Figure 4.22	Positive vertical temperature gradient in concrete and steel superstructures (Figure 3.12.3-2 and Table 3.12.3-1 from the AASHTO LRFD Bridge Design Specifications [9]).....	148
Figure 4.23	Thermocouples used to calculate thermal gradient magnitudes on the Ramp P superstructure..	149
Figure 4.24	Measured thermal gradient magnitudes on Ramp P for the month of March 1997.....	150
Figure 4.25	The maximum measured positive gradient on Ramp P (from March 20, 1997).....	151
Figure 4.26	The maximum measured negative gradient on Ramp P (from March 6, 1997).....	152
Figure 4.27	Statistical occurrence of daily maximum $T_{1,meas}$ values on Ramp P before application of the asphalt blacktop.....	153
Figure 4.28	Statistical occurrence of daily maximum $T_{1,meas}$ values on Ramp P after application of the asphalt blacktop.....	153
Figure 4.29	Statistical occurrence of daily minimum $T_{1,meas}$ values on Ramp P before application of the asphalt blacktop.....	154
Figure 4.30	Statistical occurrence of daily minimum $T_{1,meas}$ values on Ramp P after application of the asphalt blacktop.....	154
Figure 4.31	Division of the Ramp P cross section into tributary areas for each thermocouple gauge.....	155
Figure 4.32	Comparison of measured and calculated positive thermal gradient stresses for segment P16-2 (near diaphragm).....	156
Figure 4.33	Comparison of measured and calculated positive thermal gradient stresses for segment P16-10 (quarter point).....	157
Figure 4.34	Comparison of measured and calculated positive thermal gradient stresses for segment P16-17 (midspan).....	158
Figure 4.35	Comparison of measured and calculated negative thermal gradient stresses for segment P16-2 (near diaphragm).....	159

Figure 4.36	Comparison of measured and calculated negative thermal gradient stresses for segment P16-10 (quarter point)	160
Figure 4.37	Comparison of measured and calculated negative thermal gradient stresses for segment P16-17 (midspan)	161
Figure 4.38	Minimum top flange stress load combinations for P16-2, P16-10 and P16-17.....	162
Figure 4.39	Maximum top flange stress load combinations for P16-2, P16-10 and P16-17	163
Figure 4.40	Comparison of measured and calculated transverse flexural stresses from positive and negative thermal gradients for P16-17	164
Figure 4.41	Measured stress changes in the Ramp P external tendons from the maximum positive gradient	165
Figure 4.42	Measured stress changes in the Ramp P external tendons from the maximum negative gradient	165
Figure 4.43	Thermocouples used to calculate thermal gradient magnitudes on the mainlane girder D5	166
Figure 4.44	Measured thermal gradients on mainlane girder D5 for the month of June 1996	167
Figure 4.45	The maximum measured positive gradient on mainlane girder D5 (from June 17, 1996)	168
Figure 4.46	Measured negative gradient on mainlane girder D5 (from November 11, 1995)	169
Figure 4.47	Statistical occurrence of daily maximum $T_{1,meas}$ values on mainlane girder D5 before application of the asphalt blacktop	170
Figure 4.48	Statistical occurrence of daily maximum $T_{1,meas}$ values on mainlane girder D5 after application of the asphalt blacktop	170
Figure 4.49	Statistical occurrence of daily minimum $T_{1,meas}$ values on mainlane girder D5 before application of the asphalt blacktop	170
Figure 4.50	Statistical occurrence of daily minimum $T_{1,meas}$ values on mainlane girder D5 after application of the asphalt blacktop	171
Figure 4.51	Division of the mainlane girder D5 cross section into tributary areas for each thermocouple gauge.....	171
Figure 4.52	Comparison of measured and calculated positive thermal gradient stresses for segment D5-9 (April 20, 1995).....	172
Figure 4.53	Comparison of measured and calculated positive thermal gradient stresses for segment D5-16 (April 20, 1995).....	173
Figure 4.54	Comparison of measured and calculated positive thermal gradient stresses for segment D5-9 (June 17, 1996)	175
Figure 4.55	Comparison of measured and calculated positive thermal gradient stresses for segment D5-16 (June 17, 1996).....	176
Figure 4.56	Comparison of measured and calculated negative thermal gradient stresses for segment D5-9 (November 11, 1995)	177
Figure 4.57	Comparison of measured and calculated negative thermal gradient stresses for segment D5-16 (November 11, 1995)	178
Figure 4.58	Measured peak positive and negative thermal gradients in degrees Celsius for segment D5-9 flanges and webs.....	179
Figure 4.59	Typical daily temperature cycle of selected thermocouples in segment PC16-5	181
Figure 4.60	Temperatures recorded through the thickness of the west wall of segment PC16-5	182

Figure 4.61	Temperatures measured along the height of pier P16.....	182
Figure 4.62	One-day cycle of thermal gradients along the north-south axis of segment PC16-5.....	183
Figure 4.63	One-day cycle of thermal gradients along the northeast-southwest axis of segment PC16-5.....	184
Figure 4.64	One-day cycle of thermal gradients along the east-west axis of segment PC16-5.....	185
Figure 4.65	One-day cycle of thermal gradients along the northwest-southeast axis of segment PC16-5.....	186
Figure 4.66	Temperature and strain changes on the north-south axis of segment PC16-5.....	187
Figure 4.67	Temperature and strain changes on the east-west axis of segment PC16-5.....	187
Figure 4.68	Temperature and strain changes through the thickness of the north wall of segment PC16-5.....	188
Figure 4.69	Temperature and strain changes through the thickness of the west wall of segment PC16-5.....	188
Figure 4.70	Concentric octagonal model for temperature representation.....	189
Figure 4.71	Projection of temperature gradient shape onto a single axis.....	190
Figure 4.72	Measured and design code maximum positive thermal gradients for pier P16.....	191
Figure 4.73	Measured and design code maximum negative thermal gradients for pier P16.....	192
Figure 4.74	Temperature changes along the east-west axis recorded by thermocouples in segment PC16-5, maximum positive gradient.....	193
Figure 4.75	Calculated strain changes and strain changes recorded by strain gauges in segment PC16-1, east-west axis, maximum positive gradient.....	193
Figure 4.76	Calculated strain changes and strain changes recorded by strain gauges in segment PC16-5, east-west axis, maximum positive gradient.....	193
Figure 4.77	Temperature changes along the north-south axis recorded by thermocouples in segment PC16-5, maximum positive gradient.....	194
Figure 4.78	Calculated strain changes and strain changes recorded by strain gauges in segment PC16-1, north-south axis, maximum positive gradient.....	194
Figure 4.79	Calculated strain changes and strain changes recorded by strain gauges in segment PC16-5, north-south axis, maximum positive gradient.....	195
Figure 4.80	Temperature changes along the east-west axis recorded by thermocouples in segment PC16-5, maximum negative gradient.....	195
Figure 4.81	Calculated strain changes and strain changes recorded by strain gauges in segment PC16-1, east-west axis, maximum negative gradient.....	196
Figure 4.82	Calculated strain changes and strain changes recorded by strain gauges in segment PC16-5, east-west axis, maximum negative gradient.....	196
Figure 4.83	Temperature changes along the north-south axis recorded by thermocouples in segment PC16-5, maximum negative gradient.....	197
Figure 4.84	Calculated strain changes and strain changes recorded by strain gauges in segment PC16-1, north-south axis, maximum negative gradient.....	197
Figure 4.85	Calculated strain changes and strain changes recorded by strain gauges in segment PC16-5, north-south axis, maximum negative gradient.....	197
Figure 4.86	Mechanism for cracking of large monolithic members during curing.....	199
Figure 4.87	Comparison of internal curing temperature to ambient air temperature, capital segment PC16-8.....	199
Figure 4.88	Maximum measured gradient shape during curing of capital segment PC16-8.....	200

Figure 4.89	Map of cracks found during curing of capital segment PC16-8.....	200
Figure 4.90	One-day cycle of pier D6 capital concrete temperatures	201
Figure 4.91	One-day cycle of pier D6 capital pipe temperatures	201
Figure 4.92	Pier D6 capital pipe temperature versus concrete core temperature, typical sunny day.....	202
Figure 4.93	Pier D6 pipe measured strains, typical sunny day.....	203
Figure 4.94	Pier D6 gauge locations	204
Figure 4.95	Measured concrete strains in the pier D6 capital over a sunny day	205
Figure 4.96	Measured concrete strains at the top of pier D6 column over a sunny day	206
Figure 4.97	Positive design gradients and measured gradients, no blacktop.....	208
Figure 4.98	Positive design gradients and measured gradients, 50mm of blacktop	209
Figure 4.99	Negative design gradients and measured gradients, no blacktop	210
Figure 4.100	Negative design gradients and measured gradients, 50mm of blacktop.....	211
Figure 4.101	Recommended positive top flange design gradient for transverse design.....	212
Figure 4.102	Recommended top flange negative design gradient for transverse design	213
Figure 4.103	Recommended web and bottom flange negative design gradient for transverse design.....	214
Figure 4.104	Recommended positive design gradient for piers	215
Figure 4.105	Recommended negative design gradient for piers	215
Figure 5.1	Shear lag deformation in a simple-span box girder.....	220
Figure 5.2	Top flange stresses in a continuous box girder	221
Figure 5.3	Response of a multiple-cell box girder to live load	223
Figure 5.4	Response of twin single-cell box girders to live load	224
Figure 5.5	Beam model of a box girder bridge	225
Figure 5.6	Analysis of twin single-cell box girders using superposition.....	226
Figure 5.7	Finite element model of a box girder bridge.....	227
Figure 5.8	Pattern of effective flange width coefficients, b_f and b_s (Figure 4.6.2.6.2-1 from the AASHTO LRFD Bridge Design Specifications [9]).....	228
Figure 5.9	Cross sections and corresponding effective flange widths, b_m , for flexure and shear (Figure 4.6.2.6.2-3 from the AASHTO LRFD Bridge Design Specifications [9]).....	229
Figure 5.10	Values of the effective flange with coefficient b_m/b , for the given values of b/l_i (Figure 4.6.2.6.2-2 from the AASHTO LRFD Bridge Design Specifications [9]).....	230
Figure 5.11	Effective flange widths, b_n , for normal forces (Figure 4.6.2.6.2-4 from the AASHTO LRFD Bridge Design Specifications [9]).....	231
Figure 5.12	Example of the effects of the diffusion of post-tensioning forces (after Kristek [44]).....	232
Figure 5.13	Mainlane girder D5 tendon locations.....	233
Figure 5.14	Longitudinal stresses in segment D5-16 from the tensioning of external tendons 1 through 6 ...	234
Figure 5.15	Longitudinal stresses in segment D5-9 from the tensioning of external tendons 1 through 6	235
Figure 5.16	Longitudinal stresses in segment D5-16 from the tensioning of internal bottom flange tendons 7 through 14	237

Figure 5.17	Longitudinal stresses in segment D5-9 from the tensioning of internal bottom flange tendons 7 through 14.....	238
Figure 5.18	Longitudinal stresses in segment D5-16 from the tensioning of bottom flange, wing and external tendons 1 through 18.....	239
Figure 5.19	Longitudinal stresses in segment D5-9 from the tensioning of bottom flange, wing and external tendons 1 through 18.....	240
Figure 5.20	Measured and calculated longitudinal stresses in segment D5-16 from post-tensioning and dead load.....	241
Figure 5.21	Measured and calculated longitudinal stresses in segment D5-9 from post-tensioning and dead load.....	242
Figure 5.22	Deflections from post-tensioning and dead load (+ deflection is camber).....	243
Figure 5.23	Live-load cases – Mainlane girders D4, D5 and D6	245
Figure 5.24	Live-load cases – Mainlane girders D4, D5 and D6 (continued).....	246
Figure 5.25	Longitudinal stresses from load case 2	247
Figure 5.26	Longitudinal stresses from load case 8	248
Figure 5.27	Deflections from load case 2	249
Figure 5.28	Deflections from load case 3	250
Figure 5.29	Deflections from load case 5	251
Figure 5.30	Deflections from load case 6	252
Figure 5.31	Deflections from load case 8	253
Figure 5.32	Deflections from load case 9	253
Figure 5.33	Diffusion of force from temporary post-tensioning in segment P16-10.....	254
Figure 5.34	Layout of segments and cantilever tendons in the P16 upstation cantilever	255
Figure 5.35	Diffusion of post-tensioning force from the cantilever tendons in segment P16-10	256
Figure 5.36	Longitudinal stresses in segment P16-2 after completion of the P16 upstation cantilever.....	257
Figure 5.37	Longitudinal stresses from selected strain gauges in segment P16-2 over the course of the cantilever construction sequence	258
Figure 5.38	Layout of internal and external continuity tendons in span P16	259
Figure 5.39	Longitudinal stresses in segment P16-2 after stressing of the continuity tendons for span P16..	260
Figure 5.40	Longitudinal stresses in segment P16-10 after stressing of the continuity tendons for span P16.....	261
Figure 5.41	Longitudinal stresses in segment P16-17 after stressing of the continuity tendons for span P16.....	262
Figure 5.42	Stresses from selected strain gauges from segment P16-2 over the course of the continuity stressing sequence.....	263
Figure 5.43	Stresses from selected strain gauges from segment P16-10 over the course of the continuity stressing sequence.....	264
Figure 5.44	Stresses from selected strain gauges from segment P16-17 over the course of the continuity stressing sequence.....	264
Figure 5.45	Live-load test cases for the Ramp P girder	266

Figure 5.46	Measured live-load longitudinal stresses in segment P16-2.....	267
Figure 5.47	Measured and calculated live-load longitudinal stresses in segment P16-2.....	268
Figure 5.48	Measured and calculated live-load longitudinal stresses in segment P16-10.....	269
Figure 5.49	Measured and calculated live-load longitudinal stresses in segment P16-17.....	270
Figure 5.50	Cross section of Unit C15, L2.....	271
Figure 5.51	(a) and (b) Live-load cases for Unit C15, L2.....	273
Figure 5.52	Deflections from load case 9.....	274
Figure 5.53	Deflections from load case 10.....	275
Figure 5.54	Deflections from load case 11.....	276
Figure 5.55	Deflections from load case 12.....	277
Figure 5.56	Deflections from load case 13.....	278
Figure 5.57	Cross section of Unit C13.....	279
Figure 5.58	(a) and (b) Live-load cases for Unit C13.....	281
Figure 5.59	Deflections from load case 2.....	282
Figure 5.60	Deflections from load case 3.....	283
Figure 5.61	Deflections from load case 4.....	284
Figure 5.62	Deflections from load case 5.....	285
Figure 5.63	Deflections from load case 6.....	286
Figure 5.64	Stresses in pier segment PC16-1 from placement of superstructure segment P16-17.....	288
Figure 5.65	Stresses in pier segment PC16-5 from placement of superstructure segment P16-17.....	288
Figure 5.66	Stresses in pier segment PC16-7 from placement of superstructure segment P16-17.....	289
Figure 5.67	Stresses in pier segment PC16-8 tie-down bars from placement of superstructure segment P16-17.....	289
Figure 6.1	Typical strut-and-tie models [52].....	297
Figure 6.2	Typical strut-and-tie models for segmental box girder design [52].....	298
Figure 6.3	Strut types [52].....	298
Figure 6.4	Anchorage details at nodes [52].....	299
Figure 6.5	Strut-and-tie model of a diaphragm from the San Antonio Y [7].....	301
Figure 6.6	Strut-and-tie model of a deviator from the San Antonio Y (after Roberts et al [7]).....	302
Figure 6.7	Types of anchorage blisters [54].....	303
Figure 6.8	Mainlane pier D6 details.....	305
Figure 6.9	Simple strut-and-tie model for mainlane pier D6.....	306
Figure 6.10	Frame model for mainlane pier D6.....	306
Figure 6.11	Measured strains in pier D6 capital from the superstructure dead load.....	308
Figure 6.12	Measured strains in pier D6 capital from live-load case 5.....	309
Figure 6.13	Measured strains in the deviator reinforcing bars from superstructure post-tensioning forces and dead load.....	310

Figure 6.14	Crack patterns in the segment D5-12 deviator	312
Figure 6.15	Measured strains in the deviator reinforcing bars from live-load case 2.....	313
Figure 6.16	Strut-and-tie model for the segment D5-12 deviator.....	314
Figure 6.17	Mainlane anchor segment D5-16 details.....	317
Figure 6.18	Crack patterns in segment D5-16 diaphragm.....	318
Figure 6.19	Crack patterns in the bottom flange of segments D5-16, D5-15 and D5-14	318
Figure 6.20	Post-tensioning and dead-load compressive force paths during construction of span D5.....	322
Figure 6.21	Dead-load support conditions during construction of span D5.....	323
Figure 6.22	Span D5 compressive force paths at ultimate load	324
Figure 6.23	Segment D5-16 diaphragm tie locations at ultimate load	325
Figure 6.24	Measured bottom flange longitudinal stresses from post-tensioning forces.....	326
Figure 6.25	Large ramp pier capital segment PC16-8 strut gauges.....	327
Figure 6.26	Large ramp pier capital segment PC16-8 tie gauges.....	328
Figure 6.27	Ramp P girder anchor segment P16-1 details	331
Figure 6.28	Crack patterns in segment P16-1	332
Figure 6.29	Strut-and-tie model at pier P16 - Side view	335
Figure 6.30	Strut-and-tie model at pier P16 - Looking down station	336
Figure 6.31	Ramp P girder segment P16-10 deviator details	337
Figure 6.32	Vertical and horizontal forces from tendons T1, T2 and T3.....	338
Figure 6.33	Crack patterns in segment P16-10	340
Figure 6.34	Strut-and-tie model for the segment P16-10 deviator	342
Figure 6.35	Ramp P girder segment P16-4 anchorage blister details.....	344
Figure 6.36	Strut-and-Tie model for segment P16-4 anchorage blister for service-load forces from Tendon T22	346
Figure 6.37	Struts and ties near anchorage blister at ultimate.....	349
Figure 6.38	Ramp P girder segment P16-10 deviator to web detail.....	350
Figure 7.1	Post-tensioning tendons on the mainlane girder.....	354
Figure 7.2	Original joint details from contract plans for U. S. 183.....	355
Figure 7.3	Actual cast-in-place joint construction.....	356
Figure 7.4	Longitudinal sections–cast-in-place joint	358
Figure 7.5	Joint details on the San Antonio Y	359
Figure 7.6	Deflections during live-load test, from Roberts, et al. [7].....	360
Figure 7.7	Strain gauge locations in cast-in-place joint–Unit D2.....	361
Figure 7.8	Live-load cases for Unit D2.....	362
Figure 7.9	Cast-in-place joint stresses–load case 2.....	363
Figure 7.10	Cast-in-place joint stresses–load case 3.....	363
Figure 7.11	Cast-in-place joint stresses–load case 5.....	364

Figure 7.12	Cast-in-place joint stresses–load case 6.....	364
Figure 7.13	Deflections from live-load test on Unit D2–load case 2	366
Figure 7.14	Deflections from live-load test on Unit D2–load case 3	366
Figure 7.15	Deflections from live-load test on Unit D2–load case 5	367
Figure 7.16	Deflections from live-load test on Unit D2–load case 6	367
Figure 7.17	Live-load cases–Unit C13.....	369
Figure 7.18	Deflections from live-load test on Unit C13–load case 2	370
Figure 7.19	Deflections from live-load test on Unit C13–load case 4	371
Figure 7.20	Live-load cases–Units C15 and L2	372
Figure 7.21	Deflections from live-load test on Units C15, L2–load case 9	373
Figure 7.22	Deflections from live-load test on Units C15, L2–load case 11	374
Figure 7.23	Measured temperatures for thermal gradient load case.....	375
Figure 7.24	Measured strains in segment D5-9 from thermal gradient load case.....	376
Figure 7.25	Measured strains in segment D5-16 and cast-in-place joint from thermal gradient load case	377
Figure A.1	US 183 Mainlane box girder daily maximum thermal gradients	395
Figure A.2	US 183 Ramp P box girder daily maximum thermal gradients.....	396
Figure A.3	US 183 segmental box pier P16 daily peak thermal gradients.....	396

LIST OF TABLES

Table 1.1	Project bid summary	2
Table 1.2	Unit construction costs	3
Table 2.1	Coefficients of thermal expansion	93
Table 2.2	Modulus of rupture test results	95
Table 3.1	Friction and wobble coefficients for post-tensioned tendons from AASHTO [23]	102
Table 3.2	Friction and wobble coefficients for post-tensioned tendons from AASHTO LRFD [9]	103
Table 3.3	Friction and wobble coefficients for post-tensioned tendons from CEB [24].....	103
Table 3.4	Friction and wobble coefficients for post-tensioned tendons from ACI 318-95 [25]	103
Table 3.5	Friction and wobble coefficients for post-tensioned internal tendons from PTI [26]	104
Table 3.6	Friction and wobble coefficients for post-tensioned internal tendons from ACI-ASCE [27]	105
Table 3.7	Bench test results	109
Table 3.8	In-place friction test results on span D2	111
Table 3.9	Measured losses and calculated wobble coefficients from in-place friction test on span D2	112
Table 3.10	Elongations from friction tests on span D2.....	112
Table 3.11	Span D5 friction test results from strain gauges	113
Table 3.12	Measured elongations from friction tests on span D5.....	114
Table 3.13	Elastic shortening losses in tendons in span D5	114
Table 3.14	Ramp P friction test results from strain gauges	116
Table 3.15	Measured elongations from friction tests on Ramp P	117
Table 3.16	Lift-off test results for tendon T3	117
Table 3.17	Elastic shortening losses–Ramp P external tendons	118
Table 3.18	Elongation measurement based wobble coefficients for all deviated external tendons, $\mu=0.25$	124
Table 3.19	Elongation measurement based wobble angles for deviated external tendons, $\mu=0.35$	124
Table 3.20	Calculated and measured elastic shortening losses in tendons in span D5	126
Table 3.21	Calculated and measured elastic shortening losses–Ramp P external tendons	127
Table 4.1	Mainlane girder D5 transverse thermal strains from the May 20, 1995, positive gradient	180
Table 4.2	Summary of maximum top fiber gradient magnitudes	208
Table 5.1	Axle weights and spacing for live-load test trucks on Unit D2.....	244
Table 5.2	Axle weights and spacing for live-load test trucks on Ramp P.....	265
Table 5.3	Axle weights and spacing for live-load test trucks on Units C15 and L2	271
Table 5.4	Axle weights and spacing for live-load test trucks on Unit C13.....	279
Table 5.5	Summary of live-load test results for multiple-cell girders.....	292
Table 6.1	Summary of tendon forces at various limit states for deviators tested by Beaupre et al. [55]	304

Table 6.2	Measured strains in anchor segment D5-16 reinforcing bars from stressing post-tensioning tendons in microstrain	319
Table 6.3	Measured strains in anchor segment D5-16 reinforcing bars from stressing post-tensioning tendons (continued) in microstrain	321
Table 6.4	Measured strain changes in segment PC16-8 gauges from post-tensioning forces	329
Table 6.5	Measured strain changes in segment PC16-8 gauges from placement of superstructure segment P16-17	330
Table 6.6	Measured strain changes in segment P16-1 gauges from placement of superstructure segment P16-17	333
Table 6.7	Measured strain changes in segment P16-1 gauges from superstructure post-tensioning forces in microstrain	333
Table 6.8	Measured strain changes in segment P16-10 gauges from post-tensioning forces in microstrain.....	339
Table 6.9	Measured strain changes in segment P16-10 gauges from live-load case 2.....	343
Table 6.10	Measured strain changes in segment P16-4 anchorage blister gauges from post-tensioning of tendon T22.....	345
Table 6.11	Element forces from P16-4 blister STM.....	348
Table 7.1	Axle weights and spacing for live-load test trucks on Unit D2.....	361
Table 7.2	Axle weights and spacing for live-load test trucks on Unit C13	368
Table 7.3	Axle weights and spacing for live-load test trucks on Units C15 and L2	373

CHAPTER 1

INTRODUCTION

1.1 THE US 183 STUDY

The data for this report came from a field study of the construction and service behavior of the US 183 segmental viaduct in north central Austin. The structure is an urban viaduct designed to separate local traffic from through traffic. US 183 is the major route for commuter traffic between IH 35 and the northwest Austin suburbs (see Figure 1.1). US 183, within the limits of the project, has extensive commercial development and a narrow right-of-way. US 183 elevated was designed to provide limited access to local roads beneath the structure, with major interchanges at IH 35, Lamar Boulevard, and Loop 1. Local businesses could be accessed from frontage roads and turnarounds beneath the elevated structure.

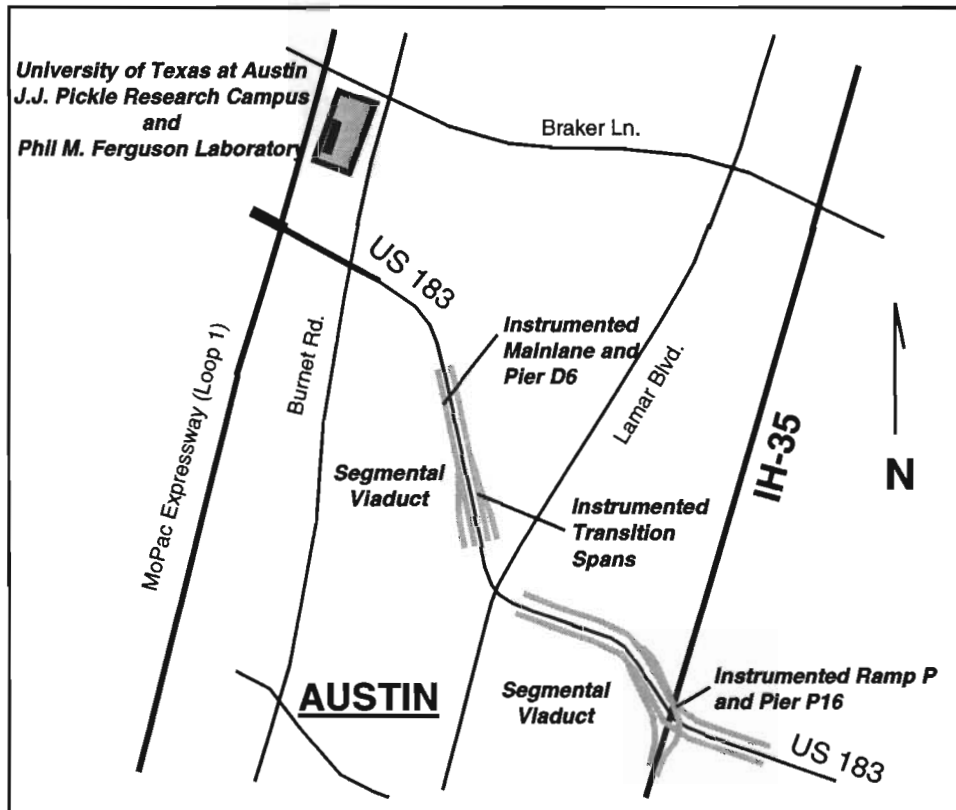


Figure 1.1 Location map

Twin precast segmental box girders constructed by the span-by-span method (Figure 1.2) were selected as the structure type most suited to much of the site for several reasons. The structure could be constructed from above the completed frontage roads while traffic could be maintained beneath. Single-column piers were used beneath the single-cell box girders allowing the frontage roads to be built beneath the structure overhangs, maximizing the number of lanes (12) in the narrow right-of-way. With over 10 kilometers of structure, precast concrete box girder construction, including fabrication of erection trusses and construction of a precasting facility, was also an economical solution. The box girder design option was the low bid at \$71.3 million over an alternate multiple precast delta and I-girder design with cast-in-place closures. Martin K. Eby Construction was the contractor in a joint venture with Flatiron Structures Company. A summary of all bids is shown in Table 1.1.

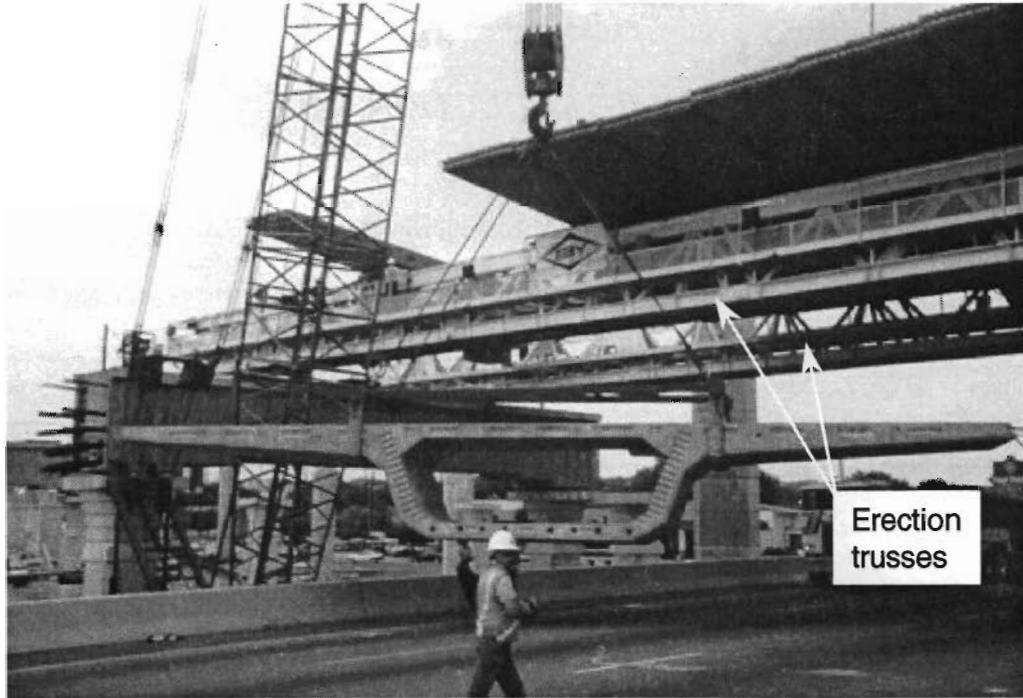


Figure 1.2 Span-by-span construction

Table 1.1 Project bid summary

Contractor	Design Option	Bid Price
Martin K. Eby Construction Co.	Precast Box Girder	\$71,328,098
Austin Bridge & Road	Precast Box Girder	\$71,792,000
H. B. Zachary Company	Precast Box Girder	\$73,456,000
Gilbert Texas Construction Co.	Precast Box Girder	\$77,495,848
McCarthy Brothers/PCL Civil Constructors	Precast Box Girder	\$82,893,263

An important consideration in selecting a box girder for the site was aesthetics. Austin residents are very sensitive to potential influences on their high quality of life in the state capital. A structure as potentially intrusive as the US 183 elevated would have to be designed as a signature structure for Austin, while minimizing visual impact. The segmental box girder option gave the designers a girder type known for its simple form and lightweight appearance. The designers, the TxDOT Bridge Division, used a spine beam-style box girder, with narrow soffit and long wings, to further enhance the light appearance of the structure. Architectural details reflecting the masonry construction of the State Capitol and The University of Texas Main Building were successfully blended into the design, especially of the single-column piers, by TxDOT engineers as seen in Figure 1.3. Table 1.2 shows the cost of the US 183 box girders and Y-shaped piers compared to the average Texas girder and pier costs [1]. The span lengths of the segmental box girders on US 183 were somewhat longer than the average span length for a pretensioned I-girder. Also, the standard multiple circular column with bent cap piers could not have been used at this site because of conflicts with the right-of-way requirement for the frontage roads.



Figure 1.3 Mainlane structure

Table 1.2 Unit construction costs

Structure Type	Unit Cost
Pretensioned I-girder	\$323/m ²
US 183 segmental box girder	\$463/m ²
Circular column with rectangular cap pier	\$420/m ³
Circular column with inverted T cap pier	\$485/m ³
US 183 mainlane Y-pier	\$556/m ³

The TxDOT Bridge Division designed the US 183 elevated segmental bridge using the knowledge they gained from the design, construction, and instrumentation of the San Antonio Y several years before (Figure 1.4). The segmental box girder superstructure design used at San Antonio was very similar in dimension and construction procedure to the superstructure used on most of US 183, but was built in fully continuous multi-span units. Most of the US 183 superstructure was constructed as simple spans. The contract for the San Antonio Y instrumentation study was with The University of Texas at Austin, as was the study on US 183. The University of Texas at Austin, particularly the Phil M. Ferguson Structural Engineering Laboratory, has had a long-term productive bridge research relationship with TxDOT and FHWA. The study of segmental bridges for Texas at the laboratory dates back to the early 1970's, when research was conducted for the design and construction of the segmental channel spans of the JFK Memorial Causeway in Corpus Christi. The knowledge gained from these field studies and from many laboratory based research projects was immediately implemented by TxDOT and the segmental bridge industry. This research provided valuable information to designers, such as effective shear key details for segment joints [2], ultimate load behavior of externally prestressed girders [3] and segmental box piers [4], and the actual behavior of discontinuity (or D-)zones for various reinforcement layouts [5] [6]. The instrumentation of the US 183 segmental project was designed to continue study of several research topics originally studied at the San Antonio Y [7], but having several new ranges of variables. More importantly this program was also able to study many new topics and structure types, including a segmentally constructed pier, a strut-and-tie model-type pier, and a five-span continuous box girder constructed in balanced cantilever. The latter is shown in Figure 1.5.

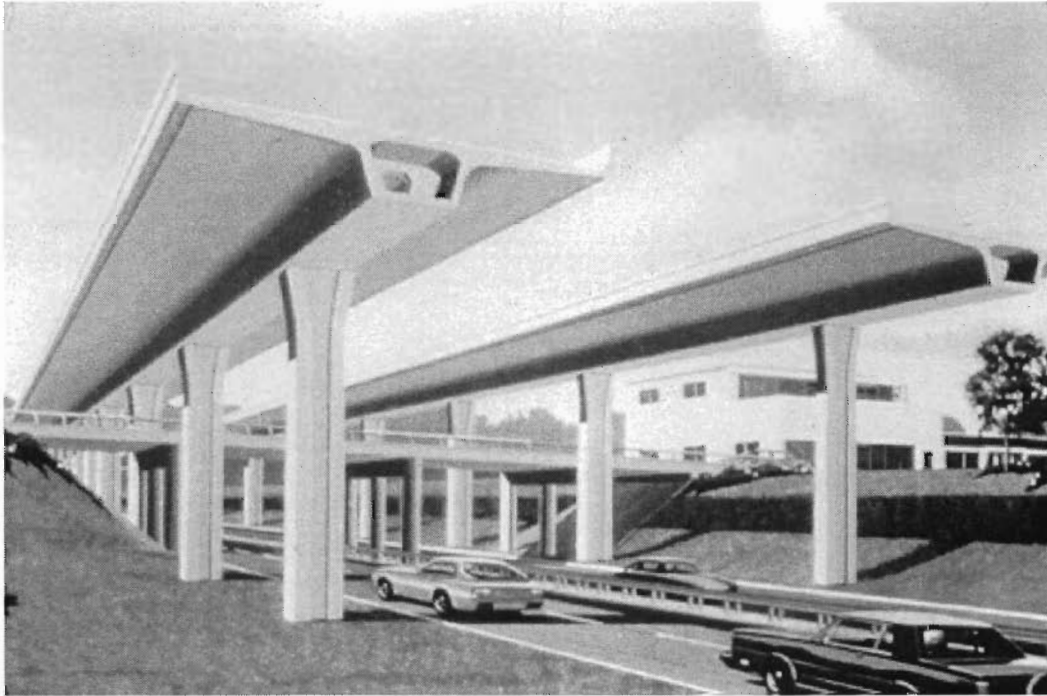


Figure 1.4 The San Antonio Y

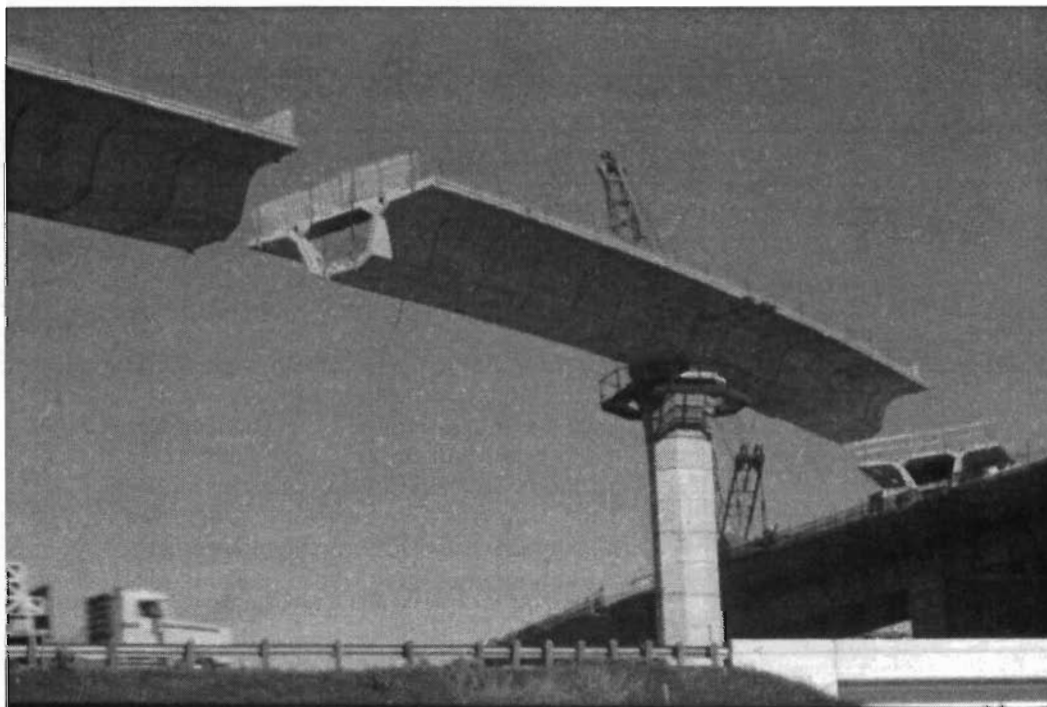


Figure 1.5 US 183 North Ramp P constructed in balanced cantilever

The close proximity of the structure to the Ferguson Laboratory (Figure 1.1) gave researchers the opportunity to conduct a very thorough, time intensive study of the bridge while under construction. Staff on the project consisted of four Master's degree candidates, one Ph.D. candidate, two supervising professors, and numerous helpers and volunteers. Over 1100 gauges and thermocouples were installed and monitored on the project. All of the data were examined. Obviously all of the data provided by these sensors could not be presented in this report, nor could a detailed study be performed on all imaginable topics. The topics presented herein were

considered to be the most important and useful to design engineers, construction engineers, and constructors. Recommendations and conclusions presented were intended to aid engineers and constructors in their decisions concerning structural behavior of segmental bridges during construction and service, as well as providing a basis for changes in the *AASHTO Guide Specification for the Design and Construction of Segmental Bridges* [8].

1.2 PURPOSE FOR THE STUDY

The main purpose for this study was to gather information through measurements and analysis that would lead to the reduction of construction and maintenance costs for segmental bridges in the state of Texas, while improving their structural performance and safety. The cost of this research project was less than 1% of the total project cost, yet historically represents a substantial investment for research by a state agency. The standard deviation of the lowest three bid prices shown in Table 1.1 was 1.6% of the low bid, which is actually a small percentage for a project of this size and complexity. This variation demonstrates that estimated construction costs can be larger than an expensive research program for the project. Table 1.2 shows that the cost of the 39m-span US 183 box girders, the span length selected as a compromise between economy and aesthetics, is somewhat higher in cost than the Texas average I-girder superstructure cast at existing plants. These I-girders are generally in the 13m to 40m-span range.

1.2.1 Structural Performance and Safety

The evaluation of structural performance by instrumentation is actually an evaluation of the design method used to analyze the structure. Structural performance of the traditional I-girders on short- to medium-span bridges is well understood from testing, and the design is generally straightforward, requiring few untested assumptions. Box girder design may require a complex time-dependent three-dimensional analysis, such as for Ramp P studied on this project. The assumptions and simplifications used in design can only be verified or calibrated using measurements on an actual structure.

Evaluation of the level of performance and safety in a structure begins with the evaluation of all critical elements of the bridge, starting with the main structural elements. If the actual structural response to known loads, environmental conditions, or time-dependent factors is poorly understood or has been poorly predicted, the level of performance and, often, of safety cannot be predicted. Predictable behavior of the main structural elements is critical in determining the safety of the entire structure. Connections and other areas with complex details or concentrated loads are designed to a higher degree of safety than the main members. Segmental box girders have numerous discontinuity zones (D-zones), where plane sections do not remain plane after loading and cracking may be expected. These D-zones, including deviators, anchorage zones, and diaphragms, can be very complex and have been the source of many problems in the past. Field measurements were taken in many D-zones on US 183 to evaluate their actual structural performance.

1.2.2 Constructibility Problems

Problems with structural elements or their assembly have a significant influence on project costs. Bridge types known for their constructibility problems are bid higher by all contractors. This was the case not long ago for segmental box girders. However, the combination of wider experience and the codification of good practice in the *AASHTO Guide Specification for Segmental Bridges* [8] has greatly reduced the problems and much of the uncertainty. Yet, since many recommendations in the Guide Specifications were based on judgment rather than studies, and since designers and constructors continue to innovate on new projects, construction problems still occur on these structures. Poor constructibility may also lead to poor quality and increased future maintenance costs.

Researchers on the US 183 project surveyed the constructibility of the project beginning at the precasting plant and continuing through to the end of construction. Construction problems occur for two distinct reasons. First, the problem may be inherent with the structural design. The engineer may be unaware of constructibility problems hidden in the design, and the problems may not even be visible to the contractor at bid time. Secondly, the construction technique and equipment used by the contractor may not be optimal, or may not be adaptable to conditions that may arise during construction.

1.2.3 Initial Cost of Future Bridges

The initial bid price of a segmental bridge can be reduced by two main factors. First, the structure can be designed to be more efficient. The instrumentation program on US 183 studied the structural response of elements that traditionally have been over-designed because of the complexity and importance of the element. Second, the structure's form and construction method can be made more simple and straightforward, with a minimum number of construction steps or tasks required building the bridge. This topic is highly related to constructibility and has the greatest influence on profit margin for the contractor.

1.2.4 Maintenance Problems

Another purpose for the study was to identify sources of future maintenance problems and recommend ways to solve these problems for future bridges. Consideration of the life cycle cost of bridges is beginning to become commonplace with highway departments. Traditional expensive maintenance items, such as painting and deck replacement, were eliminated with the US 183 segmental box girders. Potential major future maintenance items for this bridge are repair of cracks, especially in regions near post-tensioning anchorages and deviators, and replacement of tendons. The researchers noted the details that performed poorly at service load levels and also noted the details that performed well.

1.3 PROJECT OBJECTIVES

The general objectives of this research project were to:

1.3.1 Identify and Study Major Design Uncertainties

There are many design areas where engineering judgment had to be used when US 183 was designed in lieu of data from previous field or laboratory measurements. The researchers interviewed both design engineers and construction engineers to determine the major uncertainties on this project. These uncertainties included the accuracy of prestress friction loss calculations, temperature gradient effects on the box girders, transverse diffusion of post-tensioning forces into the cross section, construction stress distribution in partially completed box girders, and the actual behavior of complex D-zones including the usefulness of strut-and-tie modeling.

1.3.2 Instrument and Test Structural Elements

Many of the structural elements designed using questionable or possibly over-conservative design assumptions were instrumented. Also, many instruments were placed to record the structure's response to general load cases, in locations where the behavior was thought to be well known, to look for anomalies in both the structure's behavior and the performance of the instrumentation systems. Monitoring of instrumented segments generally began at the casting yard, continued throughout construction and was continued for about a year thereafter to record the response to thermal loads, live loads, and long-term deformations of the structure.

1.3.3 Interpret Measurements

Measurements were made of tendon forces, concrete surface and internal strains, reinforcing bar strains, structural steel pipe strains, deflections, and temperatures. After data were reduced for a given load case, the measured structural behavior could be compared to that predicted by normal design techniques used by the industry. This comparison gave an indication of the efficiency of the design, whether conservative or unconservative, and provided the actual measured response in regions that showed signs of distress, such as major cracking.

1.3.4 Make Recommendations to TxDOT and FHWA

Once the measurements had been interpreted and analysis completed, recommendations were to be made to TxDOT and FHWA engineers, the sponsors of the research. Specific recommendations were also to be made for modifications to current design codes. The *AASHTO Guide Specification for the Design and Construction of Segmental Concrete Bridges* [8] (Figure 1.6) and the *AASHTO LRFD Bridge Design Specifications* [9] are the primary codes available to guide designers in the USA. Much of the research for the Segmental Guide Specification was performed at The University of Texas at Austin. Recommendations for modifications of these two documents are given in this document.



Figure 1.6 The AASHTO Segmental Guide Specification [8]

1.4 STRUCTURAL ELEMENTS UNDER STUDY

The US 183 segmental viaduct consists of about 10km of precast concrete superstructure. The US 183 mainlanes are provided by two parallel bridges carrying three traffic lanes and one full shoulder each (see Figure 1.7). Access ramps are provided at Lamar Boulevard and IH 35 using a smaller box girder designed for one lane of traffic plus a shoulder (see Figure 1.8). The transitions from the mainlane cross section to the ramp cross section were made using a three-cell cast-in-place girder, shown in Figure 1.9, originally designed to be precast and constructed as two single-cell boxes joined by cast-in-place top and bottom slabs.

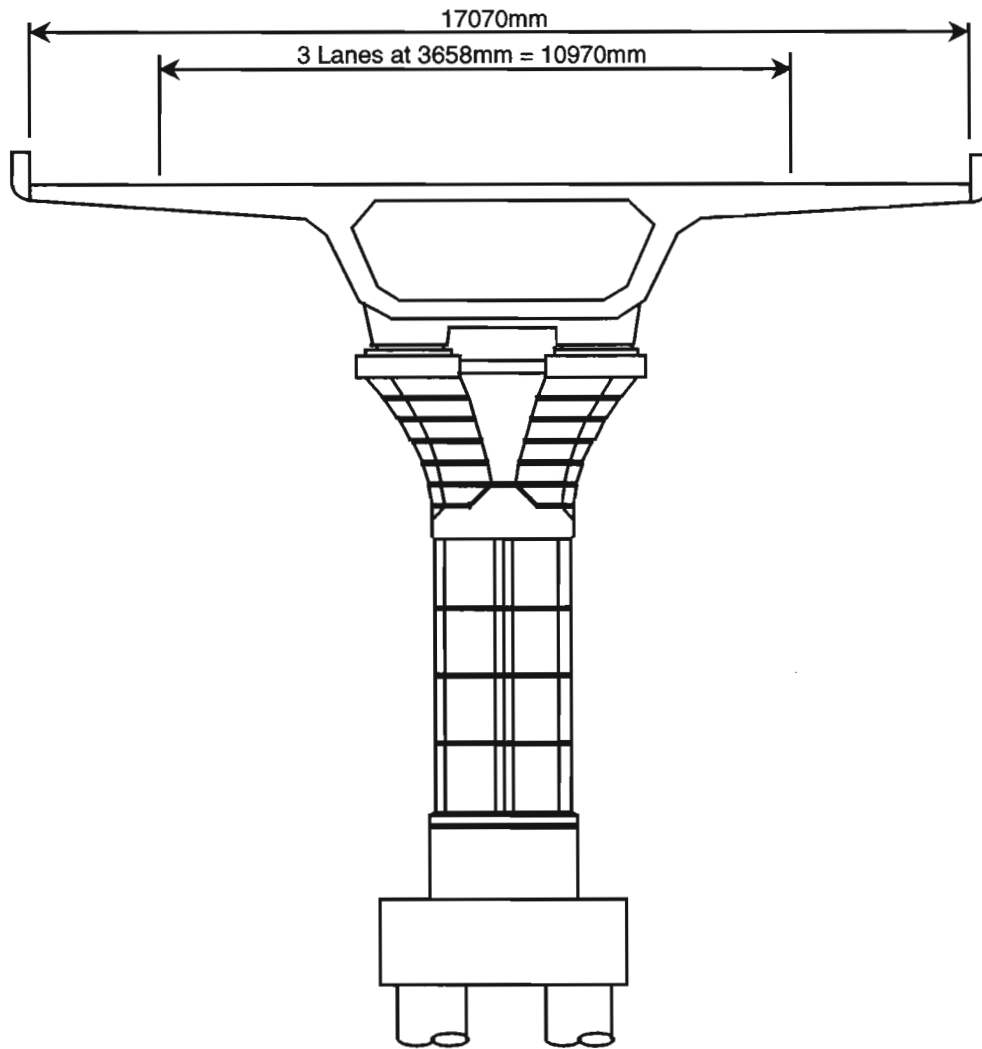


Figure 1.7 Mainlane superstructure section

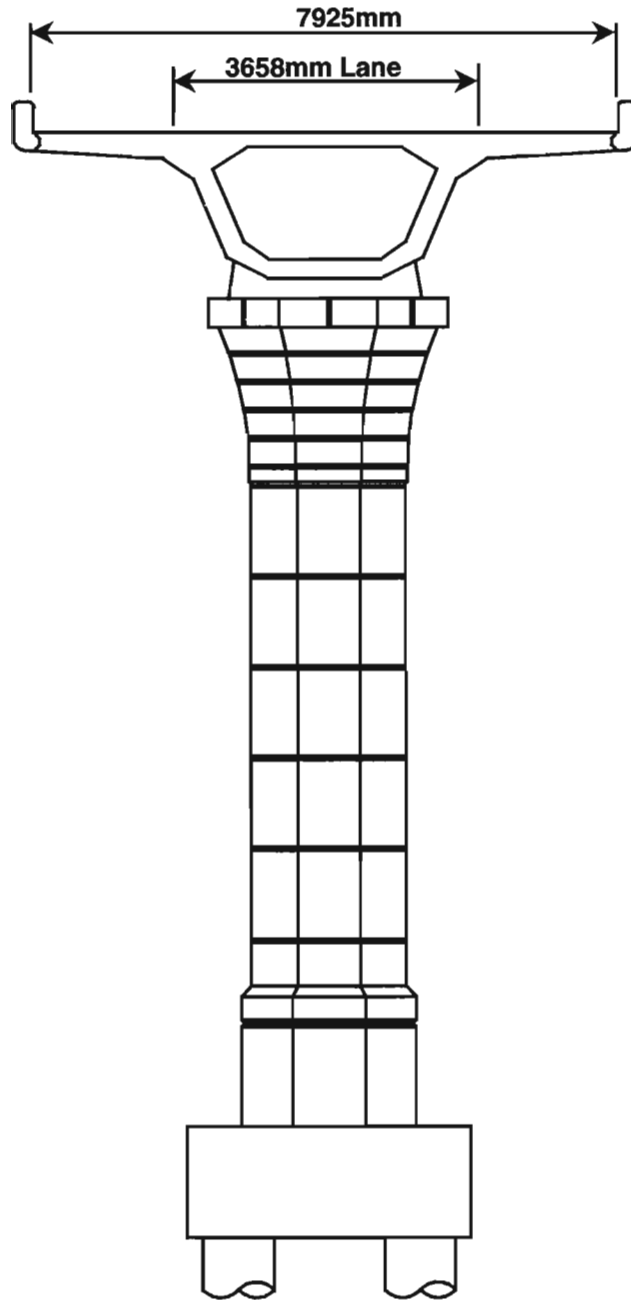
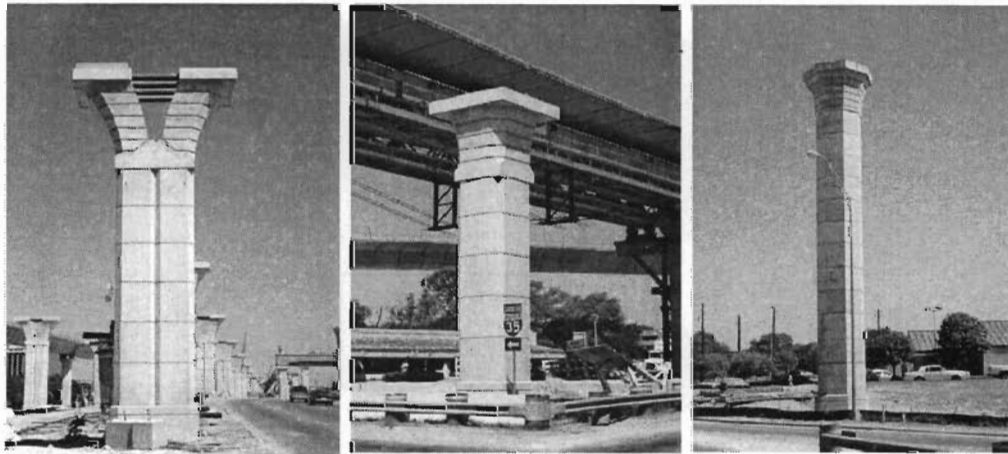


Figure 1.8 Ramp superstructure section



Figure 1.9 *Cast-in-place transition spans*

The US 183 segmental viaduct project was originally designed with three types of segmentally constructed piers (see Figure 1.10). However, the contractor opted to cast two of the pier types in place. One cast-in-place Y-shaped mainlane pier and one segmentally constructed large ramp pier were instrumented, and the small ramp piers were not selected for study.



(a) Mainlane Y-Pier

(b) Small Ramp Pier

(c) Large Ramp Pier

Figure 1.10 *Pier types*

The contractor's decision to cast most of the piers in place rather than use precast segmental construction was made due to several factors. First, the vast majority of the piers were relatively short (below 10 meters in height) and easy to reach with only small mobile cranes. Second, access to the piers for construction vehicles were relatively simple, with most of the mainlane piers located in the median of the existing frontage roads where ground conditions were excellent. Third, space was limited at the precasting and storage facility constructed for the project. The decision was made to use the large amount of land available under the bridge right-of-way as the construction preparation area for the cast-in-place piers. This decision allowed pier construction to begin as soon as the forms were constructed and shipped.

All concrete segments were cast at a precasting facility in southeast Austin that was constructed solely for the US 183 segmental project. The precasting yard, shown in Figure 1.11, was constructed in an inactive shallow quarry. The yard had as many as twelve casting machines in operation, serviced by four overhead cranes and one mobile crane (see Figure 1.12). Every pair of casting machines was surveyed from survey houses located along the central axis of the casting yard. Segments were taken to storage from the casting machines by a straddle crane. With no provision to double stack segments, the storage yard filled to near capacity at one point in time. As additional erection trusses came on line, the storage yard emptied and the casting machines were progressively staged out of service.

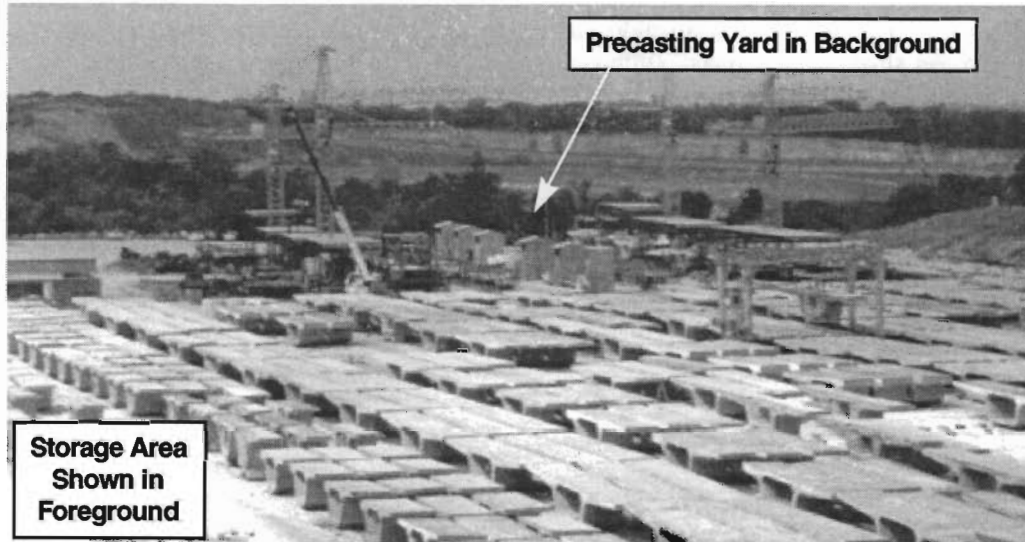


Figure 1.11 Project precasting plant

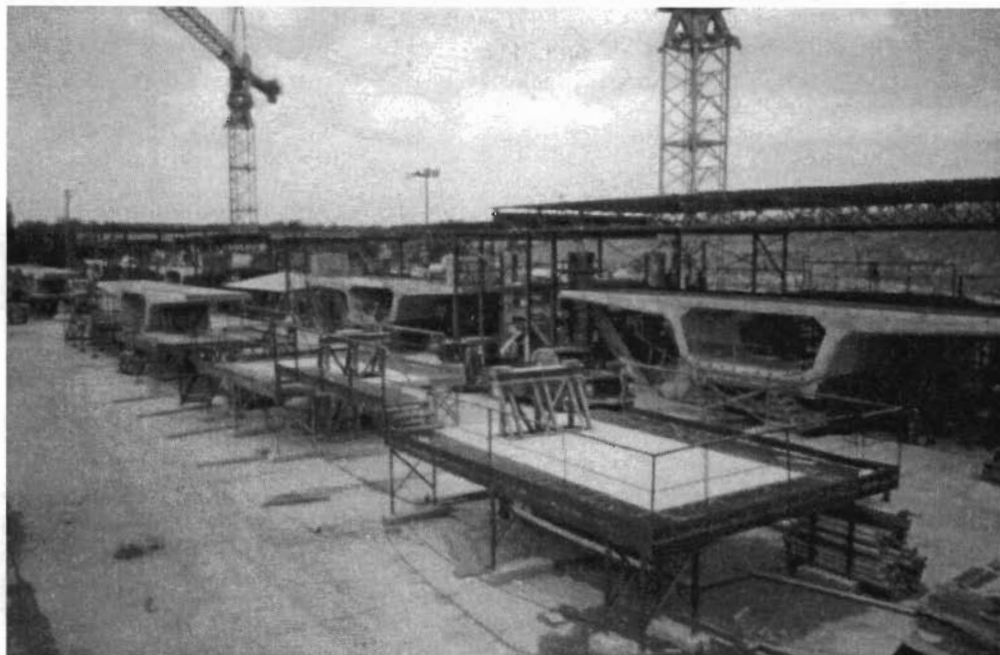


Figure 1.12 Casting machines

The casting yard quickly became a model of efficiency, with a segment produced each day from every casting machine, except from the heavy end diaphragm casting machines. Out of the total 3200 segments cast, only about 0.5% were rejected, usually for large voids in congested webs or deviator blocks. Repetition, excellent

construction engineering and quality assurance personnel, including the on-site TxDOT inspectors, and experienced construction workers resulted in very high quality segments. Project success at the precast yard was important. Sixty percent of the project construction cost occurred at the precasting yard.

1.4.1 Mainlane Pier

Bridge pier design in most state departments of transportation has become highly standardized. Design for piers that have worked well in the past are often used, and many states minimize creativity in this area of bridge design as a means of minimizing costs. The piers are conservatively designed, and minimum reinforcement ratios tend to govern. Structural problems with these standard piers do not often arise. Modern research on these standard piers has focused on modifying construction methods, such as precasting, and improving the appearance of multi-column and single-column piers. Billington predicts that both innovative and aesthetic modifications to existing standard Texas piers could be made with only a marginal increase in cost, at \$525/m³, over the cost of the standard circular column piers with rectangular or inverted T bent cap shown in Table 1.2 [1].

The standard highway piers used to support I-girder superstructures were rejected for use at US 183 for aesthetic reasons alone. The US 183 mainlane bridge piers are not, by any means, typical bridge piers. They are functional and also innovative, with great emphasis placed on aesthetics, as shown in Figure 1.13. They provide an opportunity to investigate the behavior of a nonstandard bridge substructure.



Figure 1.13 Mainlane pier

The piers for the mainlane portion of the US183 project are Y-shaped reinforced concrete piers with structural steel tension ties across the top of the "Y," as shown in Figure 1.14. The column shaft of the piers is of variable height H. The capital has a constant height of 3200mm. Each end of each pipe is anchored by steel plates at two locations, as shown in Figure 1.15. Through their form, these piers provide a visual representation of their structural behavior. Most observers will intuitively realize that as vertical load is placed on the two sets of bearings located beneath the box girder webs, the "Y" will tend to spread apart, placing the steel pipe ties across the "Y" into tension. Although this behavior is intuitive, detailing and dimensioning involved in the pier design may be quite difficult, especially since this pier is a composite structure of steel and reinforced concrete.

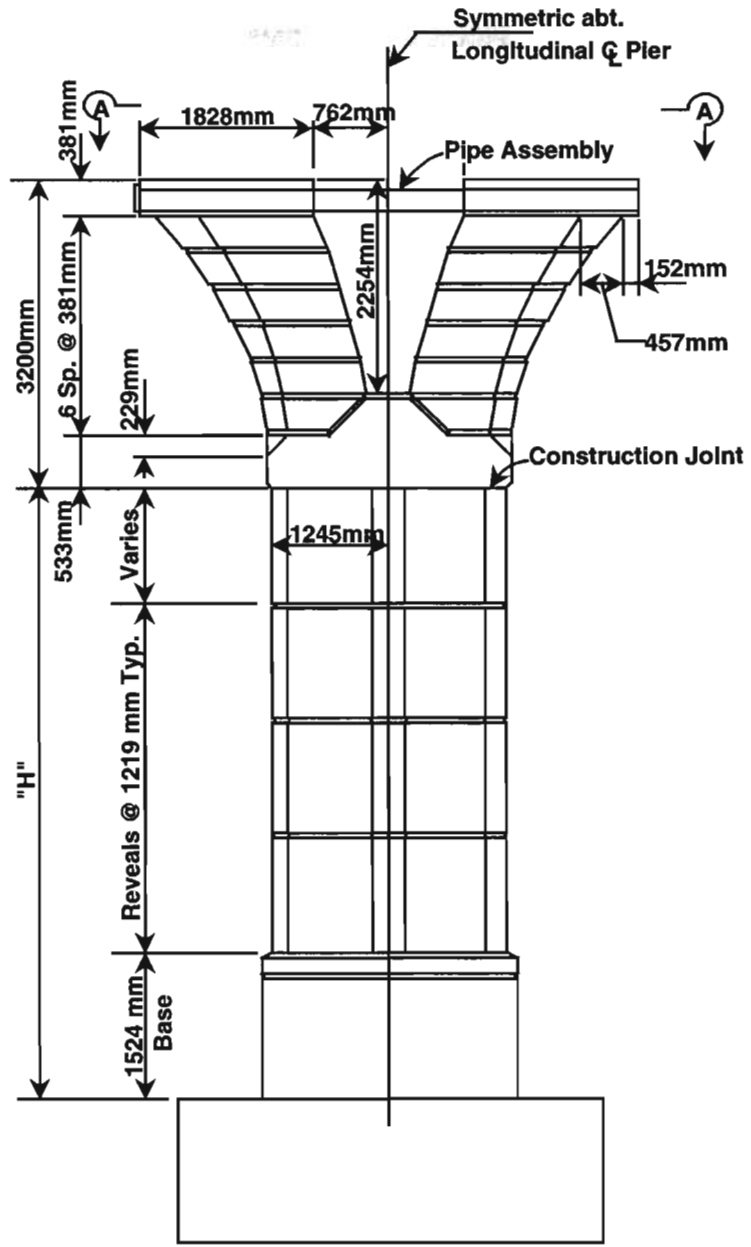
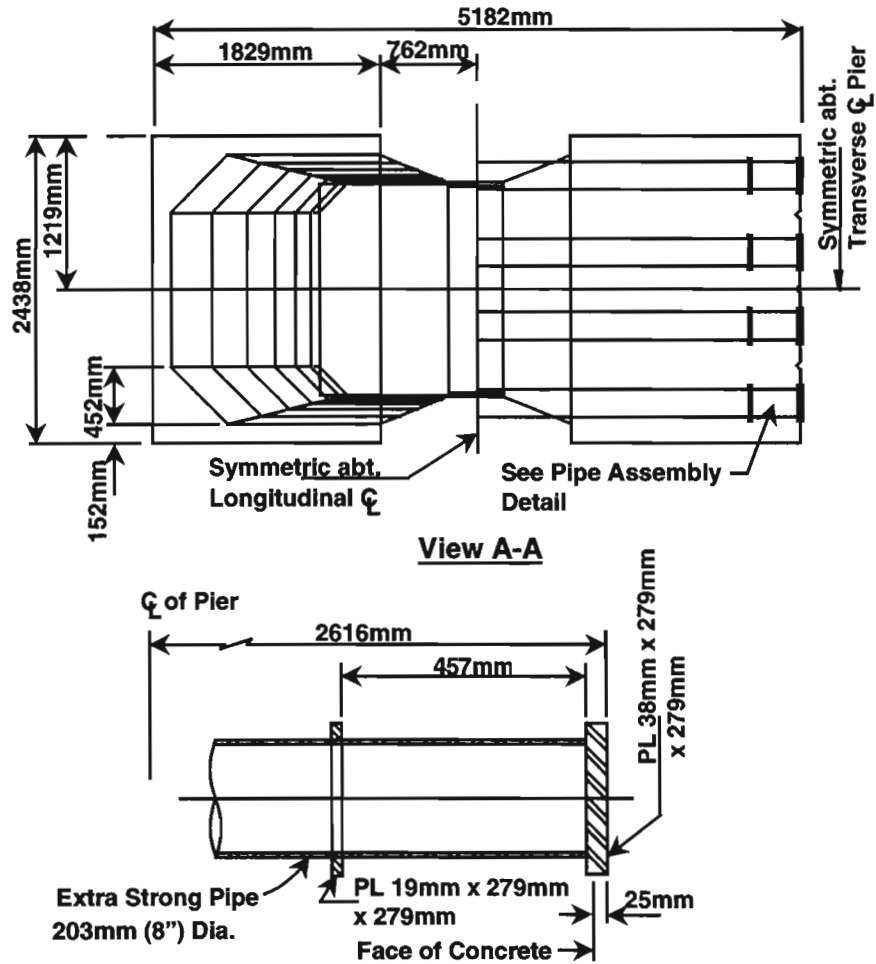


Figure 1.14 Mainlane pier elevation



Pipe Assembly Detail

Figure 1.15 Mainlane pier details

Mainlane pier D6 was selected for instrumentation, and its location is shown on the map in Figure 1.1. Pier construction began at the north end of the project and moved southward, with piers for both C and D mainlanes constructed simultaneously. Selection of pier D6 allowed research to begin as early during construction as possible. Access to pier D6 from the laboratory and from the ground was also optimal. The mainlane piers were cast in two pours above the footing for an overall height of 7700mm. The reinforcing bar cage for the capital was actually tied inside the form, as shown in Figure 1.16. The forms used maintained the appearance, including all chamfers and reveals, originally intended for the pier as a precast post-tensioned structural element.

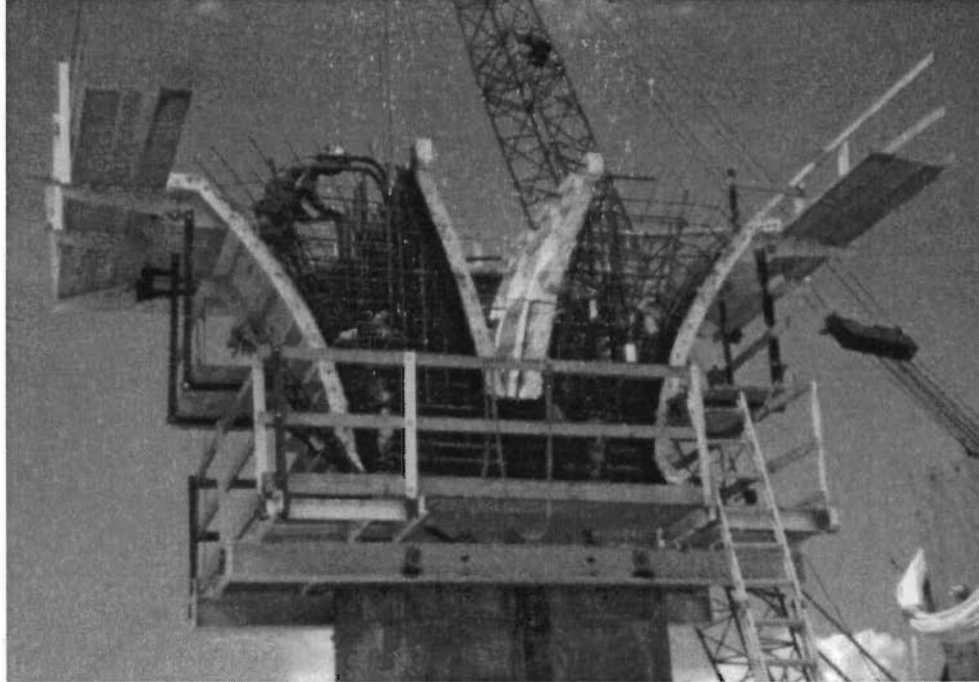


Figure 1.16 Construction of mainlane pier capital

1.4.2 Mainlane Girder

One three-span semicontinuous bridge unit of mainlane precast segmental box girder was selected for instrumentation. Unit D2 (spans D4, D5, and D6) was selected for study. Instrumented pier D6 was located at the joint between spans D5 and D6. This bridge unit was the second mainlane bridge unit constructed on the project, allowing research to begin as early as possible without interfering with the construction of the first couple of spans.

The general shape of the US 183 mainlane girder was based on a design concept by T.Y. Lin International originally intended for the San Antonio Y segmental project. The girder was conceived as a spine beam with narrow soffit, shallow structural depth, short spans, and very wide wings. The girder actually used at the San Antonio Y maintained the spine beam concept, but had slightly better structural proportions for transverse bending of the top flange. The box girder used for the US 183 mainlane, shown in Figure 1.17, was similar to the San Antonio girder in transverse proportions, but was 300mm deeper in structural depth to accommodate longer spans (39m for US 183 versus 33m at the San Antonio Y). One major difference between the US 183 mainlane girders and the San Antonio Y mainlane girders is the lack of fully continuous spans at U. S 183.



Figure 1.17 Mainlane girder

The economical method of erecting precast segmental girders up to about 46m in length is by the span-by-span method. This method uses a pair of erection trusses (see Figure 1.18) to construct the bridge one span at a time. All segments are loaded onto the trusses and stressed together generally from one end of the girder. The girder, with ungrouted tendons at this point, must support its own dead load plus the enormous live load of the construction equipment and segments passing over to construct the next span. The flexural stiffness benefits of a fully continuous structure are not realized until after the most critical loads the bridge may ever see have already been placed on the structure. Furthermore, construction of a continuous structure requires that continuity tendon post-tensioning operations, bearing placement, and closure pours occur directly behind the advanced erection trusses, complicating and possibly slowing down construction of the span on the trusses, as seen at the San Antonio Y. From a design standpoint, a continuous box girder must be designed for a thermal gradient load case that creates bending moments over interior piers of a multispan bridge unit opposite to those induced by live-load forces. This requires additional continuity post-tensioning over the interior piers of a continuous bridge unit. For these reasons, TxDOT engineers designed the mainlane structure and most of the ramp spans as simple spans. A two- or three-span partially continuous bridge unit was created, after construction of the girders had been completed, by casting a deck slab between the box girder top flanges. This "poor-boy" continuity, as it is known to TxDOT, provides an inexpensive and smooth riding surface at locations other than the finger joints (see the "poor-boy" cast-in-place deck joint under construction in Figure 1.19).



Figure 1.18 Construction of a mainlane girder

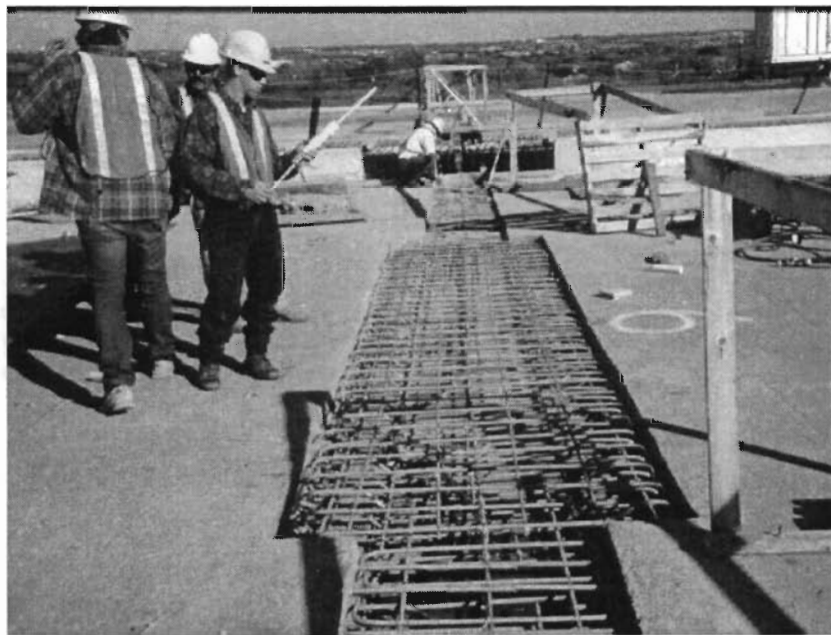
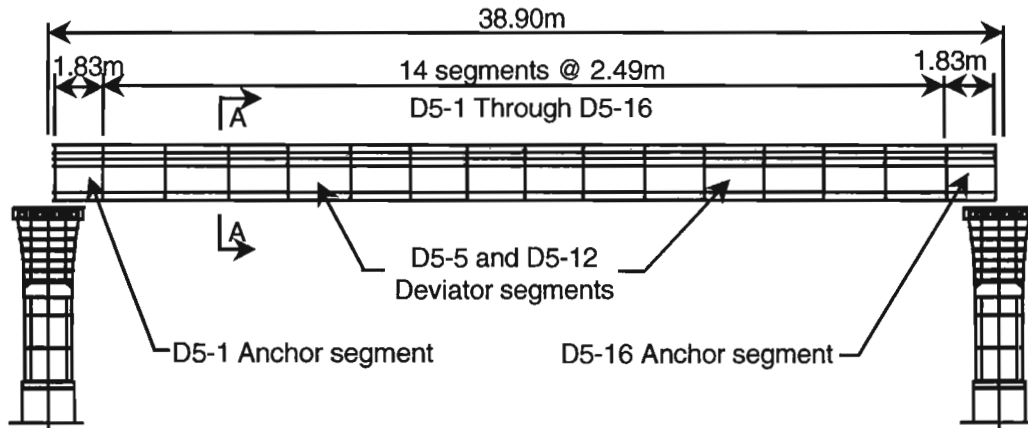


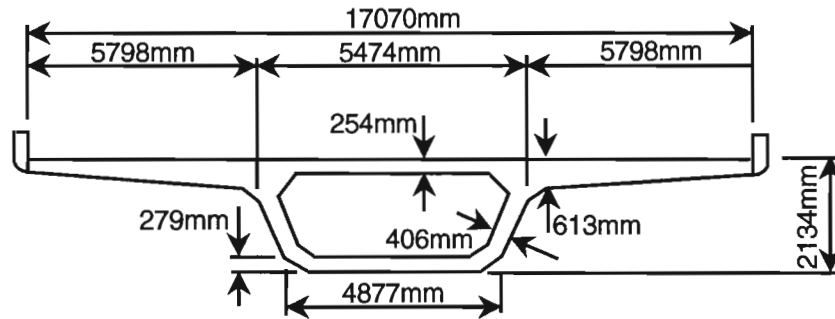
Figure 1.19 Construction of a cast-in-place deck joint

The simple-span construction was a great success, with the contractor constructing one span every two days from each set of erection trusses. Construction could have proceeded even faster except for the requirement that all heavy lifting be done at night, when the frontage roads beneath could be narrowed to a single lane.

Mainlane spans generally consist of sixteen or seventeen segments. Span D5 is 38.9m long with two heavy end diaphragm or anchor segments, two deviator segments, and twelve typical segments, as shown in Figure 1.20.



Elevation



Section A-A

Figure 1.20 Cross section and elevation—Span D5

Six deviated external and 8 straight bottom slab internal 19-15mm diameter strand tendons and four smaller straight wing tendons were used to post-tension the span. Transverse prestressing of the top flange was mostly completed at the casting yard. Most of the casting machines had bulkheads for pretensioning the top slab. Transverse post-tensioning was used only in the anchor segments.

All casting machines used the short-line method of casting, with a fixed bulkhead rear form and the previous day's segment mounted on adjustable hydraulic jacks as the front form. The exterior web and wing form could be lowered slightly and the core form articulated inward to release a newly cast segment from the form. The soffit form traveled with the segment as it was rolled on tracks out of the form to the match casting position, or from the match casting position to the finishing rack. The surveying house was located at the front of the form to measure the segment as-cast from the previous day, and then later to adjust it correctly in the match casting position. Reinforcing bar cages were prefabricated to the rear of the form in a jig shaped like the exterior form. Photographs of the primary features of the casting machines are shown in Figures 1.21, 1.22, and 1.23.

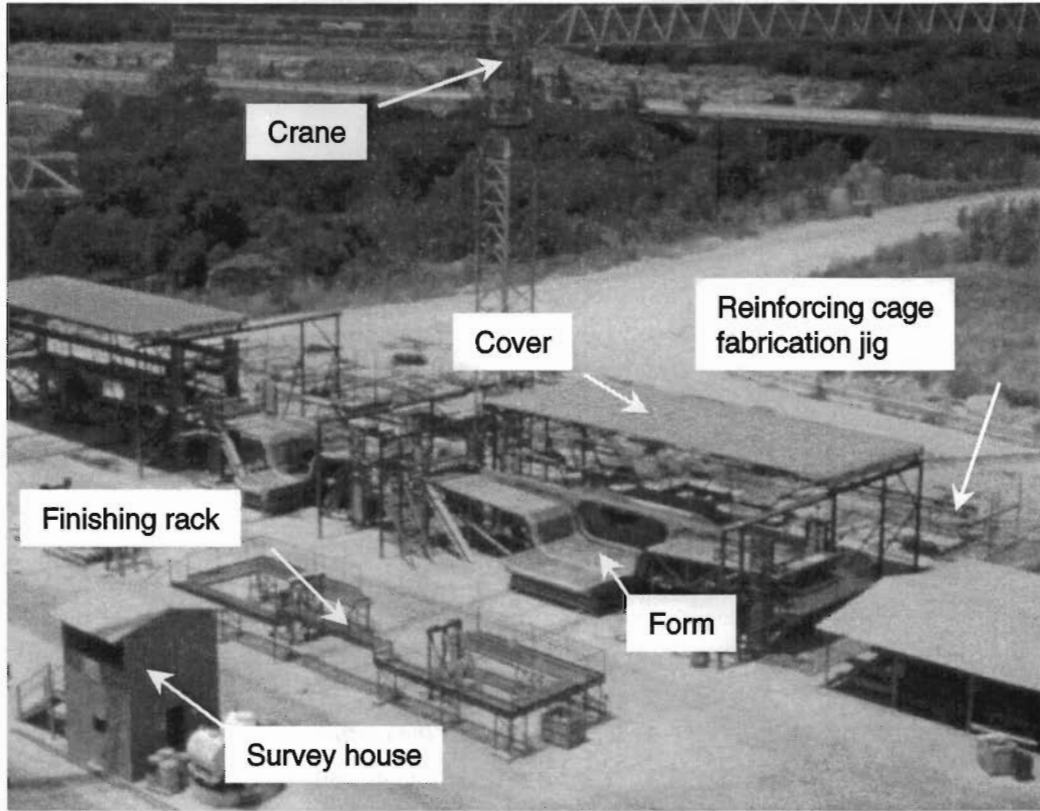


Figure 1.21 Casting machine

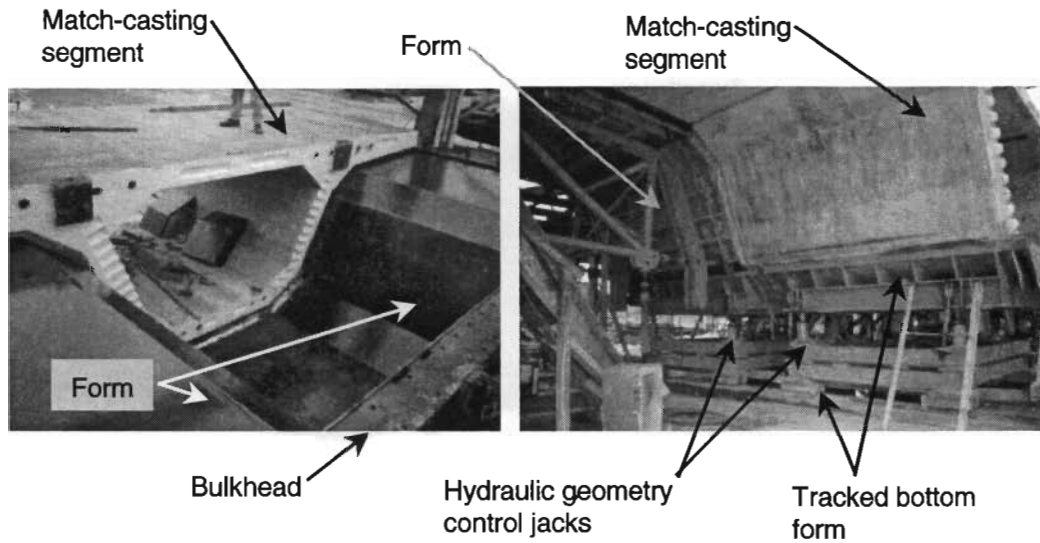


Figure 1.22 Casting machine details

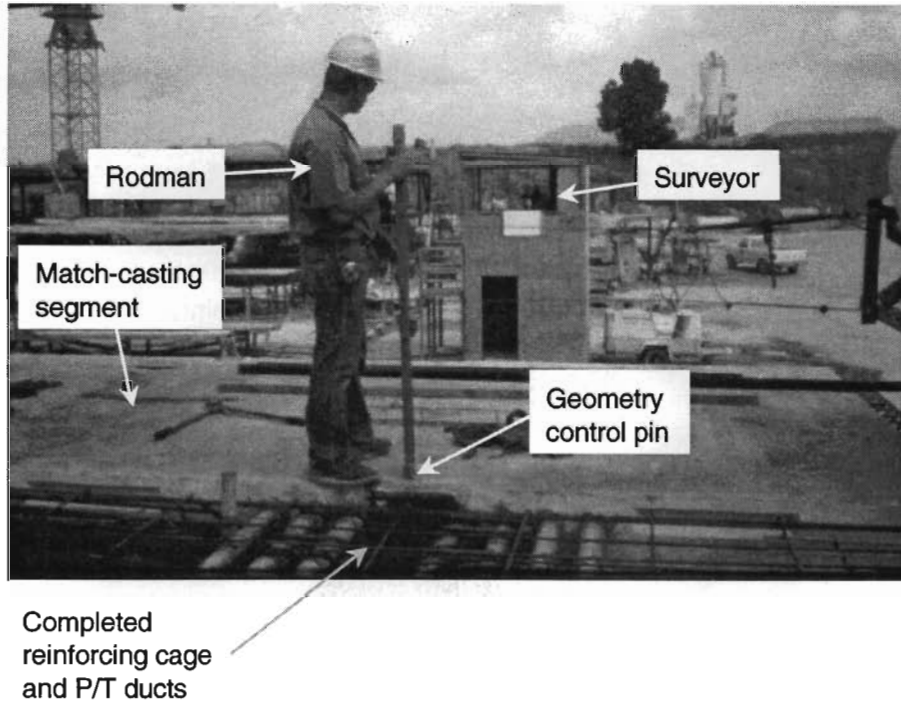


Figure 1.23 Geometry control of the casting machine

Segments were hauled from storage to the site using lowboy trailers with hydraulically adjustable axles to help distribute the heavy load of the segment (490kN for a typical mainlane segment to 620kN for an anchor segment). Segments were unloaded with a straddle crane and stored beyond the abutment of the newly constructed portion of the bridge on the approach roadway (see Figure 1.24).

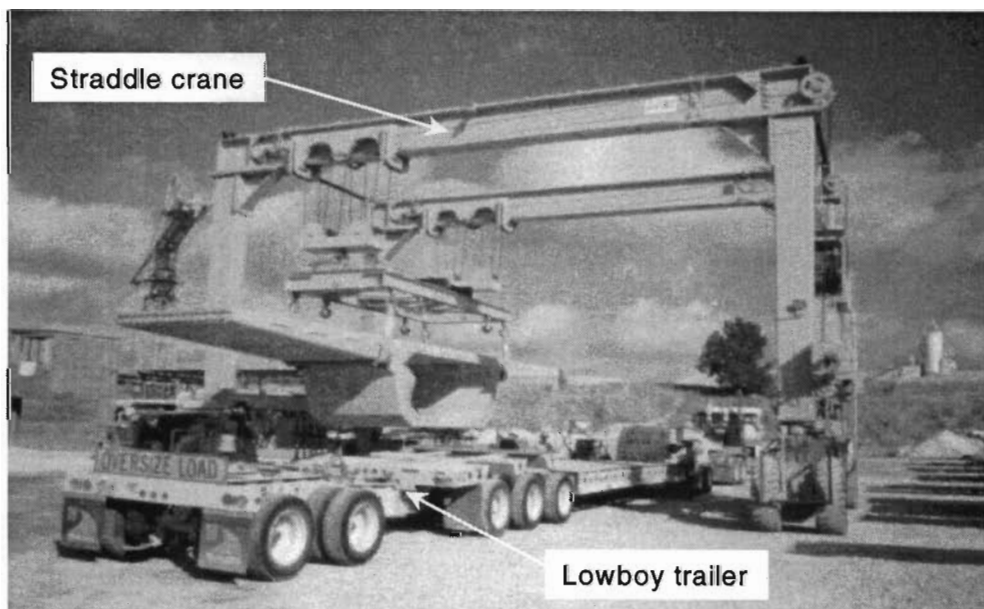


Figure 1.24 Transporting segments

Once the twin triangular erection trusses were in place, supported by brackets on the piers, segments were lifted onto a heavy-duty flatbed truck and hauled to the end of the previously constructed span. The "Texas lifter," a different type of straddle crane, would lift the segments off the flatbed truck and move them forward over the trusses while turning them 90°. The segments were lowered onto three sets of roller jacks, adjustable in all directions, and rolled into approximate position (Figure 1.25).

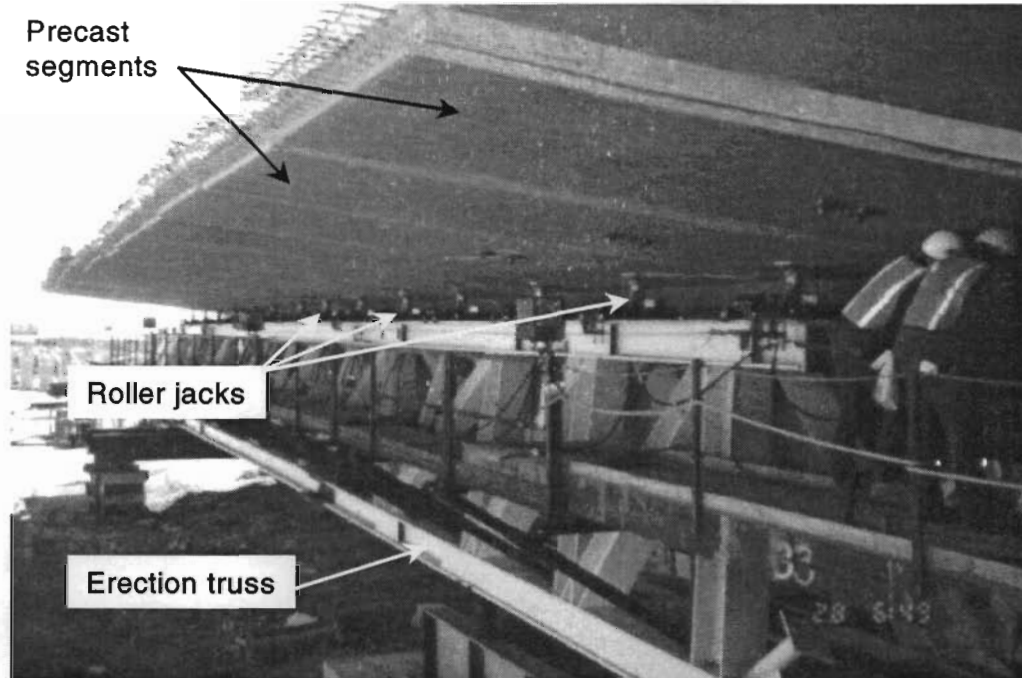
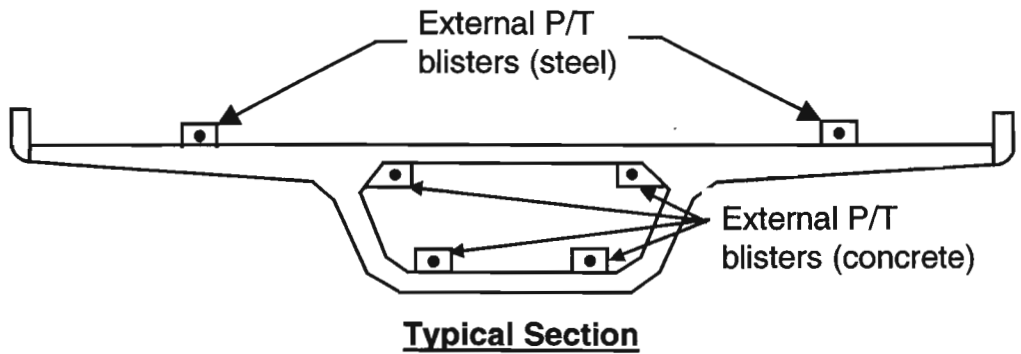
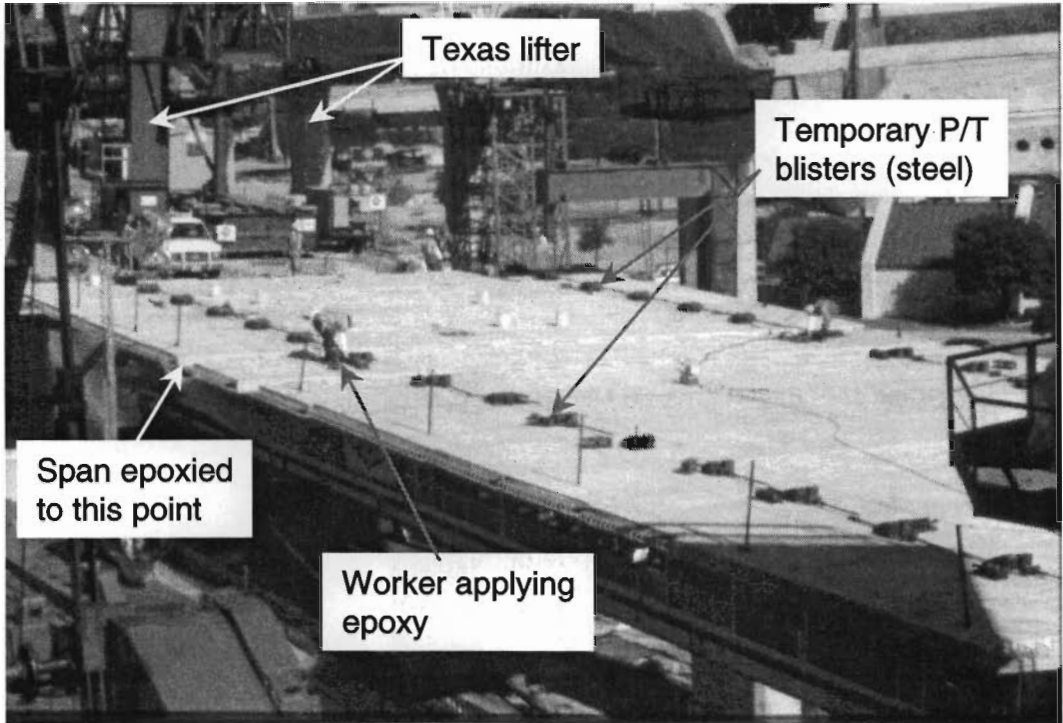


Figure 1.25 Locating segments on the erection trusses

The first anchor segment and adjacent typical segment were epoxied together, with six post-tensioning threadbars anchored in external blisters providing the temporary clamping force required for a good fit during epoxy curing. These two segments were then surveyed and adjusted into their final position, allowing for bearing compression. Then, epoxying proceeded for the remaining segments. Figure 1.26 shows epoxying in progress from the deck, with the external temporary post-tensioning blisters on the wings in view. These temporary post-tensioning anchorage blisters on the deck (2 per segment) were made of steel and could be reused. Four concrete temporary post-tensioning blisters were cast into each segment and were located near the juncture of the girder flanges and webs in the core of the box girder. The location of the six external post-tensioning blisters in each typical segment is shown at the bottom of Figure 1.26.



Typical Section

Figure 1.26 Epoxying segments

Prefabricated prestressing tendons were pulled from the dead end to the live end of the girder and stressed in pairs with two jacks and two hydraulic pumps (see Figure 1.27). The elastomeric bearing top surface to bearing plinth gap was grouted, the jacks supporting the segments on the truss were released, and the erection trusses were prepared for launching. Trusses were either self launching, requiring a launching nose on each truss, or were launched using a ground-based crane. Segments were also placed on the trusses using a ground-based crane when required, since the Texas lifter could only service one set of trusses at a time.

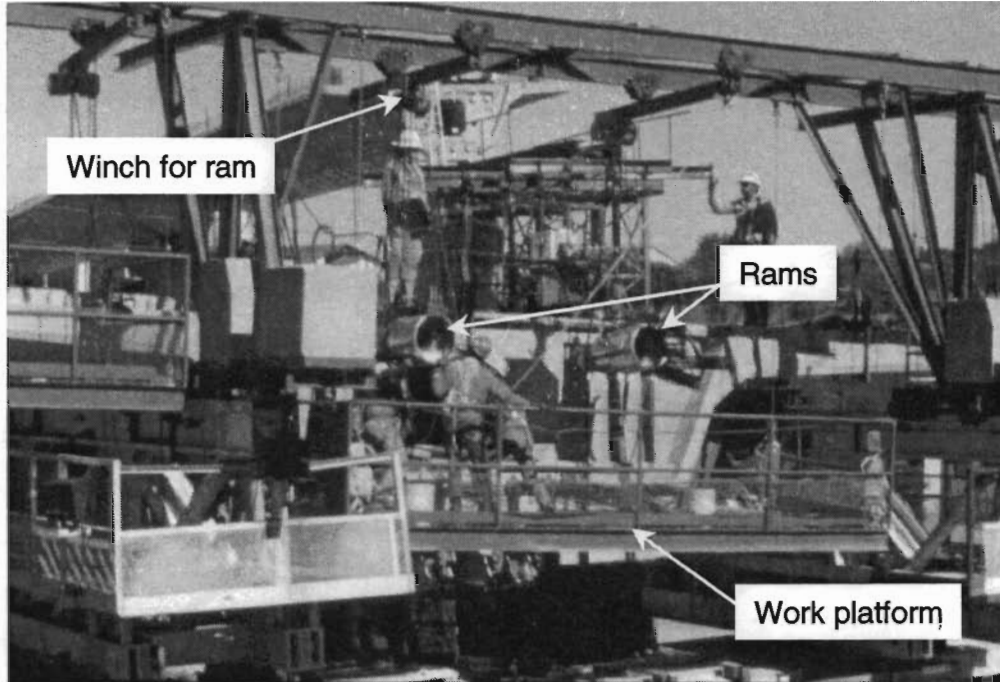


Figure 1.27 Stressing a pair of mainlane girder external tendons

1.4.3 Ramp P Girder

The alignment of the flyover Ramp P that connected northbound IH 35 with northbound US 183, shown in Figure 1.28, required that the structure pass over the mainlanes and the frontage roads of both of those highways. The congestion in the area beneath the ramp reduced the space available for supporting substructure, requiring longer spans for the ramp than were typical for the rest of the project. The alignment of the ramp also followed a fairly tight radius of 221m. Both of these constrictions made span-by-span construction, used on the mainlane girders and most ramp girders, impractical for the construction of Ramp P. Therefore, balanced cantilever construction was used to build five spans of Ramp P.

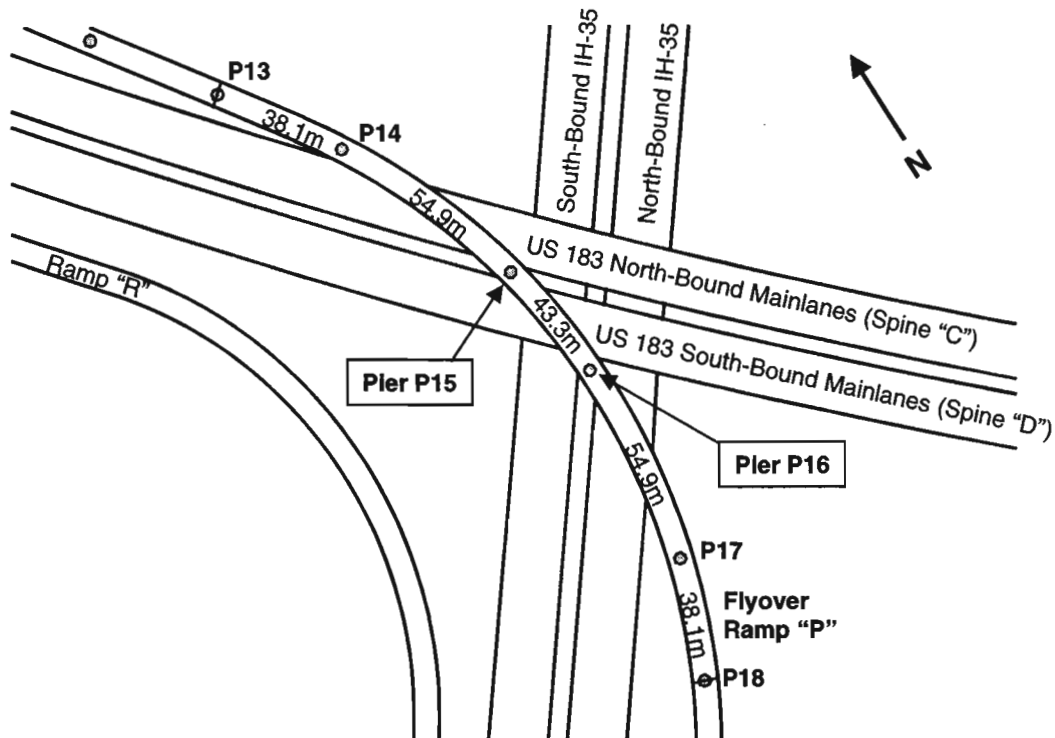
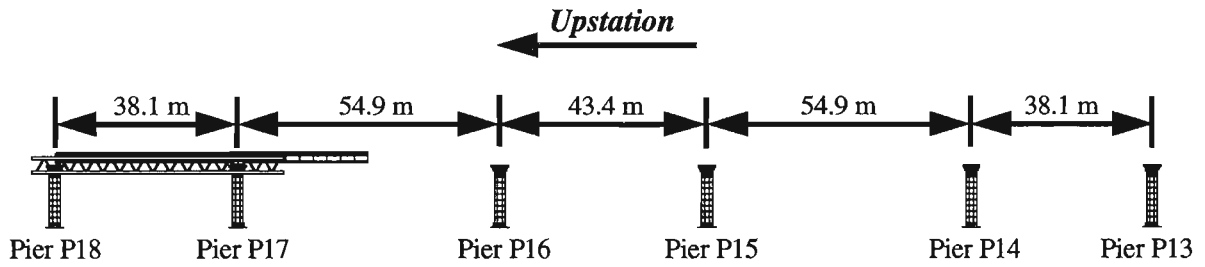


Figure 1.28 Plan of US 183 at IH 35

The balanced cantilever constructed spans of Ramp P were selected for instrumentation for several reasons. One of these was the desire to study the method of construction itself since little data are available on balanced cantilever erection. Also, the box girder shape, true continuity of the five-span bridge unit, and horizontal curvature were entirely different than for the mainlane girder. Ramp P provided additional topics for study beyond those found with the mainlane girder, such as torsional response of the box girder. Measurements for some topics, such as diffusion of post-tensioning forces and thermal gradients, could be compared with those of the mainlane using the different box girder shapes of Ramp P and the mainlane as the variable.

Figure 1.29 shows the span arrangement and construction sequence stages for Ramp P. Clearance of the mainlane and frontage roads beneath Ramp P required unequal span lengths and unique construction staging and post-tensioning sequences. Precast segments were hung in place with ground-based cranes and epoxied to previously erected segments in similar fashion to the mainlane girder. Top flange cantilevering tendons were stressed after each pair of segments had been epoxied in place, one on either end of the cantilever unit to balance moments in the pier (see Figure 1.30).



Phase I: Construction of the P17 cantilever unit and the completion of the upstation endspan.



Phase II: Construction of the P16 cantilever unit.



Phase III: Construction of the P14 cantilever unit. Construction begins on the P15 unit.



Phase IV: Completion of the downstation endspan and the P15 cantilever unit.



Phase V: The central span is completed. The free cantilever wings of the P15 and P16 units are extended by one segment.



Phase VI: Final bearing adjustments are made on P17. The upstation 54.9 m span is completed. The same process is repeated on the downstation half of the bridge.

Phase VII: The last external tendons are placed and stressed. The barriers are cast and a wearing surface is applied to the deck.

Figure 1.29 Construction sequence of Ramp P

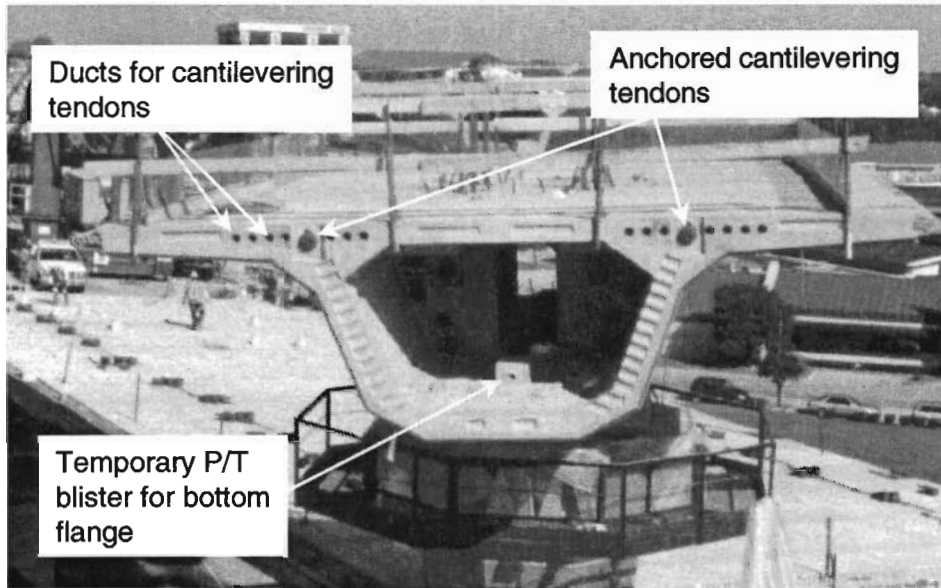


Figure 1.30 End view of balanced cantilever ramp under construction

Closure pours were made between cantilever units to make the girder continuous. A combination of bottom slab internal tendons, external multi-span tendons, and bearing elevation adjustments changed the state of stress in the box girder to that required for a five-span continuous girder subjected to traffic loads. Fixity required between the pier capital and the girder during construction was only maintained at piers P15 and P16 in the final structure. The ramp girder had heavy anchor segments for post-tensioning tendons over each pier. The dimensions of these segments are given in Figure 1.31. Typical segments had varying bottom flange thickness near the pier to increase the moment of inertia of the section for cantilevering moments. Figure 1.32 shows the typical segment dimensions. Instrumentation was concentrated in the half of the 54.9m span closest to pier P16.

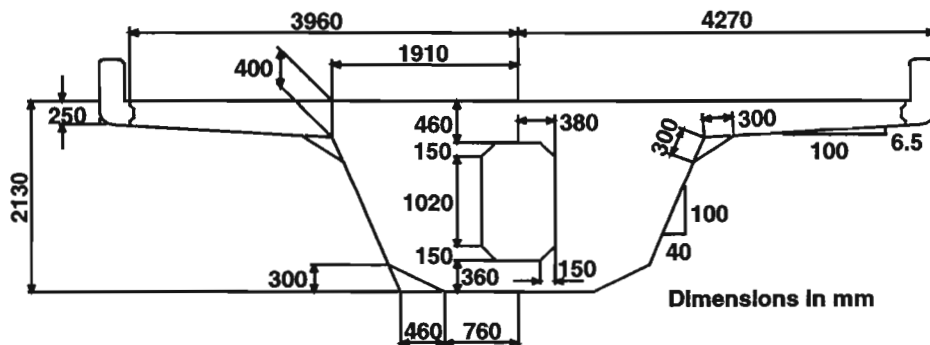


Figure 1.31 Ramp P anchor segment dimensions

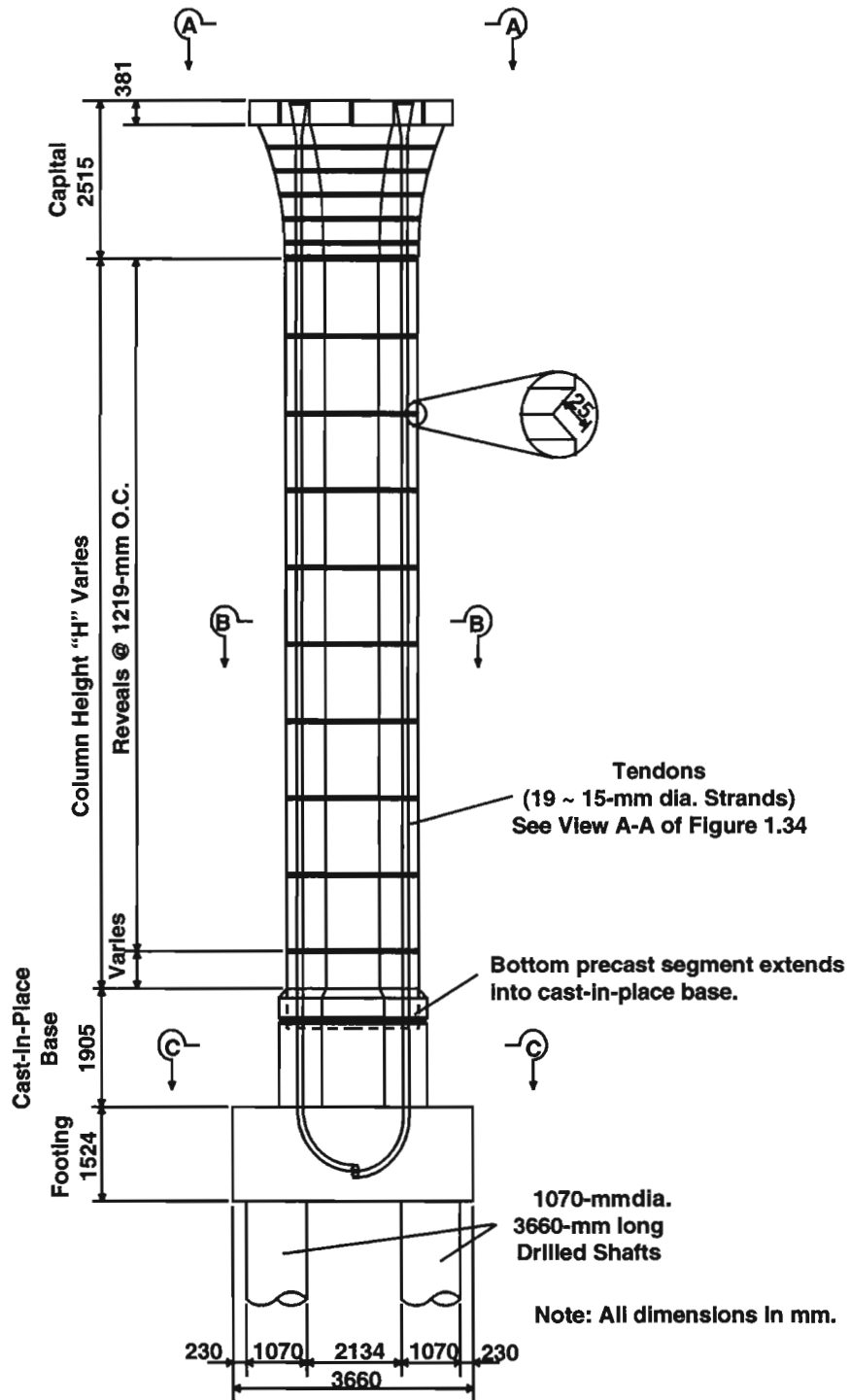
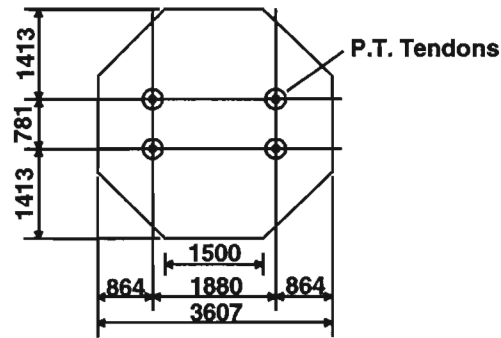
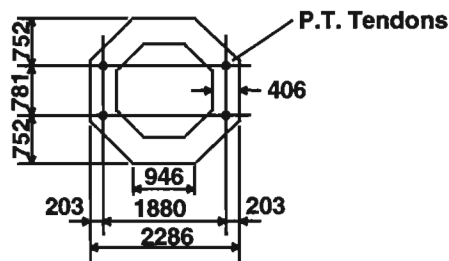


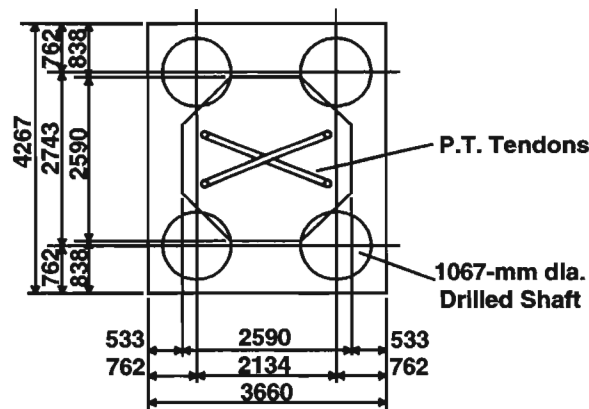
Figure 1.33 Typical large ramp pier: elevation view



VIEW A-A



SECTION B-B



SECTION C-C

Note: All dimensions in mm.

Figure 1.34 Typical sections: large ramp pier

Pier P16 was selected for instrumentation for several reasons. First, the pier had unobstructed exposure to the sun over much of its height until the ramp superstructure was constructed. This configuration allowed many months of thermal measurements to be taken without having shade as a variable. This pier was also adjacent to the longest cantilever on the structure, about 27.4m, so it would also be subjected to the largest unbalanced cantilever moment. Finally the pier was located beneath the instrumented superstructure span, so a common data acquisition system location could be used.

All of the segments for pier P16 were cast at the same precasting yard as for the superstructure segments. After precasting, the segments were placed in storage at the same site until pier erection activities began. The US 183 project plans called for 13 segmentally constructed piers, of which 12 were located along the flyover Ramp P. Large ramp piers along Ramp P ranged in height from 8.2m to 21.6m. The piers were comprised of a total of fifty-seven 2.44m segments, seven 1.22m segments, and thirteen capital segments. Variations in pier height were accommodated with a cast-in-place closure pour between the top of the footing and the first precast segment. This method eliminated the need to cast variable height segments.

Precast pier segments were cast in a specially designed casting bed at the precasting facility. The bed consisted of tandem casting platforms, each with hydraulic jacks to control segment attitude and alignment (see Figure 1.35). Two platforms were utilized to enable constructors to cast one pier segment per day. Figure 1.36 illustrates the typical cycle for casting pier segments.

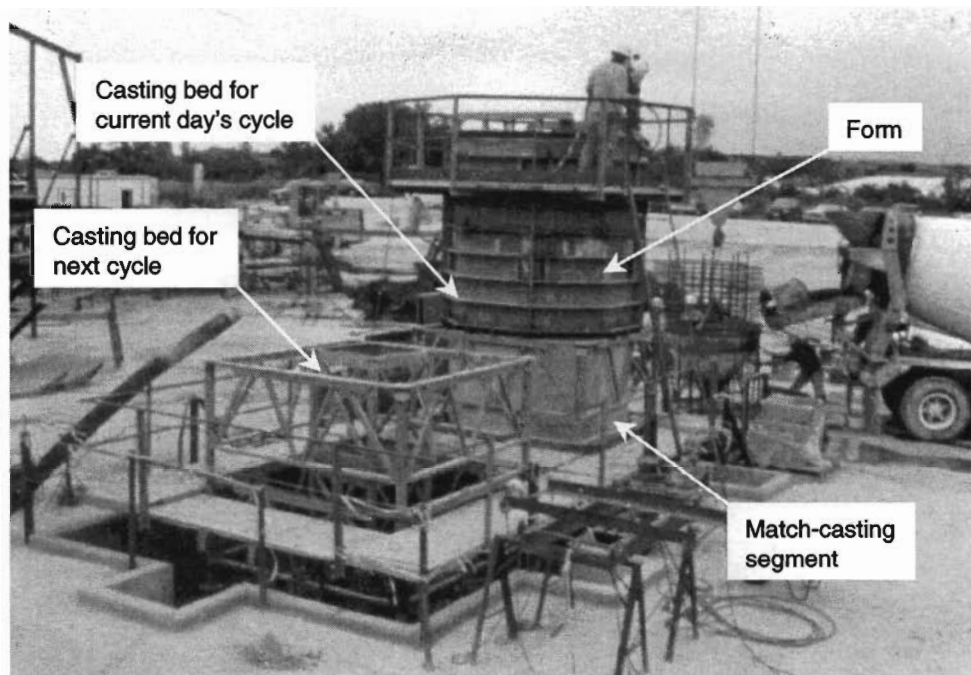


Figure 1.35 Pier segment casting machine

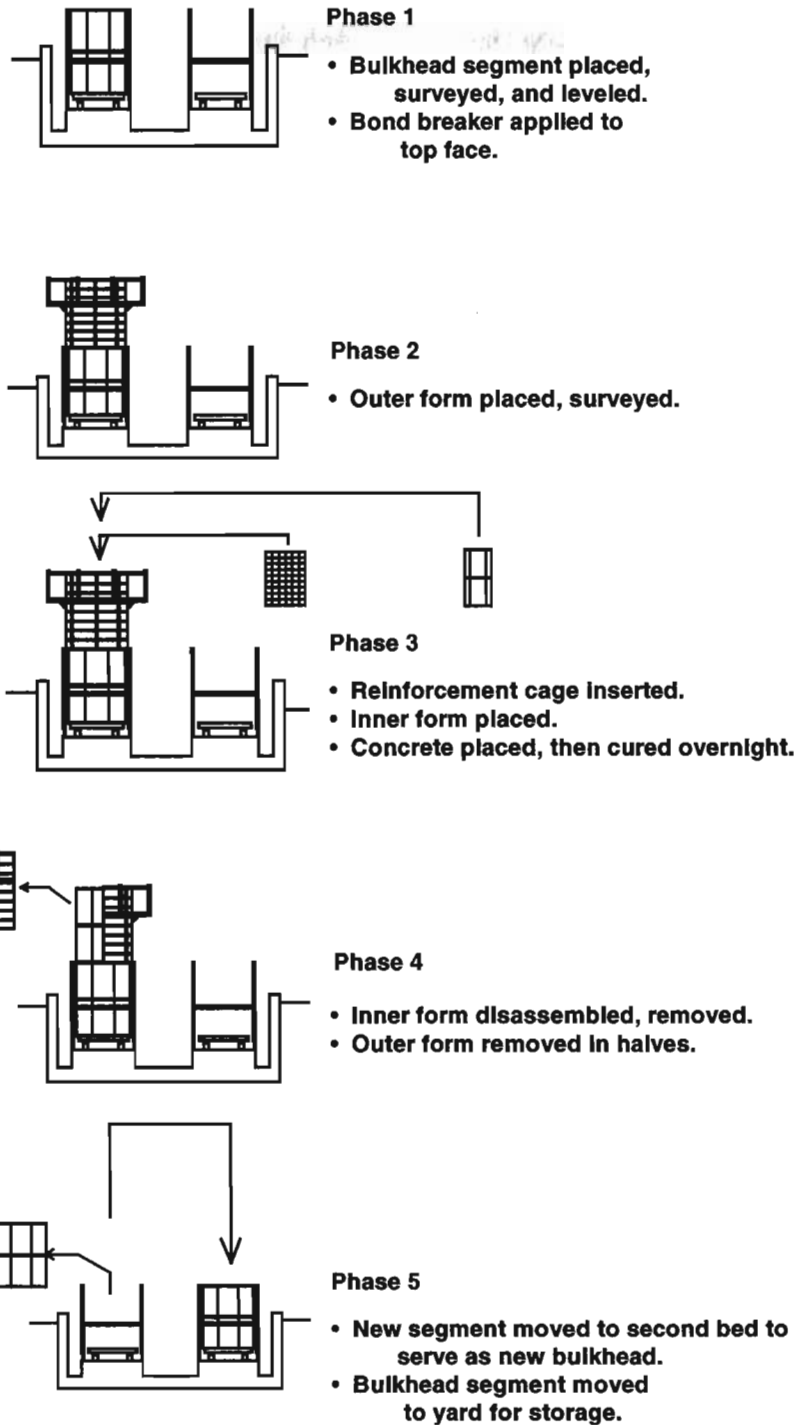


Figure 1.36 Typical segment-per-day casting sequence

The short-line method of match casting was used to cast all pier segments. A typical casting cycle began with the stripping of the forms and placement of the previous day's segment into one of the sides of the tandem casting bed using the straddle crane. This segment served as the match casting segment against which the current day's segment was cast. The match casting segment from the previous day was then hauled to storage with the straddle crane. This technique ensured a perfect fit between segments and reduced systematic alignment errors. The match-casting segment was then checked by surveyors to ensure that it was plumb and aligned correctly.

The cycle continued with the placement of the steel outer form onto the top of the match casting segment (see Figure 1.37). The form was supported by the segment and a steel support cage with a set of jacks that could be leveled independently of those supporting the bulkhead segment (Figures 1.38 and 1.39). The reinforcement cage, that had been assembled in a jig during the previous day's casting operations, was then lowered into the outer form. Steel ductwork for the post-tensioned tendons and temporary post-tensioning bars, PVC drainage piping, and electrical wiring ducts were placed at this point in the cycle. Steel pipe mandrels were inserted into all ducts to ensure good duct alignment between segments. The inner core form was placed and blockouts were installed in the top face for temporary post-tensioning bar anchor plates. Lifting hooks were also installed so that the segment could be carried by the yard's straddle crane. Shear keys were formed into the top segment face with small, hand-held key forms inserted into the fresh concrete. The form was made plumb with the match casting segment by the surveyors, then concrete was cast.



Figure 1.37 Placement of outer pier segment form

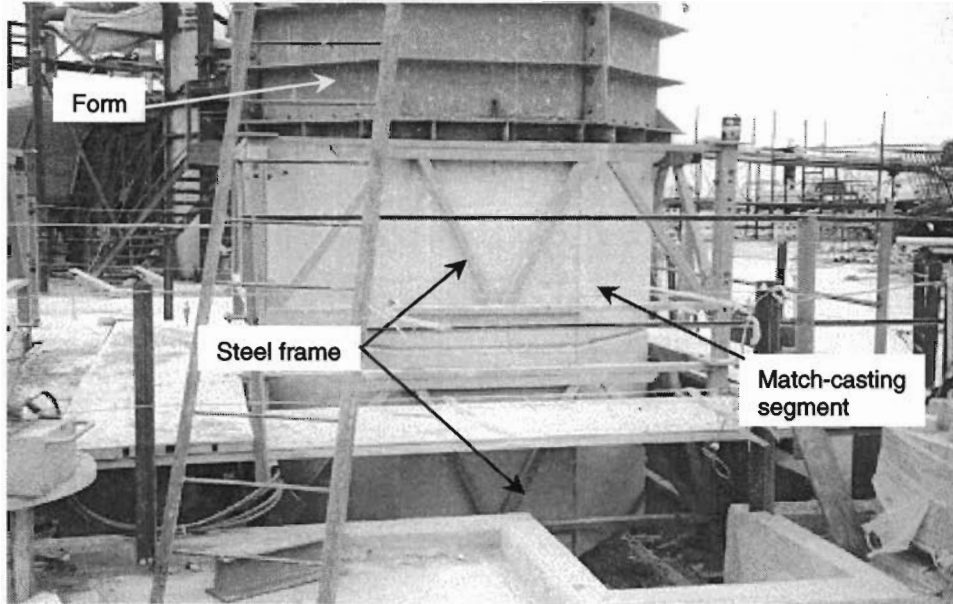


Figure 1.38 Casting bed with steel support frame for formwork

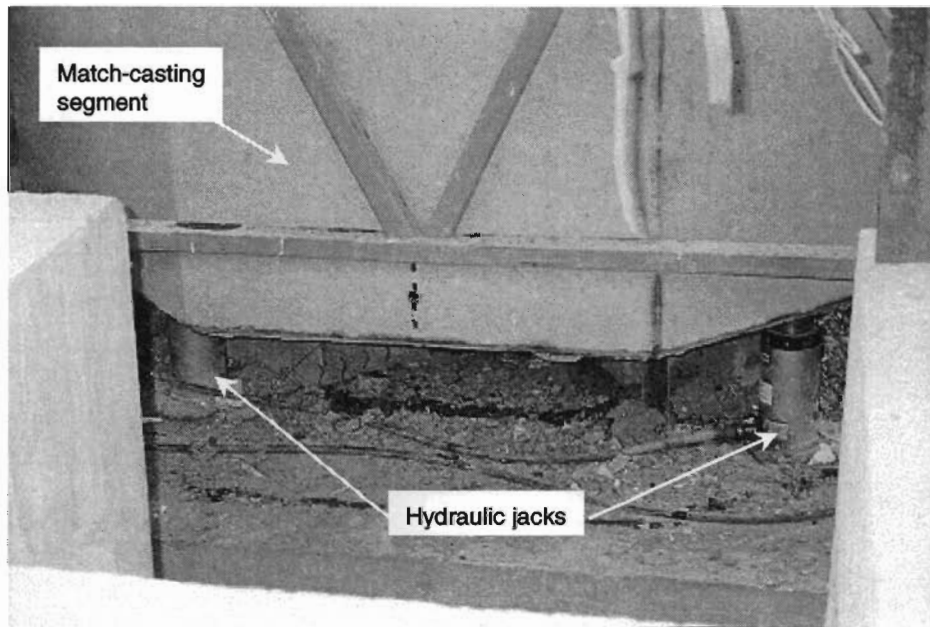


Figure 1.39 Hydraulic jacks used to align the bulkhead pier segment

The segmental piers on the US 183 project were designed to be post-tensioned from the top of the capital segment. For this reason the post-tensioning ducts were designed with a U-shaped bend at the base of the pier. Figure 1.40 shows this duct configuration at the pier's foundation. After completion of the cast-in-place foundation, an adjustable steel frame was installed on top of the footing to support the first segment, PC16-1, on pier P16 (see Figure 1.41).

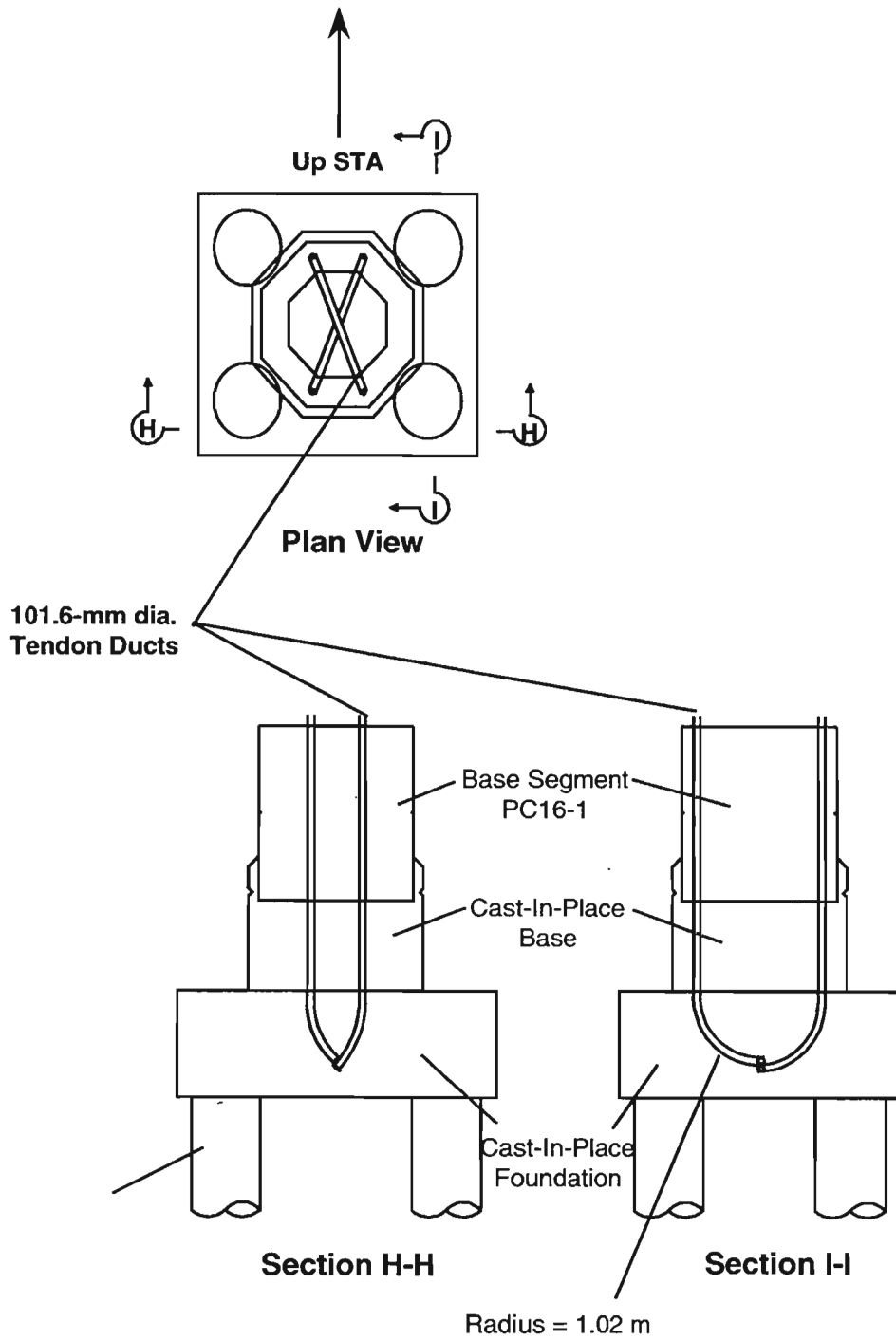


Figure 1.40 U-shaped tendon ducts located in pier foundation

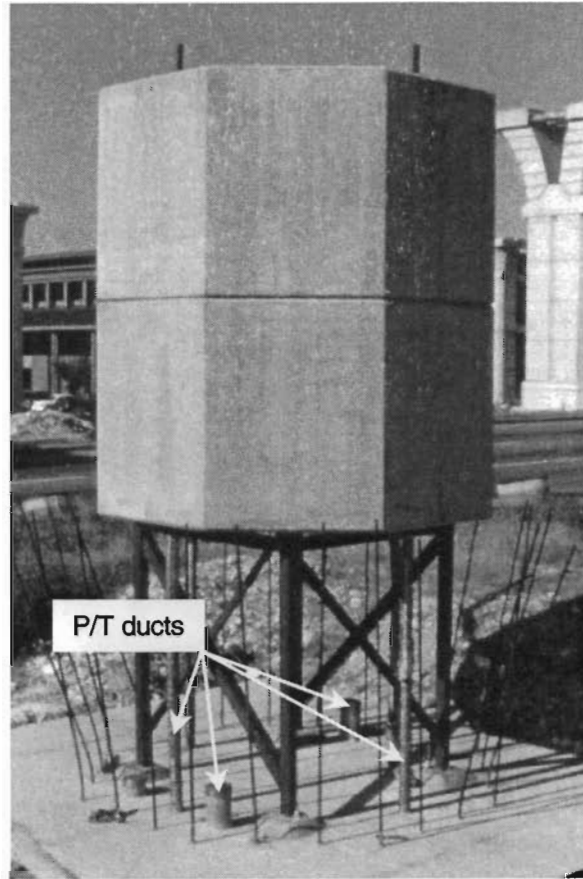


Figure 1.41 Steel support frame for first precast segment

After alignment and leveling of the first segment, a concrete base was cast around it. During construction of the cast-in-place base, the concrete was mechanically vibrated and forced to flow up against the bottom face and into the core void of the segment, ensuring good contact between the base and the bottom segment. Figure 1.42 shows the cast-in-place base during erection of the pier segment PC16-2.

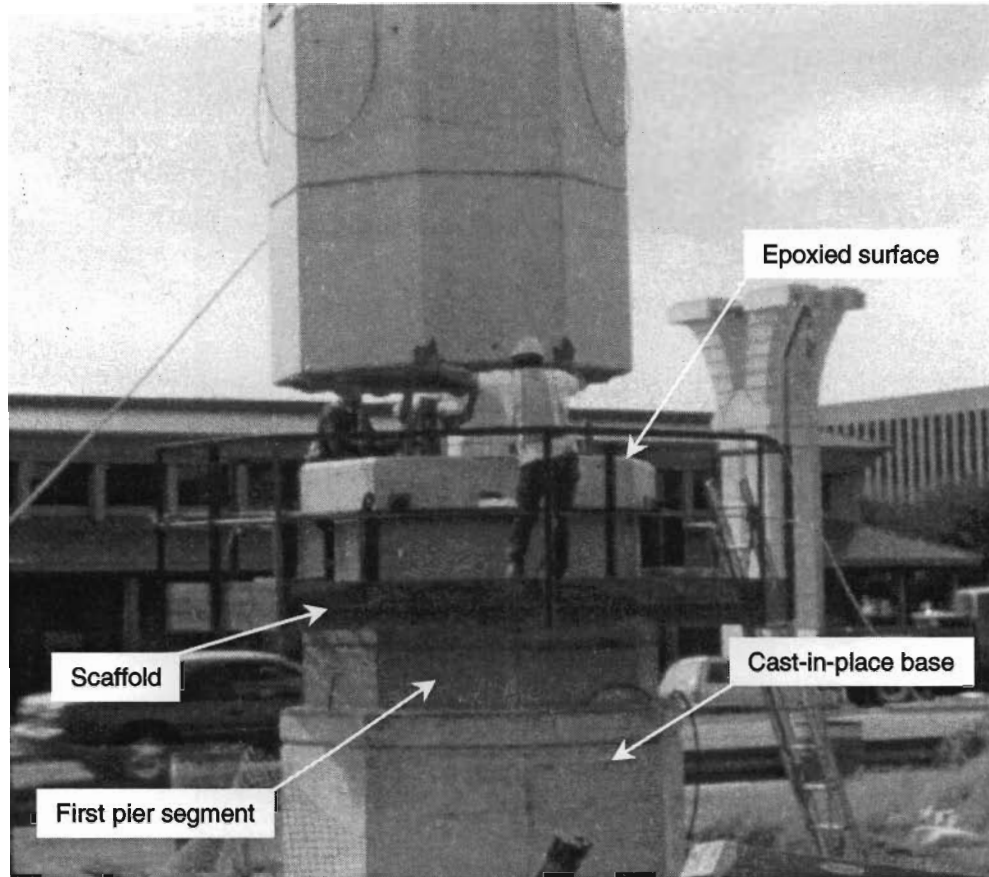


Figure 1.42 Cast-in-place base forming a rigid moment connection between base segment PC16-1 and foundation

Subsequent segments, as shown in Figure 1.42, were placed using a mobile crane. Segment joints were epoxyed like the superstructure segments, but the post-tensioning threadbars used to provide the squeezing force on the joint were left in place permanently. Figure 1.43 shows the hydraulic ram used for post-tensioning the threadbars. A portable scaffold was slipped up the pier by the crane as construction proceeded.

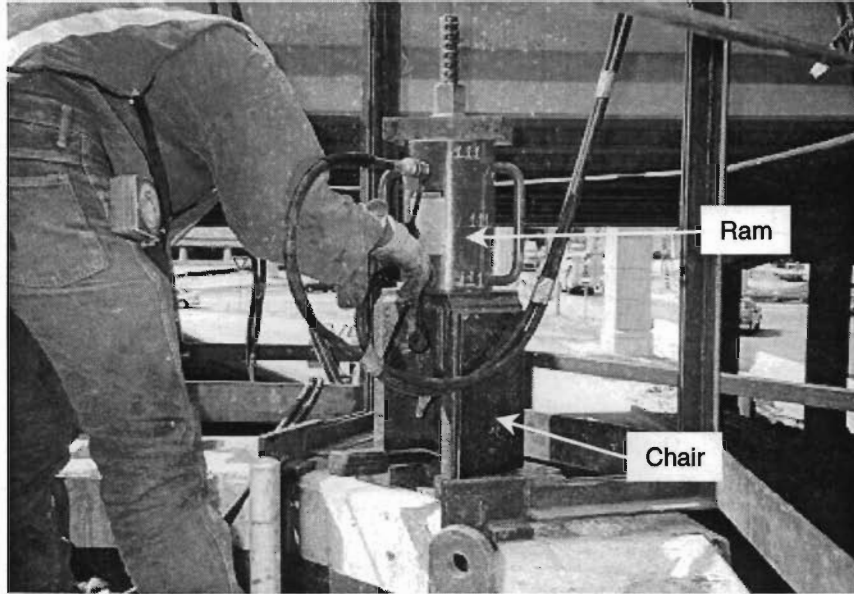


Figure 1.43 Hydraulic ram stressing temporary post-tensioning bars

Post-tensioning of the pier's two main tendons followed the placement of the capital segment PC16-8. Tendons consisting of 19-15mm diameter strands were cut to an approximate length, lifted by crane to the top of the pier, and inserted into the tendon ducts. The crane was then used to pull the tendons through the full lengths of the ducts using a fish wire. The tendons were stressed with a ram hung from the crane.

1.4.5 Transition and Modified Spans

Since the US 183 segmental project is an urban viaduct, limited access ramps had to be provided to the structure at various points. The transition and modified spans joined the single-cell box girder ramps to the single-cell mainlane girders at Lamar Boulevard and at IH 35. The transition spans were designed as three-celled box girders, thus providing the four webs necessary where the ramps split from the mainlane girder (see Figure 1.44). The transition spans were originally designed to be constructed as two single-cell, single winged girders with cast-in-place top and bottom flanges completing the central cell. The contractor decided not to modify the erection trusses used on the project to handle the eccentric load of a single winged girder and not to purchase the two additional casting machines required for the transition segments. Instead, he opted to cast the entire set of transition spans in place on timber falsework. Precast or not, the transition spans provided an opportunity to study a wide three-celled girder under various live loads. Two-span unit C13 was selected for study.

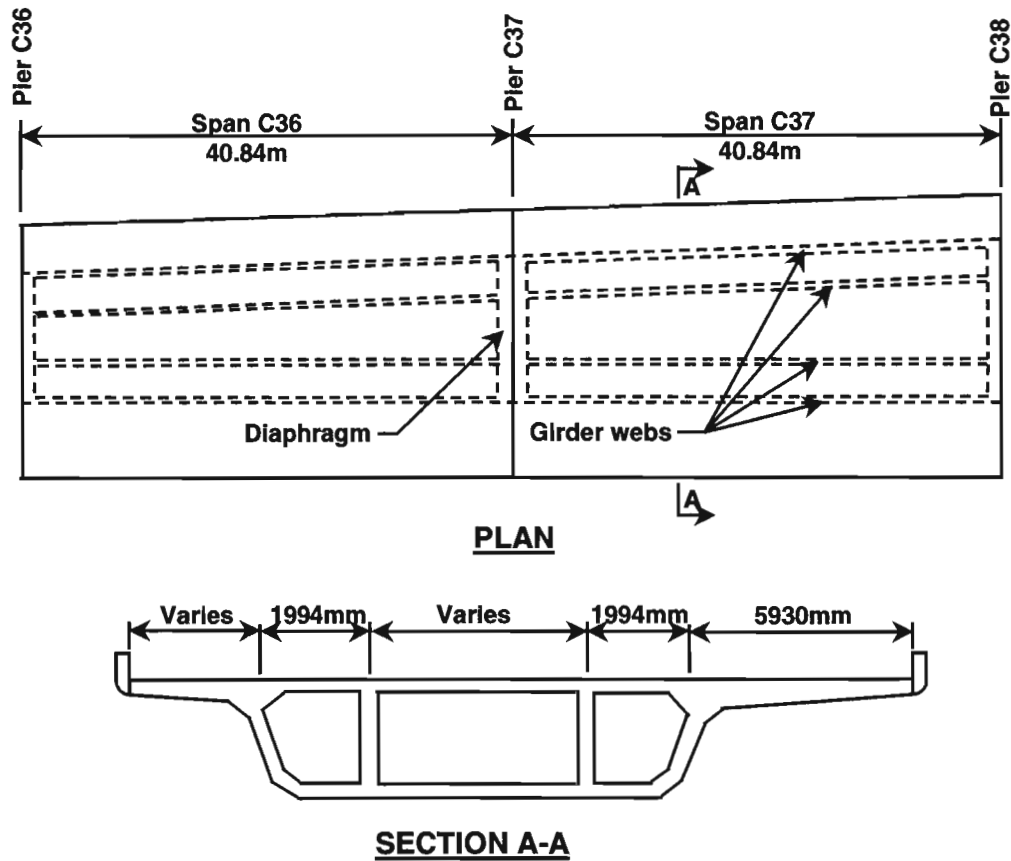


Figure 1.44 Plan and section of transition Unit C13

Modified bridge unit C15-L2 was also selected for study. This modified bridge unit was constructed using three spans of modified ramp girder and three spans of modified mainlane girder, with truncated wings on one side and a cast-in-place closure (see Figure 1.45). This detail is similar to many twin single-cell box girder bridges that are joined longitudinally at their interior wing tips to share live loads. Construction of the modified spans required little modification to the erection equipment for the mainlanes and ramps, with the gore closure formed and cast entirely from above. Longitudinal post-tensioning tendon layouts were very similar to those in the mainlane girders. Transverse prestressing was provided by a combination of pretensioned strands and post-tensioning tendons for the modified spans, and by post-tensioning only for the transition spans.

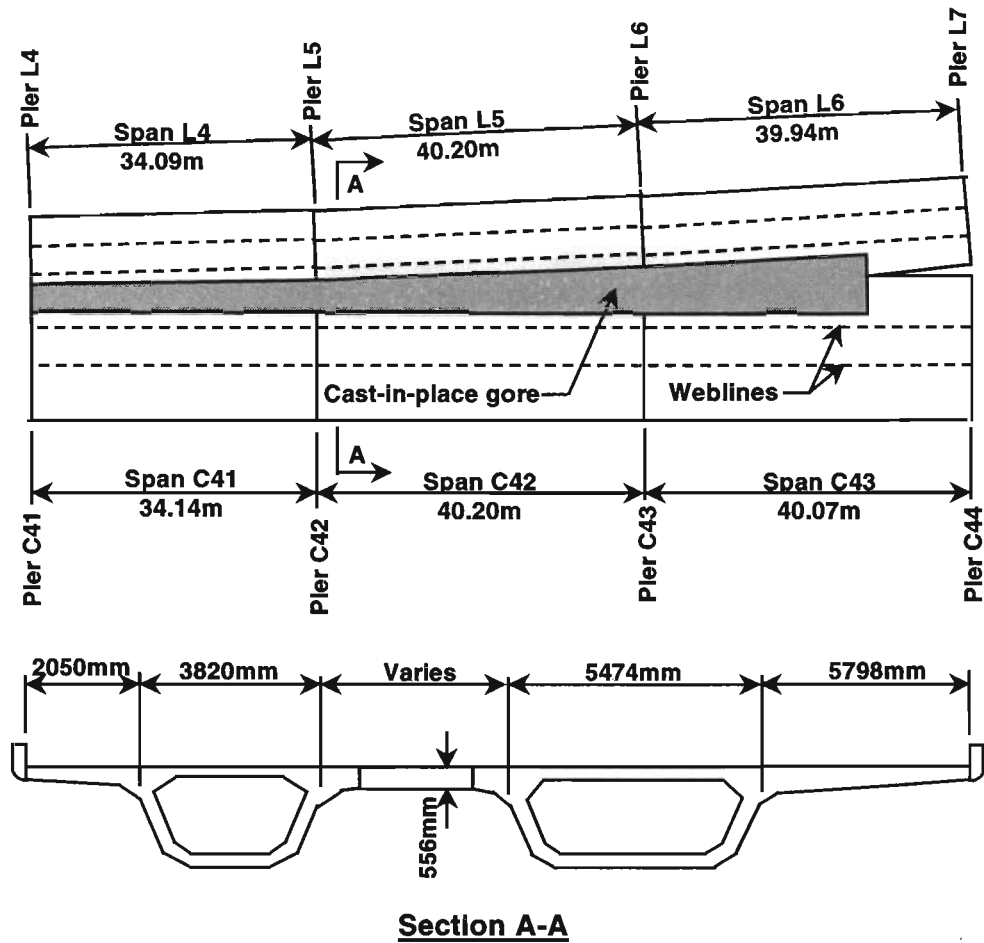


Figure 1.45 Plan and section of modified Unit C15-L2

1.5 TOPICS STUDIED ON THE US 183 SEGMENTAL PROJECT

The major topics studied in the current research study were:

1.5.1 Friction losses in post-tensioning tendons

Although considerable research has been conducted measuring friction losses in post-tensioning tendons, the wide variety of possible geometric configurations for a tendon makes any additional data useful to a designer. The external tendons on US 183 were of a common design (Figure 1.46), making friction loss test results for these tendons important. Other prestress losses include elastic shortening and shrinkage and creep losses. Tendon strains were measured using strain gauges, so tendon forces could be tracked over time. Gauges in the concrete of the box girders also allowed comparisons between tendon strain changes and the response of the entire bridge to prestressing forces, temperature changes, and creep and shrinkage.

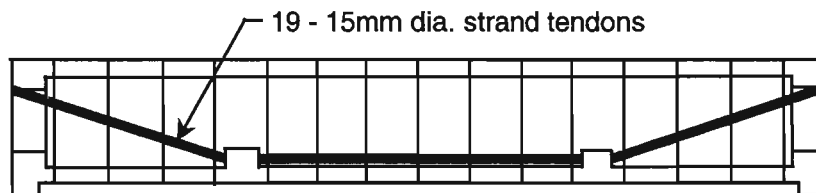


Figure 1.46 External tendon layouts for the US 183 box girders

1.5.2 Thermal gradients and their effects

Thermal gradients can cause stresses in continuous box girders of the same magnitude as stresses from live loads. The daily heating and cooling of a box girder top flange causes the bridge to deflect up and down, leading to induced moments for continuous structures (Figure 1.47) that may be opposite in direction of moments from dead load and live load. Overestimation of the magnitudes for the design thermal gradient for a structure can lead to great amounts of extra prestressing. Underestimation can lead to a cracked structure. Measurements were taken on US 183 to determine the actual thermal gradients as a check of the recommended design thermal gradients, to record the frequency of the magnitudes of thermal gradients, and to measure the response of the structure to thermal loads. The traditional analysis technique used to calculate concrete stresses from thermal loads makes broad assumptions as to the response of the girder.

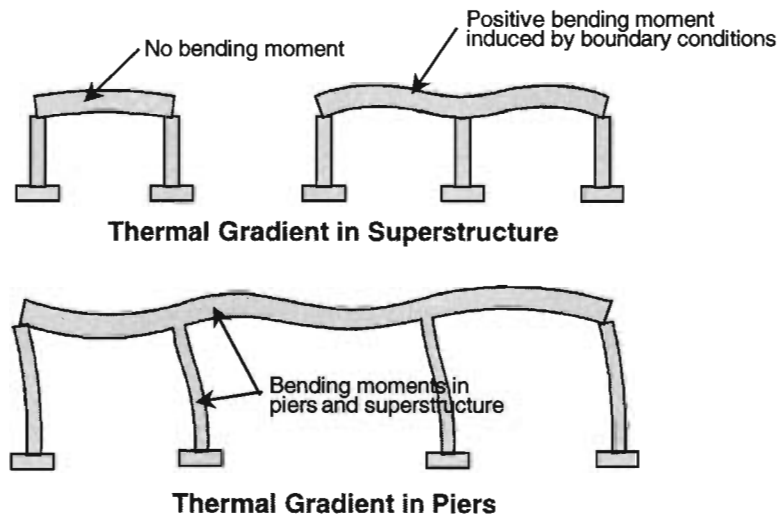


Figure 1.47 Structural response to thermal gradients

1.5.3 Strut-and-tie design regions

Concrete box girders have many local regions called D-zones, or discontinuity zones that can not be designed using normal design techniques for beams or columns. Strut-and-tie modeling of the regions gives the designer a useful method for the design of D-zones, such as for the anchor zone in Figure 1.48. D-zones under study at US 183 included two different deviators, two different anchor diaphragms, an anchorage blister, and two different pier capitals. Each of these D-zones was designed for strength and safety, yet had to be detailed to give satisfactory performance at service load levels. Instrumentation gave an indication of why some of these D-zones behaved very well at service load levels, while some others behaved poorly with large cracks.

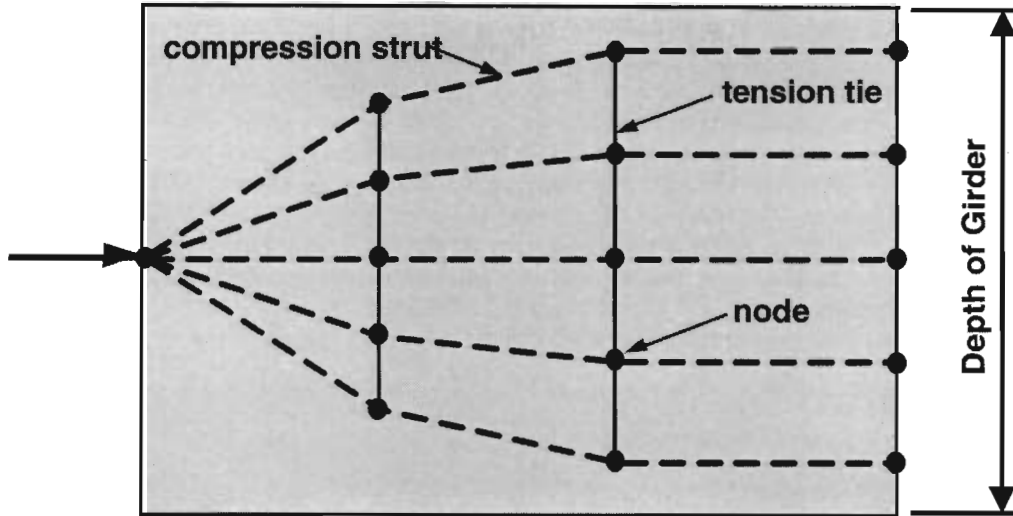


Figure 1.48 Strut-and-tie model for diffusion of a point load

1.5.4 Stress distributions in box girders

Low-level viaduct-type bridges such as US 183 generally have short- to medium-span lengths, yet may need to have a wide deck for three lanes of traffic or more. These proportions for a single-cell concrete box girder make predictions of stress using simple beam theory inaccurate, particularly near the post-tensioning anchorage zones, as shown in Figure 1.49. Stress distributions can also be difficult to predict because of the construction sequence and curved alignment of a structure, such as on Ramp P studied at US 183. Measurements were taken and stress distributions were plotted for many load cases on two different box girders and the segmental pier.

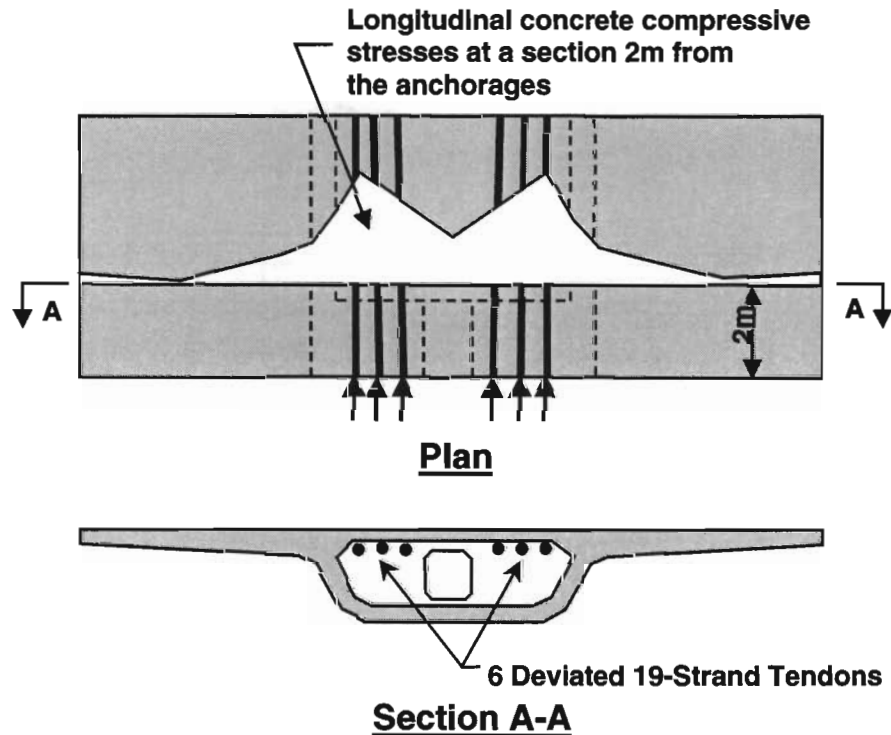


Figure 1.49 Diffusion of post-tensioning forces

1.5.5 Behavior of semicontinuous multiple-span units

The mainlane spans and many of the ramp spans were designed to be simple spans under dead load and live load, with "poor boy" continuity of the deck elements over the piers. This "poor boy" continuity was obtained by using an inexpensive cast-in-place deck slab to provide a riding surface between these simple-span girders at locations other than the finger joints, while no connection was provided between successive girder webs or bottom slabs. The joint also served to maintain alignment of the bridge unit, since guided bearings were provided at a minimum of locations. Construction of this joint is shown in Figure 1.50. Measurements were taken to determine how much negative moment this detail was carrying under live load. The moment couple would be developed between the slab as a tension member and the elastomeric bearings in shear. The development of a negative moment was not a performance characteristic desired by the TxDOT design engineers. Also, the response of the joint to thermal gradients in the box girder was measured.

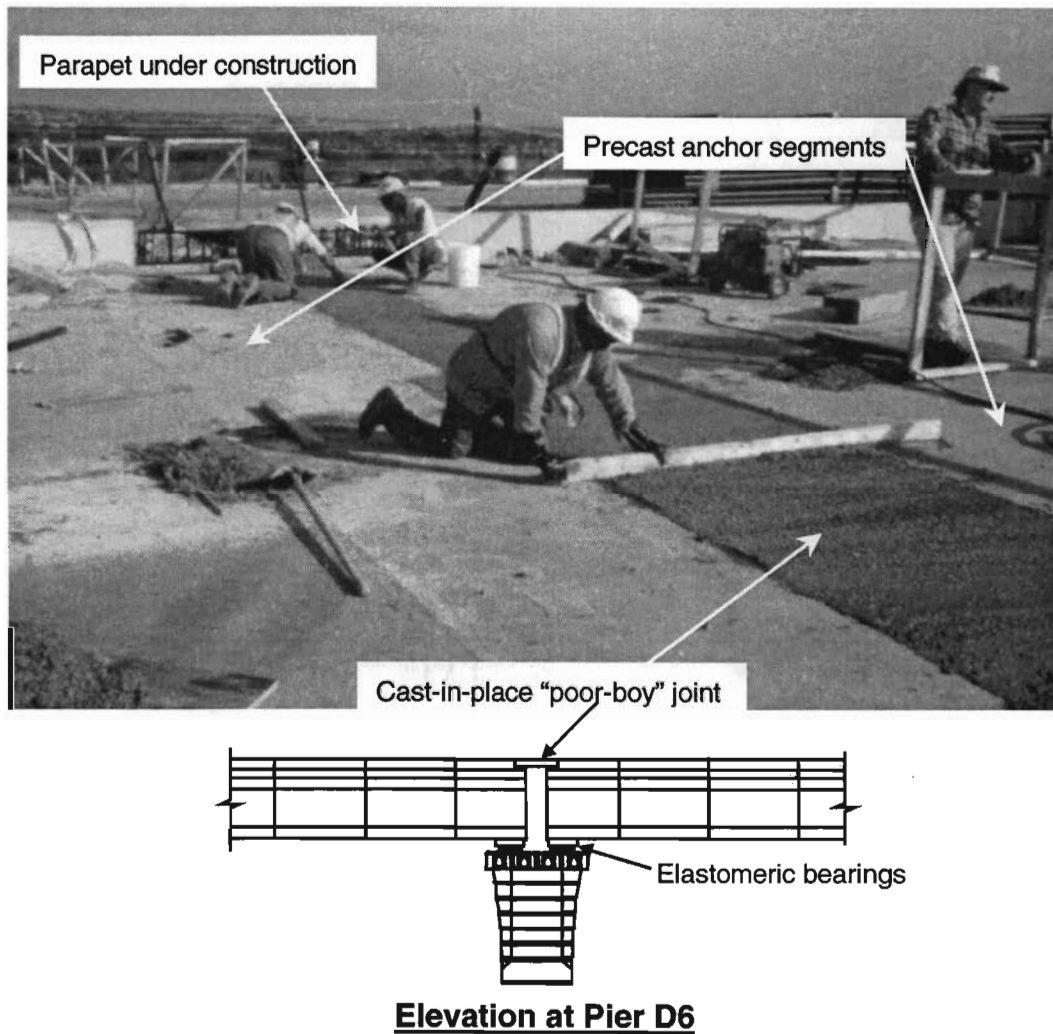


Figure 1.50 Construction of a cast-in-place continuity joint

1.6 SCOPE AND CHAPTER ORGANIZATION

The topics selected for study on US 183 were thought to be those most important to the segmental bridge industry at the present time. The information gained on some of the topics, such as friction losses and diffusion of post-tensioning forces, can be applied to many types of structures. Research on other topics, such as deviator behavior and thermal gradient effects, applied only to concrete box girders. The primary intent of the research was to verify the behavior of as many structural elements as possible through measurements. Therefore, this report emphasizes the measured results, using calculated results only for purposes of comparison. It was not

within the scope of this report to refine all design procedures that proved to be deficient. Instead suggestions were made and data presented to help aid in future designs. Furthermore, much of the data presented was intended to quantitatively verify design code provisions, especially the recommended design thermal gradient.

The chapters that follow contain details of the instrumentation used and background information on the structure, the study of the five main topics, and a summary of recommendations and conclusions. The Appendix has a summary of the thermal gradient records for the mainlane and ramp box girders. These chapters are:

1. Introduction
2. Instrumentation Program
3. Prestressing Force Losses in Post-Tensioning Tendons
4. Thermal Gradients and Their Effects
5. Load Response of Box Girders
6. Behavior of D-zones
7. Behavior of a Semicontinuous Unit
8. Observations, Recommendations, and Conclusions

Appendix

Chapters 3 through 7 are generally organized as follows:

1. Problem description and technical background
2. Literature review and previous field experience
3. Instrumentation program and field measurements
4. Comparison of results with calculated results
5. Recommendations

Every chapter has been written and illustrated as an individual document. Chapter 8 provides a summary of the findings and requires a previous understanding of the topics studied.

CHAPTER 2

INSTRUMENTATION PROGRAM

2.1 GENERAL APPROACH TO MEASUREMENTS

The important measurements taken on this research project can be classified into two main categories: Temperatures and deformations. The measurement of concrete, steel, or air temperatures was easily made with thermocouples located in or on the material in question. Deformations, on the other hand, had to be measured with a variety of instruments from strain gauges to extensometers, each with unique installation requirements and wiring circuitry, as required. Other categories of measurements included the measurement of force, using a load cell and the measurement of pressure, using a pressure transducer. These instruments basically are capable of measuring deformations internally and give an electrical response proportional to force or pressure.

The instruments used on the project can also be placed into two main categories: those that could be read automatically with a datalogger, and those that had to be read manually. Measurements that had to be taken at frequent intervals, such as once every minute during a live-load test, were read electronically with a datalogger. Measurements that had to be taken hourly for long periods of time, such as cross-sectional temperatures, also were taken electronically with a datalogger. Instruments requiring manual readings often served as a redundant system for the electronic instruments. For example, the manually read Demec extensometer was used to measure external strains as a check on internal strain meters. Manual reading sets often required 45 minutes to complete during each interval of a test, limiting their usefulness and inviting human error. Most of the electronic transducers used on the project were cast within concrete and therefore had to be read with a datalogger. These transducers, mainly strain gauges and thermocouples, were prefabricated at the laboratory to the greatest extent possible, then tied into the rebar cage as is shown in Figure 2.1. The construction or precasting schedule often required that instrumentation be installed in the course of one day.

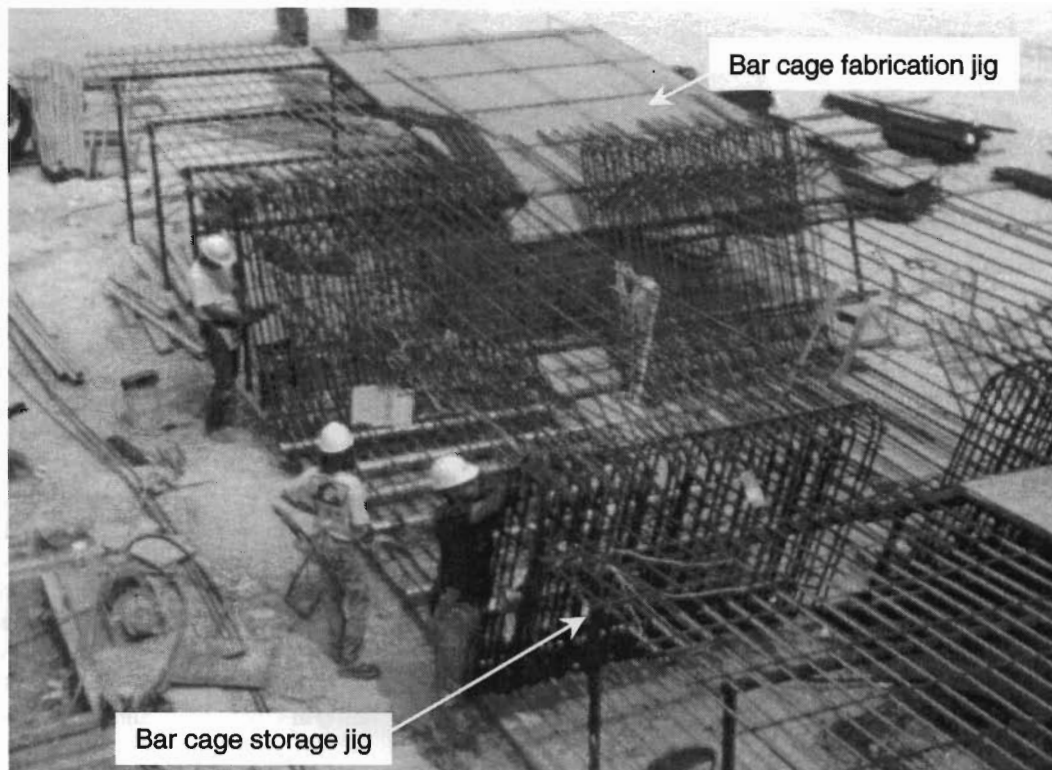


Figure 2.1 Gauge installation

Durability of the instrumentation and of the data acquisition systems was a primary concern. Many of the transducers were quite fragile, especially the strain gauges. The gauges were protected from direct impact with

multiple layer coatings, but could not readily be protected from vibration, such as during concrete placement shown in Figure 2.2, or more critically from a hammer impact. Many strain gauges were lost entirely during concrete placement, or showed evidence of delamination from the steel to which they were bonded. Since much of the project was precast, many of the gauges had to be installed months ahead of the time they would be needed to take measurements. Although most of the gauges that survived the casting procedure worked well for months or years afterward, some of the gauges demonstrated erratic output or quit working altogether. Thermocouples had nearly a 100% survival rate for the length of the project, easily surviving the casting process and not suffering any long-term degradation. The dataloggers selected for the project were built for field use and had been used with great success on previous field studies, especially at the San Antonio Y [10]. Many of the instrumentation systems used were developed in a study by Arrellaga [11]. Testing and further refinement of the systems was performed on this research project based on recommendations by Roberts [10] and Arrellaga [11].

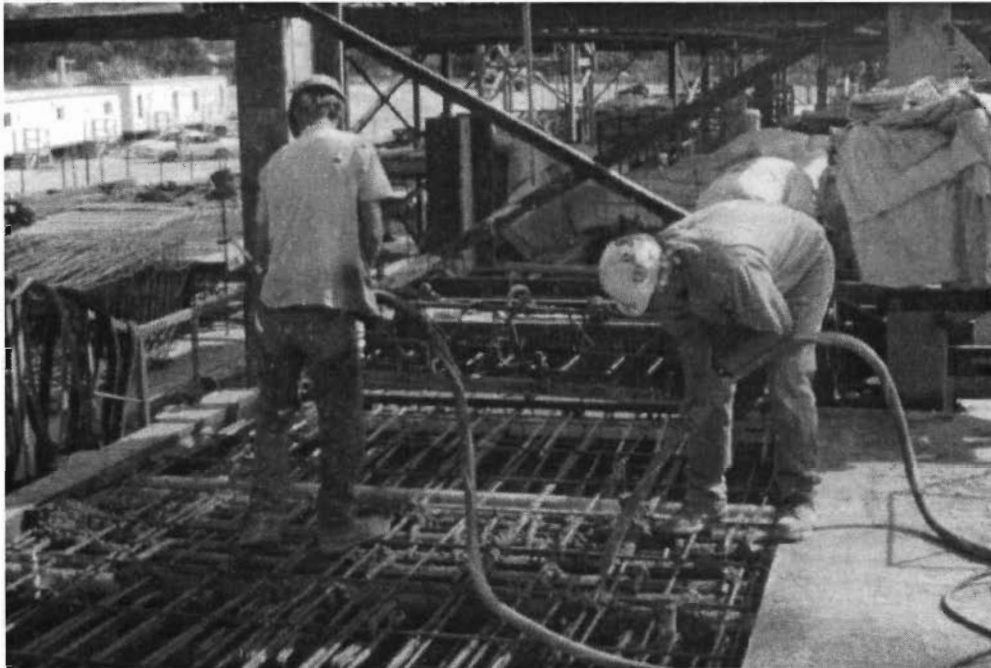


Figure 2.2 Vibrating concrete near instrumentation

2.2 INSTRUMENTATION

2.2.1 Strain Gauges

The electronic resistance type strain gauges selected for the project were all Micromasurements Group 350 Ω gauges. This nominal gauge resistance was selected because many of the anticipated measured strains were quite small, and the excitation voltage was only 5 volts. A 350 Ω gauge would increase the output voltage over a standard 125 Ω gauge. The gauge dimensions were chosen such that the gauge could be easily installed on a single wire of a 15mm, 7-wire strand. The electronic resistance gauge, as shown in Figure 2.3, works by changing its resistance linearly with changes in gauge length. The gauges used on the project were also thermally compensated for use on a material with a particular coefficient of thermal expansion, which was steel and concrete in this case. The resistance of the gauge changes with its own temperature such that thermal strain in the gauged material does not produce any appreciable output over a wide temperature range. Therefore, strain output from the gauge has a stress associated with it, since uniform contraction and expansion strains have been subtracted out automatically.

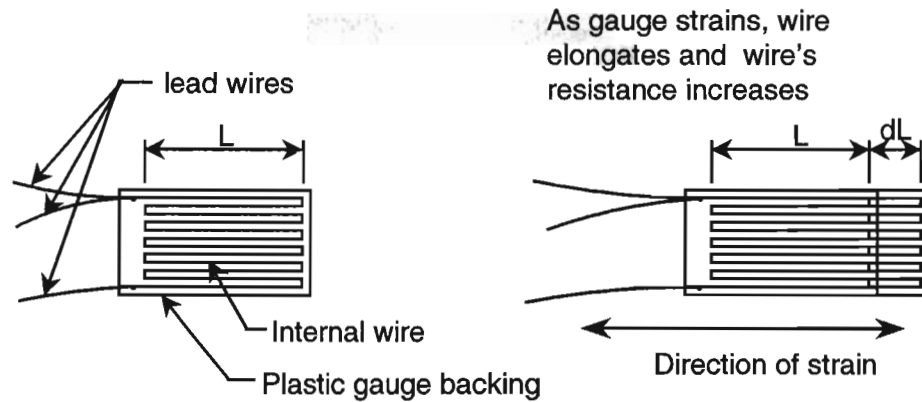


Figure 2.3 Electronic strain gauge

All strain gauges on the project were wired as one quarter of a Wheatstone bridge circuit, shown in Figure 2.4. The output voltage is produced when current is not equal on the left and right sides of the bridge. A three-wire system was used with all strain gauges to eliminate any output from temperature-induced resistance changes in the gauge lead wires.

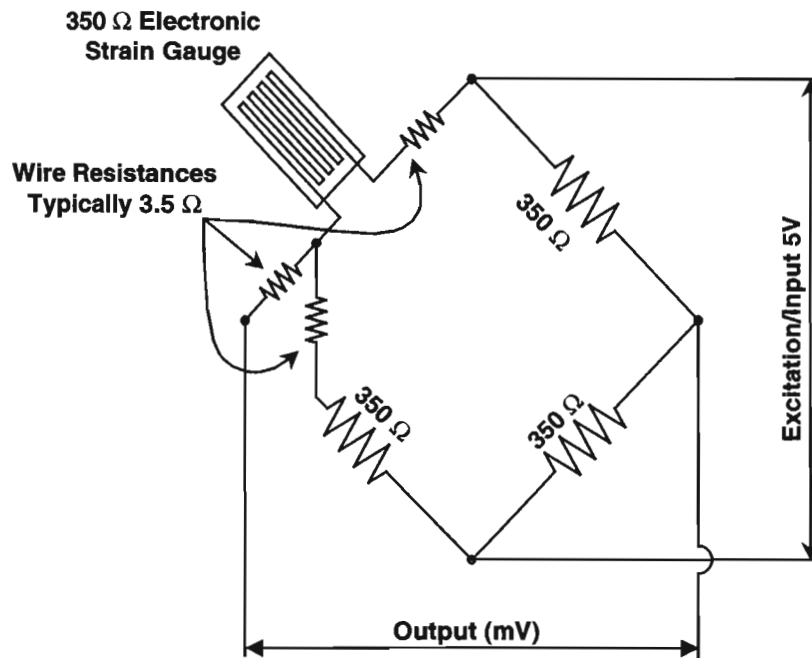


Figure 2.4 Wheatstone bridge circuit

Strain gauges were always installed on steel. The "S" series gauges were installed directly on important steel elements, such as reinforcing bars, while "C" series gauges were installed on small lengths of steel embedded in the concrete with the intention of measuring concrete strains. S-gauges were installed extensively on the heavy reinforcing bars in D-zones, such as in the anchorage blister shown in Figure 2.5. Gauges were located where cracks were expected to form so that the measured strain could easily be converted into a force. S-gauges were also installed on post-tensioning tendons and post-tensioning threadbars for the same reason. Gauges on the main external post-tensioning tendons, shown in Figure 2.6, had to be installed in the girder with the duct cut away. Gauges on the threadbars, such as the tiedown bars in the capital and anchor segments at pier P16, could be installed at the laboratory.

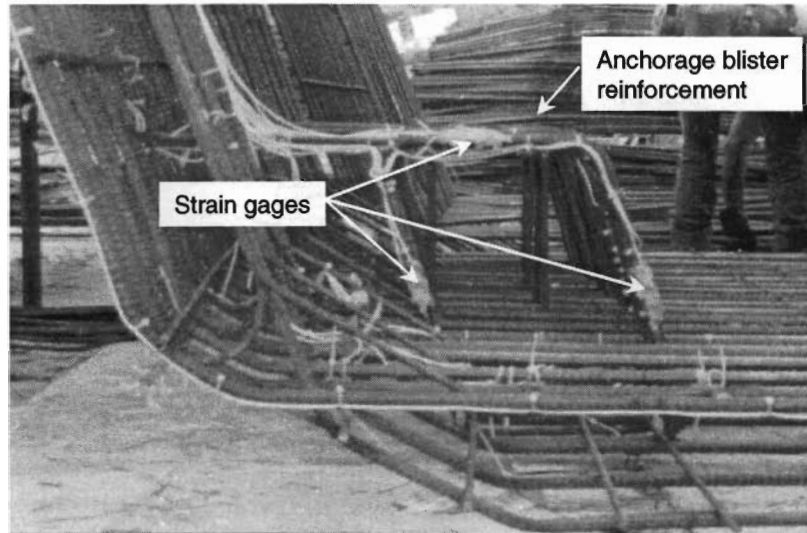


Figure 2.5 "S" series gauges installed on rebar

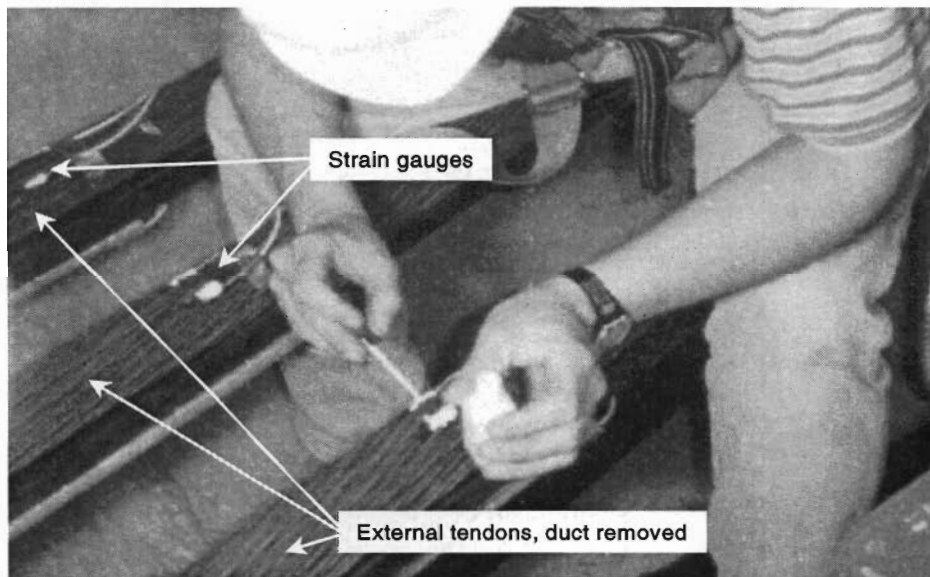


Figure 2.6 "S" series gauges installed on prestressing tendon

The laboratory-installed gauges almost always gave better performance and had a longer life than gauges installed at the site under uncontrolled temperature and humidity. The temperature of the material to be gauged apparently had the greatest influence. S-gauges were installed on the structural steel pipes for the mainlane Y-pier, shown in Figure 2.7, in direct sunlight. This exposure caused great temperature fluctuations in the pipe itself. The glue selected for all the strain gauging on the project, Micromeritics Group M-Bond 200, would work over a wider temperature range than many of the more expensive glues. Heat was used to raise the temperature of the material to be gauged if it was below 15°C. The glue would not set up otherwise and often would not bond to the gauge or the steel.

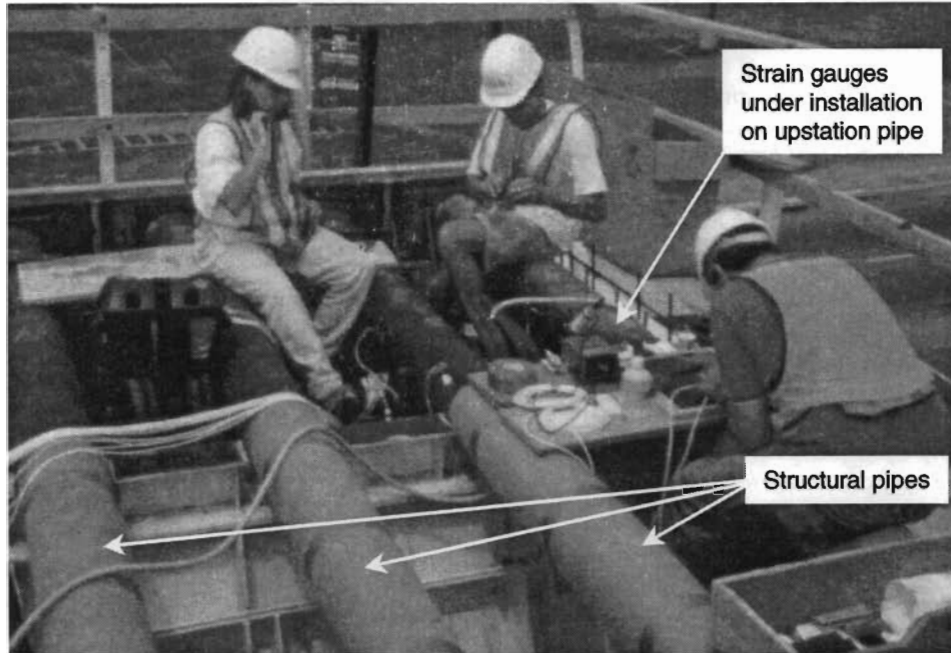


Figure 2.7 "S" series gauges installed on structural pipe

The "C"-series gauges consisted of a strain gauge bonded to a small steel rod, which was threaded on each end for 2 nuts and a washer. A plastic sleeve was provided so that only the end nuts and washers bonded to the concrete. The C-gauge was embedded in the concrete at time of casting. This device, shown in Figure 2.8, was originally designed by Stone [12] as a modified Mustran Cell. The C-gauge was tested and further refined on this project.

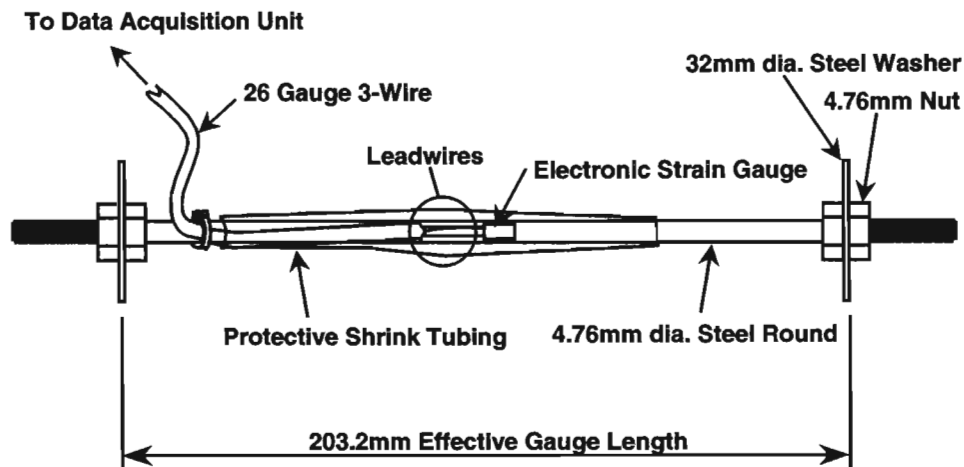


Figure 2.8 "C" series gauge construction

The gauge in its final form used throughout the project consisted of a cold-rolled steel rod 4.76mm in diameter approximately 235mm long, and was threaded approximately 20mm on each end. The effective gauge length between washers was 203mm. The strain gauge was the same 350 Ω electrical resistance strain gauge used for gauging the tendon wires and reinforcing bars. This strain gauge was bonded at the center of the steel rod. An acrylic coating and a small piece of butyl rubber were applied to the strain gauge after the electrical leads were installed and isolated from the steel rod. Approximately 165mm of heat shrink plastic tubing was slipped over the strain gauge, leads, and steel rod. The nuts were #10x32 USC and the washers were approximately 25mm in diameter. The nuts and washers were placed on each end, giving a 203mm gauge length, and tightened to yield the threads of the 4.76mm rod. The heat shrink tubing was shrunk to hold wire leads in place and protect

the strain gauge. Finally a coating of epoxy or silicone rubber was applied to the ends of the heat shrink tubing for waterproofing.

Tests were performed to determine the overall length for the C-gauge. If the gauge were too short it would act as a stiff inclusion in the concrete, reducing the strain measured by the gauge below acceptable limits. The 4.76mm rod was selected because it was small enough in diameter to reduce inclusion effects with reasonable gauge lengths, yet large enough for consistent quality gauging. C-gauges with lengths of 102mm, 152mm, and 203mm were constructed, cast within concrete specimens, and tested in a load machine. The test results are described in detail by Andres [13]. All the gauges performed satisfactorily, but the 203mm gauge was selected for use because of its ease of handling. A longer gauge was not considered because of its tendency to be easily bent and yield with relatively small transverse loads between the washers.

The 203mm gauge was tested further in 152mm by 152mm by 610mm concrete prisms tested in compression. The C-gauge was cast down the center of the specimen and Demec extensometer points, described in Section 2.2.7, were placed on the four exterior faces. Strains were measured mechanically with the Demec gauge and electronically by the C-gauge and a datalogger. The results of these tests are shown in Figure 2.9. The C-gauges gave very consistent results, and compared well to the strains measured by the Demec extensometer.

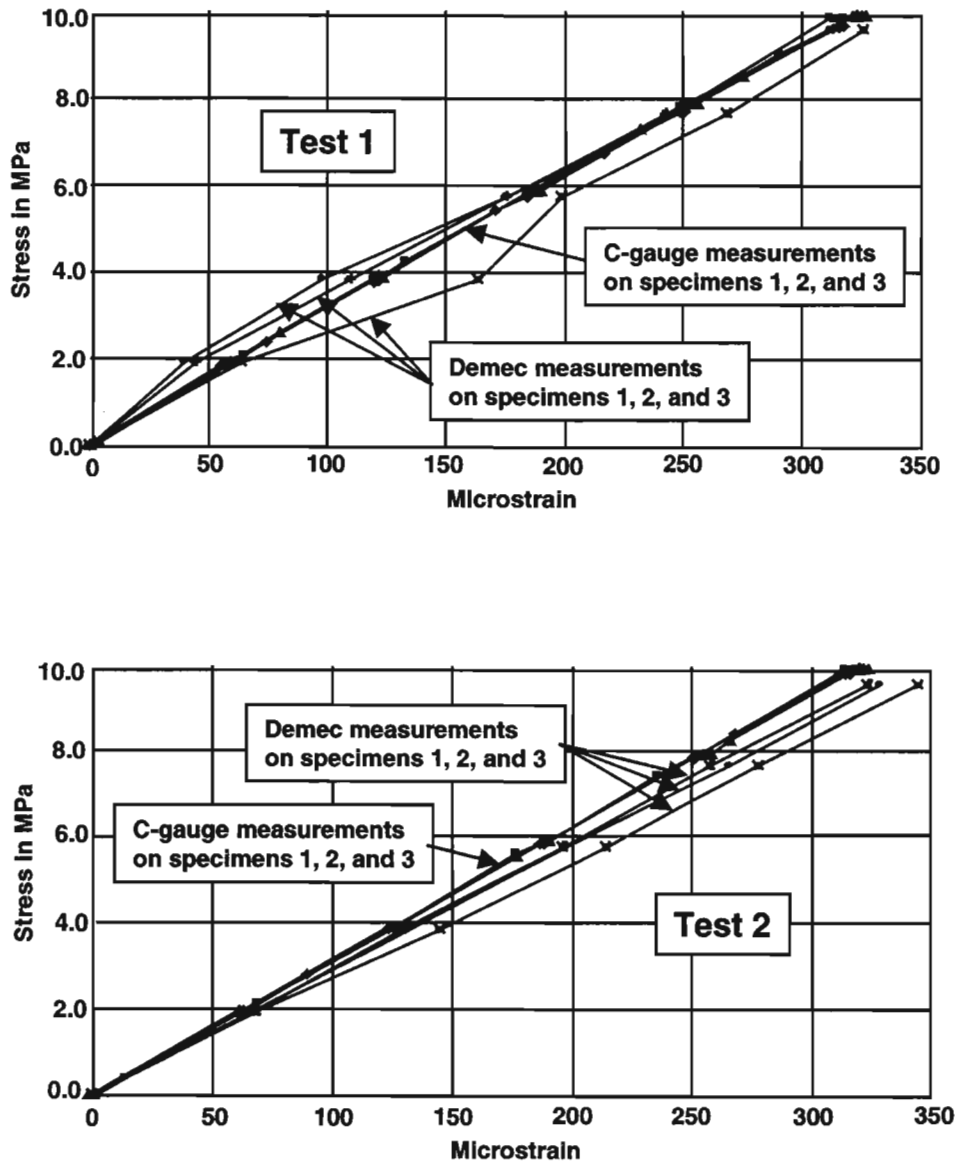


Figure 2.9 C-gauge tested against the Demec extensometer

Since the C-gauges were threaded on each end, they were easily installed in a test frame and pulled in tension. Every C-gauge used on the project was tested in this way and checked for linearity and slope compared to other C-gauges in the test group. The results of these tests for gauges C30 through C49 is shown in Figure 2.10. The one bad gauge in the plot was disassembled, rebuilt, and tested again. Slight variations in slope on the plot were caused by bending stresses in gauges that were slightly bent initially, and did not effect the accuracy of the gauge once it was cast in concrete.

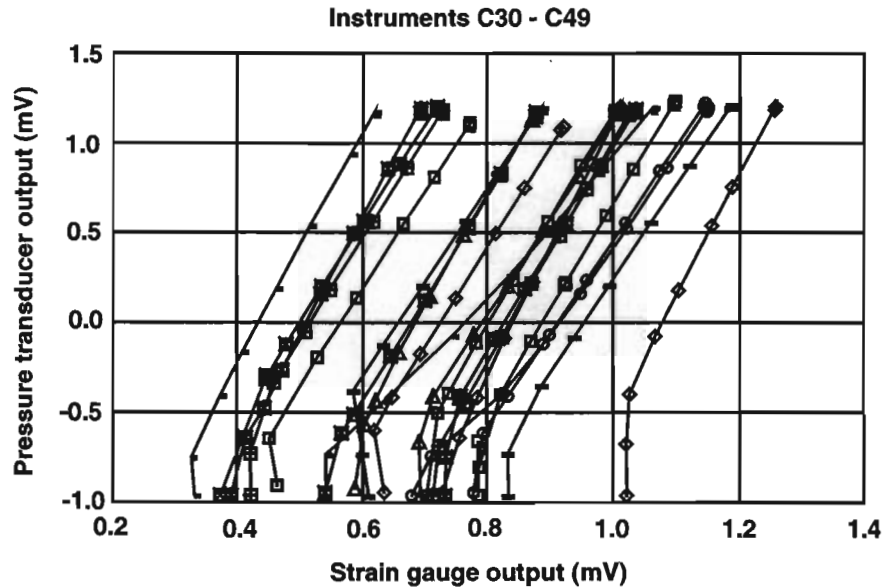


Figure 2.10 C-gauge calibration

The C-gauges were tied directly to the reinforcement cage, as shown in Figure 2.11. Additional bars often had to be added to the cage to hold one end of the gauge, since its length was only 203mm. Lead wires were run along the bars to an outlet blockout. It was found to be essential to leave some slack where wires crossed bar intersections or changed directions to allow for adjustments of the bar cage once it was lifted into the form. In retrospect, the C-gauges worked extremely well in the laboratory and very well in the field when they were not damaged by flowing concrete or vibration. The gauges' lifetime was adequate for monitoring all construction operations and the load distribution live-load tests. However, they did not have long-term stability. For monitoring very long-term service load behavior, a few vibrating wire strain gauges should have been installed. The C-gauges were too small to be quickly installed in the field, and were too easily bent by foot traffic and flowing concrete, especially in the girder webs. The gauge could be fabricated in a similar manner using a 500mm piece of rebar with threaded ends for testing, and deformed surfaces for bonding to the concrete. The life of this strain gauge may still be quite short compared to vibrating wire gauges, which function reliably for several years.

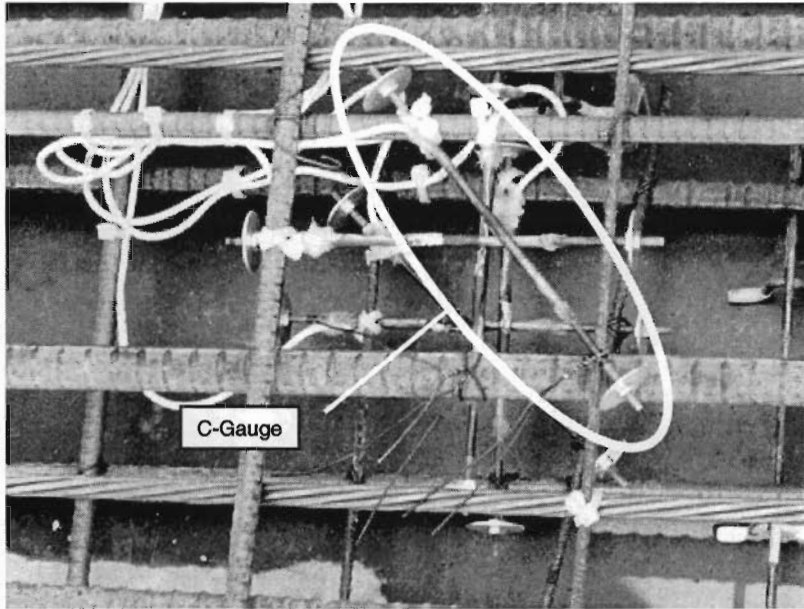


Figure 2.11 Installation of C-gauges

2.2.2 Thermocouples

Type T thermocouples were selected for the project because of the temperature range of the measurements to be taken. A typical type T thermocouple circuit is shown in Figure 2.12. The thermocouples proved to be the most durable gauge type used on the project. The thermocouple wire selected for the project was heavy gauge, wire mesh shielded with a Teflon outer case. The wire was tough and had high tensile strength, unlike the wire leads used for the strain gauges. The thermocouple end at the measurement temperature location was twisted and silver soldered, then protected with heat shrink tubing. A typical thermocouple installation is shown in Figure 2.13. The stiff constantan wire allowed the lead to be bent away from the rebar that the thermocouple was mounted on so that concrete temperatures could be measured without the local influence of the highly heat conductive steel rebar. Thermocouples were also installed in small holes drilled into the structural steel pipes in the mainlane Y-pier, installed within the strand group of some external tendons, and hung out drain holes in the girders to measure ambient outside air temperature.

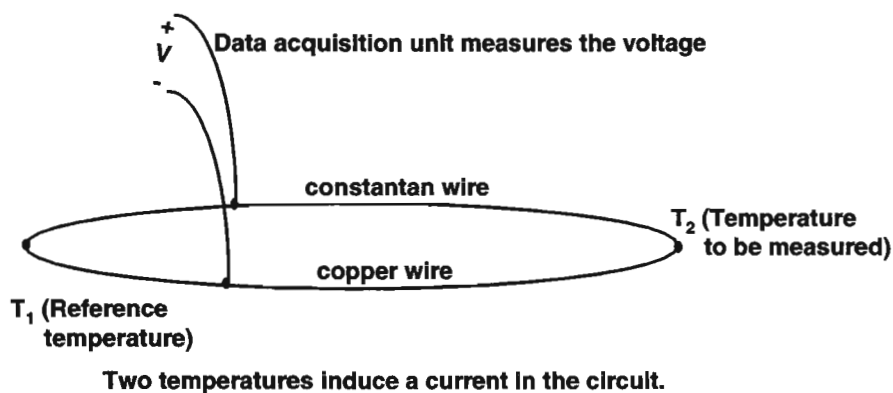


Figure 2.12 Thermocouple circuit

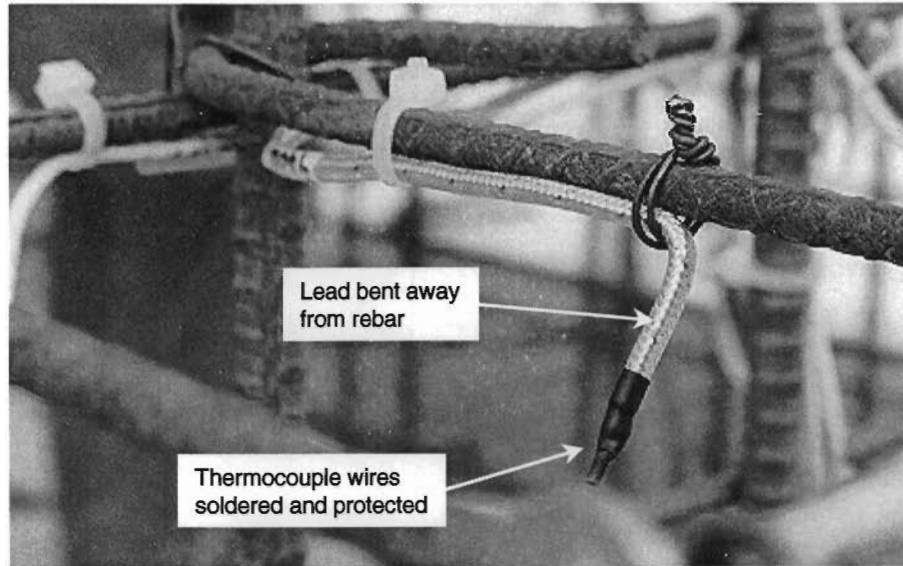


Figure 2.13 Installation of a thermocouple

2.2.3 Linear Potentiometers

Linear potentiometers were used on the project to measure movements of the superstructure with respect to the pier. This device, shown in Figure 2.14 gives an output voltage signal that changes directly in proportion to the distance the plunger is moved in or out of the housing. A linear potentiometer can accurately measure length changes on the order of millimeters, but cannot be used to measure strains in a material because of mounting irregularities, temperature changes, and the precision of the device itself.

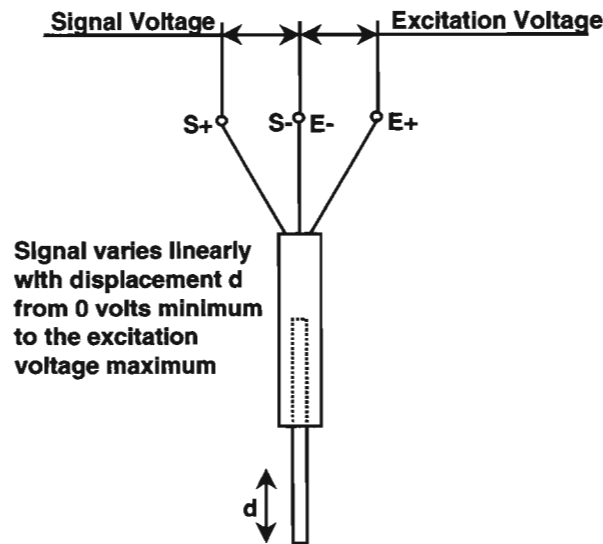


Figure 2.14 Linear potentiometer schematic

2.2.4 Pressure Transducers

Hydraulic rams were used extensively on the project by the contractor to jack the prestressing force into the post-tensioning tendons, and by the researchers in various laboratory tests. A pressure transducer, shown in Figure 2.15, gives an output signal linearly changing with pressure. This device was wired into the dataloggers during post-tensioning to record tendon force at the same time strain gauges were read.

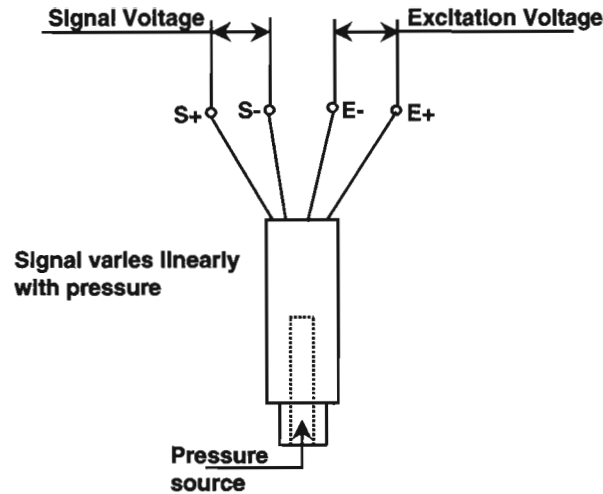


Figure 2.15 Pressure transducer schematic

2.2.5 Load Cells

Load cells were used during post-tensioning tests to measure force at the dead end of a tendon. A load cell, shown in Figure 2.16, operates much like a pressure transducer but with the signal voltage changing with applied force on the sides of the load cell. A load cell actually has strain gauges inside wired into a Wheatstone circuit. The load cells used on the project had a hole through their center for the tendon to pass through.

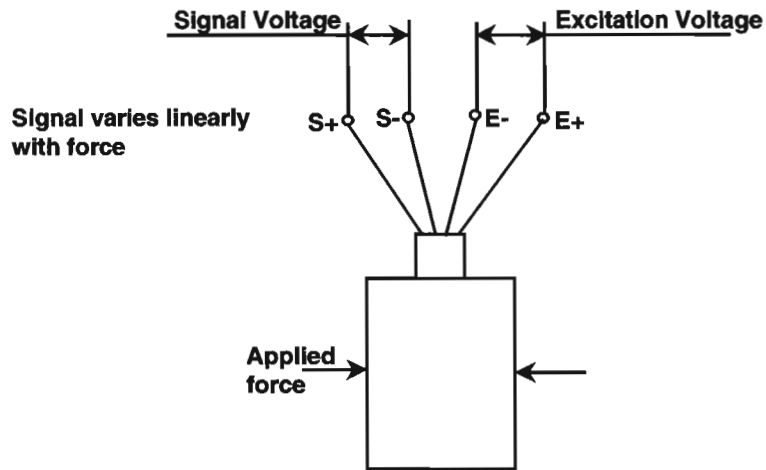


Figure 2.16 Load cell schematic

2.2.6 Data Acquisition System

The data acquisition systems used on the project all consisted of Campbell 21X dataloggers, Campbell AM416 relay multiplexers, a 12V marine battery, and a laptop personal computer. The containment for the data acquisition systems varied at different locations on the project, as shown in Figure 2.17. The mainlane girder had two cages containing the dataloggers, terminal boards, multiplexers, and a battery. The data acquisition system nearest pier D6 is shown in the top photo in Figure 2.17. Instrumentation for the mainlane Y-pier was also wired to this data acquisition system after temporarily being wired to the weatherproof box shown in the middle photo in Figure 2.17. This weatherproof box later housed the data acquisition system for pier P16. Each segment of Ramp P with large amounts of instrumentation had its own data acquisition system, with the dataloggers and multiplexers stored in individual sealed electrical junction boxes. This system allowed readings to be taken as the segments were being hung in balanced cantilever. This system proved to be far superior to the cages and terminal boards used in the mainlane girder. The ramp data acquisition systems were installed

and tested while the segments were in storage, while the mainlane girder systems had to be assembled inside the partially constructed span. All terminal connections were also eliminated in the ramp girder data acquisition systems.

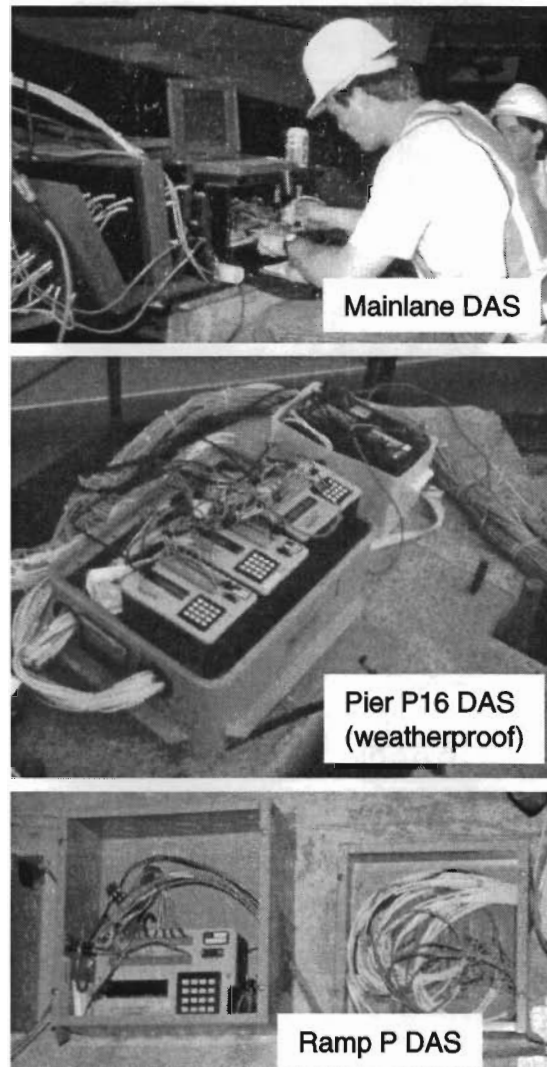


Figure 2.17 Data acquisition systems used on the project

The 21X datalogger has 8 channels for differential voltage measurements, and four terminals for switched excitations. The number of datalogger input channels are expanded with the use of up to four AM416 relay multiplexers. The 21X is programmed to control the multiplexers with signals from the excitation and control ports shown in Figure 2.18. The multiplexers are also powered through the 12V supply on the face of the 21X. Each multiplexer has 16 full-bridge channels, which can be divided into 32 quarter-bridge, or differential, voltage channels. Each of the two COM terminals on the multiplexer are wired to a different input channel on the 21X, providing a maximum of 128 differential voltage channels to be read with one datalogger.

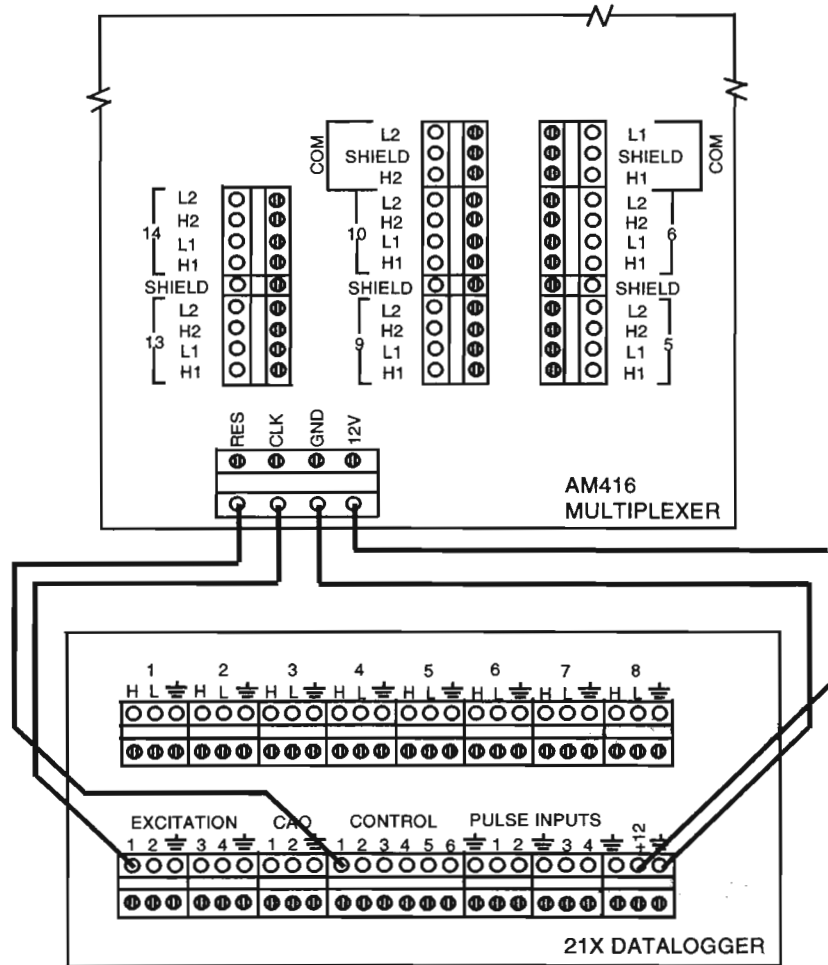


Figure 2.18 *Wiring the AM416 Multiplexer to the 21X Datalogger*

Strain gauges were wired as a quarter bridge on the multiplexer, with the remaining three-quarters of the bridge wired on the 21X datalogger, as shown in Figure 2.19. Actually two individual Wheatstone bridge circuits are shown in Figure 2.19, with the multiplexer acting as two 16-channel multiplexers. The H1 and L1 switched terminals are internally wired to the H1 and L1 COM, and the H2 and L2 switched terminals are wired to the H2 and L2 COM. Variations in resistance at the relays, which would show as gauge output, are small. The AM416 multiplexer has gold clad silver alloy contacts rated at a resistance of 50 m Ω . Current is supplied to the gauge through the multiplexer switches at an amperage well below the maximum current rating for the switch. A variation of 50 m Ω resistance at the switches would correspond to only a 14 microstrain apparent output by the gauge being switched. All leads for the 350 Ω precision resistors were identical in size and length to keep resistances equal on all sides of the bridge circuit.

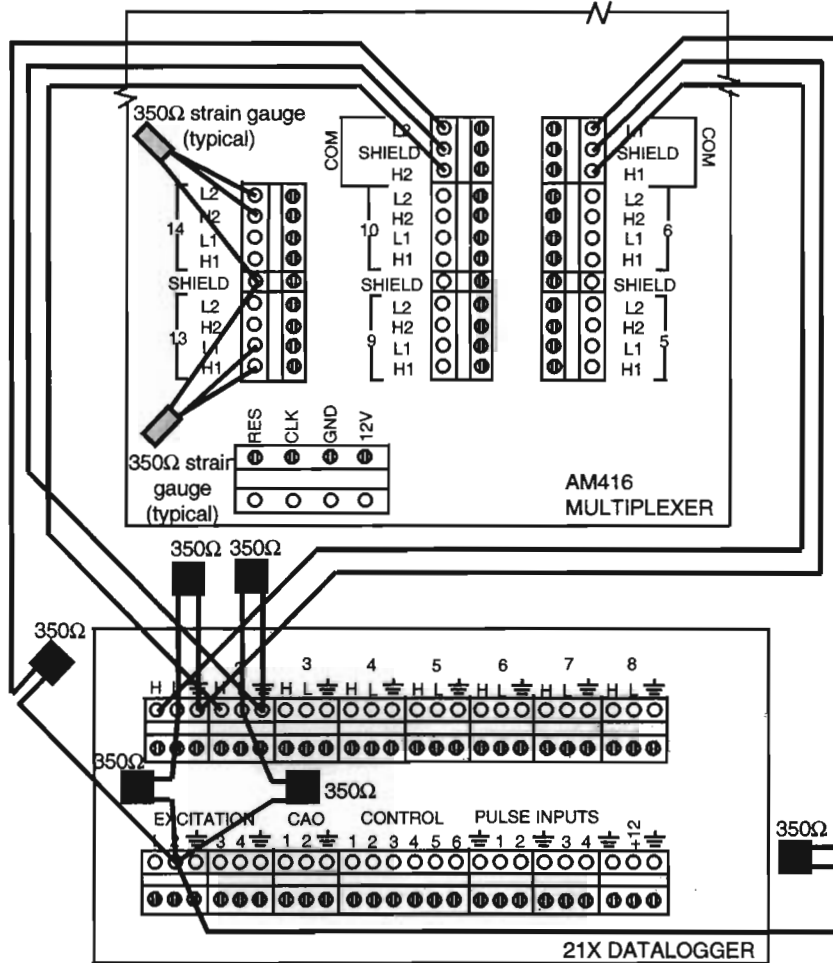


Figure 2.19 Wiring diagram for 350Ω strain gauges including the Wheatstone circuit

A test was performed to find if apparent gauge output was being recorded because of temperature variations at the datalogger or at the gauge. Temperature changes at the datalogger and the completion circuit for the bridge were expected to change resistances that could not be compensated by the Wheatstone bridge circuit. Also the strain gauges were compensated for a coefficient of thermal expansion of the gauged material of $10.8/^{\circ}\text{C}$ while the actual coefficient of thermal expansion of the concrete produced by the batch plant at the casting yard was about $9.9/^{\circ}\text{C}$. Figure 2.20 gives the temperature of the datalogger and the temperature at a thermocouple located next to a C-gauge cast within a 152mm by 305mm concrete cylinder. A 25°C temperature variation was used because that is approximately the seasonal temperature variation at the bridge site. The concrete specimens were given 24 hours to achieve uniform temperature. Prior to this a thermal gradient exists and the gauges would measure a strain caused by self-equilibrating internal stresses in the concrete cylinder. Toward the end of each 24-hour period, as seen in Figure 2.21, the gauges in cylinders 1, 3 and 4 showed nearly identical output. The gauge in cylinder 2 showed signs of partial debonding. Using the gauge factor of 0.0019002, the maximum gauge output variation was about 9.5 microstrain.

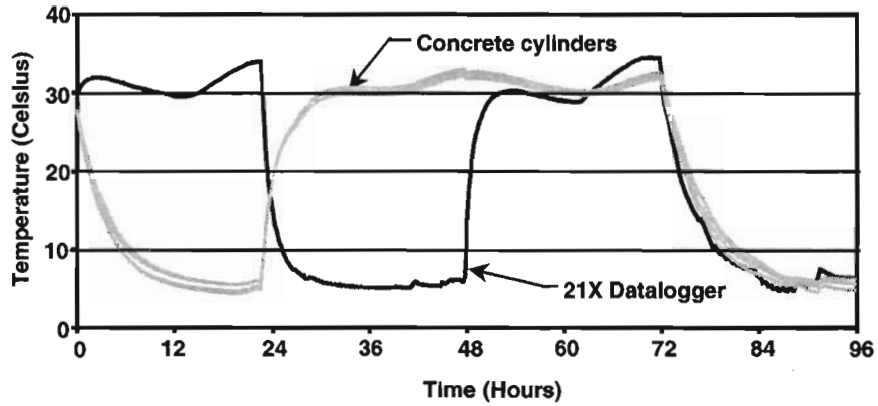


Figure 2.20 Concrete specimen and 21X datalogger temperatures recorded during temperature effects test

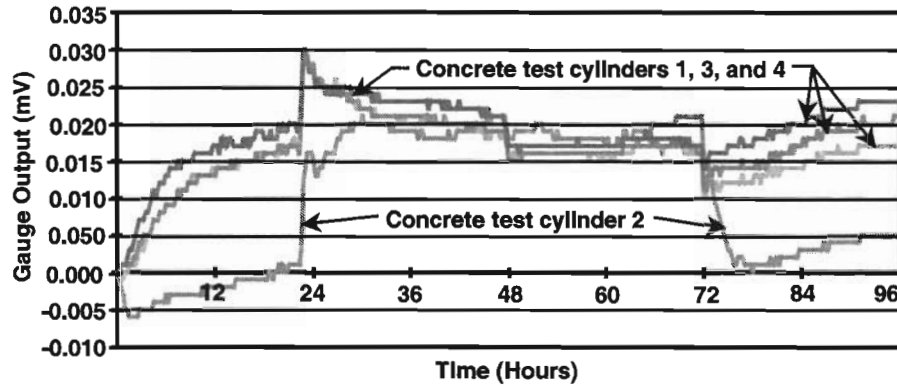


Figure 2.21 C-gauge output recorded during temperature effects test

Thermocouples were wired for differential voltage measurement, as shown in Figure 2.22. The thermocouple circuit does not require any excitation or completion circuits, and is the simplest device used on the project.

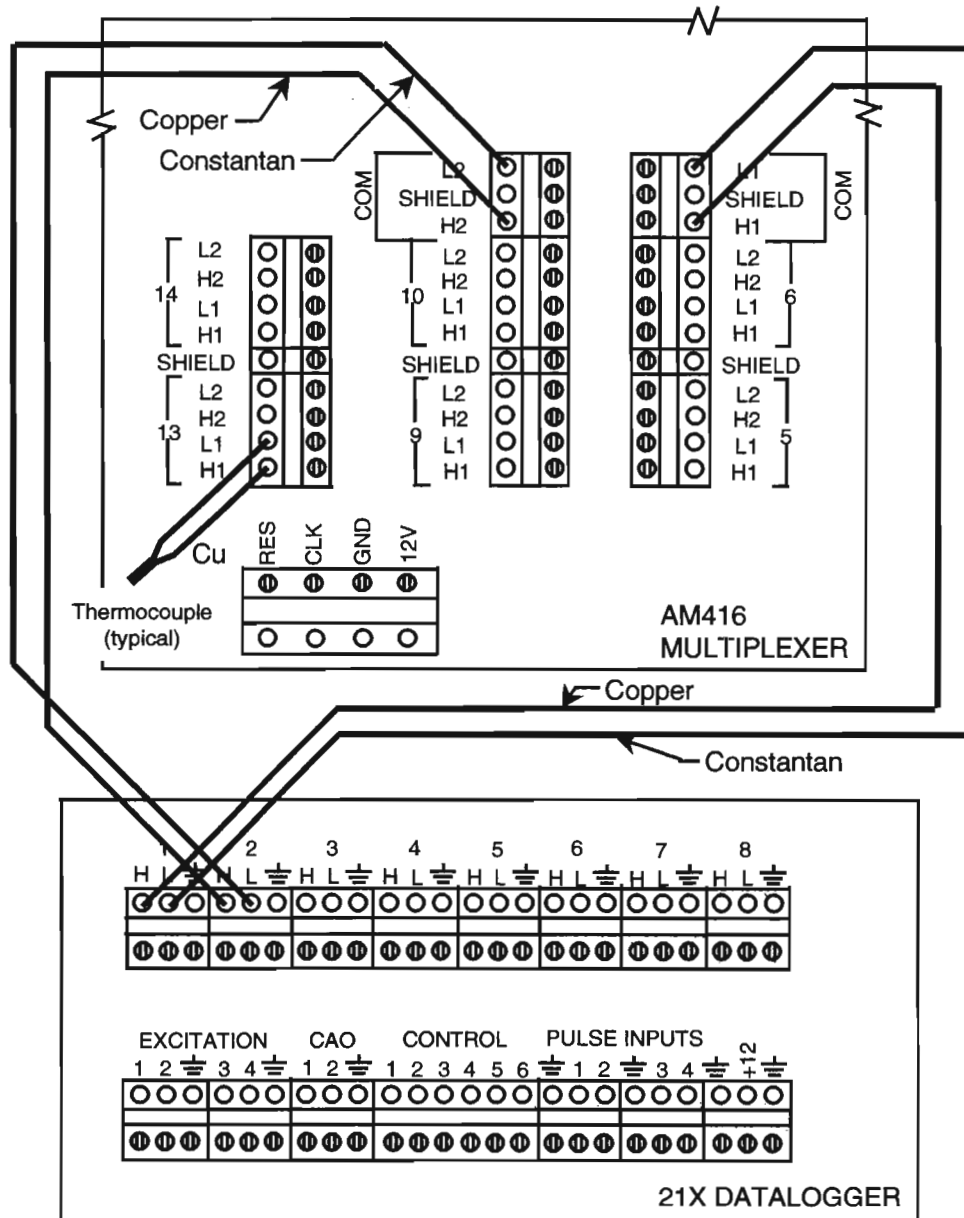


Figure 2.22 *Wiring diagram for thermocouples*

The excitation and the signal for linear potentiometers have a common ground, therefore the device can be read as a single ended measurement. With the wiring shown in Figure 2.23, one multiplexer can switch 32 channels of linear potentiometers.

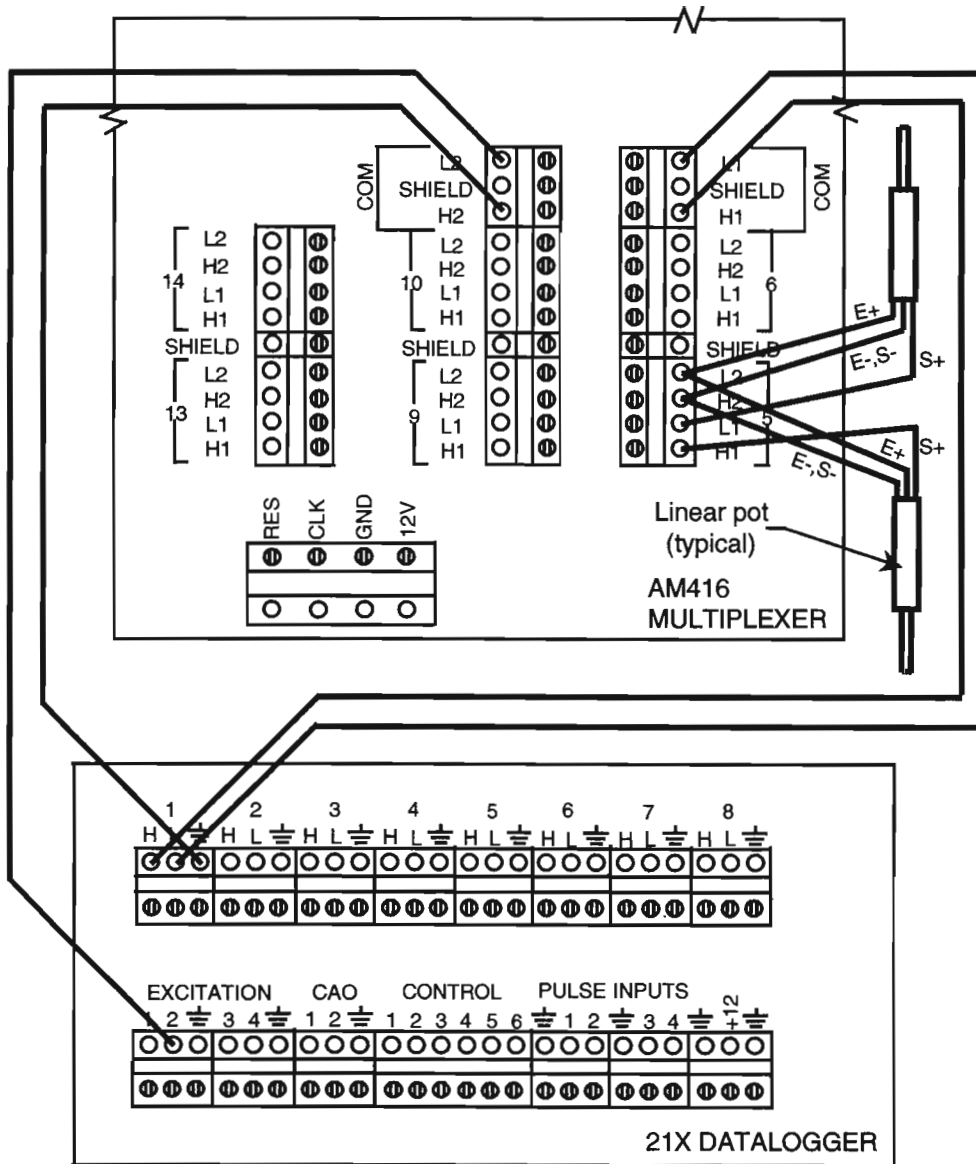


Figure 2.23 Wiring diagram for linear potentiometers

Pressure transducers and load cells are both full-bridge devices requiring a separate excitation circuit and differential voltage signal circuit. The wiring used for these devices is shown in Figure 2.24. Each device requires one entire channel on either the 21X datalogger or the AM416 multiplexer.

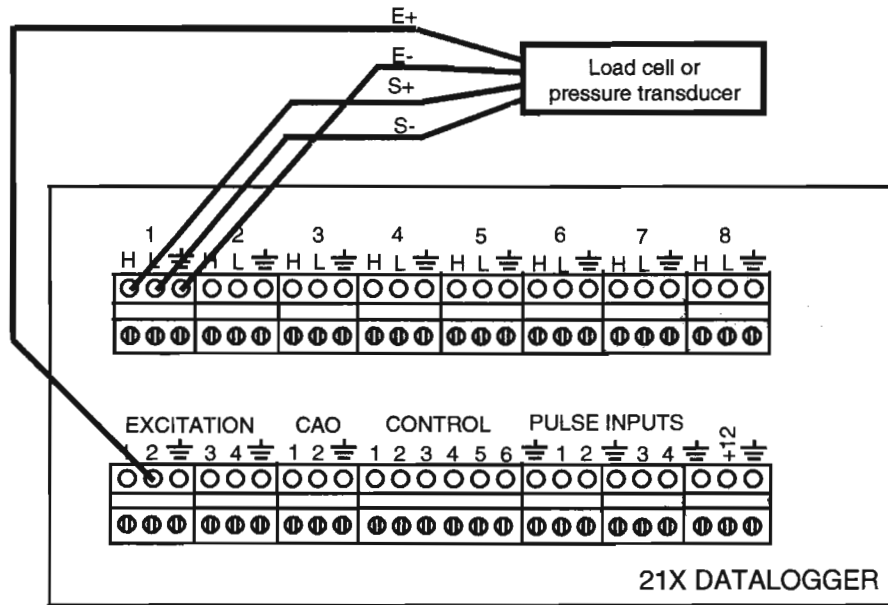


Figure 2.24 Wiring diagram for pressure transducers and load cells

2.2.7 Demec Extensometer

Despite the reliability of the C-gauges, gauges were often damaged during casting. Often the damage was obvious because the signal was lost entirely, or the steel rod for the C-gauge was bent enough to cause plastic strains in the steel beneath the gauge. These plastic strains often led to erratic behavior of the gauge. Gauges often debonded from the steel after a certain amount of time. If one of the two latter problems occurred, it would not be known until analysis of the data began. It is difficult to make the judgment that a gauge has gone bad by visually inspecting the raw data or even the plotted data in some cases. A simple and reliable backup to the concrete strain gauge was to use a Demec extensometer.

A Demec extensometer shown in Figure 2.25, is a mechanical device that measures strain on the surface of concrete or any material. Two steel points are installed into the concrete after it has hardened. These points can be glued to the concrete surface. However, HILTI® brand Hit anchors were used on this project to anchor the points into the concrete to a depth of about 32mm. A small 0.8mm diameter hole was drilled into the steel nail head of the Hit anchor. The Hit anchor was installed into the concrete at the precasting yard storage area. A 10mm hole was drilled into the concrete. A small amount of epoxy was injected into the hole. The Hit anchor was placed in the hole and hammered firm. Another Hit anchor was then placed a distance of 400mm away from the first point, and in the direction that the strain was to be measured. The Demec extensometer has points on each of its ends that fit into the holes in the Hit anchors, shown in Figure 2.26. One of the points can pivot to accommodate movement between the Hit anchors, and a dial gauge on the reader registers the amount of movement. The Demec extensometer mechanically measures changes in the distance between the two 0.8mm holes in the Hit anchors and gives readings in terms of strain. The Demec extensometer used in the US 183 study had an accuracy of 4×10^{-6} m/m. Demec measured strains gave alternative strain data to compare with the electronic data from the C-gauges.



Figure 2.25 The Demec extensometer

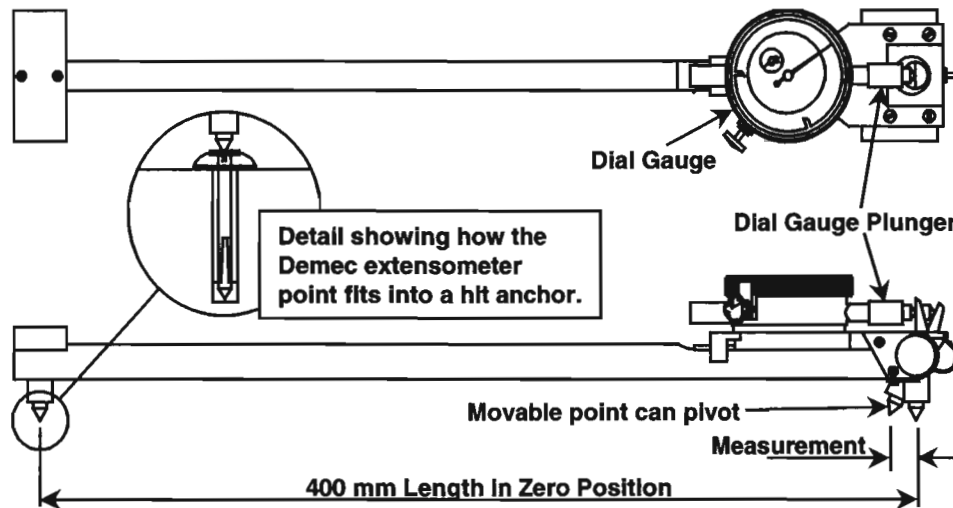


Figure 2.26 Demec extensometer schematic

Demec strains are less accurate and slower to read than data from the electronic strain gauges. Because Demec readings are taken manually, they can suffer from human error. Also the drilled Hit anchors were damaged on several occasions, and tended to accumulate dirt and grout dust in the drilled locating holes. The Demec extensometer gave values of strains at the surface level of the concrete, whereas the concrete gauges were embedded a certain depth and provided strain readouts for concrete beneath the surface level. Therefore, there was not a direct comparison between strain values from the two instruments located adjacent to one another. The Demec points or gauge are also not temperature compensated. Thermal strains that have no stress associated with them will appear in the data from the Demec points. Therefore, Demec points were most useful for reading short term changes in concrete strain under controlled loading conditions, where the temperature of the concrete did not vary significantly. If read properly by a person who has experience with the Demec gauge, it can provide useful comparison data to that from the electronic concrete strain gauges. A detailed study of the use and accuracy of Demec points was performed by Arrellaga [11].

2.2.8 Deflection Measurements

The taut wire baseline system was used to measure deflections in the mainline girders, and the transition and modified girders. This system, shown in Figure 2.27, could not be used in Ramp P because of the horizontal curvature. The system consisted of a piano wire anchored at the centerline of bearing at one end of a span and hung through a pulley at the centerline of bearing at the other end of the span. A 222N weight drew the wire consistently tight from test to test. Measurements were made using a digital extensometer, shown in Figure 2.28, mounted on a rail that allowed the gauge roller to travel up and down. A reference plate made of magnetic stainless steel was mounted on the bottom of the top flange of the girder. A magnet on the top end of the gauge shaft held the instrument to the reference plate while the cross arm was lowered by the reader down onto the wire. Measurements were taken at the span quarter points, as well as near the span ends to check the geometry

of the wire from test to test. This deflection measurement system was very accurate and reliable, although somewhat dangerous when in use.

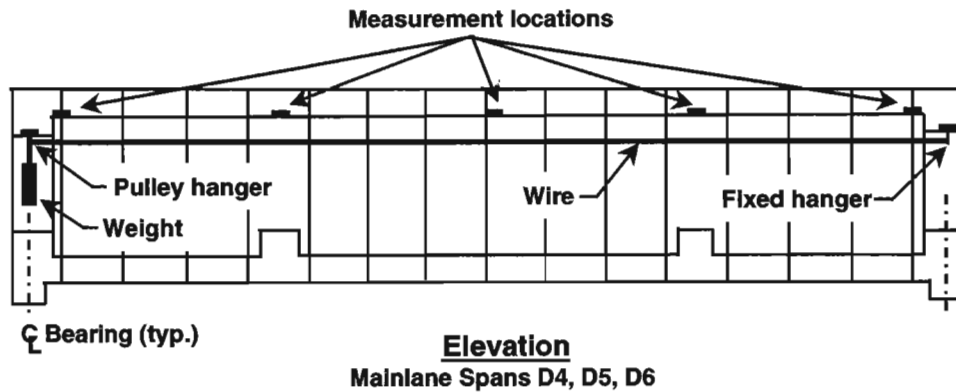


Figure 2.27 Piano wire deflection measuring system schematic

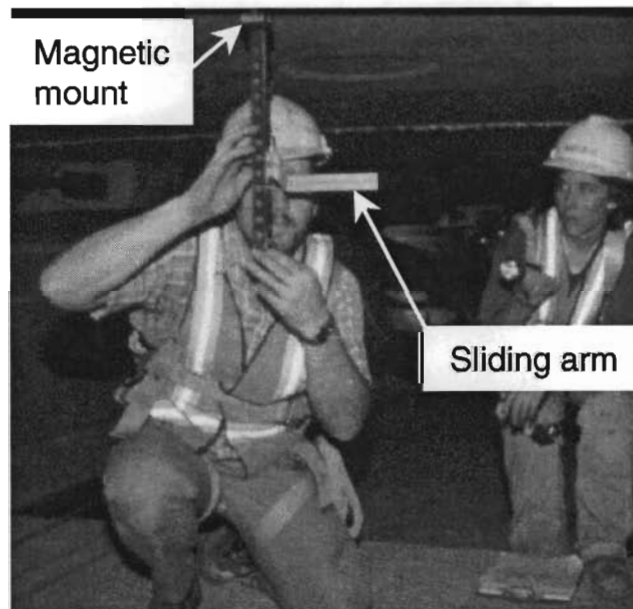


Figure 2.28 Taking deflection measurements

Deflections were also measured with Global Positioning System survey equipment during several tests. The measurements were taken by Michael Hyzak from Applied Research Laboratories of The University of Texas in Austin as an exercise in the use of GPS. Accuracy of the equipment is about 5mm, which was on the same order of magnitude as the measured span deflections under live load. The GPS receiving units were placed at various points along the spans during testing, as seen in Figure 2.29.



Figure 2.29 GPS deflection measurement equipment

2.2.9 Tiltmeter

The tiltmeter used to measure slope and twist of the pier P16 cantilevers during construction was a Model 800P Portable Tiltmeter manufactured by Applied Geometrics. Use of the tiltmeter also came through the cooperation of the Applied Research Laboratories. The 800P Tiltmeter uses electrolytic resistance cells to measure angles from the baseline gravity vector (a straight line towards the center of the Earth, or in other words, a very precise plumb line). The precision of the 800P is smaller than 1 microradian (1 mm in 1 km). Ceramic tiltplates (also manufactured by Applied Geometrics) were cemented to the deck of the bridge. The tiltplates, shown in Figure 2.30, are mounts for the tiltmeter that allow precise placement and orientation of the tiltmeter for every measurement. The 800P tiltmeter device has indexing bars attached to its bottom surface so that it can be precisely fitted to the tiltmeter plates every time measurements are taken. Four measurements were made with the tiltmeter at each tiltplate during tests, and these measurements were used to calculate the magnitude and direction of tilt. The data were read using a voltmeter. Further study of the use of tiltmeters for bridge instrumentation has been conducted by Hyzak, and is currently unpublished.

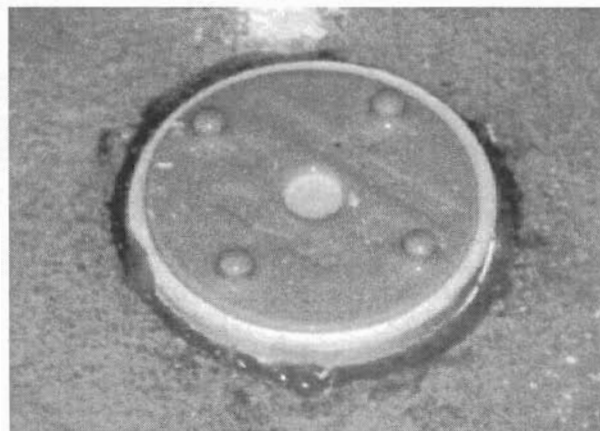


Figure 2.30 Tiltmeter gauge mounting plate

2.2.10 Epoxy Sleeve System

An epoxy sleeve strain measurement system was used to measure tendon strains in the mainlane girder. The system consists of a pair of cylindrical sleeves cast in epoxy around a group of strands. Two sets of Demec

points are mounted in each pair of epoxy sleeves. The system was originally developed by Arrellaga [11], and used by Roberts [10] at the San Antonio Y. Because of problems with grouting the ducts after removal of an entire section of duct at the San Antonio Y, only half the duct was removed on US 183, as seen in Figure 2.31. Although tests in the laboratory, such as the bench test shown in Figure 2.32, successfully used the epoxy sleeve system to measure strains, field installation allowed only a partial depth sleeve, which was very difficult to seal. Each epoxy sleeve took about 2 hours to construct. The time would have been better spent installing several more electronic strain gauges at each location. Data from the epoxy sleeves used on the mainlane were quite erratic.

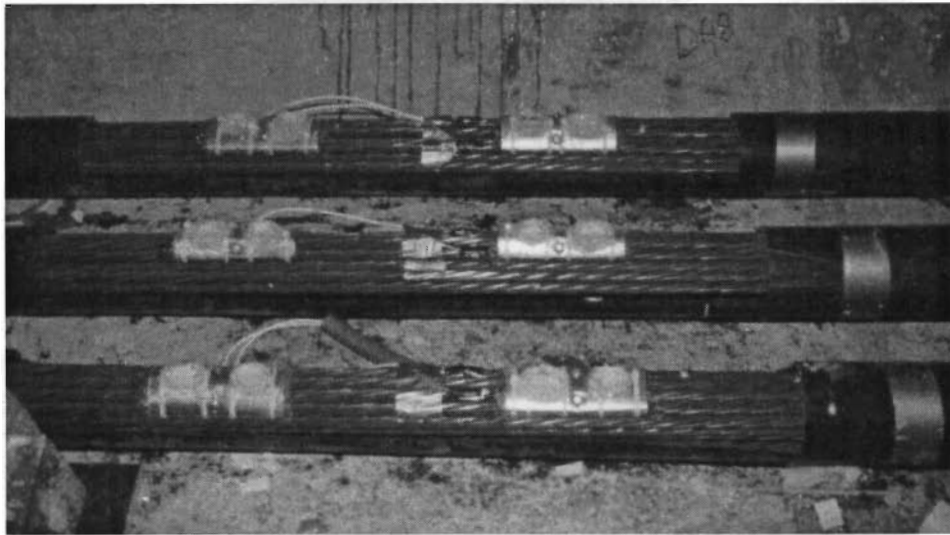
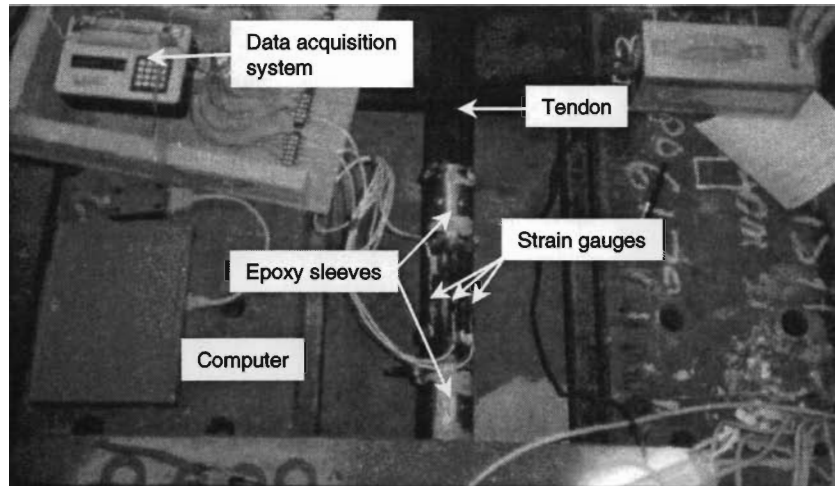


Figure 2.31 Epoxy sleeve strain measurement system



View A-A

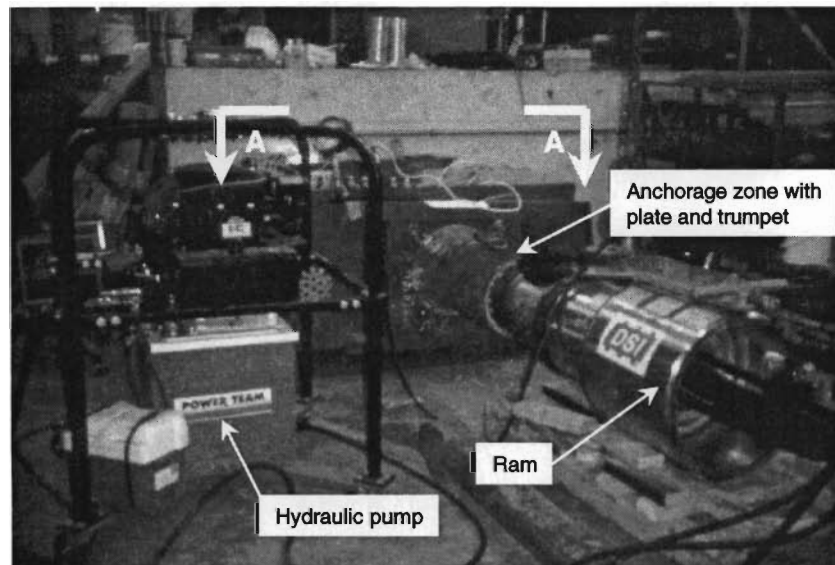
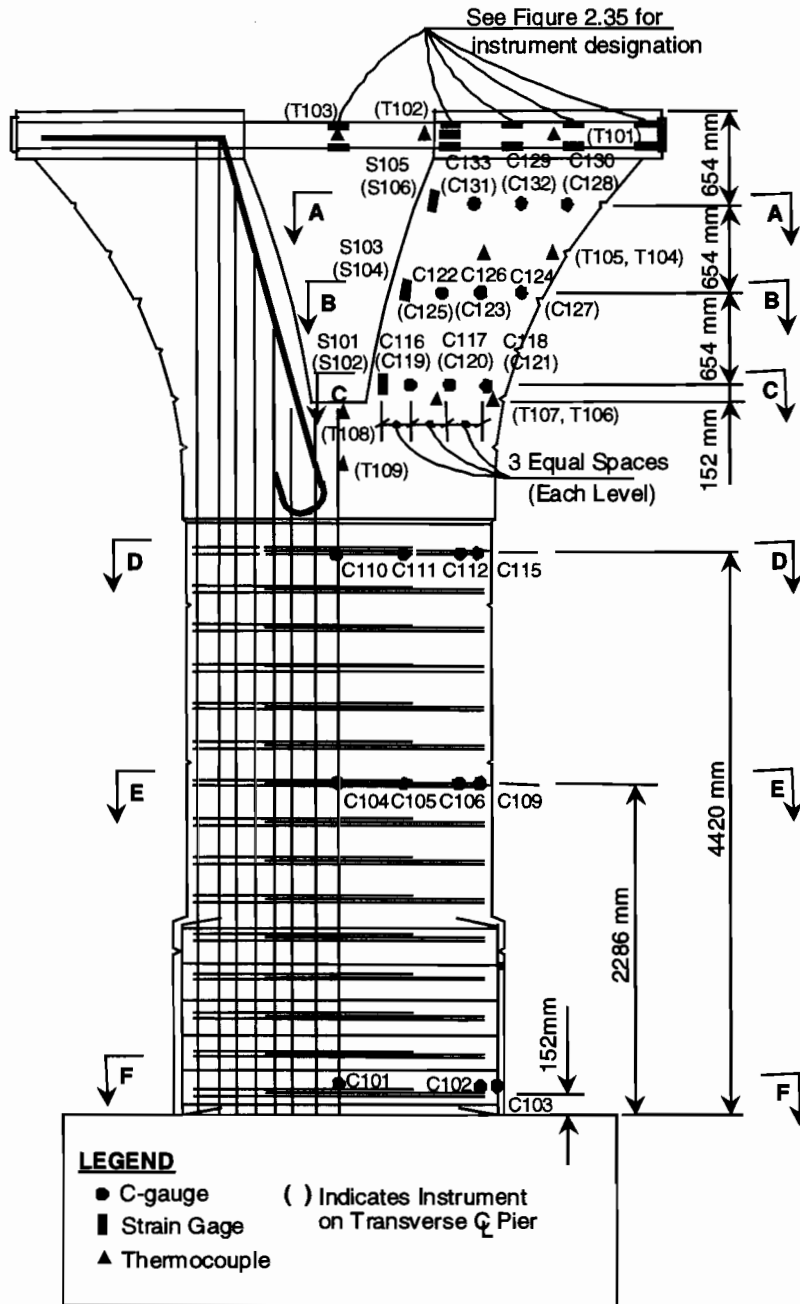


Figure 2.32 Epoxy sleeves tested during the bench test

2.3 INSTRUMENT LOCATIONS

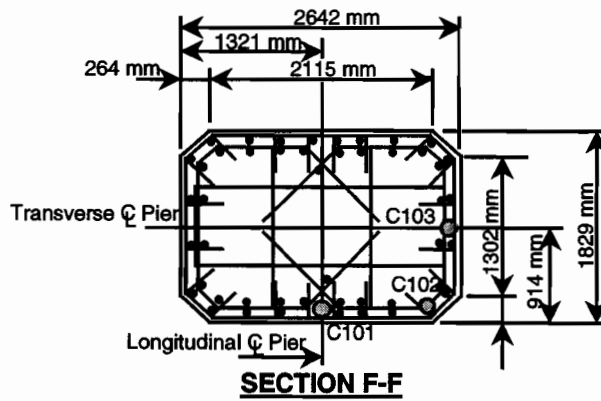
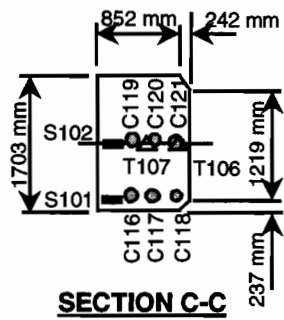
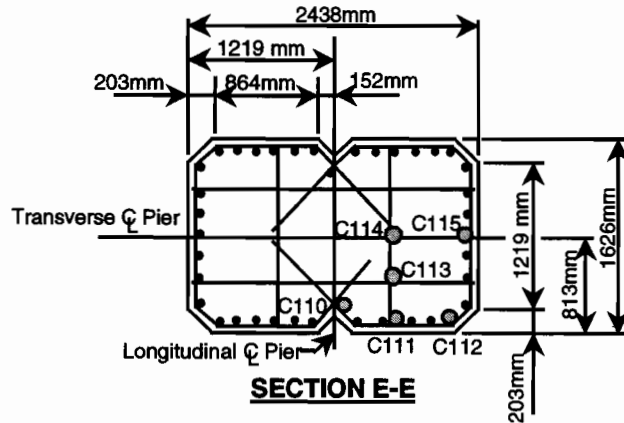
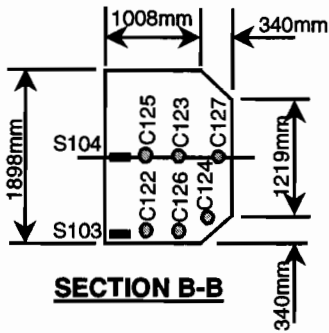
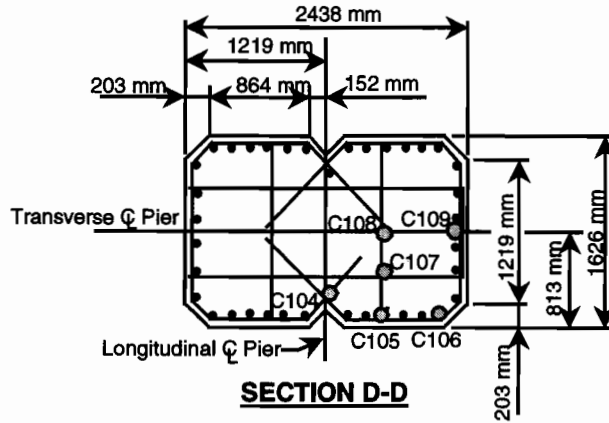
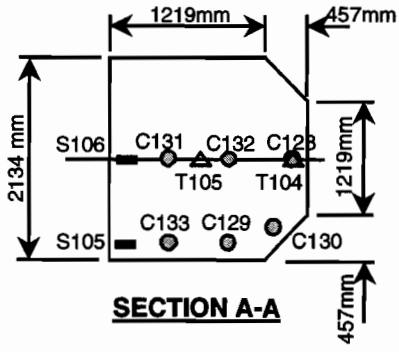
2.3.1 Mainlane Pier

The downstation right side quadrant of mainlane pier D6 was instrumented with C-gauges, S-gauges, and thermocouples. Figure 2.33 shows that C-gauges were placed at six sections along the height of the pier. These gauges were intended to follow the flow of compressive forces from the bearing pedestal to the footing. Demec points were also located on the outside of the pier at the same elevations as the C-gauges. When the pier was redesigned as a cast-in-place pier, heavy reinforcement was added to the capital, particularly on the inside face of the Y. Strain gauges S101 through S106 were installed on the hooked bars detailed in the left half of the capital in Figure 2.33. These S-gauges and the C-gauges were located as shown in the sections in Figure 2.34. Several thermocouples were also installed to measure the thermal gradient between the surface concrete and the core of the pier. The structural steel pipes had an array of strain gauges installed on their surface, both inside and outside of the concrete. The S-gauges on the pipes were intended to measure the force in the pipes, and measure the change in force in the pipes near the anchor plates at the end of each pipe. The location of the pipe gauges is shown in Figure 2.35. Thermocouples were also installed in the pipes so that thermal-induced stresses could be evaluated. Even though the loading on the pier was always symmetric from the superstructure, both sides of the pier should have been gauged for redundancy.



Note: Sections A-A through F-F shown in Figure 2.34

Figure 2.33 Elevation of Y-pier with gauge locations



LEGEND

- C-Gauge
- Strain Gauge
- ▲ Thermocouple

Figure 2.34 Y-pier sections showing gauge locations

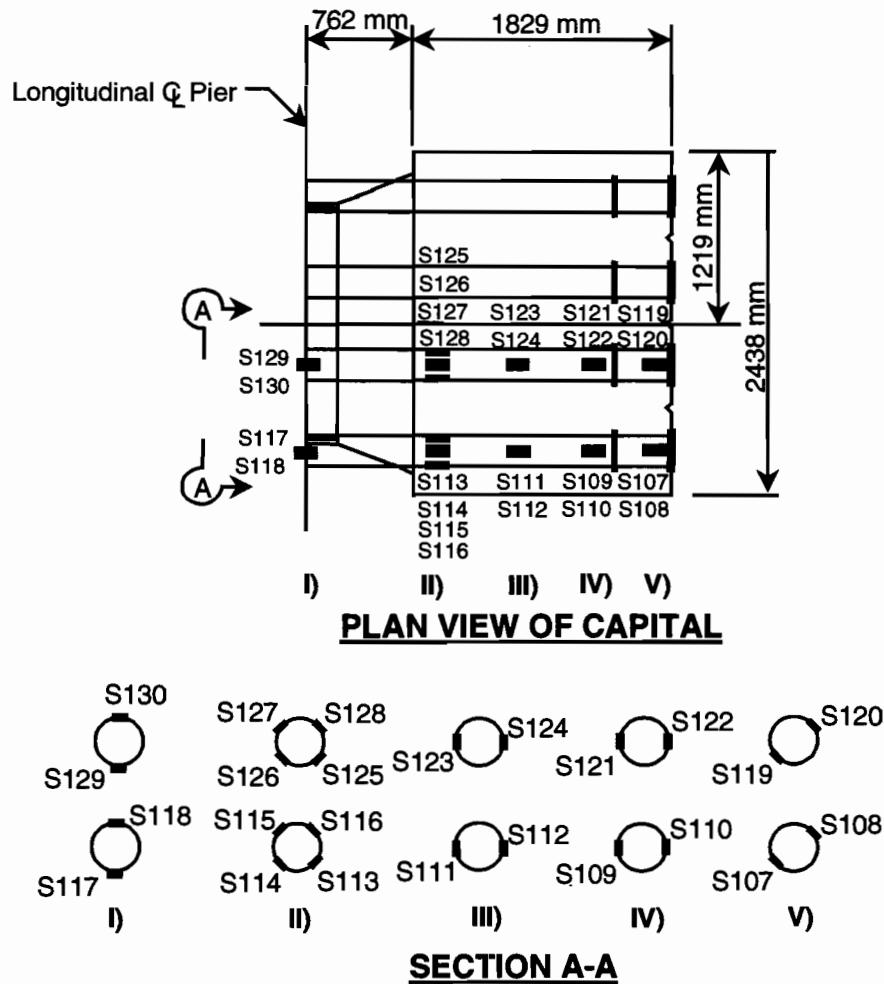


Figure 2.35 Plan view of Y-pier showing gauge locations

2.3.2 Three-Span Mainlane Box Girder Unit

The mainlane girder for span D5, shown in Figure 2.36, had two segments heavily instrumented, D5-9 and D5-16. Deviator segment D5-12 also had considerable instrumentation. The taut wire measurement system was used in span D5, as well in spans D4 and D6, during post-tensioning of tendons and during live-load tests. Tendon gauges and epoxy sleeve mounted Demec points are shown in Section A-A in Figure 2.37. Gauges were located along the tendon to measure friction losses through the deviators during post-tensioning, and to measure changes in tendon force from live loads.

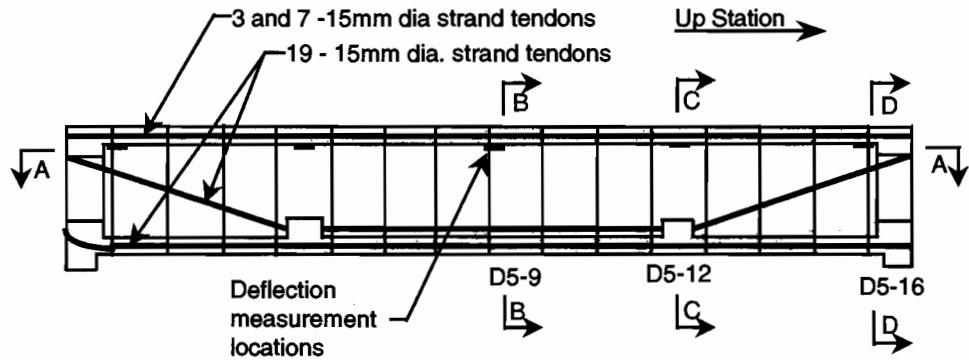
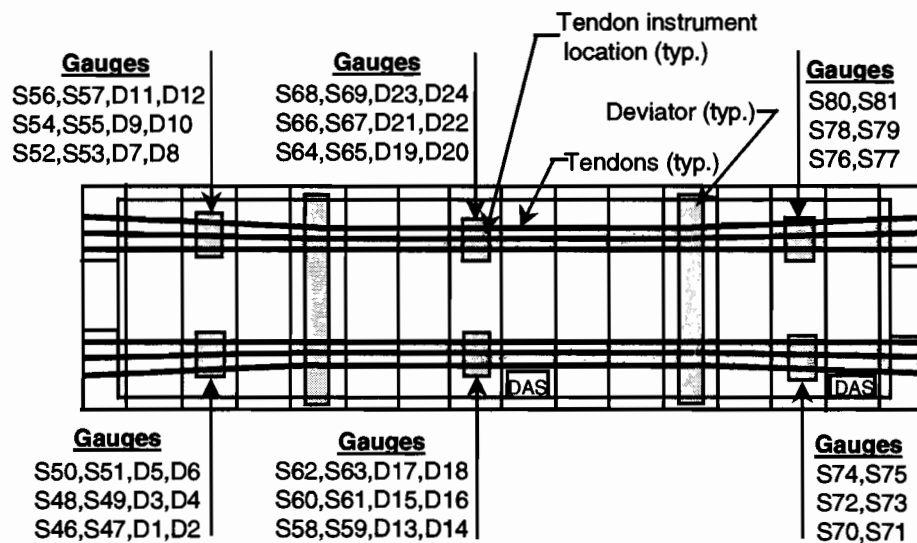


Figure 2.36 Elevation of mainlane girder D5 with deflection measurement locations



SECTION A-A

Figure 2.37 Tendon gauge locations for mainlane girder D5

Section B-B in Figure 2.38 shows the location of the longitudinally oriented C-gauges and Demec points in segment D5-9. The right half of the section was more heavily instrumented than the left half. Gauges were spaced closely above the right web to measure changes in strain transversely due to shear lag effects from bending moments. C-gauges were also located transversely around the cross section to measure strains from transverse bending, tension and compression in the webs and flanges. Section B-B in Figure 2.39 shows the location of thermocouples in segment D5-9. This segment was chosen for the thermal gradient study because its heat flow would not be influenced by large volumes of concrete such as the deviator beams and diaphragms, and could use the same data acquisition system as the midspan C-gauges. Thermocouples were placed densely on the right side of the section, including across web and flange widths, and vertically up the left web for redundancy and directional effects.

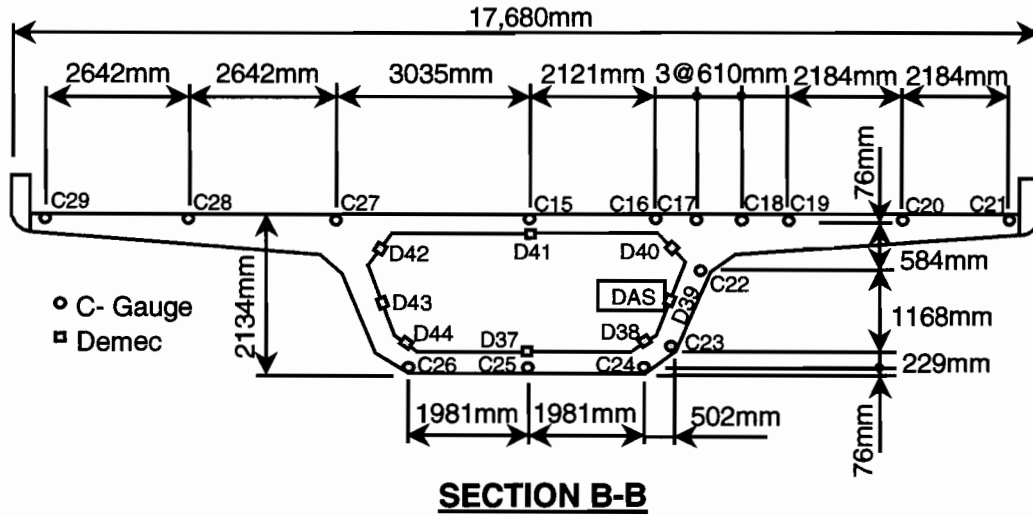


Figure 2.38 Strain gauge locations for segment D5-9

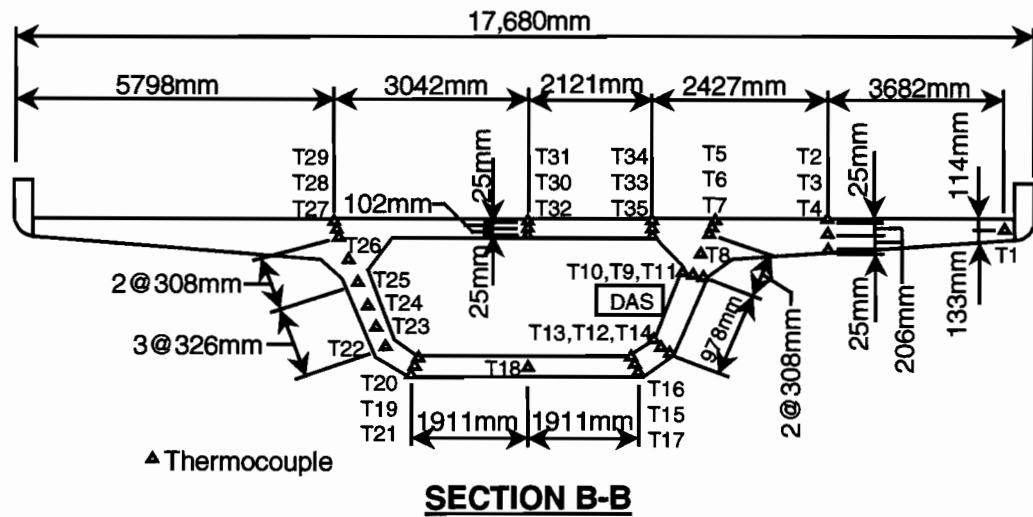


Figure 2.39 Thermocouple locations for segment D5-9

The longitudinally oriented C-gauges in D5-16, the upstation anchor segment, are shown in Figure 2.40. The anchor segment has a short length of typical section cast onto it downstation from the diaphragm for match casting purposes. This is where the C-gauges were located. The Demec points shown in Figure 2.40 were actually located in segment D5-15. The distribution of these gauges was similar to that in segment D5-9, but was symmetric for redundancy. The density of the longitudinally oriented C-gauges should have been more dense, especially in the top flange, as was done later for the Ramp P girder.

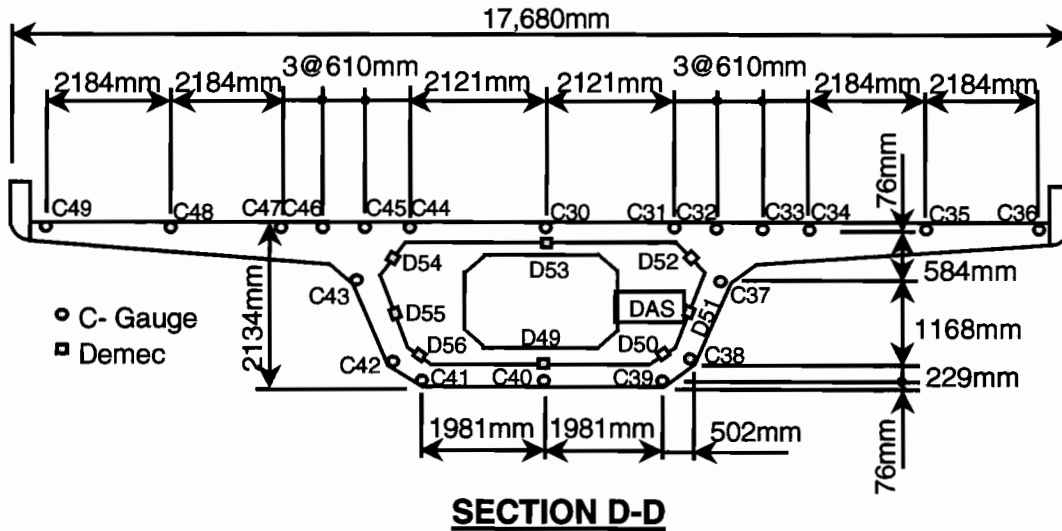


Figure 2.40 Longitudinal strain gauge locations for segment D5-16

The deviator segment shown in Figure 2.41 was instrumented with strain gauges near the deviation pipes on the right hand side of the section only. Gauges were installed directly on the rebars at locations of anticipated cracks. Section G-G in Figure 2.41 shows that the gauges were installed on three transverse planes. Since the deviator was designed as an inverted T-beam, S-gauges should also have been installed on the heavy top bar near the centerline of the cross section. This installation pattern was later done on the deviator in Ramp P. However, cracks only occurred in the anticipated locations.

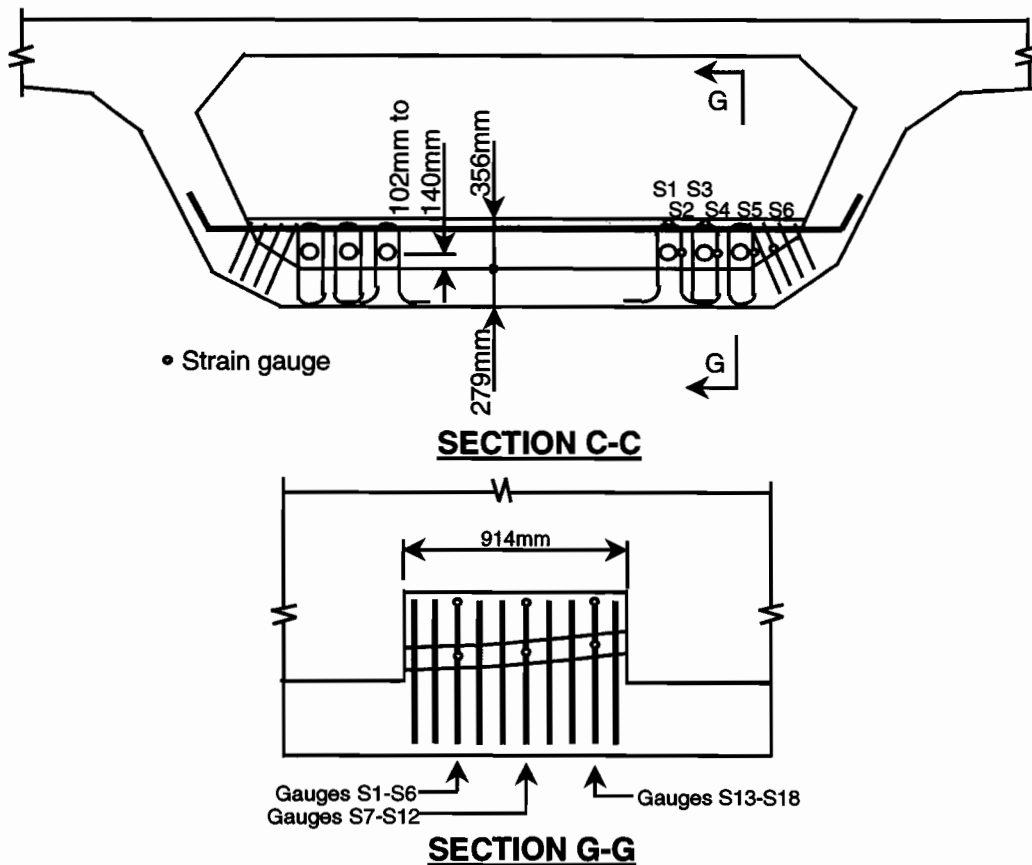


Figure 2.41 Strain gauge locations for deviator segment D5-12

Strain gauges were also located directly on the heavy bars in the anchor segment D5-16, as shown in Figure 2.42. The diaphragm was designed using the strut-and-tie method. The bars placed to act as ties from the design were the ones that received the most instrumentation. Gauges were located on these bars at locations of anticipated cracks, such as near chamfered corners.

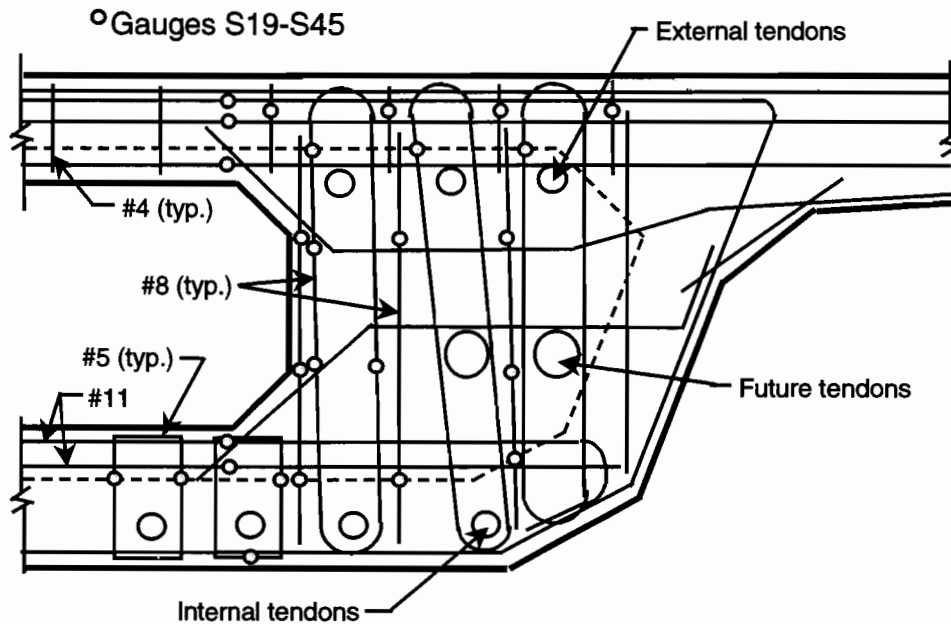
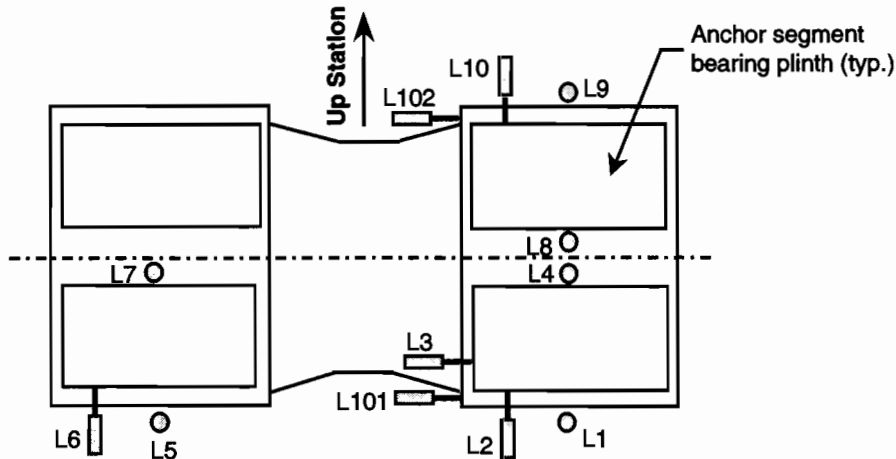


Figure 2.42 Strain gauge locations for anchor segment D5-16

Linear potentiometers were placed around the bearing plinths at pier D6 to measure girder end rotations during live-load tests, and measure any horizontal movement of the superstructure. The location of these instruments is shown in Figure 2.43. The movements were so small that the measurements were of little value during the live-load tests, but did provide good data for daily thermal fluctuations. This data were used to time the casting of the cast-in-place deck joints to reduce tension in the joint during the initial curing period.

Legend

- Vertically oriented linear pot
- ▭ Horizontally oriented linear pot



Plan View - Pier D6

Figure 2.43 Linear potentiometer locations at pier D6

The cast-in-place deck joint between spans D5 and D6 was instrumented with an array of longitudinally oriented C-gauges, similar in transverse distribution to those in the top flange of segment D5-16. The deck joint was expected to go into tension and compression from thermal forces, and possibly from live-load forces. Gauges were located top and bottom of the deck joint, as shown in Figure 2.44, to measure bending strains as well.

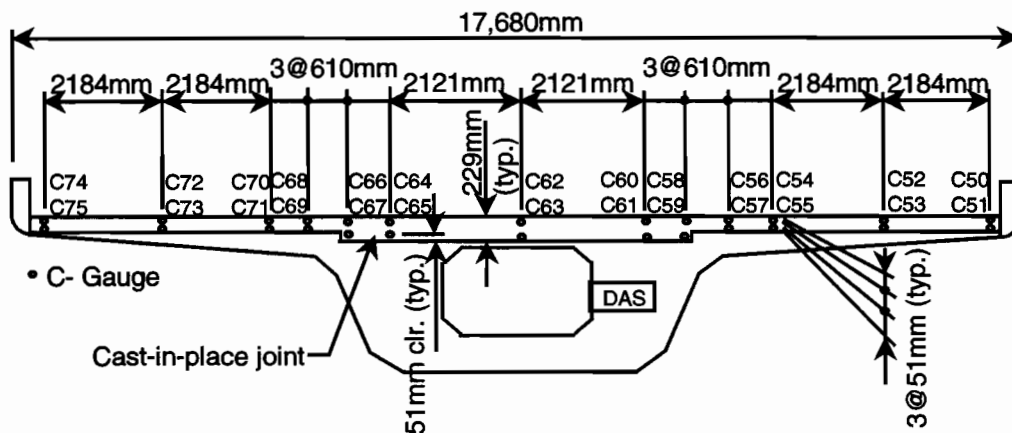


Figure 2.44 Strain gauge locations for the cast-in-place joint over pier D6

2.3.3 Segmental Large Ramp Pier

The segmental large ramp pier P16 was instrumented at three sections in the column, and throughout the capital. Figure 2.45 shows an elevation of the pier and the location of the instrumented segments. Figure 2.46 shows the instrumentation in segment PC16-1. The gauges were located just above the cast-in-place base. The segment is heavily instrumented with C-gauges, and lightly instrumented with thermocouples to compare its temperature with that of the other instrumented segments. Figure 2.47 shows the instrument locations in segment PC16-5. This segment was selected for the thermal gradient study. It had optimal exposure to the sun, and was sufficiently far from the capital and the shaded sections of the bottom of the pier to prevent vertical

heat flow. Figure 2.48 shows the gauge locations in segment PC16-7. The gauge distribution is identical to that in segment PC16-1, with the plane of gauges located 610mm beneath the solid capital segment.

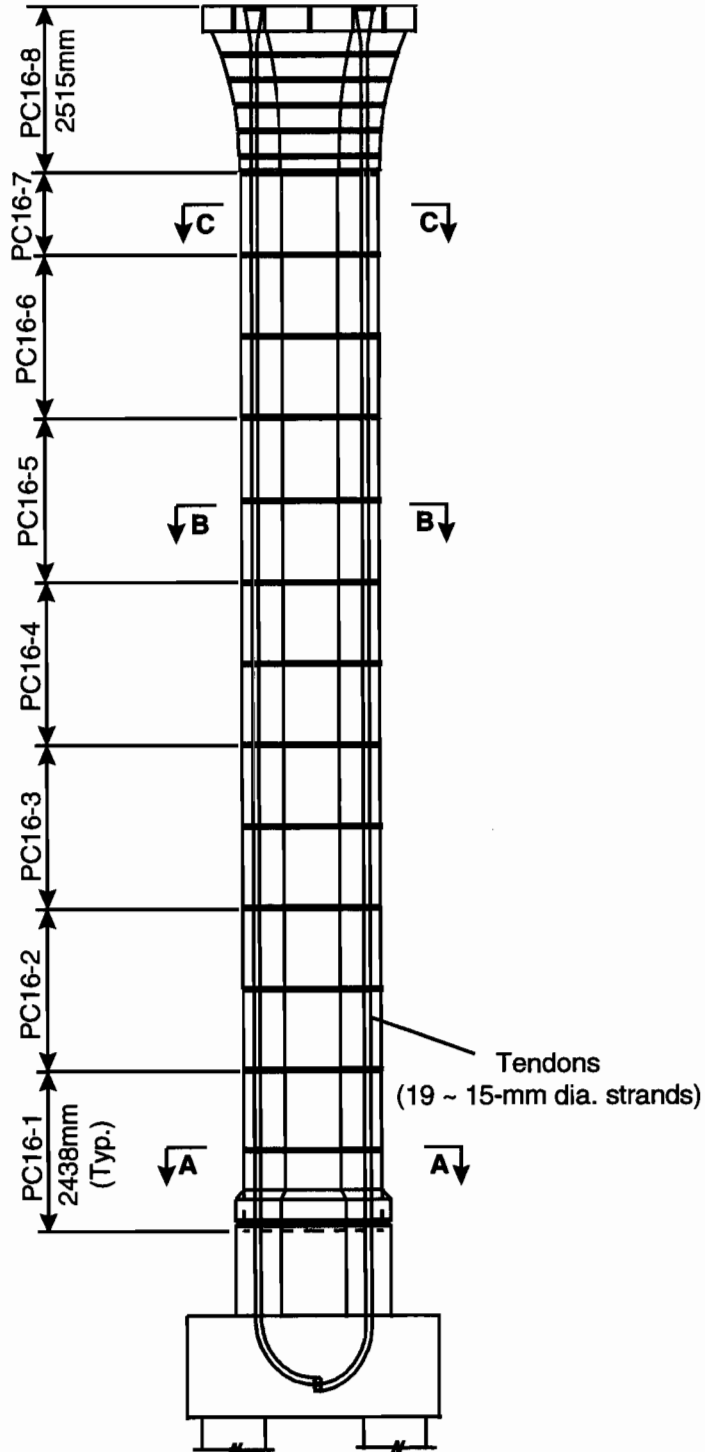
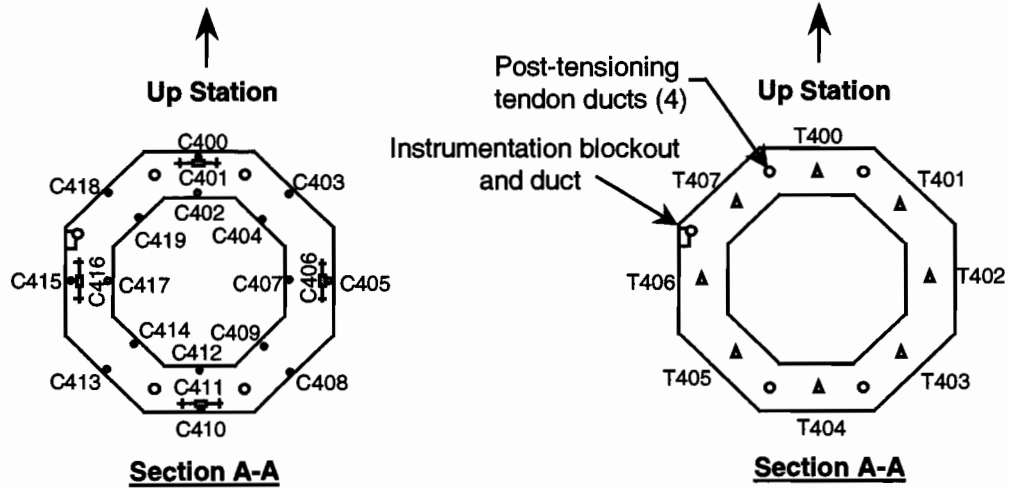


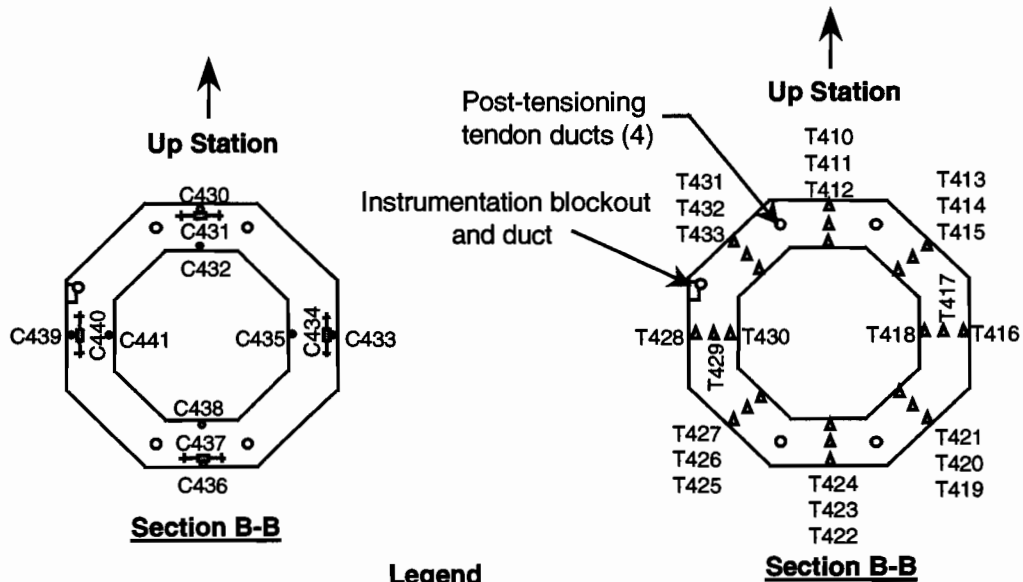
Figure 2.45 Elevation of large ramp pier P16 with segment identification



Legend

- +□+ Concrete Strain Gauge Oriented Horizontally
- Concrete Strain Gauge Oriented Vertically
- ▲ Thermocouple

Figure 2.46 Segment PC16-1 sections with gauge locations



Legend

- +□+ Concrete Strain Gauge Oriented Horizontally
- Concrete Strain Gauge Oriented Vertically
- ▲ Thermocouple

Figure 2.47 Segment PC16-5 sections with gauge locations

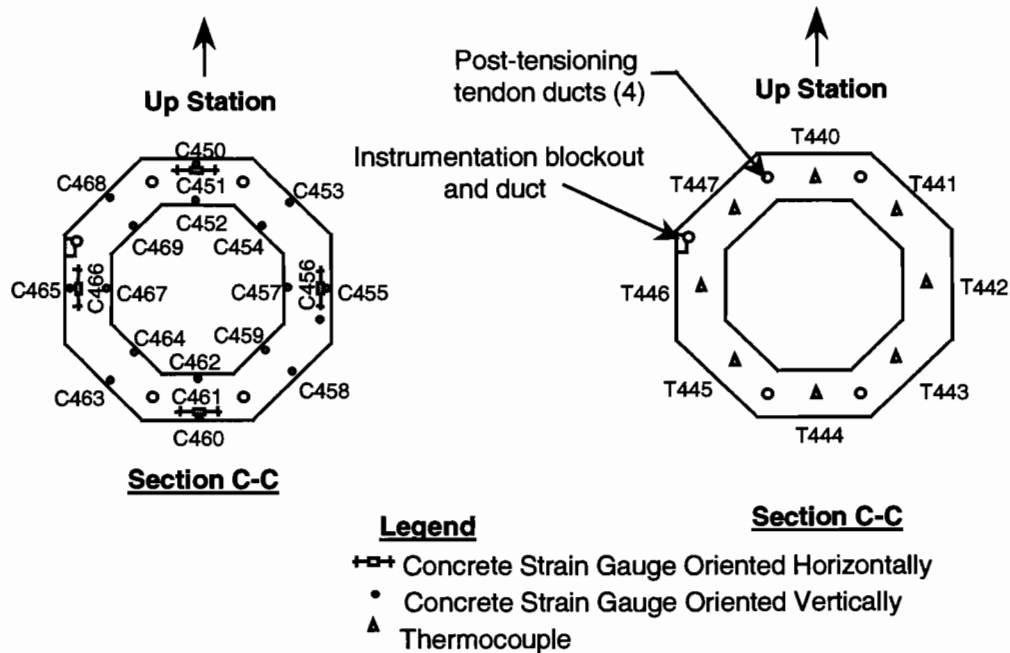
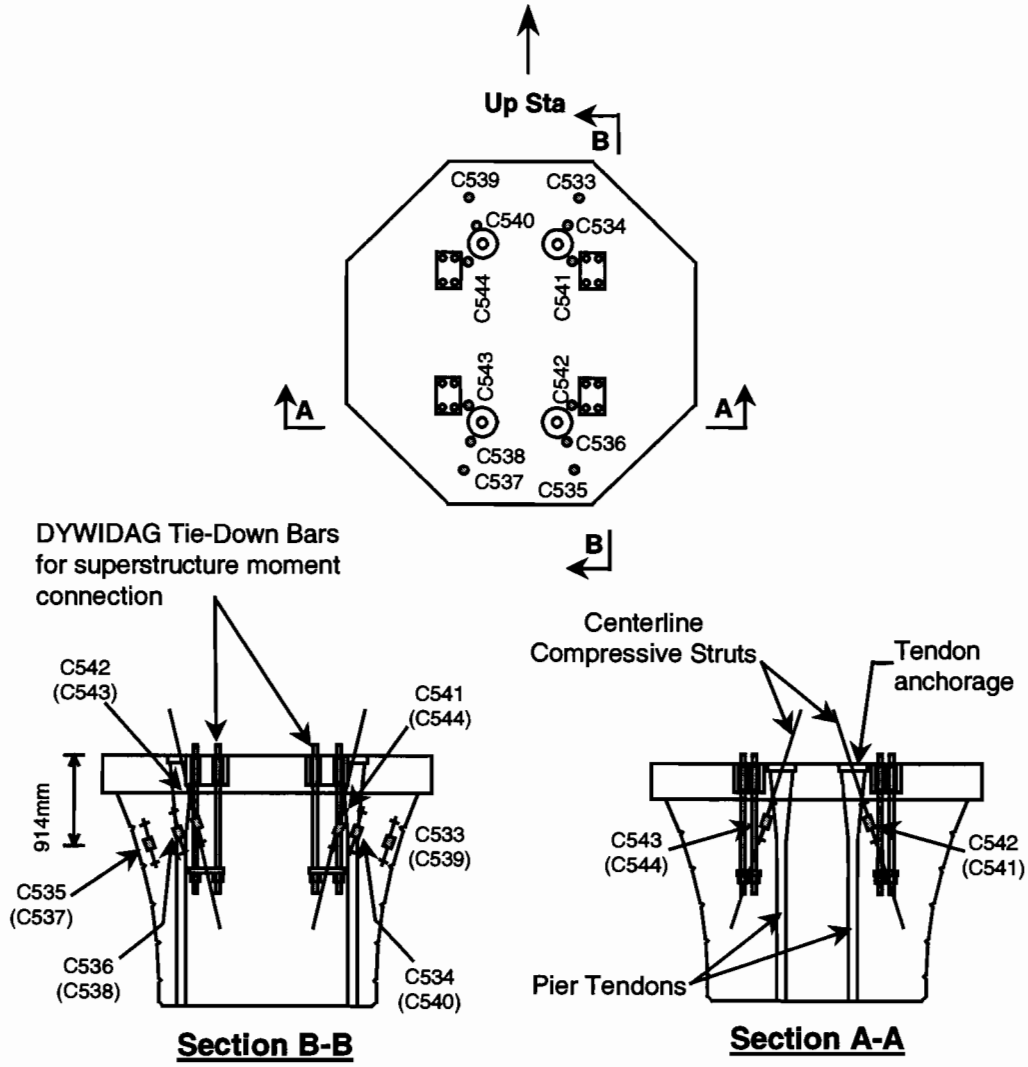


Figure 2.48 Segment PC16-7 sections with gauge locations

The capital segment PC16-8 was heavily instrumented with C-gauges, S-gauges, and thermocouples. Figure 2.49 shows the location of the C-gauges intended to measure compressive forces from the girder bearings and main post-tensioning anchorages, and the anchor plates of the tie down bars. The C-gauges in Figure 2.50 are similar in distribution to the gauges in segment PC16-7, and were intended to measure compressive strains from the superstructure dead-load axial forces and bending moments.



(Gauges C533, C535, C537, C539 located at 75mm clear cover.)
 (Gauges C534, C536, C538, C540 located at 455mm clear cover.)

Legend

- C-gauge oriented along compressive struts
 () denotes gauges on rear strut
- Concrete Strain Gauge
 (Top View)

Figure 2.49 Segment PC16-8 top C-gauge locations

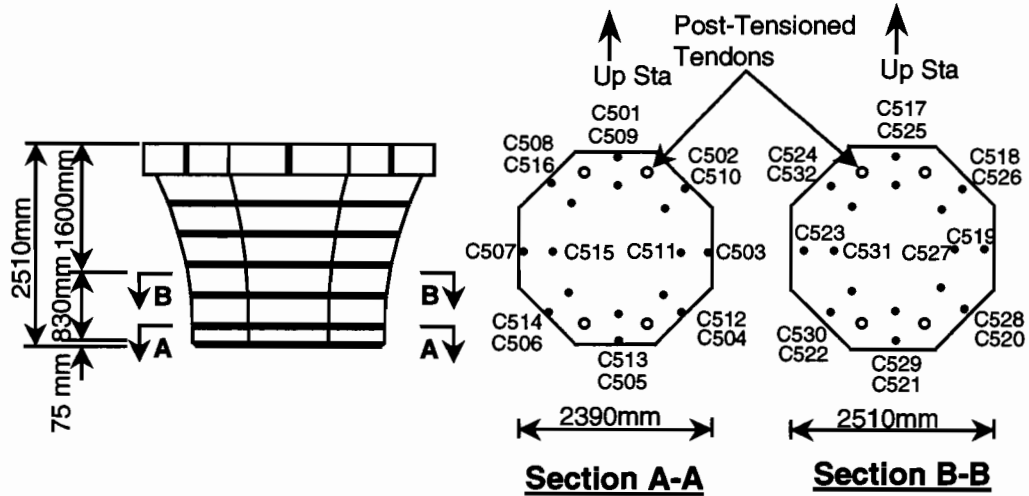


Figure 2.50 Segment PC16-8 bottom C-gauge locations

Since the capital is an excellent example of a strut-and-tie structure, the heavy reinforcing bars located in the top and bottom of the pier intended to act as ties were instrumented. Figure 2.51 shows the S-gauge locations on these tie bars. The ramp girder anchor segments were post-tensioned to the capital with the 16 threadbars shown in Figure 2.52 to form a moment connection. These threadbars were cast into the capital, then coupled to bars extending up to the deck of the anchor segments. Force in these bars was monitored at three elevations by the strain gauges shown in Figure 2.52.

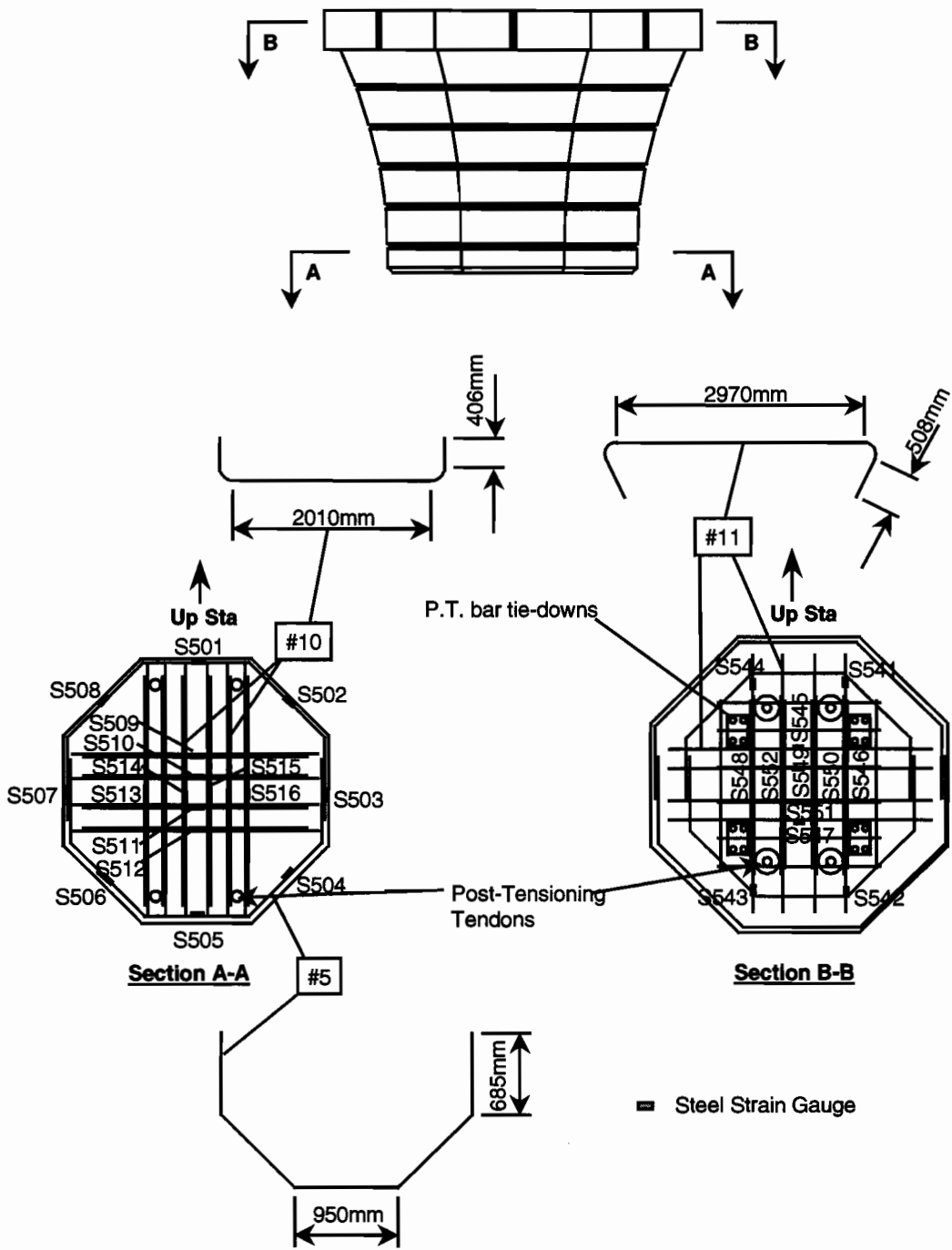
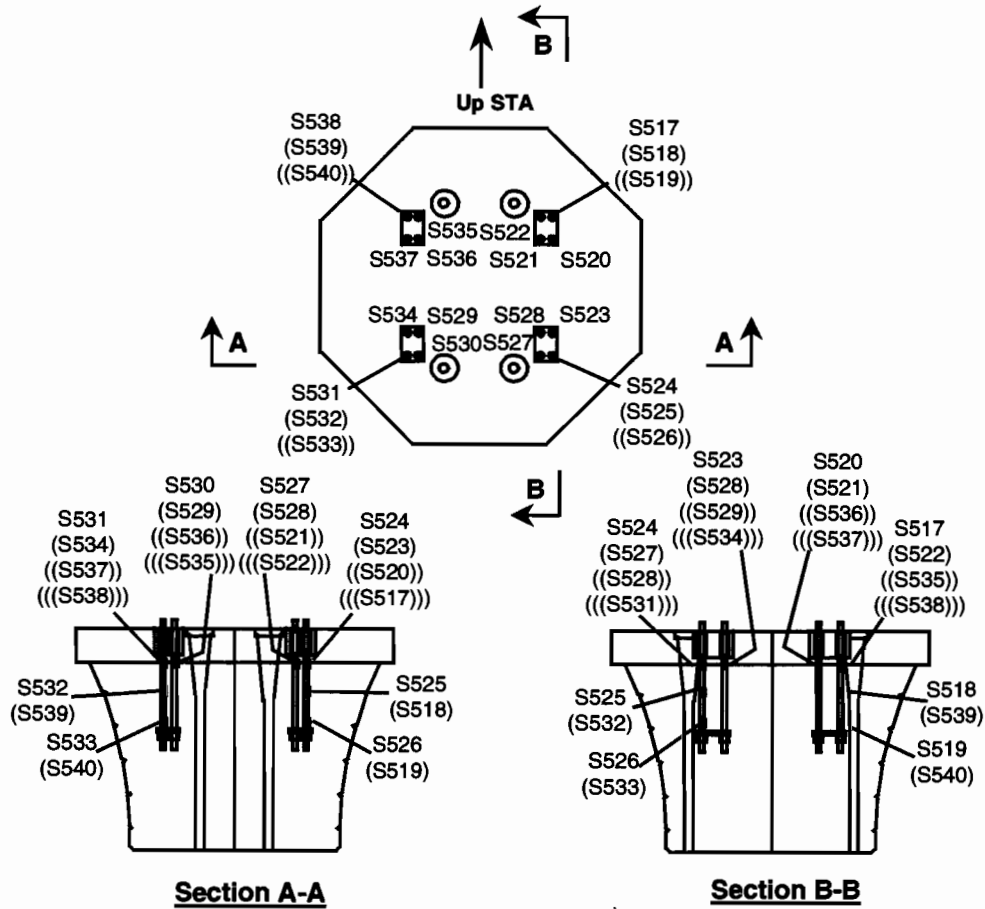


Figure 2.51 Segment PC16-8 S-gauge locations on rebar



Notes:
 Gauges denoted by () located "behind" gauges shown.
 Gauges denoted by (()) located "behind" gauges denoted by ().
 Gauges denoted by ((())) located "behind" gauges denoted by (()) .

Figure 2.52 Segment PC16-8 S-gauge locations on tie-down bars

2.3.4 Five-Span Ramp Box Girder Unit

The half-span of Ramp P upstation from pier P16 was heavily instrumented. Three full cross sections were instrumented for axial, bending and torsional strains. Three D-zones were also instrumented for strains, and one section was thoroughly instrumented for concrete temperatures. Tendons on either side of one vertical deviator were instrumented with strain gauges to measure friction losses during post-tensioning, and strain changes during live-load tests. The instrumented segments are shown in the elevation in Figure 2.53, along with the location of tiltmeter plates on the deck used during balanced cantilevering. The location of tendon gauges is shown in Figure 2.54.

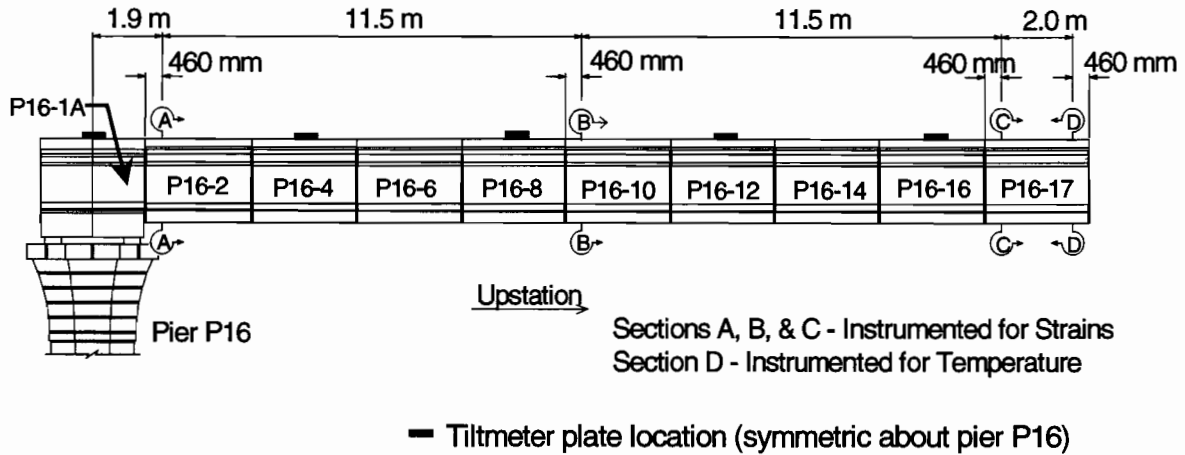


Figure 2.53 Elevation of Ramp P, span P16, with segment identification

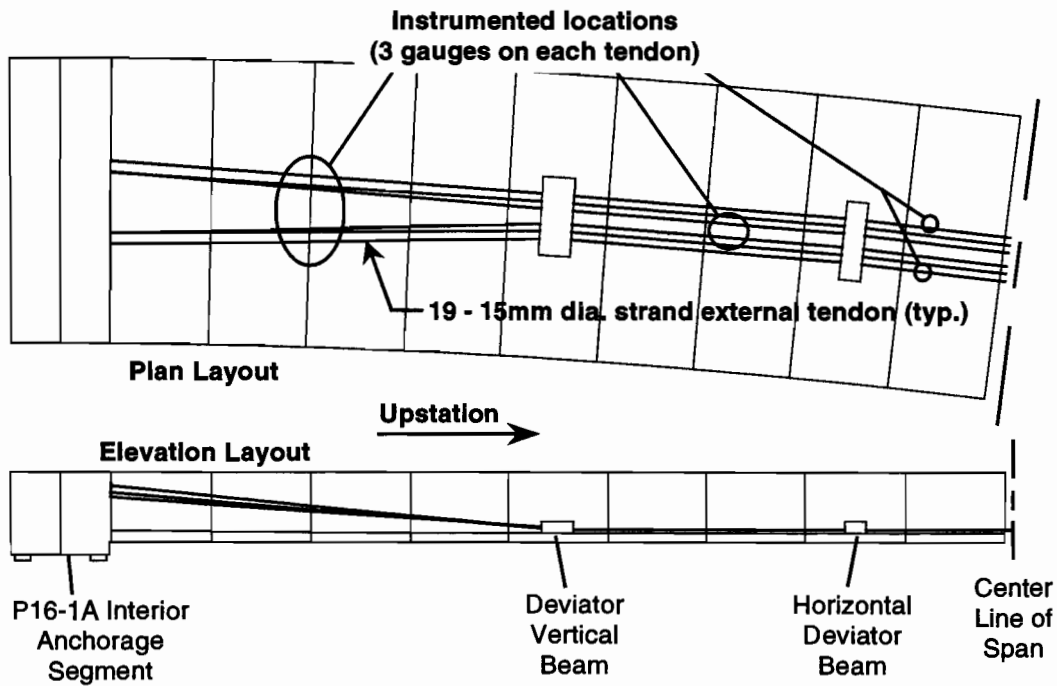


Figure 2.54 Ramp P tendon gauge locations

Anchor segment P16-1A was designed by the strut-and-tie method, but was post-tensioned vertically. This greatly reduced the cracking in this segment when compared to the mainlane anchor segments. Strain gauges were located on the diaphragm face shown in Figure 2.55 at locations where minor cracking did occur. These few S-gauges were wired into the data acquisition system in segment P16-2. P16-2 was instrumented with a symmetrical array of C-gauges and Demec points, as shown in Figure 2.56. Eight strain gauge rosettes were in the segment to measure shear strains and torsional effects.

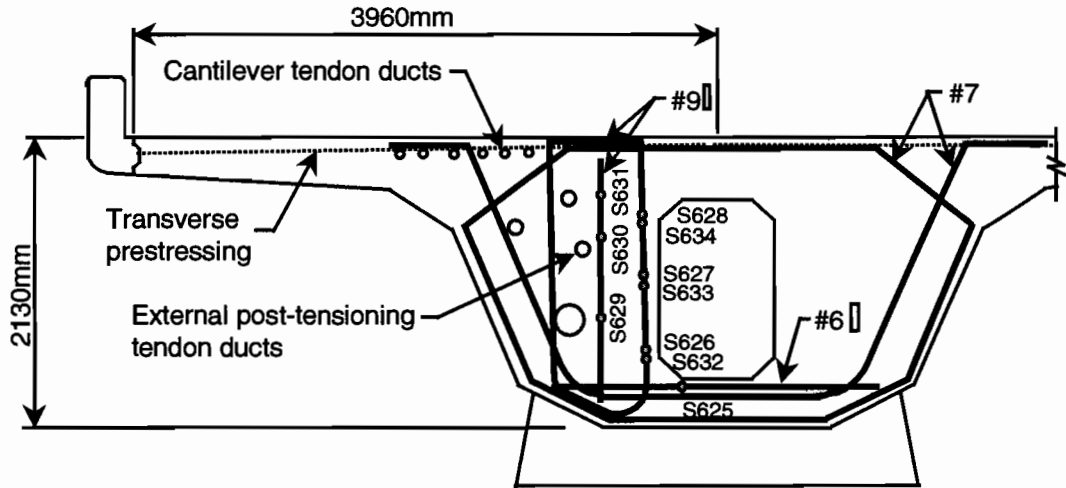


Figure 2.55 Anchor segment P16-1A section with gauge locations

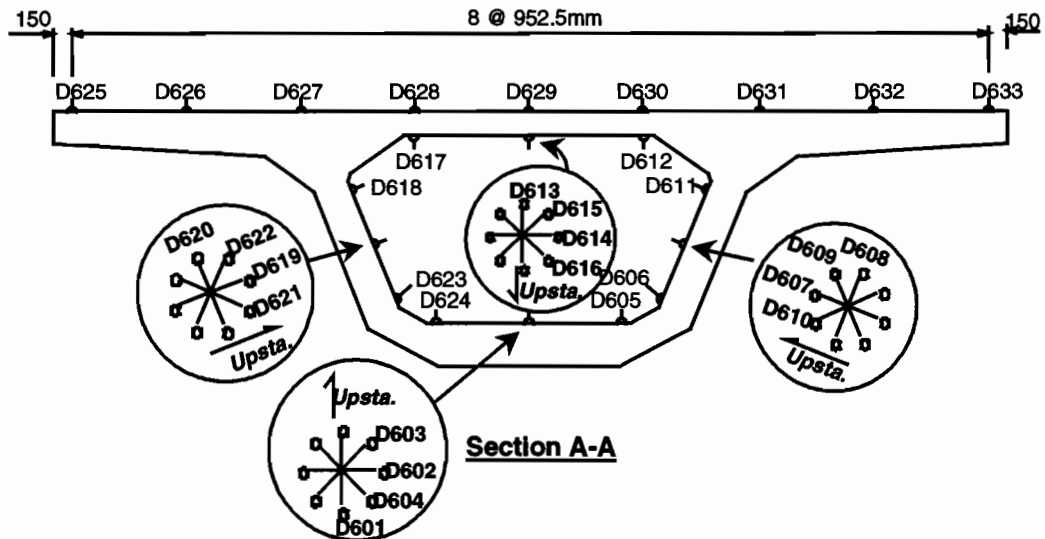
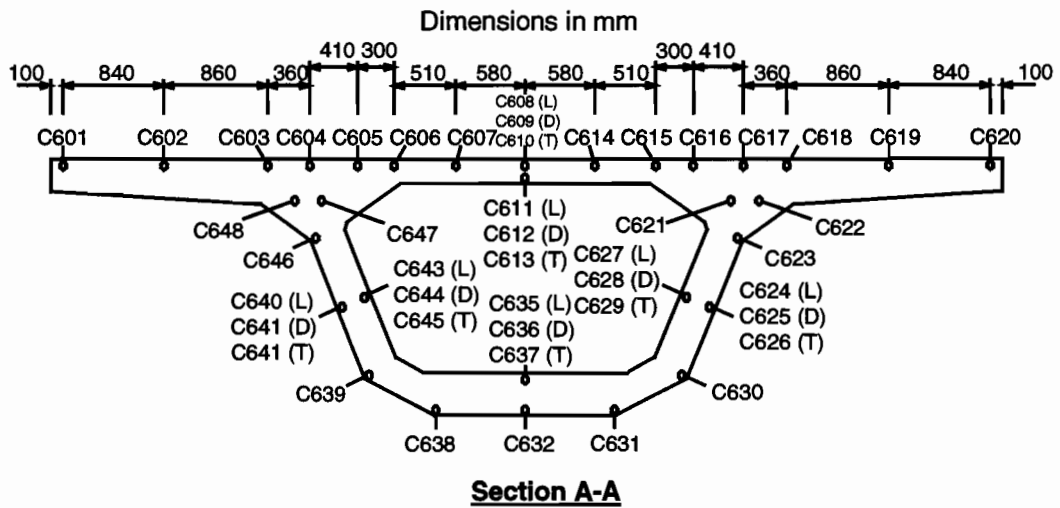


Figure 2.56 Segment P16-2 sections with gauge locations

Segments P16-10 and P16-17 were instrumented with an array of C-gauges and Demec points identically to segment P16-2, as shown in Figures 2.57 and 2.58. Segment P16-17 is the midspan segment and P16-10 is at the quarter point. The gauging density in these segments was sufficiently increased over that of the mainlane, but more cross sections needed to be instrumented since the gauges in P16-2 were quite close to the heavy end diaphragm, and the gauges in P16-10 were too close to the vertical deviator.

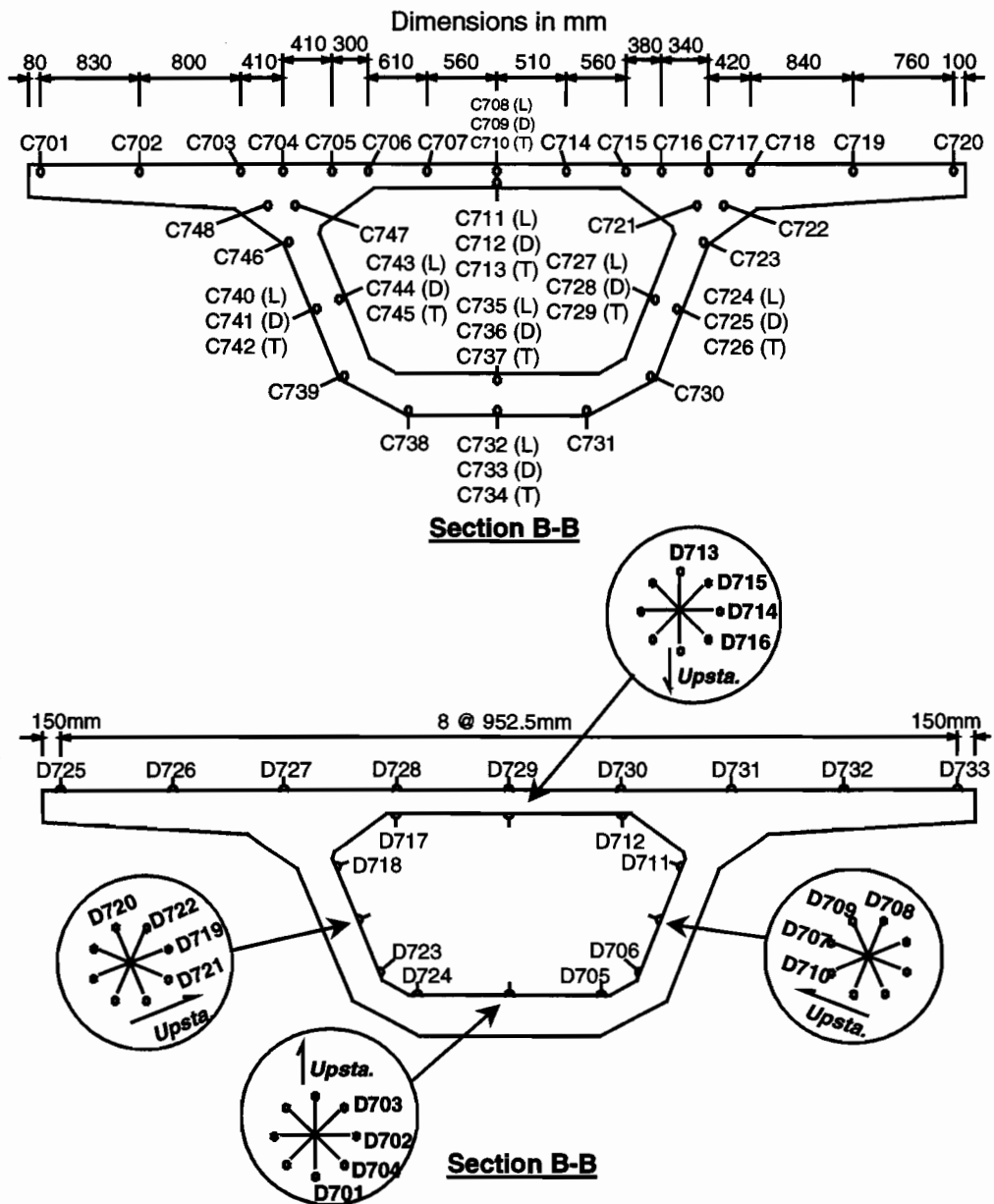


Figure 2.57 Deviator segment P16-10 sections with gauge locations

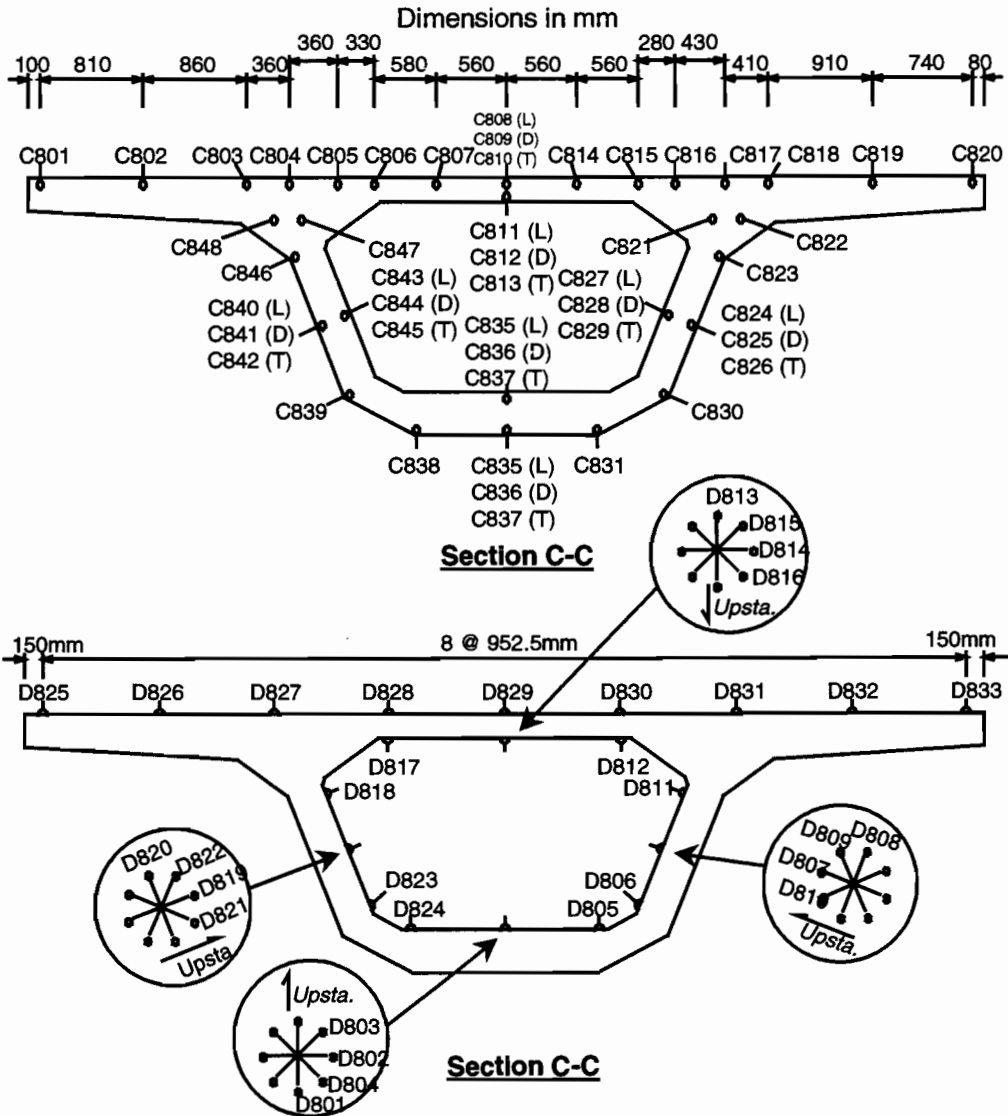


Figure 2.58 Segment P16-17 sections with strain gauge locations

Segment P16-17 was selected for the thermal gradient study. The array of thermocouples, shown in Figure 2.59, was more dense than the mainlane and symmetrical. This instrumentation was as thorough as has been done in any study to date, and was possible because 128 channels were available for the gauges in segment P16-17.

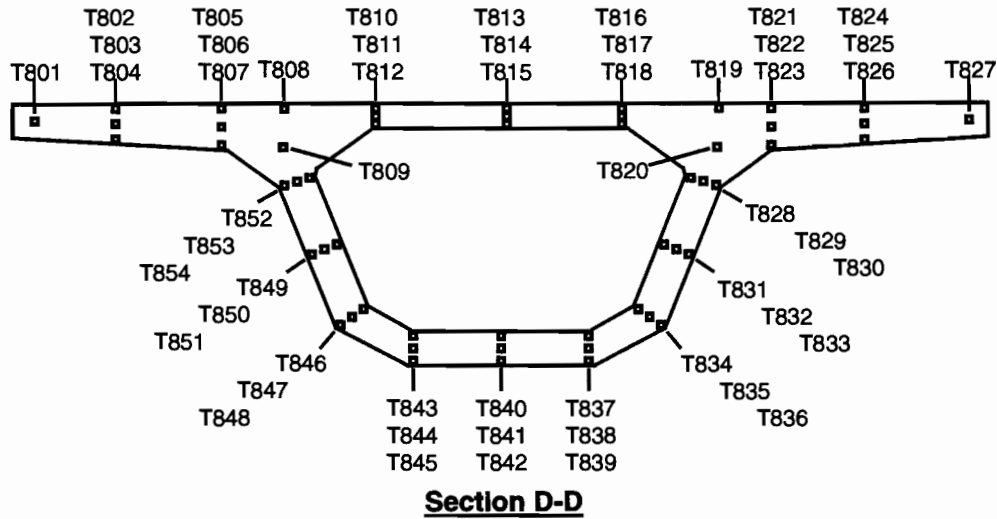
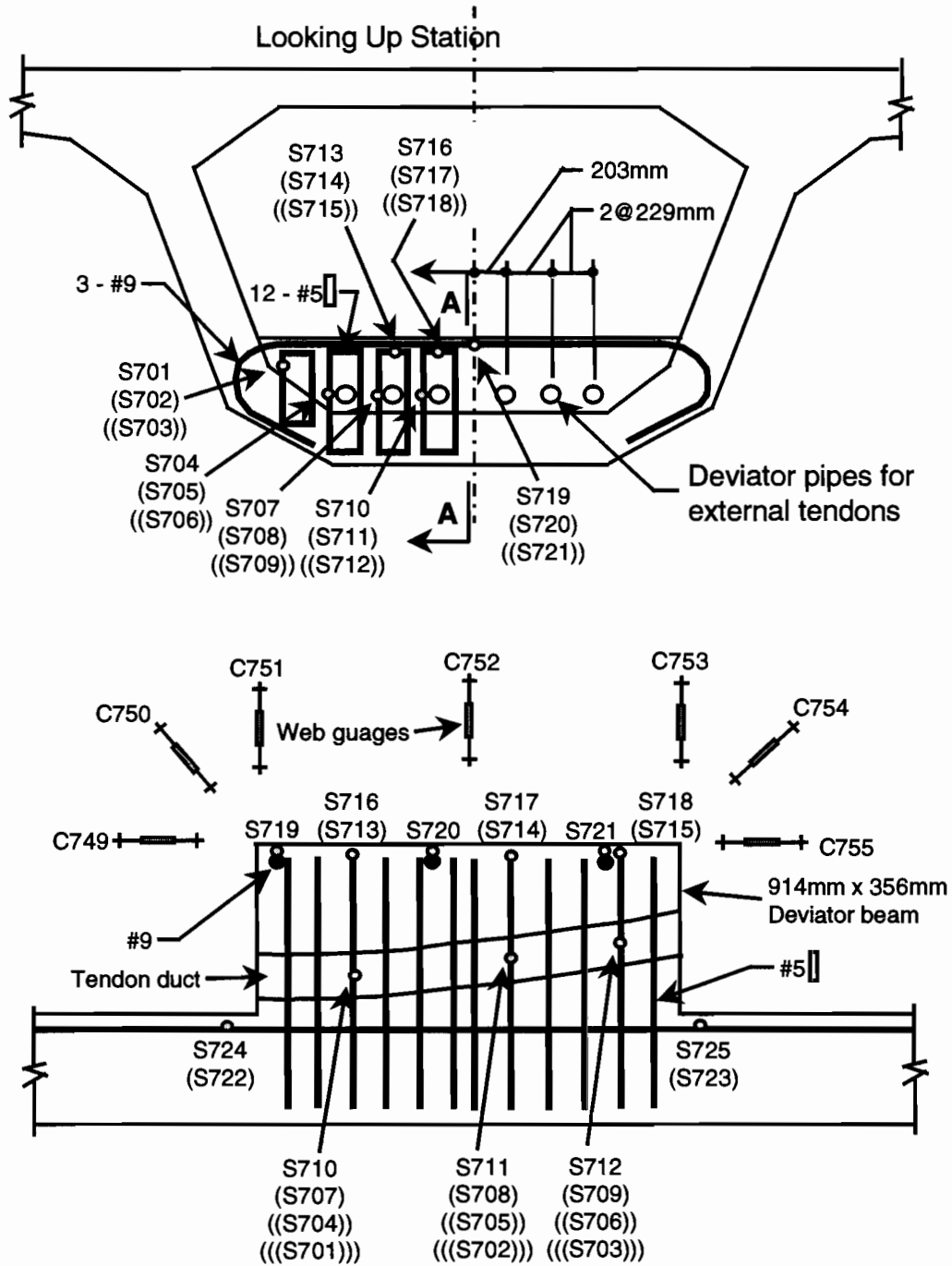


Figure 2.59 Segment P16-17 section with thermocouple locations

The deviator beam in segment P16-10 was similar in instrumentation to the deviator on the mainlane, with the addition of gauges mounted on the heavy top bars, and C-gauges located in the web, as shown in Figure 2.60. Unfortunately, gauges S719, S720 and S721 were all destroyed during segment casting. Concrete for the deviator was poured through a hole in the center of the top flange form, and had to be knocked off the deviator bars between lifts so that it would not dry on the bars.



Section A-A

Figure 2.60 Deviator segment P16 section with S-gauge locations on rebar

The bottom slab post-tensioning tendon anchorage blister in segment P16-4 was the third D-zone in Ramp P to be instrumented. S-gauges were located on bars that were expected to go into significant tension. C-gauges were located in the bottom slab and webs of the segment behind the anchorage blister to measure the tensile strain in this region. The location of these gauges is shown in Figure 2.61.

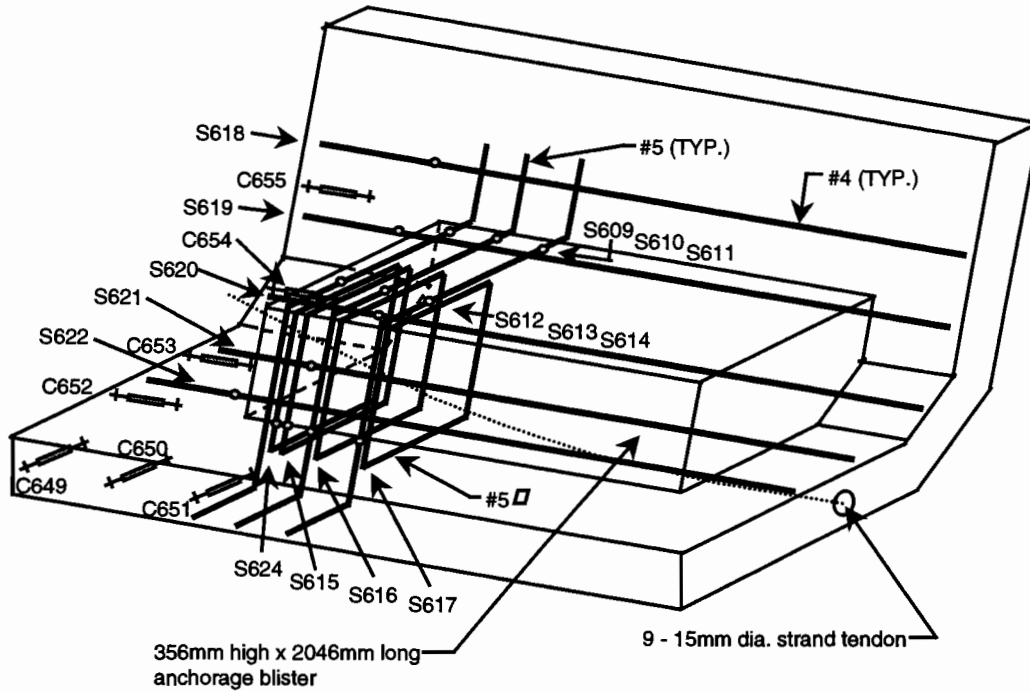


Figure 2.61 Segment P16-4 anchorage blister strain gauge locations

2.3.5 Multiple-Celled Box Girder Units

The cast-in-place transition spans shown in Figure 2.62 were instrumented for deflections only during a live-load test using the taut wire deflection measuring system. Wires were hung down the center of each of the three cells in each span. Deflections were measured at the quarter points of the span, as well as at the girder ends.

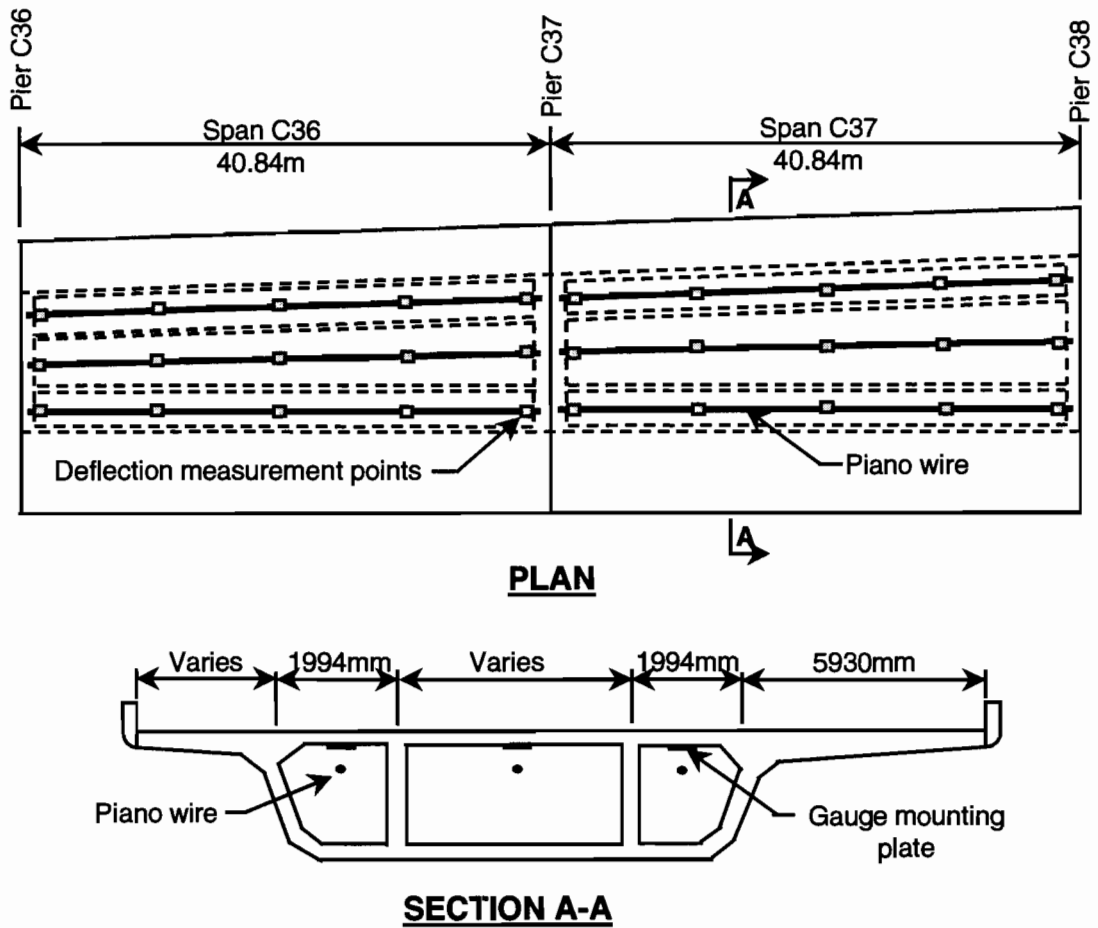


Figure 2.62 Plan and section of transition spans showing instrumentation locations

Three modified spans with cast-in-place gore closure strip were also instrumented for deflections only, as shown in Figure 2.63. The wires were hung down the center of each single-celled box girder.

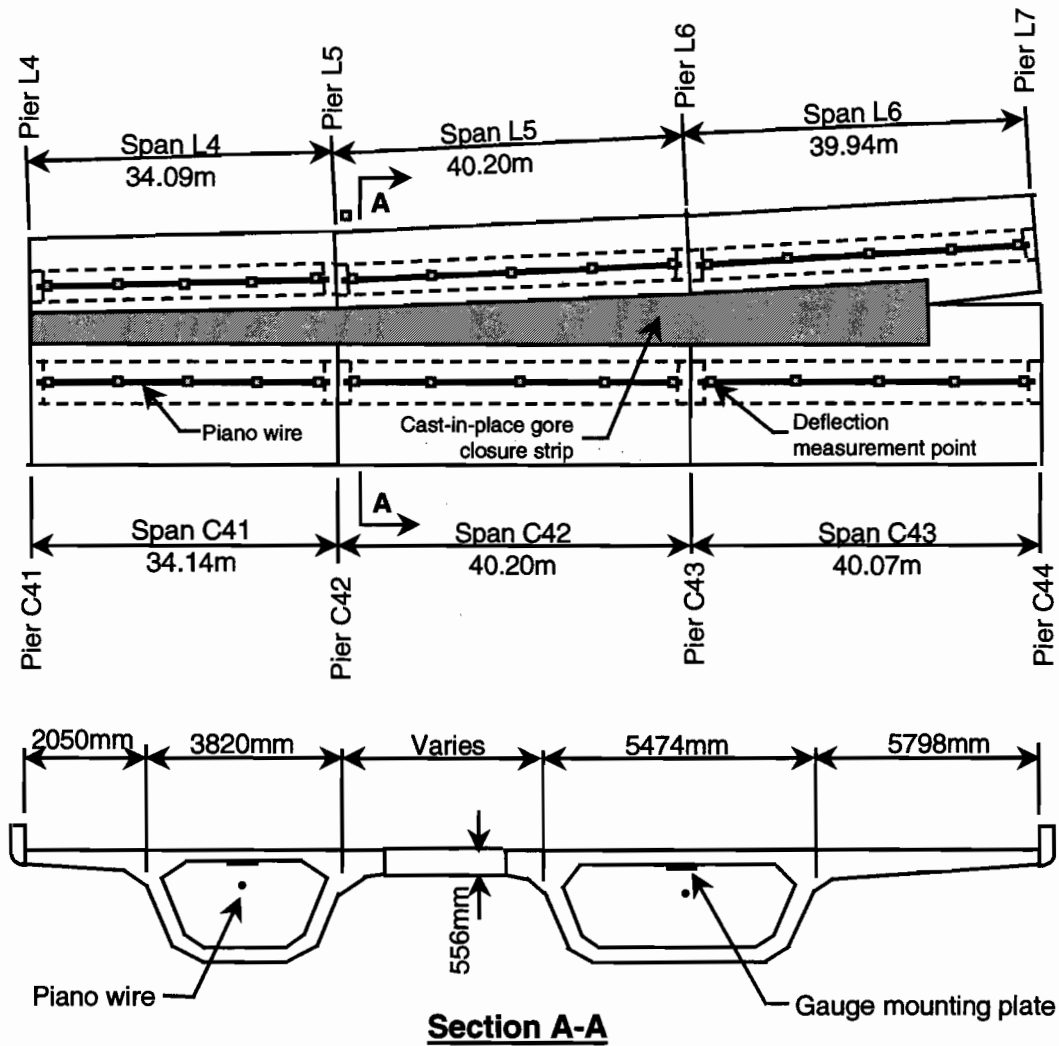


Figure 2.63 Plan and section of modified spans showing instrumentation locations

2.4 MATERIAL PROPERTY TESTS

Three 152mm by 152mm by 533mm concrete prism samples were made for each segment instrumented on the project. These specimens were tested for their moduli of elasticity and coefficients of thermal expansion using the Demec extensometer and a test machine. A concrete prism test specimen is shown in Figure 2.64

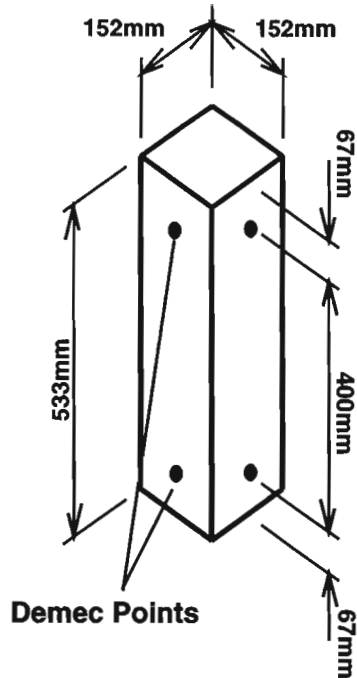


Figure 2.64 Concrete modulus of elasticity test specimen

The results of the modulus of elasticity tests are shown in Figure 2.65 through Figure 2.68. The concrete for the mainlane pier did not come from the batch plant at the precasting yard. The mainlane pier concrete (Figure 2.65) was not as stiff as that used for the precast segments (Figure 2.67). Interestingly enough, the modulus of elasticity of the concrete decreases as the specimens age, and dry out. This was seen in every specimen.

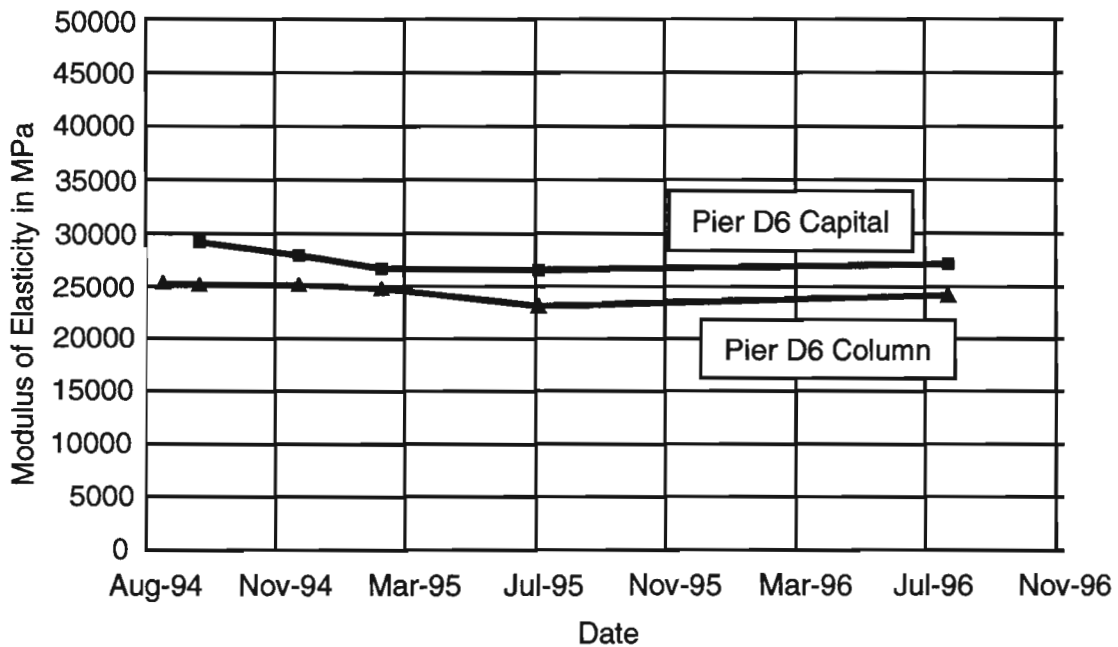


Figure 2.65 Modulus of elasticity test results for mainlane pier D6

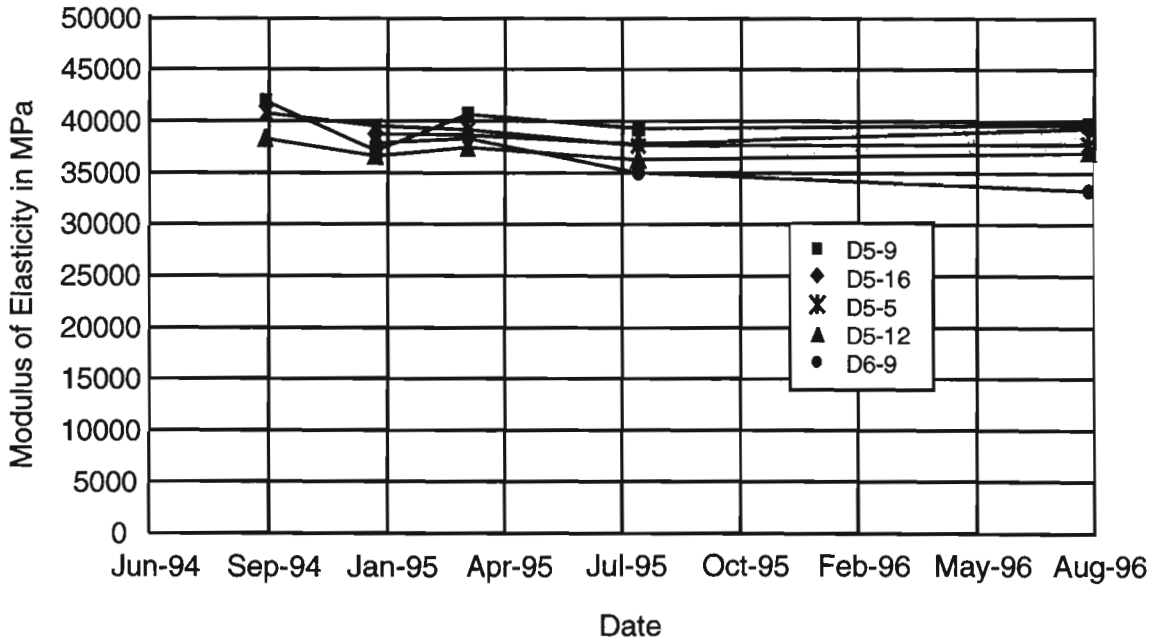


Figure 2.66 Modulus of elasticity test results for mainlane superstructure Unit D2

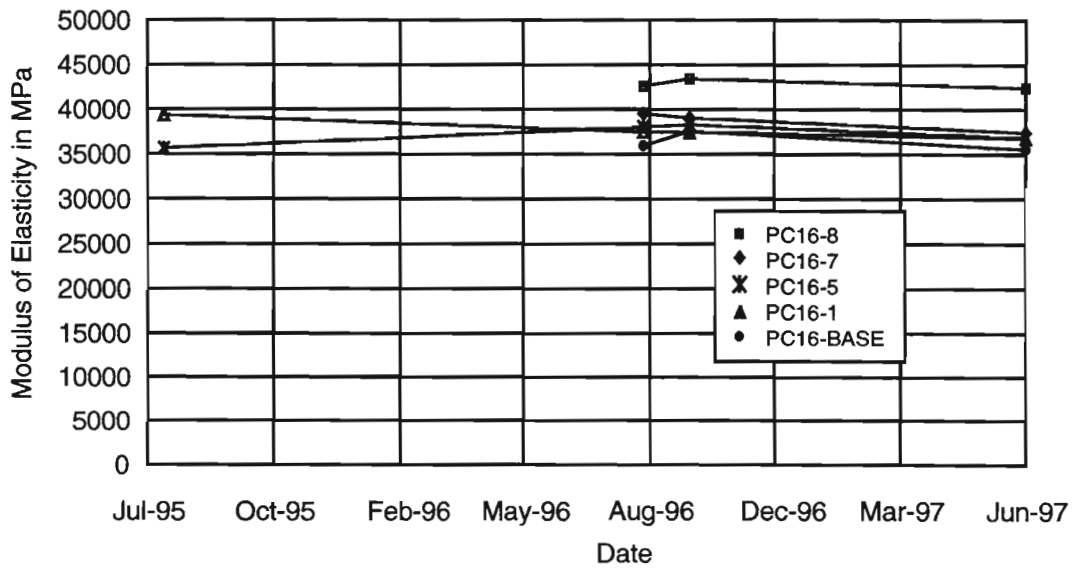


Figure 2.67 Modulus of elasticity test results for large ramp pier P16

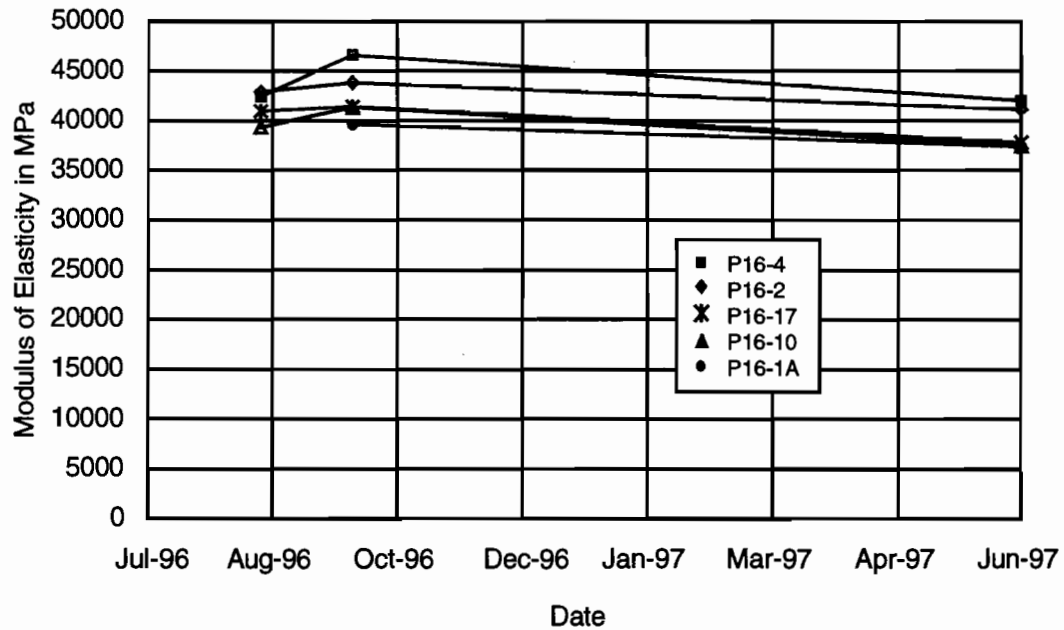


Figure 2.68 Modulus of elasticity test results for Ramp P superstructure

Coefficient of thermal expansion tests were also performed on several of the test specimens. The results are in Table 2.1. The concrete in the mainlane pier once again proved to be substantially different in this material property compared to the concrete in segments from the precasting yard.

Table 2.1 Coefficients of thermal expansion

Segment	Coefficient of Thermal Expansion ($^{\circ}\text{C}^{-1}$)
Pier D6 Column	8.28×10^{-6}
Pier D6 Capital	8.35×10^{-6}
D5-5	9.59×10^{-6}
D5-9	9.79×10^{-6}
D5-12	9.99×10^{-6}
D5-16	10.40×10^{-6}
D6-9	10.40×10^{-6}
PC16-1	9.90×10^{-6}
PC16-5	9.90×10^{-6}
PC16-7	9.00×10^{-6}
PC16-8	10.01×10^{-6}
P16-2	9.00×10^{-6}
P16-10	9.72×10^{-6}
P16-17	9.36×10^{-6}

Concrete compressive strengths (f'_c) measured at the precasting yard for mainlane D are shown in Figure 2.69. Very few of the compressive test cylinders were tested beyond the 7-day break because the 28-day design strength of 37.9Mpa was usually achieved by this point in time. Concrete strengths of over 62Mpa were the norm at 28 days. Strengths probably continued to increase beyond the 28-day strength since 25% of the cementitious material was fly ash.

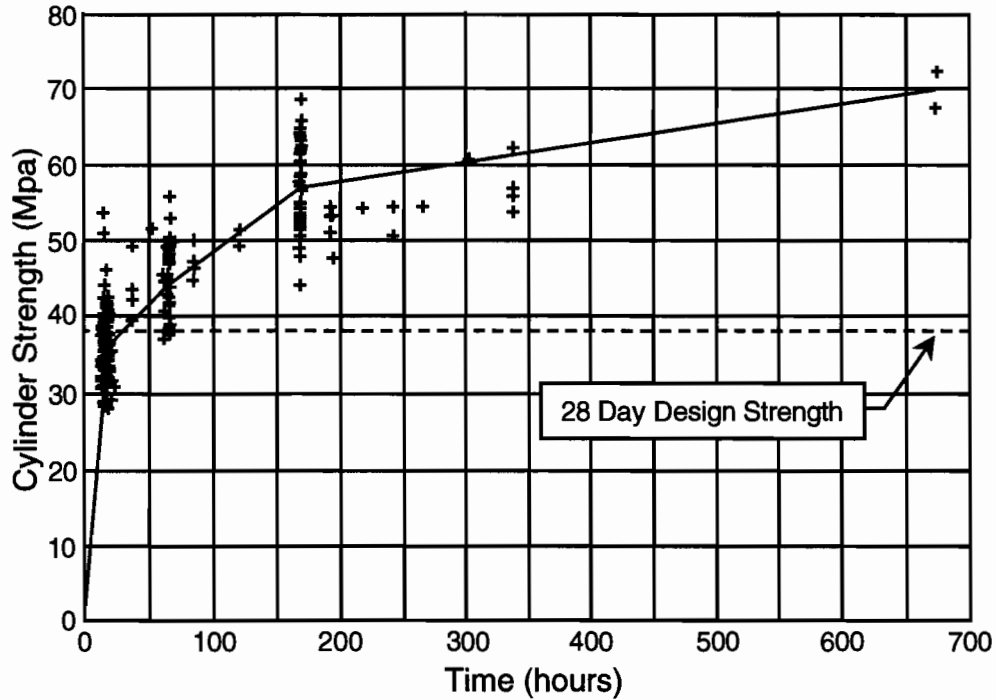


Figure 2.69 Concrete compressive strengths for mainlane D

The results of modulus of rupture tests are given in Table 2.2 for selected concrete samples. The specimens used in these tests were the same as used in the modulus of elasticity tests and the coefficient of thermal expansion tests. Table 2.2 presents the average measurements from three tests specimens for various segments, except for segments P16-2 and PC16-5 that used two specimens. The test results were not very consistent among specimens from the same segment, as indicated by the large standard deviations in the far right column of Table 2.2, or among various segments. The average rupture tensile strain for the concrete specimens from the precasting yard was $172\mu\epsilon$, while the average for the PC-16 cast-in-place base concrete specimens was higher, averaging $200\mu\epsilon$.

Table 2.2 Modulus of rupture test results

Segment	Concrete Age (days)	Tensile Stress (Mpa)	Modulus of Elasticity (Mpa)	Tensile Strain at Rupture ($\mu\epsilon$)	Standard Deviation ($\mu\epsilon$)
P16-1a	948	5.49	37000	148	9.9
P16-2	1006	7.48	41000	183	12.4
P16-4	1001	7.48	42000	178	13.3
P16-10	995	6.24	37000	169	5.6
P16-17	989	6.40	37500	171	13.8
PC16-Base	1100	7.10	35500	200	17.0
PC16-1	1372	5.87	36500	161	26.8
PC16-5	1363	6.36	37000	172	1.6
PC16-7	1329	6.99	37500	186	24.1
PC16-8	1255	7.70	42500	181	29.2
Average (except base)		6.71	38300	172	

CHAPTER 3

PRESTRESSING FORCE LOSSES IN POST-TENSIONING TENDONS

3.1 PROBLEM DESCRIPTION AND TECHNICAL BACKGROUND

Prestressing force losses in post-tensioning tendons may be divided into two categories: losses occurring at the time of stressing and losses occurring over time thereafter. When using low-relaxation strands, the largest prestressing losses in a post-tensioned structure usually come from friction losses during stressing. Friction loss of the post-tensioning force in a tendon occurs when the tendon comes in contact with its duct or other guiding device during stressing. The normal force between the tendon and duct can be small, such as for a straight tendon with its duct internal to the concrete. The normal force can also be large, especially for external tendons deviated at discrete locations in a bridge girder. The coefficient of friction between tendon and duct can vary substantially depending on the normal force generated between the two materials. The three basic elements that are involved in the friction of unlubricated solids are [14]:

1. the true area of contact between mating rough surfaces;
2. the type and strength of bond formed at the interface where contact occurs; and
3. the way in which material in and around the contacting regions is sheared and ruptured during sliding.

Because these variables are difficult to quantify, design coefficients of friction for various duct materials and normal forces have been determined empirically and are usually presented as a range of values. The engineer must select an appropriate coefficient of friction when designing a tendon. The accuracy of his selection may not be known until the bridge is under construction.

Friction loss during post-tensioning of a tendon may substantially reduce the prestressing force in the tendon. This loss occurs in tendons with large cumulative angular deviations over the length of the tendon. Multi-span deviated tendons may lose 40% to 50% of the prestressing force at the jacking end of the tendon. Accurate calculation of the friction losses in this case is essential for an economical, safe, and constructible design.

Elongations measured during post-tensioning give an indication of the cumulative friction loss in a tendon. The *AASHTO Guide Specifications for the Design and Construction of Segmental Concrete Bridges* [8] require measured elongations to be within 5% of those calculated by the engineer, unless otherwise approved by the owner. This specification is insensitive to the level of prestress force friction loss in a tendon. The tolerance is difficult to satisfy for two distinct reasons in tendons with high friction losses. First, the engineer may not be able to select a friction coefficient with sufficient accuracy. Second, the constructor may not install ducts to the degree of accuracy that the engineer assumed in his calculation. These factors will not have a significant impact on the accuracy of elongation calculations for tendons with little friction loss. Selection of the proper modulus of elasticity for the tendon and knowledge of the friction losses near the live end anchorage may become more important in this case. Consistently high friction losses on a project can be overcome by increasing overall prestressing force by adding additional strands to the tendon, where possible, or by lubricating the tendon and duct with graphite to reduce the friction.

The commonly used friction loss model for bridge design calculations is shown in Figure 3.1. The model assumes that the tendon to duct contact surface is planar when computing the normal force. The total normal force for a multistrand tendon in a circular duct would be somewhat larger.

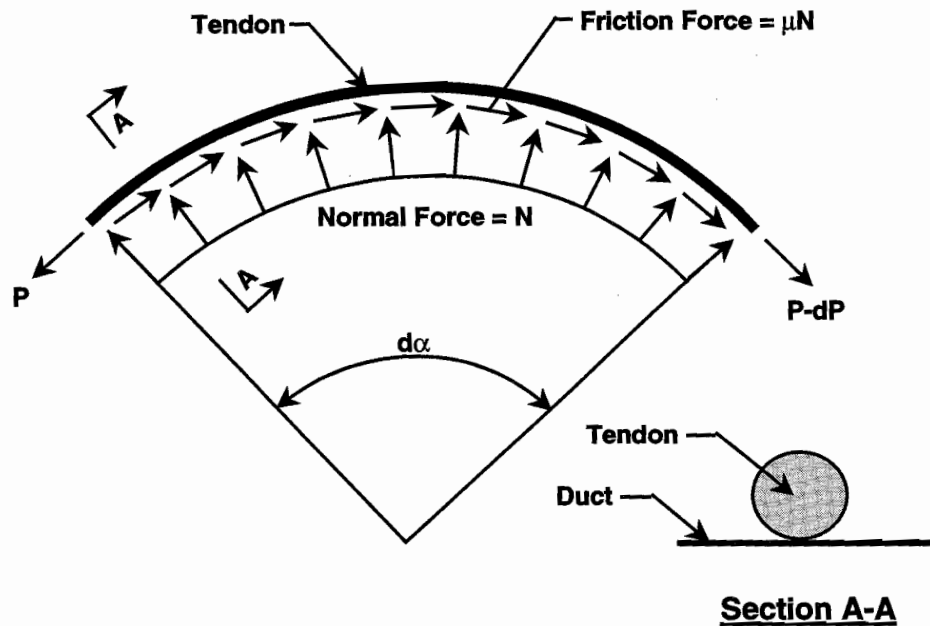


Figure 3.1 Friction loss model

Equilibrium in the tendon for the differential length of duct in Figure 3.1 gives:

$$dP = -\mu N \quad (3-1)$$

where

dP = differential change in tendon force

μ = coefficient of friction

N = normal force

$N = Pd\alpha$

P = tendon force

$d\alpha$ = differential angle change

Integrating both sides gives:

$$P_x/P_0 = e^{-\mu\alpha} \quad (3-2)$$

This equation gives the relationship between the known tendon force at point 0 and the tendon force at some point x as a function of the cumulative angle change α between point 0 and point x . To account for duct placement construction tolerances, an additional angle change is added to α in one of three ways. First, the angle change can be an absolute value β , the wobble angle, applied at deviators or other locations.

$$P_x/P_0 = e^{-\mu(\alpha+\beta)} \quad (3-3)$$

Second, the angle change can be a percentage k of the design angle change.

$$P_x/P_0 = e^{-\mu(\alpha+k\alpha)} \quad (3-4)$$

Third, the angle change can be a function of the length of the duct L , as is used for internal tendons, with an appropriate wobble coefficient K .

$$P_x/P_0 = e^{-\mu\alpha-KL} \quad (3-5)$$

The accuracy of these equations depends on proper selection of the coefficients of friction μ and the wobble angle β or coefficients of wobble k or K .

Deformation of a structure also occurs when prestressing is applied. Tendons are usually stressed in some sequence. Thus, tendons stressed later will have an effect on the force in tendons stressed earlier in the sequence. This prestress force change is known as the elastic shortening loss and is mainly a function of the geometry of the structure and the modulus of elasticity of the concrete and obviously the magnitude and sequence of the applied post-tensioning forces.

Long-term prestress losses occur when the length of a tendon changes from creep and shrinkage of the girder concrete and because of prestressing steel relaxation. Long-term prestress losses are a function of material properties as well as the geometry of the structure. The use of low relaxation strand has reduced the relaxation loss in a tendon to below 3% of the jacking force [8]. Therefore, a reasonable estimate of the relaxation loss by the engineer using current code equations is quite adequate. Accuracy of the relaxation loss calculation has little effect on the accuracy of the total tendon force loss estimate.

On the other hand, creep and shrinkage-induced losses in post-tensioning tendons may be difficult to predict at the time of the structure's design. The magnitude of both creep and shrinkage strains causing post-tensioning losses is directly related to the amount of water remaining in the pore volume of the paste in the concrete at the time of stressing [15]. The concrete elements in a post-tensioned structure may have been cast well in advance of the time prestressing or other loads were applied, such as is usual in a precast segmental bridge. Creep and shrinkage losses may be low in this case because much of the water in the concrete not used for hydration has escaped into the atmosphere, and the crystalline structure of the paste is dense, restricting movement of the remaining water. On the other hand, a cast-in-place segmental bridge is usually prestressed very early, as soon as the concrete comes to the required strength, so that construction may continue. The accuracy of creep and shrinkage loss calculations may become more important than the accuracy of friction loss calculations in the cast-in-place case. The designer must estimate the casting and post-tensioning schedule for the project at the time of design and estimate the concrete creep and shrinkage behavior for concrete available at the particular project site. Figure 3.2 shows the effect of concrete creep and shrinkage on prestress force for concrete of various ages.

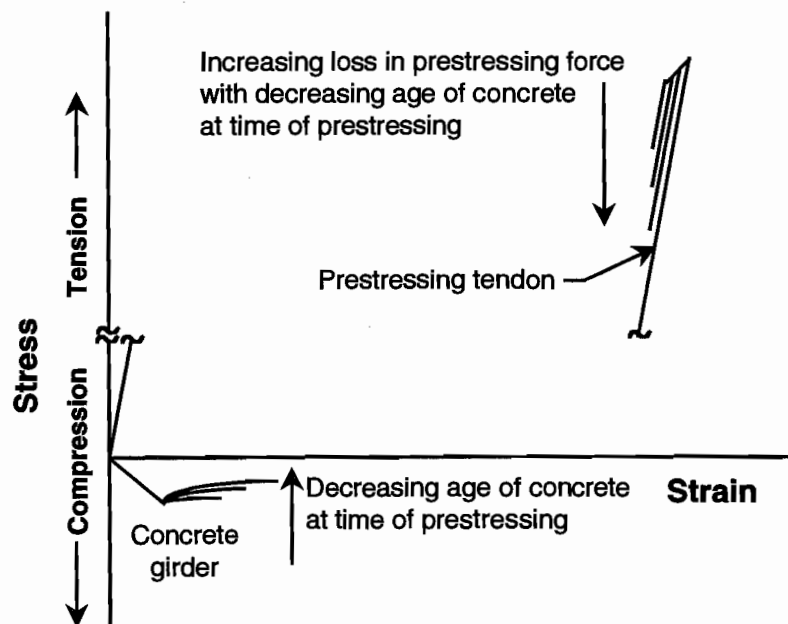


Figure 3.2 Prestress force loss from creep and shrinkage

Simple methods for roughly estimating the prestress loss from creep and shrinkage strains are included in concrete design codes and other special publications. The accuracy of these methods is sufficient for

preliminary designs and many final designs. More accurate time-dependent analyses will be required to predict losses and control deflections on some structures, such as bridges constructed in balanced cantilever.

The post-tensioned box girders under study on US 183 had both internal and external tendons, as shown in Figures 3.3 and 3.4. The internal tendons were placed essentially on straight profiles in the bottom flange of the girders and in the wings. The external tendons were deviated at two or more points on various profiles. The main objectives for the research on these tendons were:

1. to measure friction losses in the anchorage zones,
2. to determine the magnitude and consistency of wobble friction along the tendon profiles,
3. to measure tendon force changes other than friction losses including elastic shortening, creep and shrinkage, and
4. to compare the measured results to values calculated using normal design techniques.

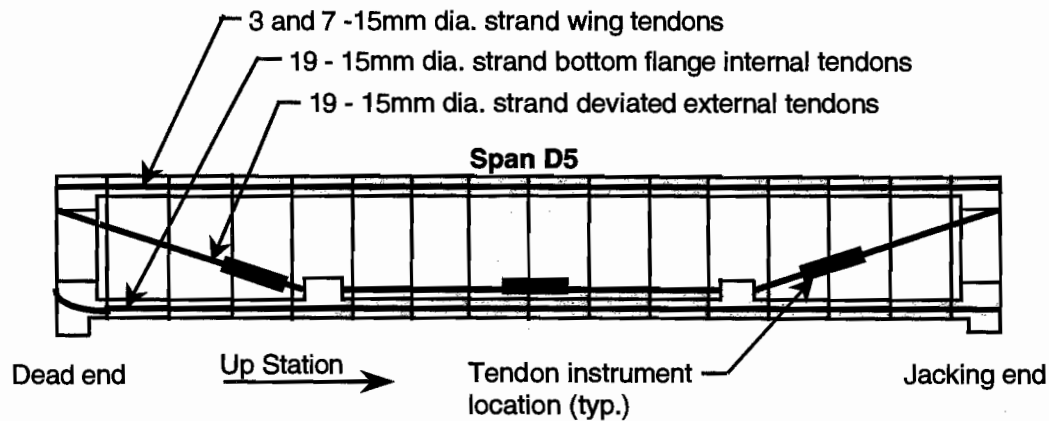


Figure 3.3 Mainlane girder tendons

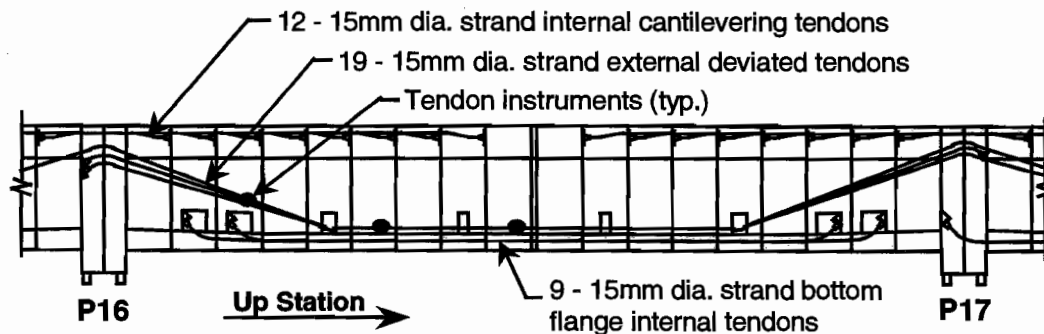


Figure 3.4 Ramp P girder tendons

3.2 LITERATURE REVIEW AND FIELD EXPERIENCE

3.2.1 Friction Losses

Post-tensioning tendons can be classified into two basic groups, internal and external. Internal tendons are in ducts cast within the concrete of the bridge girders over their entire length. Ducts may be curved on a vertical profile in response to the shape of the bending moment diagram for the member. Ducts may be placed essentially straight, such as in the top and bottom slabs of box girders. With some exceptions, internal tendon profiles have high radii of curvature (>30m) resulting in low normal forces between strand and duct, and the tendon and duct are in contact over much of the length of the profile.

External tendons are located in ducts that are cast within the concrete only at discrete points, such as at a deviator or saddle. Required curvature changes only occur at these points, resulting in curvature profiles with low radii (8m) and tendon to duct contact over little of the length of the profile. Coefficients of friction and wobble are much different than those for internal tendons.

Internal Tendons

Internal tendons were commonplace before the use of external tendons became common practice. A duct commonly used in the 1960's in the United States for internal tendons was flexible steel tubing. High wobble loss was experienced by the industry and was experimentally verified by Bezouska [16]. Wobble friction coefficients (K) were found to be 0.0049m^{-1} when used with a coefficient of friction of 0.25. Soon afterward, the State of California and the rest of the country began using rigid or semirigid steel duct in bridge construction. This duct could be tied in place more accurately than the flexible duct and remained in place when concrete was cast. Wobble friction coefficients (K) were then found by Bezouska [17] to drop to 0.0007m^{-1} when used with an assumed curvature friction coefficient of 0.25. After a review of their construction records, California eventually decided to use a friction coefficient of 0.20 with no wobble term for all internal tendons.

More modern field tests performed by Dywidag [18] gave a coefficient of friction of 0.24 in galvanized semirigid duct when the wobble coefficient was assumed to be 0.0007m^{-1} . Tran [19], testing a laboratory-prepared girder with galvanized semirigid duct found that the wobble coefficient was closer to 0.0013m^{-1} , and that the coefficient of friction was 0.16. Assuming $K=0.0013\text{m}^{-1}$ in Dywidag's test girder, their coefficient of friction becomes 0.17, similar to Tran's coefficient of friction.

Harstead, Kummerle, Archer, and Porat [20] performed full-scale tests in galvanized semirigid steel duct with strand tendons. Using an assumed K of 0.0013m^{-1} , their test results also give a coefficient of friction of 0.17 in a duct with a minimum radius of 20m and 0.24 in another duct with a minimum radius of 6m. Bezouska [17] also saw the relationship between increased curvature and increased friction loss. Tests by Yasuno, Kondo, Tadano, Mogami, and Sotomura [21] in specimens with minimum radii of curvature similar to those of Tran [19] (8m–21m) gave $\mu=0.14$ and $K=0.0011\text{m}^{-1}$ as friction coefficients.

Test results for internal segmentally constructed tendon profiles by Davis, Tran, Breen, and Frank [22] corresponded well with previously measured results, shown in Figure 3.5, with a coefficient of friction of 0.16 and wobble coefficient of 0.0016m^{-1} . The coefficient of friction between galvanized semirigid duct and strand tendons apparently changes from values typical when normal forces correspond to curvature radii between about 15m to 40m radii in draped internal ducts (with an upper bound of $\mu=0.25$) to much higher values under high normal forces which accompany radii less than 10m. Friction coefficients used in Equation 3-5 for external deviator pipes, with radii usually less than 10m, are approximately $\mu=0.25$ with $K=0.0007\text{m}^{-1}$ or greater for the wobble coefficient, as recommended by AASHTO [23].

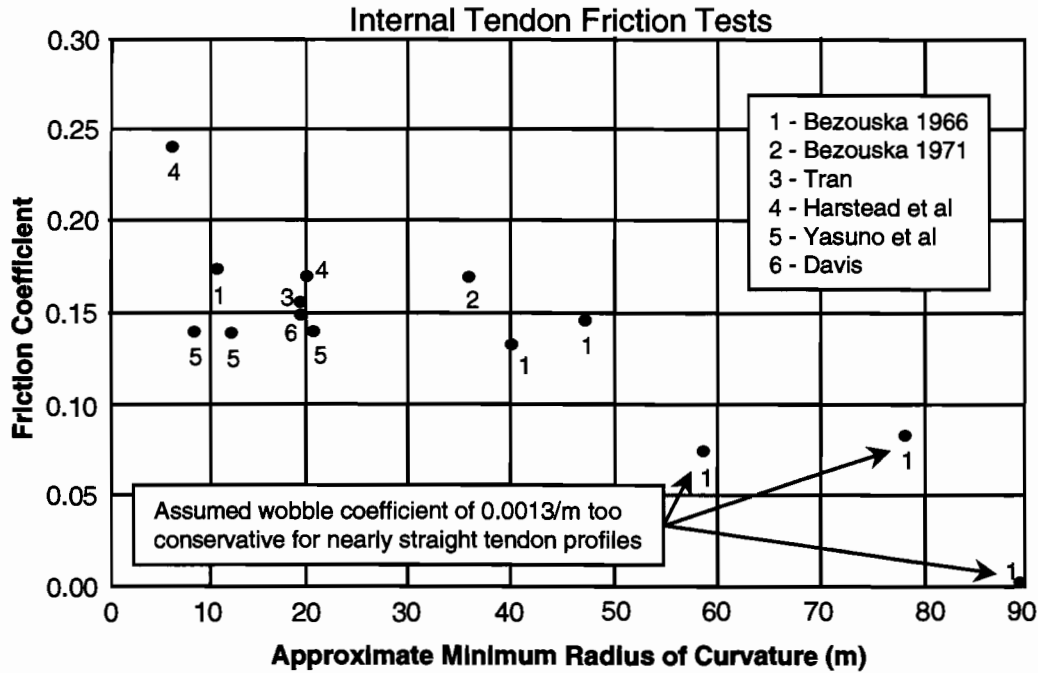


Figure 3.5 Results from previous friction tests

External Tendons

Coefficients of friction used by design engineers for external tendons are largely based on field experience. This experience is reflected in the *AASHTO Guide Specification* [23]. AASHTO suggests using $\mu=0.25$ and no wobble or additional angle change term when lubrication is used at the deviator. A realistic coefficient of friction and wobble term for unlubricated external tendons was suggested by Roberts, Breen, and Kreger [7]. They suggested using the usual coefficient of friction of 0.25, but based on field observations they recommended supplementing it with an inadvertent angle change term (β from Equation 3-3) of 0.04 radians or 2.29 degrees added to the intended angle change at each deviator.

Design coefficients for internal and external tendons recommended by various authorities and shown in Tables 3.1 through 3.6 tend to be somewhat conservative, or give a range of values. In Table 3.3, the CEB recommended coefficient of friction is modified, depending on the degree of duct filling. Higher tendon area to duct area ratios generate higher total normal forces because the tendon bears on a greater part of the perimeter of the duct. Therefore, the basic coefficient of friction for flat surfaces is multiplied by a squeezing factor.

Table 3.1 Friction and wobble coefficients for post-tensioned tendons from AASHTO [23]

Materials	Friction Coefficient μ	Wobble Coefficient K (m^{-1})
For strand in galvanized metal sheathing	0.15–0.25*	0.0007
For deformed high strength bars in galvanized metal sheathing	0.15	0.0007
For strand in internal polyethylene duct	0.23	0.0007
For strand in straight polyethylene duct (external to the concrete)	0	0
Rigid steel pipe deviators	0.25**	0.0007

* A friction coefficient of 0.25 is appropriate for 12-strand tendons. The coefficient is less for larger tendon and duct sizes.

** Lubrication will probably be required.

Table 3.2 Friction and wobble coefficients for post-tensioned tendons from AASHTO LRFD [9]

Type of Tendons and Sheathing	Wobble Coefficient, K (m ⁻¹)	Curvature Coefficient, μ (1/RAD)
Tendons in rigid and semirigid galvanized ducts - 7-wire strands	0.0007	0.05–0.25
Pregreased tendons - wires and 7-wire strands	0.0010–0.0066	0.05–0.15
Mastic-coated tendons - wires and 7-wire strands	0.0033–0.0066	0.05–0.15
Rigid steel pipe deviators	0.0007	0.25 Lubrication probably required

Table 3.3 Friction and wobble coefficients for post-tensioned tendons from CEB [24]

Tendon Type	Physical Coefficient of Friction* μ_0	Coefficient of Friction** μ	Wobble Coefficient K (m ⁻¹)
Cold drawn wire	0.13	0.17	0.005–0.010
Strand	0.15	0.19	0.005–0.010
Deformed bar	0.50	0.65	0.005–0.010
Smooth and round bar	0.25	0.33	0.005–0.010
Monostrands (single or grouped) in slabs or reservoirs		0.05–0.07	0.006–0.010
Greased multistrand or wire tendons (e.g. in nuclear containments)		0.13–0.15	0.004–0.008
Dry multistrand or wire tendons (e.g. in nuclear containments with dry air as subsequent corrosion protection)		Factors as for ordinary p.t. tendons	Factors as for ordinary p.t. tendons
External multistrand tendons: naked dry strands over steel saddle***		0.25–0.30	0
External multistrand tendons: greased strands over steel saddle***		0.20–0.25	0
External multistrand tendons: dry strands inside plastic pipe over saddle***		0.12–0.15	0
External multistrand tendons: bundle of monostrands over saddle***		0.05–0.07	0

* Values can be multiplied by 0.9 if slight lubrication is present, e.g. by soluble oil.

** The coefficient of friction μ is the product of the physical coefficient of friction μ_0 and the squeezing factor χ , where χ is dependent on the degree of filling of the duct. Where more exact investigations are not available, this factor can be assumed to be 1.3 to 1.35 for tendons filling the duct between 50% and 60%. The values in the table assume 50% filling.

***These values correspond to a saddle radius of 2.5m to 4.0m. For lower radii further test evidence is needed.

Table 3.4 Friction and wobble coefficients for post-tensioned tendons from ACI 318-95 [25]

Tendon Type	Duct	Tendon	Wobble Coefficient K (m⁻¹)	Curvature Coefficient μ
Grouted	Metal sheathing	Wire tendons	0.0033–0.0049	0.15–0.25
Grouted	Metal sheathing	High strength bars	0.0003–0.0020	0.08–0.30
Grouted	Metal sheathing	7 - wire strand	0.0016–0.0066	0.15–0.25
Unbonded	Mastic coated	Wire tendons	0.0033–0.0066	0.05–0.15
Unbonded	Mastic coated	7 - wire strand	0.0033–0.0066	0.15–0.15
Unbonded	Pregreased	Wire tendons	0.0010–0.0066	0.05–0.15
Unbonded	Pregreased	7 - wire strand	0.0010–0.0066	0.05–0.15

Table 3.5 Friction and wobble coefficients for post-tensioned internal tendons from PTI [26]

Type of Duct	Range of Values μ	Range of Values K (m⁻¹)	Recommended for Calculations μ	Recommended for Calculations K (m⁻¹)
Flexible tubing non-grouted	0.18–0.26	16–66 x 10 ⁻⁴	0.22	25 x 10 ⁻⁴
Flexible tubing galvanized	0.14–0.22	10–23 x 10 ⁻⁴	0.18	16 x 10 ⁻⁴
Rigid thin-wall tubing nongalvanized	0.20–0.30	3–16 x 10 ⁻⁴	0.25	10 x 10 ⁻⁴
Rigid thin-wall tubing galvanized	0.16–0.24	0–13 x 10 ⁻⁴	0.20	7 x 10 ⁻⁴
Greased and wrapped	0.05–0.15	16–49 x 10 ⁻⁴	0.07	33 x 10 ⁻⁴

Table 3.6 Friction and wobble coefficients for post-tensioned internal tendons from ACI-ASCE [27]

Type of Steel	Type of Duct or Sheath	Usual Range of Observed Values K (m ⁻¹)	Usual Range of Observed Values μ	Suggested Design Values K (m ⁻¹)	Suggested Design Values μ
Wire cables	Bright metal sheathing	0.0016–0.0098	0.15–0.35	0.0066	0.30
Wire cables	Galvanized metal sheathing	0.0016–0.0098	0.15–0.35	0.0049	0.25
Wire cables	Greased or asphalt coated and wrapped	0.0098	0.25–0.35	0.0066	0.30
High strength bars	Bright metal sheathing	0.0003–0.0016	0.08–0.30	0.0010	0.2
High strength bars	Galvanized metal sheathing	0.0003–0.0016	0.08–0.30	0.0007	0.15
Galvanized strand	Bright metal sheathing	0.0016–0.0066	0.15–0.30	0.0049	0.25
Galvanized strand	Galvanized metal sheathing	0.0016–0.0066	0.15–0.30	0.0033	0.20

Other Sources of Friction

Substantial friction losses occur within the anchorage region of the tendon. Individual strands are deviated to enter the anchor head causing a normal force between the strands and the walls of the trumpet and anchor plate. At the live end, the force lost in the tendon can be 2% to 3% of the jacking force, as measured by Roberts, *et al.* [7]. A similar loss occurs at the dead end anchorage but is of little consequence. The engineer must include the live-end loss in order to accurately predict friction losses and elongations in the girder.

3.2.2 Elastic Shortening Losses

Elastic shortening losses for a post-tensioning tendon depends on the time that tendon was stressed relative to the other tendons in the structure. It also depends on the change in strain in the concrete along the tendon profile in question for an internal tendon, or the translation of the anchorage and deviation points for an external tendon. Calculation of the elastic shortening stress loss is usually calculated for a group of ungrouted post-tensioning tendons using an equation such as Equation 3-6 suggested by Zia, Preston, Scott and Workman [28].

$$ES = 0.5E_s f_{cpa} / E_{ci} \tag{3-6}$$

ES = Stress change in a tendon from elastic shortening of the girder

E_s = Modulus of elasticity of the prestressing steel

E_{ci} = Modulus of elasticity of the concrete at the time of stressing

f_{cpa} = Average compressive stress in the concrete along the member length at the center of gravity of the tendons immediately after the prestress has been applied

This equation is also used in the *AASHTO Standard Specification for Highway Bridges* [23] for use in bridge design. The equation requires that the designer know the modulus of elasticity of the concrete and the stress in the concrete along the tendon profile. The stress in the concrete may be difficult to predict in girder cross sections with significant shear lag and the resultant poor diffusion of post-tensioning forces. The modulus of elasticity of the concrete depends greatly on the modulus of elasticity of the coarse aggregate used at the site.

The concrete modulus of elasticity may differ from the modulus calculated from the simple equation in *AASHTO* [23].

3.2.3 Creep and Shrinkage

Losses due to creep and shrinkage depend on environmental factors, material properties of the concrete and its constituents, and the proportions of the structural member. *AASHTO* [23] uses Equation 3-7 for shrinkage loss in post-tensioning tendons. It is a function of relative humidity only. The 0.80 factor is intended to reduce the loss because of the potential age of a post-tensioned member at the time of stressing. This equation is adequate for preliminary designs.

$$SH = 0.80 (117000-1030RH) \quad (3-7)$$

SH = Tendon loss due to shrinkage in MPa

RH = Average relative humidity in %

Equation 3-8 for the stress loss in a tendon from shrinkage was given by Zia, Preston, Scott and Workman [29] for ACI-ASCE Committee 423. The equation estimates the amount of water leaving the concrete pore volume as a function of time, relative humidity and shape, although it does not account for differences in concrete mixes, such as water to cement ratio or percentage of aggregate.

$$SH = 8.2 \times 10^{-6} K_{sh} E_s (1-0.0018V/S)(100-RH) \quad (3-8)$$

SH = Tendon stress lost due to shrinkage in Mpa

E_s = Modulus of elasticity of the prestressing tendon

V/S = Volume to surface area ratio of the concrete

RH = Average relative humidity in %

K_{sh} is a function of the time elapsed between moist curing and prestressing

ACI Committee 209 studied the effects of concrete constituents and other factors on creep and shrinkage [29]. Equation 3-9 was developed for estimating shrinkage strain in concrete and includes these factors:

$$\epsilon_{sh} = \epsilon_{shu} S_t S_h S_{th} S_s S_f S_e S_c \quad (3-9)$$

$\epsilon_{shu} = 0.0008$ for moist cured concrete

$\epsilon_{shu} = 0.00073$ for steam cured concrete

$S_t = t/(35+t)$, t = time in days from age 7 days
(moist cured)

$S_t = t/(55+t)$, t = time in days from age 1 to 3 days
(steam cured)

$S_h = 1.4 - 0.01RH$, 40% < RH < 80%

$S_h = 3.0 - 0.03RH$, 80% < RH < 100%

$S_{th} = 1.0$, minimum thickness < 152mm

$S_{th} = 0.84$, minimum thickness < 229mm

$S_{th} = 0.80$, minimum thickness < 356mm

$S_{th} = 0.72$, minimum thickness < 508mm

$S_{th} = 0.70$, minimum thickness < 610mm

$S_s = 0.89 + 0.00157*(Slump)$, Slump in mm

$S_f = 0.33 + F/75$, F < 50%

$S_f = 0.88 + F/430$, F > 50%

$F = \% \text{ fines by weight of total aggregate}$

$S_e = 0.95 + A/120$, $A = \text{air content in \%}$

$S_c = 0.72 + C/14544$, $C = \text{cement content in } N/m^3$

These equations shown above are for girders free to contract along their length. The calculation of shrinkage losses becomes more complicated when additional boundary conditions are placed on continuous girders, such as a moment connection to a pier.

The calculation of prestressing losses from creep is similar to that for shrinkage. The *ACI Committee 209 Report* [29] gives the following equation for calculating creep strain in concrete:

$$C_t = \epsilon_{cr}/\epsilon_{elastic} = \text{creep coefficient} \quad (3-10)$$

$\epsilon_{elastic}$ = immediate strain response to a constant load

ϵ_{cr} = creep strain from a constant load

$$C_t = C_u K_t K_a K_h K_{th} K_s K_f K_e \quad (3-11)$$

$C_u = 2.35$, ultimate creep coefficient

$K_t = (t^{0.6})/(10 + t^{0.6})$, $t = \text{days of load application}$

$K_a = 1.25 t_i^{-0.118}$, (moist cured)

$K_a = 1.13 t_i^{-0.095}$, (steam cured)

$t_i = \text{age in days when loaded}$

$K_h = 1.27 - 0.0067H$, for $H > 40\%$

$H = \text{relative humidity}$

$K_{th} = 1.0$, minimum thickness $< 152\text{mm}$

$K_{th} = 0.85$, minimum thickness $< 305\text{mm}$

$K_{th} = 0.75$, minimum thickness $< 457\text{mm}$

$K_{th} = 0.70$, minimum thickness $< 610\text{mm}$

$K_s = 0.82 + (\text{slump})/381$, slump in mm

$K_f = 0.90 + F/500$, % fines by weight

$K_e = 1.0$, for air content $< 6\%$

$K_e = 0.45 + A/11$, for air content $A > 6\%$

Once again, this equation provides the means for calculating the creep strain in plane stress members. The problem becomes more complicated when the actual boundary conditions are applied.

3.3 INSTRUMENTATION PROGRAM

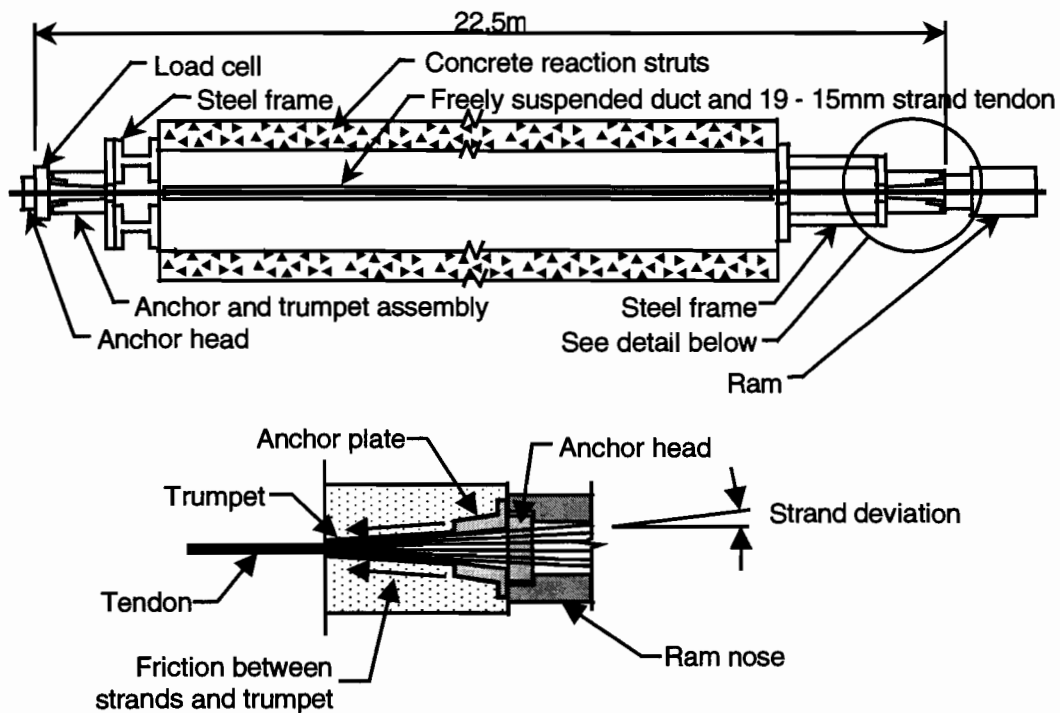
Measurements were taken on tendons tested in the laboratory, on tendons in two spans in the mainlane superstructure, and on tendons in one span of Ramp P. Span D5 on the mainlane and span P16 on Ramp P had strain gauges installed permanently on the tendons. Tendons tested in the bench test at the laboratory and in span D2 during the in-place friction test were only temporarily instrumented for strain readings during stressing.

3.3.1 Bench Test

Tendons under study on US 183 were 19-15mm strand tendons. The stressing equipment, tendons, and instrumentation for measuring tendon strains were tested and calibrated in a bench test shortly before construction of the bridge superstructure. The bench test was probably unnecessary from a construction standpoint since the first girder to be constructed had nearly straight tendons in the bottom flange. Calibration of the ram could have been verified during the in-place friction test. From the researchers' standpoint, the bench

test provided the means for measuring friction losses in the anchorage zones and ram separately from friction in the duct profiles. The bench test also allowed side-by-side calibration of the strain gauges, epoxy sleeve system, load cell, and pressure transducer used to measure tendon strains in the field tests.

The bench test, shown in Figure 3.6, was conducted at the Ferguson Structural Engineering Laboratory at The University of Texas at Austin. The test specimen was a 19-15mm strand tendon 22.5m long. Dead-end and live-end bulkheads were constructed from steel and were seated on either end of an access passage beneath the laboratory's structural load floor. The tendon was hung freely in a duct down the length of the access passage. Both the live end and dead end anchor plates and trumpets were cast into steel pipe lined cylinders of concrete to more accurately represent the anchorage zones. A load cell was placed between the anchor head and the anchor plate at the dead end to measure tendon force. Pressure on the ram was measured with a pressure transducer. Strain in the tendon was measured using electronic strain gauges on individual wires of the tendon, a Demec extensometer with Demec points mounted in epoxy sleeves around the tendon, and by elongation measurements with a ruler. As the tendon was stressed, the individual strands of the tendon were deviated in the trumpet in order to match the geometry of the anchor head. This deviation caused a normal force and friction to occur between the tendon and the trumpet. The loss in tendon force between the live end and the dead end of the tendon is shown in Table 3.7. Confirming measurements by Roberts [10], the loss through the stressing equipment and anchorage hardware was over 2%. The load cell was calibrated face to face with the ram in a previous test. The load cell gave a slightly nonlinear response in this test, with maximum error being 0.93% of the jacking force. This error was accounted for in the tests to follow, when this load cell was used, by using the actual nonlinear calibration curve. The live end and dead end anchorage zone losses in Table 3.7 were calculated based on the angle changes of the strands in the trumpet and anchor plate. The angle change at the dead end was less than that at the live end because the load cell increased the distance of the anchor head to the anchor plate.



Detail

Figure 3.6 Bench test

Table 3.7 Bench test results

Measured Ram Force (kN)	Measured Load Cell Force (kN)	Total Loss (%)	Calculated Live End Anchorage Zone Loss (kN)	Calculated Dead End Anchorage Zone Loss (kN)
0	0	0	0	0
445	441	0.8	2.5	1.5
890	887	0.3	1.9	1.1
1334	1335	0.0	-0.6	-0.4
1779	1761	1.1	11.4	6.6
2224	2176	2.1	30.4	17.6
2669	2607	2.3	39.3	22.7
3114	3050	2.0	40.6	23.4
3558	3486	2.0	45.6	26.4
3959	3871	2.2	55.8	32.2

The bench test provided an apparent modulus of elasticity of the tendon for use with the electronic strain gauges. The strain gauges were placed parallel to the helical outer wires of the prestressing strands. As would be expected, the strains measured by the strain gauges differed from those measured from the elongation of the entire tendon. The strains measured from the epoxy sleeve system were somewhat inconsistent in both the bench test and in tests to follow. The epoxy sleeve system measured strains therefore were used only as a backup to the electronic gauges. The final results for the instrumentation in the bench test are shown in Figure 3.7.

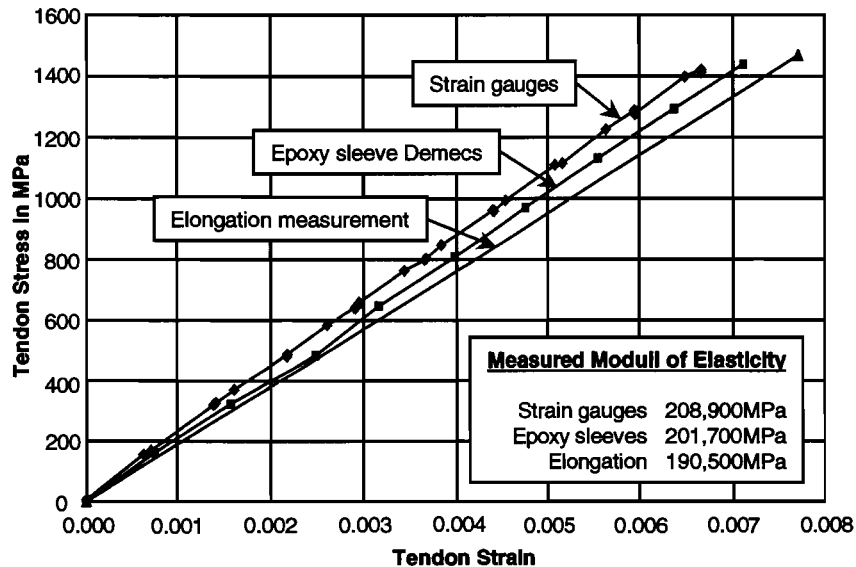


Figure 3.7 Instrumentation calibration from bench test

The tendon modulus of elasticity determined from the elongation measurements, at 190,500MPa, was 1.3% lower than the AASHTO [23] suggested value of 193,000MPa.

3.3.2 Mainlane Girder Tests

The mainlane girders were constructed as simple spans. The internal and external tendon profiles are shown in Figures 3.8 and 3.9.

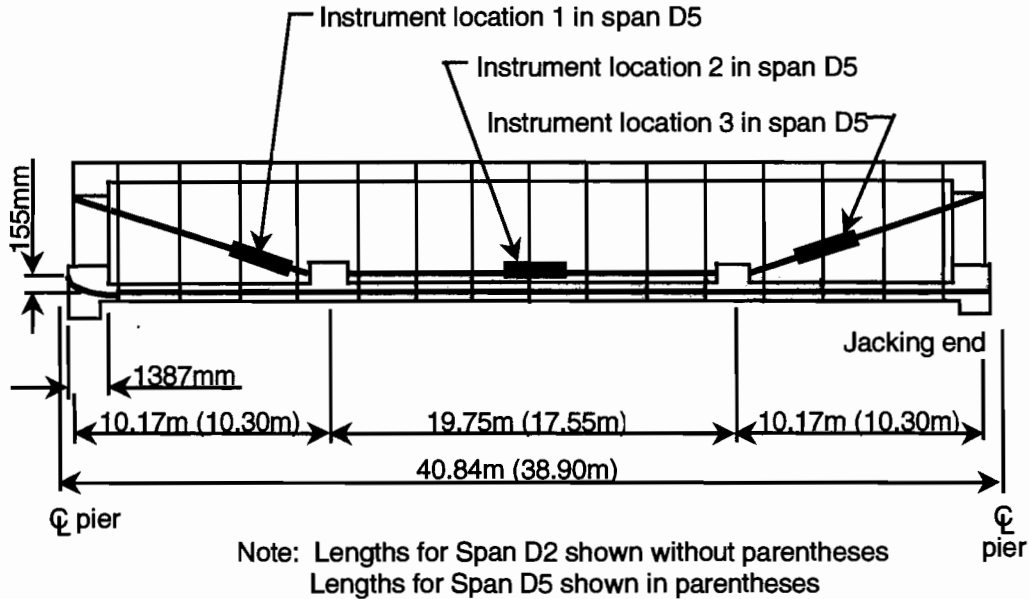


Figure 3.8 Mainlane girder D5 tendon profiles—elevation

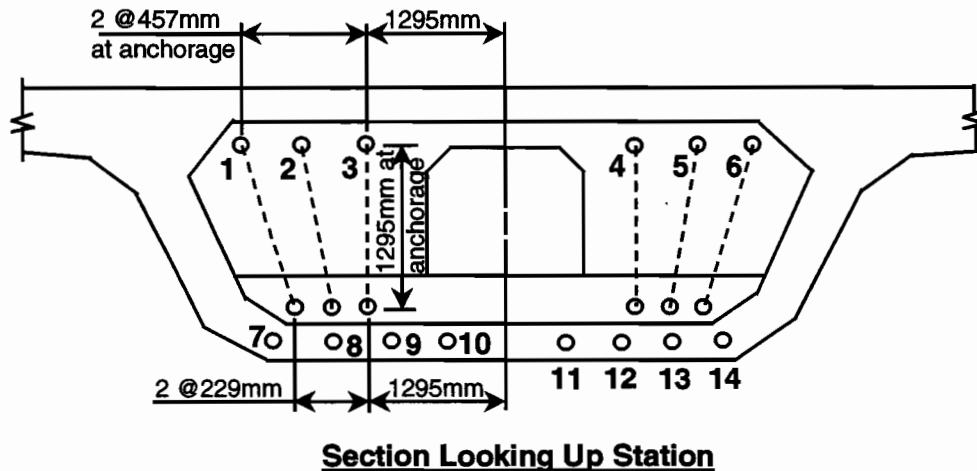


Figure 3.9 Mainlane girder D5 tendon profiles—end view

All tendons were 19-15mm strand tendons, with the exception of the four wing tendons. The six deviated external tendons had no intended angle change at any point other than at the two deviators. A summary of the deviation angles is given in Tables 3.9 and 3.11.

The eight bottom flange internal tendons followed the geometry of the bridge girder except for an angle change at the dead end of the profile. This angle change was provided to ease installation of the tendons. The tendons were pulled into their ducts from the dead end to the live end. In retrospect, the angle change was unnecessary and required that the dead end anchor segment have different anchorage geometry than the live end anchor segment.

In-Place Friction Tests on Span D2

Strand forces for four profiles of 19-15mm strand tendons were measured in span D2 on the mainlane. Ram pressure was measured at the live end with a pressure transducer and a hydraulic dial gauge. Dead end force was measured with a load cell. The entire test setup was identical to that of the bench test with the exception of the tendon length and profile. Two bottom flange internal tendons were tested (tendons 12 and 13), and two

deviated external tendons were tested (tendons 2 and 3). The results of these tests are shown in Table 3.8. The anchorage zone losses shown in columns (4) and (5) of Table 3.8 were assumed to be proportional to those determined in the bench test. The live end anchorage zone losses were calculated by dividing the appropriate measured live end force in column (1) of Table 3.8, by the measured live end force from the bench test in column (1), then multiplying this ratio by the live end anchorage loss in column (4), measured in the bench test. The dead end anchorage zone losses in column (5) of Table 3.8 were calculated by dividing the appropriate measured dead end force in column (2) of Table 3.8, by the measured dead end force from the bench test in column (2), then multiplying this ratio by the dead end anchorage loss in column (5), measured in the bench test. The losses at the deviators or dead end curvature shown in column (6) of Table 3.8 were determined by taking the difference between the total measured losses and these assumed anchorage losses. Based on these measurements and assumptions the average force loss through two deviators was 7.5% of the live end force. The average loss in tendons 12 and 13, caused by the curvature in the duct near the dead end of the tendon, was only 0.4%, much less than the losses assumed to occur in the live and dead end anchorage zones.

Table 3.8 In-place friction test results on span D2

Test Tendon	(1) Measured Live End Force (kN)	(2) Measured Load Cell Force (kN)	(3)=(1)-(2) Measured Total Loss (kN)	(4) Assumed Live End Anchorage Loss (kN)	(5) Assumed Dead End Anchorage Loss (kN)	(6)=(3)-(4)-(5) Calculated Deviators 1 and 2 Loss or Dead End Curvature Loss, (kN) or % of live end force	
Bench	3959	3871	88	56	32	-	
2	3904	3512	392	55	29	308	7.89%
3	3818	3461	357	54	29	274	7.18%
Ave. 2-3	3861	3487	374	55	29	290	7.51%
12	3824	3733	91	54	31	6	0.16%
13	3849	3742	107	54	31	22	0.57%
Ave. 12-13	3837	3738	99	54	31	14	0.36%

The friction coefficients and wobble angles and coefficients, used in Equations 3-3, 3-4 and 3-5, have been calculated based on the measured and calculated values given in Table 3.8. The friction coefficients and wobble angles and coefficients are presented in Table 3.9. The angle change given in column (1) in Table 3.9 is the intentional angle change and was calculated using the contract drawings. The percentage loss in column (2) is the loss occurring over the length of tendon under consideration. For the deviated external tendons 2 and 3 this percentage loss includes only the losses occurring in the deviator pipes. For the internal tendons 12 and 13 only the loss occurring within the curvature in the ducts near the dead end of the tendon was considered. The friction coefficient of 0.25 in column (3) was assumed for the deviated external tendons. Using the percentage loss in column (1), the assumed friction coefficient from column (3), and Equations 3-3 and 3-4, the wobble angles β in column (4) and the wobble coefficients k in column (5) were calculated. The average β for each deviator was 0.036 radians, which compares well with Robert's [7] recommended value of 0.04 radians per deviator. The friction coefficient μ (column (3) of Table 3.9) was calculated for the internal tendons 12 and 13 assuming no wobble losses. The percentage loss for tendons 12 and 13 in column (2) was so small as to be unbelievable. The assumed dead end or live end anchorage zone losses for these tendons from Table 3.8 must have been too large, or errors were made during the tendon force measurements.

Table 3.9 Measured losses and calculated wobble coefficients from in-place friction test on span D2

Test Tendon	(1) Angle Change (Degrees)	(2) Calculated % Loss	(3) μ Fiction Coefficient	(4) β (Radians)	(5) k	(6) K (m^{-1})
Bench	0	0	0.25***	0	0	-
Deviated External						
2	14.162**	8.00%**	0.25***	0.086**	0.349	-
3*	14.102**	7.28%**	0.25***	0.056**	0.228	-
Straight Internal						
12	11.242	0.16%	0.0082	-	-	0
13	11.242	0.58%	0.0296	-	-	0

* Visible misalignment of anchorage and deviator noted

** Includes 2 deviators

*** Assumed friction coefficient

Table 3.10 gives the measured and the calculated elongations for tendons 2, 3, 12 and 13. Column (1) of Table 3.10 contains the elongations measured during stressing of the tendons, adjusted for elastic shortening of the box girder and wedge seating at the dead end. The measured elongations in column (1) of Table 3.10 were consistently shorter than the calculated elongations in column (3). The elongations in column (3) were calculated using the losses from Table 3.8 and the tendon's elastic modulus determined from the bench test shown in column (4). The predicted elongations in column (3) assumed that each deviator performed identically. This identical performance was most likely not the case. Also, the loss in the live end anchor segment was probably larger than that seen in the bench test because of the additional duct length in the anchor segment beyond the anchorage device. The measured moduli of elasticity in column (2) of Table 3.10 were calculated using the measured elongations in column (1) and the losses from Table 3.8. The measured moduli were inconsistent between the deviated external tendons and the internal tendons. The average measured modulus of elasticity was larger for the external tendons, indicating the tendon force was lower than expected over its entire length. The average modulus measured for the internal tendons indicates that the bench test modulus may have been lower than the actual modulus of elasticity for these tendons.

Table 3.10 Elongations from friction tests on span D2

Test Tendon	(1) Measured Elongation (mm)	(2) Measured Modulus (MPa)	(3) Calculated Elongation (mm)	(4) Bench Test Modulus (MPa)	(5) Assumed Friction Coefficient μ	(6) Resultant Wobble Angle β (Radians)
Deviated External						
2	275	203,400	294	190,500	0.25	0.307*
3	277	198,200	288	190,500	0.25	0.166*
Ave. 2-3	276	200,800	291	190,500	0.25	0.237*
Straight Internal						
12	296	193,500	301	190,500	0.15	0.211
13	293	196,800	303	190,500	0.15	0.563
Ave. 12-13	294.5	195,200	302	190,500	0.15	0.387

* Angle applied at each deviator (2 total)

The wobble angle β in column (6) of Table 3.10 was calculated using only the design geometry of the tendons from Table 3.9, an assumed live end anchorage zone loss of 2%, the tendon's elastic modulus determined from the bench test, and the measured elongations. The unrealistically large β angles in column (6) indicate that the bench test modulus was different from that of the in-place friction test tendons. The load cell may also have given erroneous readings. There is a question as to the accuracy of the load cell since nonlinear output was observed during the bench test and load cell calibration. It is likely that the load cell was not functioning properly since the 11.242° tendon deviation in tendons 12 and 13 produced only about 0.5% force loss. In a best case scenario this friction loss should have been about 3%, assuming a coefficient of friction of 0.15 and no wobble. The load cell calibration was not checked after the friction tests.

Mainlane Girder Friction Tests on Span D5

Strand forces for six sets of 19-15mm strand deviated external tendons were measured on span D5 on the mainlane. Ram pressure was measured at the live end with a pressure transducer, and tendon strains were measured with strain gauges and epoxy sleeve systems on either side of the deviators. The strain measurements taken between the live end anchorage and the first deviator gave an indication of the effective wedge seating loss beyond the anchorage zone itself. Very little strain change was measured in the two tendon lengths beyond the first deviator that was caused by wedge seating. The wedge seating length shown in column (6) of Table 3.11 was calculated from the measured strain change in gauges on the adjacent length of tendon. The average wedge seating length was 5.19mm with a small standard deviation of 0.55mm. The wobble coefficients determined in this test using the strain gauge data are shown in columns (5) and (6) of Table 3.11. The percentage loss through the deviators measured by the strain gauges, shown in column (2) of Table 3.11, was consistently nearly twice the loss measured with the load cell on span D2. The location of the gauges on the top strands of each tendon may not have provided strains representative of those in the entire tendon, even though the data were very consistent. Arrellaga has shown that substantial force differences can exist between the various wires and strands in the same tendon [11]. The calculated wobble angles and coefficients β and k in columns (5) and (6) of Table 3.11 varied considerably from tendon to tendon because the friction coefficient μ in column (3) was assumed to be constant at 0.25. Thus, the calculated wobble friction also have included any reduction or increase in friction resulting from errors in the selection of μ . The standard deviations for the measured wobble values were on the order of the wobble values themselves, and the averages were unrealistically large.

Table 3.11 Span D5 friction test results from strain gauges

Test Tendon	(1) Intentional Angle Change*	(2) Measured Loss*	(3) Assumed Friction Coefficient μ	(4) Calculated β^*	(5) Calculated k	(6) Calculated Wedge Seating Length
1	7.122°	7.16%	0.25	0.173rad	1.39	-
2	7.017°	7.22%	0.25	0.177rad	1.45	4.50mm
3	6.966°	4.84%	0.25	0.077rad	0.63	5.84mm
4	6.966°	6.78%	0.25	0.159rad	1.31	5.28mm
5	6.975°	5.62%	0.25	0.110rad	0.90	5.13mm
6	7.040°	6.80%	0.25	0.159rad	1.29	-
Ave. 1-6		6.40%		0.143rad	1.16	5.19mm
σ 1-6				0.040rad	0.32	0.55mm

* Measured through one deviator

Another way of determining the wobble coefficients and angles is to compute them based on measured elongations. Table 3.12 gives the measured elongations in column (1) and the wobble angles and coefficients β and k in columns (4) and (5) calculated using these elongations and the elastic modulus found in the bench test. Once again, the losses in span D5 appear to be larger than those measured in span D2. However, the measured elongations were consistent with those measured in span D2 when the differences in tendon length were

accounted for. The assumed loss distribution over the length of the tendons and the modulus of the steel strand both have uncertainties. Because of the calculation method, any variation in actual strand area would be perceived as a change in elastic modulus. The average values for β and k in Tables 3.11 and 3.12 actually compare quite well on average, even though the standard deviation of the individual wobble angles and coefficients is 28% of the average based on the strain gauge data, and 22% of the average based on the elongation data.

Table 3.12 Measured elongations from friction tests on span D5

Test Tendon	(1) Measured Elongation (mm)	(2) Bench Test Modulus (MPa)	(3) Assumed Friction Coefficient	(4) Calculated β^* (Radians)	(5) Calculated k
1	262	190,500	0.25	0.190	1.53
2	267	190,500	0.25	0.116	0.95
3	265	190,500	0.25	0.146	1.20
4	264	190,500	0.25	0.164	1.35
5	267	190,500	0.25	0.116	0.95
6	267	190,500	0.25	0.115	0.94
Ave. 1-6	265	190,500	0.25	0.141	1.15
σ 1-6	2.1			0.031	0.25

* Measured through one deviator

Elastic Shortening Losses

The elastic shortening losses measured in the instrumented external tendons are given in Table 3.13. Strain changes in the tendons were symmetric about the longitudinal centerline of the bridge since the tendons were stressed in pairs using two rams and one hydraulic pump. Instrument locations 1, 2, and 3 are shown in Figure 3.8. Tendon locations and deviations are shown in Figure 3.9. In general, the data were very consistent. Stressing of the deviated external tendons tended to cause more elastic shortening loss in the deviated legs of the previously stressed tendons at gauge locations 1 and 3. Stressing of the bottom slab internal tendons produced more elastic shortening loss in the middle leg of the instrumented deviated tendons than stressing of the deviated tendons. This loss is because the bottom slab internal tendons had greater eccentricity with respect to the girder cross section than did the deviated external tendons.

Table 3.13 Elastic shortening losses in tendons in span D5

Tendon Stressed	Strain (Stress) Change from Elastic Shortening Average for All Stressed Tendons at Each Gauge Location in $\mu\epsilon$ (MPa)		
	1	2	3
Deviated			
2 and 5	-48.9	-51.9	-41.2
1 and 6	-38.2	-52.1	-39.9
Ave. Deviated	-43.6 (-9.1)	-52.0 (-10.9)	-40.6 (-8.5)
Straight			
10 and 11	-39.9	-58.7	-40.1
9 and 12	-40.7	-59.3	-40.7
8 and 13	-41.4	-58.7	-40.2
7 and 14	-37.7	-57.6	-37.4
Ave. Straight	-39.9 (-8.3)	-58.6 (-12.2)	-39.6 (-8.3)

3.3.3 Ramp Girder Tests

The five-span continuous girder on Ramp P was constructed in balanced cantilever from the four interior piers, then made continuous with cast-in-place closures and both internal and external post-tensioning. The interior anchor segment anchorage zones for the external tendons were constructed as deviation saddles. The anchorages deviated downward at the live end to facilitate stressing inside the box girder core. Therefore, even though the tendons used were 19-15mm strand tendons, the anchor zone configuration did not exactly match that of the bench test.

Friction Losses

The test program consisted of strain measurements of six external tendons on either side of two deviators using multiple electronic strain gauges. Measurements were taken near the downstation deviator and the adjacent horizontal deviator in span P16 (see Figure 3.10). Tendons T1 and T2 were continuous over spans P16 and P17 and were jacked from the downstation end only, near the instrumentation. Tendon T3 was continuous over spans P14, P15 and P16 and was jacked from both ends. The geometry of the tendons through the deviators under study is shown in Figures 3.10 and 3.11, with the angle changes given in column (1) of Table 3.14. The results from the friction tests are also given in Table 3.14.

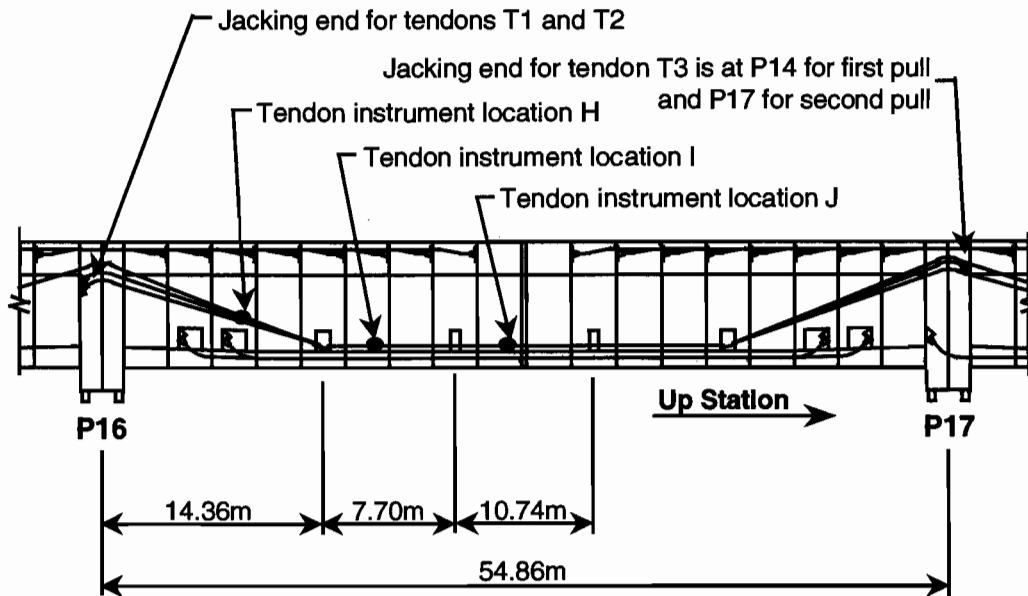
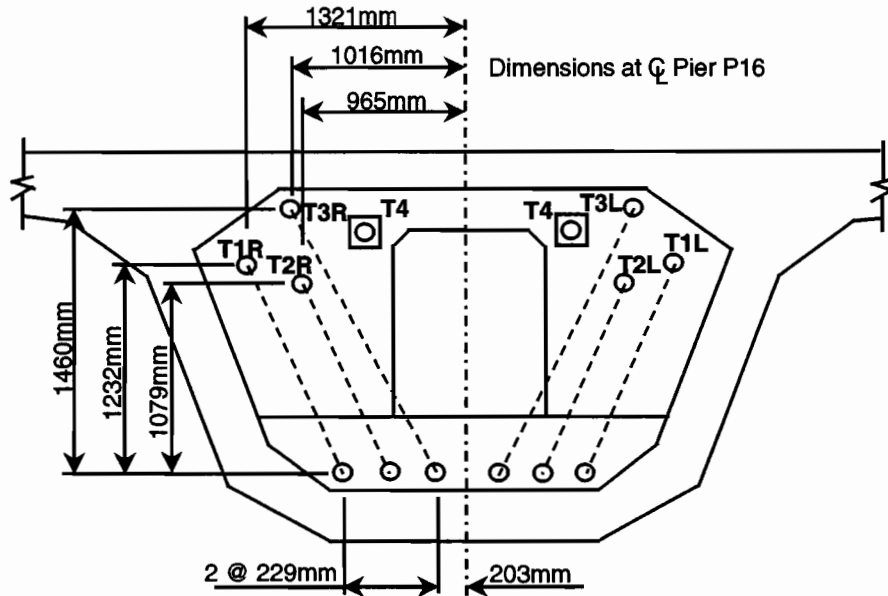


Figure 3.10 Ramp P tendon geometry-elevation



Section Looking Down Station

Horizontal curvature not shown

Figure 3.11 Ramp P tendon geometry—end view

Table 3.14 Ramp P friction test results from strain gauges

Test Tendon	(1) Angle Change	(2) Measured % Loss	(3) Assumed Friction Coefficient	(4) Calculated β^* (Radians)	(5) Calculated k
T1L	4.870°	18.2	0.25	0.719	8.45
T1R	7.449°	15.6	0.25	0.548	4.22
T2L	4.344°	6.6	0.25	0.197	2.60
T3R	9.695° **	11.8	0.25	0.333	1.97
Ave.					4.31

* Additional angle β is applied at each deviator and each anchor or pier segment (9 total for tendons T1L, T1R, T2L and T2R, and 14 total for tendons T3L and T3R)

**Angle change through two deviators

The strain gauges consistently measured a large amount of friction loss through the deviators, as shown in column (2) of Table 3.14, as was the case in span D5. The measured loss was as high as 18% through the deviator for tendon T1L. Expected loss through this deviator would be 3% using $\mu=0.25$ and $\beta=0.04$ in Equation 3-3. Since the gauges were all located on the top strands of the tendon, and these were the strands in direct contact with the deviator pipe, the measured values may be representative of these outer strands and may not be accurate for the tendon stress on average. The average wobble coefficient $k=4.3$ in column (5) of Table 3.14 is unrealistic. A wobble of this magnitude would require a construction error resulting in an angle change of about 40° at each deviator.

The wobble angles β and wobble coefficients k , shown in columns (4) and (5) of Table 3.15, calculated based on the bench test tendon modulus and the measured elongations, also indicated high friction in the Ramp P tendons. The results were based on the measured elongation data in column (1) of Table 3.15 and the bench test modulus in column (2). The calculated wobble coefficients in Table 3.15 were sensitive to the value of the tendon elastic modulus. Based on the elongations and dead end force measurements on the mainlane girder D2,

the bench test modulus was most likely smaller than the elastic modulus of the tendons in Ramp P. Therefore, the average calculated wobble coefficient $k=1.1$ in column (5) of Table 3.15 most likely was unrealistically large. The friction loss in tendons T3L and T3R, measured by a lift-off test when stressing the downstation end of the tendon, revealed much less apparent friction loss. The results of the lift-off test are shown in Table 3.16. The calculated wobble terms in columns (4) and (5) are small, with $k=0.11$ on average. Since the downstation end of the tendon was stressed many hours after the upstation end, the force distribution along the tendon may have changed over time. This phenomenon has been measured both in the laboratory [22] and in the field [10] and is more pronounced in tendons with high friction loss. Force near the live end of these tendons may have decreased, while force at the dead end increased. Therefore, using the lift-off test to measure friction loss may lead to overestimation of the average stress in the tendon because of the lapse in time.

Table 3.15 Measured elongations from friction tests on Ramp P

Test Tendon	(1) Measured Elongation (mm)	(2) Bench Test Modulus (MPa)	(3) Assumed Friction Coefficient	(4) Calculated β^* (Radians)	(5) Calculated k
T1L	593	190,500	0.25	0.0404	0.393
T1R	550	190,500	0.25	0.132	1.190
T2L	558	190,500	0.25	0.128	1.287
T2R	552	190,500	0.25	0.144	1.374
T3L	798	190,500	0.25	0.124	0.976
T3R	760	190,500	0.25	0.157	1.161
Ave.					1.06

* Additional angle β is applied at each deviator and each anchor or pier segments (9 total for tendons T1L, T1R, T2L and T2R, and 14 total for tendons T3L and T3R)

Table 3.16 Lift-off test results for tendon T3

Test Tendon	(1) Dead End Force/ Live End Force	(2) Assumed Friction Coefficient	(3) Total Angle Change (Radians)	(4) Calculated β * (Radians)	(5) Calculated k
T3L	0.645	0.25	1.775	-0.0195	-0.011
T3R	0.558	0.25	1.893	0.441	0.233
Ave.				0.023**	0.11

* Total additional angle β for all deviators and anchor or pier segments

** Applied at each of the 14 deviators and saddles

Elastic Shortening Losses

The measured elastic shortening losses are given in Table 3.17. Losses in some tendons could not be measured because gauges were lost when three of the tendons failed during stressing. Instrument locations H, I, and J are shown in Figure 3.10. The elastic shortening strains from stressing each of the external tendons are not directly comparable to each other. Since the bridge was built on a substantial horizontal curve, no two tendon profiles were alike. The first tendon stressed, tendon T1L, had the most elastic shortening loss at -30.4MPa. This elastic shortening loss was small, at less than 2.5% of its stress after jacking. The total elastic shortening stress loss at location I was only 1.4% on average for the group of 6 tendons.

Table 3.17 Elastic shortening losses–Ramp P external tendons

Tendon Stressed	Gauge Location	Strain (Stress) Change from Elastic Shortening in Each Stressed Tendon in $\mu\epsilon$ (MPa)				
		T1L	T1R	T2L	T2R	T3R
T1R	H	-16.4				
T2L	H	-19.6	-17.8			
T2R	H	-17.8	-26.0	-21.5		
T3R	H	-16.4	-19.6	-17.1	-15.2	
T3L	H	-8.6	-7.6	-6.3	-8.9	-12.0
Total Loss	H	-78.8 (-16.5)	-71.0 (-14.8)	-44.9 (-9.4)	-24.1 (-5.0)	-12.0 (-2.5)

T1R	I	-27.2				
T2L	I	-30.4	-30.4			
T2R	I	-31.1	-35.5	-27.6		
T3R	I	-33.2	-32.3	-32.3	-33.6	
T3L	I	-23.8	-23.8	-25.6	-22.8	
Total Loss	I	-145.7 (-30.4)	-122.0 (-25.5)	-85.5 (-17.9)	-56.4 (-11.8)	

T3L	J					-36.7
-----	---	--	--	--	--	-------

Long-Term External Tendon Strains

Although almost all of the span D5 tendon gauges became debonded from the tendon after only a week beyond the time of stressing, the gauges on the Ramp P external tendons performed well for months after stressing. Figure 3.12 shows a plot of tendon stress over time for tendon T1 on either side of a vertical deviator. The most pronounced loss apparent in the figure is the initial friction loss between the gauges at location H and at location I at about 200MPa, although one of these plots is for T1L and the other is for T1R and the tendons were stressed at different times. About 40MPa of the total time dependent loss at location H occurred in the first month after stressing. Tendon T1 at location I only lost about 20MPa in the first month after stressing. The tendons were not grouted during this month, so it is conceivable that some of the force in the tendon at location H migrated through the deviator to the tendon length at location I during this time period because of tendon slippage through the deviator. The additional loss seen to occur between April 1997 and June 1997 may be due in part to the average seasonal temperature variation and the difference in the coefficients of thermal expansion between the tendon steel and the girder concrete. The total loss over the ten-month period was about 70MPa on average, amounting to 6% of the original tendon force following stressing. The tendon forces plotted in Figure 3.12 appear to be stable by August 1997.

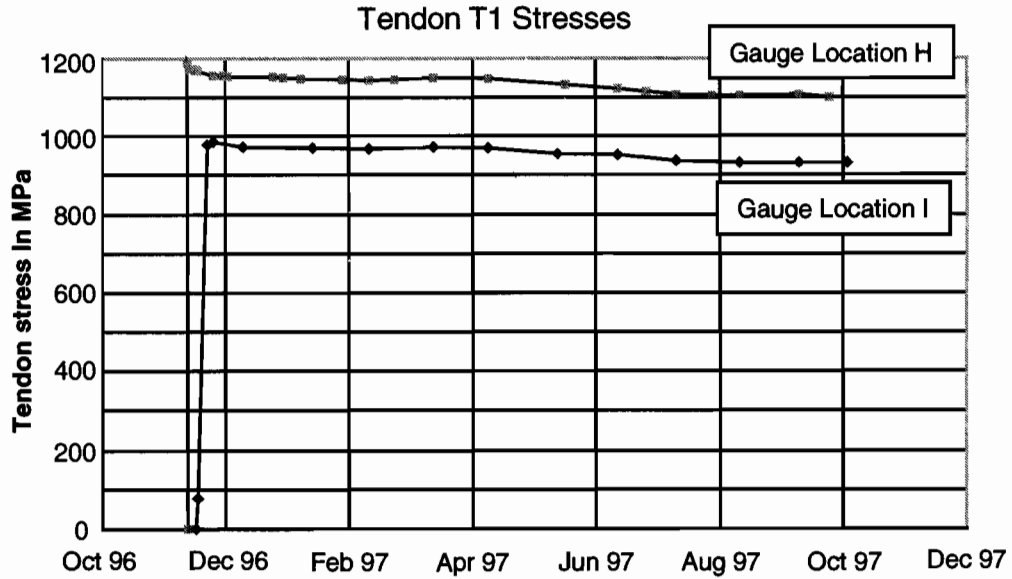


Figure 3.12 Strain change in ramp tendons over time

3.3.4 Large Ramp Pier Tests

Pier P16 was the only post-tensioned pier studied on the project. The pier had two 19-15mm strand U-shaped tendons. The U-bend was provided by rigid pipes cast in the footing, as shown in Figure 3.13. The anchorage zone geometry was straight, so that a direct comparison could be made between anchorage zone losses measured in the bench test and the pier tendon tests. Tendons were cut to an approximate length, lifted by crane to the top of the pier, and inserted into the tendon ducts. The crane was then used to pull the tendons through the full lengths of the ducts. After installation of the post-tensioning anchorage heads and wedges, the tendons were stressed in the order shown in Figure 3.14. The tendon ducts were placed so as to cross each other within the footing in plan. Thus, the anchorages at points 1 and 2 belonged to the same tendon.

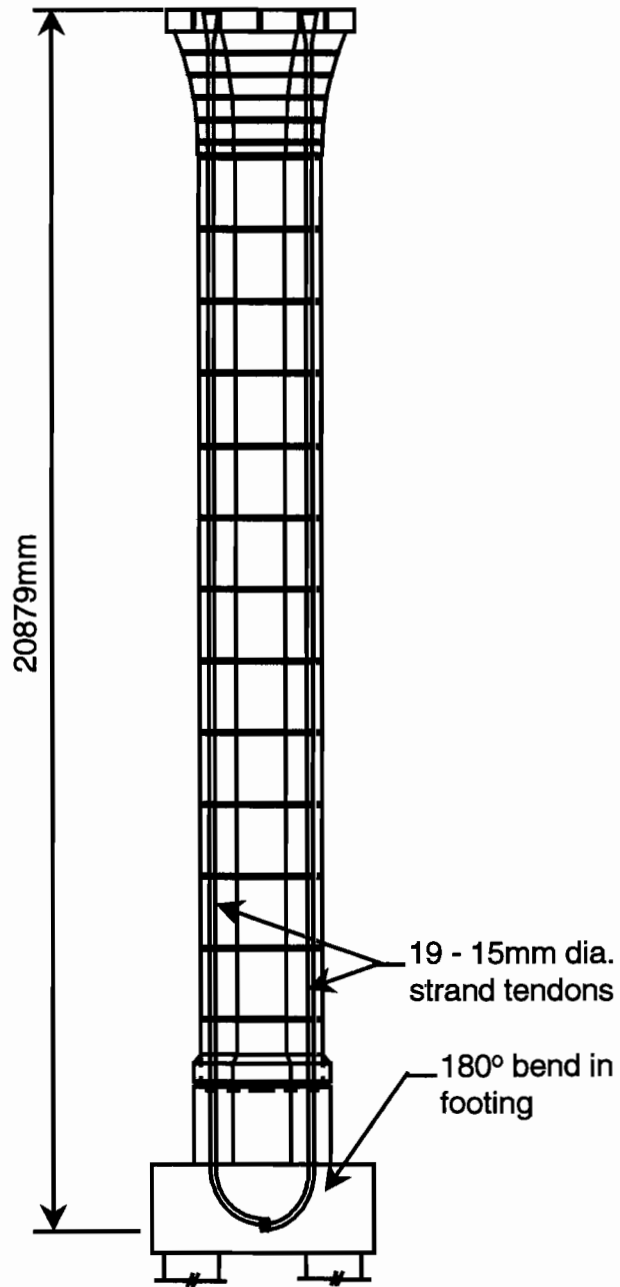
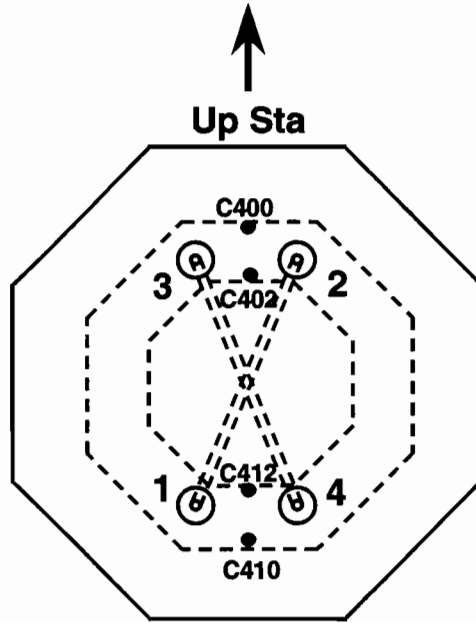


Figure 3.13 Pier P16 elevation and tendon profiles



Plan View - Pier P16

Figure 3.14 Sequence of final post-tensioning of pier P16 tendons

Friction Losses

The force at the dead end of the tendon was measured after stressing the other end by performing a lift-off test with the ram. The lift-off stress on the dead end of the tendon was about 49% of the live end stress on average after one pull. Subtracting out the anchorage zone losses based on the results of the bench test, the measured coefficient of friction μ in the rigid steel pipe with 180° angle change was 0.240 in the first tendon and 0.214 in the second tendon. This agrees well with the usual friction coefficient $\mu=0.25$ chosen for rigid pipe deviators in the first tendon. The friction loss in the U-bend pipe of the pier was of little consequence since the tendons were stressed from both ends, and no substantial friction occurred at any point other than in the U-bend pipe.

Elastic Shortening Losses

Concrete strains were measured once every minute during the post-tensioning process. In addition, a pressure transducer was attached to the hydraulic ram to measure jacking forces at the four tendon anchor locations. Figure 3.15 shows a plot of readings taken by the pressure transducer and strain gauges oriented along the vertical axis of the pier in segment PC16-1 over the course of the post-tensioning process. The tendons were stressed in the order indicated adjacent to the plot of the pressure transducer output.

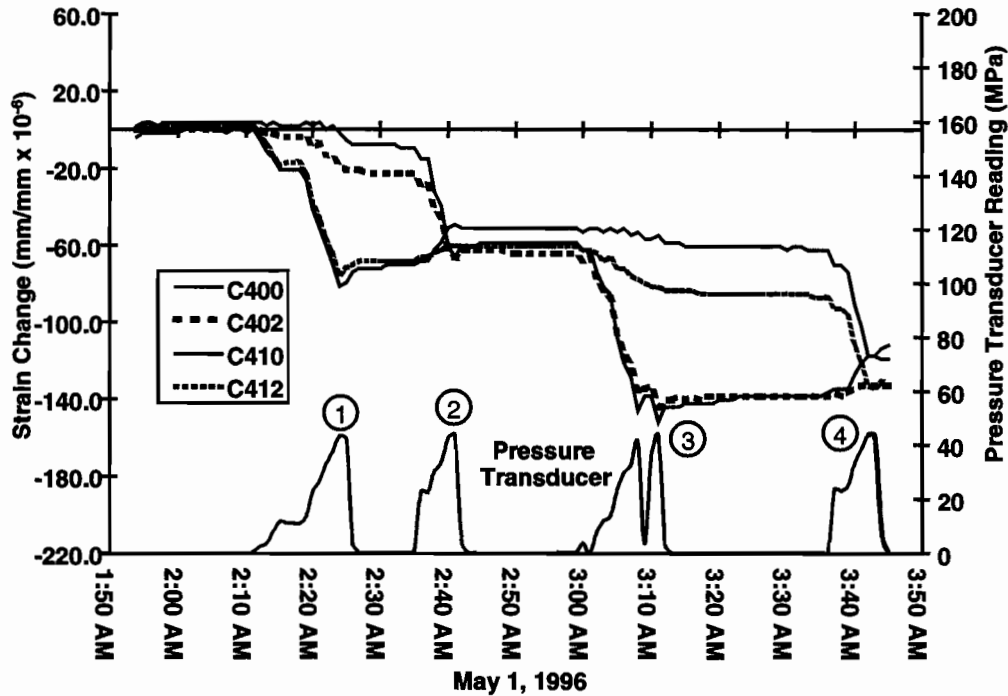


Figure 3.15 Selected axial strains in segment PC16-1 during pier post-tensioning, north-south axis locations

As shown in Figure 3.15, gauges located along the axis running north-south through the pier's cross section showed several well-defined trends during post-tensioning. The different strain responses after stressing at location 1 and 3 that are seen on opposite sides of the cross section were caused by the eccentricity of effective prestress force on the pier due to friction losses. In a frictionless tendon the forces at 1 and 2 would be equal after stressing from one end. Thus the axial stress would be uniform. However, due to friction the tendon force was not equalized until the tendon was jacked from location 2 and then again from location 4. Because position 1 was primarily eccentric with respect to the east-west centroidal axis, large differential strains occurred in the north and south faces.

After stressing at position 2 was complete, the post-tensioning loads experienced by the pier were nearly symmetric about the east-west axis. During stressing at point 2, concrete strains at gauges C410 and C412 were increasing because of the eccentricity of the jack at point 2 was beyond the Kern point for the cross section. This strain increase produced a gain in force of the tendon length anchored at point 1. The same behavior was seen in the tendon anchored at points 3 and 4. Concrete strain changes measured by the gauges during stressing at locations 3 and 4 produced an elastic shortening loss in the tendon anchored at points 1 and 2 of approximately $82\mu\epsilon$ or 16MPa.

3.4 DISCUSSION OF RESULTS

The results from these post-tensioning force and strain measurements can be compared to the results of other studies, field data, and typical design solutions based on methods recommended in bridge design codes. These comparisons should give bridge designers some insight into the accuracy of their design calculations, and most importantly, show which variables have the greatest impact on accuracy.

3.4.1 Friction Losses

Friction losses were measured for internal tendons, for external deviated tendons, and in the anchorage zones. The impact of wedge seating length is also directly related to the frictional performance of the tendon.

Internal Tendons

The internal tendons studied on the project were straight bottom slab tendons. Curvature changes over the majority of the length of the tendon were very small. Almost all of the friction loss in these tendons was due to

losses in and near the anchorage regions, not from wobble friction along the length of the duct. The segments for this project were cast using the short-line method. The bulkhead had permanent holes cut for locating the bottom slab tendons. The semirigid steel ducts were held in place between the bulkhead and match-casting segment with an inflatable mandrel. This mandrel was capable of holding the ducts solidly in place during the casting process. Measured wobble losses in these ducts were very small, as seen in Table 3.9. The modulus of elasticity of the tendons calculated from the elongation data for tendons 12 and 13 in span D2 was somewhat higher than that calculated in the bench test. If the tendon modulus of elasticity is assumed to be 193,500MPa, as measured for tendon 12 in Table 3.10, the β angles in Table 3.10 would decrease substantially. β for tendon 12 would become 0.0013 radians, which relates to $K=0.0000048\text{m}^{-1}$. β for tendon 13 would become 0.2260 radians, or $K=0.00084\text{m}^{-1}$. The change in elastic modulus from 190,500MPa to 193,500MPa represents a 1.6% increase in stiffness. Such a change could have resulted from a 0.8% or 0.04mm increase in wire diameter, which is within the wire ASTM Specification A 416-74 [30] limits for prestressing wire.

Most of the internal tendon research data presented in Section 3.2 primary was concerned with determining the coefficients of friction and wobble in draped internal tendons. Draped profile internal tendons primarily are used in non-segmental cast-in-place box girders, although they can also be used in segmental precast and cast-in-place girders. The ducts can not be held in place using mandrels and therefore are subject to placement error during construction. Wobble coefficients were found in other studies to range from 0.0007m^{-1} to 0.0016m^{-1} for commonly used semirigid steel duct.

An appropriate approach for the design of tendons similar to the US 183 bottom slab 19-strand tendons would not include these latter high wobble loss coefficients if the use of mandrels during construction is to be specified and their effectiveness verified. When using such mandrels, a wobble loss coefficient of 0.0007m^{-1} and a friction coefficient of about 0.16 should be chosen for use along the majority of the length of the tendon. Friction will be generated from curvature changes due to the vertical and horizontal alignment of the bridge, as well as in the live end anchorage region. Friction calculation using these coefficients would provide a conservative result compared to the measured data presented in Table 3.9.

External Tendons

The external tendons used in the US 183 box girders were 19-15mm strand tendons, a common size and efficient tendon for the span-by-span construction used on the mainlane girders. The large jacks used to stress these tendons were hung from rigging at the open end of the mainlane girder and stressed from one end only. On the other hand, the multi-span 19-strand external tendons in Ramp P had to be stressed with these same large rams from inside the core of the girder. Handling and clearances became a problem, particularly because of the obstructions on the bottom slab and the horizontal curvature of the bridge.

Since the short-line method of casting was used, the forms holding the rigid ducts for the deviators and anchor segments allowed little adjustment for geometry changes. Small placement errors were bound to occur and had a measurable impact on friction. Roberts recommended that an additional inadvertent angle change of 0.04 radians be applied at each deviator to account for duct misalignment. This recommendation was primarily based on results measured in girders constructed by the span-by-span method. The inconsistency of the measured moduli of the tendons in span D2 shown in Table 3.10 indicates that a misalignment loss may have occurred in the live end anchor segment, and therefore the β values in Table 3.9 may actually be smaller than shown. If 0.04 radians of additional angle change is applied only at the two deviators, the calculation of the dead end force as measured by the load cell in span D2 is quite accurate. The average force in the tendon, however, is lower than the calculation predicts, and the elongations are lower than predicted as well.

Using the modulus of elasticity measured for tendon 12 in Table 3.10, at 193,500MPa, and the elongation data for all the deviated external tendons tested in spans D2, D5, and Ramp P, the β values shown in Table 3.18 were calculated. The table uses the commonly applied coefficient of friction for external tendons of $\mu=0.25$. The galvanized steel deviator pipes used in the first several spans of mainlane D spine were inadvertently bent with a 2m radius instead of the 7.5m radius drawn in the plans. The large β angles in Table 3.18 for the mainlane span D2 and D5 tendons indicate that the 0.25 coefficient of friction chosen was too small for the tight radius pipe bend. The large β angles in Table 3.18 would have revealed themselves as visible duct misalignments in the bridge, but these were not apparent. For these tight bends, the coefficient of friction is more likely closer to 0.35, the maximum of the range specified by ACI-ASCE [27] for wire cables on metal sheathing. The wobble angles for all the span D2 and D5 deviated external tendons based on the measured elongations are recalculated

in Table 3.19 using 0.35 as the friction coefficient. These β angles appear to be more realistic for spans D2 and D5, with an average of $\beta=0.0373$ radians. The standard deviation of the wobble angle β was high, at about $\sigma=0.04$ radians, regardless of the friction coefficient used.

Table 3.18 Elongation measurement based wobble coefficients for all deviated external tendons, $\mu=0.25$

Test Tendon	Span	Measured Elongation (mm)	Assumed Elastic Modulus (MPa)	Total Angle Change α (rad)	Assumed Friction Coefficient μ	Resultant Wobble Angle β^*
2	D2	275	193,500	0.2472	0.25	0.2217
3	D2	277	193,500	0.2461	0.25	0.1034
1	D5	262	193,500	0.2486	0.25	0.1271
2	D5	267	193,500	0.2449	0.25	0.0634
3	D5	265	193,500	0.2432	0.25	0.0843
4	D5	264	193,500	0.2432	0.25	0.0994
5	D5	267	193,500	0.2435	0.25	0.0540
6	D5	267	193,500	0.2457	0.25	0.0530
Ave.	D2, D5					0.1008
σ	D2, D5					0.0554
T1L	Ramp P	593	193,500	0.9256	0.25	0.0277
T1R	Ramp P	550	193,500	0.9982	0.25	0.1181
T2L	Ramp P	558	193,500	0.8945	0.25	0.1144
T2R	Ramp P	552	193,500	0.9423	0.25	0.1297
T3L	Ramp P	798	193,500	1.7748	0.25	0.1139
T3R	Ramp P	760	193,500	1.8926	0.25	0.1469
Ave.	Ramp P					0.1085
σ	Ramp P					0.0415

* β angle applied at each deviator segment (2 total for all tendons on spans D2 and D5), or each deviator and anchor segment (9 total for tendons T1L, T1R, T2L, and T2R, and 14 total for tendons T3L and T3R)

Table 3.19 Elongation measurement based wobble angles for deviated external tendons, $\mu=0.35$

Test Tendon	Span	Measured Elongation (mm)	Assumed Elastic Modulus (MPa)	Total Angle Change α (rad)	Assumed Friction Coefficient μ	Resultant Wobble Angle β^*
2	D2	275	193,500	0.2472	0.35	0.1231
3	D2	277	193,500	0.2461	0.35	0.0385
1	D5	262	193,500	0.2486	0.35	0.0553
2	D5	267	193,500	0.2449	0.35	0.0131
3	D5	265	193,500	0.2432	0.35	0.0255
4	D5	264	193,500	0.2432	0.35	0.0363
5	D5	267	193,500	0.2435	0.35	0.0038
6	D5	267	193,500	0.2457	0.35	0.0027
Ave.	D2, D5					0.0373
σ	D2, D5					0.0392

* β angle applied at each deviator segment (2 total for all tendons on spans D2 and D5)

The high β values for the tendons of Ramp P in Table 3.18, averaging $\beta=0.11$ radians, may be correct. The horizontal and vertical curvature of the bridge would have required that most every deviator pipe have a different radius bend, and that all pipes be carefully measured into place. This placement was not practical, nor was the provision for adjustment of the holes in the deviator form that held the pipes in place. To simplify the construction of deviators without increasing friction, "diabolos" have been used to replace the bent deviator pipes [31]. A diablo is a deviator pipe with a trumpet bell shape on each end. The radius of the bell can be designed to accommodate many deviation angles, so a few standard diabolos can be used in all the deviator segments on a project. These diablo pipes were used successfully on the Second Stage Expressway System (SES) elevated bridges in Bangkok, Thailand. High density polyethylene ducts passed continuously through the diabolos on these bridges.

Based on the measured data, the external deviated tendon design for spans D2 and D5 could be performed accurately by choosing 0.30 or 0.35 as the coefficient of friction and using the $\beta=0.04$ at each deviator as suggested by Roberts [10]. The normal coefficient of friction of 0.25 should not be used in this case because of the tight radius bend in the deviator pipes. This tight radius bend was detrimental to friction loss, as well as to the service -level performance of the deviator. Also, the β angle need not be applied at the live end anchor segment since the duct at that location is short and straight, even though the potential for misalignment does exist.

The friction performance for the external tendons tested in Ramp P would be much more difficult to predict than that of the mainlane tendons. Both the elongation and strain gauge data showed that friction loss was large through the deviators. On the other hand, the lift-off data for tendons T3L and T3R revealed that the friction forces did not stay locked in at the deviators and pier segments. The force in the tendon tended to average out over time, and a normal design calculation using $\mu=0.25$ and $\beta=0.04$ applied at all deviators and pier segment saddles would predict the force in the dead end of the tendon quite well. Unfortunately, the short measured elongations meant that the average stress in the tendon was below that calculated using the coefficients above. These long tendons were good candidates for lubrication with graphite since the elongations were consistently short. The lubrication may not have helped in this case since much of the friction loss may have occurred very near the live end.

The saddle-shaped duct immediately adjacent to the inclined jacking anchorage did not allow strands that tangled upon insertion into the anchor head to untangle, as was the usual case with the straight anchorages and ducts of the mainlane tendons. Furthermore, the large jack used for the 19-strand tendons within the core of the girder had to be hoisted up to be level with the anchorage plate by a cable attached to its lifting flange, then rotated to avoid hitting its hydraulic connections on the top flange of the girder. This necessary maneuver added a twist to the tangle that had probably already formed. Total elongation including removal of slack was over 1m for tendons T3L and T3R. Strands could be heard rearranging themselves in the anchor segment saddle during the entire stressing process. Entangled strands evidently were being pulled into the anchor head. This entanglement resulted in three failed tendons, with breakages immediately beyond the anchor head. The long elongations, deviation saddle adjacent to the anchorage, and difficult access to the large tendons were to blame. The tangled strands in contact with the saddle-shaped duct adjacent to the stressing anchorage probably increased friction at this location and reduced the average stress over the entire length of the tendon.

Misalignments and duct obstructions were noted, but not consistently of the magnitude needed to produce the β angles in Table 3.18. Most likely the coefficient of friction between tendon and duct in Ramp P was closer to 0.30 than 0.25. A design β angle higher than 0.04 radians may be warranted in spans with significant horizontal curvature, unless a diablo-type deviator pipe is used.

Anchorage Zone Losses

The friction losses occurring in the anchorage zone as the strands of the tendon are flared to enter the anchor head need to be considered. This loss at the jacking end of the tendon reduces the stress over the entire length of the tendon and reduces elongations accordingly. The loss at the jacking end anchorage of the 19-15mm strand tendons was measured to be 2.2% of the jacking force. Losses for different tendon and stressing systems may vary from this, but losses at the stressing end of strand-type tendons are generally in the 2%-3% range [10]. The anchorage zone loss measured for the 3-strand wing tendon tested in mainlane span D2 was 1.74% for live end. The loss measured for the 7-strand wing tendon was slightly larger at 2.33% for the live end.

Wedge Seating Losses

The wedge seating lengths shown in Table 3.11 indicate that the average seating length for this jack and anchorage system was about 5.2mm. Designers usually assume a wedge seating displacement of 6mm after the wedges are power seated. All measured seating displacements were smaller than 6mm, so the common design value would be appropriate in this case.

3.4.2 Elastic Shortening

Table 3.20 gives the measured and calculated strain change in the deviated external tendons of span D5 due to elastic shortening of the girder from the tensioning of adjacent tendons. The measured data, given in Table 3.13, are quite consistent from tendon to tendon. The elastic shortening stress losses are usually calculated for a group of similar tendons that are stressed in some sequence. The total elastic shortening of the girder along the tendon path is calculated from the tensioning of the entire tendon group, and one half of this strain is assumed to act on every tendon as an average elastic shortening loss. The calculated elastic shortening strains for the tendons in Table 3.20 are from the stressing of a pair of external tendons or a pair internal tendons, all 19-15mm strand tendons. In this way, the calculated values could be directly compared to the measured values. Gauge locations 1, 2 and 3 are shown in Figure 3.8.

Table 3.20 Calculated and measured elastic shortening losses in tendons in span D5

Pair of Tendons Stressed		Strain Change from Elastic Shortening Average for All Stressed Tendons at Each Gauge Location in $\mu\epsilon$		
		1	2	3
Deviated External	measured	-43.5	-52.0	-40.6
	calculated	-31.4	-71.8	-37.2
Bottom Slab Internal	measured	-39.9	-58.6	-39.6
	calculated	-49.3	-88.9	-49.3

The calculated strains in Table 3.20 for the central leg of the tendons are generally larger in magnitude than the measured strains. This difference exists for three reasons. First, the modulus of elasticity of the concrete used in the calculations was taken from test results of concrete samples. The modulus of elasticity of the samples, though taken from the same batch of concrete as the structure, consistently was lower than that of concrete in the structure. Differences in curing conditions and moisture content at the time of loading resulted in significantly different concrete stiffnesses. A design engineer usually has little information available to aid in the selection of the proper modulus of elasticity. This lack of information can adversely effect the accuracy of the calculations. Fortunately, elastic shortening losses are not usually substantial, and great accuracy is not needed. The second reason that the magnitude of the calculated values would be larger than the measured is that shear lag effects were not accounted for in the calculation. Shear lag effects would reduce or increase the elastic shortening of the installed tendons, depending on the tendon stressed, when compared to an ideally behaving beam.

The third and most important reason for the difference between the measured and the calculated strains is the slippage of the ungrouted tendons in the deviator pipes. The calculation assumed that the tendons would not move with respect to the deviator. It is evident that the tendons did slip, but not enough to cause equal strain change in the central and inclined legs of the tendons. A conservative approach for design would be to calculate the minimum and maximum possible elastic shortening strains of each leg of the tendons using either infinite or zero friction at the deviator pipes. This calculation is easily done since the strain change in each leg must be calculated for the infinite friction case. The worst case of loss could then be used for the design of the girder.

Table 3.21 gives the calculated and the measured elastic shortening loss strains for the deviated tendons of Ramp P. Gauge locations H and I are shown in Figure 3.11. The same characteristics are seen in these external tendons as were seen in the external tendons in the mainlane span D5. The calculated elastic shortening losses in the inclined and horizontal part of the tendons tended to be inaccurate because of slipping of the tendons in the deviator and a low assumed modulus of elasticity of the girder concrete.

Table 3.21 Calculated and measured elastic shortening losses–Ramp P external tendons

Pair of Tendons Stressed	Gauge Location	Strain Change from Elastic Shortening in Each Stressed Tendon in $\mu\epsilon$		
		T1	T2	T3
T2	H measured	-40.6		
	H calculated	-45.5		
T3	H measured	-26.1	-23.8	
	H calculated	-32.1	-28.8	

T2	I measured	-63.8		
	I calculated	-79.8		
T3	I measured	-56.6	-57.2	
	I calculated	-74.3	-74.3	

3.4.3 Long-Term Losses

Losses due to creep and shrinkage should be analyzed after two years or more of data collection so that seasonal effects can be separated from the permanent losses. Since the project segments were all precast 5 months or more before erection of the structural elements under study, most of the shrinkage strain had occurred in the concrete segments before any strain gauges were recording data. Also, the concrete was quite aged before loading, thereby greatly reducing its creep potential. For these reasons, long-term losses may not be as important as seasonal losses and gains in stress from average ambient temperature changes.

As seen in Figure 3.12, tendon stress losses from creep and steel relaxation are only about 6% of the total tendon force. It is doubtful that the state-of-the-art methods for creep calculation would be useful or necessary for this case. Steel relaxation could be responsible for up to 3% of the long-term loss. To predict the seasonal stress change in the tendons, the designer must know the coefficient of thermal expansion of the concrete, which is mostly a function of the coarse aggregate, the coefficient of thermal expansion of the prestressing steel, the seasonal temperature fluctuation, and the time of year and temperature of the materials on the day of stressing. Approximations will be necessary since the bridge design would be completed well before construction began.

3.5 CONCLUSIONS

The following conclusions have been made based on the measured data, other field and laboratory data, and field observations:

1. Measurements of live end anchorage zone friction losses in the laboratory bench test and in-place friction test indicated that an assumed design loss of 2% would be sufficient, unless actual live end losses are known from previous measurements.
2. Measured wedge seating losses were slightly less than the design value of 6mm. The current design value is adequate.
3. The bench test proved to be of little value to all parties except the researchers, other than as a basic calibration trial of the various pieces of the stressing system. The modulus of elasticity determined in the bench test did not prove to be representative of most of the tendons used in the structure, presumably because of slight variations in strand area. The in-place friction test was much more useful for providing information to the engineers and constructors. Accurate elongation calculations must be based on the results of an in-place friction test, otherwise the measured elongation tolerance may not be easily met.
4. Wobble friction in the straight internal ducts of the structure was quite small. These ducts were effectively held in position during concrete placement by inflatable mandrels. Friction coefficients for internal tendons in ducts constructed using mandrels can conservatively be taken as $\mu=0.16$ and $K=0.0007m^{-1}$. For draped

internal ducts, friction coefficients are $\mu=0.16$ and $K=0.0013\text{m}^{-1}$ for monolithic girders and $K=0.0016\text{m}^{-1}$ for segmental girders, based on other studies [19] [22].

5. The friction coefficient for external tendons in smoothly bent deviator pipes with consistent radius can be taken as $\mu=0.25$. The friction coefficient in the sharply bent deviator pipes used in some of the US 183 girders, at about a 2m radius, generated a coefficient of friction of about $\mu=0.35$. The sharp radius bend also caused large cracks in the deviator concrete and should be avoided.
6. The extra wobble angle $\beta=0.04$ radians suggested by Roberts [7] was found to be sufficient when applied at each deviator of the mainlane girders, if the proper coefficient of friction (0.35) was used in the calculation. The wobble angle $\beta=0.04$ radians was recommended based on studies of girders constructed span by span with straight or large radius horizontal geometry. The β angles measured in Ramp P, with a horizontal curvature of 221m, were higher at $\beta=0.11$ radians with an assumed friction coefficient of $\mu=0.25$. The horizontal curvature of the girder makes accurate deviator pipe placement more difficult, thereby warranting a higher design β angle. The β angle should be applied at all deviators and saddles. The use of a diabolo, or double trumpet-bell-shaped deviator pipe, would help reduce the β angles on curved structures. The diabolo-style deviator pipe was not necessary for the mainlane girders because the total friction loss was small for the one-span tendons, and the bridge alignment was nearly straight.
7. Anchorage of the long 150m (3-span) external tendons in Ramp P adjacent to a deviation saddle in the anchor segment proved to be unacceptable. The large elongations caused entangled tendons to be drawn close to the back of the anchor head where they broke. Straight anchorage geometry would have allowed the 19-strand tendons to untangle to some extent in the long distance between the anchorage and the deviator. No strand breakages of this type occurred in any of the 14 tendons in each of 162 spans of mainlane girder. The mainlane girders had straight anchorage geometry. If deviation saddles are required adjacent to a live end anchorage where a first pull must be made, the length of elongation should be limited to that of one span. Proper support of unstressed tendons over their deviated length prior to stressing would help reduce the total elongation substantially by reducing the slack length.
8. Elastic shortening loss calculations for the external deviated tendons were found to be inaccurate if slippage was not assumed to occur at the deviators. The measured values fell between the cases calculated using a deviator with infinite friction and zero friction between the deviator pipe and the stressed tendon. The more conservative loss from these two cases should be used for design.
9. Long-term losses were found to be small when compared to other losses for the girders under study. The segments were well aged before they were erected and prestressed.

CHAPTER 4

THERMAL GRADIENTS AND THEIR EFFECTS

4.1 PROBLEM DESCRIPTION AND TECHNICAL BACKGROUND

Structures of any common building material undergo strain changes when the temperature of all or part of the structure changes. Whether or not forces are generated in the structure depends on the distribution of temperature change in the structure, the shape of the structure, and the boundary constraints on the structure. In general, heat is conducted well in steel structures, tending to cause more uniform temperature changes in the whole structure when one part or surface is heated or cooled. Concrete structures, on the other hand, conduct heat poorly. Concrete structures can maintain temperature gradients from uneven heating or cooling that are larger and are maintained longer than in steel structures of similar proportion. Hybrid structures, such as steel plate girder bridges with concrete decks, have characteristics of both concrete and steel structures.

A thermal gradient is defined as a temperature distribution throughout the depth of a cross section relative to the minimum temperature, measured or predicted, which is taken as the zero reference point of the thermal gradient. When structures such as the US 183 box girders are designed, both an average temperature change in the structure, to reflect seasonal temperature changes, and nonlinear design thermal gradient through the depth of the structure must be applied. The thermal gradient design cases are used to predict stress changes in a girder that occur over a relatively short period of time, perhaps daily. The numerical values for these design cases are given in the *AASHTO Guide Specification* [23] or the *AASHTO LRFD Guide Specification* [9]. The design thermal gradients are discussed in Section 4.2.9 and 4.2.10. The accuracy of the thermal gradient design calculation, in predicting what is actually occurring in the structure over its lifetime, relies on both realistic design values and correct solution techniques. The measurements taken using thermocouples on US 183 were intended to check the current superstructure design code values for thermal gradient design. Two different cross sections were instrumented, one on the mainlane girder D5 and the other on Ramp P. The strain measurements taken in the structure were also compared to results calculated using common design methods. There has been much concern by the bridge industry as to the accuracy of the current recommended design thermal gradients for concrete box girders. Overly conservative design thermal gradients can increase the cost of a bridge, mostly through unnecessary prestressing. Thermal gradients can cause bending moments in continuous structures that are opposite in sign or the same in sign as the bending moments from live loads, thus enlarging the entire moment envelope.

Traditionally the bridge industry has ignored thermal gradient effects in bridge piers. Substructure elements should respond to thermal gradients just as would a superstructure member. Temperature and strain measurements were taken in mainlane pier D6 that is solid in cross section and in ramp pier P16 that is voided in cross section. The measured thermal gradients were compared to those measured in the superstructure for both distribution and magnitude. The importance of the stress changes from the measured thermal gradients was then evaluated, since a pier is a bending and compression member and not just a bending member like the superstructure.

4.1.1 Superstructure Behavior and Analysis Techniques

Thermal gradients in a box girder or other bridge girder are caused by changes in weather conditions combined with daily heating and cooling. Conditions needed for the development of a positive thermal gradient are shown in Figure 4.1(a). A positive thermal gradient is defined to exist when the temperature of the box girder deck surface (T_{deck}) is hotter than the minimum average temperature at some depth in the section (T_{min}). T_{min} usually occurs somewhere near the top of the girder webs, as seen in Figure 4.1(a). The sun primarily heats the deck surface over the course of a day. The maximum possible magnitude of the positive thermal gradient at deck level for a bridge girder occurs when a long period of cold and cloudy weather is followed by a day of clear and sunny weather. The deck-level magnitude of the positive thermal gradient is larger when the total amount of solar radiation reaching the structure over the day is increased. The location of the bridge determines the peak amount of solar radiation. Altitude, latitude, and relative humidity are all important in determining the peak amount of solar radiation. The magnitude of the gradient is decreased when heat is removed from the deck by wind or rain.

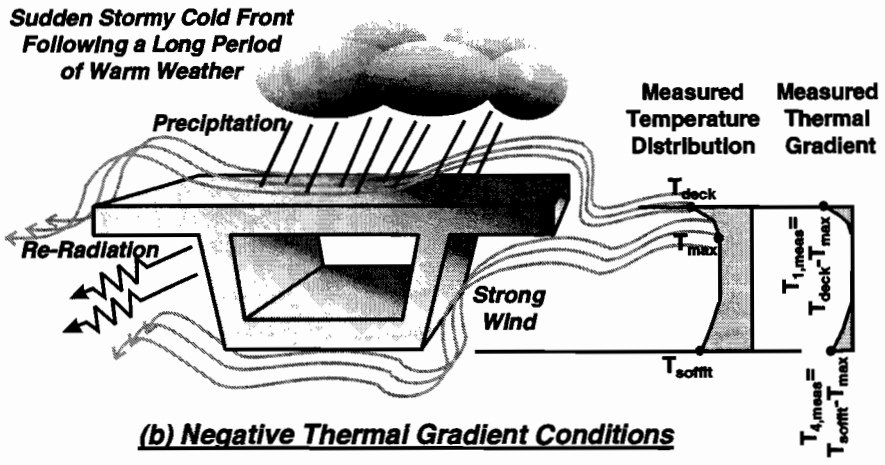
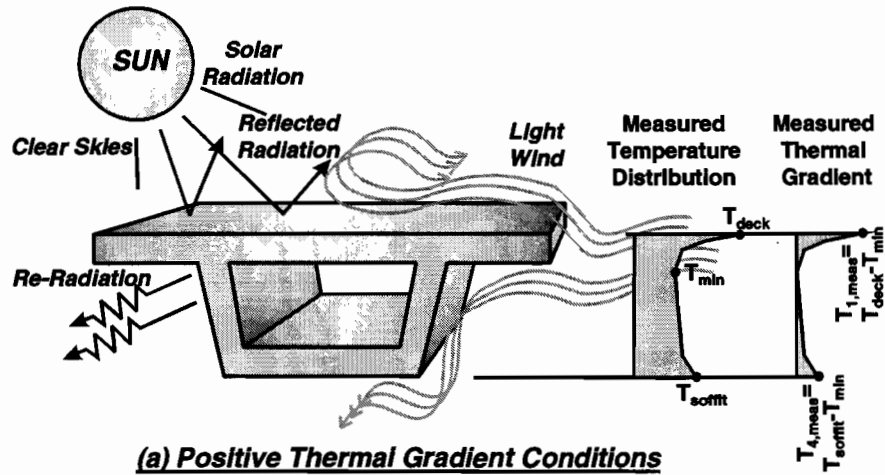


Figure 4.1 Climatic influences on superstructure thermal gradients

The maximum measured deck-level magnitude of the positive thermal gradient is defined as $T_{1,meas}$ and is calculated from the measured temperatures $T_{deck} - T_{min}$, as shown in Figure 4.1(a). Deck-level temperatures (T_{deck}) were taken 25mm below the actual deck-level concrete surface. The measured soffit-level magnitude of the positive thermal gradient is defined as $T_{4,meas}$ and is calculated from the measured temperatures $T_{soffit} - T_{min}$, as shown in Figure 4.1(a). Since much of the cross-sectional area of a box girder is in the top flange, the deck-level magnitude of the positive thermal gradient has much greater influence on the structure's response than the magnitude of the thermal gradient at other depths in the cross section.

The conditions necessary for the formation of a negative thermal gradient are shown in Figure 4.1(b). A negative thermal gradient exists when the deck surface of the girder (T_{deck}) is colder than the maximum average temperature in the webs (T_{max}). Negative gradient conditions of maximum negative deck-level magnitude ($T_{1,meas}$) occur when a relatively warm bridge girder is cooled rapidly by cold rain on the deck. Both peak positive and negative deck-level thermal gradient magnitudes occur most frequently in the spring, when solar radiation intensity is high and weather conditions change radically.

The deck-level magnitude of the thermal gradients is also dependent on the shape of the girder cross section. Figure 4.2 shows that an increase in the number of webs or a decrease in web spacing will lead to more heat conduction from the deck into the webs, reducing $T_{1,meas}$ for the positive thermal gradient case. In fact, measurements showed a decrease in deck-level temperature over the girder webs under positive thermal gradient conditions when compared to other portions of the deck surface. The massiveness of the cross section will also have an effect on the shape and deck-level magnitude of the thermal gradients. Design thermal gradients are only modified over the structural depth and are assumed constant across the width of a girder.

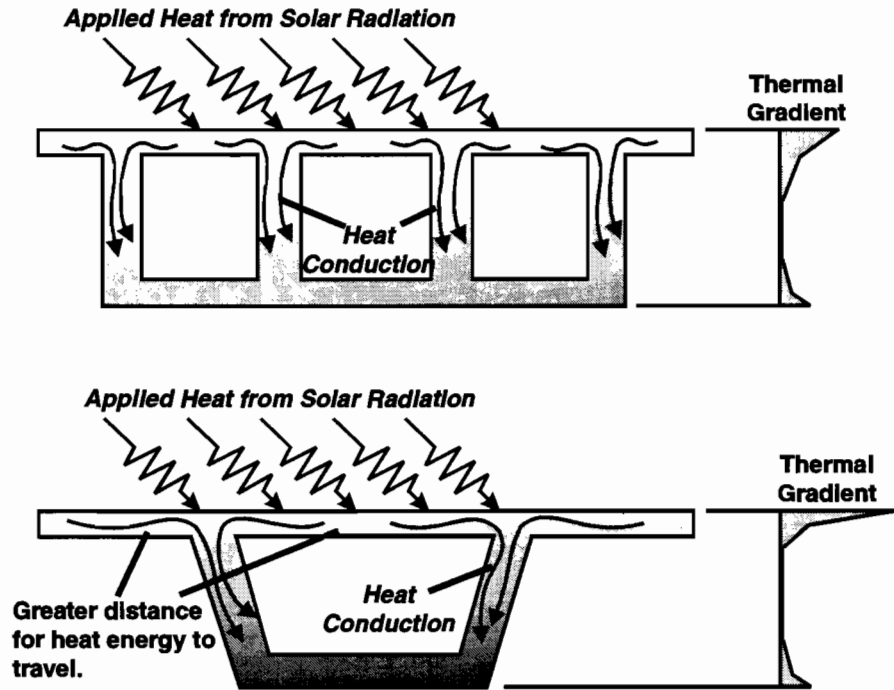


Figure 4.2 The effects of cross-section shape on thermal gradient shape

Design of a girder with the random cross section in Figure 4.3 for a thermal gradient usually begins by breaking the thermal gradient into the sum of three parts. The thermal gradient in Figure 4.3 is divided into a uniform temperature, a linear temperature gradient that is zero at the neutral axis of the girder, and a nonlinear temperature distribution that results in self-equilibrating stresses in the cross section. The division of the applied thermal gradient into these three parts greatly simplifies the analysis of the girder, if transverse plane sections in the girder are assumed to remain plane under the thermal loading. Figure 4.4 shows the structural response of a simple-span bridge to the first two of the three components of a nonlinear thermal gradient. The figure shows that the uniform temperature change results in only an expansion of the girder with no forces generated in the girder or at the supports. Similarly, the linear gradient causes a curvature change in the girder. The girder deflects into a circular arc with no resultant internal stresses and no reactions at the supports. The analysis of the simple span for thermal effects is elementary, except in the case of the nonlinear thermal gradient.

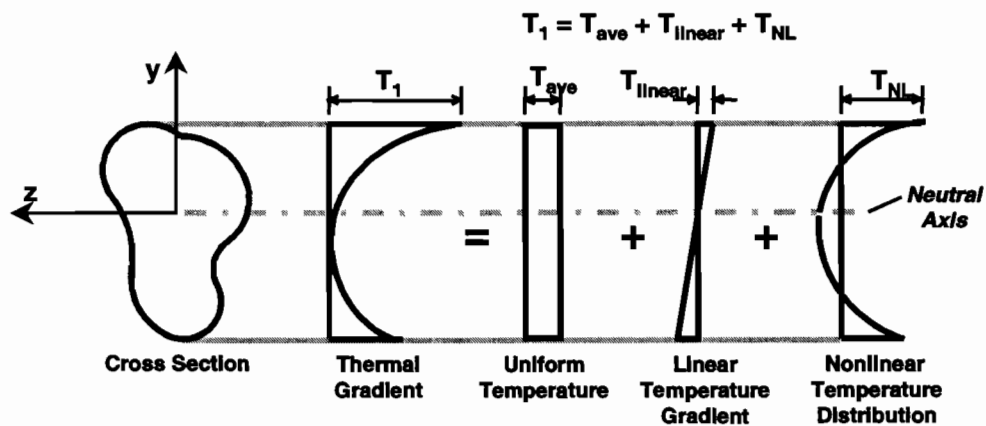


Figure 4.3 Components of a nonlinear thermal gradient

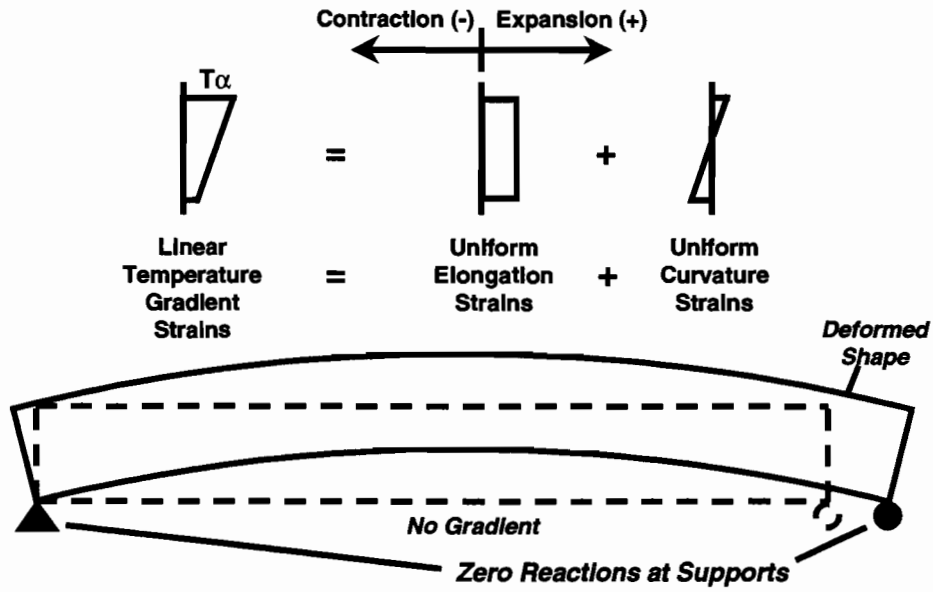
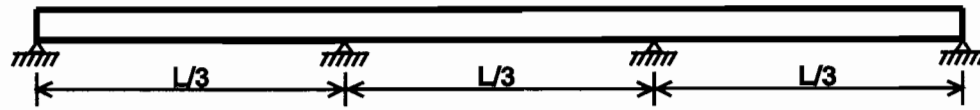


Figure 4.4 Effect of linear thermal gradient components on a statically determinate span

Figure 4.5 shows the response of a three-span continuous structure under the same linear thermal gradient loading as shown for the girder in Figure 4.4. In this case, the uniform elongation from the uniform temperature change is accommodated by expansion bearings at three of the four bearing locations. On the other hand, the girder cannot assume its new equilibrium position in a circular shape because of the dead weight of the structure or restraint at the bearings. The new equilibrium shape of the girder causes bending in the girder and reactions at the bearings.

Three-Span Structure



Support Reactions
Necessary to Make $\delta = 0$

Unrestrained Deformation with Uniform Curvature



Moments Due to Restraining Force at Center Supports



Actual Deformation

Figure 4.5 Effect of linear thermal gradient components on a statically indeterminate bridge structure

A girder with various boundary conditions subjected to a nonlinear thermal gradient can be analyzed the same way any girder is analyzed for other loads. Figure 4.6 shows how the stresses generated by the nonlinear thermal gradient are broken down into three components. Basically, the fixed end forces for the member are calculated. Once these fixed end forces are known, the member can be assembled into a structural analysis model. The thermal gradient stresses that do not contribute to the fixed end forces are the self-equilibrating stresses and are found by default. The fixed end forces and self-equilibrating stresses can be calculated using the following equations.

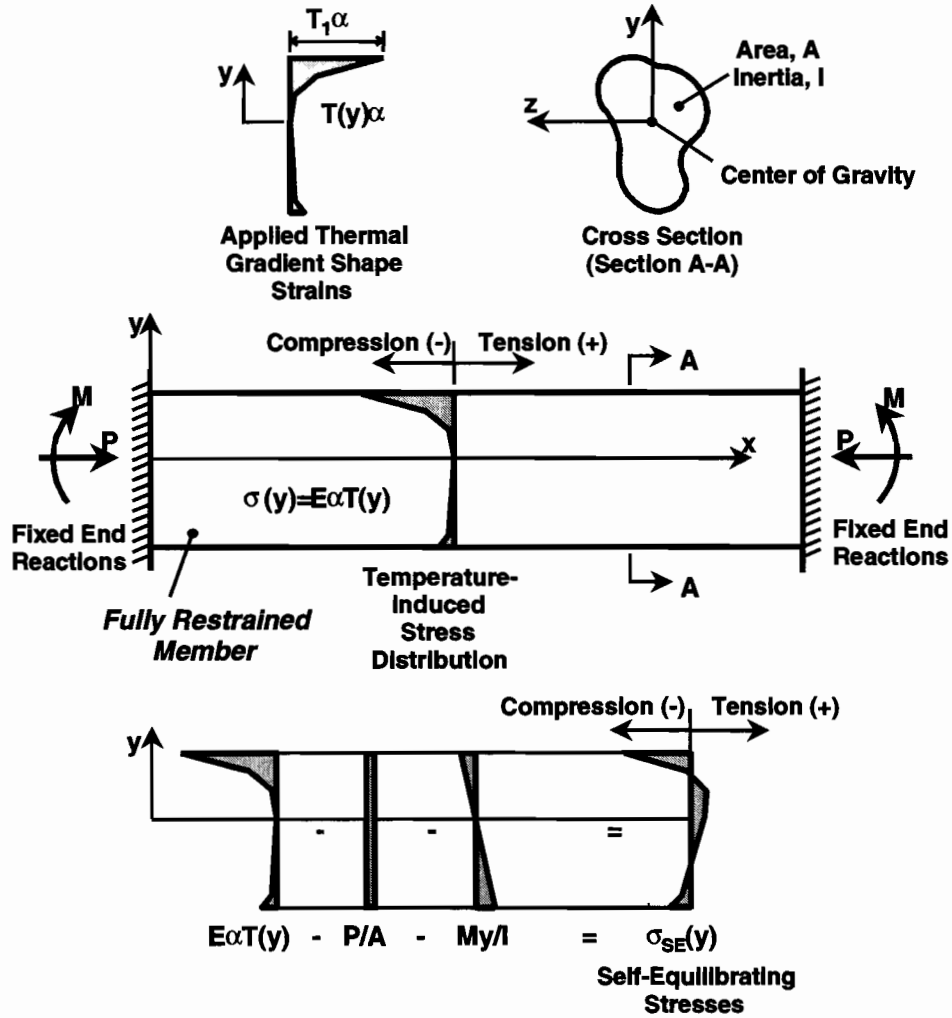


Figure 4.6 Calculation of self-equilibrating stresses from a nonlinear thermal gradient when plane sections remain plane

The axial fixed end force P is calculated by:

$$P = \int_{depth} E\alpha T(y)b(y)dy \quad (4-1)$$

The fixed end moment M is calculated by:

$$M = \int_{depth} E\alpha T(y)b(y)ydy \quad (4-2)$$

and the self-equilibrating stresses are calculated by:

$$\sigma_{SE}(y) = E\alpha T(y) - P/A - My/I \quad (4-3)$$

where:

y = distance measured perpendicular to the longitudinal axis at the center of gravity of the cross section

$T(y)$ = temperature at a depth y

- $b(y)$ = net section width at a depth y
- E = modulus of elasticity
- α = coefficient of thermal expansion
- $\sigma_{SE}(y)$ = self-equilibrating stress at a depth y
- A = cross-sectional area
- I = moment of inertia

If the thermal gradient varies over the vertical and transverse axes of the member, as shown in Figure 4.7, these equations simply change to:

$$P = \int_{depth} \int_{width} E\alpha T(z,y) dz dy \quad (4-4)$$

The fixed end moment about the z -axis is calculated by:

$$M_z = \int_{depth} \int_{width} E\alpha T(z,y) z dz dy \quad (4-5)$$

The fixed end moment about the y -axis is calculated by:

$$M_y = \int_{depth} \int_{width} E\alpha T(z,y) y dz dy \quad (4-6)$$

and the self-equilibrating stresses are calculated by:

$$\sigma_{SE}(z,y) = E\alpha T(z,y) - P/A - M_z y/I_z - M_y z/I_y \quad (4-7)$$

where:

- y = vertical distance measured to the center of gravity of the cross section
- z = transverse distance measured to the center of gravity of the cross section
- $T(z,y)$ = temperature at transverse distance z and depth y
- $\sigma_{SE}(z,y)$ = self-equilibrating stress at transverse distance z and depth y
- I_z = moment of inertia about z axis
- I_y = moment of inertia about y axis

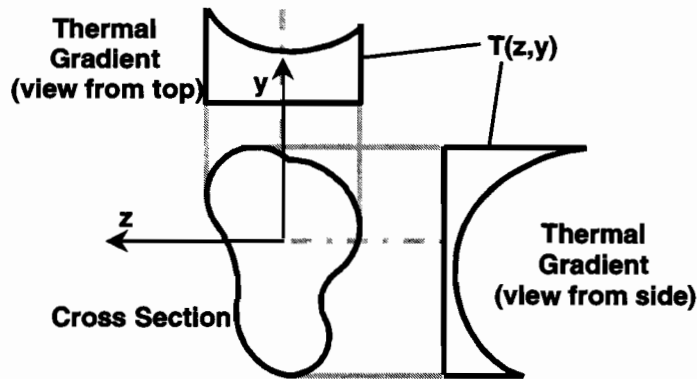


Figure 4.7 Thermal gradient that varies across the width and depth of a cross section

The magnitude of structural response of a bridge girder to thermal gradients is greatly dependent on the peak magnitude of the thermal gradient at deck level. The deck of a box girder contributes greatly to the moment of inertia of the cross section, so temperature-induced stresses integrated over the full deck width have great influence on the longitudinal stresses in the entire cross section. Transverse stresses from thermal gradients through the deck, webs and bottom slab must also be calculated. In this case the axial and bending stiffnesses of the slabs and webs are dependent only on their thicknesses, thus simplifying the calculations and reducing their sensitivity to nonlinear thermal gradients from that of a flanged section. The magnitude of the measured thermal gradients through the webs and bottom slabs of the US 183 box girders were found to be moderate to small. The deck-level magnitude of the thermal gradient and average temperature change in the top slab between webs was found to be quite large. Therefore, the thermal gradient design case is an important part of the box girder's transverse design. Figure 4.8 shows a typical model of a box girder used for transverse design for all load cases. The fixed end forces from the design thermal gradients in the top slab, webs and bottom slab are calculated using the same approach used for the longitudinal analysis. Bending moments induced in the top slab are especially important since they must be combined with truck wheel loads. The moments produced at the top of the webs from the temperature expansion of the top slab can also be large.

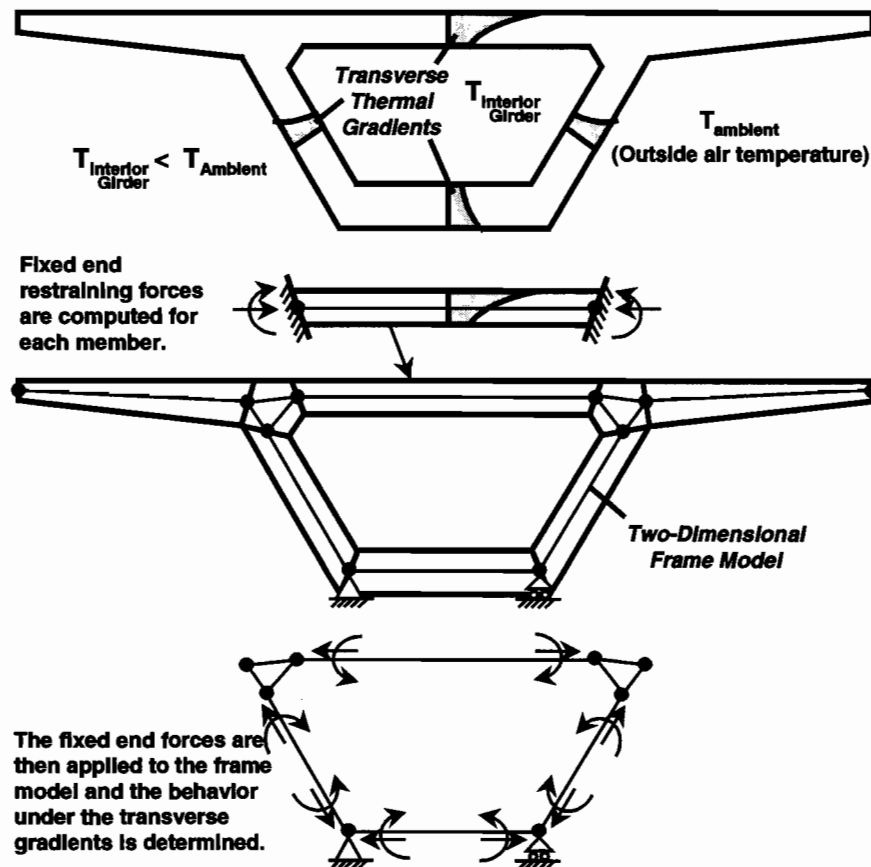


Figure 4.8 *Transverse analysis for thermal gradients*

Transversely plane sections of a box girder are usually assumed to remain plane under a thermal load to greatly simplify the calculations. If warping of the cross section will occur, usual design procedures allow removal of portions of the cross section, such as the wing tips, to account for the reduced stiffness of the girder. The designer proceeds from this point assuming once again that plane sections will remain plane. This assumption has proven to be a valid design method for computing box girder response to external loads, dead loads and even post-tensioning loads. When the fixed end forces are calculated for these known loads, equilibrium must be satisfied regardless of any warping occurring in the cross section. Error in the calculation may occur after the elements are assembled in the structural model, since the assumed stiffnesses of the elements may be incorrect. For the thermal gradient load case, the fixed end forces for the member are calculated assuming plane

sections are going to remain plane. If this is not the case, the fixed end forces will not be correct, and therefore the assumed loading on the structure will not be correct.

An example of warping in a cross section is shown in Figures 4.9 and 4.10. The applied thermal gradient in the top slab is very large when compared to the rest of the box girder. If continuity to the webs is released, the top slab will bow upward both longitudinally and transversely. If the transverse curvature is ignored, since it will have little effect on the longitudinal response of the girder for this example, the top slab would have the shape shown in Figure 4.9. The forces required to achieve continuity with the webs and bottom slab result in the final deformed shape shown at the bottom of Figure 4.9. The forces and stresses at the top slab to web juncture are complex. Longitudinal stresses may vary considerably across the top slab, as shown in Figure 4.10. The measured longitudinal stresses taken from the US 183 box girders were compared to the same stresses calculated using common design procedures to evaluate the effects of warping.

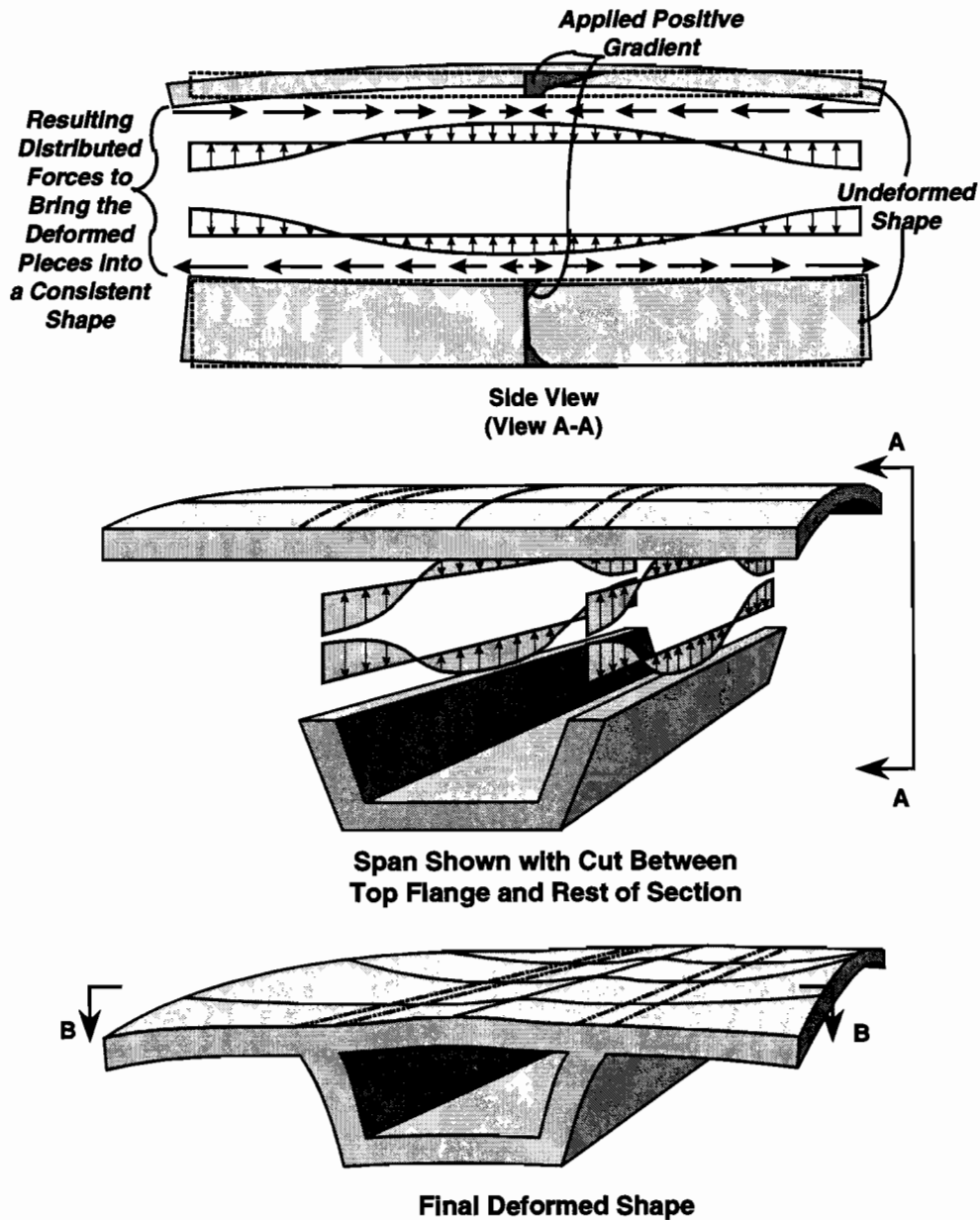


Figure 4.9 Girder response to an applied positive thermal gradient when warping occurs

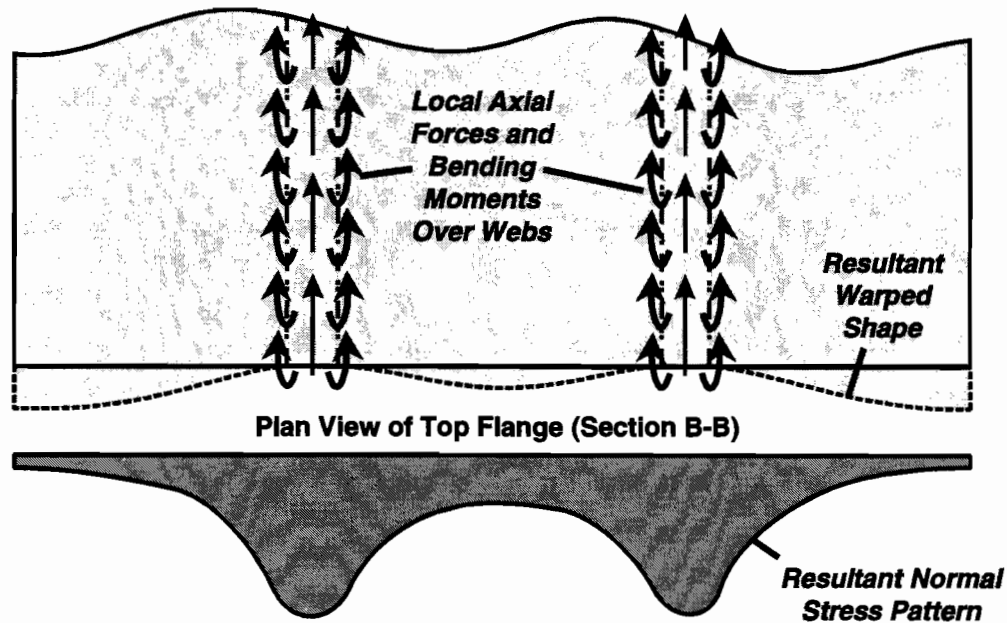


Figure 4.10 Girder response to an applied positive thermal gradient when warping occurs

4.1.2 Substructure Behavior and Analysis Techniques

Bridge piers are subjected to thermal gradients and average temperature changes. For common bridges, the thermal gradient design load for substructures is ignored altogether, even though a pier would respond to a thermal gradient much in the same way that a superstructure girder would behave. For example, the flagpole-type single pier in Figure 4.11 would behave similarly to the simple-span girder of Figure 4.4. The analysis procedure would be the same for calculating the internally balanced stresses in the cross section. Figure 4.12 shows a single pier subjected to a thermal gradient that will produce bending stresses both in itself and in the monolithically connected superstructure. Figure 4.13 shows a two column bent subjected to a thermal gradient. The thermal gradient case on the left of the figure produces only internally balanced stresses, while the case on the right produces both bending stresses and internally balanced stresses. A thermal gradient case that is capable of producing large internally balanced stresses in massive solid piers is demonstrated in Figure 4.14. Temperature changes on the surface of the pier produce stresses analogous to those produced by the mating of two materials with dissimilar thermal expansion properties subjected to a uniform temperature change.

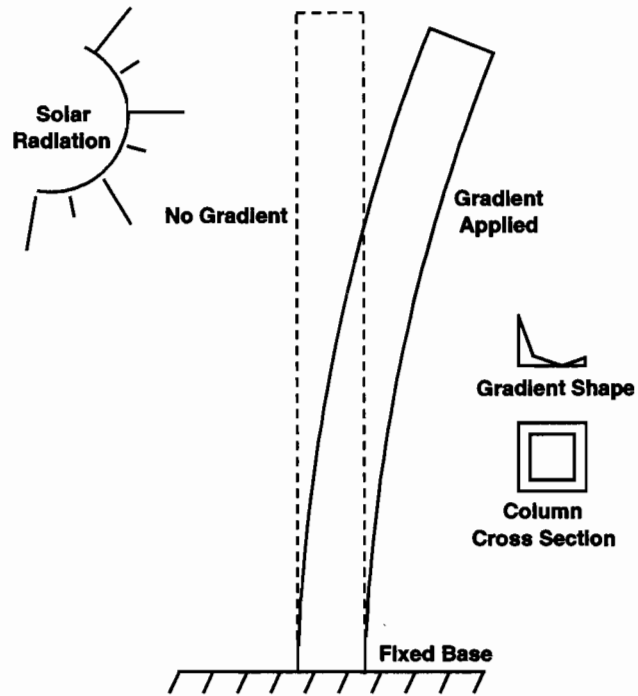


Figure 4.11 Response of a single column to a thermal gradient

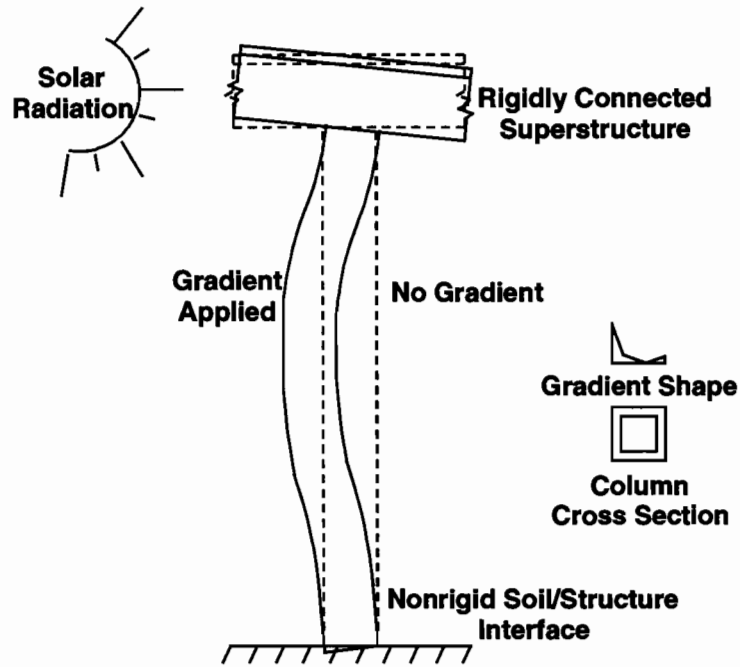


Figure 4.12 Response of a single-column bridge pier to a thermal gradient

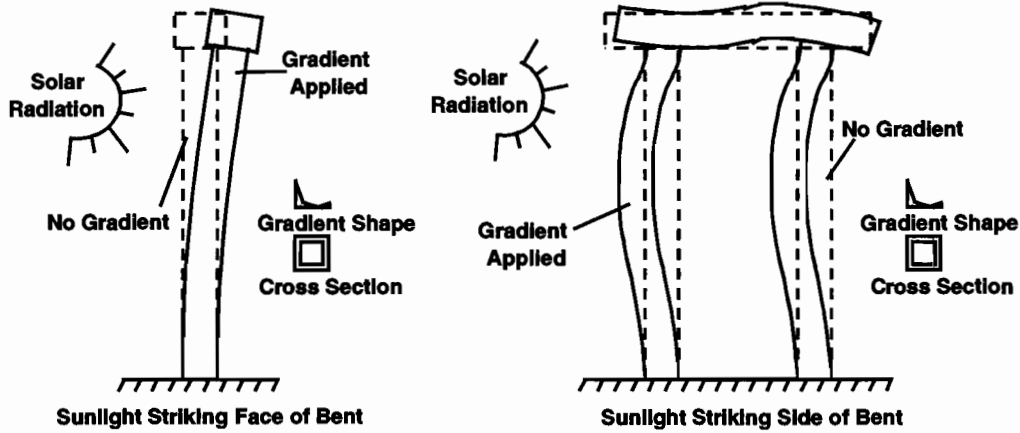


Figure 4.13 Response of a multiple column bridge pier to a thermal gradient

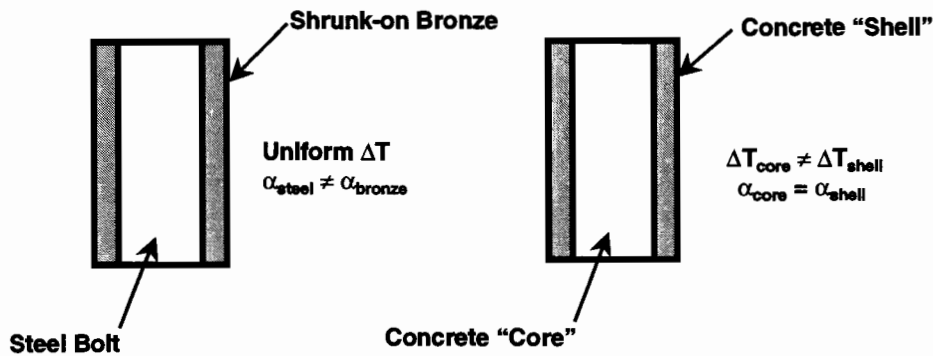


Figure 4.14 Response of solid column to thermal gradients

The shape and magnitude of the thermal gradient in a vertical pier will differ from that of a superstructure member because of its varying exposure to the sun over the course of the day. The largest magnitude of positive thermal gradient in a superstructure girder occurs when an extended cloudy cool period is followed by a clear, calm and hot day with high solar radiation intensity. These conditions would also produce a large magnitude thermal gradient in a bridge pier, but the changing orientation of sun exposure would tend to reduce the magnitude of the gradient from that produced with a single orientation. Figure 4.15 shows the thermal gradient shapes that might be produced at different times of the day on the octagon piers of Ramp P. The heat from the sun exposure at sunrise and mid-morning on the east face of the pier dissipates into the cross section by afternoon, effectively reducing the potential magnitude of the gradient at this time. Radiation from the sun also strikes the pier at an acute angle during mid-afternoon, the time when peak positive gradient magnitudes are produced in the superstructure.

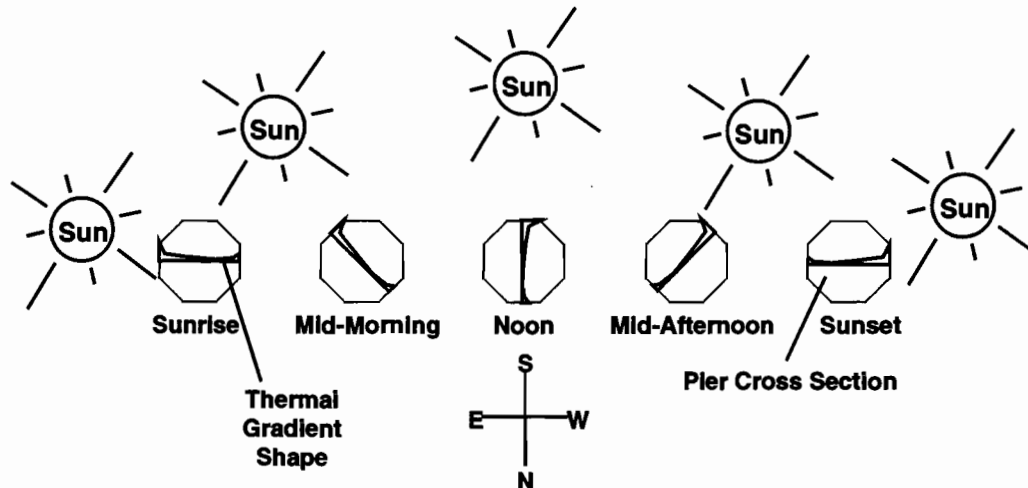


Figure 4.15 Thermal gradient orientations at different times of the day

Analysis of a bridge pier for thermal gradients would proceed identically to that for the superstructure. One major difference is that the design thermal gradient in the superstructure will vary only over the depth of the girder and not the width. A design thermal gradient applied to a pier will no doubt have its orientation governed by sun exposure and not the pier's major or minor bending axes. The response of a pier to a thermal gradient may also differ from that of a superstructure box girder. Piers are generally of a compact cross-sectional shape, so the assumption that plane sections remain plane might very well be valid. Also, the peak magnitude of the thermal gradient is applied at deck level and over the large width of the deck in a superstructure box girder, resulting in an appropriately large response of the entire girder. The compact shape of a bridge pier results in proportionately less of the cross section being subjected to the peak magnitude of the gradient. The temperature measurements taken from the instrumented piers on US 183 allowed a direct comparison of the magnitudes and shapes of the superstructure thermal gradients and the pier thermal gradients. The importance of the thermal gradient design case depends on the magnitude of the thermal gradient selected and magnitude of the stresses produced in the pier when compared to the stresses from other load cases.

4.2 PREVIOUSLY MEASURED GRADIENTS AND DESIGN GRADIENTS

Several research studies have been conducted to determine the magnitude, shape, and frequency of positive and negative thermal gradients in concrete bridges. Some studies were conducted on actual bridges, others on laboratory constructed girders, and some studies were analytical. The frequency and duration of readings for these studies varied considerably, as did the number of thermocouples. The distance of the topmost thermocouple to the deck surface no doubt affected the accuracy of some of the measured peak thermal gradient magnitudes, based on an inspection of the gauge location drawings. Very little has been done to verify a structure's response to thermal gradients.

4.2.1 Hoffman, McClure and West [32]

These researchers at Penn State constructed a full-scale segmental box girder with the cross section shown in Figure 4.16. Thermocouples were placed primarily across the thicknesses of the top slab, webs and bottom slab. Readings were taken eighteen times daily from October 25, 1978 to October 16, 1979. The peak positive and negative thermal gradient magnitudes are plotted in Figure 4.16. The peak negative thermal gradient deck-level magnitude is only a small fraction of the magnitude of the peak positive gradient at deck level. The peak positive gradient magnitude at deck level measured about 29°C, much higher than the 22.8°C recommended by the AASHTO LRFD design specification for the Penn State area. The shape of the gradient may actually vary considerably from that plotted because of the absence of any gauges between the tops of the webs and the middle of the webs.

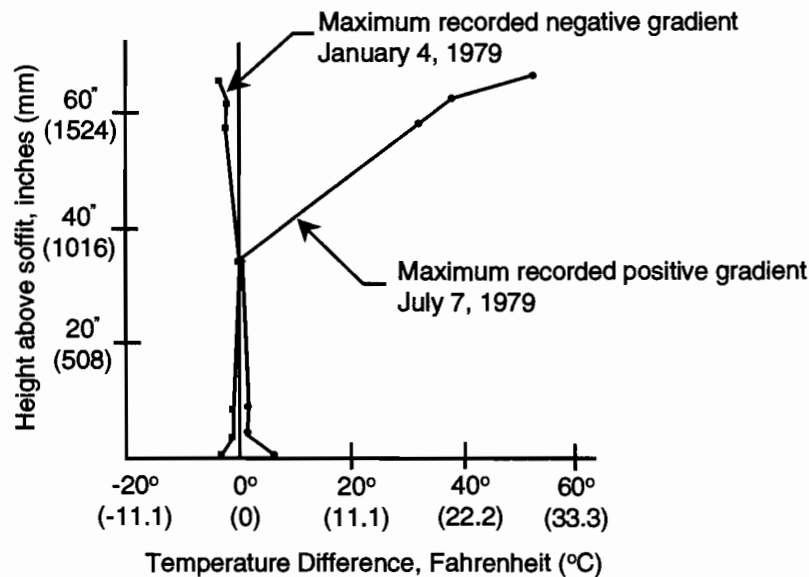
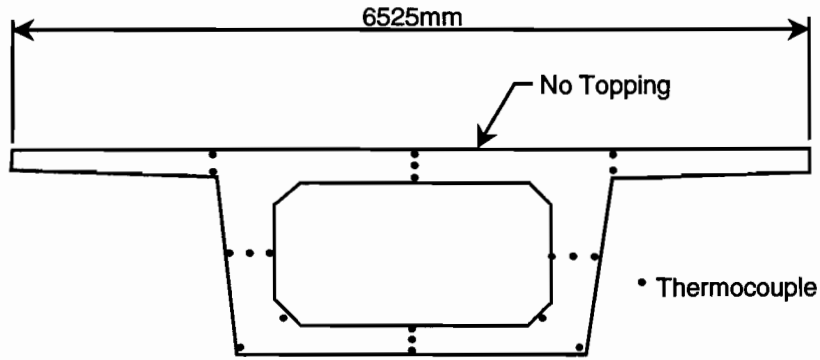


Figure 4.16 Thermocouple locations and maximum recorded thermal gradients for the Hoffman, McClure and West study [32]

4.2.2 Hirst and Dilger [33]

Their study compared the results from an analytical model to the measured thermal gradients from a light rail bridge in Canada and a box girder in Australia. The results from the analytical model compared well with the measured results, thus verifying their method. The maximum measured positive gradient magnitude at deck level was only 10°C.

4.2.3 Shui [34]

Temperature measurements were taken on three bridges in various parts of the country. These were the Kishwaukee River Bridge in Illinois, the Denny Creek Bridge in Washington, and the Linn Cove Viaduct in North Carolina. The measured thermal gradients were similar for all with a maximum positive thermal gradient magnitude at deck level of 11°C and a maximum negative gradient magnitude at deck level of -5.5°C.

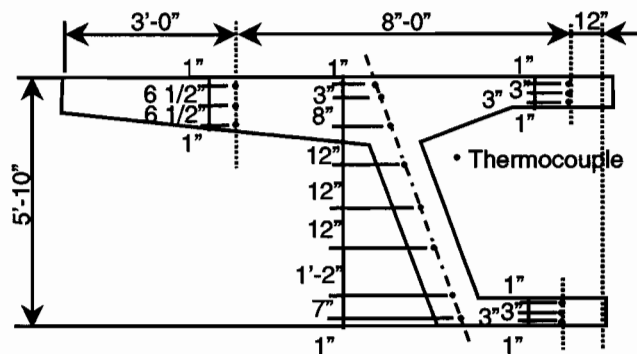
4.2.4 Priestley [35]

This study was another study in which analytical results were compared to measurements. The measurements were taken on a quarter-scale box girder subjected to laboratory-controlled ambient temperature and radiation intensity. Once again, good correlation was found between the analytical results and the measured results. The peak simulated positive thermal gradient was 32°C at deck level for use in New Zealand. The addition of

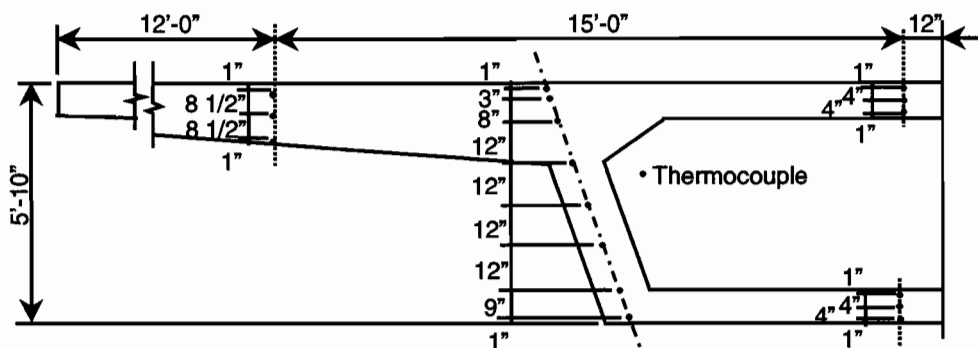
blacktop reduced the peak thermal gradient magnitude at deck level at the rate of 0.2°C per millimeter of blacktop.

4.2.5 Roberts, Breen, Kreger [7]

This study measured temperatures in two box girders on the San Antonio Y segmental viaduct in Texas. The results of this study would be expected to compare directly with the measurements taken on US 183, since Austin and San Antonio are similar in climate, elevation and latitude. The box girders under study were also similar in proportion to those on US 183, with long wings and massive fillet area, but were 356mm less in depth at 1778mm. A fine distribution of thermocouples, seen in Figure 4.17, was placed down the center of the webs and readings were taken hourly for several years, including one year without any blacktop. The maximum positive thermal gradient magnitudes measured at deck level were 12.2°C without blacktop and 15.6°C with 50mm of blacktop. The maximum measured magnitudes of negative thermal gradients at deck level were -8.3°C without blacktop and -4.4°C with 50mm of blacktop. The first year of data without blacktop most likely did not include the peak positive gradient possible for this area, judging by the variability of the data from US 183 over several years.



**Type I Segment Thermocouple Layout
Segments 11C-5 and 11C-10**



**Type III Segment Thermocouple Layout
Segments 44A-6 and 44A-15**

Figure 4.17 Thermocouple layout for the San Antonio Y study by Roberts [7]

4.2.6 Arockiasamy and Reddy [36]

An analytical study using a program called FETAB (Finite Element Temperature Analysis of Bridges) was used to predict temperatures measured in two bridges. Thermocouples were retrofitted into each structure. The maximum recorded positive thermal gradient magnitude at deck level was 25.6°C . Temperature variations were recorded transversely across the deck.

4.2.7 Pentas, Avent, Gopu, and Rebello [37]

A precast pretensioned girder bridge was instrumented in Louisiana with the cross section and gauge locations shown in Figure 4.18. Measurements were taken approximately once a month for two years. The maximum positive thermal gradient magnitude at deck level was about 13°C, and the maximum negative thermal gradient magnitude at deck level was about -4°C. These measurements do not compare directly to those of a box girder because the I-girders were exposed to ambient air on all surfaces.

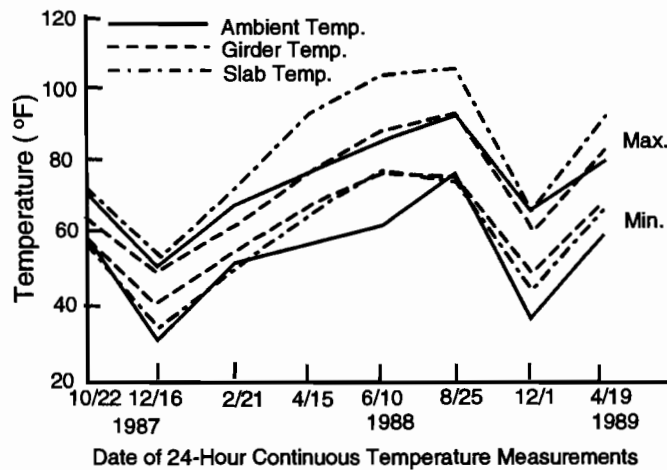
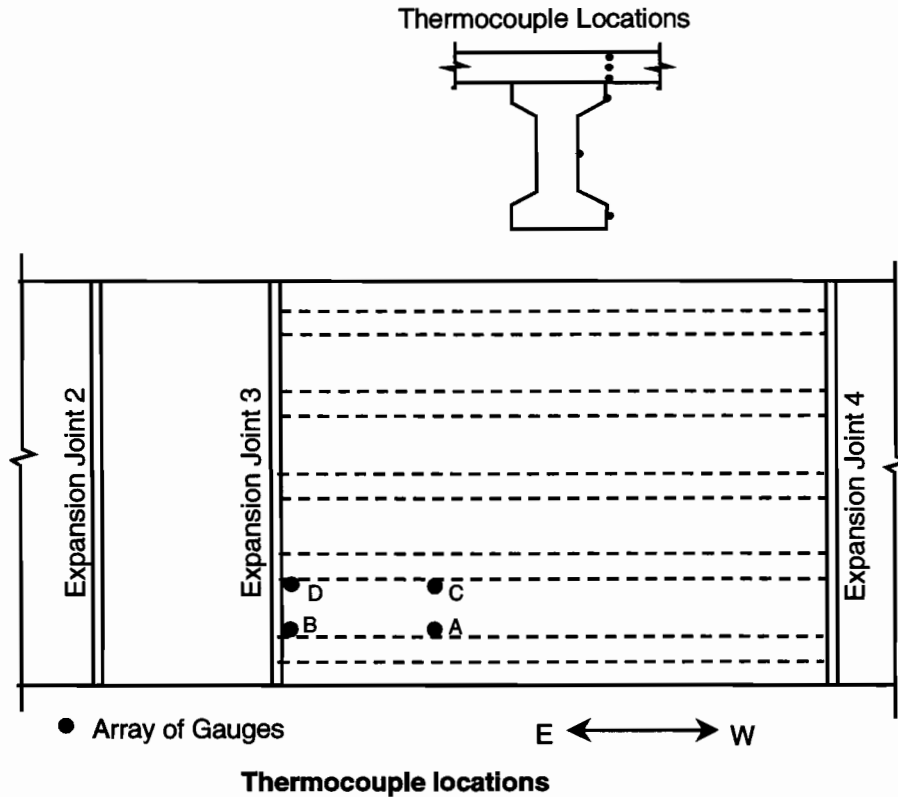


Figure 4.18 Temperature distributions through the depth of the section for the US 190 Atchafalaya River Bridge study by Pentas et al. [37]

4.2.8 Potgieter and Gamble [38]

Data from 26 weather stations from around the country were used as input in an analytical model to predict thermal gradients in concrete bridges and the frequency of peak magnitude thermal gradients. Two days of field measurements were taken on the Kishwaukee River Bridge in Illinois to verify the results of the model. The results of this study were used to develop the design recommendations in the NCHRP 276 report. The researchers recommended further field studies be performed to verify the model for all areas of the country.

4.2.9 NCHRP 276 [39]

This report gave an overview of thermal effects in concrete. The recommendations for design thermal gradients given in the NCHRP report were adopted by AASHTO to be used to design the nation's concrete bridges. The positive design thermal gradients were taken from the results of the Potgieter and Gamble study [39] and vary with location and thickness of blacktop. The various thermal gradient zones are shown in Figure 4.19. The recommended shape and magnitude for the positive design thermal gradients for box girders are shown in Figure 4.20. Temperatures T_2 and T_3 should be reduced by 2.8°C for beam and slab bridges. The shape and values of the negative thermal gradients shown in Figure 4.21 were based on the gradient specified in the British Standard BS 5400 [40]. There was no substantial analytical or measured basis for the specified negative gradients or their shapes. They were chosen based on engineering judgment. It is not clear why the temperatures in the webs and bottom slab are functions of the amount of blacktop.

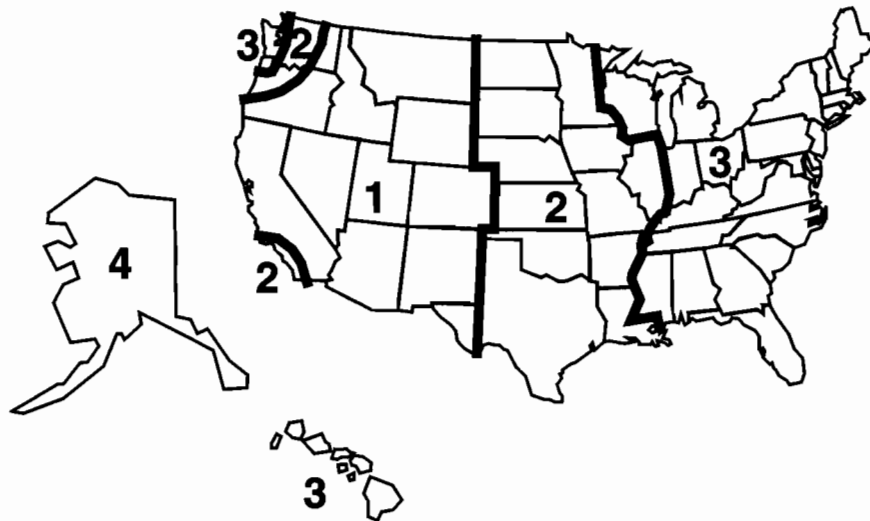
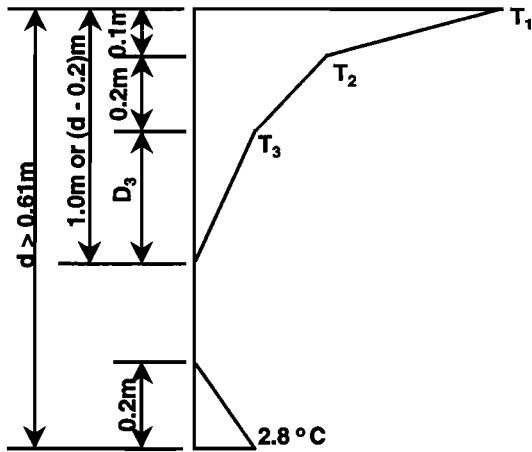


Figure 4.19 Proposed maximum solar radiation zones by Imbsen, et al. [39]



Gradients are for box girders

Zone 1

mm of Blacktop	Temperature, °Celsius		
	T ₁	T ₂	T ₃
0	30	11	6
50	24	11	5
100	17	8	4

Zone 2

mm of Blacktop	Temperature, °Celsius		
	T ₁	T ₂	T ₃
0	26	9	5
50	20	9	5
100	14	8	4

Zone 4

mm of Blacktop	Temperature, °Celsius		
	T ₁	T ₂	T ₃
0	21	8	4
50	16	8	4
100	12	9	4

Zone 3

mm of Blacktop	Temperature, °Celsius		
	T ₁	T ₂	T ₃
0	23	9	5
50	18	9	4
100	13	9	4

Figure 4.20 Recommended positive vertical temperature gradient by Imbsen, et al. [39]

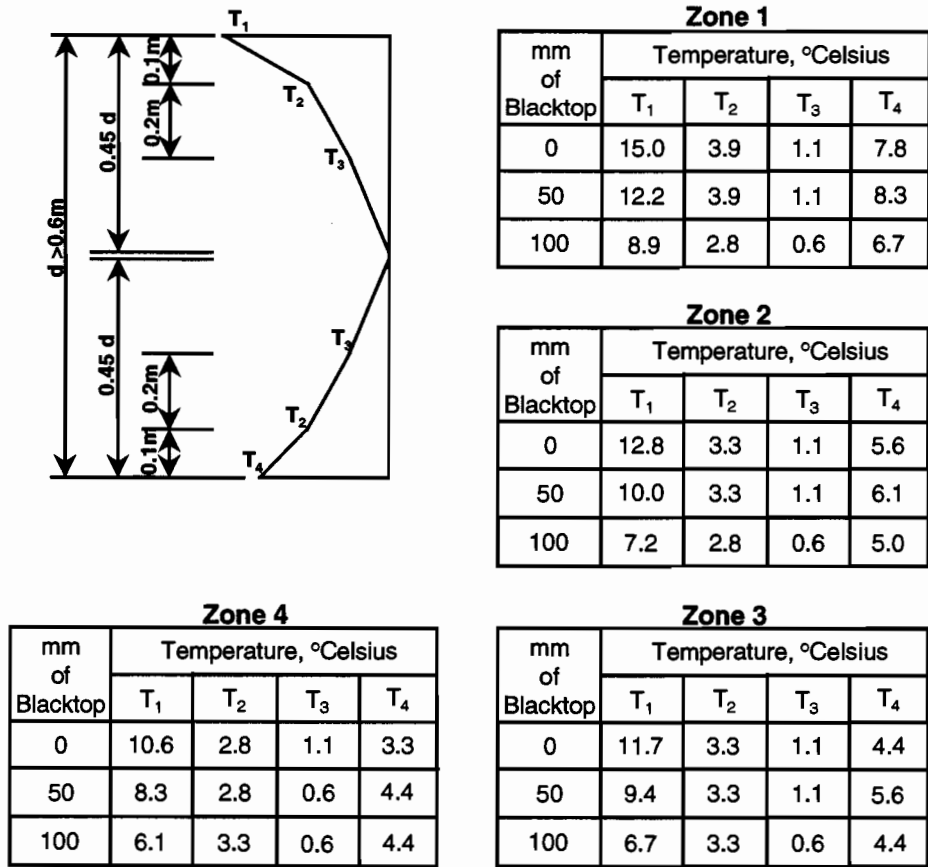


Figure 4.21 Recommended negative vertical temperature gradient by Imbsen, et al [39]

4.2.10 AASHTO LRFD [9]

The design thermal gradients adopted for the AASHTO LRFD design specifications were also based on the recommendations of NCHRP 276, with some simplifications. The AASHTO LRFD thermal gradient values are given in Figure 4.22. The upper part of the design gradient shape is composed of two lines. The bottom portion of the thermal gradient has a magnitude $T_3=0$, unless determined otherwise by a site-specific study, but need not exceed 2.8°C for the positive thermal gradient case. A full-scale research project would have to be done prior to the design of the bridge for an accurate estimate of T_3 . The negative thermal gradients are derived by multiplying the applicable positive gradient by -0.5 . This approximation reduces the amount of calculation involved for computing stresses almost in half, depending on the method used. The dimension A varies with the depth of the superstructure. A is equal to 300mm for concrete superstructures that are 400mm in depth or greater. A is equal to 100mm for concrete superstructures that are less than 400mm in depth.

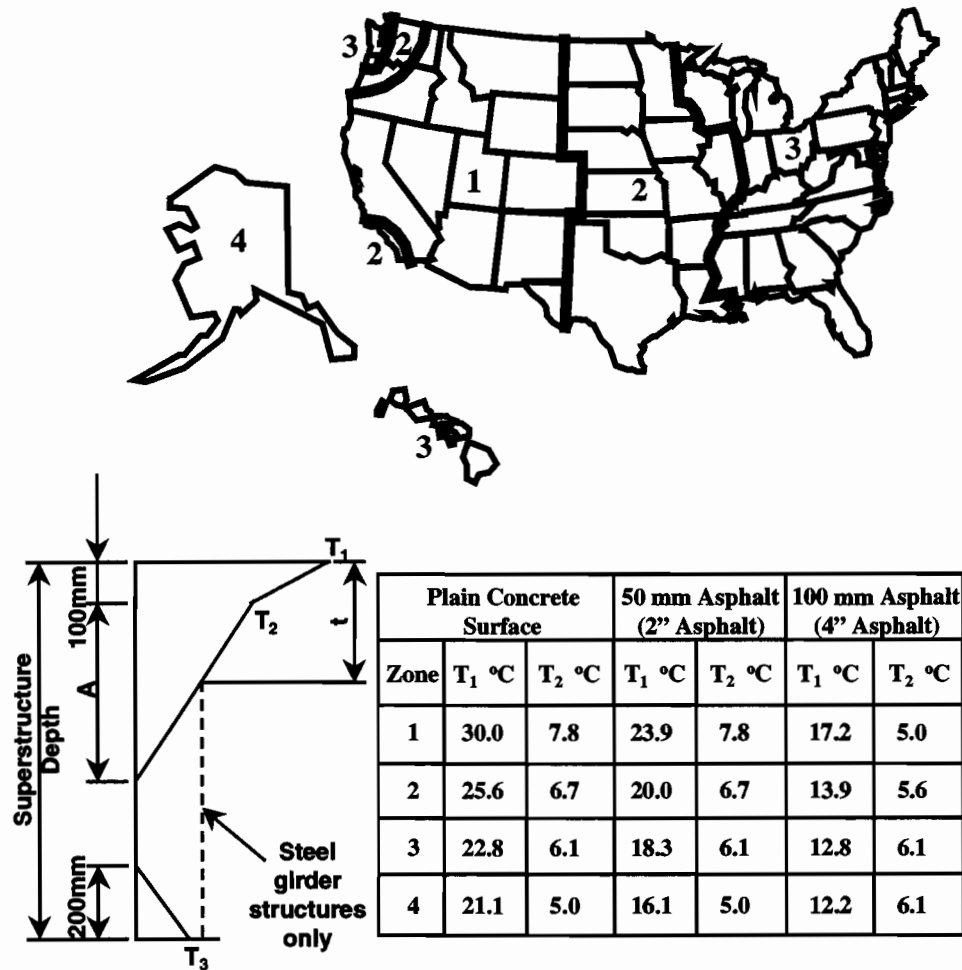


Figure 4.22 Positive vertical temperature gradient in concrete and steel superstructures (Figure 3.12.3-2 and Table 3.12.3-1 from the AASHTO LRFD Bridge Design Specifications [9])

4.3 DATA COLLECTION AND ANALYSIS

4.3.1 Ramp P Superstructure

Temperature measurements were taken hourly in one cross section of the Ramp P superstructure with a dense grid of thermocouples. Strain measurements were also taken at three sections in the girder at the same time intervals. The thermocouples used to evaluate thermal gradient magnitude are shown in Figure 4.23. The six thermocouples located at the top of the webs were usually at the lowest temperature on average of any horizontal plane of thermocouples. This condition was particularly true at the times peak positive gradients were occurring and when negative gradients of any importance were occurring. The positive gradient shape shown in Figure 4.23 was typical for positive gradients. $T_{1,meas}$ is the measured deck-level magnitude of the thermal gradient. $T_{1,meas}$ is the average temperature measured with the top thermocouples minus the average temperature (T_{min}) measured by the six baseline thermocouples. Similarly, $T_{4,meas}$ is the soffit-level gradient occurring at the same time as $T_{1,meas}$.

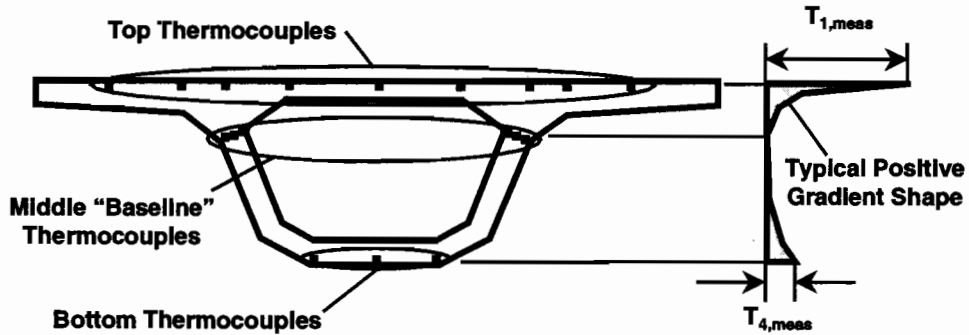


Figure 4.23 Thermocouples used to calculate thermal gradient magnitudes on the Ramp P superstructure

The deck-level thermal gradient magnitude, soffit-level thermal gradient magnitude, and the ambient air temperature beneath the box girder are plotted in Figure 4.24 for the month of March 1997. One deck-level positive gradient magnitude of interest during this month was $T_{1,meas}$ created when hot asphalt was applied to the deck. This gradient magnitude was the largest deck-level positive gradient magnitude measured for the Ramp P girder, but should be considered a construction load and not a normal service load. The maximum measured positive $T_{1,meas}$ on Ramp P under normal conditions occurred after the asphalt blacktop was in place on March 20, 1997. A full year of data for this girder without blacktop could not be measured because of the construction schedule. The maximum possible positive $T_{1,meas}$ for this girder without blacktop most probably was not measured. Maximum $T_{1,meas}$ on March 20, 1997, followed a period of cool weather. The maximum $T_{1,meas}$ for the days following this cool period were all similar in magnitude and persisted until the onset of the next cool period. In general, the spring of 1997 did not have conditions favorable for producing maximum positive thermal gradients. The positive thermal gradients measured in the mainlane superstructure for the springs of 1995 and 1996 were substantially higher in magnitude than those measured in the spring of 1997. Persistent mild, cloudy and rainy weather was to blame. The $T_{1,meas}$ values for the entire study period are summarized in the Appendix.

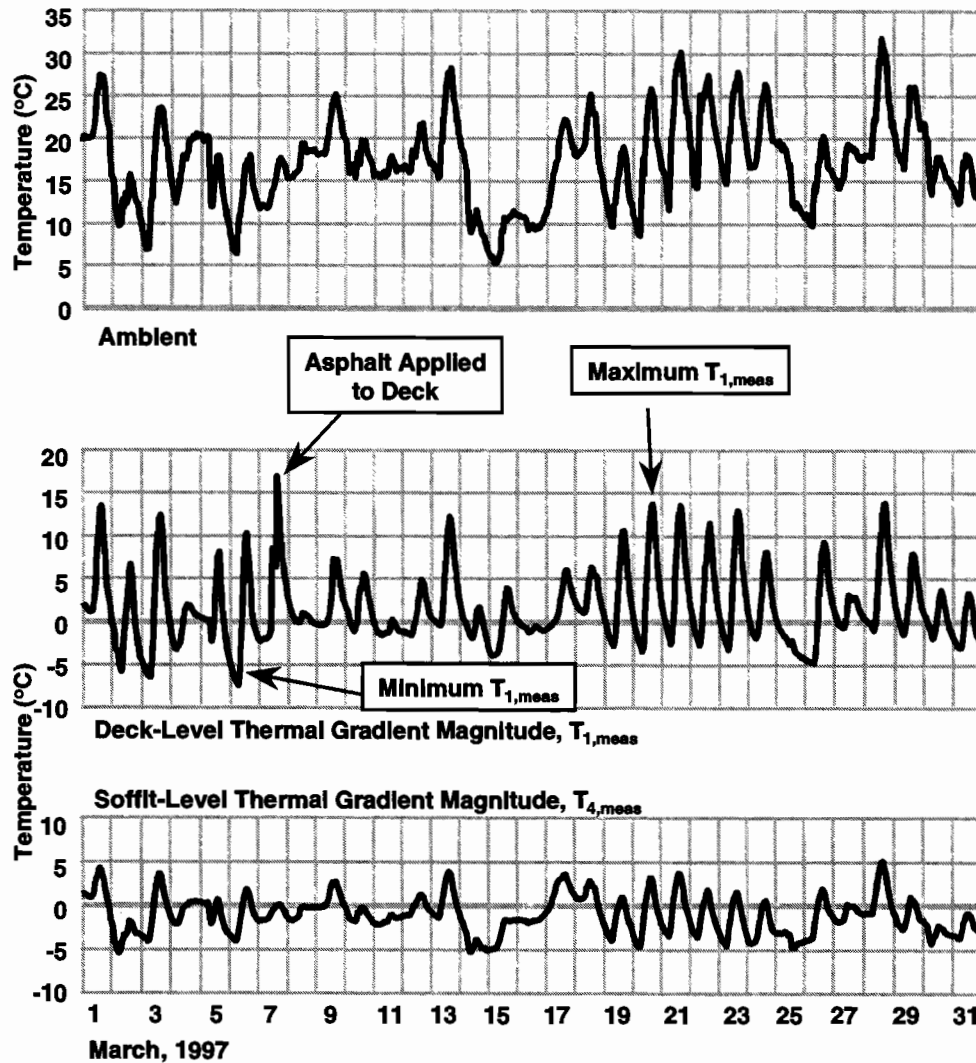
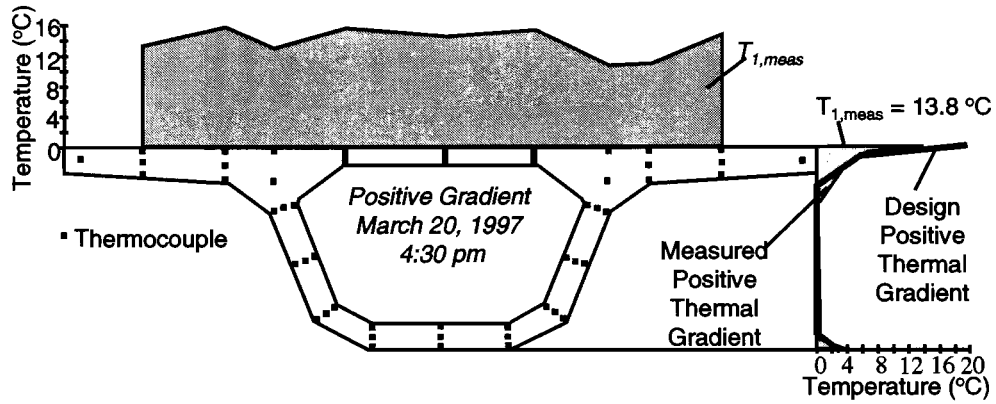


Figure 4.24 Measured thermal gradient magnitudes on Ramp P for the month of March 1997

The measured thermal gradient of March 20, 1997, is tabulated for each thermocouple location in Figure 4.25. $T_{1,meas}$ values plotted over the width of the top slab show that the webs acted to draw heat from the top of the cross section, thus a line of thermocouples located up the centerline of a web would not have measured the peak deck-level temperatures. Both the positive design thermal gradient shape and magnitude recommended by the AASHTO LRFD design specification, shown in the plot at the right in Figure 4.25, do not accurately represent the positive thermal gradient measured in this girder. The massiveness of the top flange to web fillets may have had some effect on this. The maximum measured negative thermal gradient from March 6, 1997, is presented in Figure 4.26. Once again, the recommended negative design thermal gradient, which was patterned after the shape of the positive design gradient, poorly represented the measured negative gradient in shape and magnitude. Substantial negative thermal gradients occur when there are extreme changes in weather over very short periods of time, so the gradient shape is not entirely predictable. Maximum positive thermal gradients occur when a relatively stable, cool and cloudy period is followed by a day of bright sunshine and resultant warmer weather. The positive thermal gradient develops from a cross section of nearly uniform temperature and therefore the shape is much more predictable.



T802	T805	T808	T810	T813	T816	T819	T821	T824
13.4	15.8	13.1	15.5	14.6	15.3	10.8	10.9	14.7
T801	T803	T806	T811	T814	T817	T822	T825	T827
3.1	5.7	4.7	3.4	8.9	8.6	3.8	6.1	4.7
T804	T807	T809	T812	T815	T818	T820	T823	T826
4.8	3.9	3.2	5.9	6.0	5.2	1.9	3.4	5.1
T854	T853	T852	T828	T829	T830			
1.7	-0.1	-0.9	-1.5	-0.6	1.5			
T851	T850	T849	T831	T832	T833			
2.3	0.6	-0.5	-1.5	-0.4	1.7			
T848	T847	T846	T834	T835	T836			
3.6	1.5	-0.2	-1.3	-0.1	3.1			
T843	T840	T837						
-0.6	-1.4	0.1						
T844	T841	T838						
0.3	0.2	0.5						
T845	T842	T839						
3.4	2.9	3.4						

Thermocouple Temperature

Temperatures for thermocouples are presented in degrees Celsius.

Figure 4.25 The maximum measured positive gradient on Ramp P (from March 20, 1997)

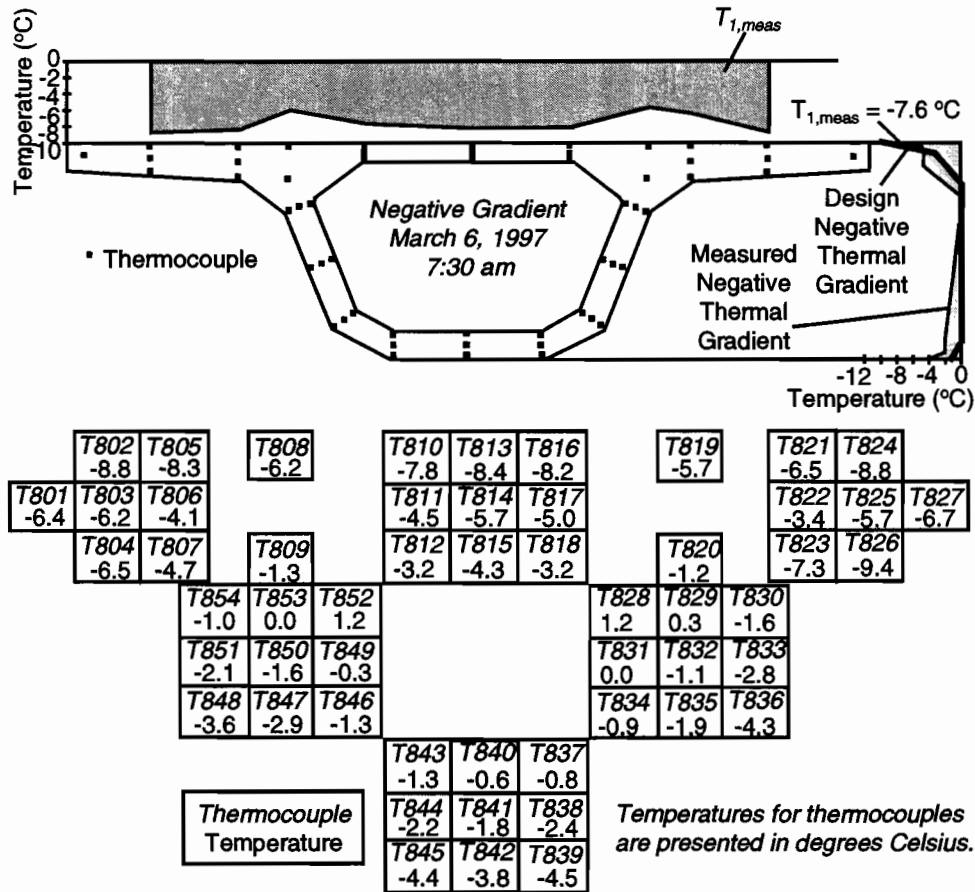


Figure 4.26 The maximum measured negative gradient on Ramp P (from March 6, 1997)

The statistical occurrence of peak positive and negative thermal gradient deck-level magnitudes is of primary concern when selecting gradient magnitudes for design. Figure 4.27 shows the occurrence of maximum daily $T_{1,meas}$ values from November 1996 to March 1997, when no blacktop was in place. This time range did not allow a complete or even realistic distribution of gradients. Figure 4.28 presents the occurrence of maximum daily $T_{1,meas}$ values from March 1997 through February 1998, with 50mm of blacktop in place. This graph reveals an entirely different distribution than that in Figure 4.27 and is more representative of an actual year. These figures show that the peak magnitude $T_{1,meas}$ values occurred on small percentage of days over the course of a year, but $T_{1,meas}$ values only two or three degrees smaller than the peak occurred frequently.

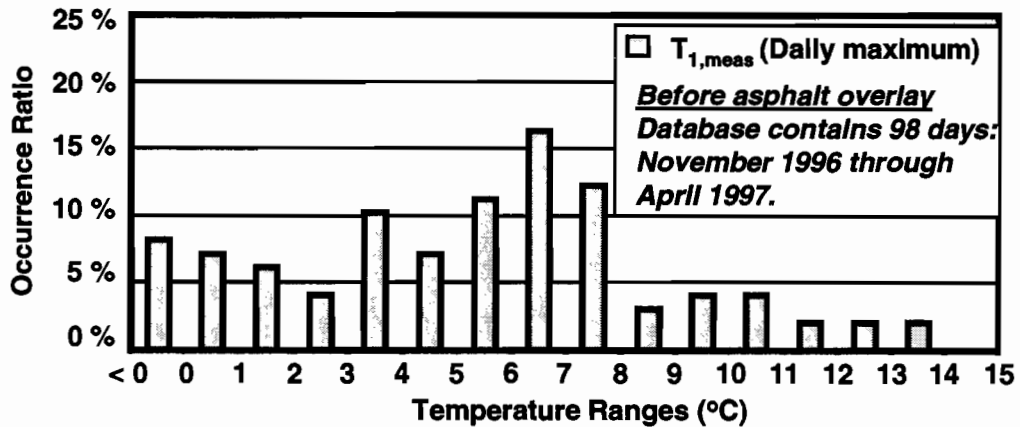


Figure 4.27 Statistical occurrence of daily maximum $T_{1,meas}$ values on Ramp P before application of the asphalt blacktop

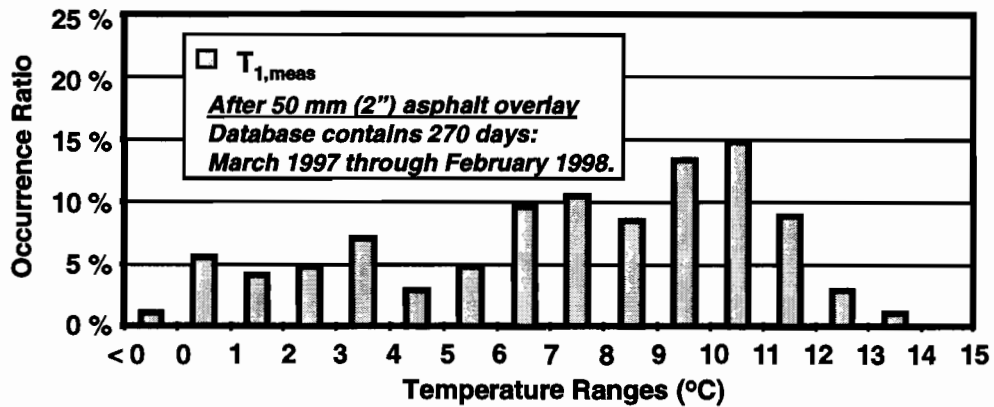


Figure 4.28 Statistical occurrence of daily maximum $T_{1,meas}$ values on Ramp P after application of the asphalt blacktop

Figures 4.29 and 4.30 give the occurrence distribution of peak daily minimum $T_{1,meas}$ values. Figure 4.29 demonstrates once again that the daily peak minimum deck-level thermal gradient magnitude occurred only a small percentage of days. The distribution of daily minimum $T_{1,meas}$ values, measured without the blacktop in place, differed from the distribution of daily maximum $T_{1,meas}$ values in that minimum $T_{1,meas}$ values of half the magnitude of the peak value occurred most of the time. Figure 4.30 shows that the magnitude of peak daily minimum deck-level gradient, with the 50mm of blacktop in place, was about half that without the blacktop.

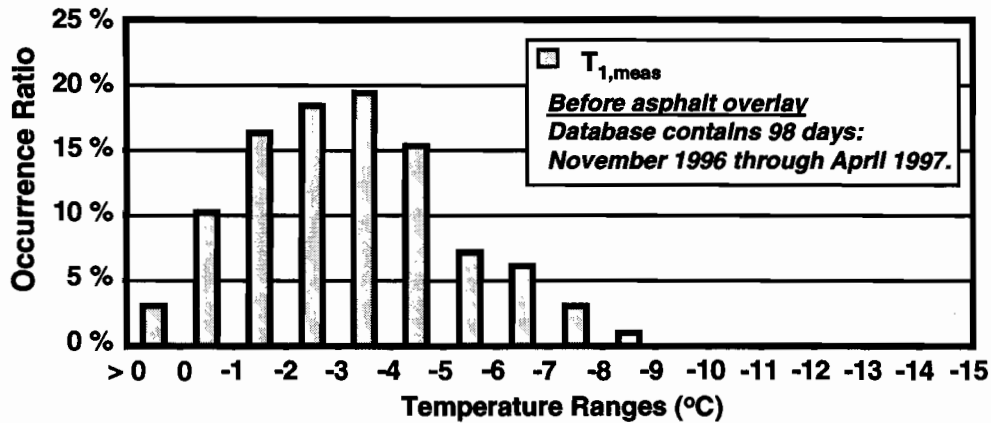


Figure 4.29 Statistical occurrence of daily minimum $T_{1,meas}$ values on Ramp P before application of the asphalt blacktop

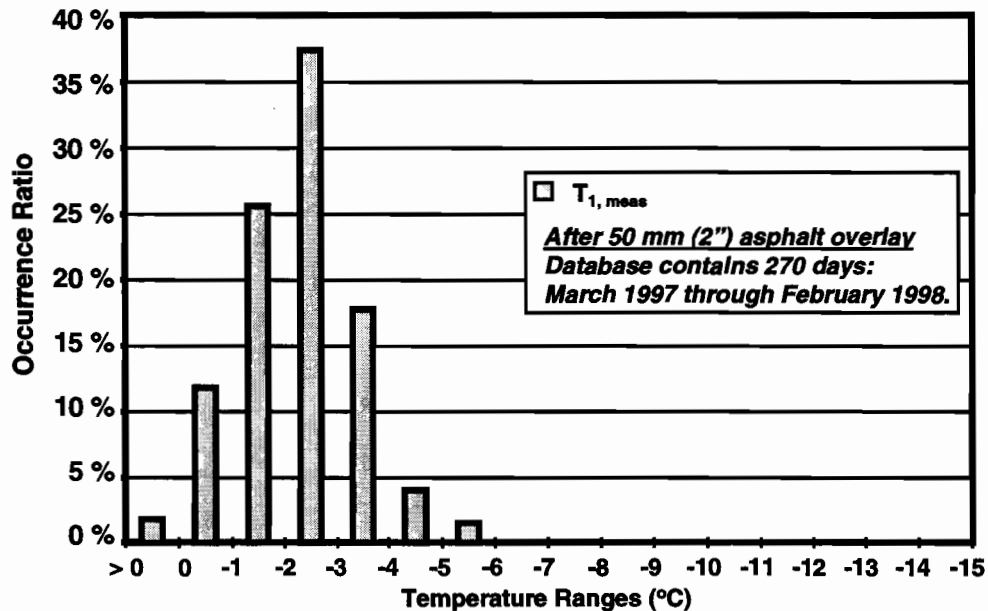


Figure 4.30 Statistical occurrence of daily minimum $T_{1,meas}$ values on Ramp P after application of the asphalt blacktop

The primary reason the design thermal gradients have been established is for the calculation of cross-sectional stresses and transverse stresses. Strain gauges were placed both longitudinally and transversely at three cross sections in the five-span continuous Ramp P girder. These cross sections were all in one half of span P16. The first cross section was in segment P16-2 near the face of the anchor segment diaphragm over pier P16. The second cross section was located at the quarter point of the span. The third cross section was located at midspan, which was the same location as the plane of thermocouples. The measured strains converted to stresses are plotted against calculated stresses in the figures to follow. The gauges used automatically subtracted out the strain that occurred from unrestrained thermal expansion, leaving only a strain caused by stresses. Stresses have been calculated using both the measured maximum gradients and the gradients recommended by AASHTO LRFD. The measured maximum gradients were taken as the change in temperature at each thermocouple over a certain period of time and were similar to the maximum positive and negative gradients presented in Figures 4.25 and 4.26. The measured temperature changes were distributed over the cross sections as shown in Figure 4.31, each area taking the temperature change of one thermocouple. The design method used was the same one recommended in the AASHTO LRFD and presented in section 4.1.1.

Plane sections were assumed to remain plane in this analysis. Since the structure was continuous, the longitudinal concrete stresses were the sum of bending stresses and self-equilibrating stresses.

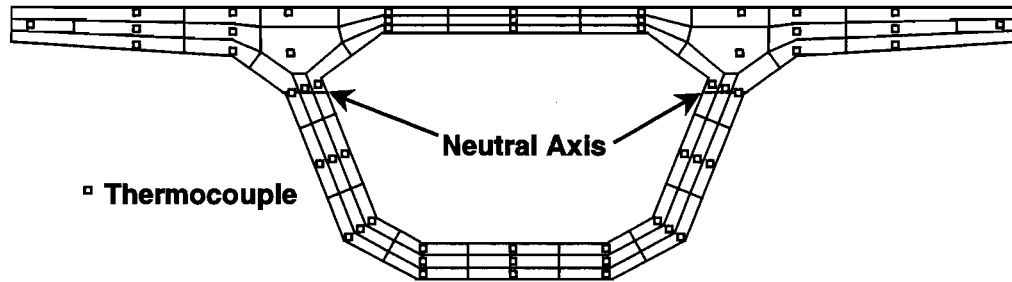


Figure 4.31 Division of the Ramp P cross section into tributary areas for each thermocouple gauge

The measured and calculated stresses for segment P16-2 for the maximum positive gradient load case are plotted in Figure 4.32. The plot of top fiber stresses shows good correlation between the measured and the calculated values, except at the wing tips. The design thermal gradient stresses were uniform across the cross section, since the gradient did not change over the width of the girder and plane sections were assumed to remain plane. The stresses calculated using the measured thermal gradient were distributed transversely in proportion to the measured temperature change at each gauge. The measured stresses definitely revealed a reduction in sectional stiffness at the wing tips. The measured stresses were almost constant between webs in the top flange. Very little strain change was measured in the lower portion of the webs and the bottom flange. The location of the web strain gauges near the exterior of the girder resulted in a strain measurement higher in compression than the average across the web width. The temperature differential across the thickness of the webs was about 4°C. The stress distribution from thermal stresses was not as readily interpreted at this section for thermal gradients as it was for other load cases because of the proximity of the web gauges to the exterior of the concrete.

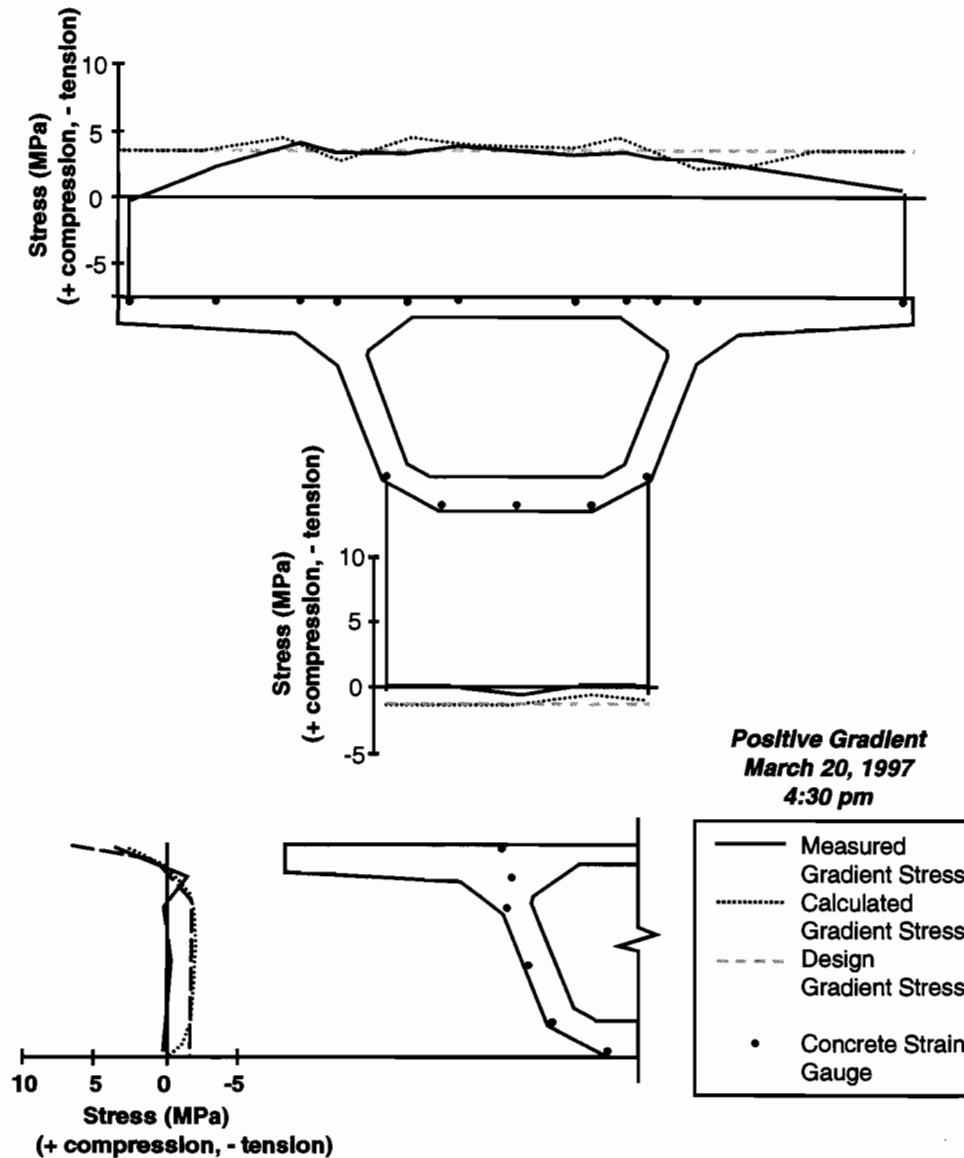


Figure 4.32 Comparison of measured and calculated positive thermal gradient stresses for segment P16-2 (near diaphragm)

Figure 4.33 shows that the distribution of measured stresses in segment P16-10 at the quarter point of the span was not predicted well by the standard calculation procedure, even on average. The measured stresses were low at the wing tips, as was seen in segment P16-2 and peaked over the webs in the top flange. The distribution of measured stresses in the lower portion of the webs and bottom flange was also similar to that in segment P16-2. The measured and predicted stresses for the positive thermal gradient case for segment P16-17 near midspan are plotted in Figure 4.34. The distribution of measured stresses in this segment was very similar to that of segment P16-10. The heavy end diaphragm located 610mm from the gauges in segment P16-2 may have been responsible for a reduction in warping at this section and a smoother distribution of stresses across the top flange. Also, the deviator beam in segment P16-10 may have contributed to the peaks in stress over the webs, which were somewhat larger than those in segment P16-17 that had no deviator beam.

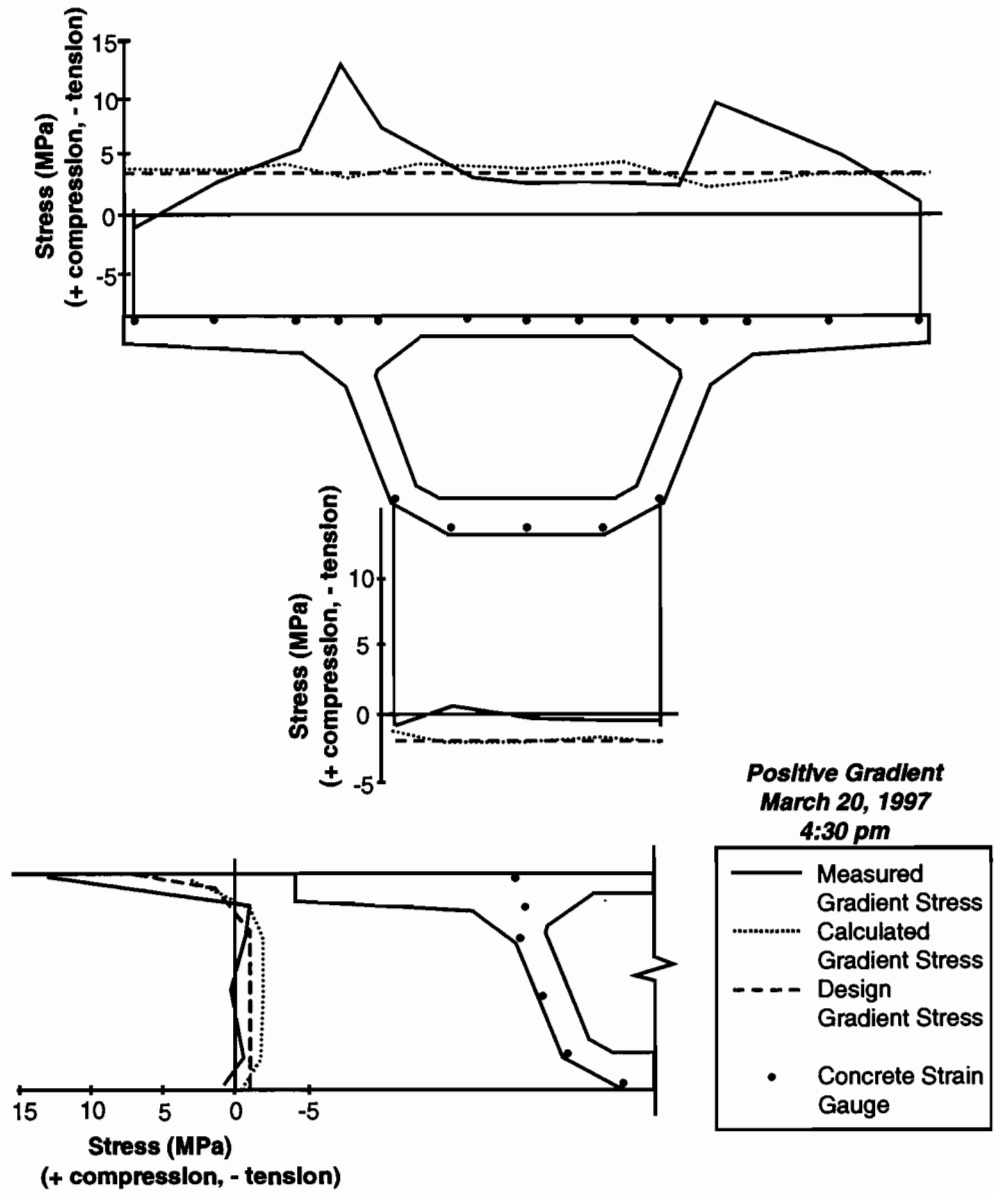


Figure 4.33 Comparison of measured and calculated positive thermal gradient stresses for segment P16-10 (quarter point)

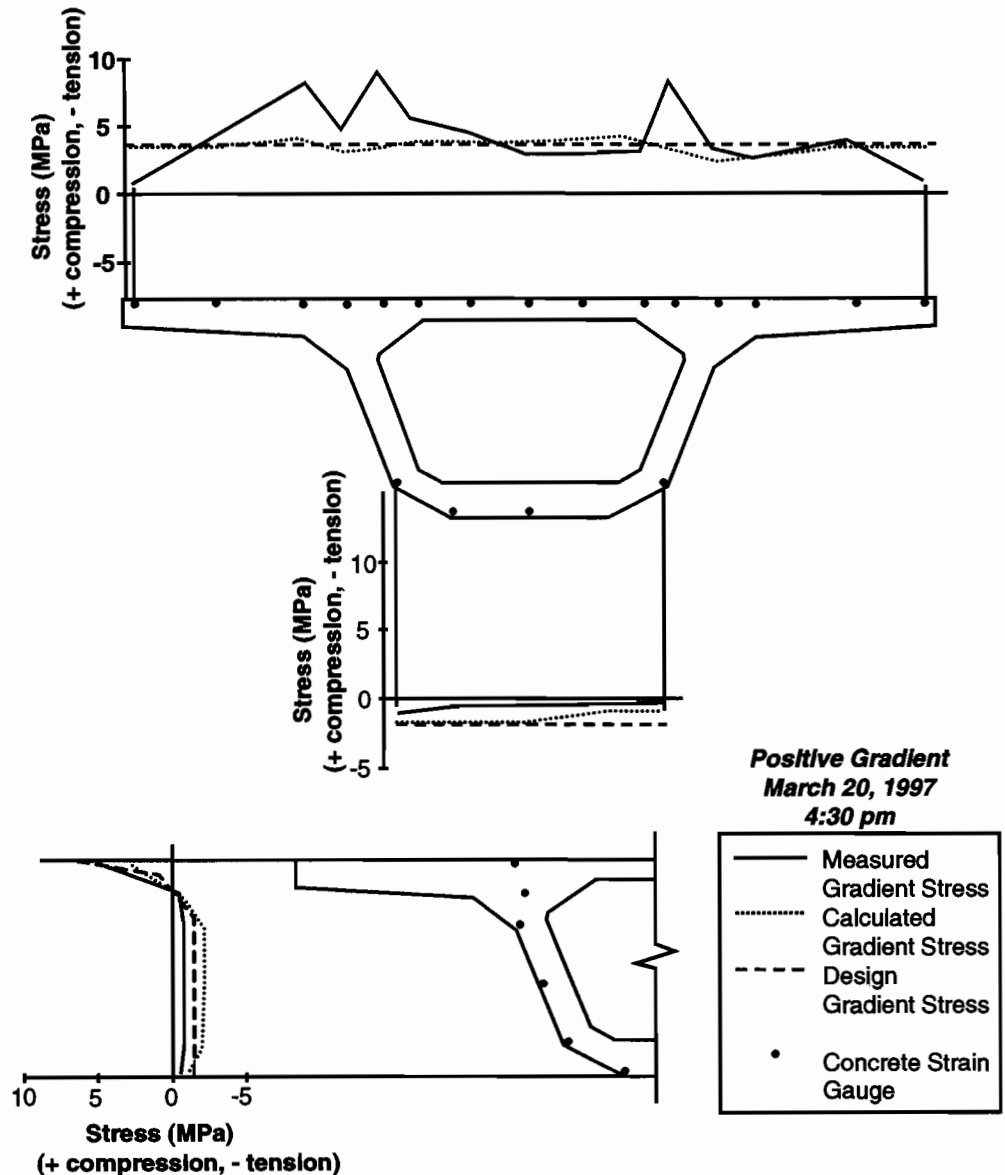


Figure 4.34 Comparison of measured and calculated positive thermal gradient stresses for segment P16-17 (midspan)

The response of the girder to the maximum negative thermal gradient case was generally similar to the response to the positive gradient, but opposite in direction. The measured and predicted stresses for the negative gradient case are plotted in Figures 4.35 through 4.37 for the three-instrumented sections. The average top flange stress in segment P16-2 was predicted reasonably well by the calculated method using the measured gradient, as was the bottom flange stress. The measured stresses and the calculated stresses did not compare well in the webs because of the negative gradient through the thickness of the web. The measured stresses over the webs in the top flange were irregular in segments P16-10 and P16-17, possibly attributable to plane sections not remaining plane, reduction of thermal forces by warping, inelastic behavior in the congested web area, or forces from the deviator beam.

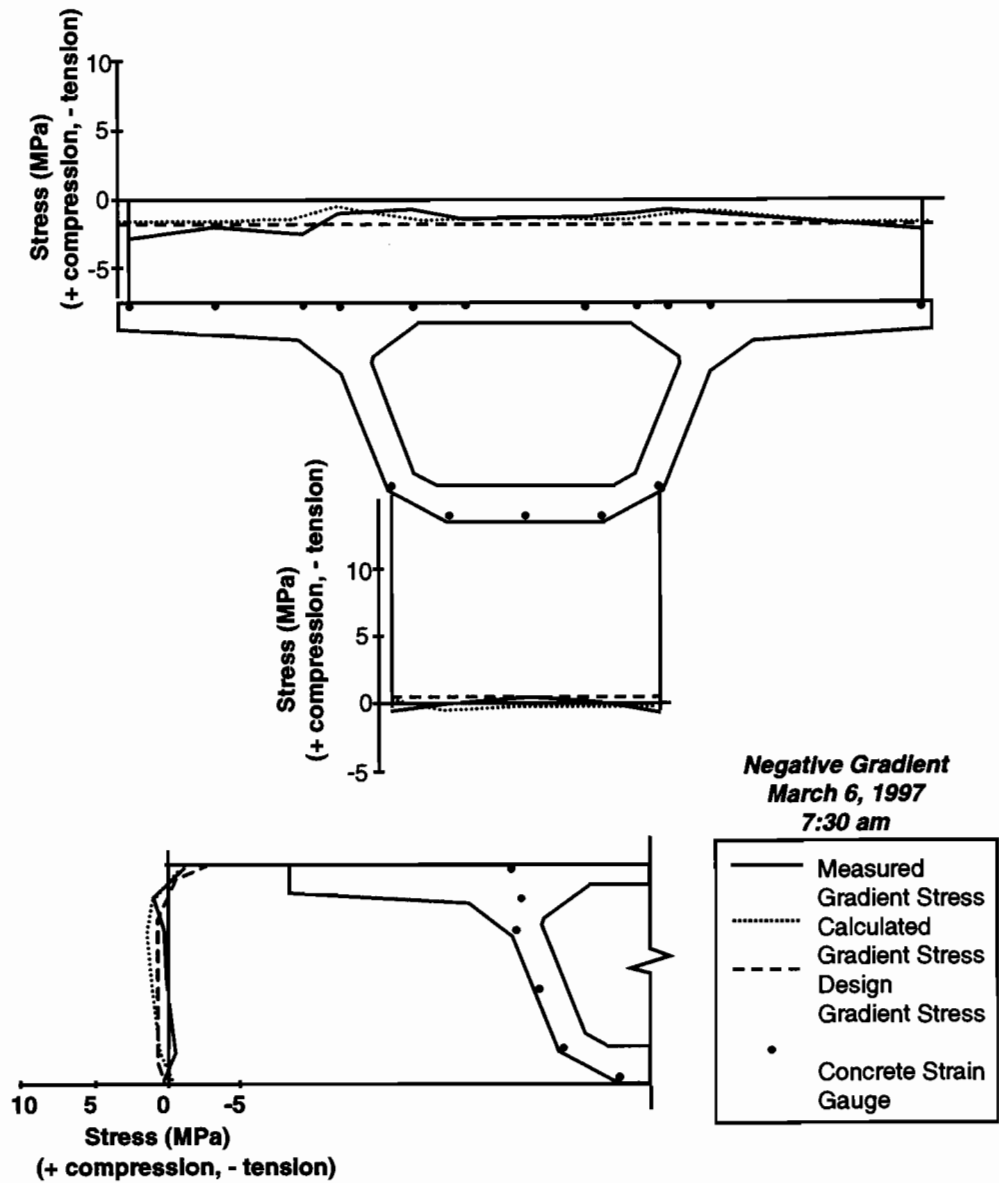


Figure 4.35 Comparison of measured and calculated negative thermal gradient stresses for segment P16-2 (near diaphragm)

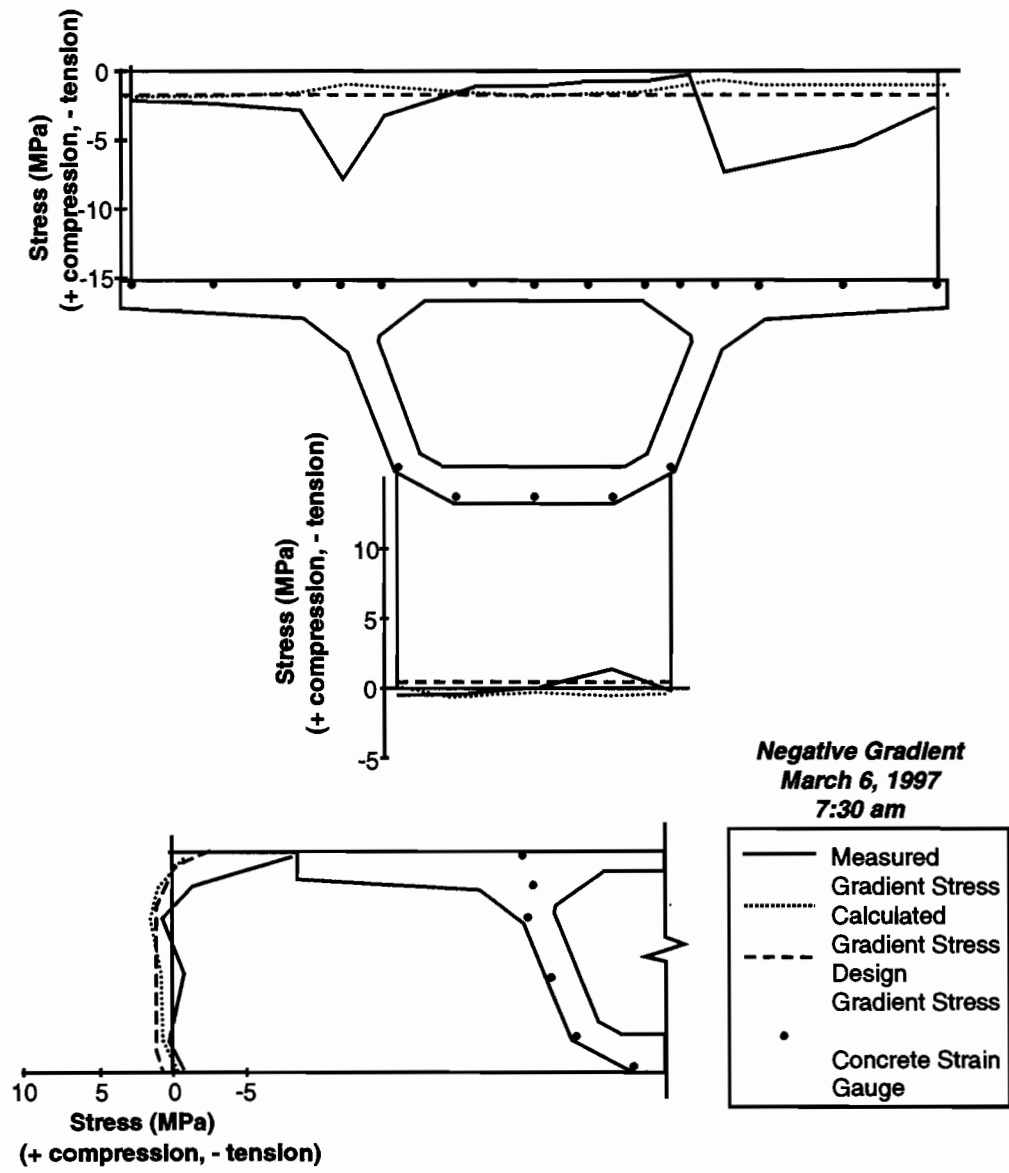


Figure 4.36 Comparison of measured and calculated negative thermal gradient stresses for segment P16-10 (quarter point)

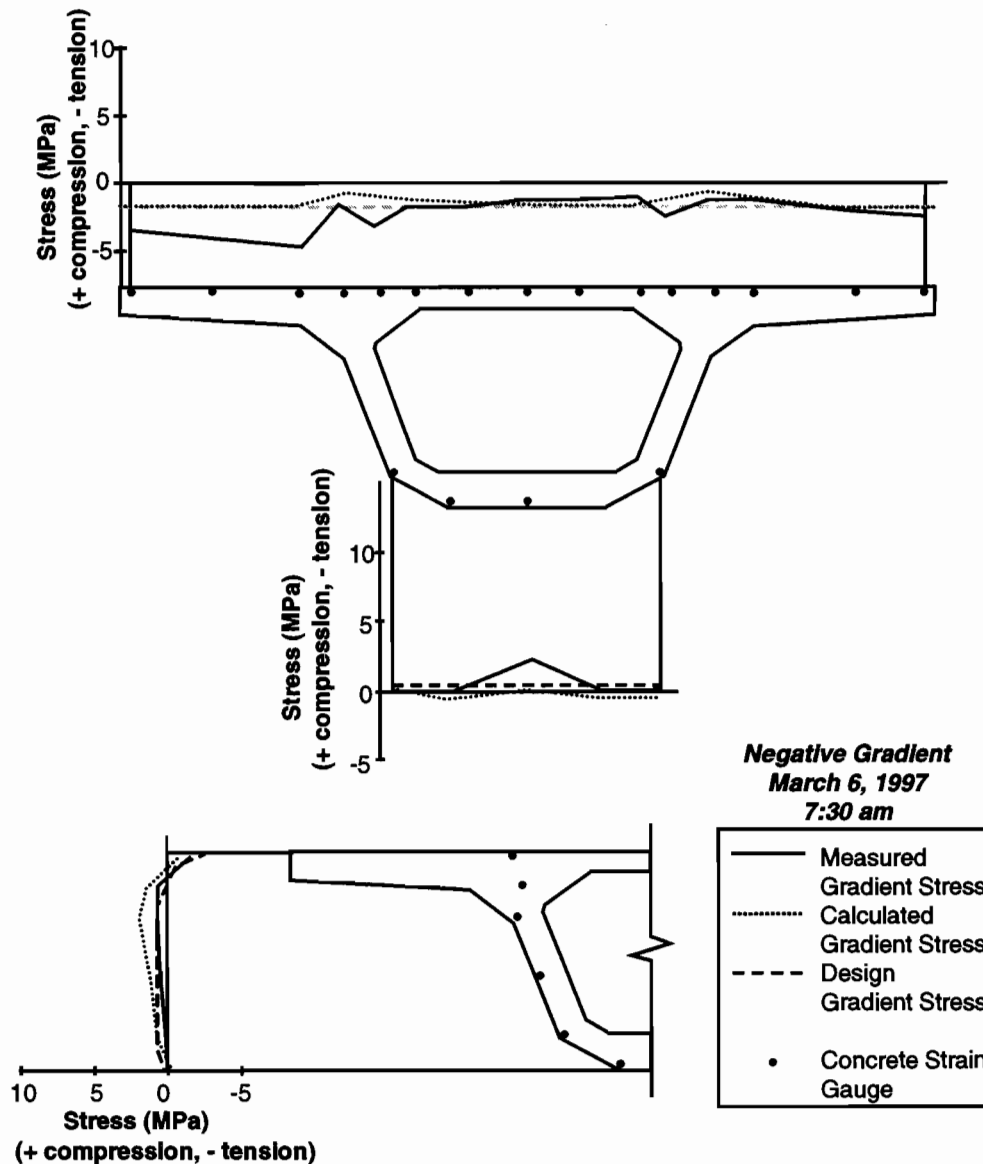
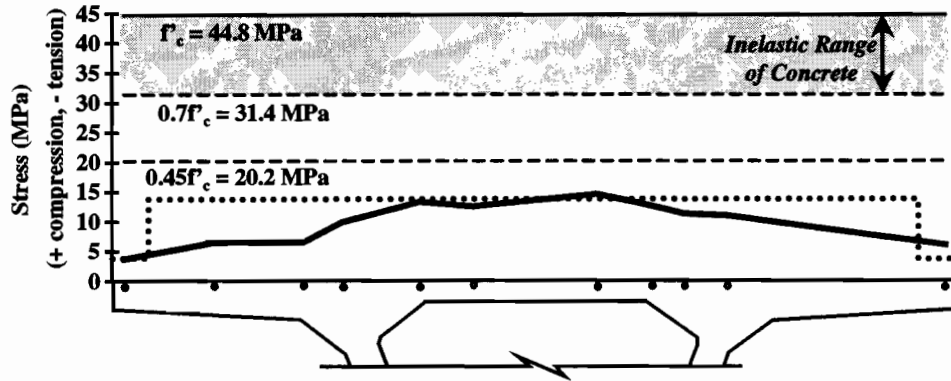


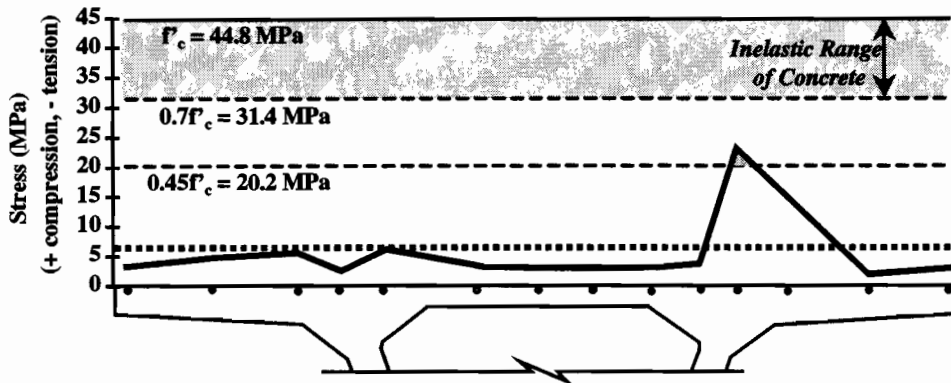
Figure 4.37 Comparison of measured and calculated negative thermal gradient stresses for segment P16-17 (midspan)

The magnitudes of the measured thermal gradients in Ramp P were lower than the AASHTO LRFD recommended gradient magnitudes, but the peak stresses at points in the section were marginally higher to much higher. Figure 4.38 shows the service load stresses from combinations of dead load, prestressing, live loads and the negative gradient case. The plots show both the measured stresses and the stresses predicted by normal calculation methods using the AASHTO LRFD design thermal gradients. The measured stresses near the diaphragm in segment P16-2 all fell below the stresses predicted by calculation. These stresses also did not approach the $0.45f'_c$ service level stress limit. The measured stress at one point in quarter point segment P16-10 exceeded the service level stress limit by a small amount, but did not approach the inelastic limit of the concrete at $0.7f'_c$. Stresses in midspan segment P16-17 all fell well below the service level stress limit. The load case at midspan did not include the live-load case because the stresses would have opposed those caused by the negative thermal gradient.

P16-2 (Near diaphragm): Dead Load + Prestressing + Live Load Case 1 + Negative Gradient



P16-10 (Quarter point): Dead Load + Prestressing + Negative Thermal Gradient



P16-17 (Midspan): Dead Load + Prestressing + Negative Thermal Gradient

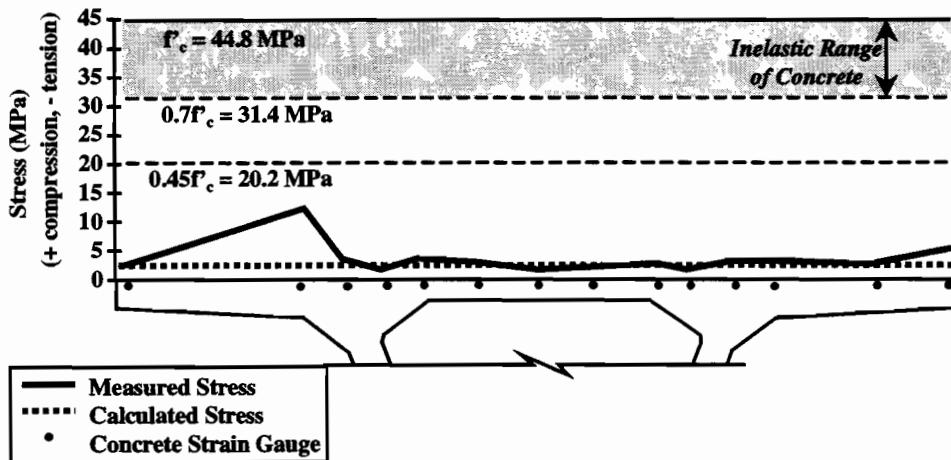
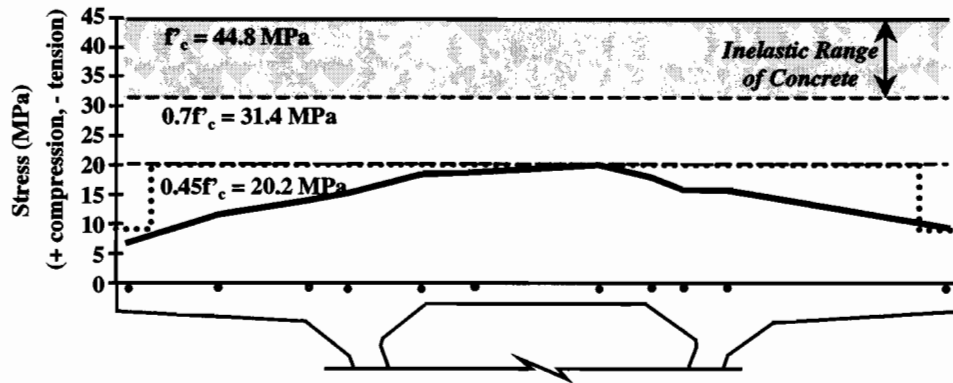


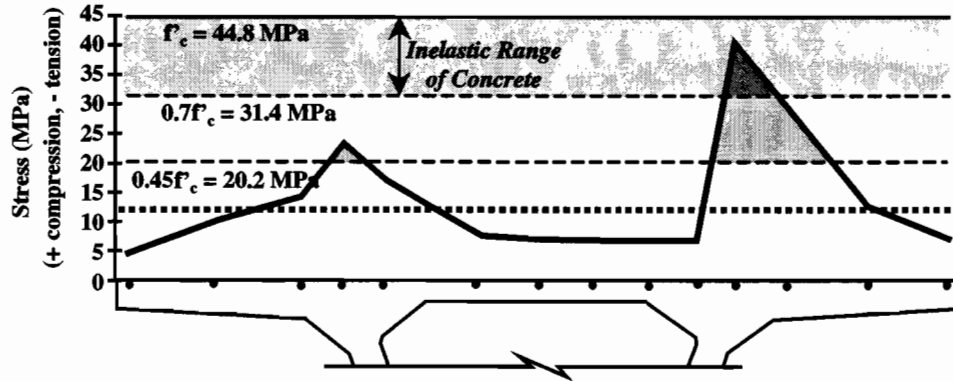
Figure 4.38 Minimum top flange stress load combinations for P16-2, P16-10 and P16-17

The stresses are plotted for various load combinations including the positive thermal gradient case in Figure 4.39. Since the maximum measured positive thermal gradient magnitude at deck level was closer to the design value than was the maximum negative thermal gradient magnitude, the measured stresses shown in Figure 4.39 exceeded the service level stress limit in more instances. The measured stresses projected well into the inelastic range in quarter point segment P16-10. No signs of distress in the concrete were noticed in this area prior to the application of the blacktop and none were noticed from the inside of the girder.

P16-2 (Near diaphragm): Dead Load + Prestressing + Positive Gradient



P16-10 (Quarter point): Dead Load + Prestressing + Live Load Case 1 + Positive Gradient



P16-17 (Midspan): Dead Load + Prestressing + Live Load Case 1 + Positive Gradient

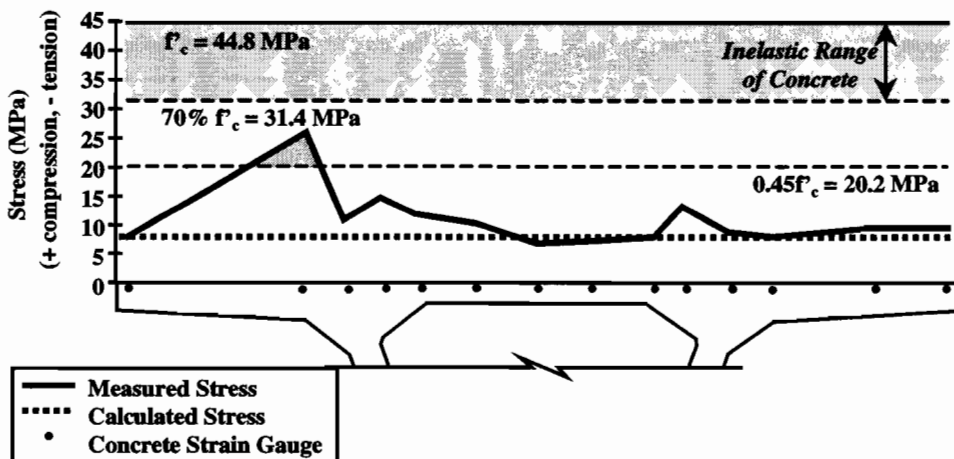


Figure 4.39 Maximum top flange stress load combinations for P16-2, P16-10 and P16-17

The transverse strains in the cross section were measured with strain gauges near each face of the top flange, bottom flange, and webs. The strains converted to stresses are plotted for midspan segment P16-17 in Figure 4.40 for the peak positive and negative thermal gradient cases. The measured stresses were compared to stresses calculated using a model of the cross section such as the one shown in Figure 4.8. The measured stresses did not compare well with the calculated stresses. For one, the calculated stresses assumed that no stresses would be created in the transverse direction from the thermal gradient response in the longitudinal direction. The primary difference between the measured and the calculated stresses was that the measured

stresses seemed to contain an additional amount of uniform compression or tension, depending on the location. The calculated stresses were dominated by bending stresses.

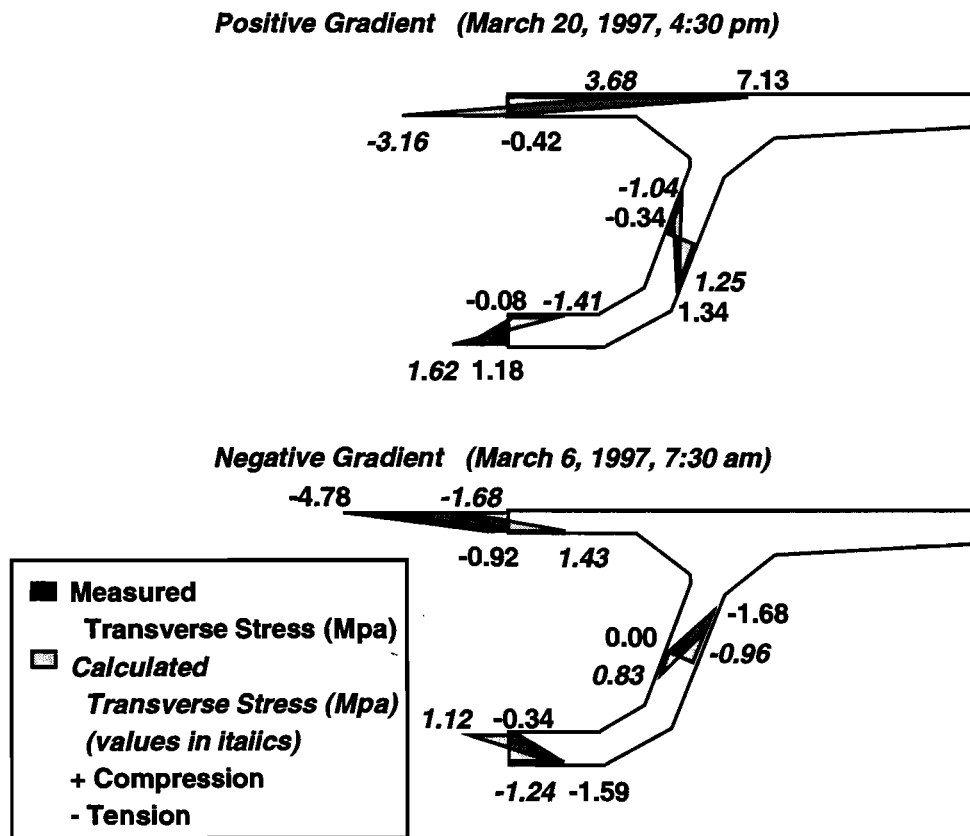


Figure 4.40 Comparison of measured and calculated transverse flexural stresses from positive and negative thermal gradients for P16-17

The strain changes in the external prestressing tendons were measured during the maximum positive and negative thermal gradient cases. Figure 4.41 shows that the stress change in any of the tendons during the maximum positive gradient day was less than 11MPa, or only 0.6% of the guaranteed ultimate tensile strength of the tendon. Figure 4.42 shows that the stress change in the tendons from the maximum negative thermal gradient was somewhat smaller at 9.5MPa. Fatigue from daily thermal stress cycles should not be a problem. Ryals [41] recommended a fatigue limit stress of 69MPa for external tendons based on traffic-induced stress cycles.

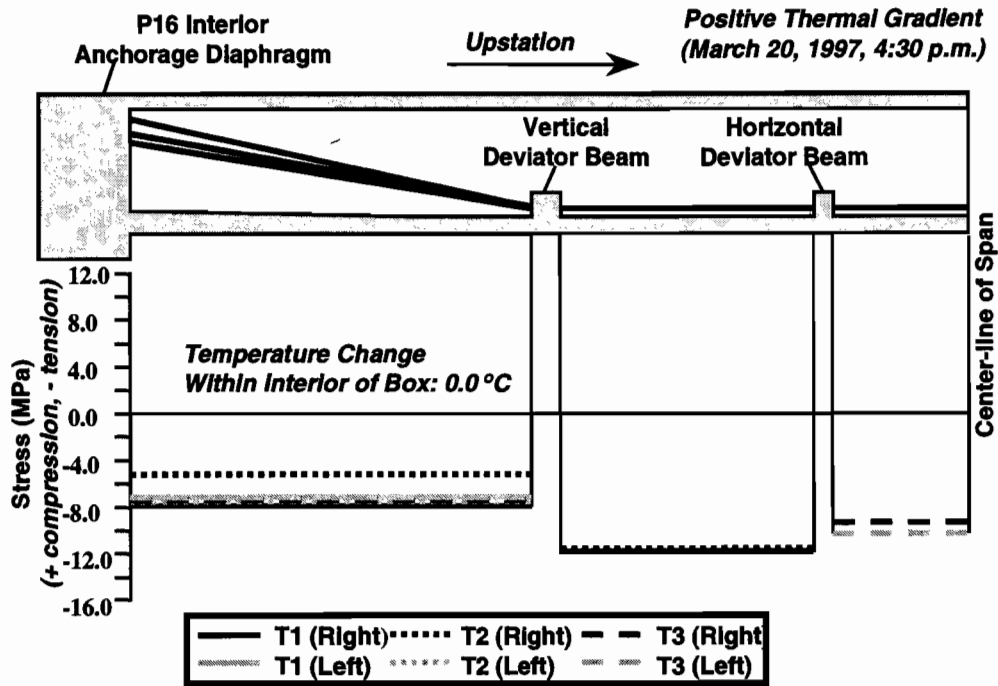


Figure 4.41 Measured stress changes in the Ramp P external tendons from the maximum positive gradient

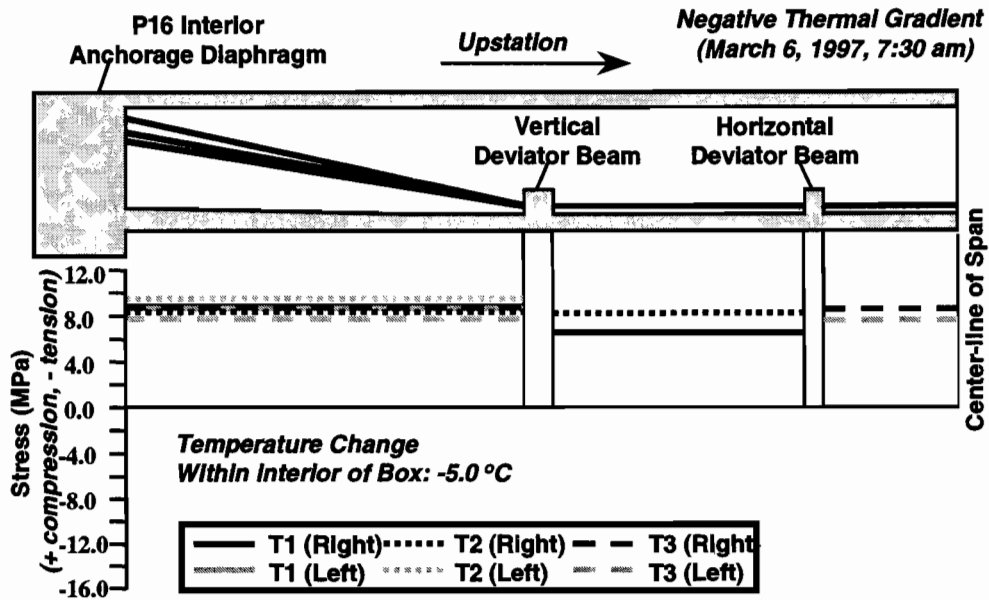


Figure 4.42 Measured stress changes in the Ramp P external tendons from the maximum negative gradient

4.3.2 Mainlane Superstructure

Temperatures were measured in the mainlane girder D5 hourly with the thermocouples distributed as shown in Figure 4.43. $T_{1,meas}$ and $T_{4,meas}$ were calculated with respect to the average temperature of the baseline thermocouples in the web. These baseline thermocouples located at the bottom of the webs recorded lower temperatures on average (T_{min}) during periods of peak positive gradients than the thermocouples located at the top of the webs. The baseline thermocouples at the top of the webs recorded higher temperatures (T_{max}) than

those at the bottom of the webs by about 2°C during periods of peak negative gradient. This behavior was different than that of the Ramp P cross section and was probably due to the huge mass of concrete at the root of the wings and the top of web fillet area. Heat absorbed through the top slab was retained in the fillet area, unable to cool completely by the end of the night. Concrete surfaces on the top interior of the box girder continued to increase in temperature until after midnight during periods of high solar intensity. The typical positive gradient shape, shown in Figure 4.43, was similar to that of Ramp P. The shape differed over that portion of the girder depth between the bottom of the top flange between webs and the bottom of the root of the wing. The shape of the negative gradients of any significant magnitude was irregular and was dependent on the gradient present in the cross section prior to the weather event that caused the high magnitude negative gradient.

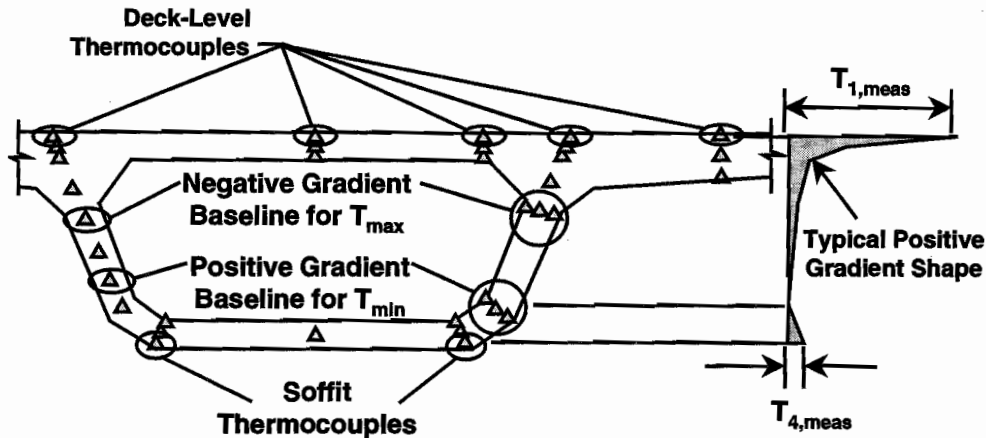


Figure 4.43 Thermocouples used to calculate thermal gradient magnitudes on the mainlane girder D5

$T_{1,meas}$, $T_{4,meas}$ and the ambient air temperature are plotted in Figure 4.44 for the month of June 1996. The maximum magnitude of the positive gradient at deck level occurred on June 17th after several days of stable weather. The maximum daily $T_{1,meas}$ values for that entire week were nearly of the same magnitude. The daily ambient temperature variation was moderate at 10°C, but the solar radiation was at its strongest of the year. $T_{1,meas}$ values of nearly this magnitude were recorded in 1995 with no blacktop in place and in other months in 1996. The spring of 1997 did not produce $T_{1,meas}$ values of significant magnitude during positive thermal gradient conditions. The $T_{1,meas}$ values recorded over the duration of the entire study are summarized in the Appendix.

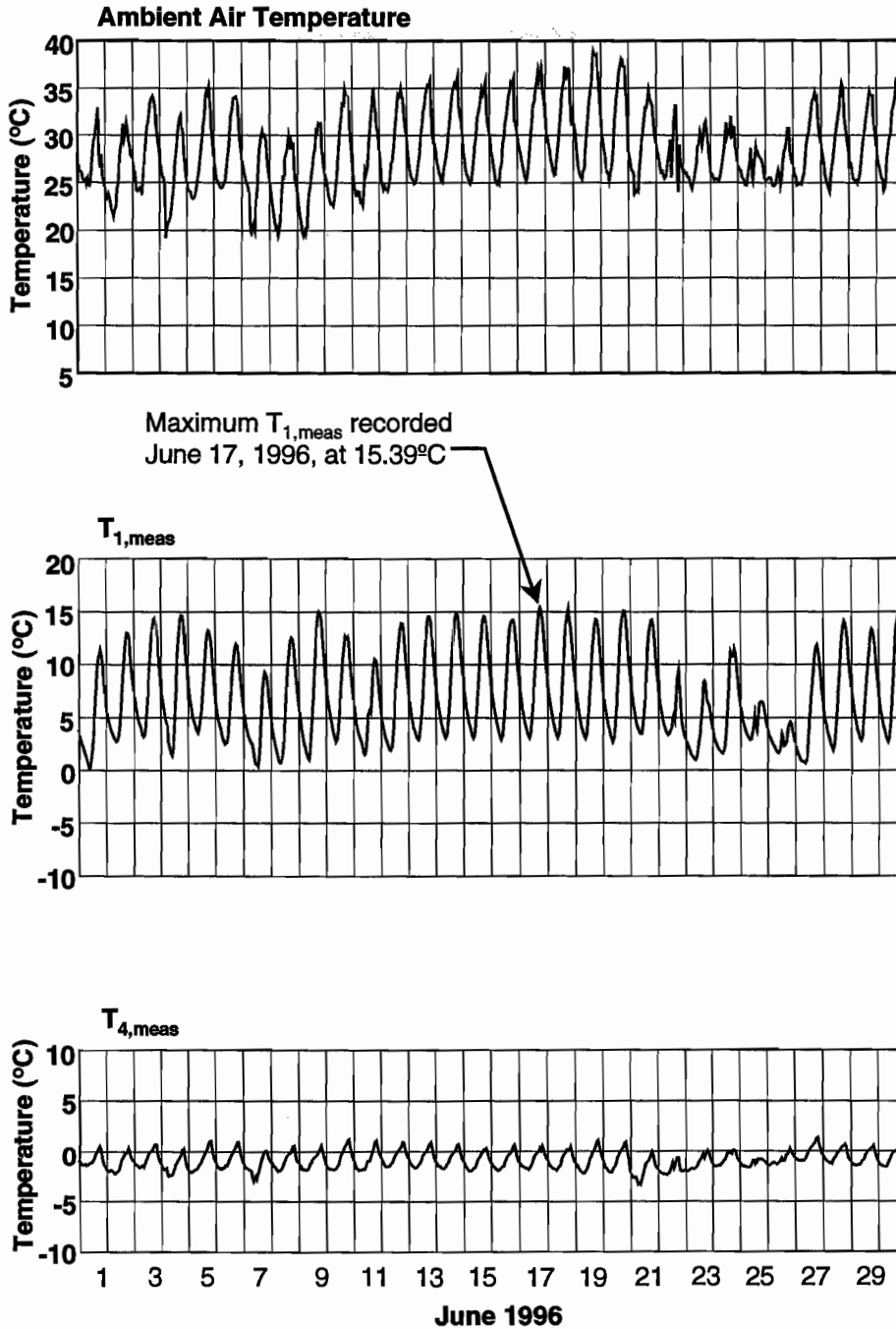


Figure 4.44 Measured thermal gradients on mainlane girder D5 for the month of June 1996

The maximum magnitude positive thermal gradient from June 17, 1996, is shown in Figure 4.45. Both the magnitude and the shape of the measured positive gradient differed from that of the design thermal gradient from AASHTO LRFD, shown in the plot at the right in Figure 4.45. $T_{1,meas}$ was lower over the webs, as was seen in the Ramp P girder. $T_{4,meas}$ was quite small at about half that of the Ramp P girder. The difference in elevation of the bottom of the top flange between webs and the bottom of the root of the wings produced an abrupt change in shape of the positive thermal gradient. This profile change was not a characteristic of Ramp P, which had proportions similar to more common box girders. The mainlane girder had the proportions of a spine girder by design for appearance.

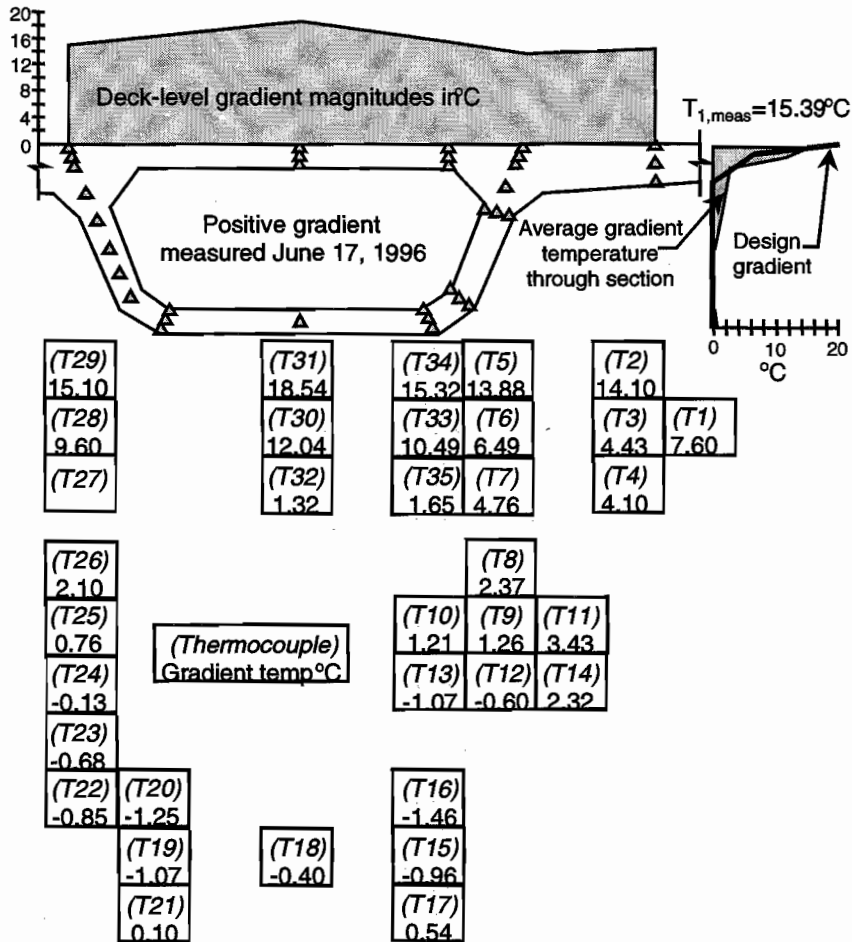


Figure 4.45 The maximum measured positive gradient on mainlane girder D5 (from June 17, 1996)

One of the maximum magnitude measured negative gradients, from November 11, 1995, is shown in Figure 4.46. The shape of the negative gradient shown in the plot at the right in the figure was regular in shape only within the depth of the top flange. The rest of the gradient shape was the sum of the previously existing gradient shape prior to the event that caused the high magnitude negative gradient and the negative gradient caused by rapid cooling of the entire exterior of the box girder. The soffit gradient magnitude ($T_{4,meas}$) was nearly as large as $T_{1,meas}$.

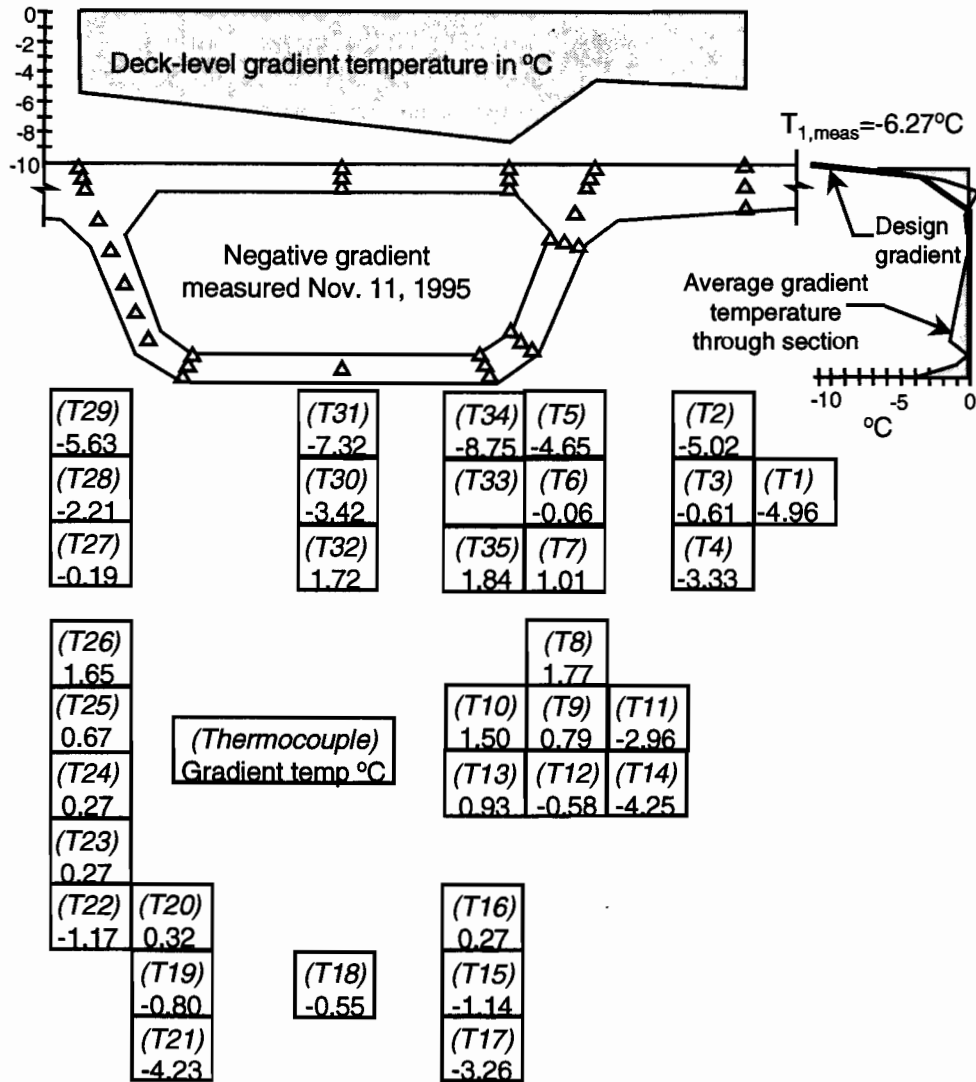


Figure 4.46 Measured negative gradient on mainlane girder D5 (from November 11, 1995)

The statistical distribution of peak daily thermal gradient deck-level magnitudes for the mainlane box girder was similar to that seen on Ramp P. The daily peak $T_{1,meas}$ values were somewhat larger on average on the mainlane for the positive gradient case, and the daily peak $T_{1,meas}$ values were about the same in magnitude and distribution for the negative gradient case. Figure 4.47 gives the distribution of daily peak $T_{1,meas}$ values for the positive gradient condition before the blacktop was in place. Gradient magnitudes measured in redundant months were only given half weight for the statistical distribution plots. The plot in Figure 4.47 includes two spring seasons, which in this case tended to unrealistically raise the percentages of the higher valued gradient magnitudes. High deck-level gradient magnitudes were consistently measured in both the spring of 1995 and 1996, while the spring of 1997 did not have such large magnitudes. Figure 4.48 gives the statistical distribution of maximum daily $T_{1,meas}$ values after the blacktop was in place. The maximum measured $T_{1,meas}$ value with blacktop was in fact larger than the maximum $T_{1,meas}$ value without the blacktop. The distribution of daily peak deck-level positive gradient magnitude substantially shifted to the lower temperatures after the 50mm of blacktop was in place. The distribution of daily minimum $T_{1,meas}$ values, shown in Figure 4.49, revealed that very few days had a substantial negative thermal gradient, with minimum daily $T_{1,meas}$ values in the -7°C to -9°C range occurring a low percentage of the time. Figure 4.50 shows that any appreciable deck-level negative gradient magnitudes had all but been eliminated once the 50mm of blacktop was placed, with over half of the days having a minimum $T_{1,meas}$ value greater than -1°C .

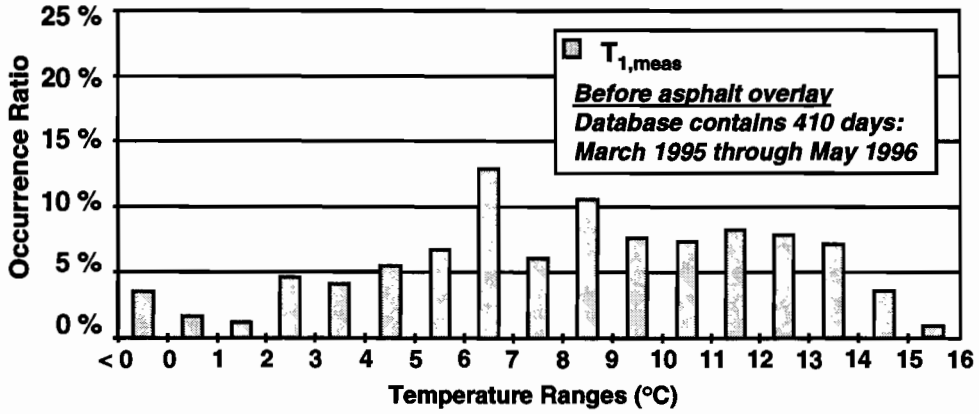


Figure 4.47 Statistical occurrence of daily maximum $T_{1,meas}$ values on mainlane girder D5 before application of the asphalt blacktop

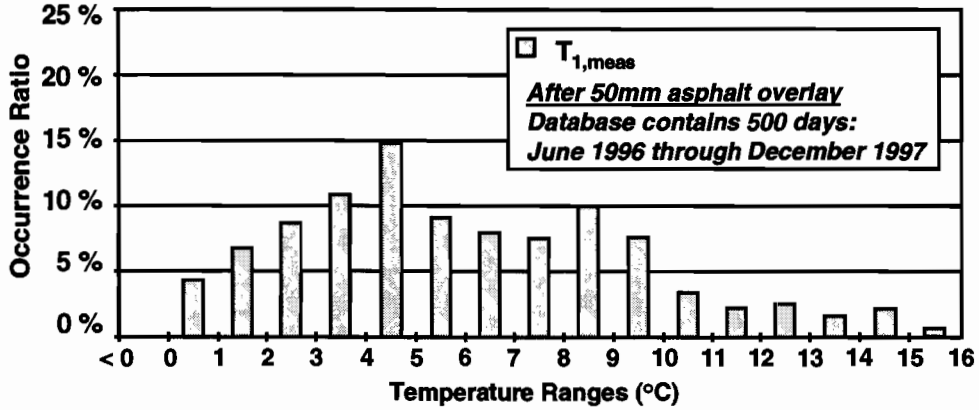


Figure 4.48 Statistical occurrence of daily maximum $T_{1,meas}$ values on mainlane girder D5 after application of the asphalt blacktop

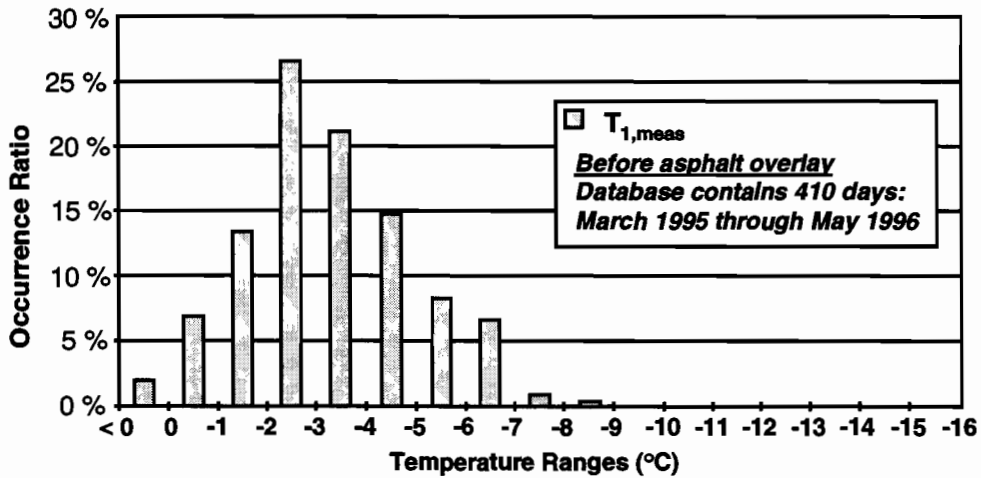


Figure 4.49 Statistical occurrence of daily minimum $T_{1,meas}$ values on mainlane girder D5 before application of the asphalt blacktop

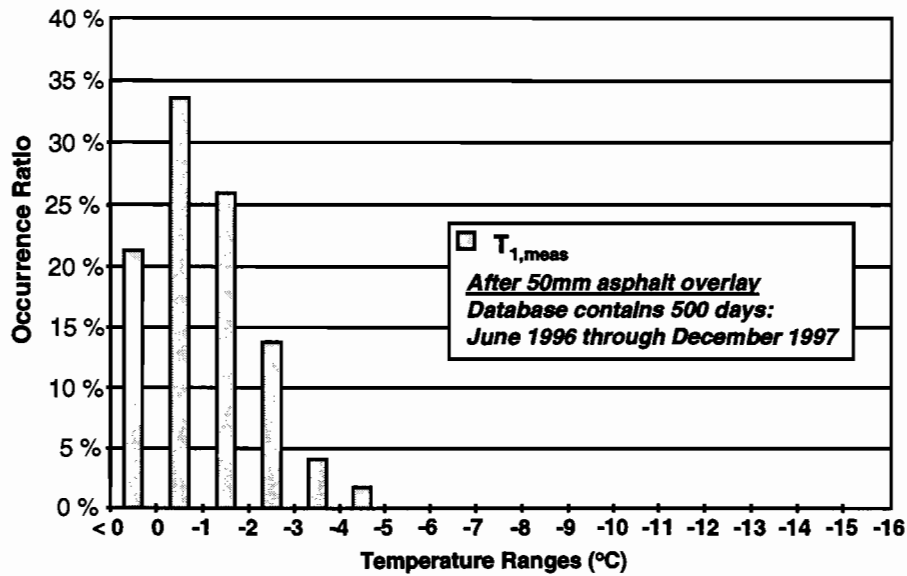


Figure 4.50 Statistical occurrence of daily minimum $T_{1,meas}$ values on mainlane girder D5 after application of the asphalt blacktop

Both measured and calculated stresses are presented in the figures to follow. Stresses were calculated using the measured temperature changes and the cross-sectional model in Figure 4.51. This calculation assumed that the measured temperatures were distributed evenly within the elements. The necessary integrations for the calculation also used these elements, and plane sections were assumed to remain plane. Stresses varied across the width of the cross section depending on the temperature change within each element. Stresses were also calculated using the appropriate AASHTO LRFD design thermal gradients. Plane sections were assumed to remain plane in this calculation, and there was no transverse variation of temperature in the design gradient. Therefore, no transverse variation of stress was calculated, as can be seen in the figures.

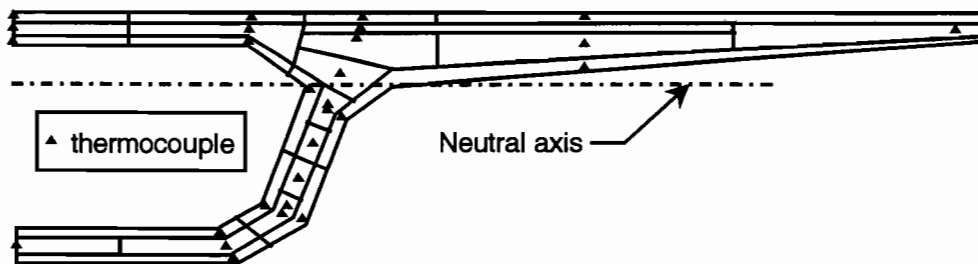


Figure 4.51 Division of the mainlane girder D5 cross section into tributary areas for each thermocouple gauge

Stresses are plotted for the positive thermal gradient case from April 20, 1995, in Figures 4.52 and 4.53. The positive thermal gradient from this day produced an extreme gradient through the thickness of the top flange between webs. The maximum temperature change at one thermocouple, located at the center of the top flange, was 17.1°C for the 9-hour interval under consideration. Figure 4.52 shows the stresses in segment D5-9 near midspan. The thermocouples were also located in this segment. Peak measured stresses in the top flange generally fell below those calculated using the AASHTO LRFD design gradient of 25.6°C. The measured stresses in the top slab were higher over the webs than in the wings. The measured soffit gradient magnitude of 3.3°C was higher than the 2.8°C recommended by AASHTO LRFD, yet the measured bottom flange stresses did not exceed those calculated using the AASHTO LRFD gradient. The measured stresses were actually predicted quite well by the calculation using the AASHTO LRFD gradient, even though the gradient shape differed substantially at some points. The best comparison can be made using the plots of stress over the depth

of the webs. The location of the strain gauges about 80mm below the surfaces of the concrete did not allow measurement of the peak top and bottom fiber stresses predicted by the calculations. The measured stresses in the top flange did compare well to the calculated values at the appropriate depth beneath the top fiber.

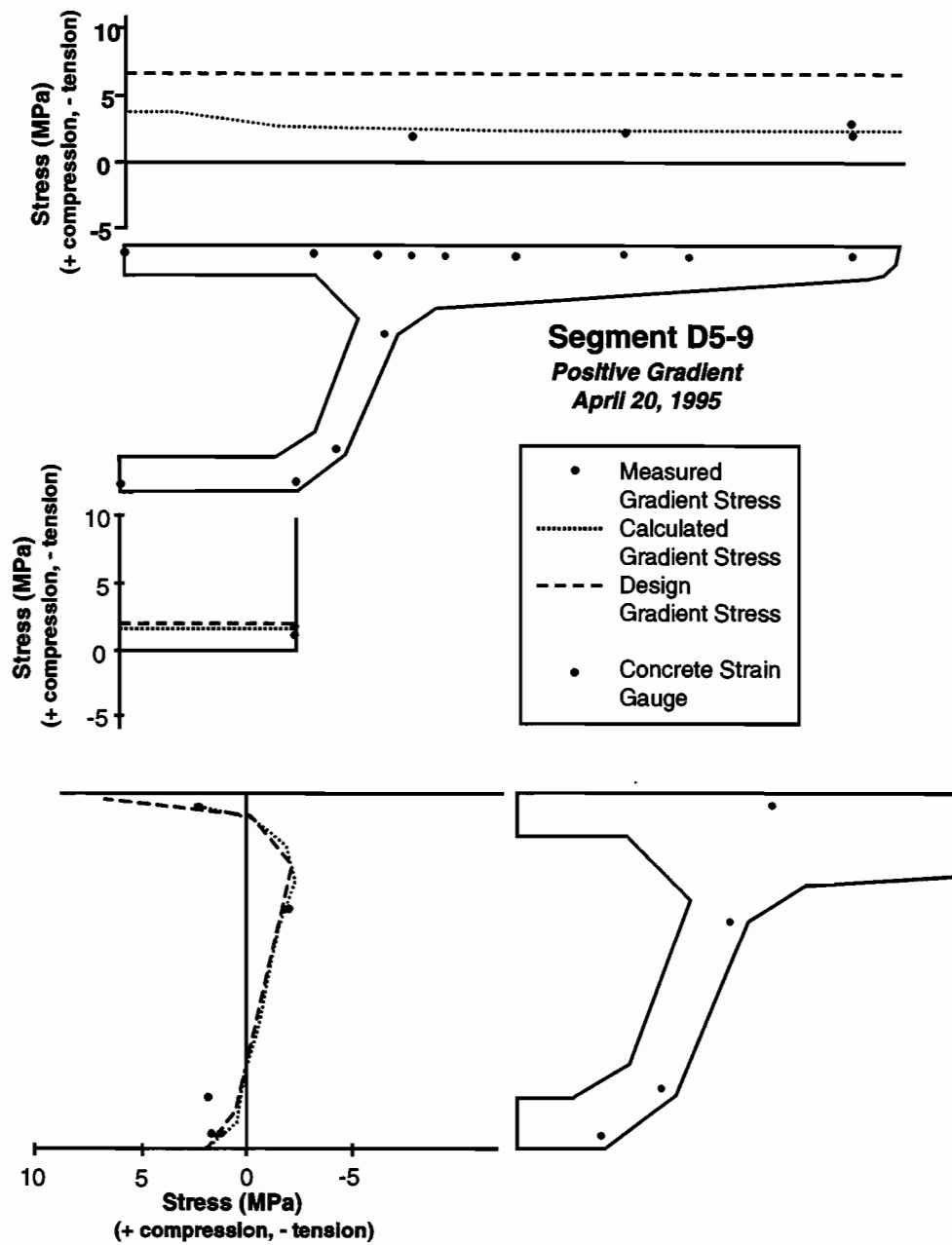


Figure 4.52 Comparison of measured and calculated positive thermal gradient stresses for segment D5-9 (April 20, 1995)

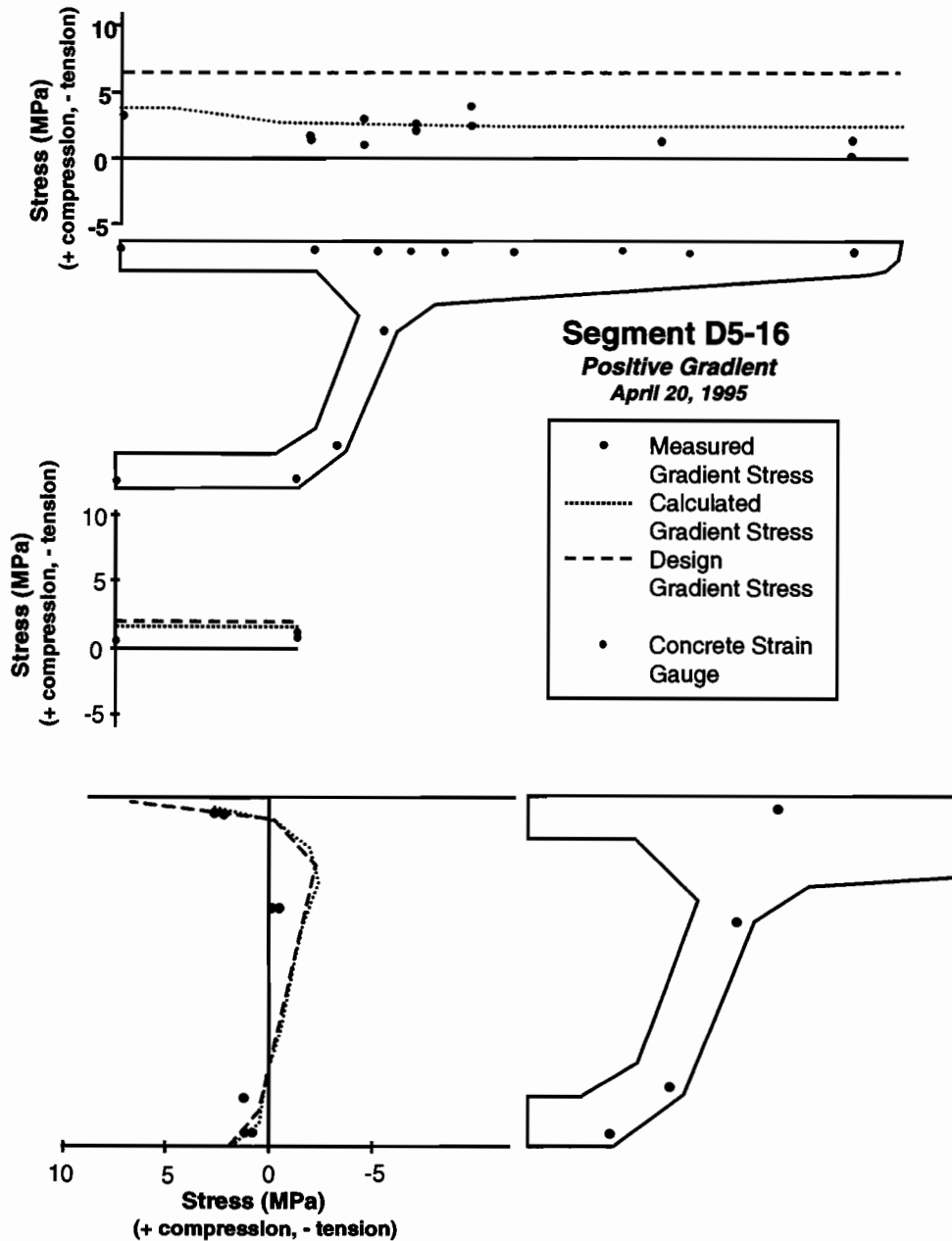


Figure 4.53 Comparison of measured and calculated positive thermal gradient stresses for segment D5-16 (April 20, 1995)

Although the positive thermal gradient in the heavy end diaphragm segment D5-16 at the longitudinal strain gauge locations probably differed somewhat from the gradient measured in segment D5-9, the measured stresses in these two segments were almost identical. The thermal-gradient-induced stresses in segment D5-16 for April 20, 1995, are plotted in Figure 4.53. The strain gauges in this segment were located only 90mm from the heavy end diaphragm, yet the measured stresses differed substantially from those in segment D5-9 only near the neutral axis of the girder. The gauges located near the neutral axis of the girder were tied to the exterior plane of the web bar cage. Therefore, the strains measured by these gauges may not reflect the true average strain change of all points at this depth in the section, since a positive thermal gradient was present across the thickness of the web. The measured stresses were also somewhat lower near the wing tip than the wing tip stresses in segment D5-9. The good comparison between the gauges at these two locations gives credibility to the measurements, especially since the internally balanced stresses being measured should have been similar

along the length of the girder. The shape of the plot of measured and calculated stresses down the depth of the web of the mainlane differed from that for the Ramp P girder. The simple-span mainlane girder had only self-equilibrating stresses, so a balance of tensile and compressive stresses was produced over the depth of the web seen at the bottom of Figure 4.52. The shape of the curve for the measured and calculated stresses was exactly like the shape of the thermal gradient. The measured and calculated stresses in the Ramp P girder seen at the bottom of Figures 4.32, 4.33 and 4.34 were influenced by a combination of bending stresses and self-equilibrating stresses because the Ramp P girder was continuous across the piers and had a moment connection to some of the piers.

Stress changes from the day of the maximum positive thermal gradient deck-level magnitude on June 17, 1996, are shown in Figures 4.54 and 4.55. At this point in time there was 50mm of blacktop in place, and the top slab closure pour had been cast between girders at the joint locations. The 50mm of blacktop changed the shape of the positive gradient from that of April 20, 1995. The most important difference was the top slab temperature variation. The 50mm of blacktop insulated the top flange concrete from heat loss during the night, nearly eliminating the formation of a daily negative gradient. The daily maximum $T_{1,meas}$ values with or without blacktop were nearly the same, at 17.1°C without blacktop and 18.5°C with 50mm of blacktop. The measured stresses from the June 17, 1996, gradient were similar to those measured for the April 20, 1995, gradient, with one major exception. Most of the gauges located in the top flange over the webs measured strains that would be well into the plastic range of the concrete. Most of these data points were not plotted in Figures 4.54 and 4.55 because they were off the selected scale. This behavior was also measured on the Ramp P girder. It is possible that the concrete in the heavily congested area over the webs had fatigued and was effectively relieving thermal stresses because of cracked concrete. This stress relief may have been the case only in the concrete area immediately adjacent to the heavy web stirrup bars, which was where the strain gauges giving the large measurements were tied in place. It is also possible that the strain gauges themselves had fatigued and were giving erroneous readings, even though they were designed for a long fatigue life over a wide temperature range. In all cases, the only gauges giving the high strain readings were located over the webs in the top flange. The measured stresses through the depth of the webs for the June 17, 1996, gradient were similar in segments D5-9 and D5-16. These stresses were also similar to those measured for the April 20, 1995, positive gradient. The measured stresses compared better to the stresses calculated using the actual measured temperature changes than to the design gradient, as was also the case for the April 20, 1995, gradient.

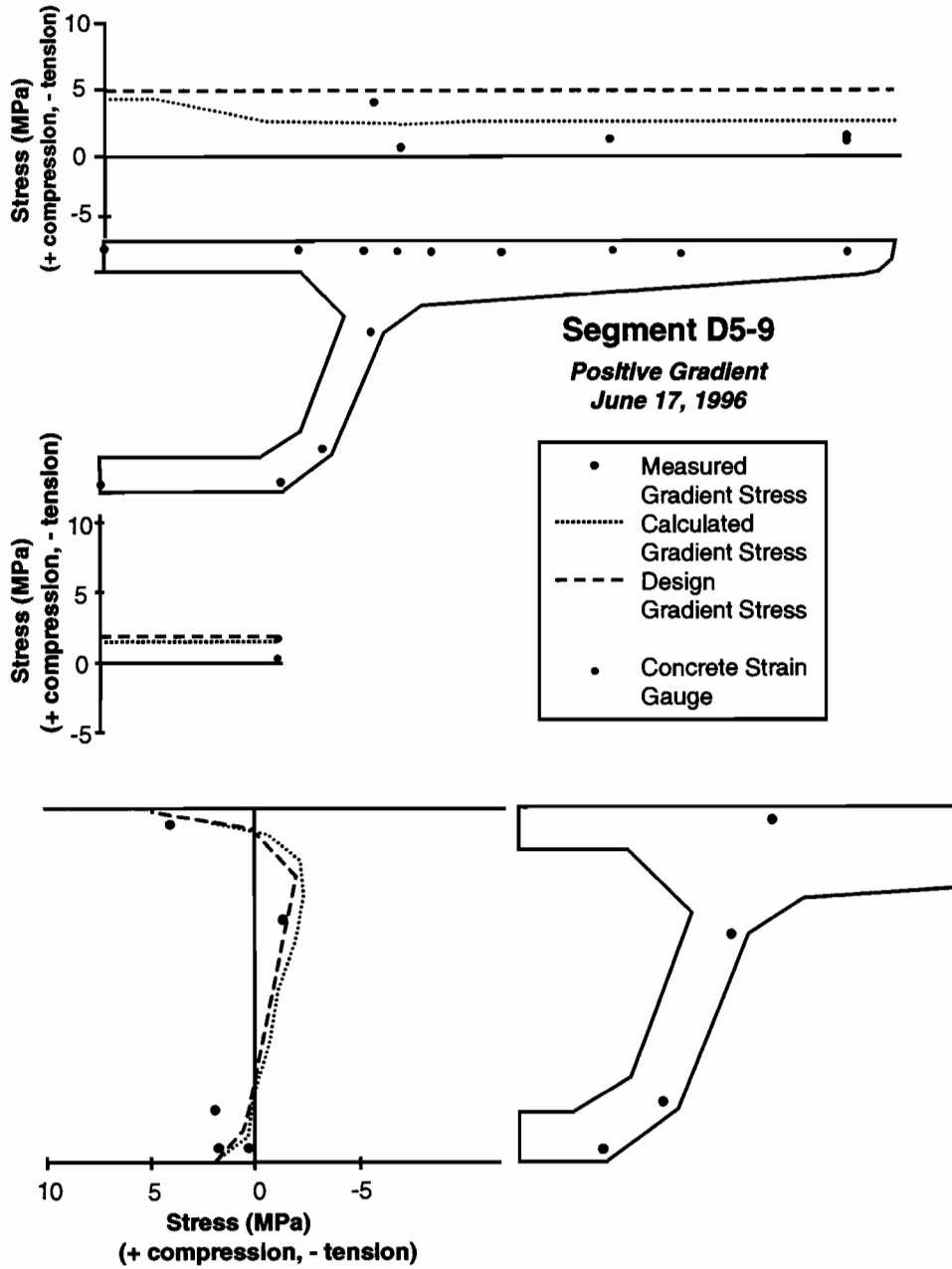


Figure 4.54 Comparison of measured and calculated positive thermal gradient stresses for segment D5-9 (June 17, 1996)

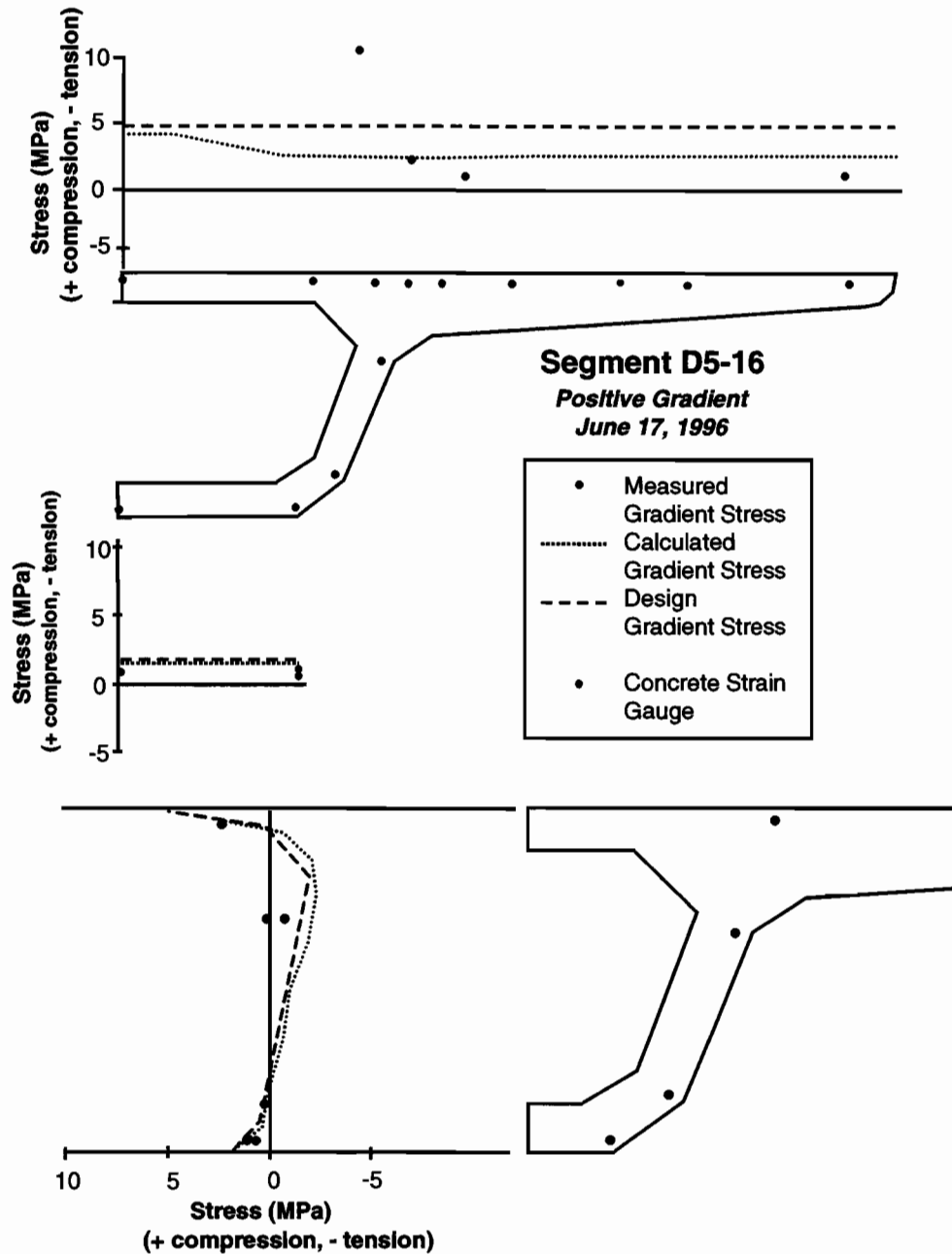


Figure 4.55 Comparison of measured and calculated positive thermal gradient stresses for segment D5-16 (June 17, 1996)

Calculated and measured stresses for the negative gradient case from November 11, 1995, are plotted in Figures 4.56 and 4.57. In general, the measured stresses were lower than the calculated stresses, especially near the neutral axis of the girder. The measured stresses in both segment D5-9 (in Figure 4.56) and segment D5-16 (in Figure 4.57) were closer to the stresses calculated using the measured gradient than that calculated using the AASHTO LRFD gradient. Neither the shape nor the magnitude of the AASHTO LRFD gradient was very similar to the actual gradient. Once again, the measured stresses in the top flange decreased from webline to wingtip, indicating plane sections were not remaining plane even at midspan.

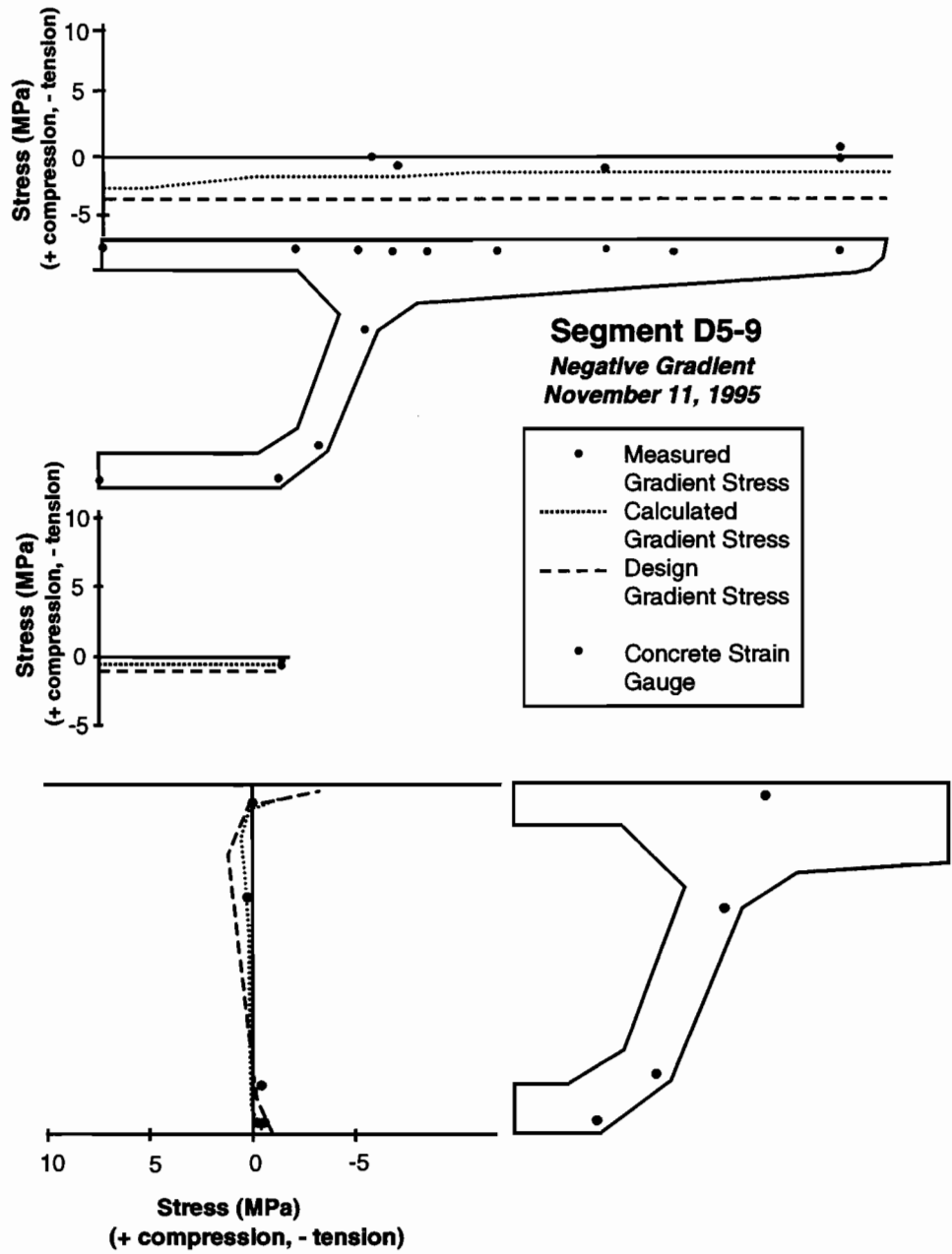


Figure 4.56 Comparison of measured and calculated negative thermal gradient stresses for segment D5-9 (November 11, 1995)

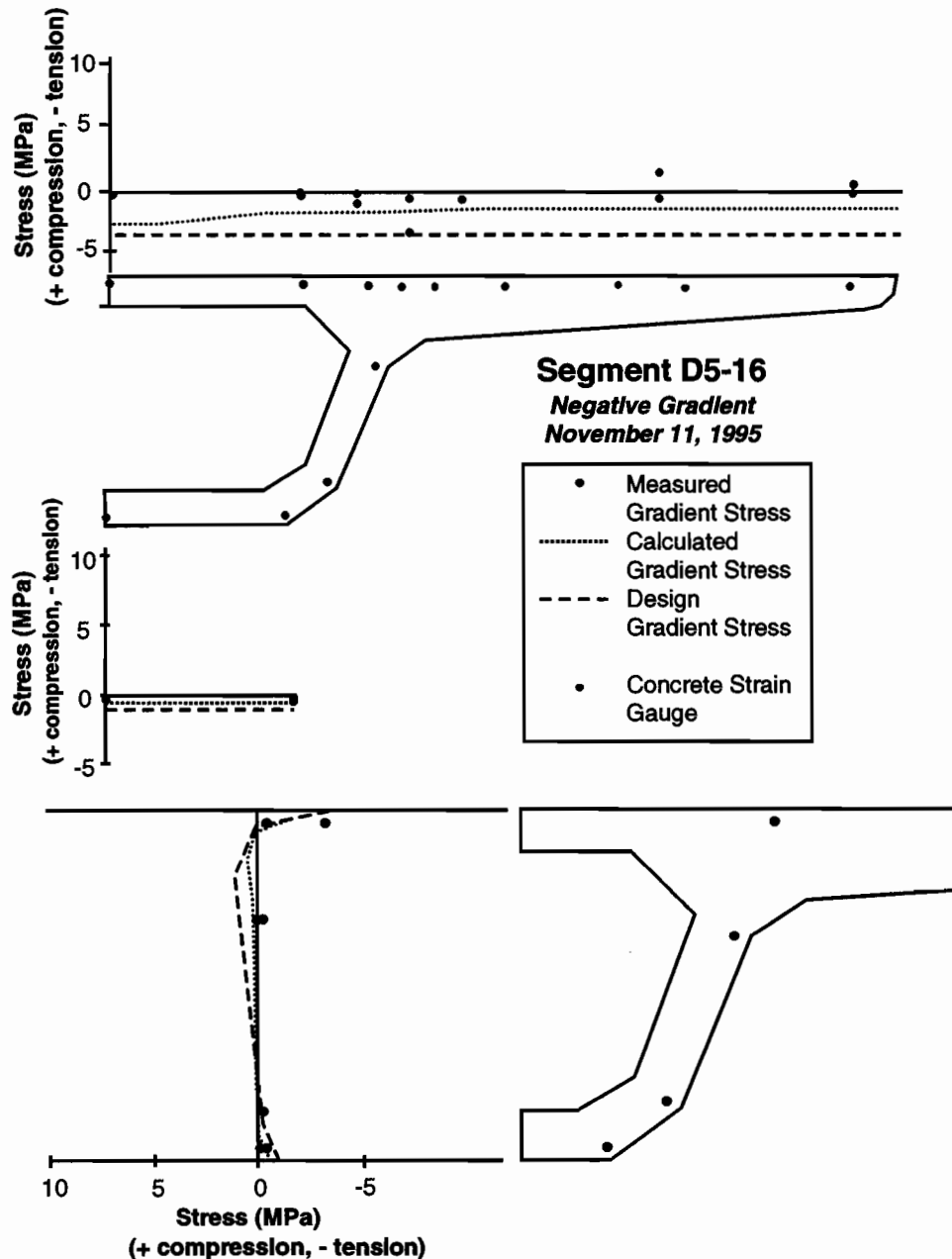


Figure 4.57 Comparison of measured and calculated negative thermal gradient stresses for segment D5-16 (November 11, 1995)

The top flange of the mainlane box girder experienced thermal gradients through its thickness of magnitudes large enough to warrant consideration during the transverse design of the section. Figure 4.58 shows the peak positive and negative gradients measured through the top flange and the corresponding gradients at other points in the section. These gradients occurred when no blacktop was in place. Measurements indicated that these peak gradients would be similar to those with 50mm of asphalt in place for the top flange. The positive thermal gradients measured through the thickness of the webs and bottom flange were of insignificant magnitude. The magnitude of the peak positive gradient in the top flange was 17.5°C, exceeding the maximum measured deck-level gradient over the depth of the entire section on that day. Significant magnitude negative thermal gradients occurred in the webs and bottom flange, as seen in the center section of Figure 4.58, with the peak negative gradient magnitude occurring in the top flange. Since the actual thermocouple locations were never closer than

25mm from any concrete surface, the peak positive and negative gradient magnitudes were most probably larger than those presented in all cases.

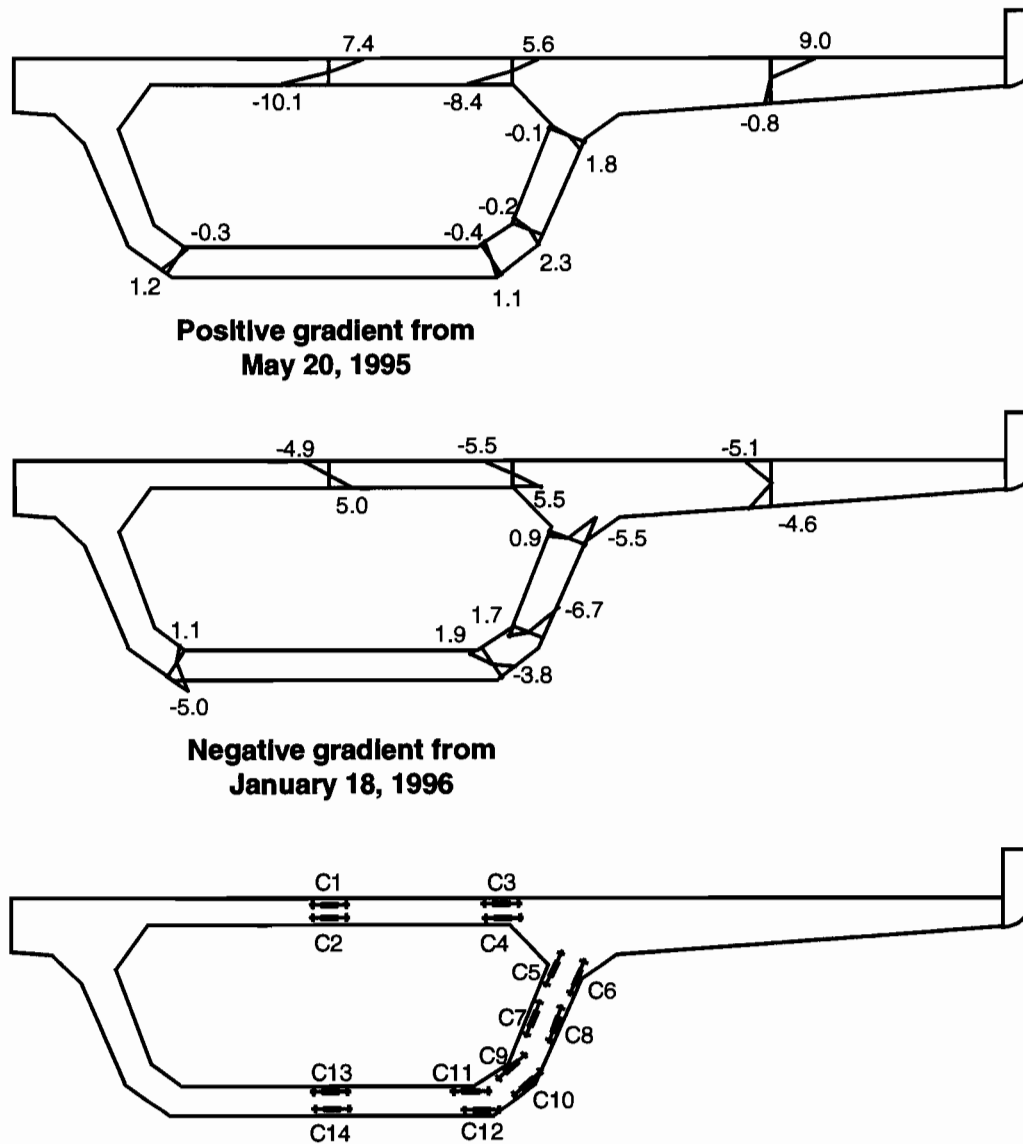


Figure 4.58 Measured peak positive and negative thermal gradients in degrees Celsius for segment D5-9 flanges and webs

Table 4.1 gives the measured strains from the May 20, 1995, positive gradient and the strains predicted by analysis using the measured gradient. The magnitude of the measured strains was less than the calculated strains at nearly every gauge location. The analytical model predicted compression on the outside face and tension on the inside face of the box girder, and the gauges measured a similar response. This was different from the response measured on Ramp P. For the positive gradient case the Ramp P girder had compression in the top flange and tension in the bottom flange, as well as bending and self-equilibrating stresses. Two major differences existed between the mainlane girder and the ramp girder. First, the mainlane girder was significantly wider for its depth than the Ramp P girder, which has an effect on the distribution of bending stresses around the section. Secondly, the mainlane box girder had a longitudinal crack at the top of both webs where the webs met the fillet on the inside of the girder. The reduction in stiffness from the crack would contribute to a reduction in bending stresses and axial stresses in the top flange and bottom flange by reduced bending moments in the webs. The crack occurred while the segments were still in the form when the concrete was relatively weak. The crack was caused by moments generated by the transverse pretensioning forces in the

top flange. The prestressing strands were cut when the concrete was less than 24 hours old. The Ramp P box girder did not crack from the pretensioning forces because the distance between webs was much shorter, reducing the elastic shortening from the prestressing. The analytical model used for calculating the strains in Table 4.1 did not account for this reduction in stiffness at the tops of the webs, which is common practice.

Table 4.1 Mainlane girder D5 transverse thermal strains from the May 20, 1995, positive gradient

Gauge Location	Measured Strains in $\mu\epsilon$	Calculated Strains in $\mu\epsilon$
C1		-99
C2		113
C3	-36	-63
C4	39	61
C5	8	26
C6	-32	-32
C7	5	19
C8	-16	-28
C9		12
C10	-9	-18
C11	18	11
C12	-12	-14
C13		12
C14	-10	-15

4.3.3 Large Ramp Pier P16

Measurements were taken to determine the importance of thermal gradient effects in the voided octagon pier P16. The relationship of the sides of the pier to the sun's exposure greatly influenced the shape and magnitude of the gradient over the course of a day. Figure 4.59 shows the temperatures measured by the thermocouples just under the concrete surface in pier segment PC16-5 near the midheight of the pier for June 17, 1996. A general and smooth cooling trend occurred overnight, with the gauges all converging to nearly the same temperature. The morning sun exposure first warmed the east face of the pier. As the sun rose, its radiation hit the pier at an increasingly acute angle. For this reason the south face of the pier underwent the lowest temperature change of any side of the pier that was directly exposed to the sun. The west face of the pier underwent the greatest temperature change due to all day ambient heating and direct exposure to the sun's radiation at the hottest part of the day. Conditions were ideal for the development of a large positive thermal gradient on this day, as was also measured on the mainlane girder.

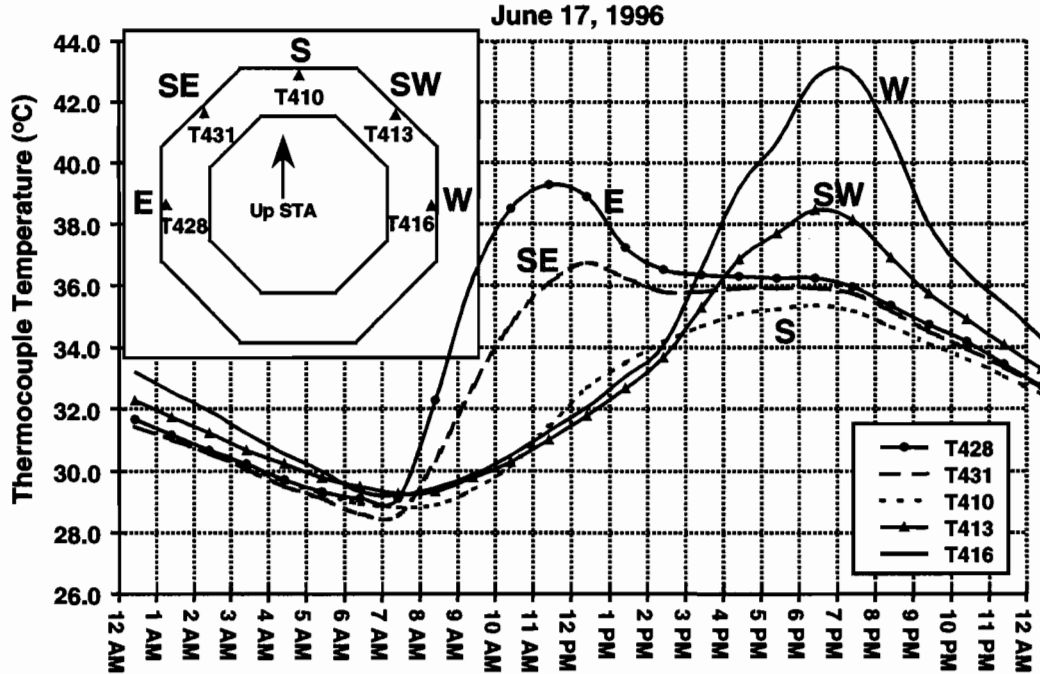


Figure 4.59 Typical daily temperature cycle of selected thermocouples in segment PC16-5

The gradient measured through the thickness of the west wall in segment PC16-5 was also substantial, plotted in Figure 4.60. The interior thermocouples T417 and T418 did not cool to the same temperature as the exterior of the concrete overnight and changed little over the course of the day. The vertical distribution of concrete temperatures on the west face is given in Figure 4.61. The temperature measured near midheight of the pier by thermocouple T417 was very similar to the temperature recorded by T442 located only 610mm from the massive solid capital segment. The superstructure was not in place so no shading of the pier's west face occurred during the entire day. Temperatures measured 610mm from the solid base of the pier were substantially lower than the temperatures further up the pier because of the heat loss to the footing and ground and from shading by the north and southbound lanes of IH 35. Temperatures recorded by thermocouple T511 in the solid capital segment did not match the peak changes at T417 and T442 because of heat loss to the solid core of that segment.

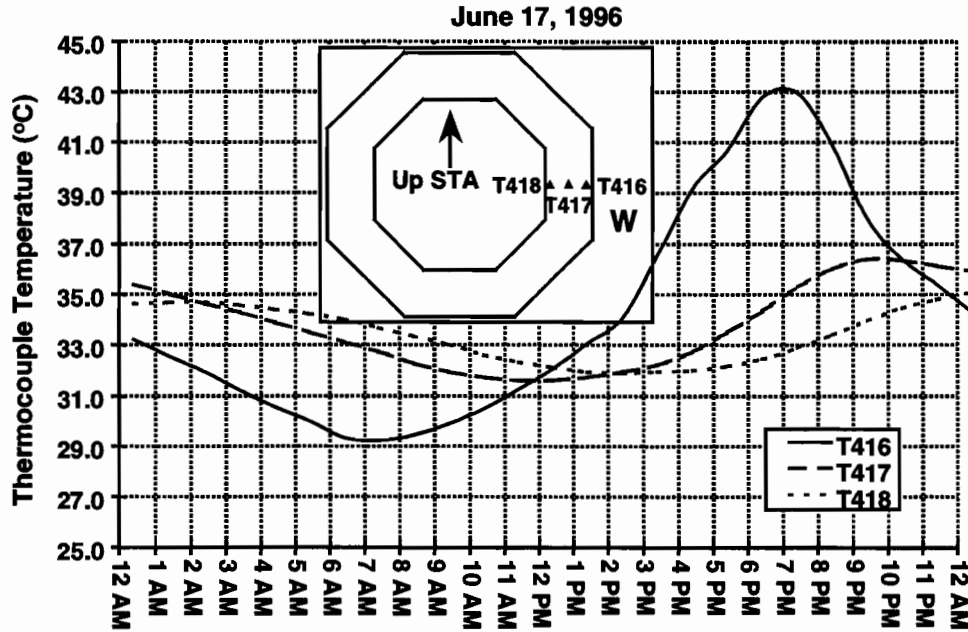


Figure 4.60 Temperatures recorded through the thickness of the west wall of segment PC16-5

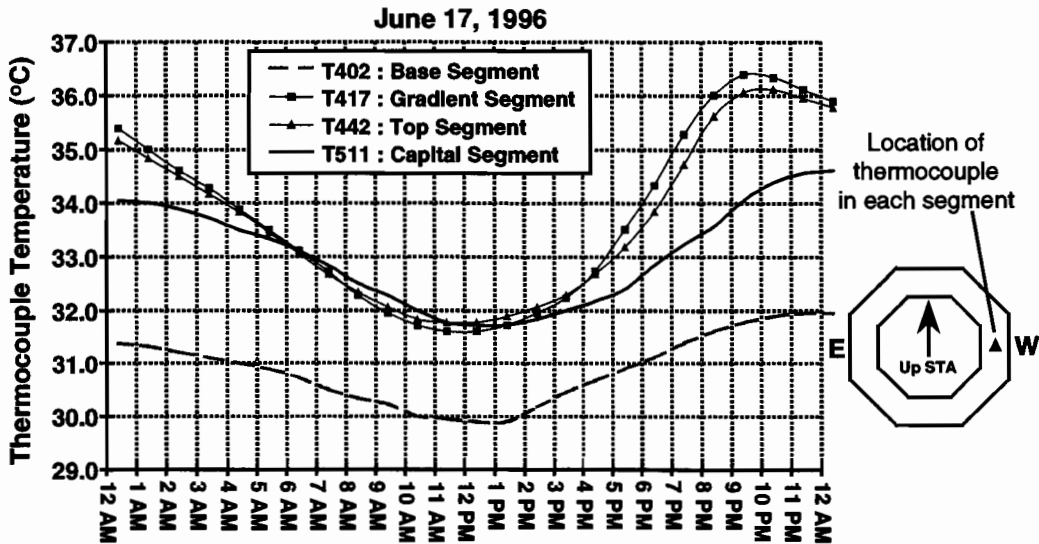


Figure 4.61 Temperatures measured along the height of pier P16

Detailed plots of the daily temperature changes in segment PC16-5 for June 17, 1996, are given in Figures 4.62 through 4.65. The plots are intended to show the gradient existing on a vertical plane of the pier. The maximum gradient magnitude that occurred on the west face was 10°C, which was considerably smaller than the 15°C positive gradient magnitude ($T_{1,meas}$) measured on the mainlane on this same day.

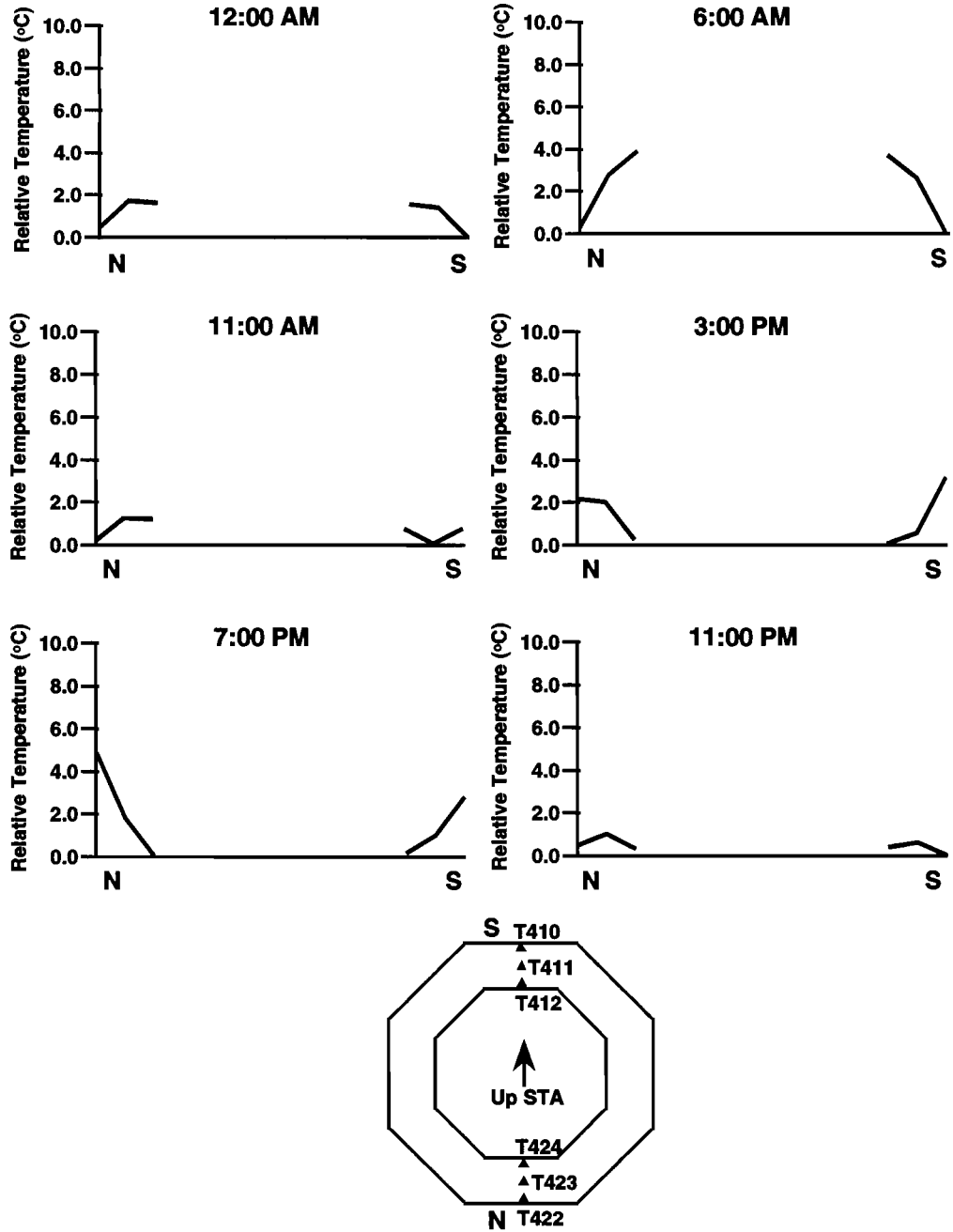


Figure 4.62 One-day cycle of thermal gradients along the north-south axis of segment PC16-5

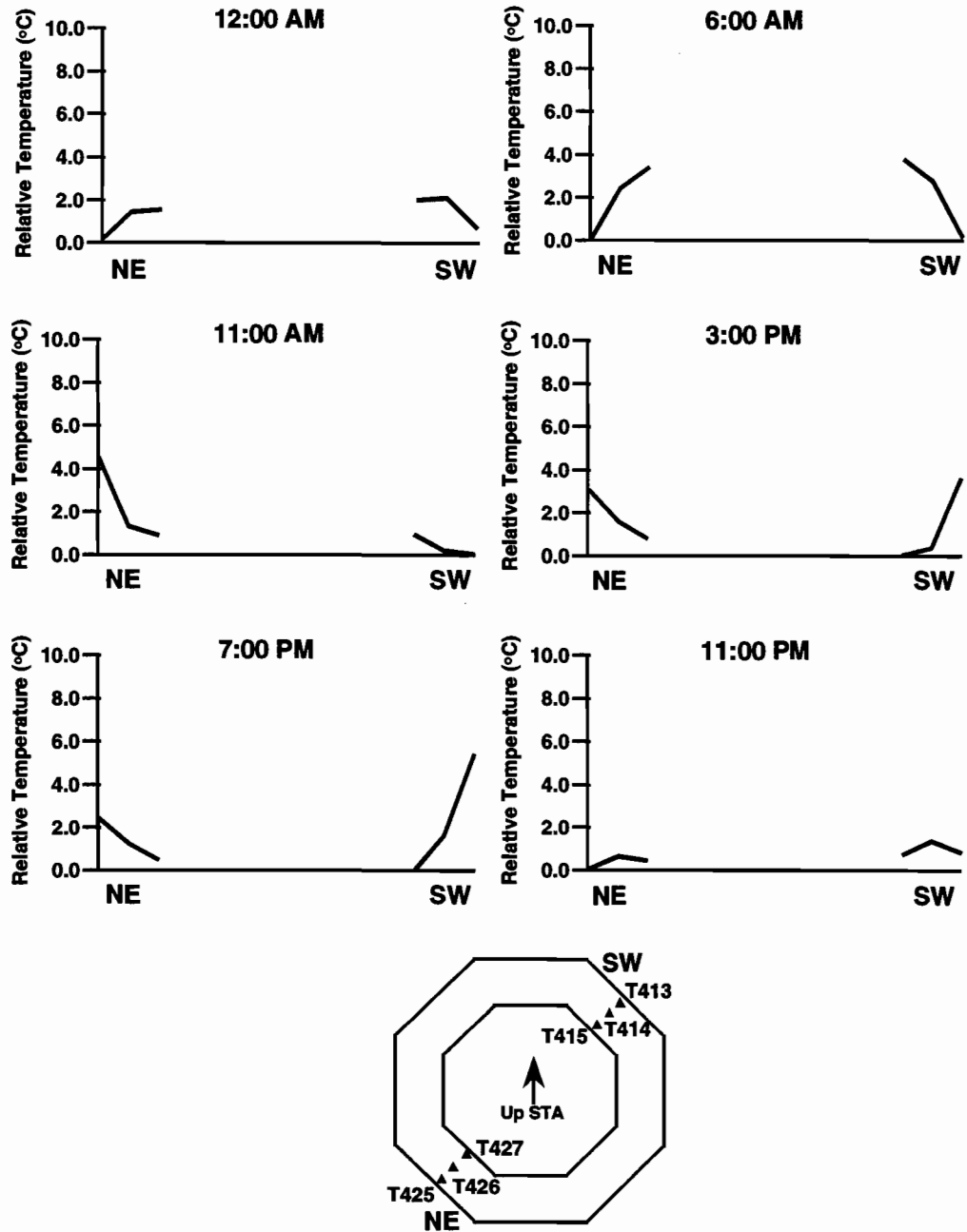


Figure 4.63 One-day cycle of thermal gradients along the northeast-southwest axis of segment PC16-5

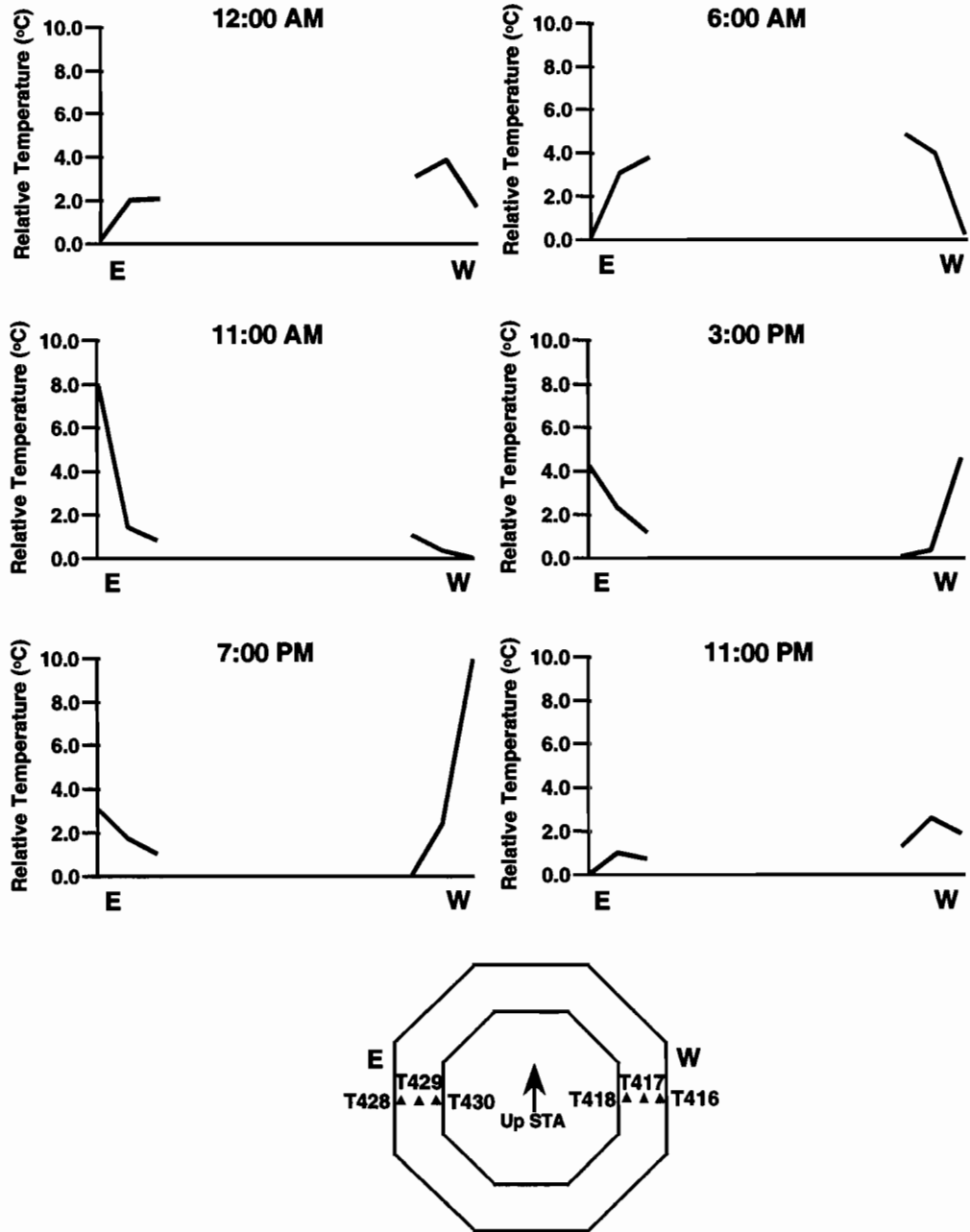


Figure 4.64 One-day cycle of thermal gradients along the east-west axis of segment PC16-5

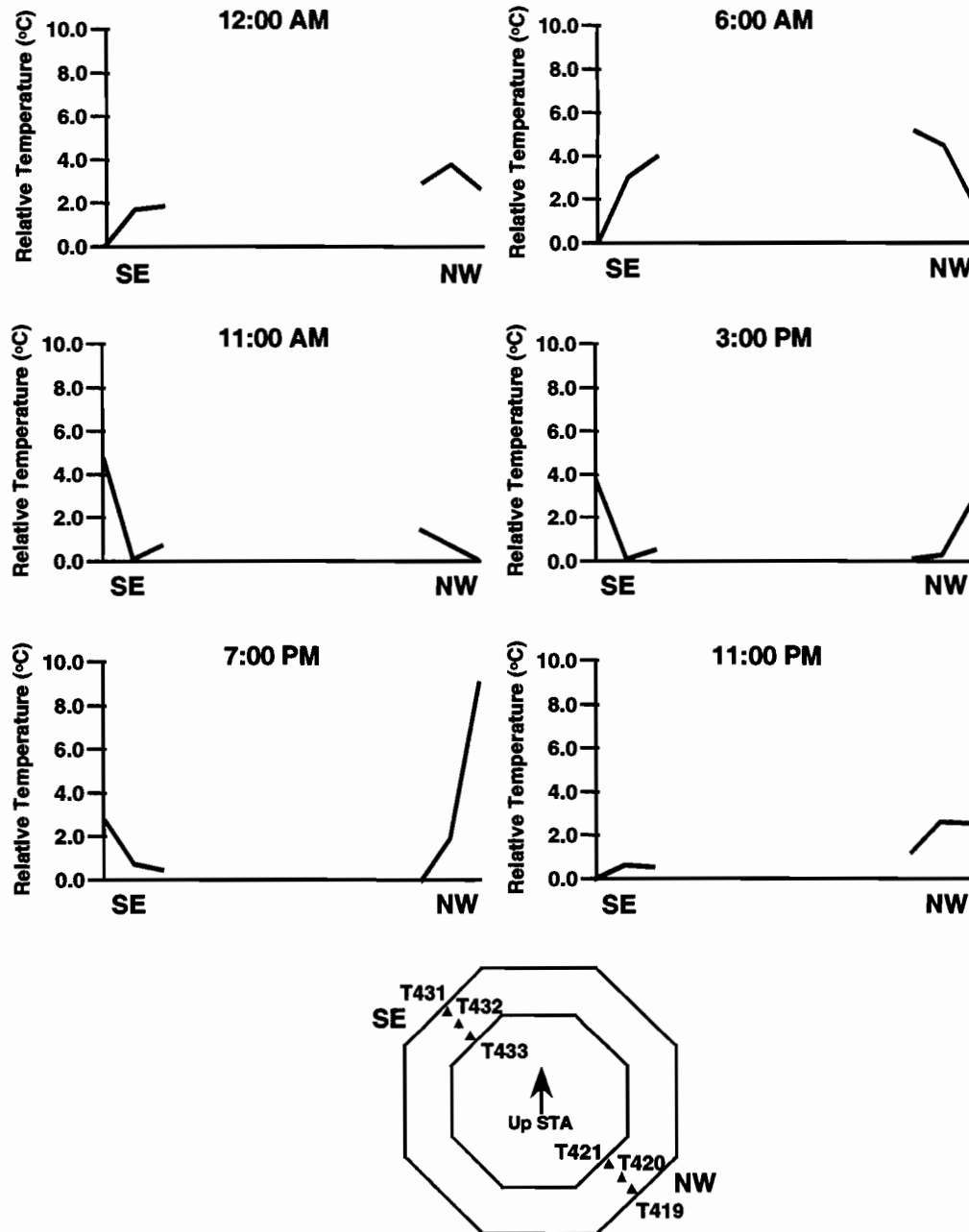


Figure 4.65 *One-day cycle of thermal gradients along the northwest-southeast axis of segment PC16-5*

Strain gauges were installed in the pier to measure the response to thermal gradients. The pier's cross section was regular and compact and was expected to behave in a predictable manner. Figure 4.66 shows the temperature changes on the north and south face of pier P16 for June 17, 1996. The temperature changes were nearly identical on both faces of the pier. The measured strain changes on both faces were also nearly identical. The strain change from unrestrained thermal expansion was not included in the presented strain. Temperature increases on the exterior of the pier resulted in compressive stresses that would be opposed by internally balancing stresses in the interior concrete. The same behavior was seen on the west face of the pier and is plotted in Figure 4.67. Strain gauge C433 responded to the temperature gradient from the entire section, as well as the gradient in the west wall. In general the gauge went into compression as the concrete on the west face was heated. The pattern was not as easily comprehended as the gauge measured response of the north and south

walls because of the cooling of the east wall and other temperature changes in the section. Gauge C439 had evidently become debonded from its mounting rod and appeared to be accurately giving the thermal strain change for an unrestrained length of concrete.

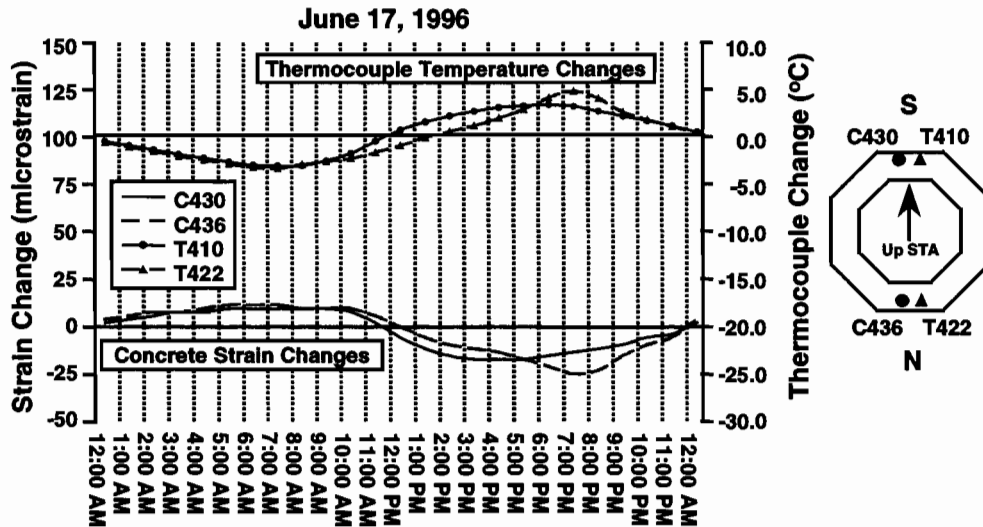


Figure 4.66 Temperature and strain changes on the north-south axis of segment PC16-5

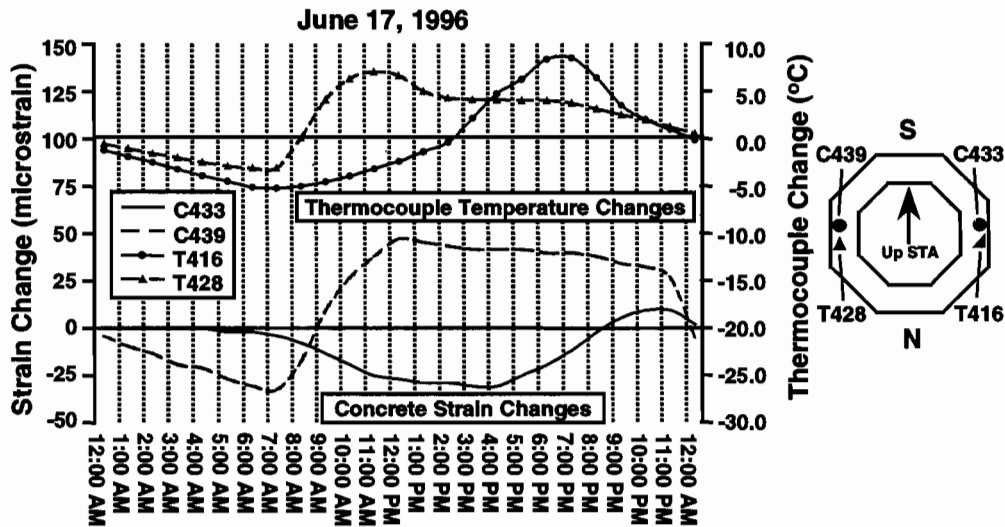


Figure 4.67 Temperature and strain changes on the east-west axis of segment PC16-5

Figure 4.68 shows the measured temperatures and strain response of the north wall. With little gradient along the north-south axis, the strains appeared to be associated purely with those from self-equilibrating stresses. Figure 4.69 gives this same data for the west wall of the pier. Even though the temperature changes through the thickness of the west wall were similar to those shown for the north wall in Figure 4.68, the strains measured were from self-equilibrating stresses in response to temperature changes in the entire cross section.

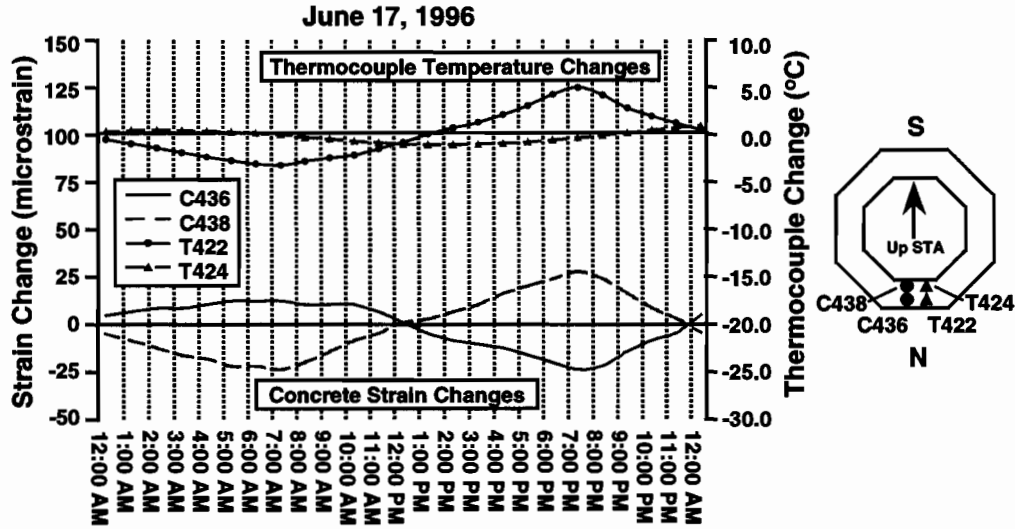


Figure 4.68 Temperature and strain changes through the thickness of the north wall of segment PC16-5

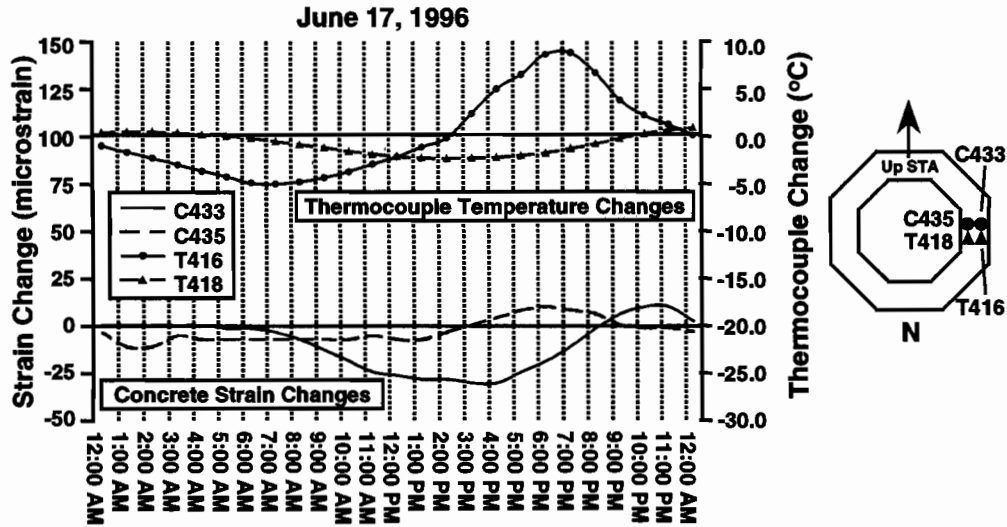


Figure 4.69 Temperature and strain changes through the thickness of the west wall of segment PC16-5

In order to compare the measured temperature gradient, which was nonlinear along two axes, to common singly nonlinear design gradients, an equivalent measured gradient had to be derived. The concentric octagon method shown in Figure 4.70 was used. Interpolation of temperatures was only employed within the same octagon shell. This interpolation procedure was used because temperatures varied greatly through the thickness of the walls. The temperatures from points of known temperature as well as interpolated temperatures could then be projected into a gradient shape as demonstrated in Figure 4.71. Irregularities caused by the octagon shape of the pier were eliminated for the sake of simplicity and applicability of the gradient to piers of different cross section.

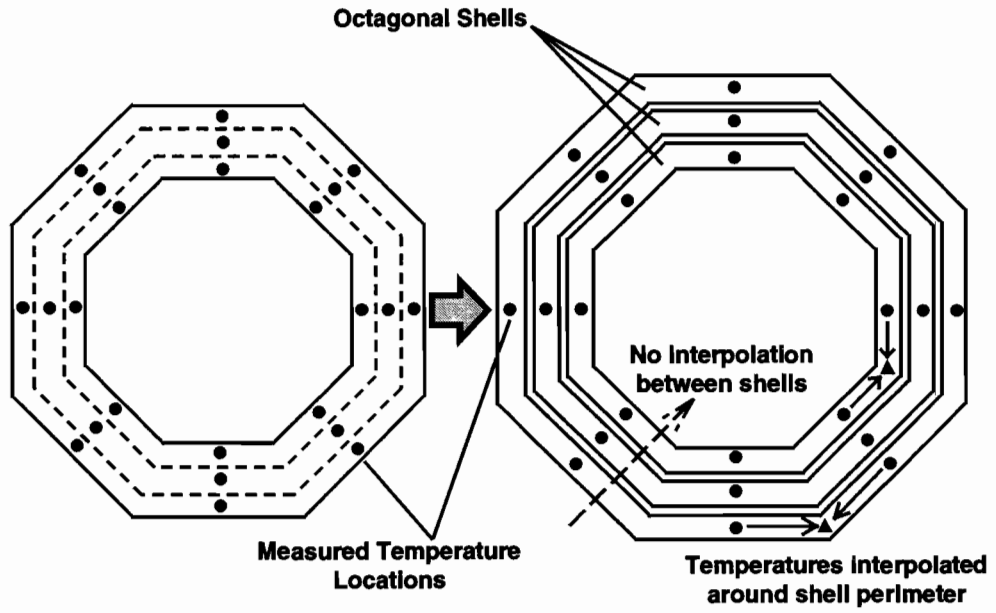


Figure 4.70 Concentric octagonal model for temperature representation

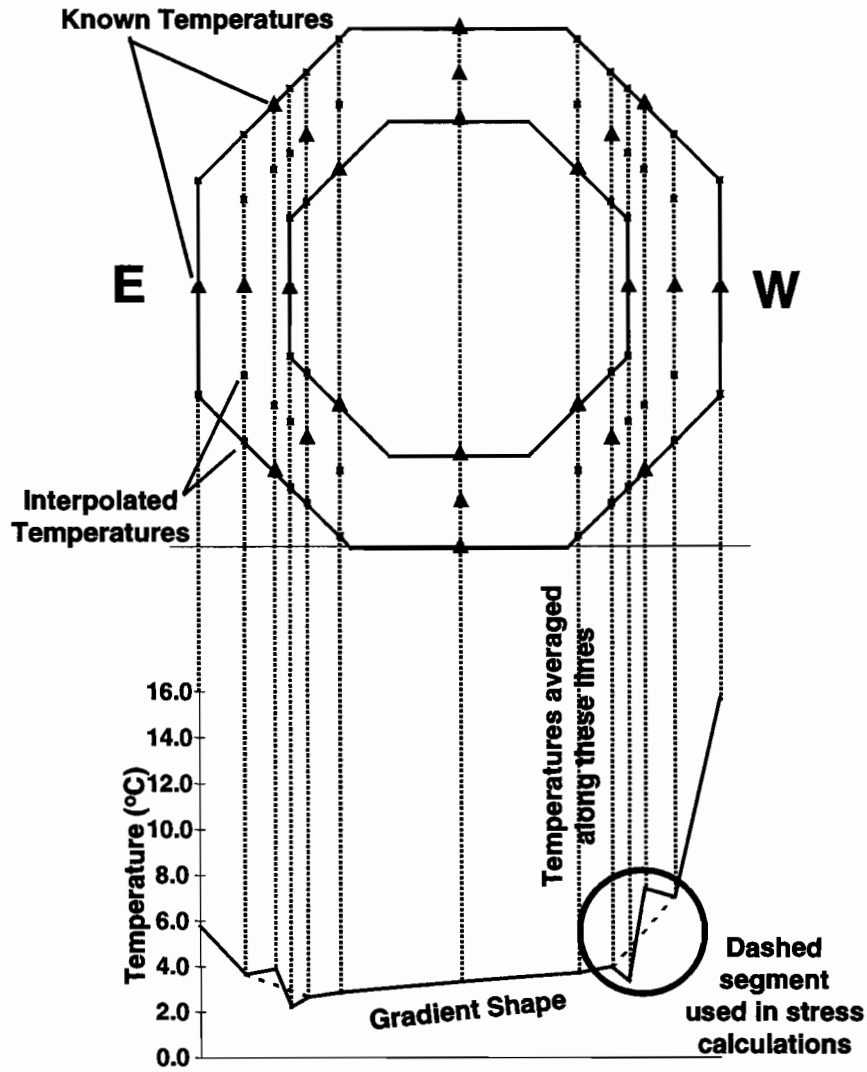


Figure 4.71 Projection of temperature gradient shape onto a single axis

Using this method, the maximum magnitude positive gradient occurred in April 1996 at 13.1°C, a time at which the pier's strain gauges had not been activated. The shape of the gradient and those recommended by AASHTO LRFD and its parent NCHRP 276 report are plotted in Figure 4.72. The magnitude of the measured gradient was only half of that recommended for superstructure design. The shape fell between the shapes recommended by AASHTO LRFD and NCHRP 276. The minimum magnitude negative gradient was measured in April 1996 at -6.8°C. This value was close to the minimum magnitude negative gradients measured in the superstructure girders. The shape of this gradient is plotted in Figure 4.73. This time, the general shape followed the original NCHRP 276 shape more closely, even though it was not derived from tests or analysis. The magnitude of the minimum measured negative gradient was, once again, only about half of that recommended for superstructure design.

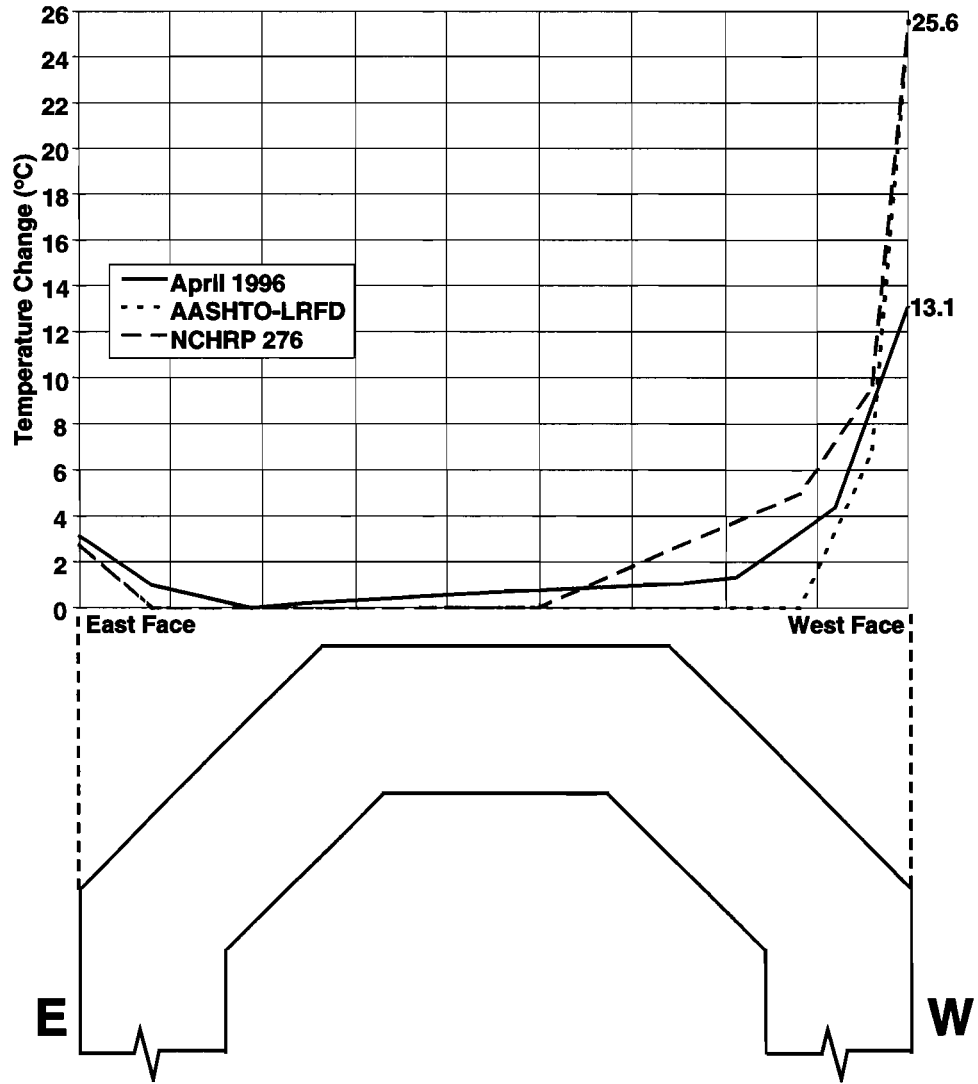


Figure 4.72 Measured and design code maximum positive thermal gradients for pier P16

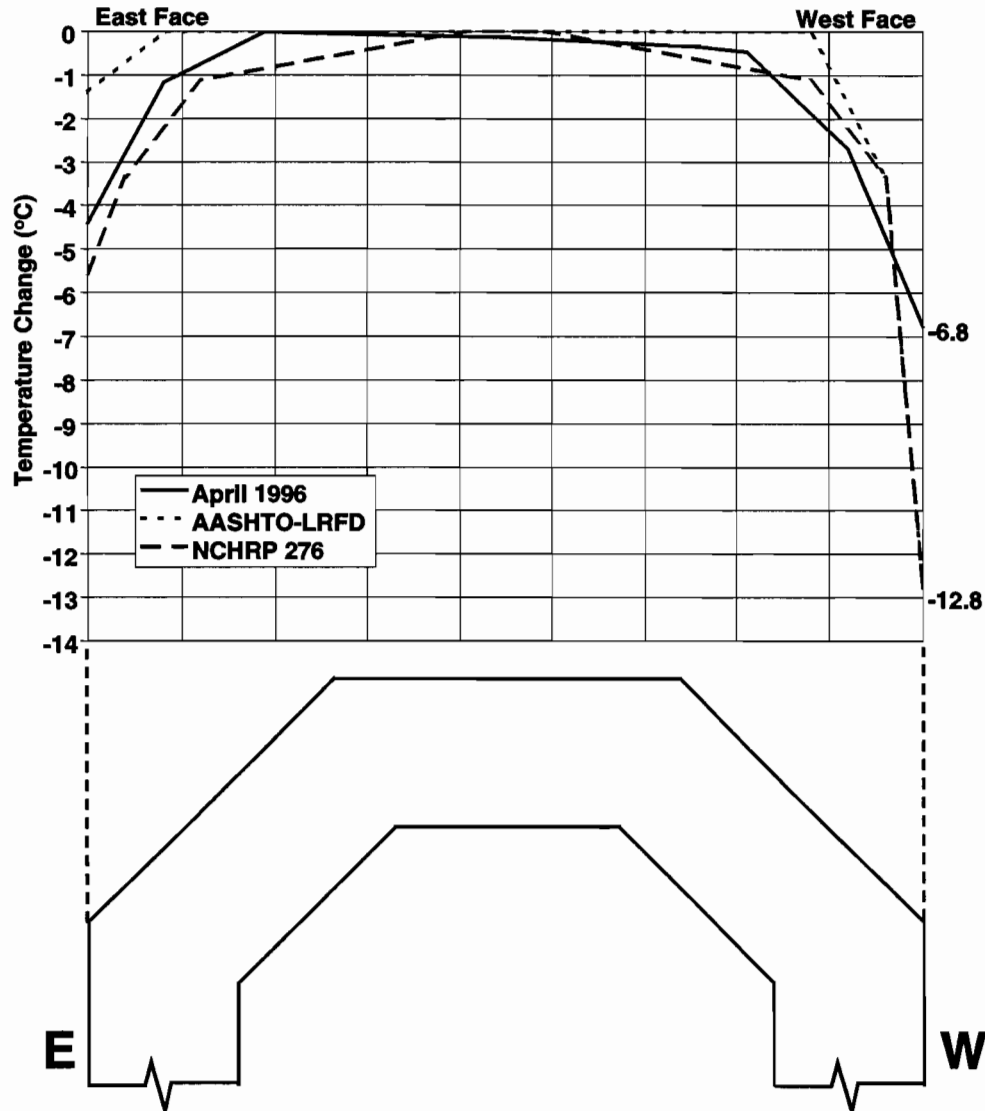


Figure 4.73 Measured and design code maximum negative thermal gradients for pier P16

To gain insight into the actual response of the pier to thermal gradients, the measured strain gauge data were plotted along with the strains predicted by three methods of analysis. The first method was the finite element method using temperature changes interpolated along the octagonal shells in Figure 4.70. The second method was the standard "classical" method described in Section 4.1.1 and commonly used by engineers. The gradient used was the one-dimensional gradient derived in Figure 4.71 and plotted in Figure 4.72. The third method was the primary bending axis method, which used the actual two-dimensional measured gradient to determine the primary axis about which self-equilibrating stresses and curvature strains were symmetric. Plane sections were assumed to remain plane in this third method.

Figure 4.74 gives the temperature changes along the east-west axis of segment PC16-5 that occurred over a portion of the day on June 17, 1996. The time period began in early morning when temperatures in the cross section were most uniform and ended at the time of the maximum positive gradient. The measured strain changes from segment PC16-1, plotted in Figure 4.75, were taken over this same time period. The gradient used to calculate the three analytical results plotted in Figure 4.75 was derived from the temperature changes that occurred over the time period in segment PC16-5. This gradient was not the thermal gradient that existed in the segment at the end of the time period. Figure 4.75 shows that the measured strain changes compared fairly well with the finite element results, even though the gradient in segment PC16-1 was not the same as the gradient from segment PC16-5 used in the analysis. Figure 4.76 gives a plot of the same analytical results and

the measured strains in the segment where the gradient under consideration did occur. The measured results in the east and west walls of segment PC16-1 were actually almost identical to the strains measured in segment PC16-5 shown in Figure 4.76. Once again, the finite element results compared most favorably with the measured results, followed by the primary bending axis method.

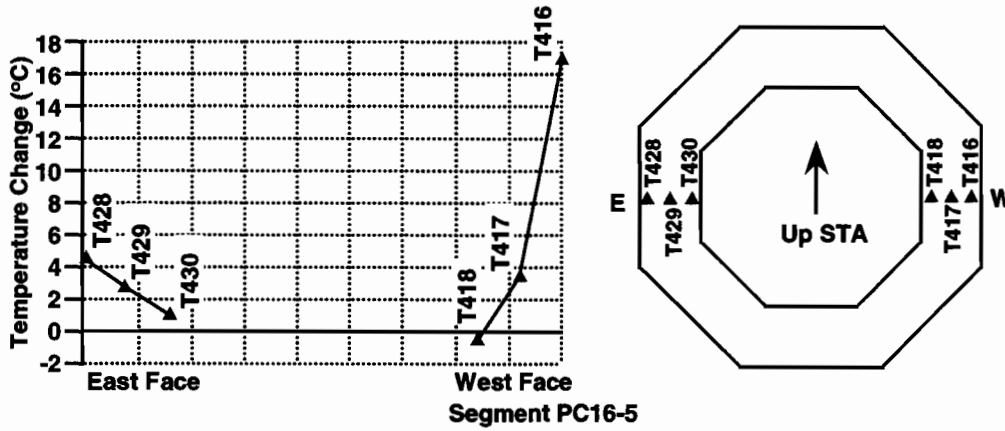


Figure 4.74 Temperature changes along the east-west axis recorded by thermocouples in segment PC16-5, maximum positive gradient

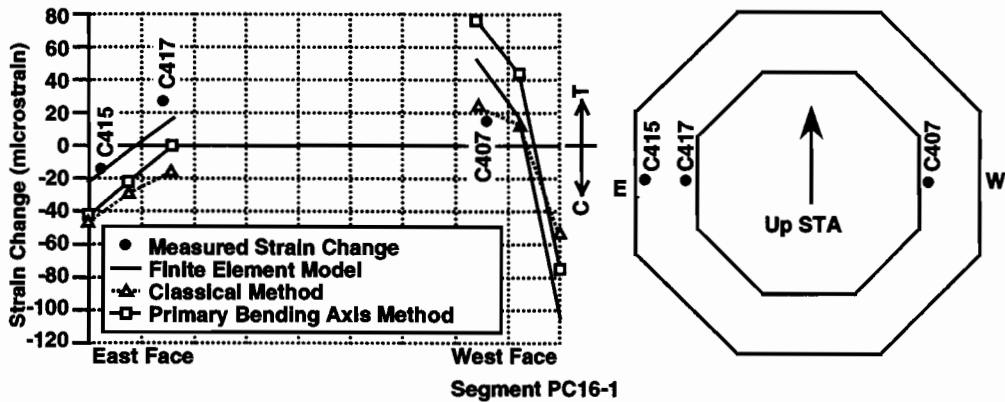


Figure 4.75 Calculated strain changes and strain changes recorded by strain gauges in segment PC16-1, east-west axis, maximum positive gradient

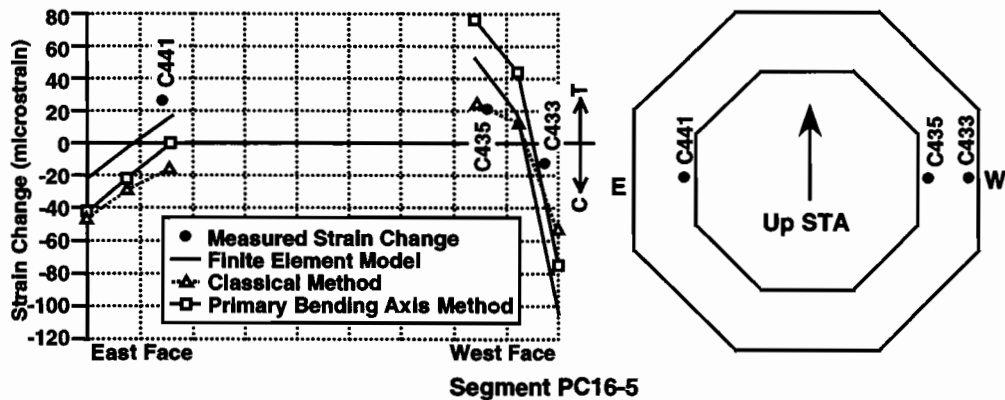


Figure 4.76 Calculated strain changes and strain changes recorded by strain gauges in segment PC16-5, east-west axis, maximum positive gradient

The temperature changes in segment PC16-5 along its north-south axis for the same time period on June 17, 1996, are plotted in Figure 4.77. The positive gradient condition produced a very unsymmetric gradient with respect to the east-west axis and produced an almost symmetrical gradient condition along the north-south axis. The strain gauge output and analytical results shown in Figures 4.78 and 4.79 were dominated by strains that were self-equilibrating within the width of the south and north walls. The primary bending axis method predicted strains that compared well to the finite element method strains for this symmetrical gradient, but did not compare well with the results calculated by the classical method along either axis. Once again, the measured strains shown in Figures 4.78 and 4.79 compared well to the finite element method results and the primary bending axis results.

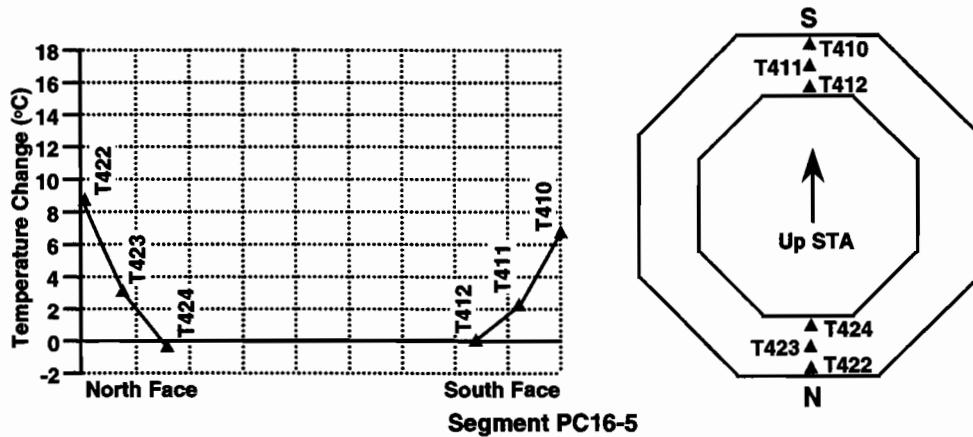


Figure 4.77 Temperature changes along the north-south axis recorded by thermocouples in segment PC16-5, maximum positive gradient

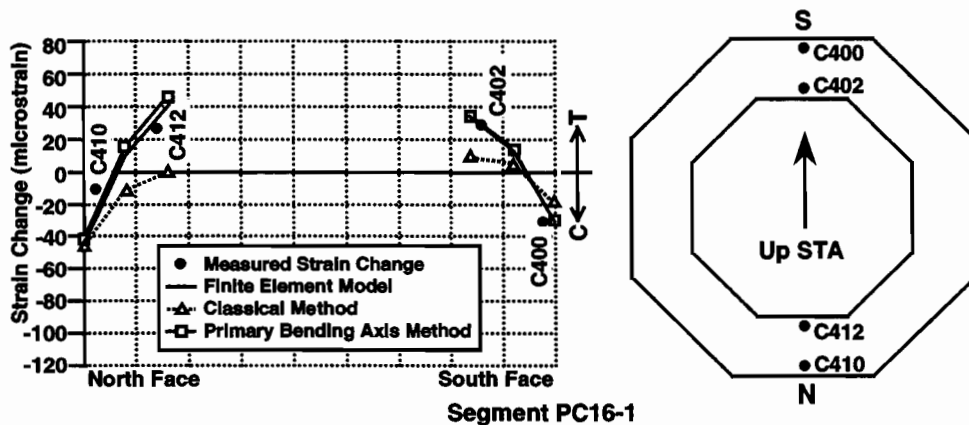


Figure 4.78 Calculated strain changes and strain changes recorded by strain gauges in segment PC16-1, north-south axis, maximum positive gradient

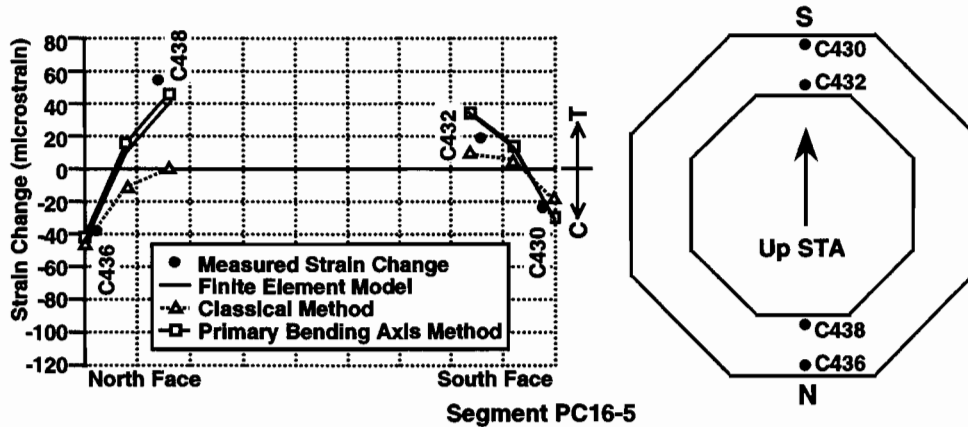


Figure 4.79 Calculated strain changes and strain changes recorded by strain gauges in segment PC16-5, north-south axis, maximum positive gradient

To evaluate the pier’s structural response to negative gradients, a time period was selected that produced a large magnitude negative gradient. The negative gradient occurred on the night of June 3-4, 1996, when intense daytime heating left the pier quite warm, and a large nighttime temperature drop cooled the exterior of the pier rapidly. The west face of the pier was the warmest after the daytime heating and cooled the greatest during the night, creating an unsymmetrical negative gradient in the pier. The temperature change along the east-west axis in segment PC16-5 for the time period under consideration is plotted in Figure 4.80. Figure 4.81 shows that the measured strains in segment PC16-1 compared well to the strains predicted by the finite element method and the primary bending axis method in the east wall. The strain measured by gauge C407 was less than predicted by these two methods of analysis. A similar response occurred for the positive gradient case plotted in Figure 4.75. The small magnitude of the strain measured by C407 could have been correct for the gradient actually occurring in segment PC16-1, or the gauge could have been poorly bonded in the concrete and was giving poor results. The measured strains in the west wall plotted in Figure 4.82 also had a magnitude smaller than that predicted by the various methods of analysis. Reasonable correlation existed between the measured strain from gauge C441 and calculated strains in the east wall.

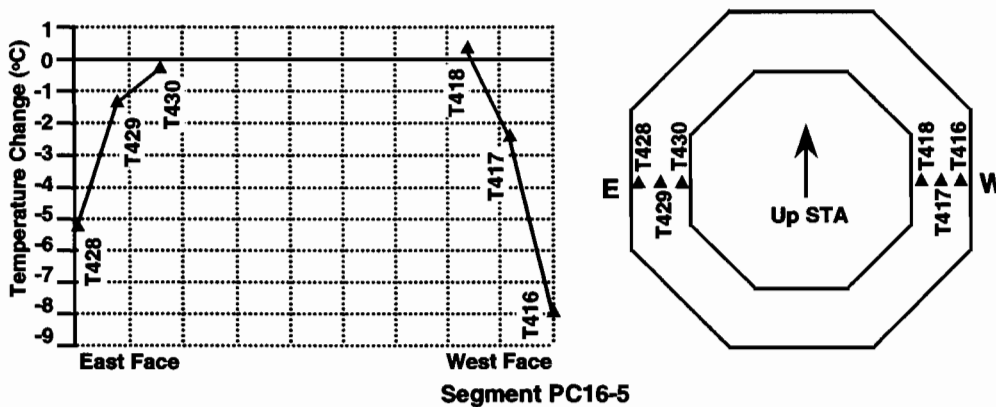


Figure 4.80 Temperature changes along the east-west axis recorded by thermocouples in segment PC16-5, maximum negative gradient

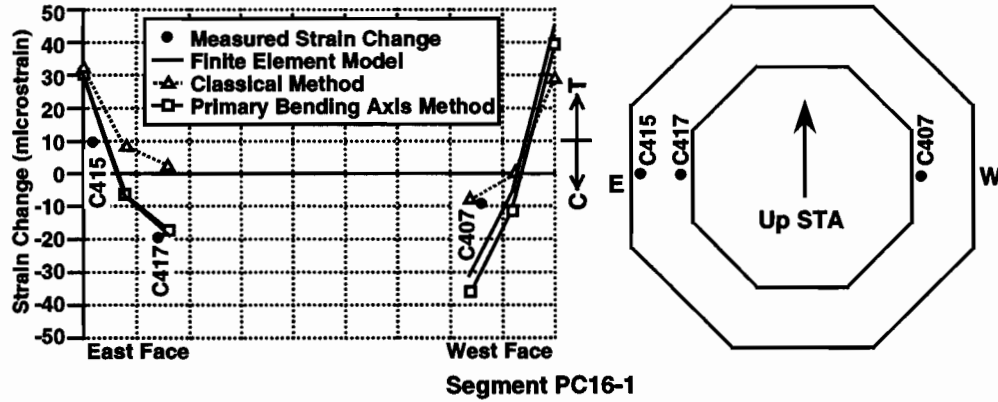


Figure 4.81 Calculated strain changes and strain changes recorded by strain gauges in segment PC16-1, east-west axis, maximum negative gradient

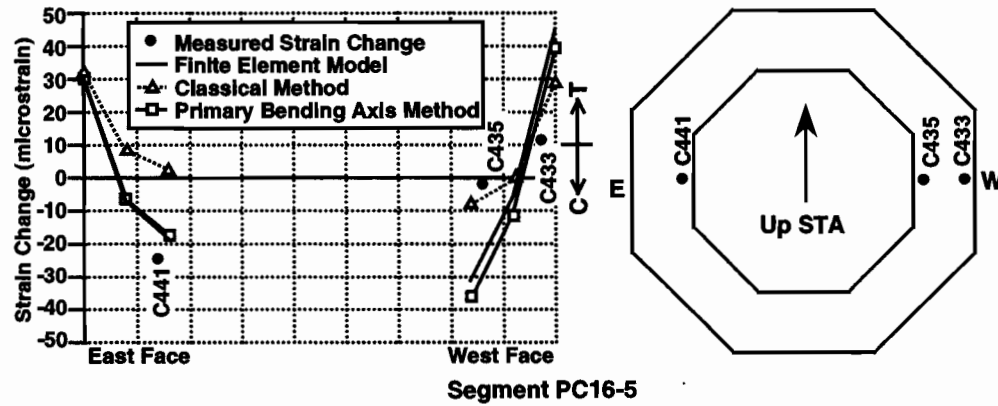


Figure 4.82 Calculated strain changes and strain changes recorded by strain gauges in segment PC16-5, east-west axis, maximum negative gradient

The negative gradient temperature changes along the north-south axis from June 3-4, 1996, are plotted in Figure 4.83. The gradient condition was nearly symmetric. The measured strains in segments PC16-1 and PC16-5, shown in Figures 4.84 and 4.85, continued to compare well with the finite element method calculated strains and reasonably well with the primary bending axis method. The classical method did not allow enough refinement of the input gradient to compare well with the measured data. Modification of the method, such as was the case for the primary bending axis method, would have to be done to get realistic results from an analysis of a two-dimensional gradient.

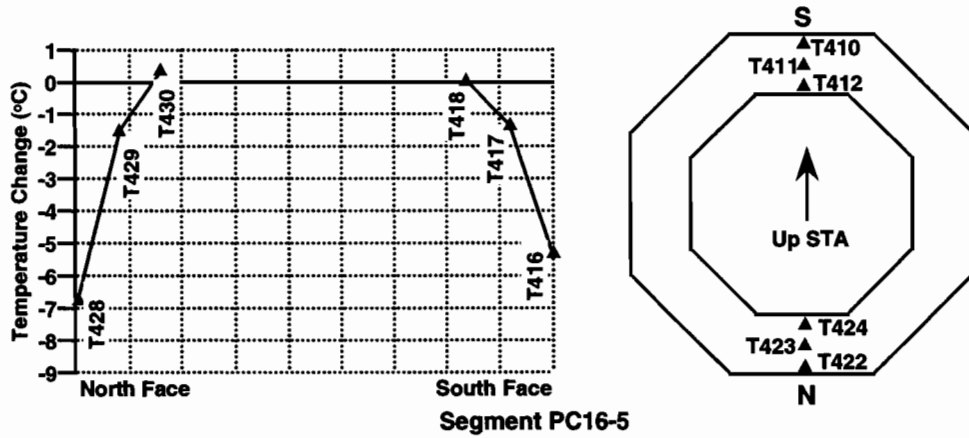


Figure 4.83 Temperature changes along the north-south axis recorded by thermocouples in segment PC16-5, maximum negative gradient

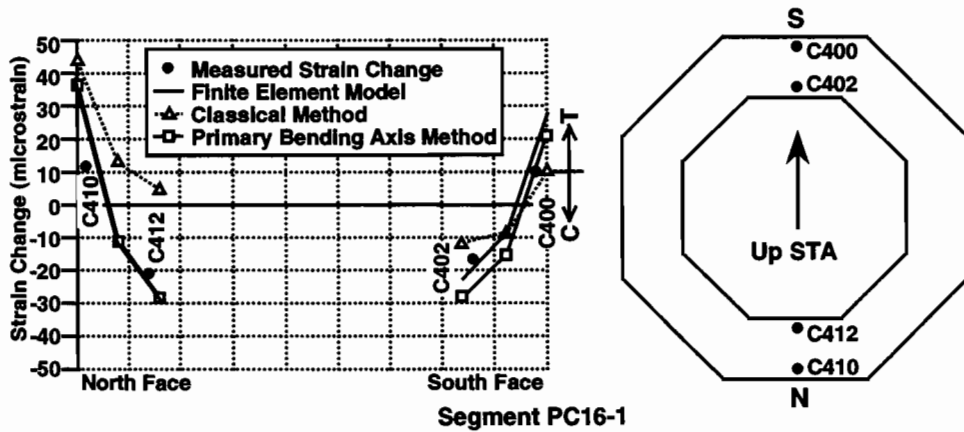


Figure 4.84 Calculated strain changes and strain changes recorded by strain gauges in segment PC16-1, north-south axis, maximum negative gradient

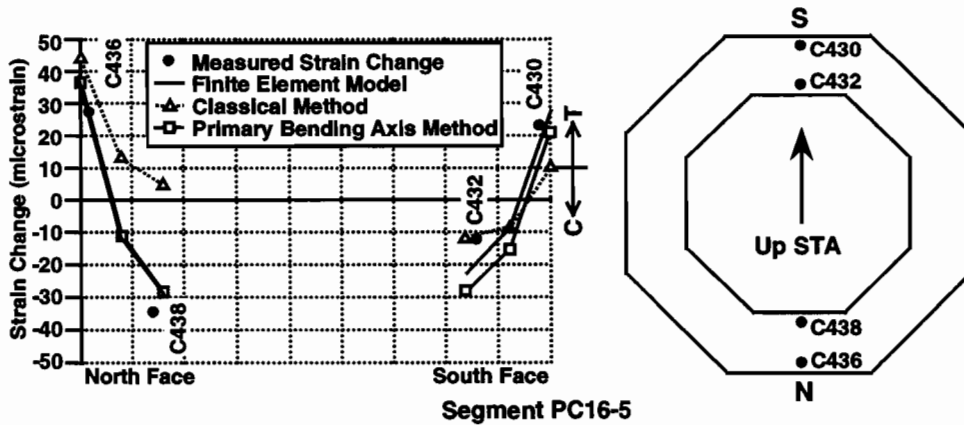


Figure 4.85 Calculated strain changes and strain changes recorded by strain gauges in segment PC16-5, north-south axis, maximum negative gradient

Substructure elements are often massive in section, whereas superstructure elements are made with efficient sections to reduce dead-load moments and shears. The dead weight of a pier seldom has much effect on the foundation costs of a bridge. Also, the additional costs of forming a voided pier section are often greater than the savings in concrete volume. For these reasons, the cross sections of many piers, or portions thereof such as the capital segment on pier P16, are often cast solid. All the piers on the US 183 project were originally designed to be voided in section and precast. Because of site conditions, the contractor elected to cast most of the piers in place, with solid sections. The Ramp P piers, including P16, were the only piers precast on the project. The design used voided piers to reduce weight for transport, which required an increase in concrete strength over that required for larger solid piers. The capital segment was solid in section to handle the multiple post-tensioning anchorages cast within it and the resultant complicated stress paths. The concrete for the ramp capital and ramp column segments had nearly the highest design strength of any concrete on the project at 51.7MPa. Concrete strengths generally fell well above their 28-day design strengths to make certain the one-day strength of the concrete would allow the segments to be removed from their forms after only one night of curing. The concrete used was very reactive because of its self-generated heat and always far exceeded the one-day strength requirement. Vertical cracks were noticed in the voided octagon column segments upon removal of the forms. The cracks generally followed an internal soft inclusion in the section, especially the 200mm PVC drainpipes. The cracks were caused by thermal gradients during curing. The concrete was taking its initial set at about uniform temperature, so no thermal gradient existed initially. Once the concrete began to react at an increased rate because of its self-generated heat, the average temperature of the concrete increased. The steel exterior form radiated this heat to the atmosphere creating a negative gradient. The concrete, still very weak shortly after its initial set, cracked vertically from tensile stresses. The transverse steel area was low at $470\text{mm}^2/\text{m}$.

Based on these observations, the thermocouples in the capital segment were activated to measure the curing temperature gradients. The solid capital segments were also found to be cracked as they sat in the form. The cracks formed at the architectural reveals in both the vertical and horizontal directions were probably caused by the mechanism demonstrated in Figure 4.86. The core of the segment was found to get quite hot during curing with a maximum of about 80°C . A plot of the core temperature over time is given in Figure 4.87. This plot shows that the core concrete did not reach the ambient air temperature for a full week. The shape of the maximum negative gradient in the capital segment is plotted in Figure 4.88, two days after the concrete was cast. This gradient magnitude was about 35°C . The gradient that occurred in the form was smaller than this, but occurred at a time when the concrete was very weak in tension and was sufficient to crack the concrete. The cracking pattern seen on the capital segment is shown in Figure 4.89. The cracks occurred mostly at the midpoint of each side, both vertically and horizontally. Once the gradient had subsided, the tension condition on the exterior face ended and the cracks closed. Over time, the cracks opened back up slightly because of shrinkage.

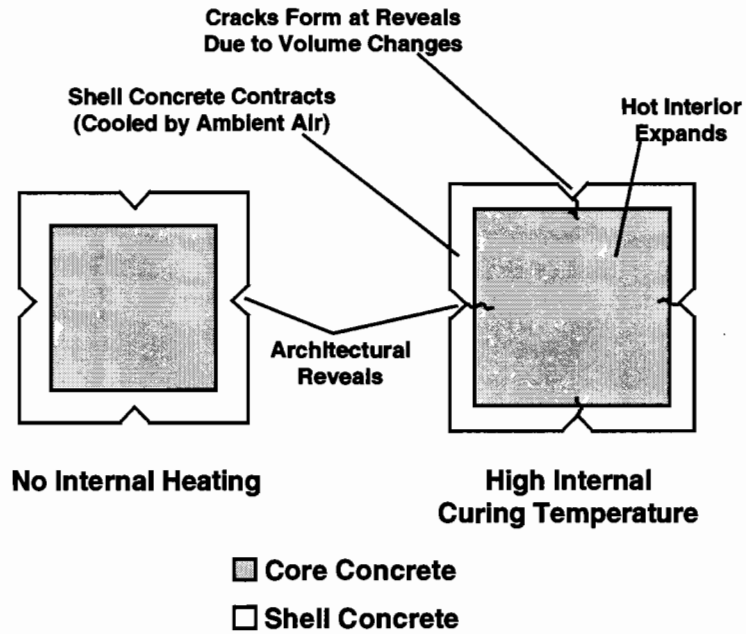


Figure 4.86 Mechanism for cracking of large monolithic members during curing

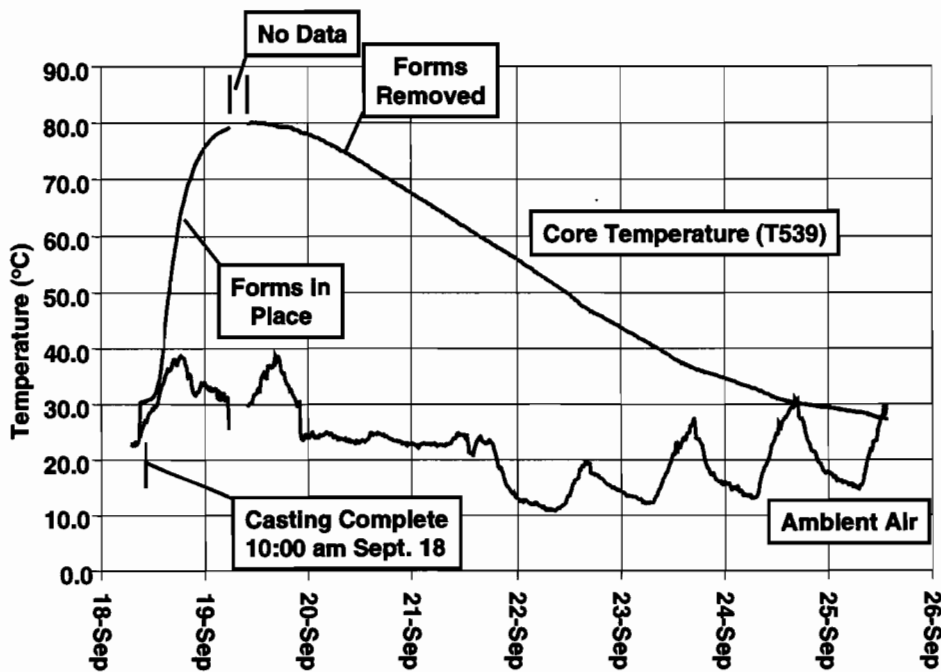


Figure 4.87 Comparison of internal curing temperature to ambient air temperature, capital segment PC16-8

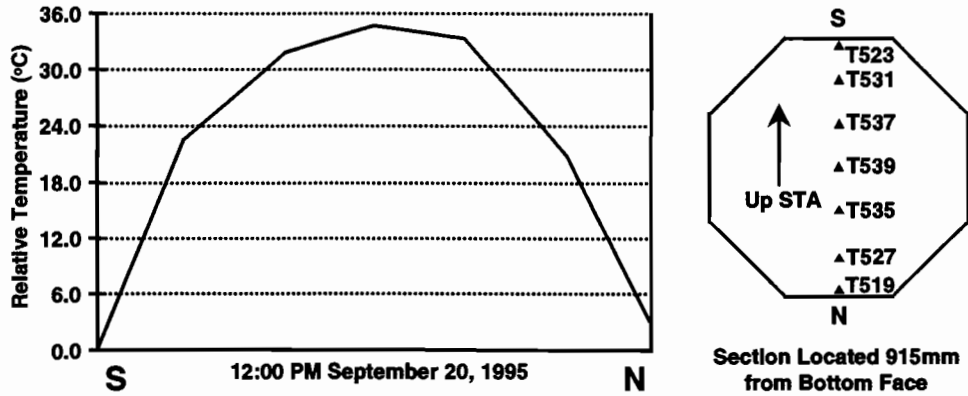


Figure 4.88 Maximum measured gradient shape during curing of capital segment PC16-8

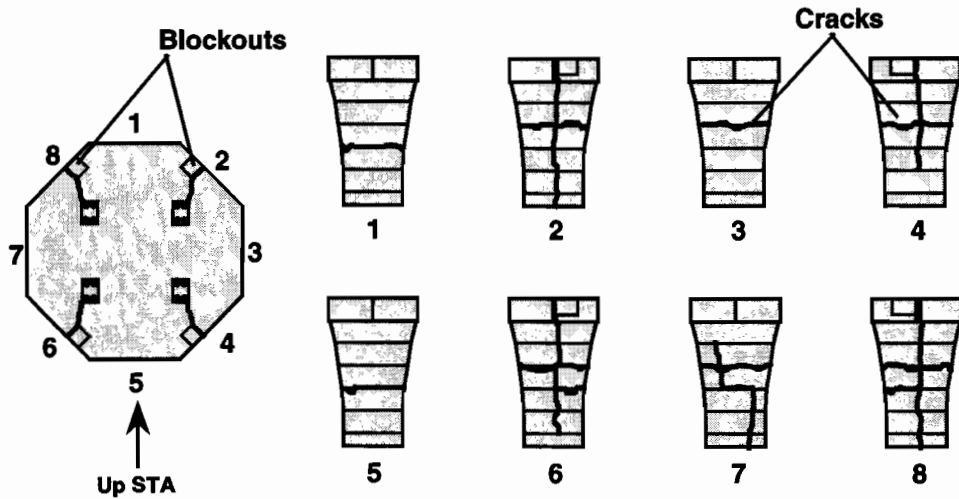


Figure 4.89 Map of cracks found during curing of capital segment PC16-8

4.3.4 Mainlane Pier D6

The mainlane Y-pier provided an opportunity to study a steel and concrete composite structure for thermal effects. The superstructure was not placed on the pier for almost a year after it was built, so the pier experienced a variety of climatic conditions under direct sunlight. The two most important types of measurements taken were those that demonstrated the behavior of the pier when the structural steel pipe ties changed temperature with respect to the concrete, and when the exterior of the solid concrete column and capital changed temperature with respect to the core of the concrete.

The difference in temperature between the exterior concrete of the capital and the core concrete is shown in Figure 4.90 for a typical sunny day in March. Thermocouples T104 and T106 had western exposure. The core concrete temperature changed little over the course of the day. The exterior concrete changed about 8°C, with a maximum positive gradient of about 8°C existing through the section. The 203mm steel pipe tie temperature, measured by T103 in Figure 4.91, changed about 11°C on the same day. The temperature of the steel pipe tie decreased rapidly as its embedment length into the concrete increased, with the temperature at T101 being only 3°C greater than that at T105. Figure 4.92 shows the change in steel pipe tie temperature versus the temperatures measured at the core concrete of the capital. The maximum gradient is about 10°C.

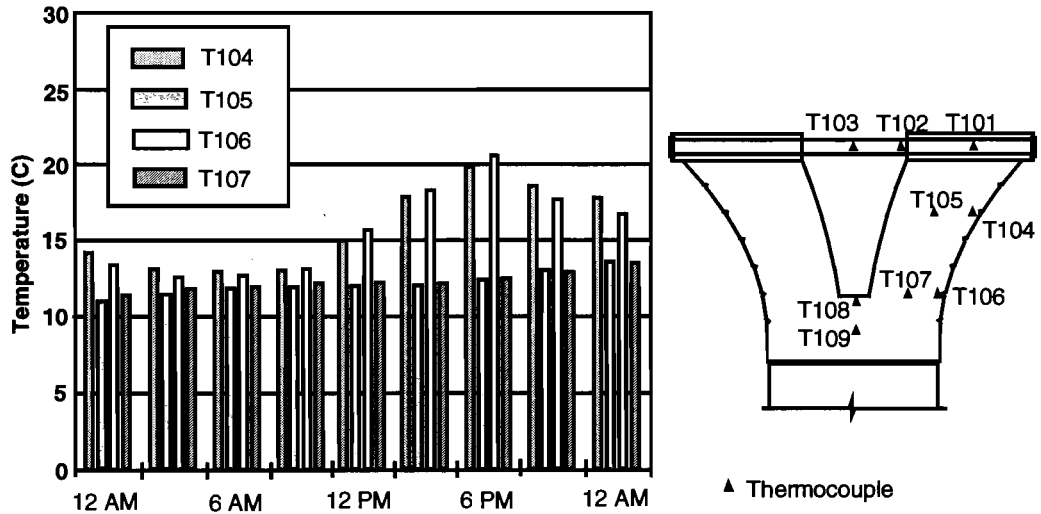


Figure 4.90 One-day cycle of pier D6 capital concrete temperatures

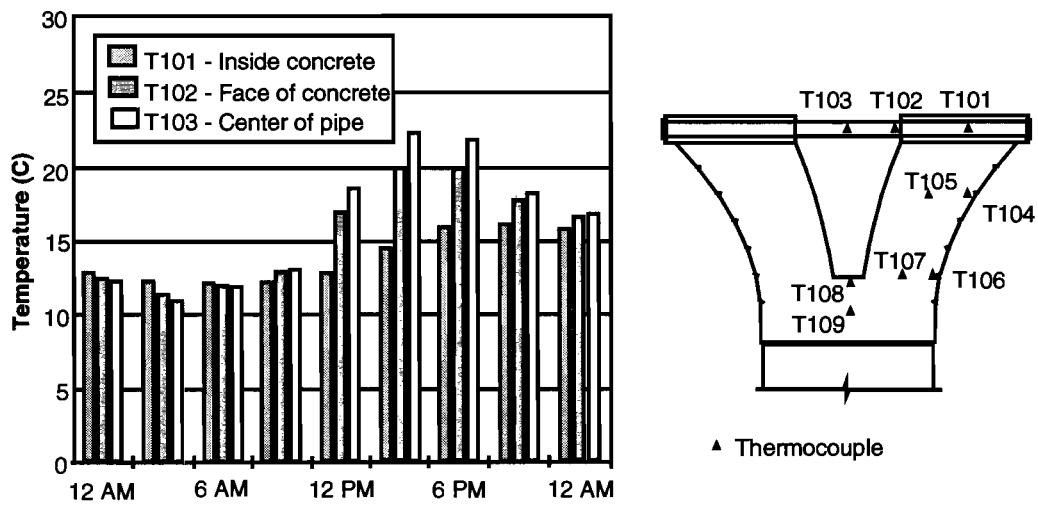


Figure 4.91 One-day cycle of pier D6 capital pipe temperatures

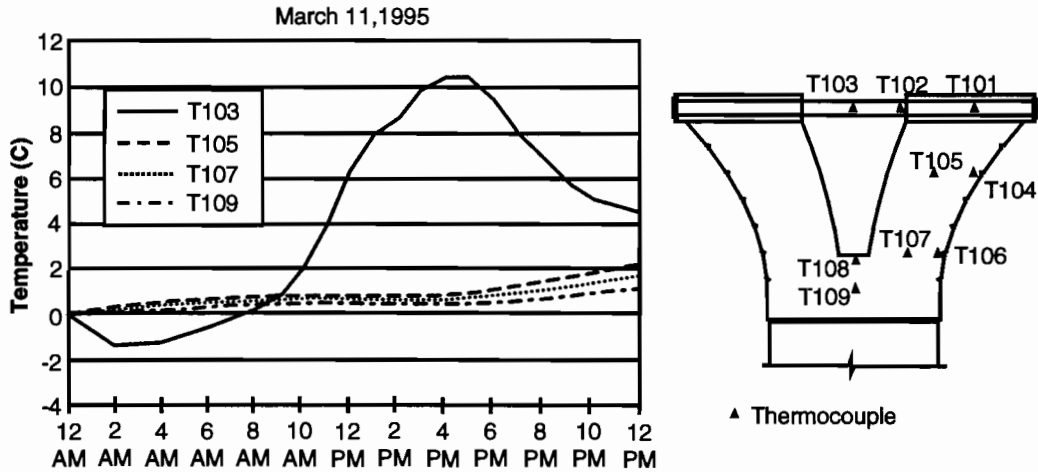


Figure 4.92 Pier D6 capital pipe temperature versus concrete core temperature, typical sunny day

Strain gauges were installed on the structural steel pipe ties, with the locations shown in Figure 4.93, to measure the structure's response to the heating and cooling of the pipes. Figure 4.93 shows a change of 12 microstrain in compression at S129 and S130 located at the center of the pipe. This change was a response to the heating of the pipes over the day and the thermal gradient in the capital. This strain related to a stress change in the pipes of only 2.4Mpa. The peak strain change for gauges S119 and S120 was at 4:00PM, when the sun was striking the anchor plate for the pipe located on the surface of the pier capital. The strain measured at S119 and S120 showed that the steel pipes were bonded to the concrete at this point in time because of their rough-galvanized finish.

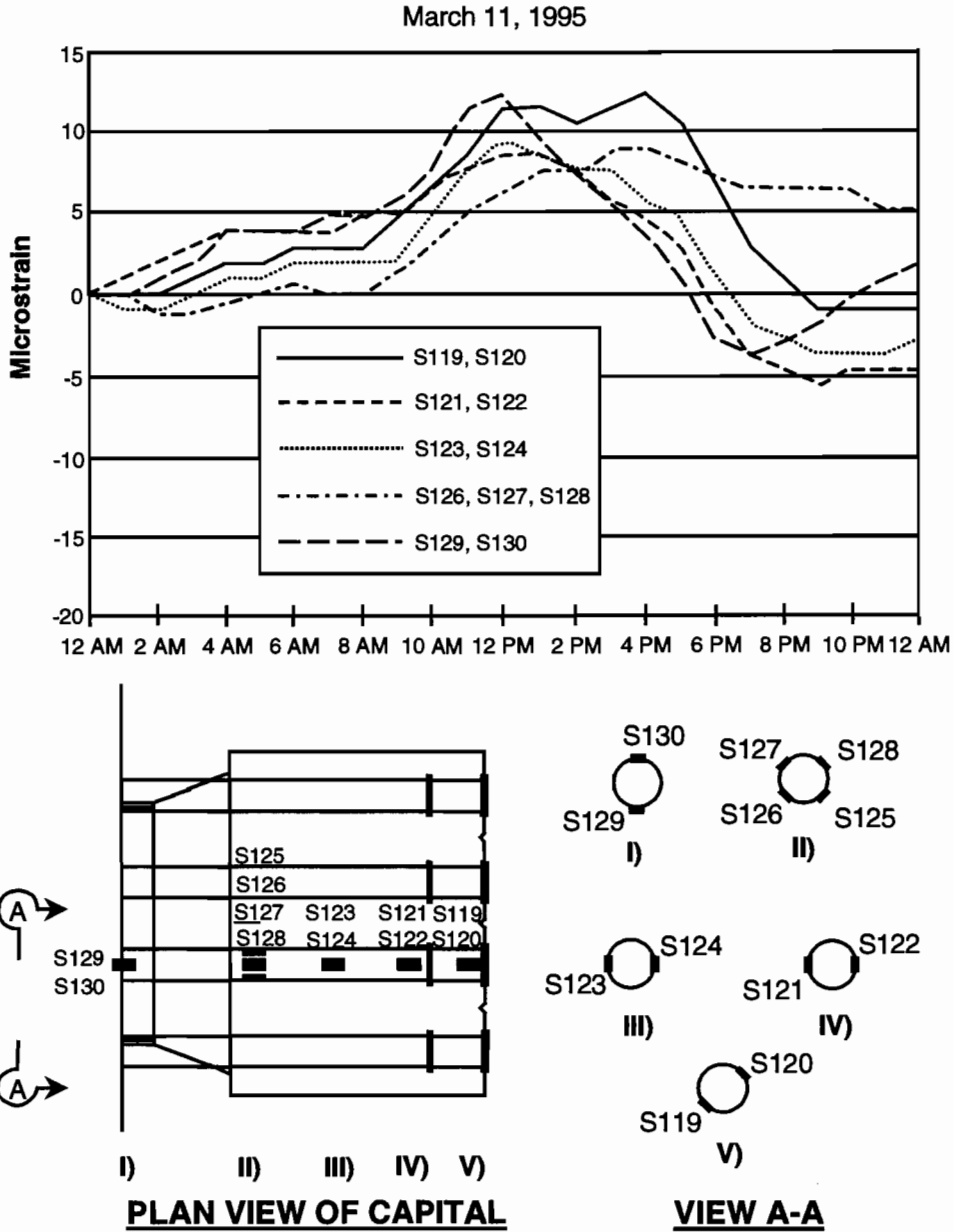


Figure 4.93 Pier D6 pipe measured strains, typical sunny day

Strain gauges were also located throughout the pier capital at the locations shown in Figure 4.94. Figure 4.95 shows that the magnitude of the strain changes over the course of this sunny day of the core concrete gauges C119 and C120 was similar to the exterior gauges C116 and C117 on the northern face, but opposite in direction. Exterior gauges on the western face of the capital measured considerable compression, with a change of 122 microstrain for C121 over the day. This strain related to a stress of about 3.3MPa, or about 20% of the normal service load level allowable stress.

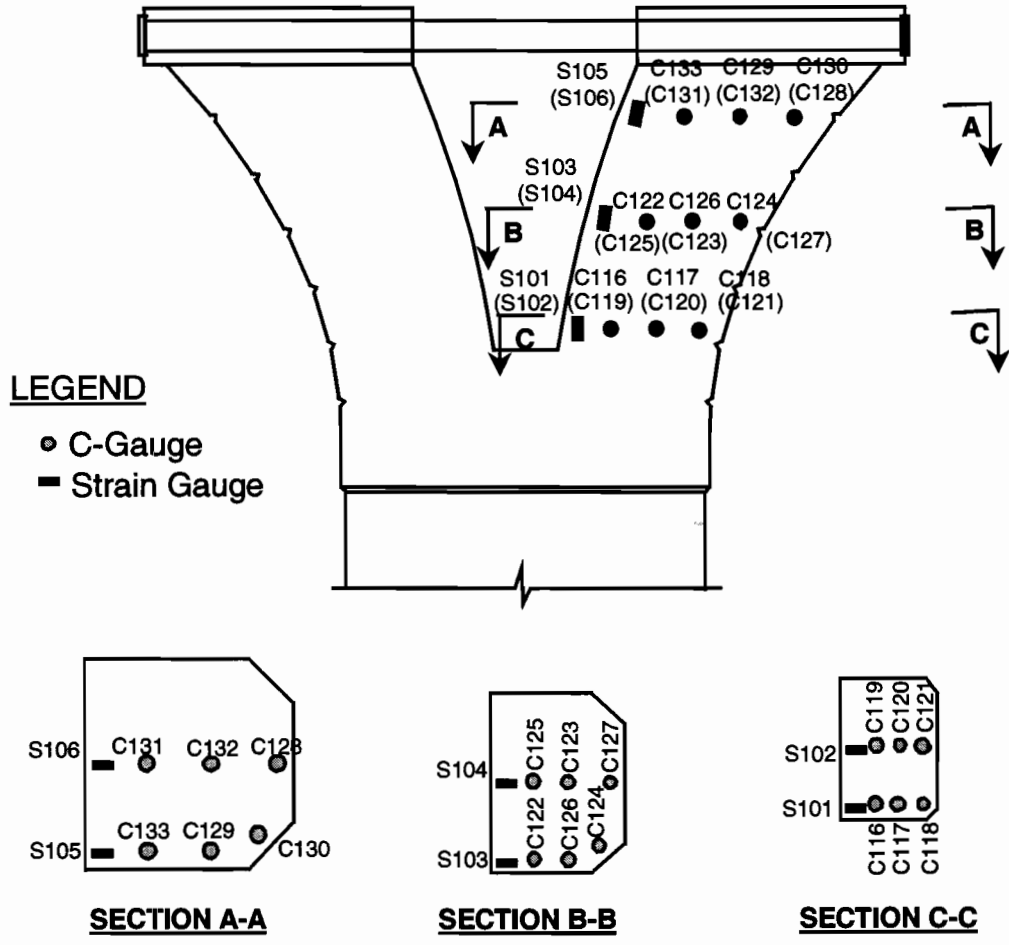


Figure 4.94 Pier D6 gauge locations

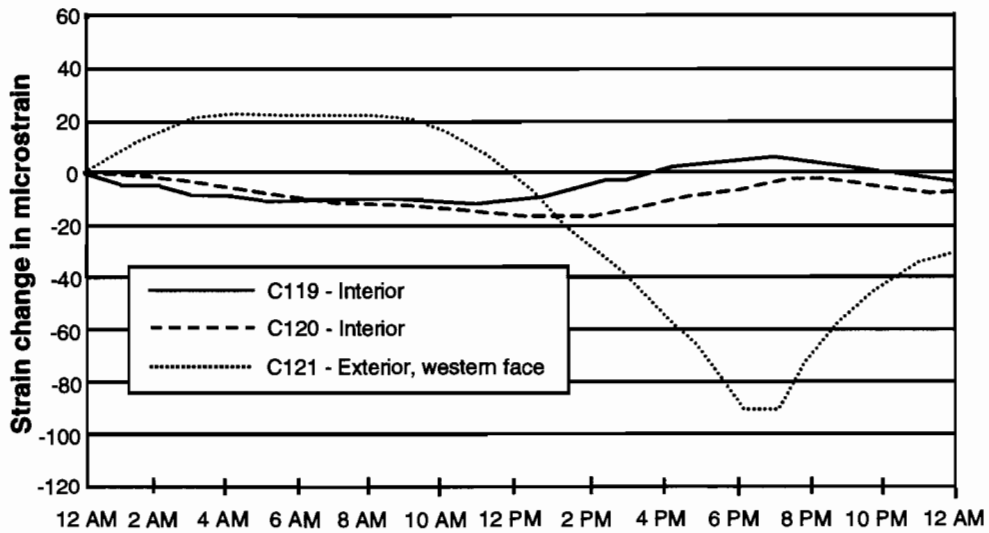
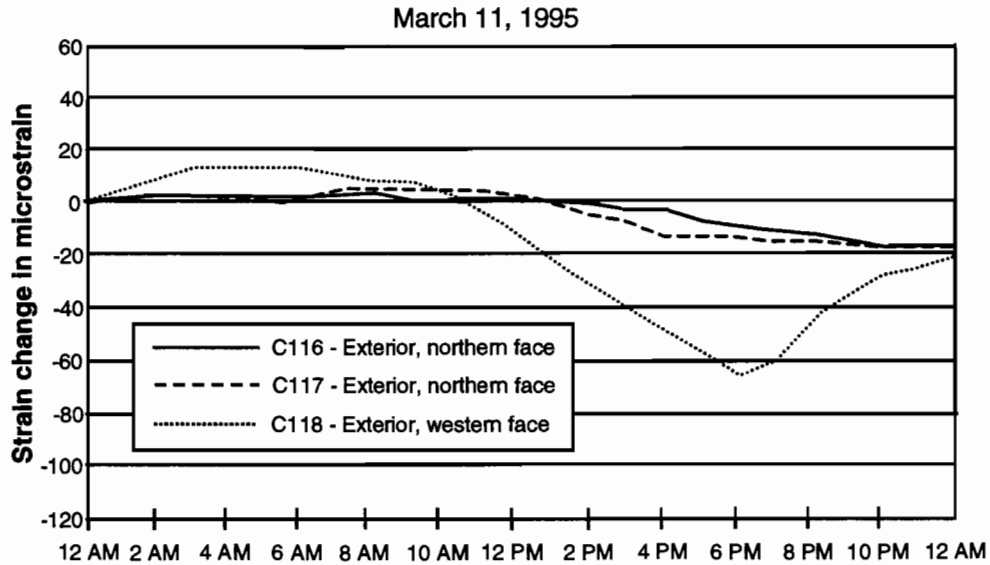


Figure 4.95 Measured concrete strains in the pier D6 capital over a sunny day

Similar behavior was seen in the pier column. Gauges were placed in the top of the column at the locations shown in the section at the bottom of Figure 4.96. Strain gauges C114 and C113 showed very similar change, even though C113 was at the quarter point of the column's thickness and C114 was at the center of the core. The strain changes measured by C111 and C112 were much larger and opposite in direction than the core gauges. The strain change measured by C112 was similar to that measured by C118 in Figure 4.95. The inoperable gauge located on the west face of the column would no doubt have produced strains similar to C121 in the capital. The positive thermal gradient did not appear to extend very deeply into the concrete, as was seen on other parts of the project. The massiveness of the core concrete kept thermal stresses low in the core and high on the exterior.

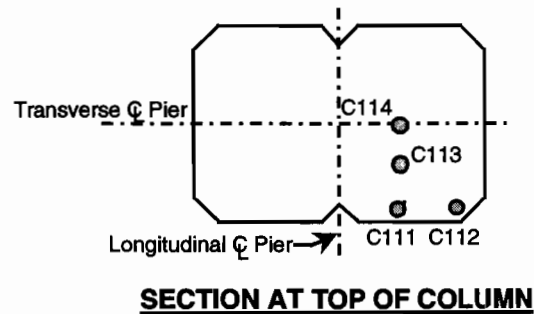
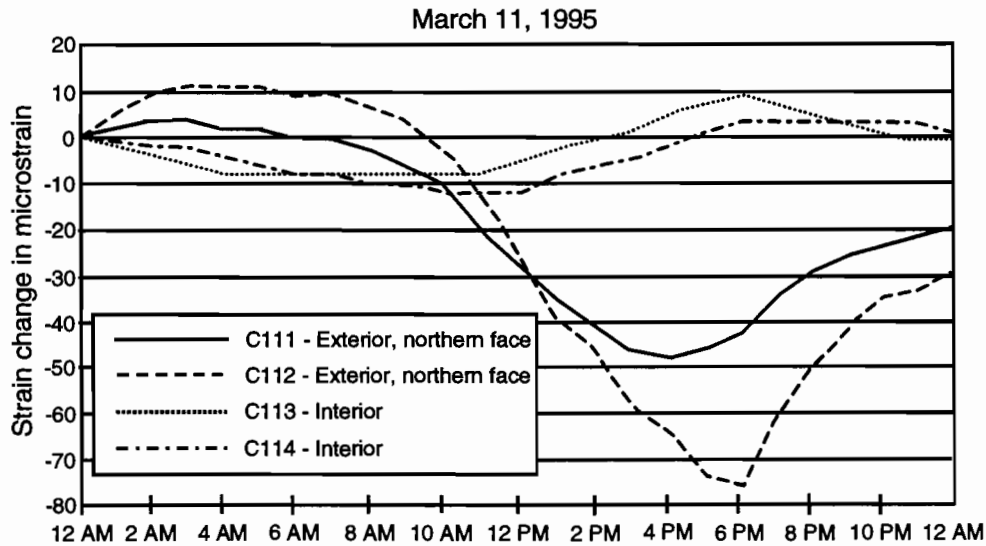


Figure 4.96 Measured concrete strains at the top of pier D6 column over a sunny day

4.4 DISCUSSION OF RESULTS

The position of the thermocouples and strain gauges in the segments was usually governed by the location of the reinforcing bars and the anticipated path of heavy concrete flow into the forms. Many of the gauges were attached to extra bars added strictly for the purpose of securing the gauges and wiring at points in the concrete where no bars existed. A reasonable amount of cover concrete, usually 50mm, was allowed for these extra bars. The gauges, particularly the thermocouples, were often extended beyond these bars or the bar cage into the cover region. The thermocouples could be extended about 25mm beyond the bar to which it was attached before the flow of concrete would move it out of position. The position of the gauges near the surface of the top slab of the superstructure segments was checked by hand just prior to the passing of the finishing machine. The flow of concrete in front of the finishing machine required that the gauges be placed no closer than 25mm from the surface. The thermocouples at other locations in the concrete could not be checked for position after the concrete was placed, and therefore could only be extended into the cover concrete a maximum of 25mm beyond their attachment point to a reinforcing bar and were usually seen to be slightly bent after the passing of concrete to about 35mm clearance to the form.

The temperatures measured by these gauges were not the actual surface temperatures at points adjacent to the gauges. The actual surface temperatures would have been somewhat higher or lower, depending on the conditions. A linear interpolation could be made from two gauges to predict the actual surface temperature, but would be unconservative because of the nonlinear temperature distribution that always existed during periods of intense heating or cooling. For this reason the peak temperatures ($T_{1,meas}$) of the measured gradients presented earlier were in most cases somewhat lower than the actual peak temperatures. The analysis using the measured gradients also probably predicted stresses that were somewhat low compared to stresses calculated from the

gradient that actually existed. The position of the strain gauges in the concrete was also governed by the flow of concrete into the form. The mounting rods for the strain gauges were easily bent if subjected to the direct flow of concrete, and therefore could not be placed in the cover region. The gauges were usually tied to the heavy bars in the reinforcing cage. For this reason, the strain gauges could not be placed directly under the surface of the concrete and attempts to do so resulted in damaged gauges most of the time from foot traffic and concrete flow. The location of the gauges, usually about 50mm or more under the concrete surface, prevented the measurement of the peak thermal stresses. A large stress gradient existed through the concrete adjacent to the surface being heated or cooled. A gauge only 50mm away from the surface would measure a strain change substantially lower than that at the actual concrete surface. The following discussions consider the reduced sensitivity of the measurements because of the proximity of the gauges to the surface of the concrete.

4.4.1 Superstructure Thermal Gradients for Longitudinal Analysis

Positive Gradients

The maximum measured deck-level positive gradient magnitude ($T_{1,meas}$), both with and without blacktop, was about 14°C for Ramp P and 16°C for the mainlane girder. A linear interpolation that took into account the concrete cover over the thermocouples usually resulted in a 2°C to 3°C increase over these measured values. The actual increase was probably higher than this because of the nonlinear shape of the temperature distribution, especially for the case without blacktop. With this increase, the maximum $T_{1,meas}$ for the mainlane would have been close to the 20°C deck-level positive gradient magnitude (T_1) recommended by the AASHTO LRFD guide specification [9] with 50mm of blacktop. The AASHTO LRFD recommended T_1 of 25.6°C for plain concrete surfaces would be about 6°C too high when compared to the maximum measured results. The measured results without the blacktop contained only one year of data, so slightly higher $T_{1,meas}$ could have been possible.

The daily temperature changes of the top flange surface were found generally to be more extreme when no blacktop was in place during periods of daily positive gradient formation, as is reflected in the statistical distribution plots of Figures 4.47 and 4.48. Higher $T_{1,meas}$ values occurred on average without blacktop. Regardless of this fact, the maximum absolute temperature change over the course of a day measured at the top layer of thermocouples was 17.1°C without blacktop and 18.5°C with 50mm of blacktop.

The statistical distribution of maximum daily $T_{1,meas}$ values, shown in Figures 4.47 and 4.48, revealed that large deck-level gradient magnitudes, from 40% to 95% of the measured maximum, occurred most of the time when no blacktop was present. After 50mm of blacktop was added, daily maximum $T_{1,meas}$ values of 60% of the magnitude of the measured maximum or less occurred most of the time. This difference indicated that the positive thermal gradient case without blacktop would warrant a higher design gradient than with blacktop. Table 4.2 gives maximum $T_{1,meas}$ values measured in the mainlane and the ramp girder. The 95% fractiles for the measured values are also given in Table 4.2. The 95% fractile value is often chosen as the appropriate design value for other types of loads. The maximum $T_{1,meas}$ values shown were most likely 2°C to 3°C lower in magnitude than at the actual concrete surface. In general, maximum $T_{1,meas}$ values were similar for both the no blacktop and 50mm of blacktop cases, but the 95% fractile was about 1°C lower for the case with the blacktop. Based on the 95% fractile results of Table 4.2 adjusted 2°C for the difference between the point of measurement and the actual concrete surface, the appropriate central Texas values for positive thermal gradient are $T_1=16°C$ for positive gradient with no blacktop, and $T_1=15°C$ for positive gradient with 50mm of blacktop. These values are substantially below the AASHTO LRFD values.

Table 4.2 Summary of maximum top fiber gradient magnitudes

	Positive Gradient No Blacktop	Positive Gradient 50mm Blacktop	Negative Gradient No Blacktop	Negative Gradient 50mm Blacktop
<u>Mainlane</u>				
Peak Measured	15.9°C	15.4°C	-8.0°C	-4.6°C
95% Fractile	13.9°C	12.8°C	-6.5°C	-3.2°C
<u>Ramp P</u>				
Peak Measured	13.4°C	13.8°C	-8.9°C	-5.8°C
95% Fractile	11.7°C	11.9°C	-6.8°C	-4.3°C
AASHTO LRFD	25.6°C	20.0°C	-12.8°C	-10.0°C

The shape of the design gradient is of less importance, within reasonable limits, than the proper selection of the T_1 value because of the influence of the width of the deck. The positive gradient shape originally recommended by NCHRP 276 [39] did appear to be more accurate than the AASHTO LRFD simplified positive gradient shape for the mainlane superstructure, as can be seen in Figures 4.97 and 4.98. The AASHTO LRFD shape more accurately represented the positive gradients measured on Ramp P. The measured positive gradients plotted in Figures 4.97 and 4.98 were typical for commonly recurring positive gradients, both with and without blacktop. The box girder shape of Ramp P was of more typical proportions to other segmental box girders than the mainlane box girder, so the AASHTO LRFD may be the better shape, especially if the dimension "A" from Figure 4.22 was adjusted to match the top of the girder web and bottom of the fillet. A value for T_3 in Figure 4.22 should be used in all cases. The value of T_3 should be a function of the appropriate deck gradient temperature T_1 with no blacktop, 3°C being suitable for central Texas. Although some warping of the girders was noted based on the measured strains, the stresses predicted by using the AASHTO LRFD design gradient did correspond fairly well with the measured values in the mainlane girder, when the proximity of the gauges to the surface of the concrete had been accounted for. The calculated stress results for the Ramp P girder thermal gradient cases poorly predicted the measured stresses at locations away from the anchor segment diaphragm. A reduction in the positive gradient magnitudes recommended by NCHRP 276 or AASHTO LRFD for central Texas would be justified based on the temperature measurements.

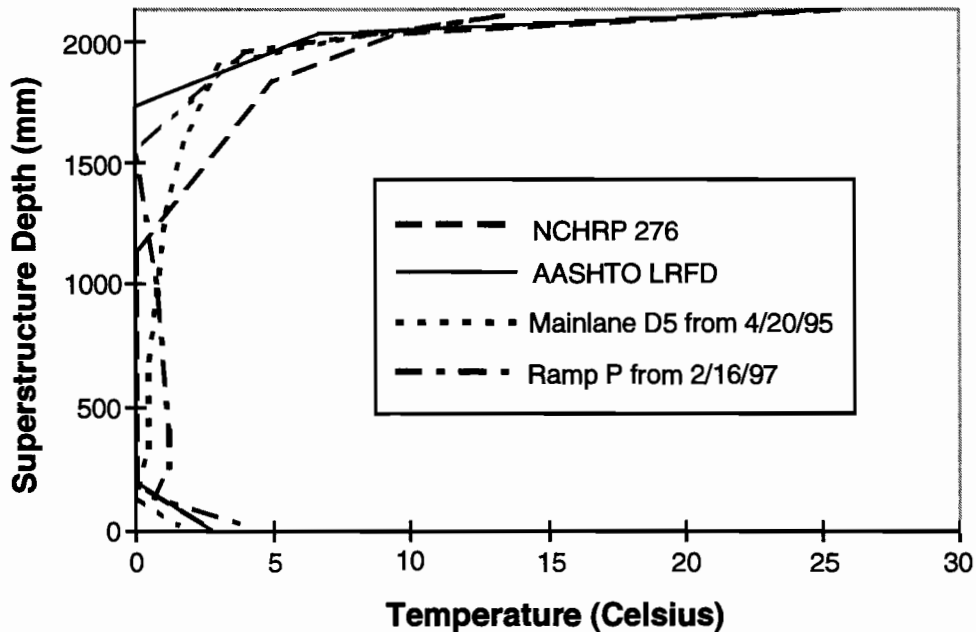


Figure 4.97 Positive design gradients and measured gradients, no blacktop

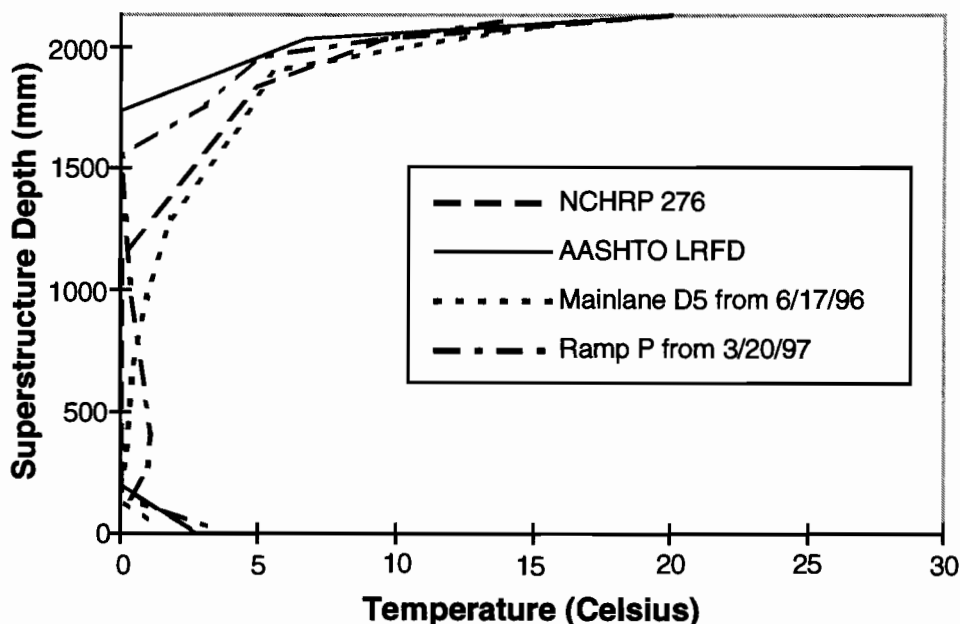


Figure 4.98 Positive design gradients and measured gradients, 50mm of blacktop

The stresses occurring from the maximum positive gradient cases with and without blacktop may not have been equal, even though the maximum $T_{1,meas}$ values were similar. Calculations usually assume that a stress-free state exists at the point in time of the day when no thermal gradient exists between the top flange and the webs. In actuality, the state of stress would not be known at any time, although the concrete would tend to creep toward a minimal state of stress at some average state of thermal strain. This state of stress would be very difficult to calculate, even if aided by measured strains. With this in consideration, it would be logical to assume that a girder with higher daily temperature changes in the top flange would have greater thermal stresses generated. This state was not reflected by the measured stress changes in Figures 4.52 through 4.55 because only the changes measured during the period of time from no gradient to maximum positive gradient at deck level were presented. The maximum positive gradient magnitudes were similar in each case, as were the changes in stress during the time periods under consideration on April 20, 1995, and June 17, 1996.

Strains measured by some gauges in the top flange over the webs in both the Ramp P girder and the mainlane girder were very large, well into the plastic range for the concrete. This behavior was only seen in the top flange over the webs, and the strains transitioned smoothly back down into the elastic range at the other strain gauge locations in the top flange. This behavior can be seen in Figure 4.55 for the mainlane and in Figure 4.33 for the Ramp P girder. The irregular measured stress distributions across the top flanges from the thermal gradient loads were not predicted by the common design technique recommended in the AASHTO LRFD. Further research into analysis techniques for thermal loads is urgently needed. Until an improved analysis is available, the obvious change to the current AASHTO LRFD or NCHRP 276 [39] positive design gradient T_1 values documented herein should be deferred. Structures designed using these current design positive gradients combined with current analysis techniques show no signs of distress.

Negative Gradients

The shape and magnitudes for minimum negative thermal gradients did not compare well with the current design gradients. The shape of the negative gradient is difficult to predict because substantial negative gradients are often produced by extreme weather events. The negative gradient caused by an extreme weather event is the superposition of the effects of the event and the gradient existing previously. The shape is also greatly affected by the exposure of the bottom of the wings, sides of the webs, and bottom of the bottom flange to the cold condition. The magnitude of the negative gradient within the thickness of the top flange is more important than the exact shape of the entire gradient when applied to a superstructure. The AASHTO LRFD negative gradient shape, however, is much different from an actual negative gradient shape and would predict

uniform curvature strains and subsequently self-equilibrating strains that may differ substantially from those actually occurring.

The minimum $T_{1,meas}$ values without blacktop were about -9°C for Ramp P and -8°C for the mainlane superstructure. Measured daily minimum $T_{1,meas}$ values less than -5°C occurred about 85% of the time without blacktop in place. Measured daily minimum $T_{1,meas}$ values less than -7°C with no blacktop and below -5°C with 50mm of blacktop occurred 95% of the time, as can be seen in Table 4.2. The AASHTO LRFD T_1 value shown in Table 4.2 is derived by multiplying the positive gradient value by -0.5 . A more realistic value, based on the measured magnitudes with no blacktop, would be -0.3 times the current AASHTO LRFD or NCHRP 276 T_1 value. If the previously recommended positive gradient design T_1 values of 16°C with blacktop and 15°C with 50mm of blacktop are adopted, then the negative gradient factor should be -0.4 with no blacktop and -0.3 with 50mm of blacktop for the deck level. The shape and magnitudes from NCHRP 276 could be used for the remainder of the gradient. During negative gradient conditions, the entire exterior of the box girder is rapidly cooled. The deck is cooled faster than the bottom flange or webs with the addition of a cold rain. The interior of the box girder is cooled very little during this period and may actually be increasing in temperature because of previous heating of the girder. The depth of the girder that cools the slowest on average is in the fillet area at the tops of the webs and at the top of the bottom flange. The bottom surface of the bottom flange undergoes a temperature drop only slightly smaller than that of the deck surface. These characteristics were reflected in the measured gradient shapes in Figure 4.99.

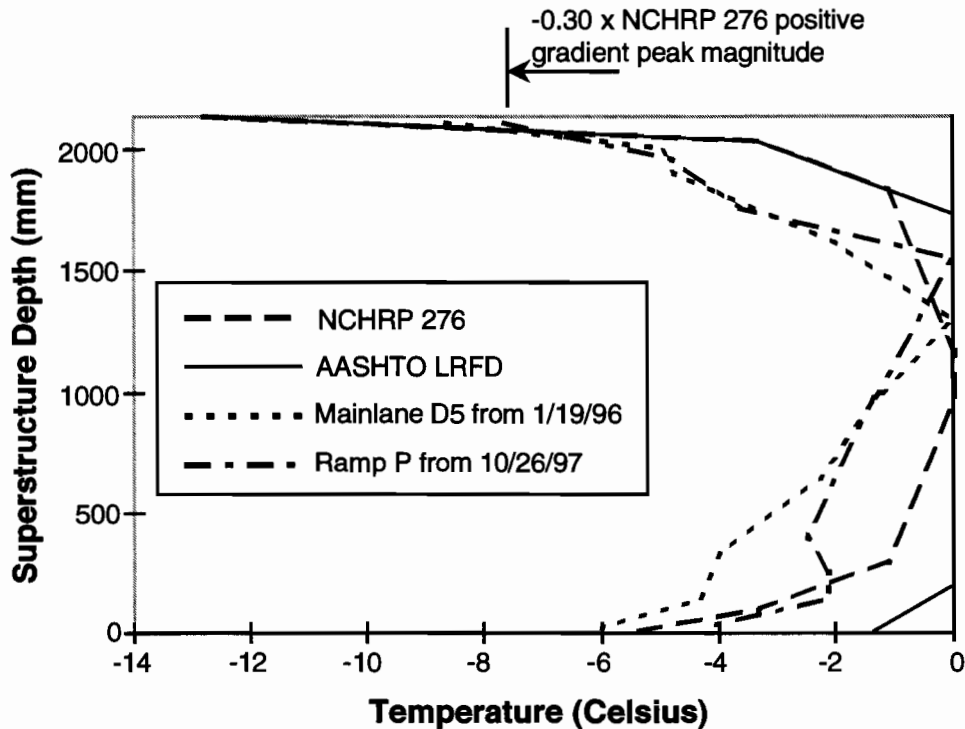


Figure 4.99 Negative design gradients and measured gradients, no blacktop

The magnitude of the measured daily minimum $T_{1,meas}$ values was reduced to -3°C or less about 85% of the time after the addition of 50mm of blacktop, and -5°C or less about 95% of the time, as seen in Table 4.2. The current recommended design negative gradient T_1 value for the US 183 girders with 50mm of blacktop is -10°C , which would be very conservative. Based on the distribution graphs in Figures 4.30 and 4.50 and the 95% fractile from Table 4.2, the design negative thermal gradient T_1 value with 50mm of blacktop also should be -5°C , which is slightly less than -0.3 times the current AASHTO recommended positive gradient T_1 value at deck level. The NCHRP 276 shape and values should be used for the remainder of the gradient. The negative gradients plotted in Figure 4.100 showed that the shape of the measured gradient was nearly the same for the case with 50mm of blacktop and with no blacktop. The temperatures in the bottom flange were predicted well by the NCHRP 276 negative gradient.

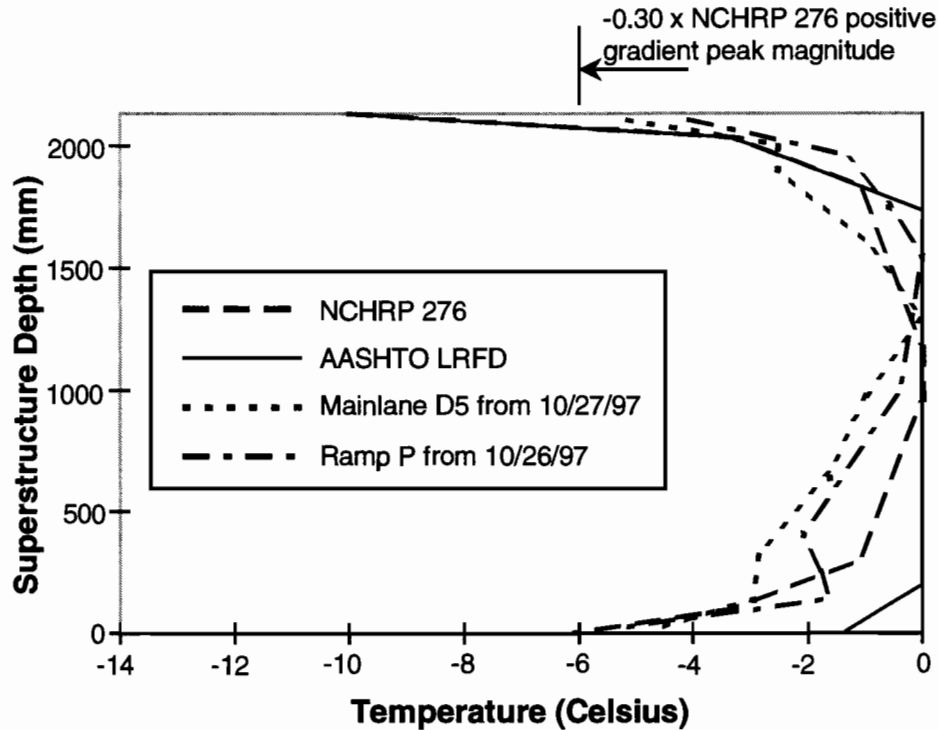


Figure 4.100 Negative design gradients and measured gradients, 50mm of blacktop

The measured stresses for the negative gradient case from November 11, 1995, shown in Figures 4.56 and 4.57 compared well with the calculated stresses using the measured gradient. The stresses calculated using the current AASHTO LRFD gradient were too conservative. The calculated stresses for the negative gradient case in the Ramp P girder did not compare well to the measured stresses at any location. The calculated bottom flange stresses for Ramp P in Figures 4.35, 4.36 and 4.37 showed that the AASHTO LRFD negative gradient predicted too much compression in the bottom fibers from uniform curvature-induced stresses. The stresses calculated from the measured gradient gave proper emphasis to the self-equilibrating stresses actually occurring and predicted tension in the bottom fibers. The shape originally recommended by NCHRP 276 was more realistic than the AASHTO LRFD shape, particularly in the bottom flange and lower part of the webs. In general, the calculated stresses using the AASHTO LRFD design negative gradient were conservative in the simple-span mainlane girder, and unconservative as well as unrealistic in the continuous Ramp P girder. Based on this observation, analytical study of the structural response of box girders to thermal loads is urgently required. Until an improved analysis is available, the obvious change in negative design gradient T_1 values recommended and documented herein should be deferred.

4.4.2 Superstructure Thermal Gradients for Transverse Design

Positive gradients

Positive thermal gradient magnitudes measured through the thickness of the top flange at points between the webs were nearly as large as the positive gradient magnitudes through the depth of the entire box girder. The maximum measured positive gradient magnitude in the top flange of the mainlane was about 17°C , both with 50mm of blacktop and without. The extrapolated temperature difference between the top fiber and bottom fiber was almost 20°C . Based on the statistical distribution of top fiber temperature gradients through the depth of the girder, the 95% fractile positive gradient magnitude would be about 18°C without blacktop, and 17°C with 50mm of blacktop. The positive gradients through the webs and bottom flange of the mainlane were much less in magnitude, which would be expected since these elements did not have direct exposure to the sun for most or all of the day. The web and bottom flange positive gradient magnitudes occurring with the maximum positive gradient in the top flange were less than 4°C and could be ignored for design purposes. The maximum measured positive gradient magnitude in the top flange of the Ramp P girder was substantially less than that of

the mainlane because the spring of 1997 did not produce positive gradients as large as the two previous springs. Also, the Ramp P box girder top flange thickness was only 203mm, compared to 254mm on the mainlane girder.

The analytical method used to calculate stresses from the measured positive gradients tended to overestimate stresses for the mainlane, probably because of the longitudinal cracks at the top of the webs, and underestimate stresses for the Ramp P girder. Also, this two-dimensional method of analysis did not consider the relationship of transverse stresses and longitudinal stresses. Measured top flange stress changes from the positive gradient were about 12% of the allowable compressive stress in the mainlane girder, and 57% of the allowable in the Ramp P girder. Calculated top flange stresses using the measured maximum positive gradients were similar in both girders at about 30% of the maximum allowable compressive stress in the concrete. These high percentages indicate that the positive gradient through the thickness of the top flange should be considered as a design case.

The design values for the thermal gradient load case for transverse design of box girders are not explicitly given in the *AASHTO Guide Specification* [23], *AASHTO LRFD Guide Specification* [9], or the *AASHTO Segmental Guide Specification* [8]. The NCHRP 276 positive gradient shape for beam and slab bridges is plotted in Figure 4.101, along with the measured positive gradients and a proposed positive top flange gradient for design in central Texas. The proposed positive gradient has a peak deck-level magnitude of 18°C for no blacktop and 17°C with 50mm of blacktop. This peak temperature decreases linearly at a gradient of $-0.072^{\circ}\text{C}/\text{mm}$ for no blacktop and $-0.068^{\circ}\text{C}/\text{mm}$ for 50mm of blacktop. Thus, the bottom fiber of a 250mm thick top flange will be 0°C. Top flanges thicker than 250mm can be assumed to have a linear temperature gradient of 18°C or 17°C, depending on the presence of blacktop. The measured gradient shown in Figure 4.101 is nearly parallel to the proposed gradient. The temperature at the bottom gauge location in the measured gradient plot was arbitrarily assigned to zero. Use of the proposed gradient results in a decreased total temperature change over the top flange depth for top flanges thinner than 250mm and also provides a realistic average temperature change in the top flange, based on the measured data. The NCHRP 276 temperatures for beam and slab bridges are plotted in Figure 4.101 for comparison purposes because the gradient magnitude through the thickness of the top flange was measured to be more severe than the gradient through the same depth of concrete directly over the webs. The NCHRP 276 positive gradient shape for box girders was intended to be applied down the centerline of the webs.

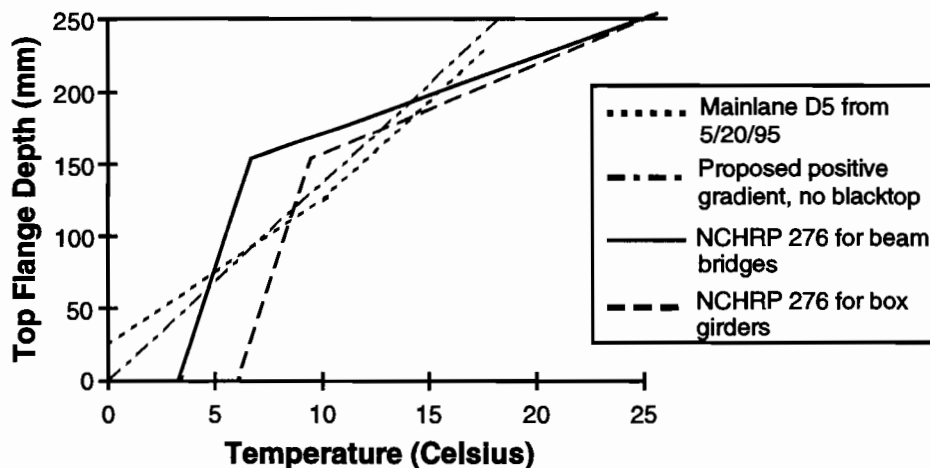


Figure 4.101 Recommended positive top flange design gradient for transverse design

Negative Gradients

The magnitude of the measured negative thermal gradient through the thickness of the top flange of the mainlane box girder was more severe than the minimum $T_{1,meas}$ for the entire depth of the girder. The minimum measured negative gradient in the top flange was about -12°C in the mainlane girder and -9°C in the Ramp P girder with no blacktop. Based on the statistical distribution of top fiber temperature gradient magnitudes through the depth of the mainlane and Ramp P girders, the 95% fractile negative gradient magnitude would be

about -10°C without blacktop, and -5°C with 50mm of blacktop for the mainlane 254mm top flange. Significant tensile stress changes were measured in Ramp P from the negative gradient, with a maximum top fiber stress change of 6.4MPa in tension. This tensile stress would be important when designing the transverse prestressing force and eccentricity for the top flange. The proposed top flange negative gradient for central Texas in Figure 4.102 has a peak deck-level temperature of -10°C for no blacktop and -5°C with 50mm of blacktop. The slope of the proposed negative top flange gradient, at $0.040^{\circ}\text{C}/\text{mm}$ for no blacktop and $0.020^{\circ}\text{C}/\text{mm}$ for 50mm of blacktop, is slightly less conservative than the slope of the measured gradient in Figure 4.102. Top flanges thicker than 250mm can be assumed to have a linear temperature gradient of -10°C or -5°C , depending on the presence of blacktop.

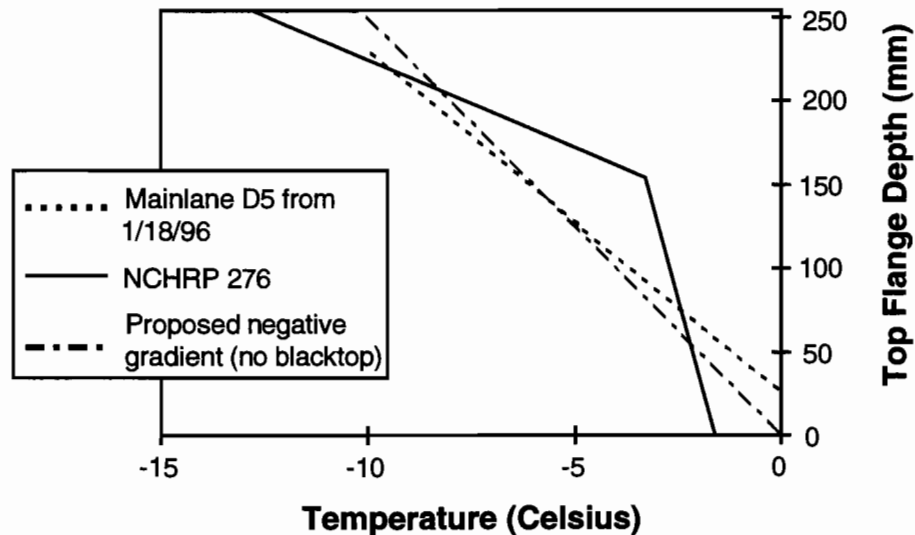


Figure 4.102 Recommended top flange negative design gradient for transverse design

The measured negative gradients through the thicknesses of the flanges and webs differed from the positive gradient case in that the negative gradients through the bottom flange and webs were of a significant magnitude. Since the negative gradients measured in the webs and bottom flange were quite large, a negative gradient in these elements should be considered for design. The magnitude of the web and bottom flange gradients was about 75% of the top flange negative gradient when no blacktop was in place. The addition of blacktop had no influence on the gradients in the webs or bottom flange. The proposed negative gradient in Figure 4.103 is derived from the proposed negative gradient for the top flange with no blacktop plotted in Figure 4.102. The recommended peak magnitude temperature in Figure 4.103 is 75% of the magnitude recommended for the top flange at deck level with no blacktop. The slope of the gradient is $0.030^{\circ}\text{C}/\text{mm}$ for webs and flanges up to 250mm thick. The overall magnitude of the temperature gradient predicted using the proposed gradient in Figure 4.103 compared well to the measured temperature difference across the webs and bottom flange. The measured gradients were not linear, as in the top flange, and therefore the proposed gradient would give slightly unconservative moments from the linearly changing component of the gradient, and slightly conservative moments and axial forces from the constant component of the gradient.

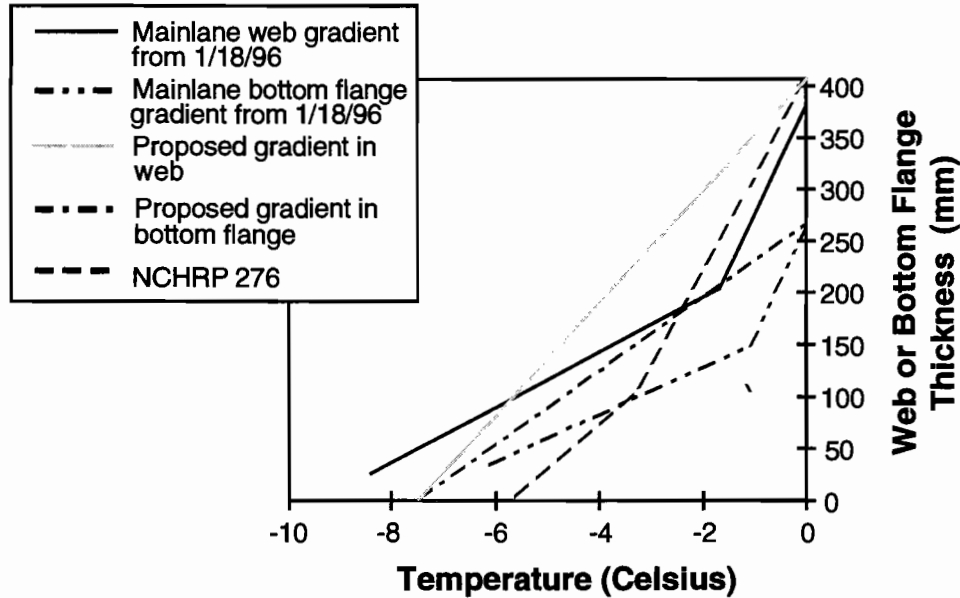


Figure 4.103 Recommended web and bottom flange negative design gradient for transverse design

4.4.3 Pier Gradients

The measured thermal gradients in the piers under study were found to be less severe than those measured in the superstructures for a given day. The positive gradient in the large ramp pier P16 had peak magnitude on the west face of the pier at the end of the afternoon. Substantial positive gradients were measured on any face of the pier that had sun exposure, including the east face. Positive gradient magnitudes measured with the sun exposure on the east face were about 80% of the magnitude of the maximum positive gradient that was to occur later in the day. The positive gradient existing when the sun exposure was on the south face was only about 50% of the maximum.

The magnitudes of the positive thermal gradients measured in pier P16 were only about 75% of those $T_{1,meas}$ values measured in the superstructure girders on the same days. The superstructure gradients were higher because the lower portions of the girders were shaded most of the day, while the pier received direct sunlight whenever skies were clear. The shape of the positive gradients in pier P16 was about the average of the NCHRP 276 gradient and the AASHTO LRFD gradient, with the peak magnitude reduced by half. The recommended shape for a positive design gradient, based on the results from pier P16, is shown in Figure 4.104. The recommended positive gradient shape is the same as recommended for the superstructure in Section 4.4.2 without blacktop, but with the entire gradient shape is multiplied by 75%. The temperature on the far side from the sun exposure should remain at 2.8°C. Until further refinement of the common analysis technique used for finding stresses from thermal gradients has been performed, this measurement-based gradient cannot be recommended. Instead, 75% of the NCHRP design positive gradient for no blacktop should be used, but with the far face temperature remaining at 2.8°C. The peak magnitude of this recommended shape is about 6°C higher than the maximum measured magnitude for three reasons. First, the time period over which data were taken may not have produced the highest possible positive gradient, although the spring of 1996 did produce substantially higher positive gradients in the mainlane girder than the spring of 1997. Second, the thermocouples used to measure the concrete temperatures were placed 25mm under the actual surface, so surface temperatures were probably higher on the exterior and lower on the interior than presented. Third, the method commonly used by design engineers to determine stresses from the one-dimensional positive gradient consistently was found to underestimate the peak stresses to an actual gradient when compared to the measured results and to calculated results using more refined design methods.

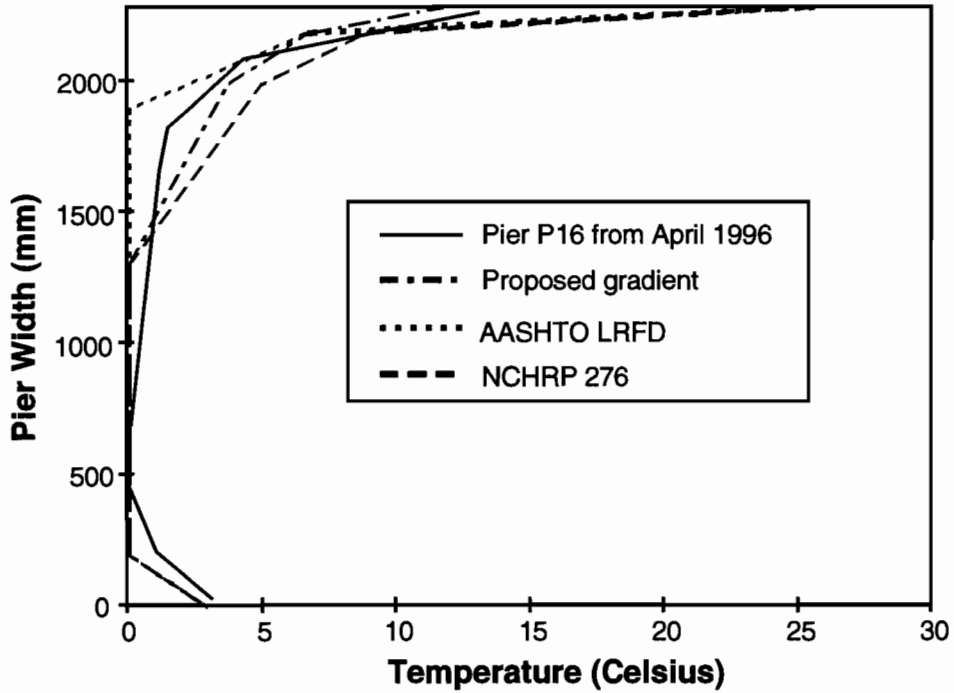


Figure 4.104 Recommended positive design gradient for piers

The negative gradients measured in pier P16 were not effected by the orientation of the sun to any extent. Also, negative gradients of significant magnitude did not occur as often as large positive gradients. The peak magnitude of the negative gradients was nearly as large as those seen in the superstructure, and the shape was predicted well by the NCHRP 276 negative gradient shape, with the exception of the peak magnitude. The recommended shape for negative design gradient (with -7°C at deck level) as shown in Figure 4.105 is recommended for piers, based on the measured results from pier P16. This is the same as recommended for superstructure box girders without blacktop in Section 4.2.2. Once again, the original NCHRP 276 values should be used until the analysis technique can be improved.

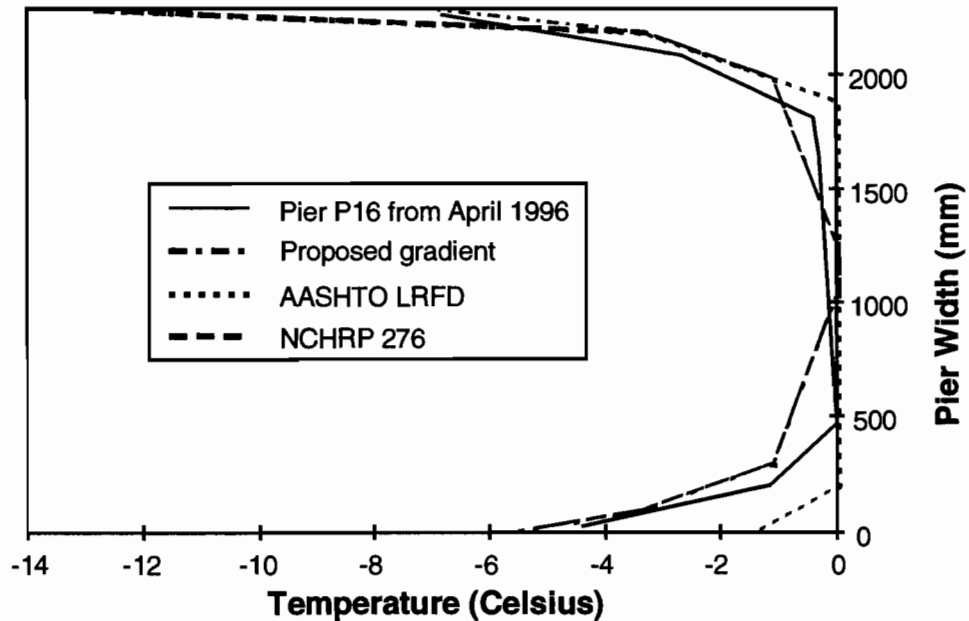


Figure 4.105 Recommended negative design gradient for piers

Thermal gradients in the solid sections of the mainlane pier and the ramp pier P16 capital were slightly smaller than those measured in the voided sections. Although the concrete in the core of these solid sections did not warm or cool appreciably over the course of the day, the exterior of the concrete was also not able to be heated or cooled to the extent of the voided piers because of heat loss to the core concrete. The net effect was a slight reduction in thermal gradient over the voided pier. Since the mainlane pier was not instrumented with the intent to define a thermal gradient shape, and the ramp pier capital segment PC16-8 was not part of a continuously solid vertical pier, the best recommendation for design thermal gradients for a solid pier would be those already given for the voided section. The peak magnitudes were found to be similar for both the voided and the solid sections. With the massive core of the solid section piers, the stresses of primary concern would be the self-equilibrating stresses on the surface of the concrete. These stresses are determined largely by the magnitude of the gradient and not by the shape of the gradient. The shape of the gradient is more important for the voided section where large areas away from the neutral bending axis of the section increase the proportion of bending stresses to self-equilibrating stresses.

Positive thermal gradients tend to cause compressive stresses on the surface of the concrete, while negative gradients cause tensile stresses on the surface of the concrete. Compressive stresses on the mainlane pier D6 from a positive gradient were measured as large as 2.7MPa, or about $0.1f_c'$ which was higher than the total axial stress from the superstructure at 1.9MPa. Compressive stresses on the ramp pier P16 were calculated to be as high as 3.9MPa from the measured peak positive gradient, or about 0.2 of the allowable compressive stress in this post-tensioned concrete. Since the design of the pier for balanced cantilever construction moments from the superstructure was dominated by control of tensile stresses in the pier, the additional compressive stress from the positive gradient was of no consequence, even during construction. Tensile stress from the maximum measured negative gradient was calculated to be -2.3MPa on the surface of pier P16. This tensile stress was calculated to cause tension in the pier concrete only during the out of balance cantilever construction load case. Significant negative gradients occur infrequently, so the addition of the negative gradient load case to the construction loads may not be necessary, depending on the bridge and the duration of construction.

In general, the importance of the addition of compressive stress from the thermal gradient load case would only be important for prestressed pier designs of uncommon shape or proportion. The decision to add the thermal gradient load case to the design should be made by the engineer. Similarly, the importance of thermal-induced tensile stresses in a compression member is of little importance, except for special load cases. The probability of a substantial negative gradient occurring during the special load case, especially during construction, should also be determined by the engineer.

Cracking on the piers or superstructure members from daily thermal loads was not observed anywhere on the project. Cracking may occur in the future because of concrete fatigue, given the daily stress range on the concrete surfaces. Since the stresses in the concrete from temperature, as well as shrinkage, are a function of exposed area and volume of the pier, a pier design that does not include the thermal gradient case should use a nominal amount of reinforcing steel in each direction and on each face of the concrete that is a function of both surface area and concrete volume. The *AASHTO LRFD* [9] gives Equation 5.10.8.2-1 for computing nominal steel percentages that meets this requirement, although for members with least dimension less than 1220mm. This equation requires a minimum steel area on each face of a member of $0.379A_g/f_y$, where A_g is the area of concrete in mm^2 between bar spacings and f_y the yield strength of the reinforcing steel in MPa. The $265\text{mm}^2/\text{m}$ reinforcing requirement in the *AASHTO Guide Specification* [23] is primarily intended for walls and may be totally insufficient for controlling local tensile stresses in more massive elements.

The $470\text{mm}^2/\text{m}$ of transverse reinforcement used in the large ramp piers, including P16, was inadequate for controlling temperature-gradient-induced stresses during the concrete curing period. The transverse steel area used was almost twice that recommended by *AASHTO* [23] and was twice that used in the original design of the piers. The *AASHTO LRFD* minimum steel requirement dictates a steel area of $372\text{mm}^2/\text{m}$, which would also have been inadequate in controlling the curing stresses. The negative thermal gradient magnitude measured in segment PC16-8 during curing was -35°C . The high strength and resultant reactivity of this concrete caused this extreme gradient. A lesser negative gradient measured while the segment was in the form was severe enough to cause cracking in the young concrete before the form was removed. The presence of these cracks could be detrimental in a corrosive environment to a precast pier made otherwise of very high quality concrete, since the cracks tend to open with time from shrinkage. Concrete with initial reactivity reduced by the use of fly ash, lower design strength, or other methods such as cooling may prove more beneficial to the structure than the use of a more efficient section and high early strengths. The amount of mild reinforcing steel used for temperature

and shrinkage crack control should be increased for piers made with more reactive concrete, since the thermal gradient during curing may be a function of the design strength.

4.5 CONCLUSIONS

The following conclusions have been made based on the measured thermal gradients in the various structural elements under study and the measured response of the structure to these gradients and the current AASHTO LRFD design thermal gradients.

4.5.1 Superstructure Gradients for Longitudinal Design

Positive Thermal Gradients

1. The peak measured positive gradient deck-level magnitudes ($T_{1,meas}$) were similar for both the cases without and with 50mm of blacktop, although thermal data without blacktop were limited.
2. The NCHRP 276 or AASHTO LRFD recommended design positive gradient T_1 value for girders with 50mm of blacktop accurately predicted peak gradients at 20°C, but the recommended T_1 value without blacktop at 25.6°C was somewhat high, based on the limited measurements. The distribution of daily positive gradient deck-level magnitudes over time indicates that the thermal gradient case without blacktop deserves a higher design gradient magnitude (at $T_1=16^\circ\text{C}$) than the case with 50mm of blacktop (at $T_1=15^\circ\text{C}$).
3. The AASHTO LRFD recommended positive gradient shape more accurately represented the measured positive gradient shape of the Ramp P girder, and the NCHRP 276 recommended positive gradient shape better represented the shape measured on the mainlane. In either case, a temperature gradient in the bottom slab should be considered, 3°C being suitable for the soffit gradient magnitude in central Texas.
4. Calculated stresses using the AASHTO LRFD recommended design positive thermal gradient compared well to stresses measured on the mainlane girder, but compared poorly and unconservatively to stresses measured on the Ramp P girder, even though the design gradient T_1 value was larger than the actual gradient. Evidence of sectional distortion or warping was measured in every thermal gradient case. Also, soon into the life of the girders, high strains were measured in response to thermal gradients in the top slab over the webs. These high strains were measured in both the mainlane girder and the Ramp P girder and would indicate plastic behavior in the concrete near the top of the heavy web reinforcement anchored in the deck.
5. Based on the measured positive gradients alone, a reduction in the magnitude of the design positive thermal gradient T_1 value would be warranted in some cases. An analytical study of the structural response to thermal loads needs to be performed before any reduction in the design positive thermal gradients could be recommended. The effects of cross-sectional shape, diaphragms, continuity, and potential plasticity should be considered in this study.

Negative Thermal Gradients

1. The shape of the AASHTO LRFD recommended negative thermal gradient did not compare well to measured negative thermal gradient shapes in either the mainlane girder or the Ramp P girder. The negative gradient shape recommended by NCHRP 276 better represented the actual shape of the negative gradient, especially in the lower part of the cross section.
2. Based on the measured negative thermal gradients, the peak top fiber gradient temperature T_1 recommended by AASHTO LRFD or NCHRP 276 was too extreme. The peak top slab negative gradient temperatures were closer to -0.3 times the NCHRP 276 recommended positive gradient temperatures for the appropriate case without or with 50mm of blacktop. All points of the negative gradient other than the top fiber temperature would be represented fairly accurately with the NCHRP 276 negative gradient shape. T_1 values should be -7°C without blacktop and -5°C with 50mm of blacktop in central Texas.
3. Based on the unconservative calculated stresses in the Ramp P girder when compared to the measured stresses, no change to the current recommended design negative gradient from NCHRP 276 can be recommended, pending further study of box girder response to thermal gradients.

4.5.2 Thermal Gradients for Transverse Design

1. Measured stresses from both positive and negative thermal gradients through the thicknesses of the top slab, webs and bottom slab were large enough to warrant a design thermal gradient for transverse design.
2. Based on the measured temperatures, a positive thermal gradient should only be applied to the top flange, and the gradient shape should be linear. A recommended shape and magnitude for the positive gradient is given in Section 4.4.2 for central Texas.
3. Based on the measured temperatures, significant negative thermal gradients occurred simultaneously in the top flange, webs, and bottom flange. The negative gradient should be assumed to be linear in the top flange, as described in Section 4.4.2. The negative gradients occurring in the webs and bottom flange should also be assumed to be linear and can be obtained by multiplying the magnitude and slope of the recommended top flange negative gradient for no blacktop by 0.75.

4.5.3 Thermal Gradients for the Design of Piers

1. Significant thermal gradients and thermal-induced stresses were measured in the voided segmental pier P16 and the solid mainlane pier D5.
2. A positive thermal gradient for the design of voided piers can be derived by multiplying the entire recommended positive gradient shape for box girders in Section 4.5.1 with no blacktop by 0.75, with the exception of the far fiber temperature, which should remain at 3°C.
3. The recommended negative thermal gradient shape for superstructures with no blacktop from Section 4.5.1 can be used for the design of voided piers.
4. Although few data were taken to define the shape of thermal gradients in solid pier sections, the magnitude of the thermal gradients were measured to be similar to those of the voided pier. The recommended thermal gradients for the design of voided piers in points 2 and 3 above are recommended for the design of solid piers until further studies can be done.
5. The stresses produced by the thermal gradients in the piers were mostly inconsequential for pier design, except for one construction load case during the construction of the balanced cantilever superstructure of Ramp P. The decision to use a thermal gradient load case for the design of piers should be made by the engineer.
6. Daily thermal-induced stress changes in the piers were measured to be on the same magnitude as those produced by the superstructure dead load. In order to control surface stresses and concrete fatigue cracking, a nominal amount of transverse steel should be selected for a pier based on both the concrete volume and surface area, such as by the AASHTO LRFD Equation 5.10.8.2-1.
7. Negative thermal gradients that occurred during curing of the pier P16 segments were large enough to crack the concrete segments while in the form. Negative thermal gradient magnitudes were measured as high as -35°C shortly after removal from the form. An area of transverse steel calculated by the AASHTO LRFD Equation 5.10.8.2-1 would not have been enough to prevent the cracking, since the transverse area of steel actually in the pier segments exceeded the amount found by this equation. A designer should consider the negative gradient produced in higher strength concrete elements during curing. Transverse steel should be increased to handle the thermal stresses, or provisions should be made to reduce the heat of hydration.

CHAPTER 5

LOAD RESPONSE OF BOX GIRDERS

5.1 INTRODUCTION

The structural response of the US 183 box girders and voided pier P16 during application of dead loads, post-tensioning forces, and live loads was measured. The measurement of the distribution of stresses across the width of the cross sections was the primary purpose for the instrumentation. Four different superstructure box girders were studied. The first was the mainlane three-span semicontinuous unit D2. This unit was constructed using the span-by-span method, which dictated that self-weight and post-tensioning forces be applied over a short period of time after the girder had been assembled. The second was the five-span continuous Ramp P girder constructed in balanced cantilever. Construction of the span P16, the span under study, occurred over several weeks because of construction staging. Application of segment dead loads and post-tensioning forces occurred over very short periods of time though, making strain measurements easy to interpret. A live-load test was performed on both mainlane unit D2 and Ramp P. Live-load tests were also performed on the two-cell box girder unit C15/L2 and the three-cell box girder unit C13 to study the sharing of live-load moments transversely from unsymmetrical load cases. Finally, measurements were taken on segmental pier P16 during the dead-load application from a superstructure segment on Ramp P. The out of balance moment from the installation of this final segment on the span P16 cantilever created large instantaneous stress changes in pier P16.

5.2 PROBLEM AND TECHNICAL BACKGROUND

Box girder bridges must be designed differently than multiple girder bridges because of potentially large horizontal shear deformations from bending moments, the distance post-tensioning forces take to diffuse into the cross section, and the lack of redundant load paths in single-cell box girders. Simplified conservative methods can be used to determine the distribution of live-load moments among girders in multiple girder bridges. A single-cell box girder must be designed to take the entire live-load moment on the span, regardless of the location of the load across the girder width. Shear lag deformations will alter the stress distribution on the cross section from that of a simple beam for live load, dead load, and post-tensioning forces and will change the moment diagram on continuous-span box girder bridges. The box girder analysis must include these considerations in order to accurately predict peak stresses.

5.2.1 *Structural Response of Box Girders to Dead Load and Live Load*

The cross-sectional shape of many box girders does not allow the designer to assume that plane sections will remain plane during a longitudinal analysis of a girder. The top flange width of a box girder is dictated by the roadway geometry above, while span lengths are dictated by pier height and ground obstructions. Box girders frequently are quite wide when compared to their span length. This proportion requires that the distance between webs and the width of the girder wings also be large when compared to the span length. Shear deformations in the top flange become important to the overall bending behavior of the girder.

Figure 5.1 shows a typical US 183 mainlane girder subjected to a point load at midspan. The plan view shows that the deflected shape of the top flange is influenced by shear deformations or shear lag and tends to relieve longitudinal stresses at points in the flanges away from their intersection with the webs. This effect is most prevalent over the part of the span under high moment gradient, where shear is high. The portions of the flanges under higher bending stress tend to have their stress relieved to some extent by shear deformations toward portions of the flanges under lower stress. For a live-load case on the simple span, shear is high over the entire span length. For the dead-load case, shear is high near the bearing reactions where the moment is low, and bending stresses are low. Measurements on the mainlane girder D5 revealed the effect of shear lag on the bending stiffness of the girder for the live-load, dead-load and post-tensioning force cases. The mainlane girders would be considered quite wide for their span lengths. Their span length to overall width ratio was about 2.3. Single-cell box girders with a span-to-width ratio of 10 or larger are generally considered to be free of significant shear lag effects for both simple and continuous-span girders.

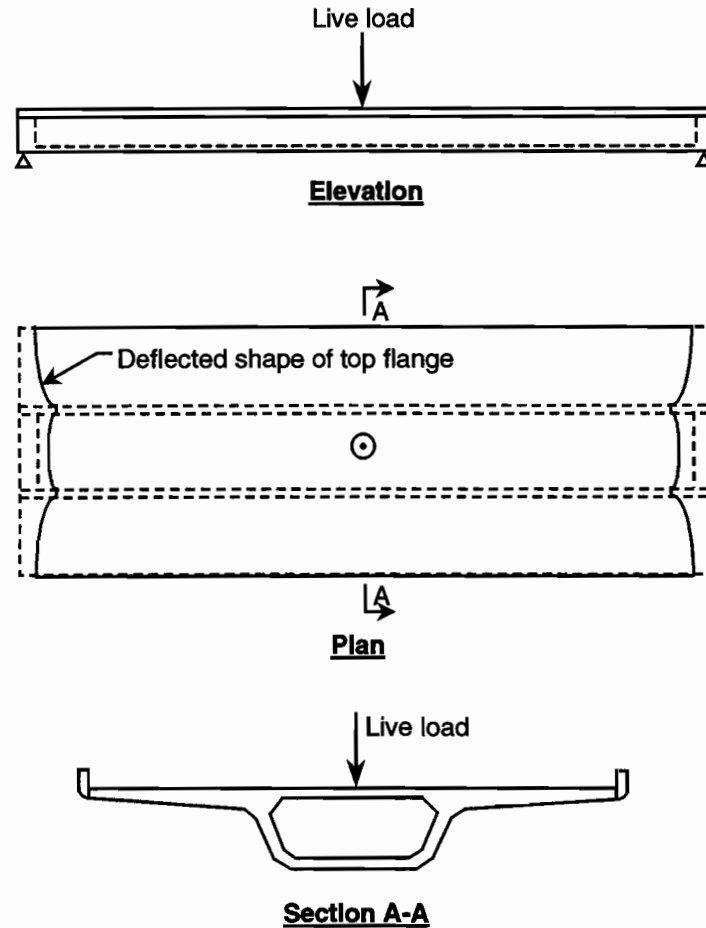


Figure 5.1 Shear lag deformation in a simple-span box girder

Shear lag effects can be more important in continuous structures. Both bending moment and moment gradient tend to be highest at interior piers. Figure 5.2 shows a continuous single-cell box girder subjected to a lane load. The pier reaction causes an abrupt point of negative moment at the pier. The average top fiber stress in the girder, as calculated using beam theory, also peaks abruptly at the centerline of the pier. Since plane sections do not remain plane in the girder because of shear lag, the longitudinal stresses at Line A and Line B are not equal. The stresses at Line A peak at the centerline of the pier because shear deformations within the web are small, especially when compared to the shear deformations at Line B. The tensile stresses along Line B are reduced from those at Line A, which effectively reduces the girder's bending stiffness, changing the moment diagram and increasing stresses at points in the cross section close to the webs.

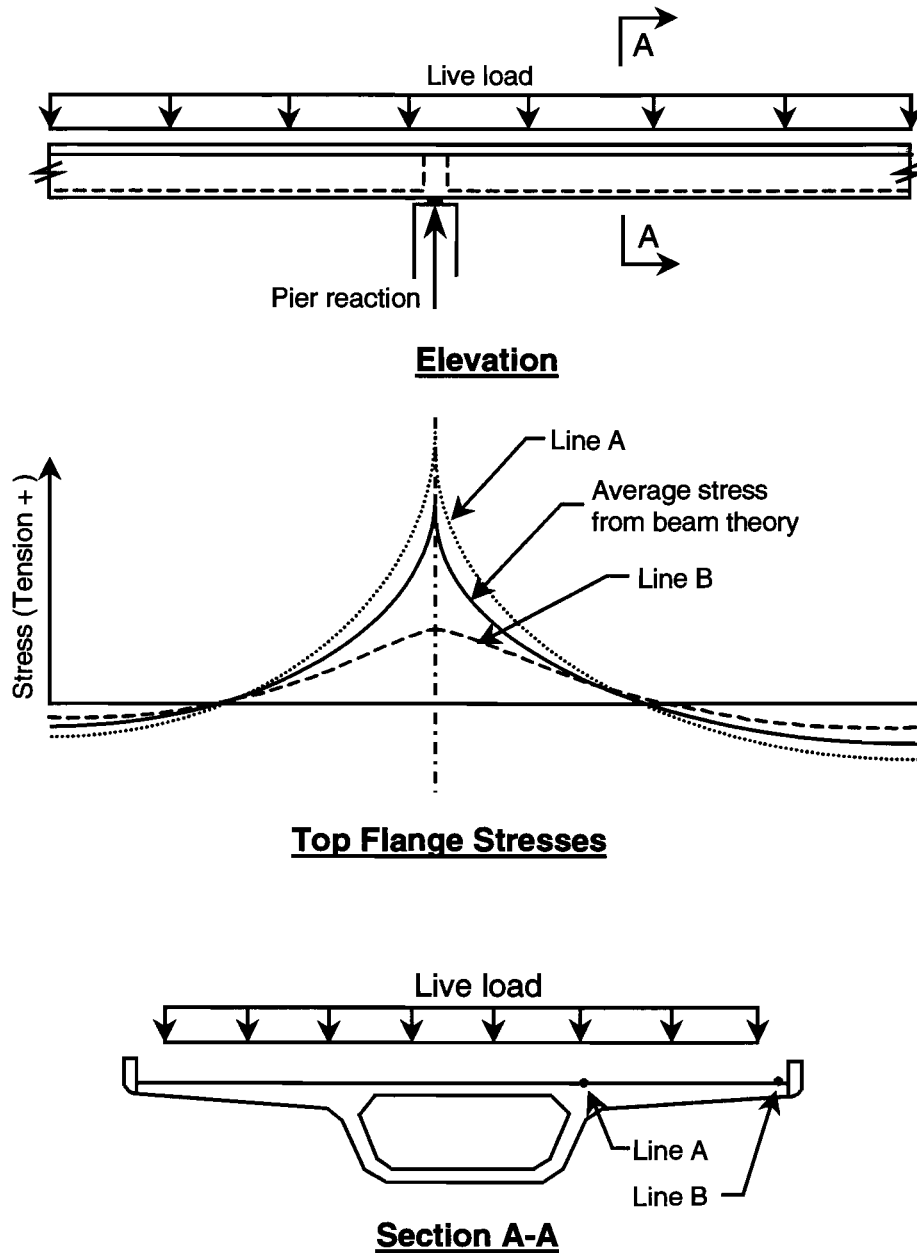


Figure 5.2 Top flange stresses in a continuous box girder

5.2.2 Diffusion of Post-Tensioning Forces

Post-tensioning tendons in box girders are often located very near, if not in, the girder webs. The diffusion of the post-tensioning forces into an entire span is effected by shear lag in the girder, as a result of the girder shape, as was the case for dead loads and live loads. Since the bending moments from the post-tensioning are designed to oppose the bending moments from dead load and live load, the peaks in stress located near the girder webs caused by shear lag will cancel themselves out to some extent. For this reason, shear lag in post-tensioned box girders is often not considered to be of any great consequence [26].

A more complicated problem is the calculation of stresses from post-tensioning forces at points very near the anchorage. A designer often needs to know when the post-tensioning force can be considered to be acting on the entire cross section. The force from the anchorage may have to diffuse from a modified portion of the cross section into the typical cross section, such as forces from an external tendon anchorage in a diaphragm. Also the concrete in the diffusion region may be cracked, further complicating the problem. For these reasons, strut-

and-tie modeling is often used when designing anchorage zones. This truss analogy method will not easily predict cross-sectional stresses at points relatively near the anchorage.

Post-tensioning anchorages may also be located within the thickness of the normal cross section of the bridge. St. Venant's Principle is often applied when trying to calculate the diffusion of the post-tensioning force into the webs and flanges of a box girder. These members are essentially plates loaded on edge. St. Venant's Principle allows the substitution of one loading with another statically equivalent loading more convenient for calculating member stresses at points beginning some distance away from the location of the original load. In the simplest example of St. Venant's Principle, a plate of some small thickness, long length, and width b is concentrically loaded with a point load on each end to produce an axial force along the length of the plate. At a distance b away from the point load, the axial stress distribution is nearly uniform across the width of the plate. The minimum stress is 0.973 of the average stress, and the maximum stress is 1.027 of the average stress [42]. For practical engineering calculations the point load could be replaced with a uniformly distributed load at a distance b away from the load. It also follows that for a wide plate with evenly spaced point loads at spacing b , the cross-sectional stresses would be nearly uniform at a distance b away from the point loads. The cross-sectional shape of a box girder, and the location and spacing of anchorages complicates the problem considerably from the previous two examples.

5.2.3 Behavior of Multiple-Cell Box Girders

Box girders may have one or more cells. Multiple-cell box girders with evenly spaced webs and a bearing at each web centerline behave only slightly differently than a multiple girder and slab bridge. The transition spans on US 183 occurred where the ramp girders intersected with the mainline girders. The design solution to this merger was a three-cell box girder with a variable width center cell and bearings located only under the outer cells. The result was a girder that was neither a multiple-cell box girder in the traditional sense, nor the union of two single-cell box girders with a gore closure between wing tips. The transition girder was difficult to analyze for live load because loads on one side of the girder would be partially shared by the other side of the girder. Since the transition spans were originally designed to have cast-in-place top and bottom slabs between two precast single-cell and single-winged box girders, all the longitudinal post-tensioning was located in the outer two cells of the girder. Figure 5.3 shows by a sketch of the deformed shape how live loads on one side of the girder would be distributed to the other side of the girder at points away from the piers. The amount of distribution of live load depends on the transverse bending stiffness of the central top and bottom slabs, the torsional stiffness of the girder cells, and the stiffness of the bearings.

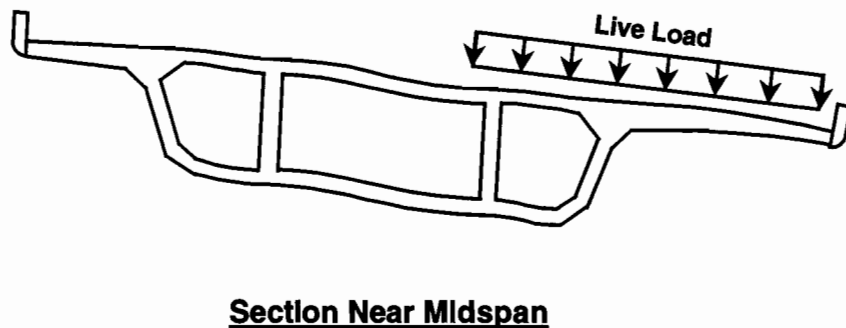
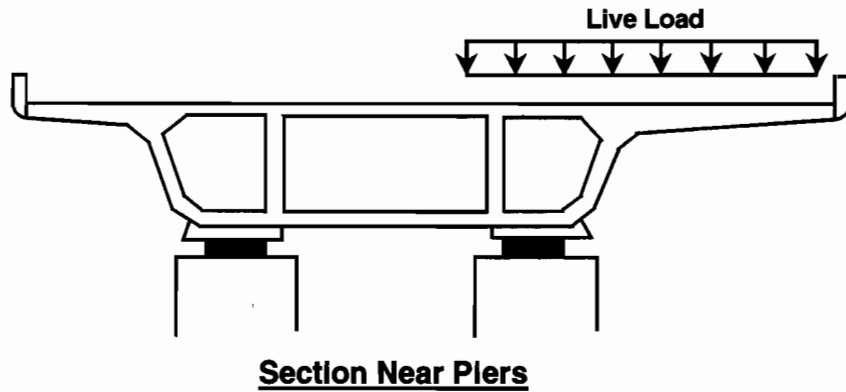


Figure 5.3 Response of a multiple-cell box girder to live load

Twin single-cell box girders are commonly joined at the wing tips and post-tensioned transversely. This arrangement allows any roadway geometry needed without the use of a longitudinal expansion joint or two parapets at the median. Also, significant sharing of live-load moments can be realized. Figure 5.4 shows the cross section of a modified span on US 183. A gore closure connects the truncated wings of the ramp girder and the mainlane girder. As for the modified spans, live loads on one girder can be distributed to the other girder at points away from the piers. The amount of sharing depends on the longitudinal bending stiffness of each girder, the transverse bending stiffness of the central top slab, and the torsional stiffness of each girder. The stiffness of the bearings effects the stiffness of all these other components.

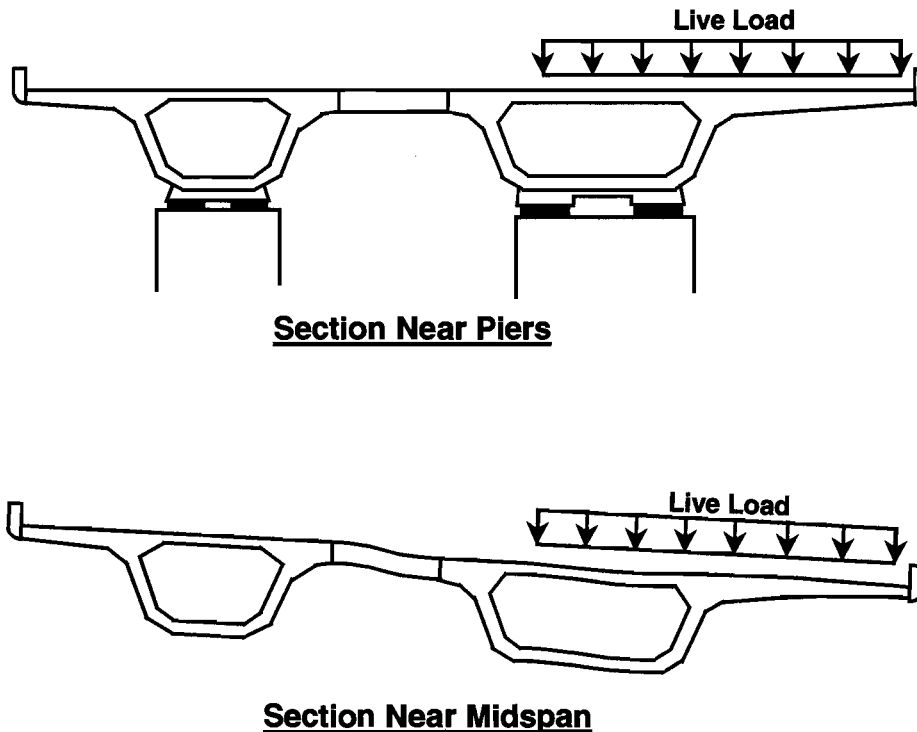


Figure 5.4 Response of twin single-cell box girders to live load

5.3 TYPICAL SOLUTIONS, DESIGN CODE METHODS, AND PREVIOUS MEASUREMENTS

A tremendous amount of resource material is available to engineers describing methods of structural analysis for box girders. The methods discussed in this chapter are the most commonly used methods that are widely used by engineers for box girder designs. The results using these design methods are evaluated by comparing them to the measured data.

5.3.1 Analysis of Box Girder Structures

The methods used for the analysis of box girder bridges range greatly in complexity. Some bridges may be designed using a two-dimensional frame model, with only a rough estimation of moment redistribution from creep. This type of bridge would be constructed by the span-by-span method and made continuous with closure pours at the piers or left as simple spans. Bending moments in the girders are dominated by positive moments from the construction as a simple span. In other box girder bridges, such as the three-span continuous bridge in Figure 5.5, the two-dimensional frame model would have to include provisions for creep and vertical displacements of the girder at the bearing locations. This bridge would be built by the balanced cantilever method, as indicated by the post-tensioning tendon profiles in the figure. Deflection calculations must include creep in order to construct the bridge to the correct geometry. The bending moments in the structure are tuned by continuity post-tensioning, bearing elevation changes, and redistribution from concrete creep. The two-dimensional frame model at the bottom of Figure 5.5 has nodes located at all the points needed for the application of dead loads and post-tensioning forces during construction and at enough points to accurately model the changes in cross section. The nodes are also located at the survey points used to track structural deflections during construction. The cross-sectional properties of bridges designed using a frame model are usually modified for shear lag effects using one of the design code recommended methods.

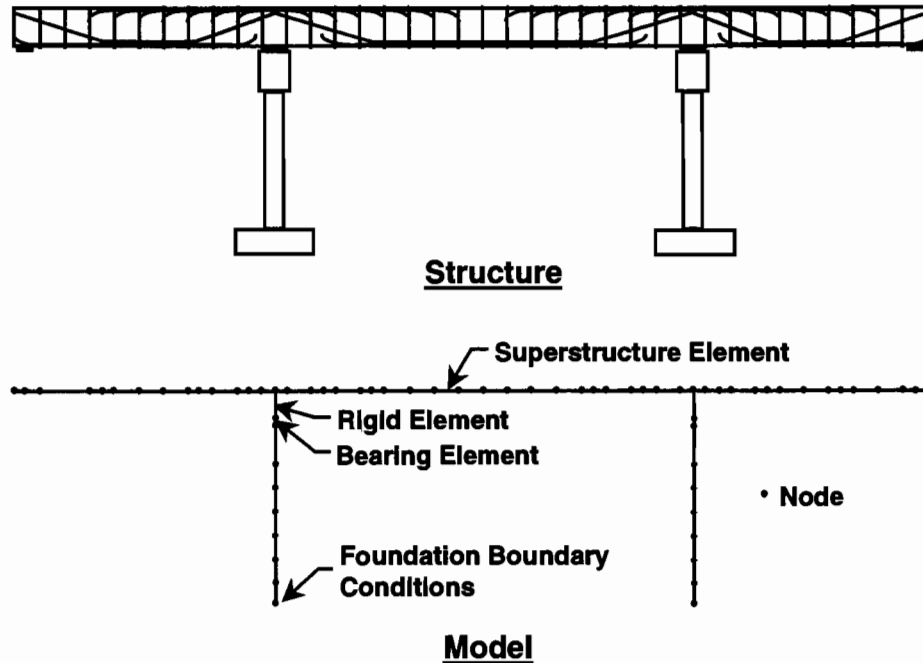


Figure 5.5 *Beam model of a box girder bridge*

Box girder bridges on a horizontal curve may have to be designed using a three-dimensional frame model, or a two-dimensional frame model with added consideration for the torsional moments. Torsion effects need not be considered when the factored torsional moment is less than one-third of the factored torsional cracking moment of the girder [8]. One problem with three-dimensional frame models of box girder bridges is that the center of gravity of the girder in bending most likely will not be at the shear center for the girder in torsion.

Box girders subjected to unsymmetrical loading or torsional loading can be analyzed using several techniques, including folded plate methods and analysis of the structure as a continuum. For some box girder bridges certain load cases can be solved by resolving the loads into the superposition of many loads. These individual load cases are easily solved using common design techniques. Figure 5.6 shows a box girder bridge consisting of two single-cell girders connected with a gore closure at their wing tips. The live-load case is symmetrical to the bridge as a whole, but will cause transverse bending, longitudinal bending and torsion in each of the girders. The loads and boundary conditions are modified into the superposition of six easily solved cases (cases 2, 4, 6, 8, 10 and 11).

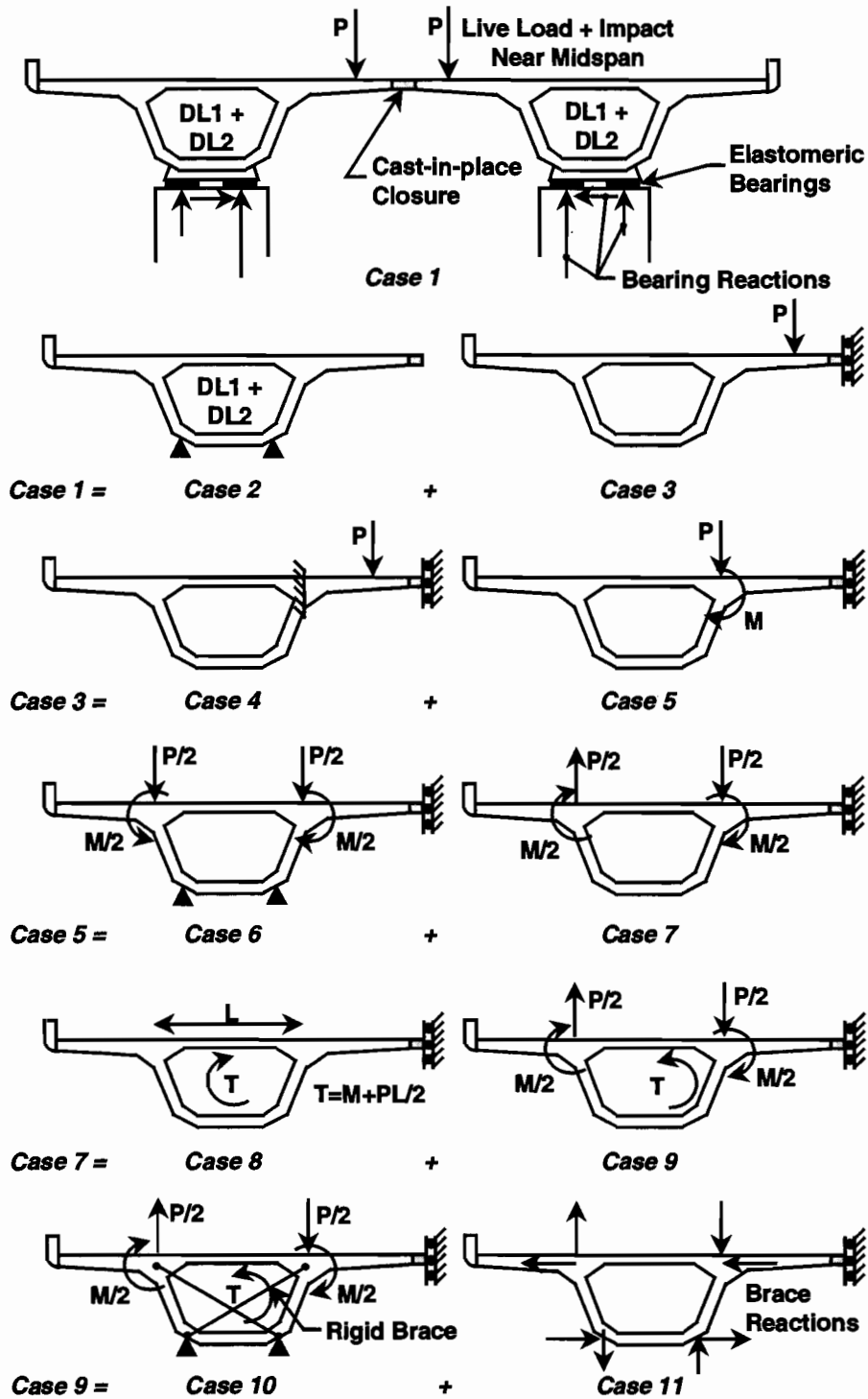


Figure 5.6 Analysis of twin single-cell box girders using superposition

Some bridges, because of their geometric complexity, can only be modeled accurately using a continuum model. In modern times, the finite element method has become the predominant method used to solve continuum models. The method lends itself to computerization because it inherently accepts the general case. The shape functions are always polynomials, not a family of custom functions used by other methods designed for hand solutions, so the stiffness matrix of each element is easily generalized. Also, the global stiffness matrix is directly assembled from the element stiffness matrices and is symmetric. General boundary conditions are easily applied after the matrix is assembled, unlike the finite difference method. The continuum is divided

into many finite elements, with a grid across the girder cross section and along the girder length. Figure 5.7 shows a bridge that may need to be designed using a finite element program. The bridge geometry includes a horizontal curve, skewed piers and bearings, and a light rail live load on one side. The girder is unsymmetrical with inclined webs and external post-tensioning. One benefit of using the finite element method is that stresses in the D-zones are known and can be used to develop STM for use in the design of the D-zones such as anchorage diaphragms.

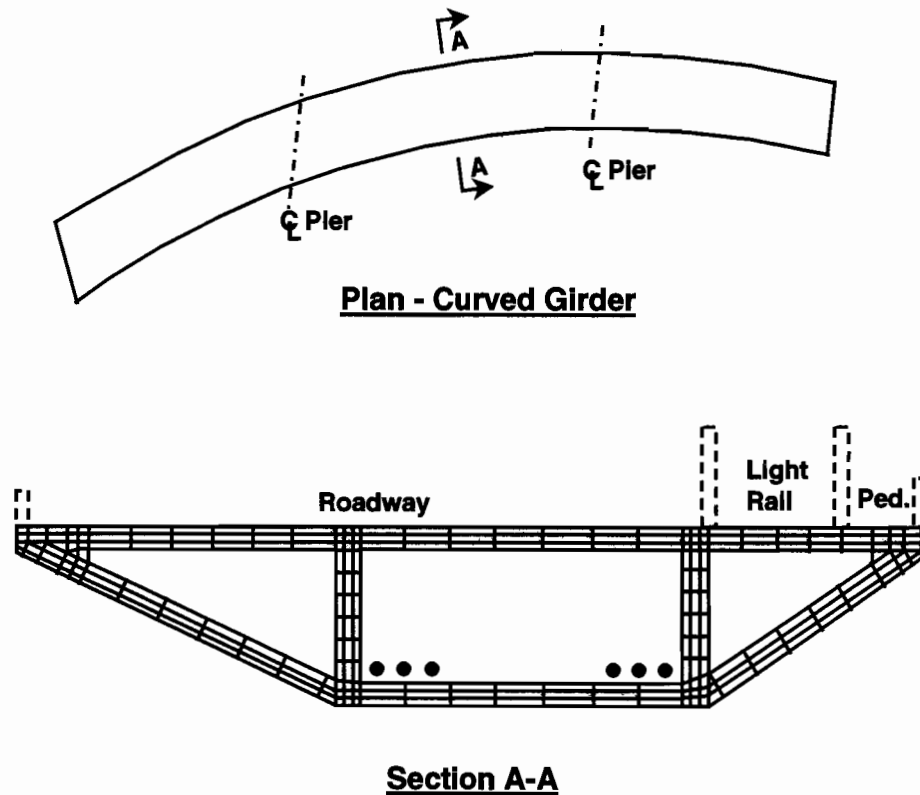


Figure 5.7 Finite element model of a box girder bridge

5.3.2 Design Code Methods of Analysis

Design codes, such as the *AASHTO Guide Specification for the Design and Construction of Segmental Concrete Bridges* [8], do not rigidly specify the method of analysis to be used by the engineer. However, design aids for analysis of a girder as a beam or part of a frame are given. To compensate for shear lag effects, an effective flange width method is given in the *AASHTO LRFD Bridge Design Specification* [9]. In this method, portions of the flanges are removed if the ratio of the flange width to effective span length exceeds 0.1. Figure 5.8 shows the modified shape of a flange after using the method for simple span, continuous and cantilever girders. The girder widths b_s and b_f are found by determining the original flange width b from Figure 5.9, dividing it by the effective span length l_e from Figure 5.8, then selecting values from the graph in Figure 5.10. The distance a is equal to b , the original flange width, but not to exceed $0.25l_e$, a quarter of the actual span length. This method tapers the flange width from b_f at the central part of the span to b_s near the piers, which may also be the case from a variable depth bottom flange. Other methods, such as the Ontario Highway Bridge Design Code method [43], use a step instead of a taper, somewhat simplifying section property calculations. Based on calculations and measurements by Roberts [10], the stepped flange width change simplifies calculations and is sufficiently accurate. Stress distributions in the flanges are determined using part c) of Figure 5.9 when using the AASHTO LRFD method. The extreme fiber stresses calculated using the modified section properties are assumed to be the maximum stresses and occur only over the width of the webs.

System		Pattern of b_m/b
Single-span Girder $l_1 = 1.0 l$		
Continuous Girder	End Span $l_1 = 0.8 l$	
	Interior Span $l_1 = 0.6 l$	
Cantilever arm $l_1 = 1.5 l$		

Figure 5.8 Pattern of effective flange width coefficients, b_f and b_s , (Figure 4.6.2.6.2-1 from the AASHTO LRFD Bridge Design Specifications [9])

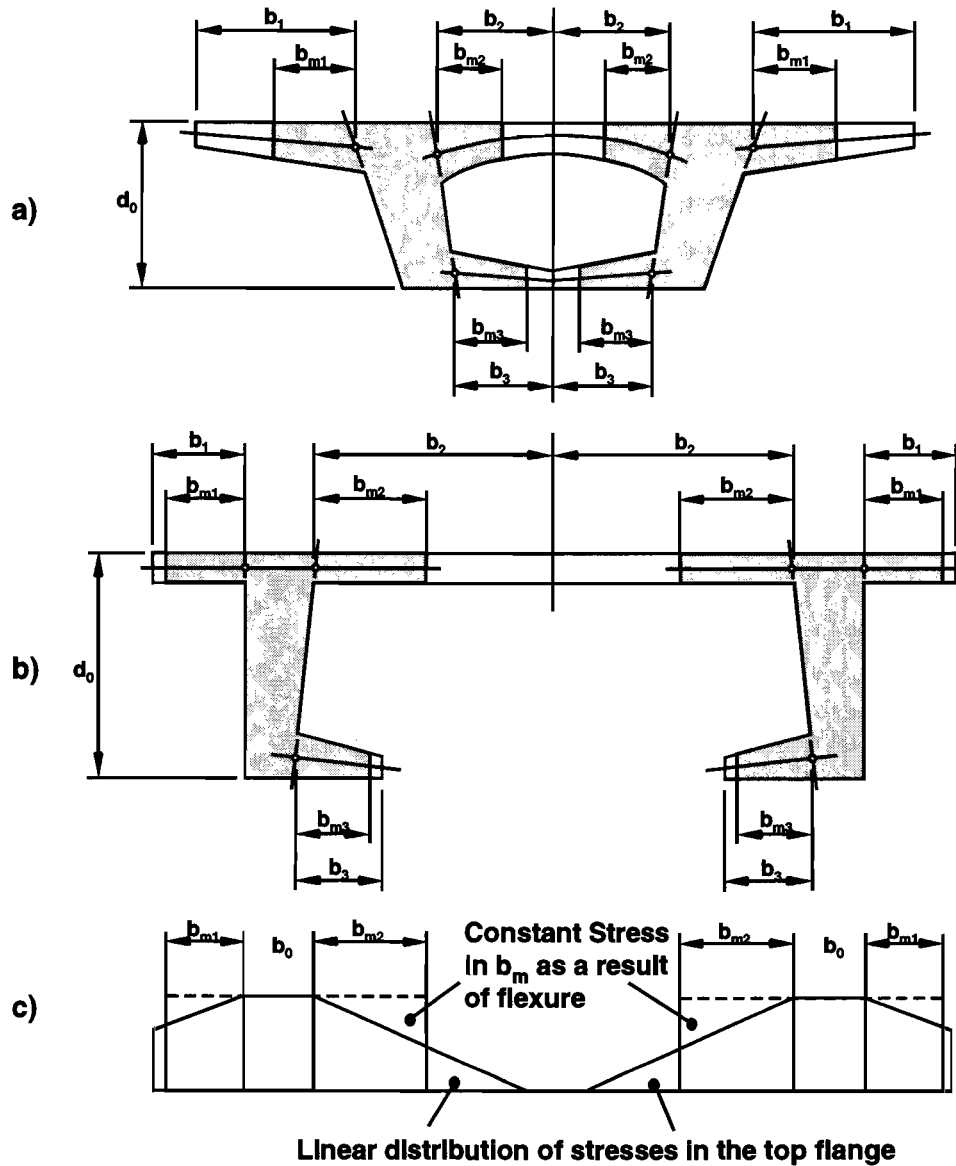


Figure 5.9 Cross sections and corresponding effective flange widths, b_m for flexure and shear (Figure 4.6.2.6.2-3 from the AASHTO LRFD Bridge Design Specifications [9])

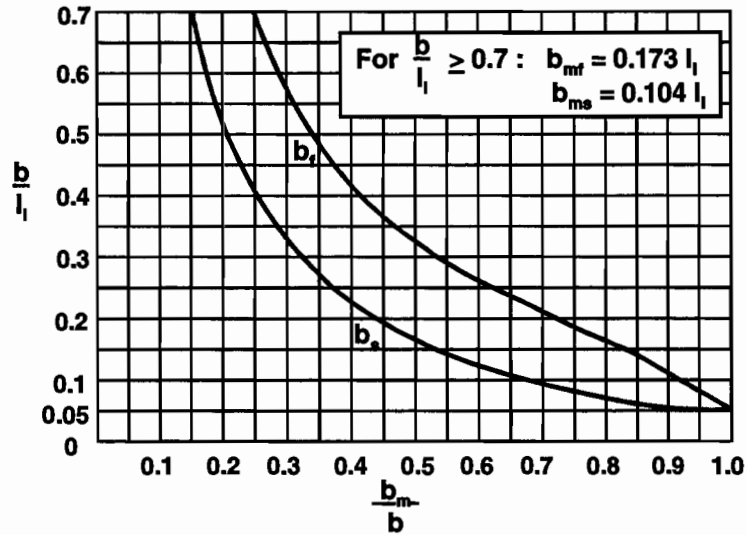


Figure 5.10 Values of the effective flange with coefficient b_m/b , for the given values of b/l_1 (Figure 4.6.2.6.2-2 from the AASHTO LRFD Bridge Design Specifications [9])

The suggested method in the AASHTO LRFD Bridge Design Specification [9] for determining the diffusion of post-tensioning forces is shown in Figure 5.11. The point loads are assumed to diffuse into the cross section within a 60° cone. This assumption means that for each distance b away from the point load, the diffusion has spread approximately to width b . The method makes calculations simple for determining the distance from the point load to a section of full diffusion. The method will not predict the actual stresses in the cross section at points closer to the point load. Figure 5.12 shows the actual distribution of stresses from two point loads on a double tee [44]. The distribution is nonlinear and produces significant transverse compressive and tensile stresses. The use of the AASHTO method for diffusion of point loads located away from the girder webs in the flanges or in a diaphragm also needs verification.

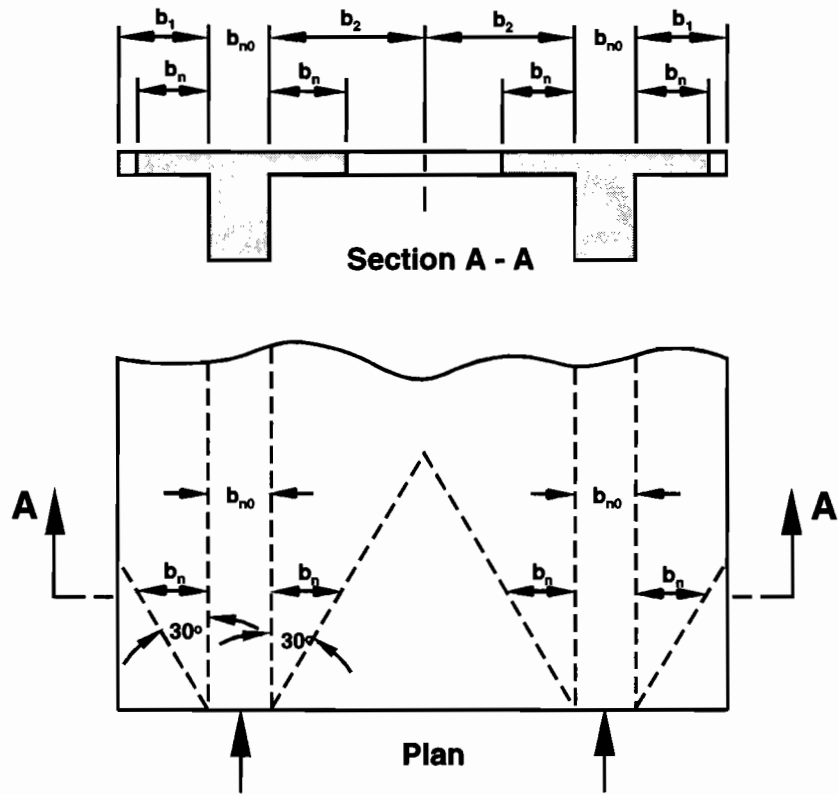


Figure 5.11 Effective flange widths, b_n for normal forces (Figure 4.6.2.6.2-4 from the AASHTO LRFD Bridge Design Specifications [9])

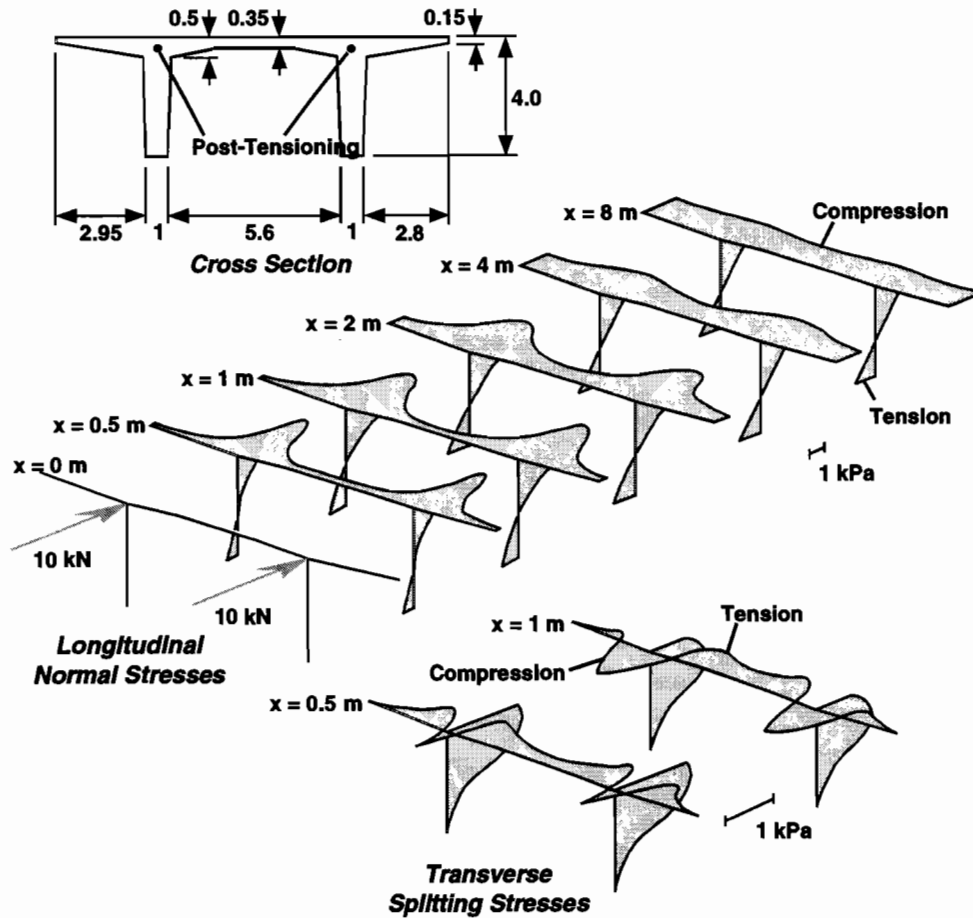


Figure 5.12 Example of the effects of the diffusion of post-tensioning forces (after Kristek [44])

5.3.3 Previous Measurements

Measurements by Roberts [10] on the box girders of the San Antonio Y were very similar to the measurements taken at US 183. The proportions of the girders tested at San Antonio were also similar to those at US 183. Measured stress distributions across flange widths were compared to stresses calculated using the AASHTO effective flange width method, beam theory with plane sections remaining plane, and a finite element computer program called SHLAG developed by Song and Scordelis [45]. The SHLAG program computes stress distributions with due consideration for shear lag in a generalized box girder cross section. Roberts found that using the beam theory approach would not predict the peak box girder stresses. On average the stresses calculated using beam theory were only 47% of the measured stresses. The AASHTO effective flange width method predicted stresses 72% of peak measured stresses on average. Roberts found the method needlessly complex and suggested another method that uses a stepped flange instead of the tapered flange of AASHTO. The SHLAG program gave the best prediction of peak stresses, at 84% of the measured peak stresses. In general, the measured stress distributions near the anchorage zones were highly irregular. Measured deflections of the girders tested were adequately predicted using the section properties from the AASHTO effective flange method.

5.4 DATA COLLECTION, ANALYSIS AND RESULTS

Measured strains, converted to stresses, and deflections were compared to results calculated using the AASHTO effective flange width method. The girders tested varied greatly in span-to-width ratio, so the effect of shear lag also varied greatly.

5.4.1 Mainlane Girder

Three-span continuous mainlane unit D2 was tested during the application of post-tensioning, dead load and live load. The central span of the unit, span D5, was instrumented with strain gauges at two cross sections. One section was near the anchorage segment, and the other section was at midspan. Deflections were measured in all three spans of the unit.

Post-Tensioning and Dead-Load Response

The post-tensioning tendon locations in span D5 are shown in Figure 5.13. Tendons were stressed immediately following the assembly of the segments on the erection trusses. Stressing began with the deviated external 19 - 15mm diameter strand tendons 1 through 6. These tendons were stressed in symmetrical pairs. Internal wing tendons 15 through 18 were stressed next to help control top flange tension during the stressing of the bottom slab tendons. The bottom slab internal tendons, also 19 - 15mm diameter strand tendons, were stressed last in symmetrical pairs. Measurements were taken at intervals during the entire post-tensioning sequence, including deflections.

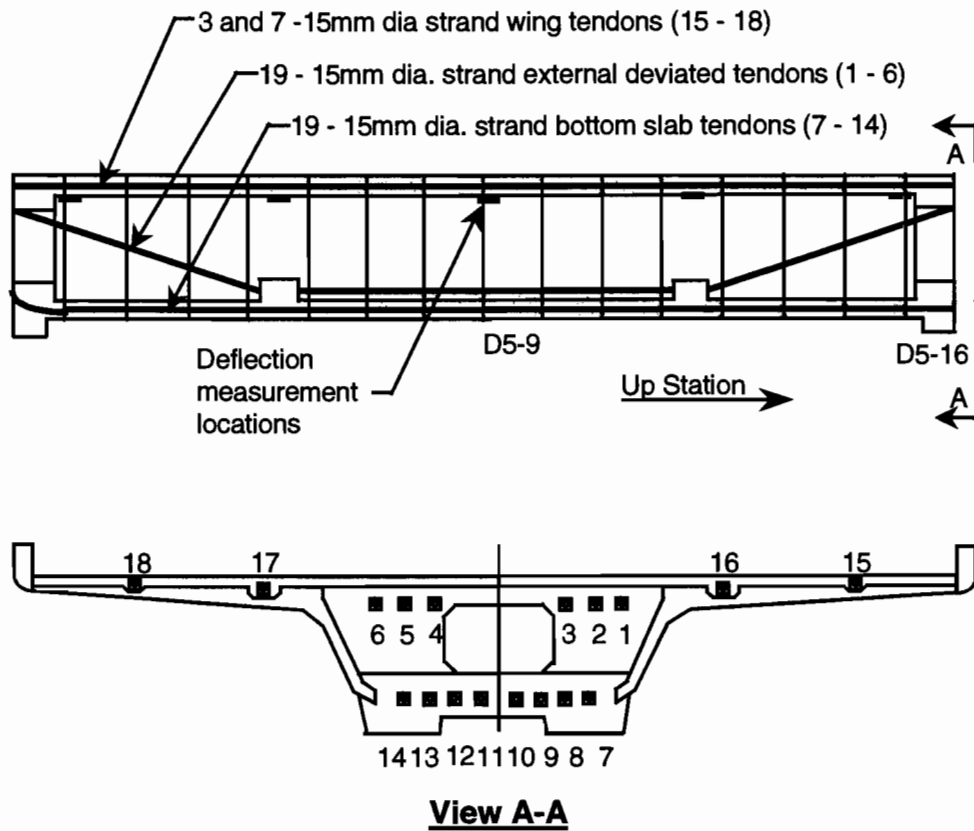


Figure 5.13 Mainlane girder D5 tendon locations

The measured longitudinal stresses in segment D5-16 from the post-tensioning of tendons 1 through 6, at the section immediately beyond the anchorage diaphragm, are shown in Figure 5.14. Strain gauges were located across the entire section, but are all plotted on the half section in the figure. Therefore, two stress changes may be shown at the same gauge location in the half section. Since the numerous jacks supporting the span continuously along its length were not adjusted during stressing, the stresses plotted include post-tensioning stresses and some dead-load stresses. The measured top flange stresses in Figure 5.14 indicate that little diffusion of the post-tensioning forces has occurred at this cross section, which was 1525mm from the anchor plates. Tendons 1 and 6 caused higher stresses toward the wing of the girder, and tendons 3 and 4 caused higher stresses toward the center of the girder, as would be expected. The heavy end diaphragm containing the anchorages was able to distribute compressive force to the middle of the bottom slab. Stress changes were

small in the bottom slab where the slab meets the web. From inspection of the lower plot in Figure 5.14, plane sections did not remain plane through the height of the web.

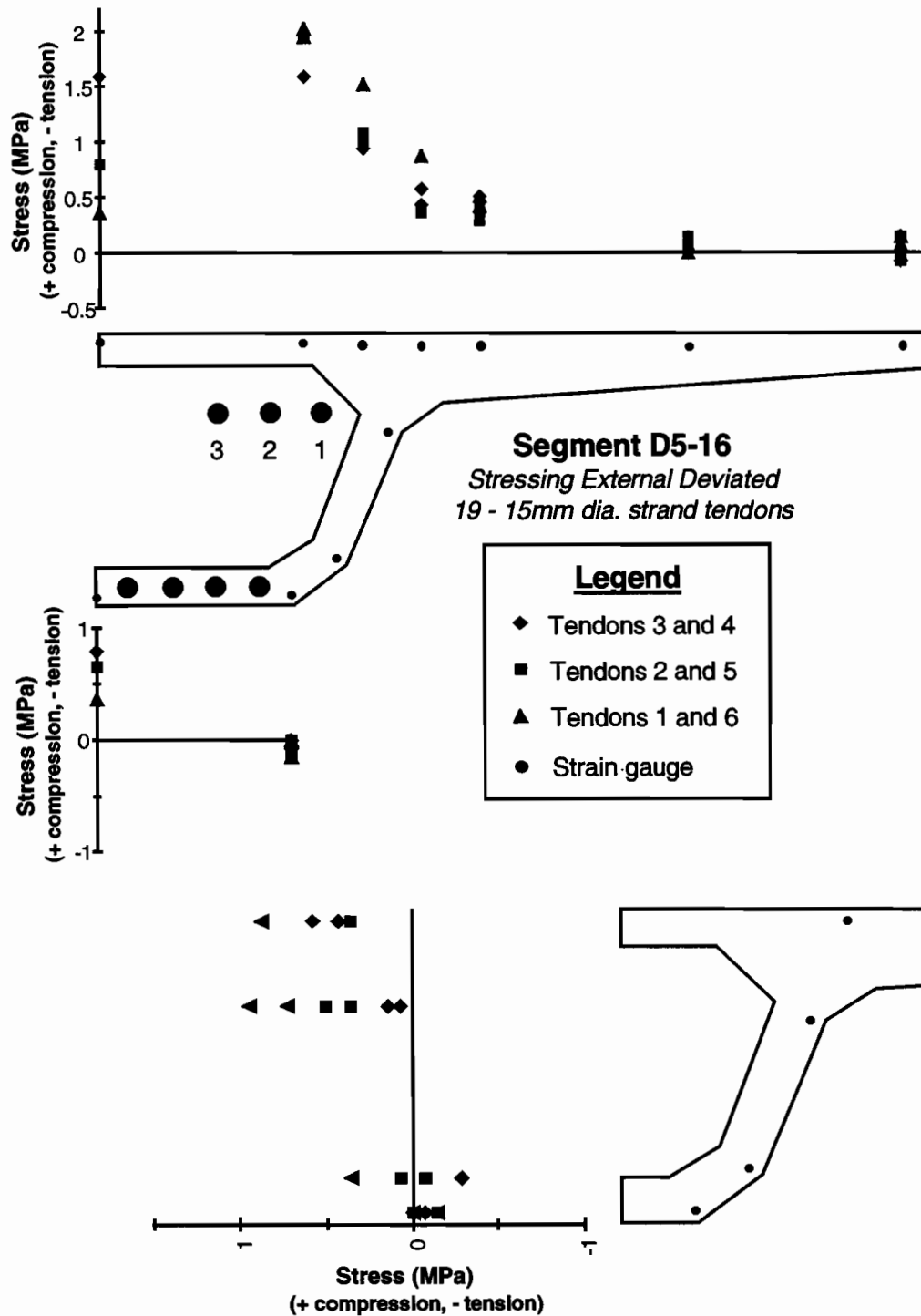


Figure 5.14 Longitudinal stresses in segment D5-16 from the tensioning of external tendons 1 through 6

Figure 5.15 shows the measured longitudinal stresses in midspan segment D5-9 from the tensioning of external tendons 1 through 6. The stresses are much more uniform across the width of the flanges at this section than in segment D5-16. The lower plot in Figure 5.15 also indicates that plane sections remained plane through the height of the web. The magnitude of the measured stresses was slightly greater when tendons 1 and 6 were

stressed than when tendons 3 and 4 were stressed. Tendons 1 and 6 were located closer to the girder webs, and therefore had a shorter distance to full diffusion of their post-tensioning force into the cross section. As a result, tendons 1 and 6 were more effective in producing negative bending moments in the girder to balance positive dead-load bending moments.

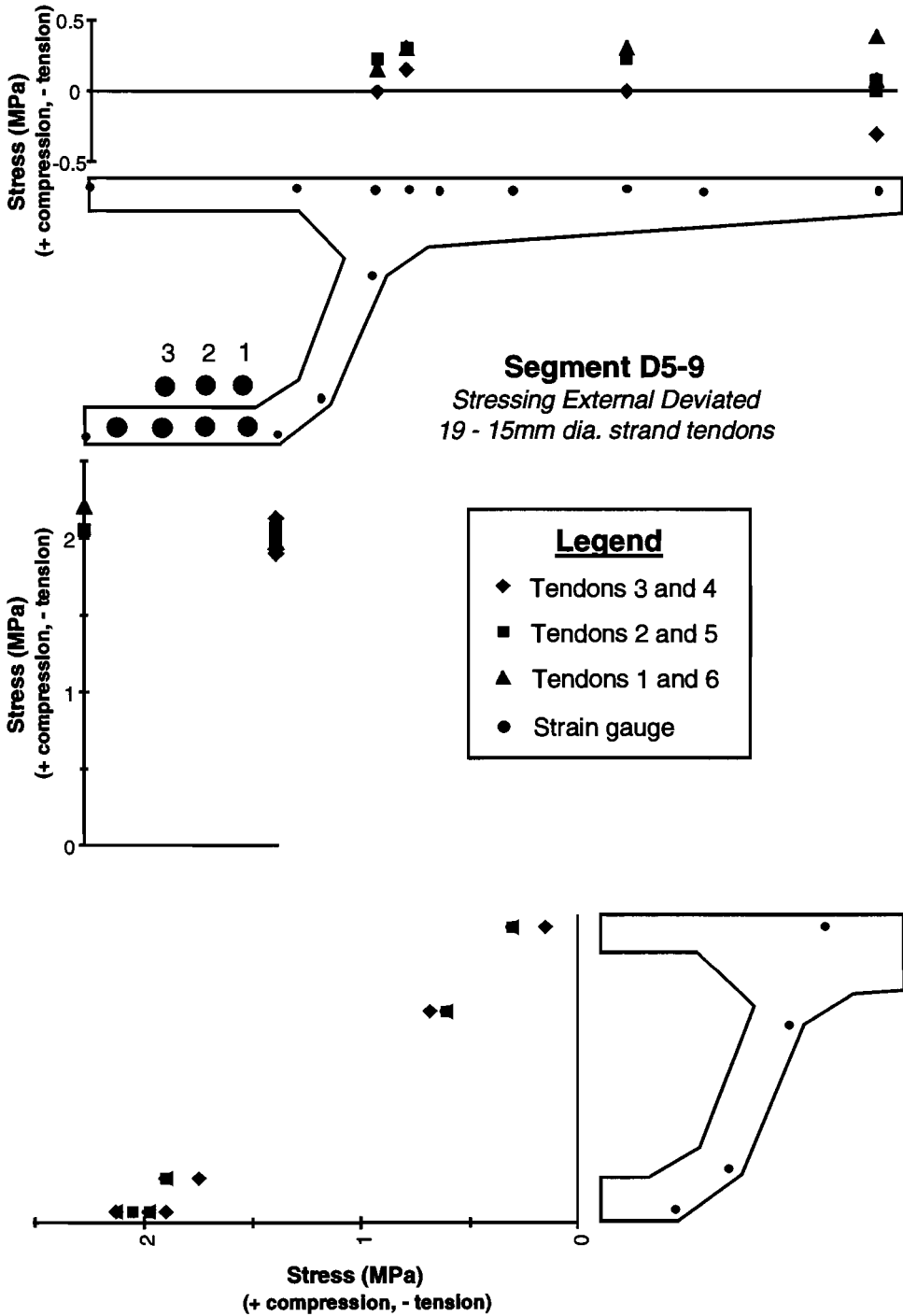


Figure 5.15 Longitudinal stresses in segment D5-9 from the tensioning of external tendons 1 through 6

Measured cross-sectional stress changes in segment D5-16 from the stressing of the eight bottom slab internal tendons are plotted in Figure 5.16. The plots adjacent to the half sections in the figure show stresses measured

on both sides of the cross section. The bottom slab internal tendons were stressed symmetrically in pairs. The gauges that measured the strains were located 1690mm from the anchorage plates and 75mm beyond the heavy end diaphragm in the typical cross section of the girder. The stress changes in the top flange were small compared to the stress changes in the bottom slab, as would be expected given the location of the tendons. The top flange stresses were higher over the webs and lower in the center of the top slab and toward the wing tips. The measured stress changes in the bottom slab were as high as 6.8MPa at the center of the bottom slab. The stresses' changes caused by the stressing of each pair of tendons was not uniform across the width of the bottom slab. The heavy end diaphragm had a large access hole located at the center of the cross section, as can be seen in Figure 2.40. The diaphragm was more effective in distributing stresses across the width of the bottom flange when tendons away from the access hole, such as 7 and 14, were stressed. The stress gradient across the width of the bottom slab from the stressing of tendons 10 and 11 was quite large at 4.9MPa. The stresses plotted at the bottom of Figure 5.16 down the depth of the webs indicate that plane sections were not remaining plane at this cross section. The stresses down the web depth were much closer to linear when tendons 7 and 14 were stressed than the other tendons. Tendons 7 and 14 were located near the bottom of the web.

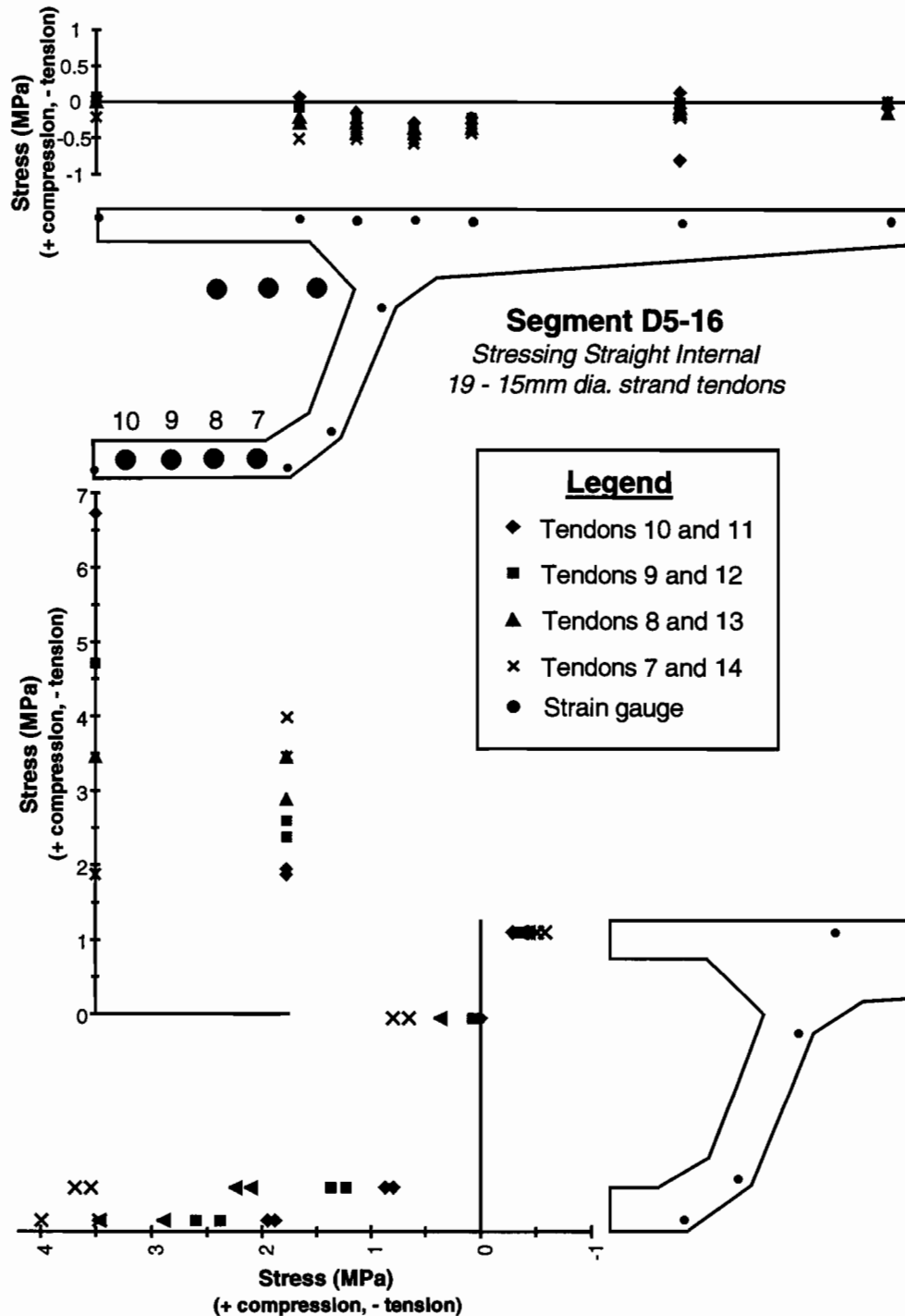


Figure 5.16 Longitudinal stresses in segment D5-16 from the tensioning of internal bottom flange tendons 7 through 14

Measured cross-sectional stress changes in segment D5-9 from the stressing of the eight bottom slab internal tendons are plotted in Figure 5.17. These stresses in segment D5-9 near midspan include some dead-load stresses, as well as the post-tensioning stresses. The plots in the figure show that the post-tensioning stresses were well distributed and linearly distributed down the depth of the webs. A small stress gradient remained across the width of the bottom slab. Based on inspection of all three plots in Figure 5.17, all the tendons appear to be equally effective in producing negative moment at midspan.

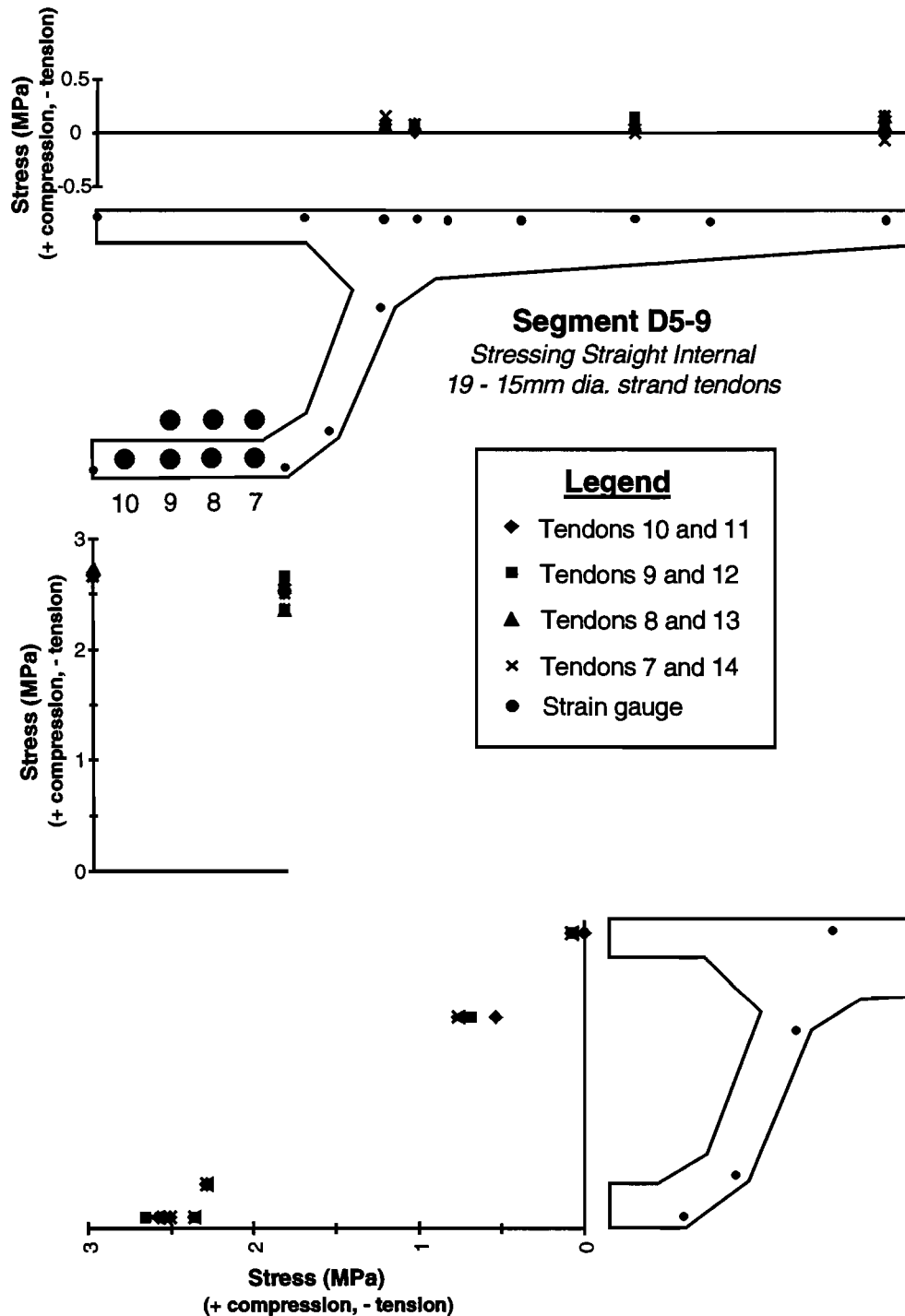


Figure 5.17 Longitudinal stresses in segment D5-9 from the tensioning of internal bottom flange tendons 7 through 14

Figure 5.18 gives a summary of the measured post-tensioning stresses in segment D5-16 at the instrumented cross section. The stresses are plotted by tendon group, including the internal wing tendons. The total stresses in the top flange were dominated by the stresses from the external deviated tendons 1 through 6. Bottom flange stresses were dominated by the stresses produced from the internal bottom slab tendons. Compressive stresses at the center of the bottom slab were very high at 49% of the design compressive strength of the concrete. A high stress gradient was measured across the width of the bottom flange. No tension was indicated at this cross

section from post-tensioning forces, although, without the wing tendons, tension would have occurred in the wings. The application of dead load would change the measured stresses in Figure 5.18 very little, since the dead-load moment was small so close to the girder bearings. A summary of the stresses in segment D5-9 produced by all the tendons is shown in Figure 5.19. The post-tensioning stresses appear to be well distributed across the cross section and nearly linear down the depth of the webs. No tension was indicated at any point in the cross section, even though the girder had not been released from the erection truss. Tension might have been expected in the top flange near midspan since the girder dead load was not applied incrementally as tendons were stressed.

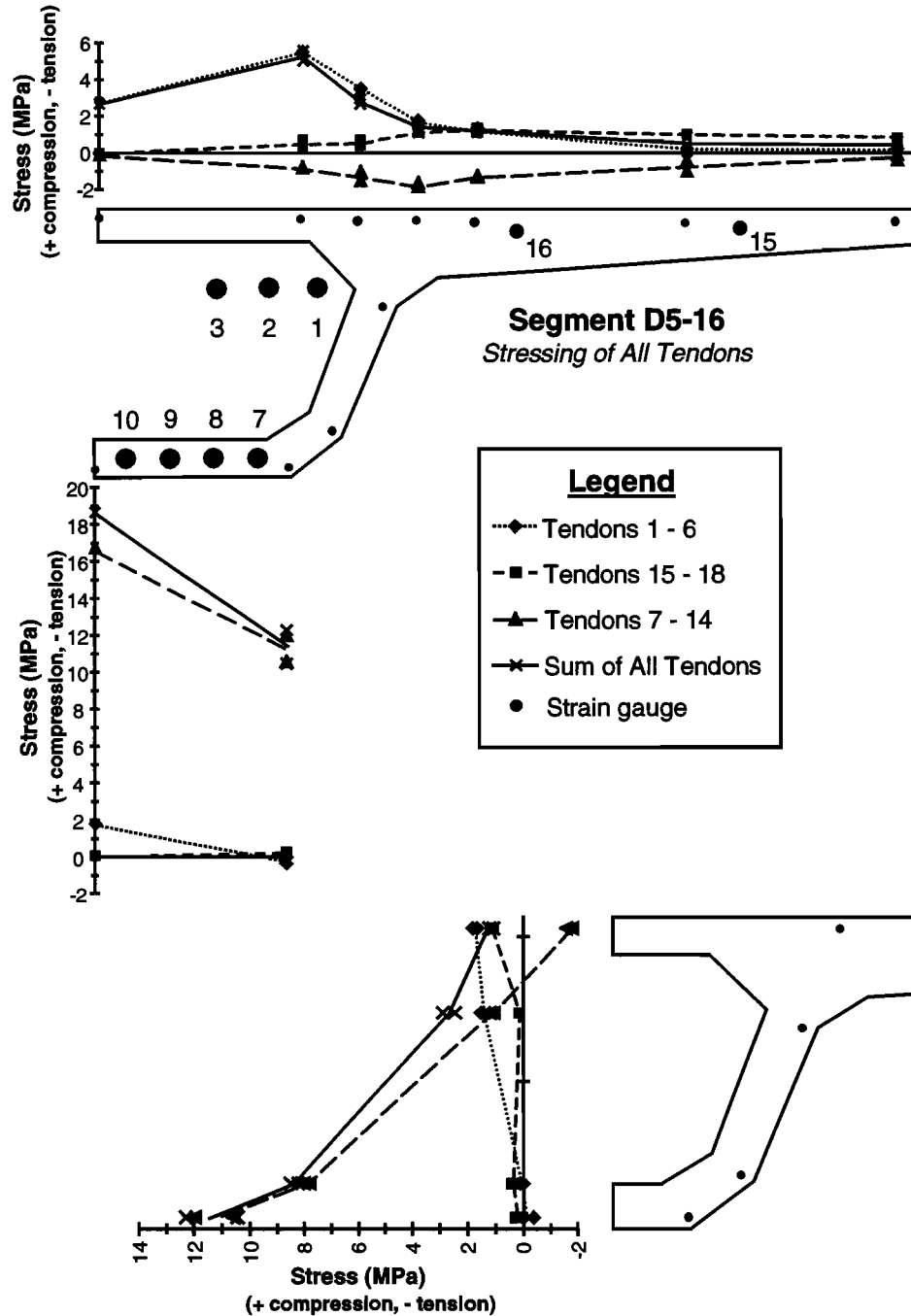


Figure 5.18 Longitudinal stresses in segment D5-16 from the tensioning of bottom flange, wing and external tendons 1 through 18

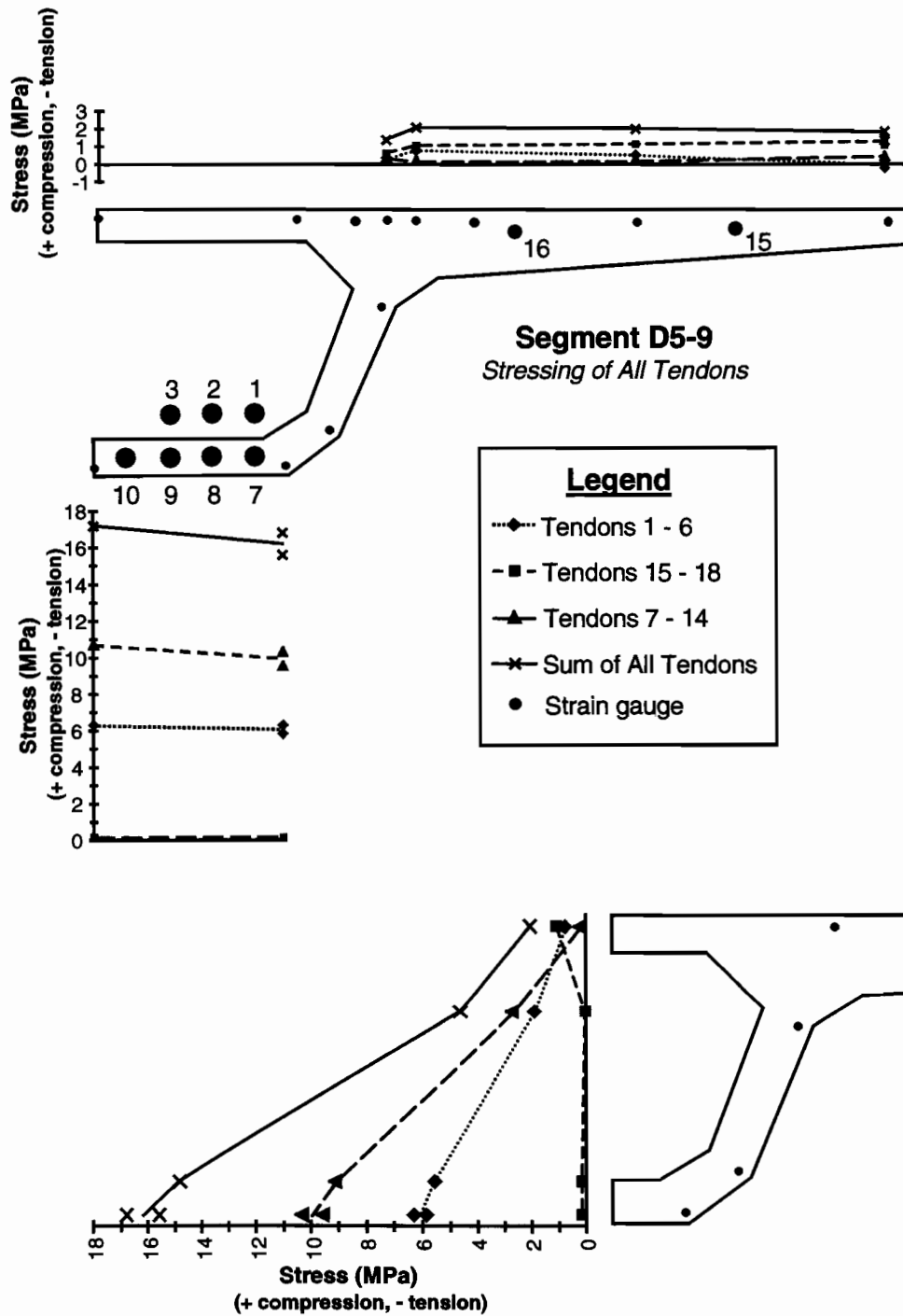


Figure 5.19 Longitudinal stresses in segment D5-9 from the tensioning of bottom flange, wing and external tendons 1 through 18

Measured stresses from post-tensioning forces and the full dead-load moment for segment D5-16 are plotted in Figure 5.20. These measurements were taken several hours after the completion of post-tensioning operations. The measured stresses in the top flange indicate that some tension might have existed at points over the webs. The large stress gradient over the width of the bottom slab remained unchanged although the magnitude of the bottom flange stresses decreased about 1MPa. Dead-load and post-tensioning stresses were calculated using the AASHTO [8] effective flange width method and 30° diffusion of post-tensioning force method. The results from this analysis are plotted as the solid lines in Figure 5.20. Post-tensioning forces were only assumed to be active

within a 60° cone propagating from the anchorage plate. Therefore, the plotted stresses look like a step function. A designer could have assumed a smoother distribution of post-tensioning stresses based on these calculated results. In general, the calculated results indicated less diffusion of post-tensioning forces than was measured. The presence of the heavy end diaphragm may have had an influence on the diffusion. The overall shape of the stress distribution in the top flange was predicted well by the calculation, although the magnitude of the peak-calculated stresses was much too high. The measured stress gradient across the width of the bottom slab was poorly predicted by the 30° diffusion method.

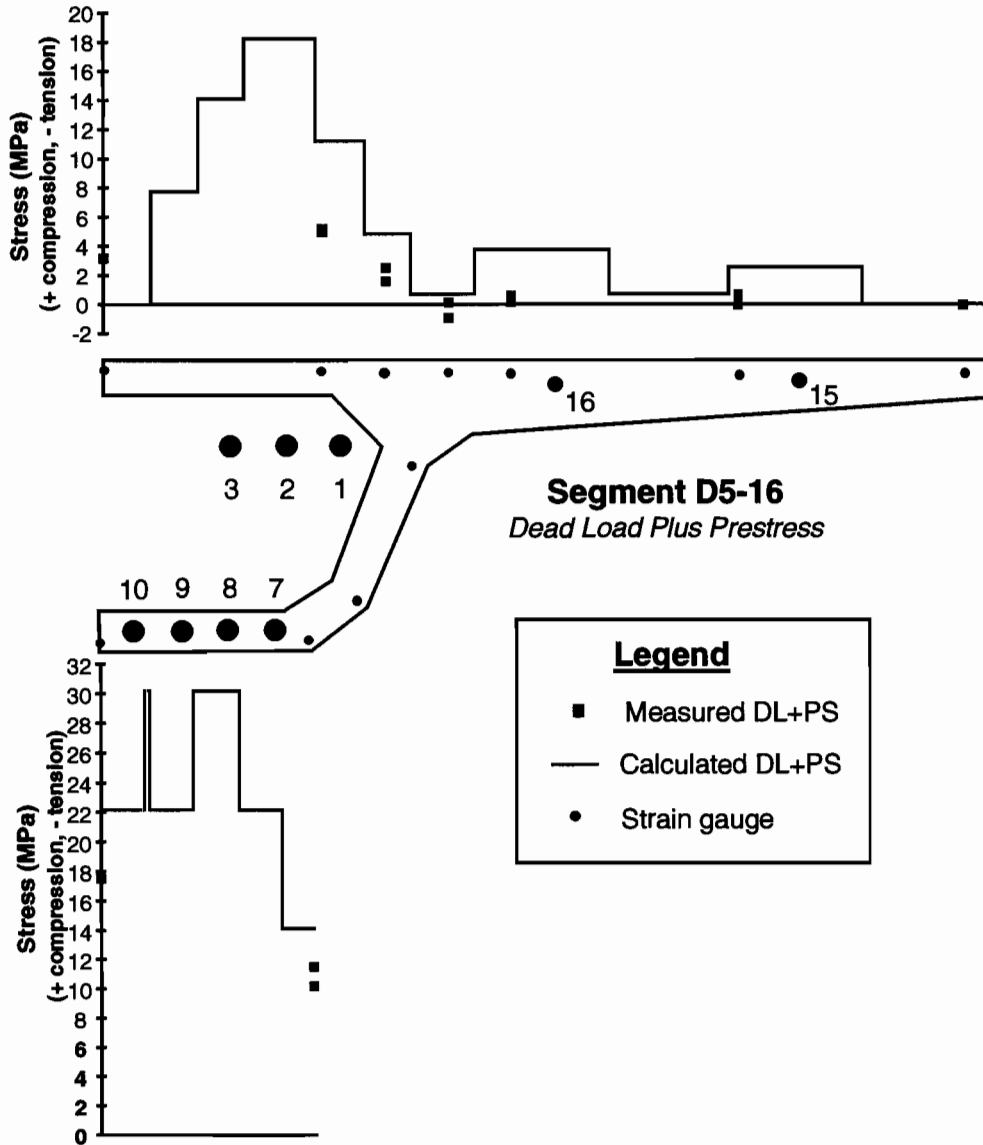


Figure 5.20 Measured and calculated longitudinal stresses in segment D5-16 from post-tensioning and dead load

The measured and calculated post-tensioning and dead-load stresses in segment D5-9 near midspan are shown in Figure 5.21. The AASHTO effective flange width method used in the calculation predicted the measured stresses quite accurately, although the measurements show more compression in the top flange and less compression in the bottom flange. The neutral axis of the girder was probably slightly lower in the cross section than predicted by the calculation.

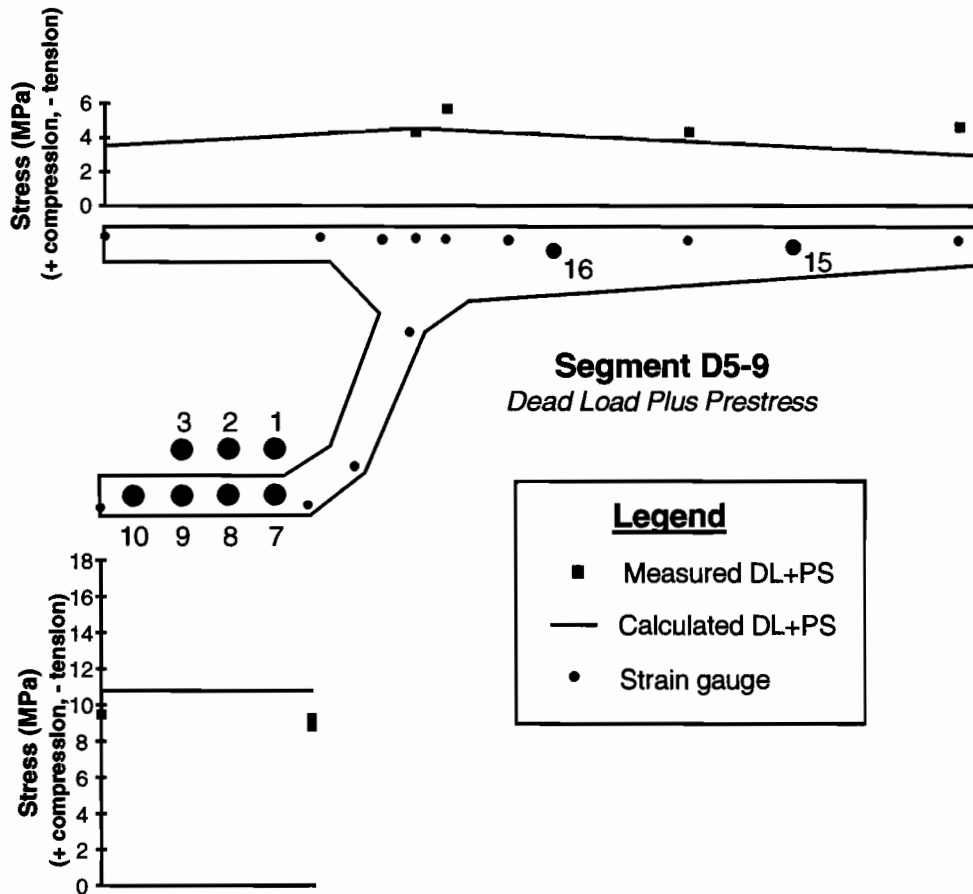


Figure 5.21 Measured and calculated longitudinal stresses in segment D5-9 from post-tensioning and dead load

Measured deflections from the construction of the three spans of unit D2 are plotted in Figure 5.22. The camber from prestressing gives an indication of the effectiveness of each post-tensioning tendon. Based on the measured deflections in Figure 5.22, the tendons located closer to the webs were slightly more effective in cambering the girders. Some variation in deflection occurred among the three spans from the application of post-tensioning and dead load. This variation could be expected since the force in the numerous hydraulic jacks supporting the segments on the truss were not monitored or adjusted during post-tensioning. Therefore the percentage of dead-load moment present during the different post-tensioning stages was not known and not easily predicted. The change in deflection from the point in time at which all tendons were stressed with the girder remaining partly on the truss, and on April 7, 1995, when all dead load had been applied indicates that dead load was not applied consistently during post-tensioning. Span D6 showed the greatest deflection change, an upward camber, and span D4 showed the least. Since the total estimated dead-load deflection was 36mm, or 1/1050 of the span length, the percentage of the total dead load applied immediately following post-tensioning was between 21% and 33% for the instrumented spans. The bridge design did not specifically call for the control of the application of dead load during post-tensioning of these spans. The erection trusses were much less stiff than the concrete girder, so the trusses deflected upward during post-tensioning without much loss in the dead-load moment they were carrying. The hydraulic jacks located on top of the truss, three supporting each segment, were locked off prior to post-tensioning so their force could not be monitored or adjusted. Camber in the girders decreased between April 7, 1995, and October 4, 1995, by about 25%. At noon on a hot day the following summer, July 11, 1996, the camber had increased 40% from the October 4, 1995, measured camber because of a positive thermal gradient.

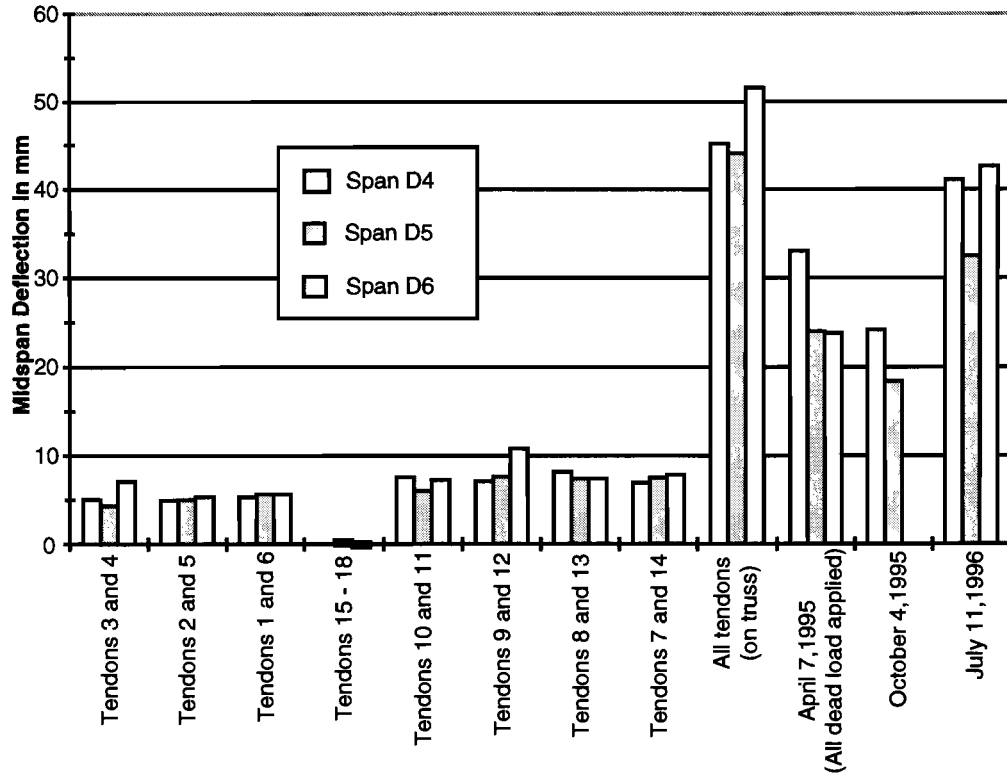


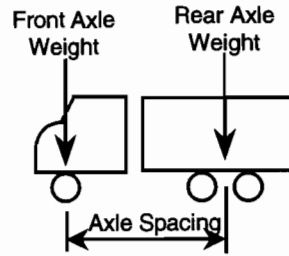
Figure 5.22 Deflections from post-tensioning and dead load (+ deflection is camber)

Live-Load Test

A live-load test was performed on the mainlane unit D2 using six dump trucks. The trucks were loaded, such that when they were placed back to back at the center of a span, the peak live-load moment produced was identical to that from an HS20-44 truck. The weights and dimensions of these trucks are given in Table 5.1. The trucks were placed both symmetrically and unsymmetrically with respect to the centerline of the bridge in three lanes. The plan view of the six live-load cases for the mainlane are shown in Figures 5.23 and 5.24.

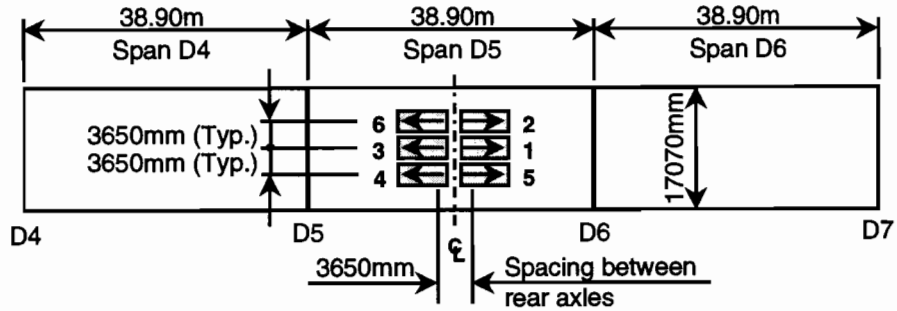
Table 5.1 Axle weights and spacing for live-load test trucks on Unit D2

Truck	Weight of Rear Axles (kN)	Weight of Front Axles (kN)	Total Weight (kN)	Axle Spacing (mm)
1	122.5	43.1	165.6	5030
2	132.0	39.6	171.6	4850
3	119.6	44.4	164.0	4890
4	119.1	40.8	159.9	4090
5	135.1	39.0	174.1	4720
6	119.7	44.1	163.8	4360

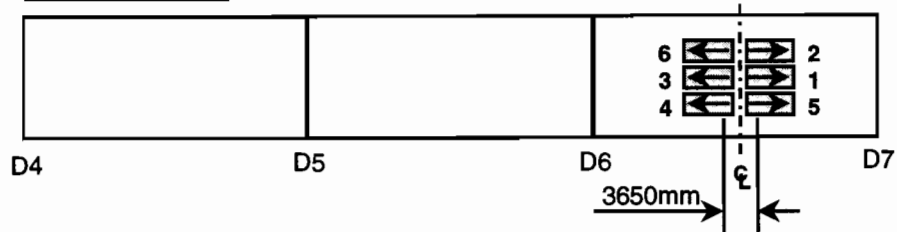


Live Load Case 2

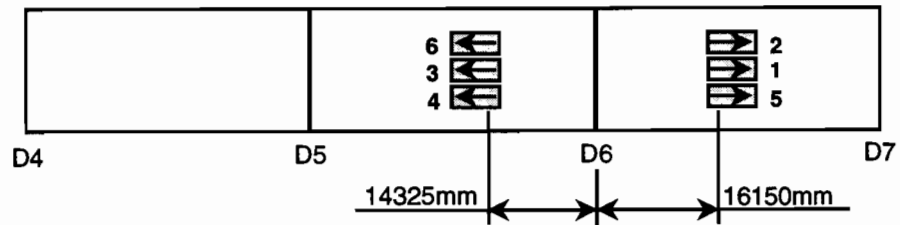
Typical Truck



Live Load Case 3



Live Load Case 5



Live Load Case 6

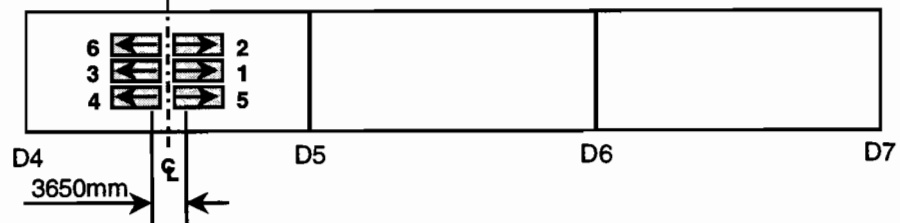


Figure 5.23 Live-load cases – Mainlane girders D4, D5 and D6

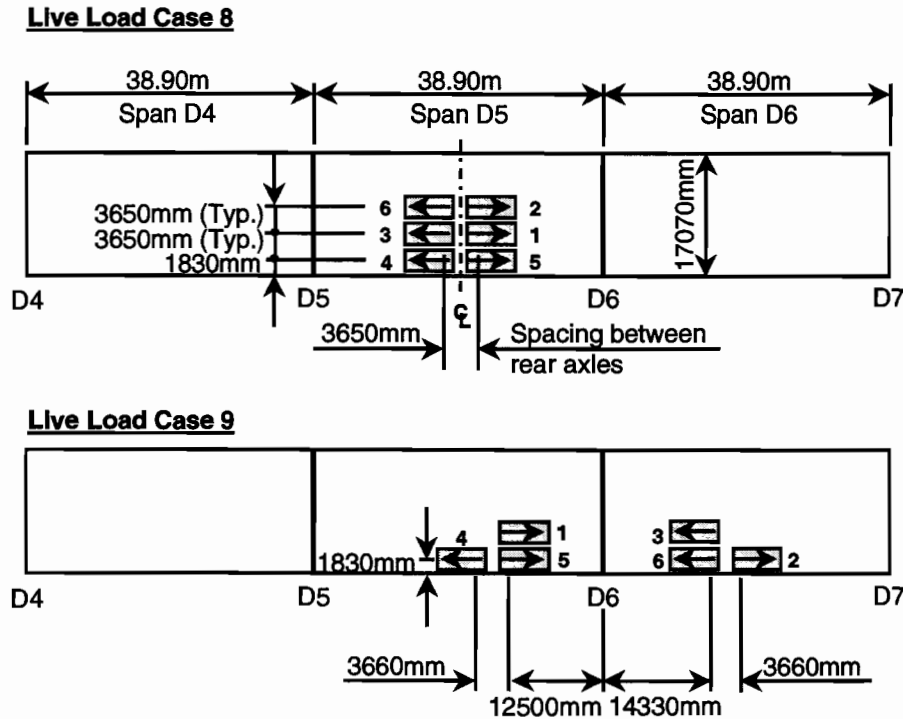


Figure 5.24 Live-load cases – Mainlane girders D4, D5 and D6 (continued)

The measured and calculated stresses in segment D5-9 for live-load case 2 are given in Figure 5.25. Live-load case 2 was a symmetric loading on span D5 intended to produce a maximum positive moment. The measured stresses are lower than the stresses predicted using the AASHTO effective flange width method. The measured stresses were calculated from the measured strains using the elastic moduli found from the test prisms described in Chapter 2. These elastic moduli were consistently found to be less than that of the actual moduli of the concrete in the girders. The measured stresses down the girder web in Figure 5.25 were nearly linear, with a neutral axis slightly below that predicted by the calculation. Also the distribution of measured stresses across the width of the top flange was nearly uniform. Since integration of the measured stresses over the cross-sectional area must result in a live-load moment equal to that applied, the modulus used to find the measured stresses from the measured strains must have been too small. The measured stresses were also less than the calculated stresses because the stiffness from the external deviated tendons was not included in the analysis. Stresses from load case 8 in segment D5-9 are shown in Figure 5.26. The measured stresses were nearly identical to those measured during load case 2 even though the load case was unsymmetric. Stresses measured in the right web, the web most directly under the live load, and the right top and bottom flanges were only 10% to 15% larger than those measured in load case 2. The calculated stresses shown for load case 8 are the same as for the symmetrical load case 2. An accurate calculation for the longitudinal cross-sectional stresses in the girder for the unsymmetrical load case would be very difficult. The actual web shear from torsion bending was effected by the connection of the top flange of the loaded girder to the adjacent girder flanges and the stiffness of the elastomeric bearings. The torsional moment may have been taken by all three spans of the unit. Therefore, for purposes of comparison, the calculated stresses for load case 2 were plotted in Figure 5.26.

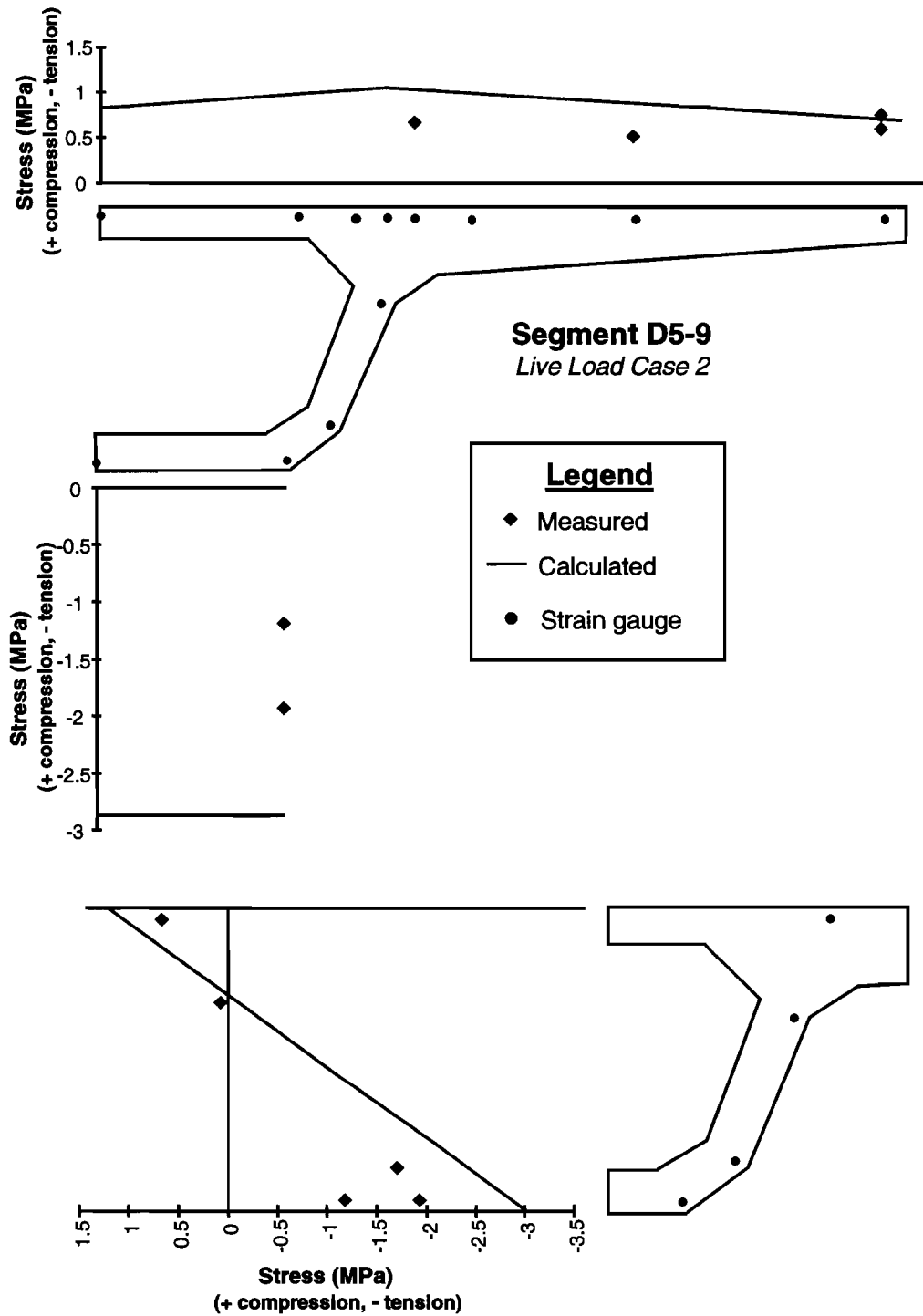


Figure 5.25 Longitudinal stresses from load case 2

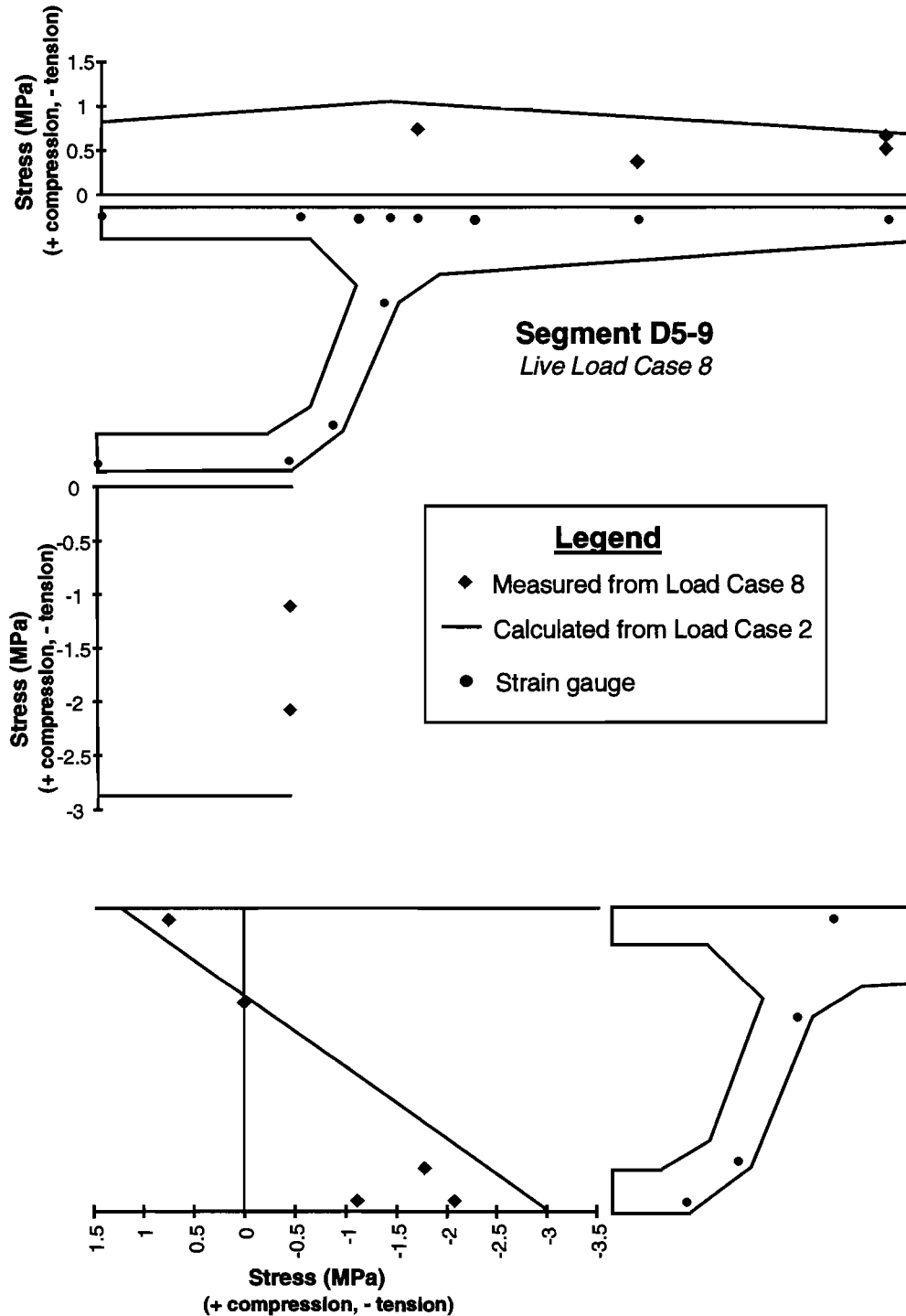


Figure 5.26 Longitudinal stresses from load case 8

Deflections were measured during all live-load cases using the taunt wire baseline deflection measuring system described in Chapter 2. The deflection of the bearings was not included in the presented deflections in the following figures. Figure 5.27 shows a plot of the measured deflections and deflections calculated using the AASHTO effective flange width method for live-load case 2. The calculated deflection was only 10% greater than the measured deflection. The difference between the calculated and measured stresses in Figure 5.25 would have predicted greater error in the deflection calculation than 10%. The deflections for load case 3 shown in Figure 5.28 gave nearly identical results. Load case 2 and load case 3 were maximum positive

moment cases for spans D5 and D6 respectively. Deflections in the unloaded spans during live-load cases 2 and 3 were essentially negligible, at less than 0.5mm at all but one point. The maximum measured midspan deflections in cases 2 and 3 were only 1/6300 of the span length.

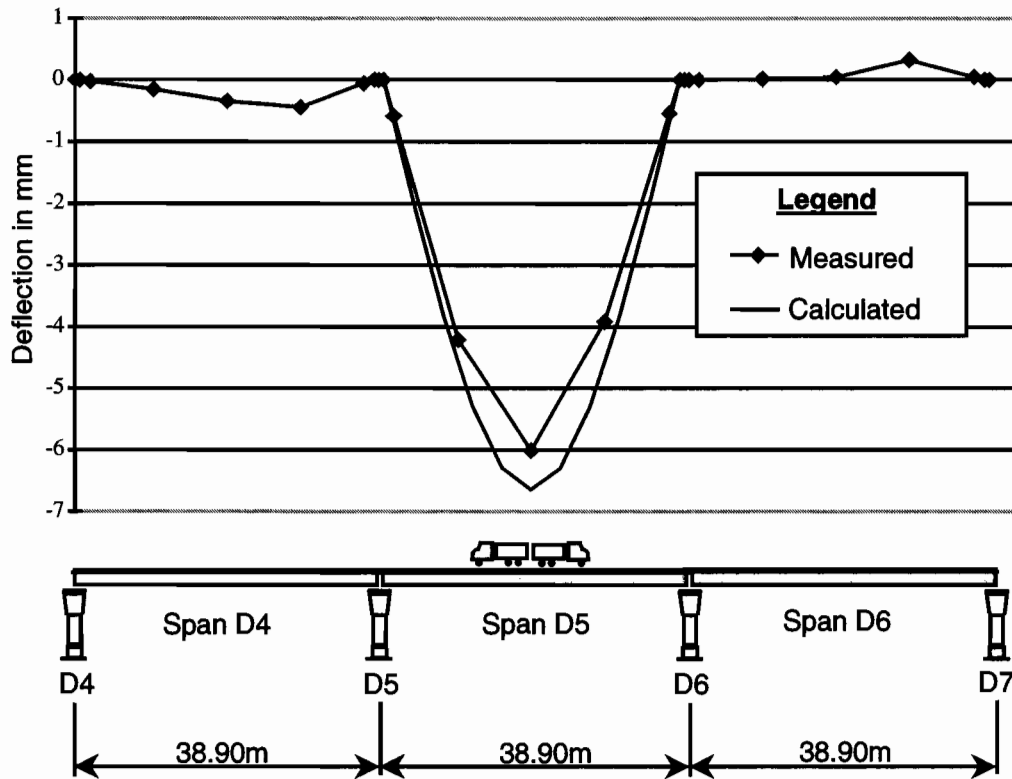


Figure 5.27 Deflections from load case 2

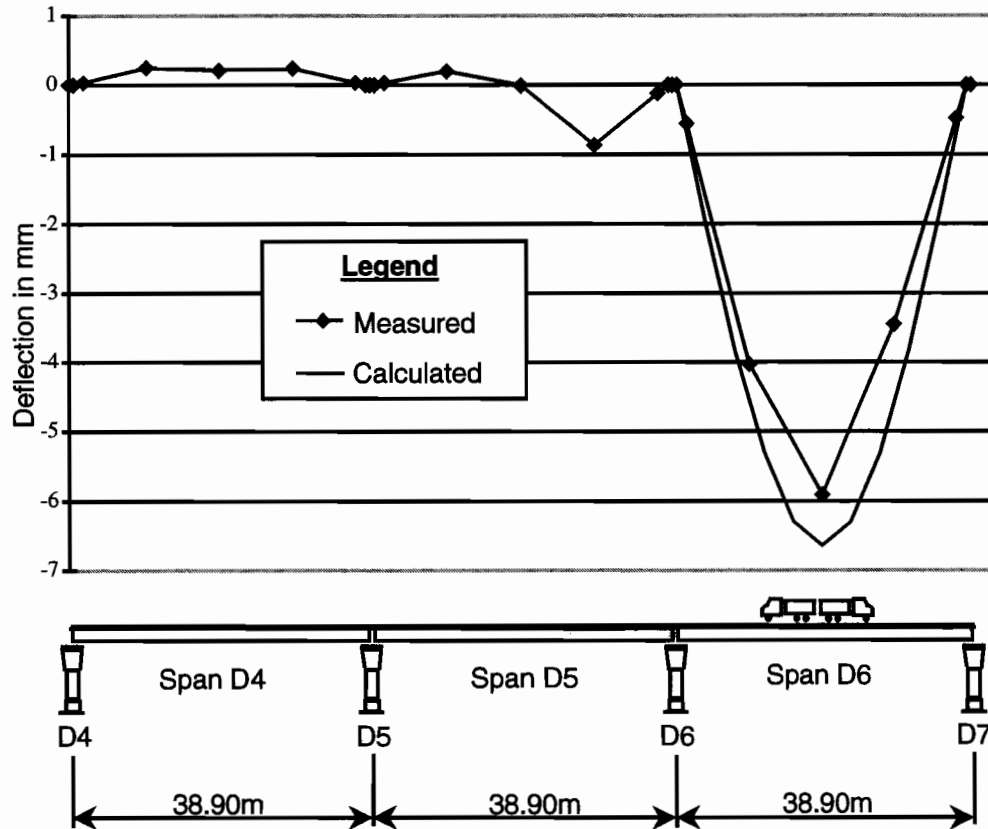


Figure 5.28 Deflections from load case 3

The test truck arrangement for load case 5 was intended to produce a negative moment couple over pier D6 between the cast-in-place deck joint and the elastomeric bearings. The deflections for load case 5 are plotted in Figure 5.29. The calculated and measured deflections were nearly identical. The deflection calculation assumed that each of the loaded spans acted as a simple span. Based on the differences between the calculated and measured deflections in load cases 2 and 3, the measured deflections for load case 5 appear to be somewhat high. The deflected shape of the spans also appears to be almost triangular. The presence of the front wheels of the test trucks immediately adjacent to the deflection measuring plates at midspan may have increased the measured midspan deflections over the actual average midspan deflections of the girders.

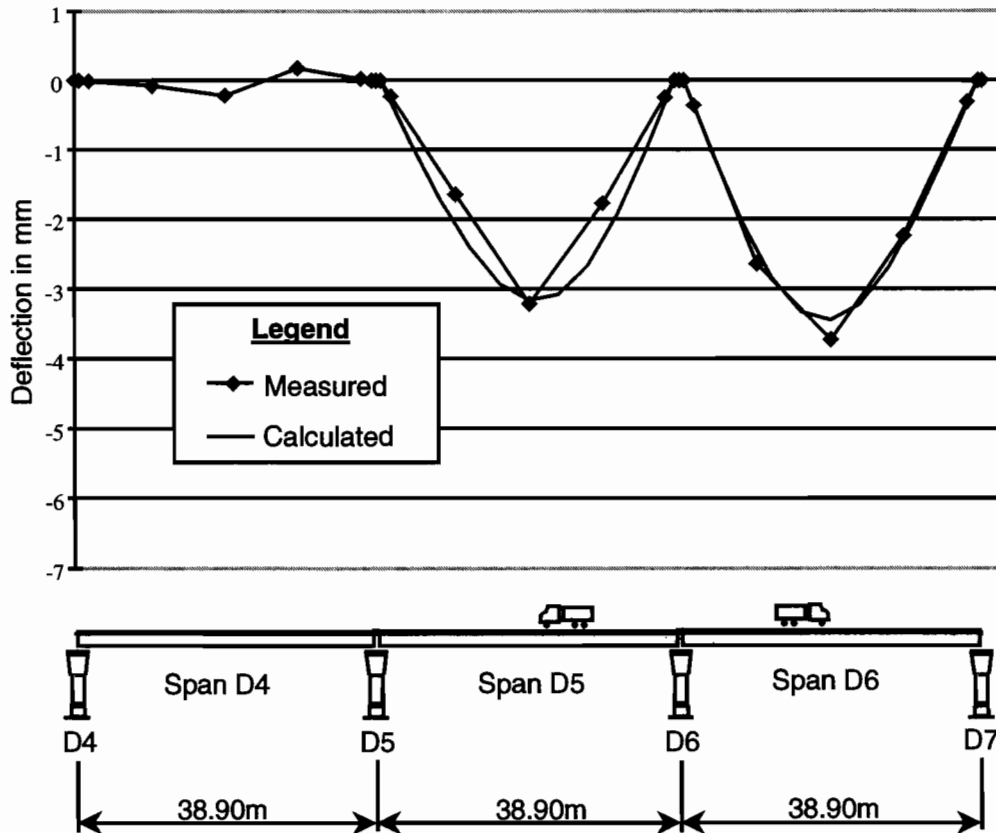


Figure 5.29 Deflections from load case 5

Live-load case 6 was similar to load cases 2 and 3 and was designed to produce a maximum positive moment in span D4. The measured deflections for this span, shown in Figure 5.30, were much smaller than the calculated deflections at only 1/10500 of the span length. The calculated deflections were for a simple span, but based on the positive measured deflections in unloaded span D5, some negative moment must have been developed in the superstructure over pier D5. In this case, a moment couple developed between the cast-in-place deck joint and the cast-in-place fixity block between the bottom flanges of girders D4 and D5. The performance of the cast-in-place joints is discussed in detail in Chapter 7.

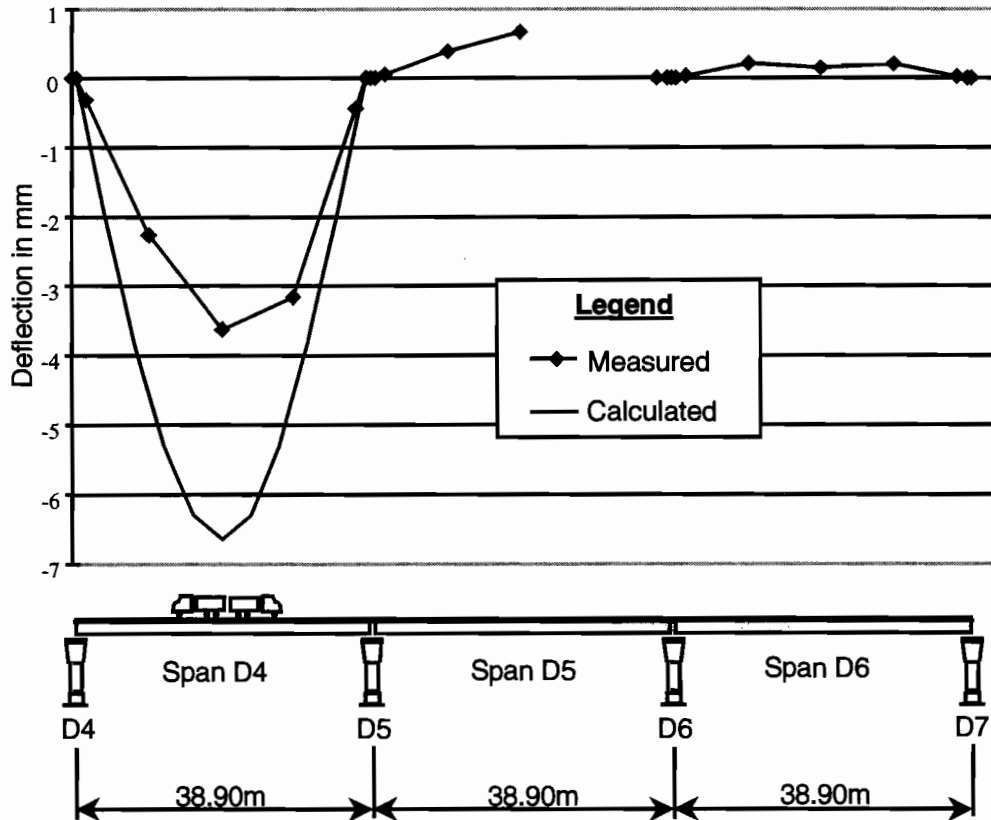


Figure 5.30 Deflections from load case 6

The deflections for live-load case 8 are shown in Figure 5.31. Load case 8 was similar to load case 2, but unsymmetrical with respect to the longitudinal centerline of the bridge. Load case 8 was intended to create maximum bending moment and torsional moment. The measured midspan deflection for load case 8 was actually smaller than the measured midspan deflection for load case 2 by 5% and 15% smaller than the deflection calculated for the symmetrical load case plotted in the figure. The slight decrease in midspan deflection over load case 2 was probably due to the high torsional rigidity of the girder combined with the deck continuity to the girder wings of the adjacent spans. The measured deflection for load case 8 was 1/6700 of the span length. Live-load case 9 was also an unsymmetrical loading intended to create transverse bending in pier D6 and negative superstructure moments over pier D6 if possible. Judging by the results of load case 5 in Figure 5.29, no negative moment was developed. In load case 5, the calculated and measured deflections were quite similar, but in load case 9 the measured deflections were 20% smaller than the calculated deflections for symmetrically loaded simple spans (shown in Figure 5.32). The cast-in-place deck joint may have stiffened the structure for this torsional case and provided some load transfer to span D4 through bending of the girder wings.

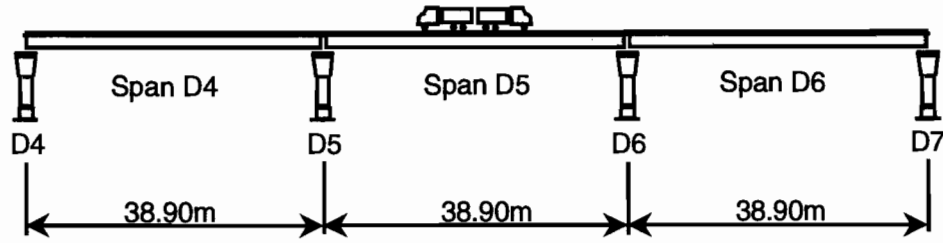
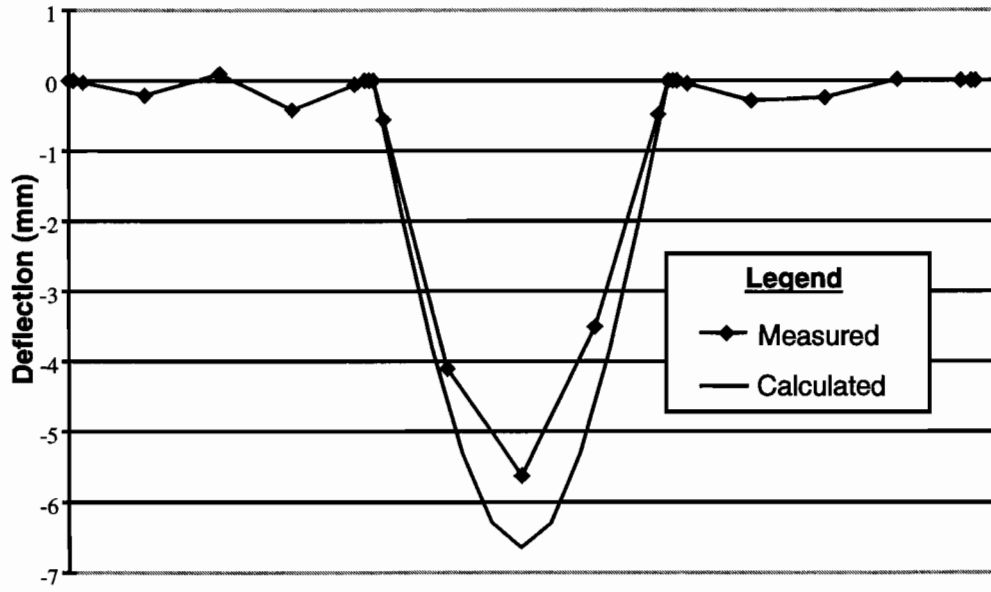


Figure 5.31 Deflections from load case 8

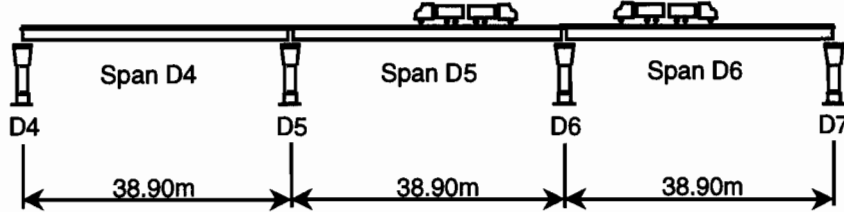
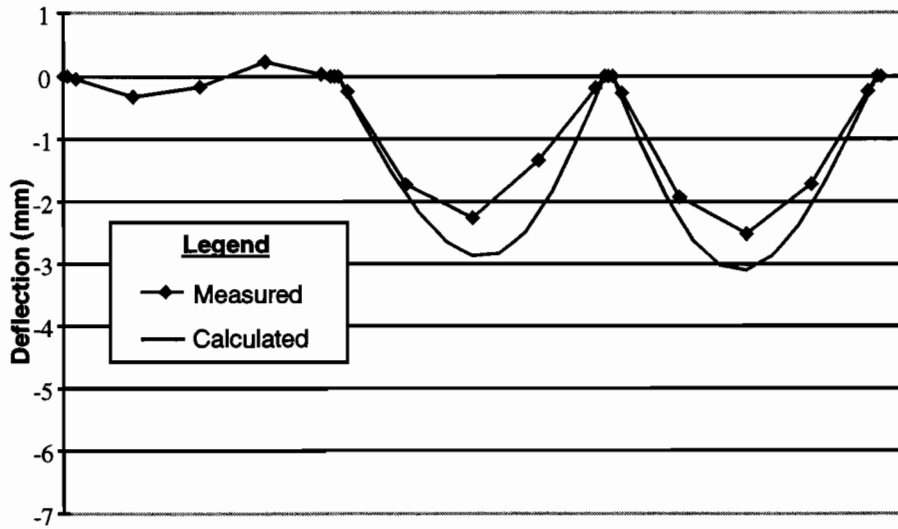


Figure 5.32 Deflections from load case 9

5.4.2 Ramp P Girder

The balanced cantilever construction of Ramp P provided the opportunity for many dead-load and post-tensioning force test cases. Measurements were taken at all stages of construction and during a live-load test. Strain changes were measured in segment P16-2 adjacent to the heavy end diaphragm at pier P16, deviator segment P16-10 at the quarter point of the span, and segment P16-17 at midspan.

Temporary Post-Tensioning

The temporary stress across a segment joint required during epoxying is 0.28MPa, as specified in the *AASHTO Segmental Guide Specification* [8]. The stress across the face of a segment when epoxied during balanced cantilever construction is provided by temporary or permanent post-tensioning and dead-load moment from the weight of the segment itself. The temporary force for epoxying the Ramp P segments was provided by 5 short lengths of post-tensioning bars anchored in blisters within the core of the girder (see Figure 5.33). Using this method, all epoxying and temporary post-tensioning could be accomplished from the deck and the core of the girder. Also, the short lengths of external post-tensioning bars easily accommodated the curvature of the structure. To avoid passing temporary post-tensioning through the congested heavy pier segment diaphragm, the cantilevering tendon ducts in the top flange over the webs were used to assemble the first two segments in balanced cantilever onto the pier segment. The straight temporary post-tensioning bars did not work well in the curved alignment of the internal cantilevering post-tensioning ducts.

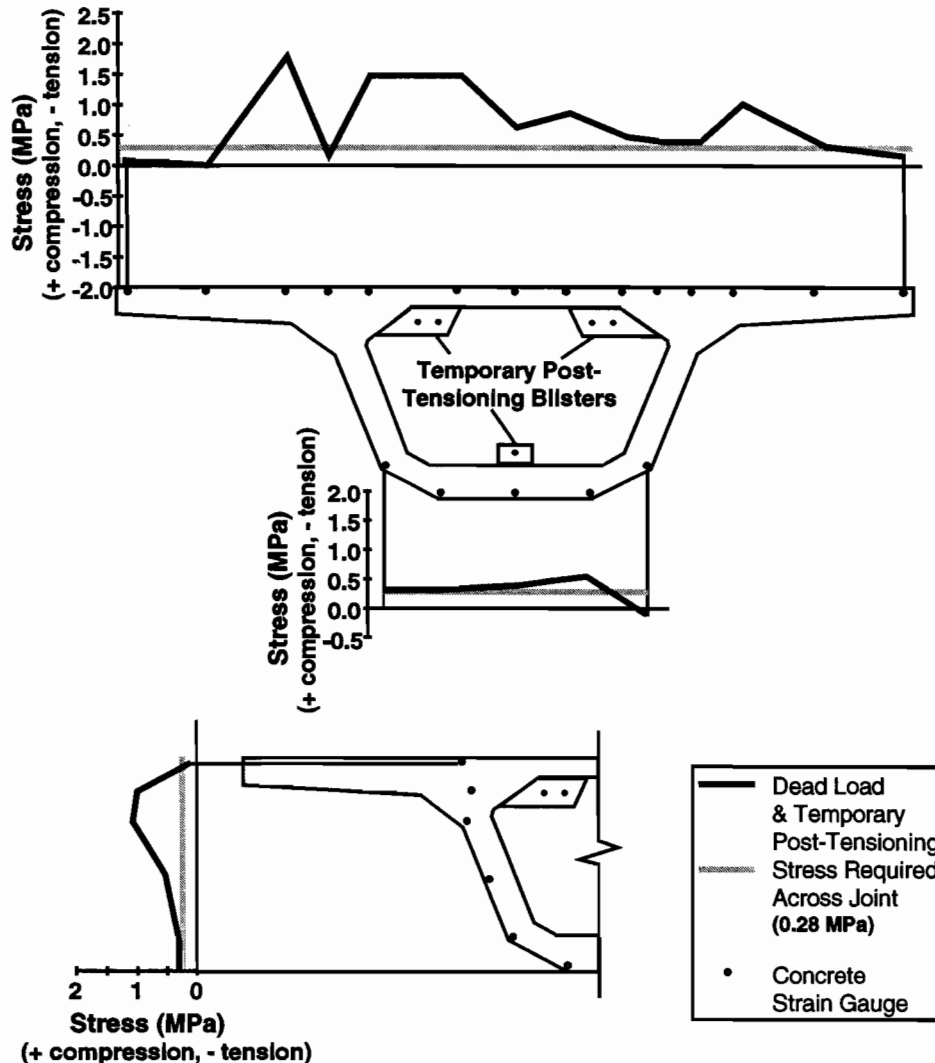


Figure 5.33 Diffusion of force from temporary post-tensioning in segment P16-10

When a segment was epoxied and stressed into place, the crane released the segment creating a negative dead-load moment from the weight of the segment. This negative moment was not enough to provide adequate squeeze of the epoxy on the bottom flange joint, so a temporary post-tensioning blister was provided on the bottom slab. Furthermore, the constructors soon realized that the bottom flange temporary post-tensioning bar must be stressed first to nearly the required force before the top temporary post-tensioning bars were fully stressed, in order to close the joint fully at the bottom flange. The measured stresses in segment P16-10 from the five temporary post-tensioning bars and self-weight are shown in Figure 5.33. The measured stresses exceeded the required joint stress for epoxying at all points except the wing tips and at one point in the bottom flange. During casting of a segment, a thermal gradient is developed in the plastic newly cast segment because of the heat of hydration generated by the match-casting segment. This gradient is present when the segment takes a set. When the segment cools to uniform temperature, the segment takes a curved shape and no longer exactly matches the segment against which it was cast. The segments tend to touch first at the wing tips. This "banana"-shaped segment behavior is more important for wider girders, such as the mainlane girders. Epoxy could be seen slipping down the joint at the center of the top flange of the mainlane girders in some instances, indicating no joint squeezing force was present at that location on the top flange. The distribution of temporary joint stresses in the top flange of segment P16-10 in Figure 5.33 did not indicate presence of a banana shape, which would have revealed itself as a stress increase near the wingtips, as seen on the mainlane. Segment P16-10 could have benefited from an increase in temporary joint force across the wing tips and on the bottom flange.

Diffusion of Cantilever Post-Tensioning

A plan and elevation of the half-span cantilever P16 is given in Figure 5.34. Construction began with the installation of the two piece pier segment, which was stressed onto the pier P16 to provide a moment connection for the balanced cantilever construction. Construction proceeded with the epoxying and temporary post-tensioning of segment P16-1 (not shown in Figure 5.34). The epoxying and temporary post-tensioning of P16-2 balanced the bending moments in pier P16. The pair of 12-strand 15mm diameter cantilever tendons T201 were then stressed to create the positive bending moments required to balance the negative moments from the dead load of the next two segments placed in cantilever. Construction proceeded by this method until midspan segment P16-17 was epoxied into place.

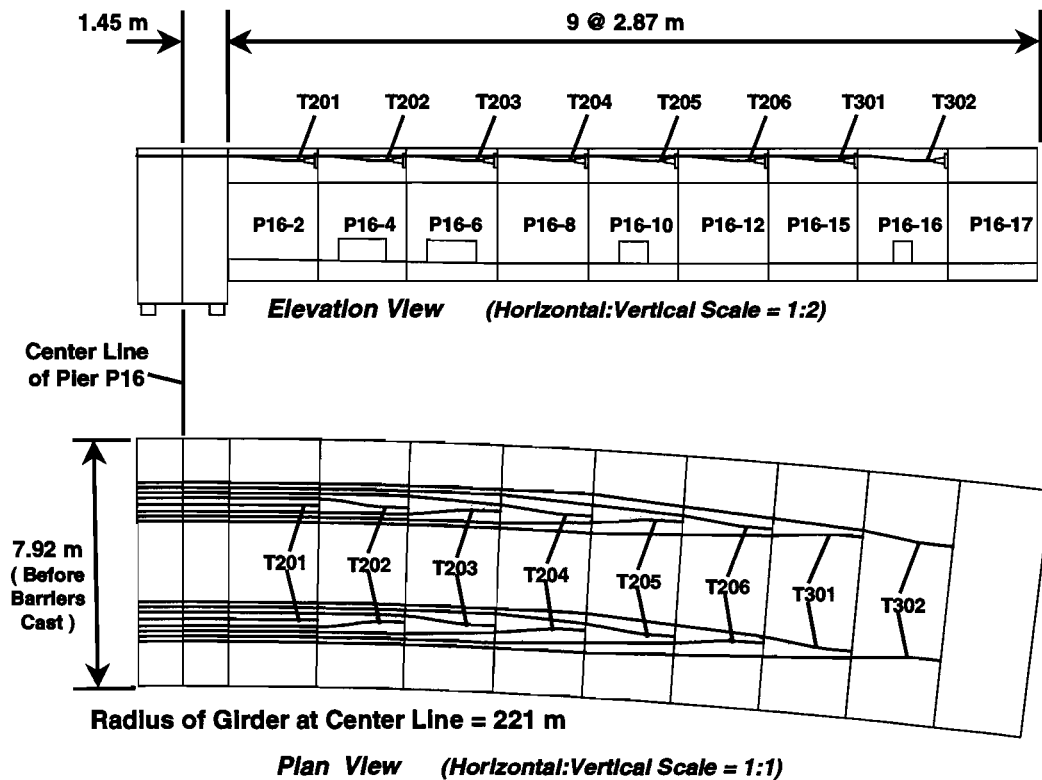


Figure 5.34 Layout of segments and cantilever tendons in the P16 upstation cantilever

Figure 5.35 shows the measured and calculated stress distribution in segment P16-10 from the stressing of cantilevering tendons T205. The instrumented section is 2410mm away from the anchor plates. The AASHTO Segmental Guide Specification method for the diffusion of post-tensioning forces is used to predict the stress at this cross section. The method assumes diffusion of the force within a 60° cone. The post-tensioning stresses are also calculated using full section properties. The measured stresses indicate that the post-tensioning force is poorly diffused at this cross section, with a nonlinear stress distribution down the depth of the web. Tension was measured across the full width of the bottom flange. Peak stresses were predicted quite well using the AASHTO 30° diffusion method, but the shape predicted by this method tends to overestimate stresses at the center of the top flange and within much of the height of the webs. The AASHTO 30° diffusion method would tend to overestimate the negative bending capacity of this section for service level stresses.

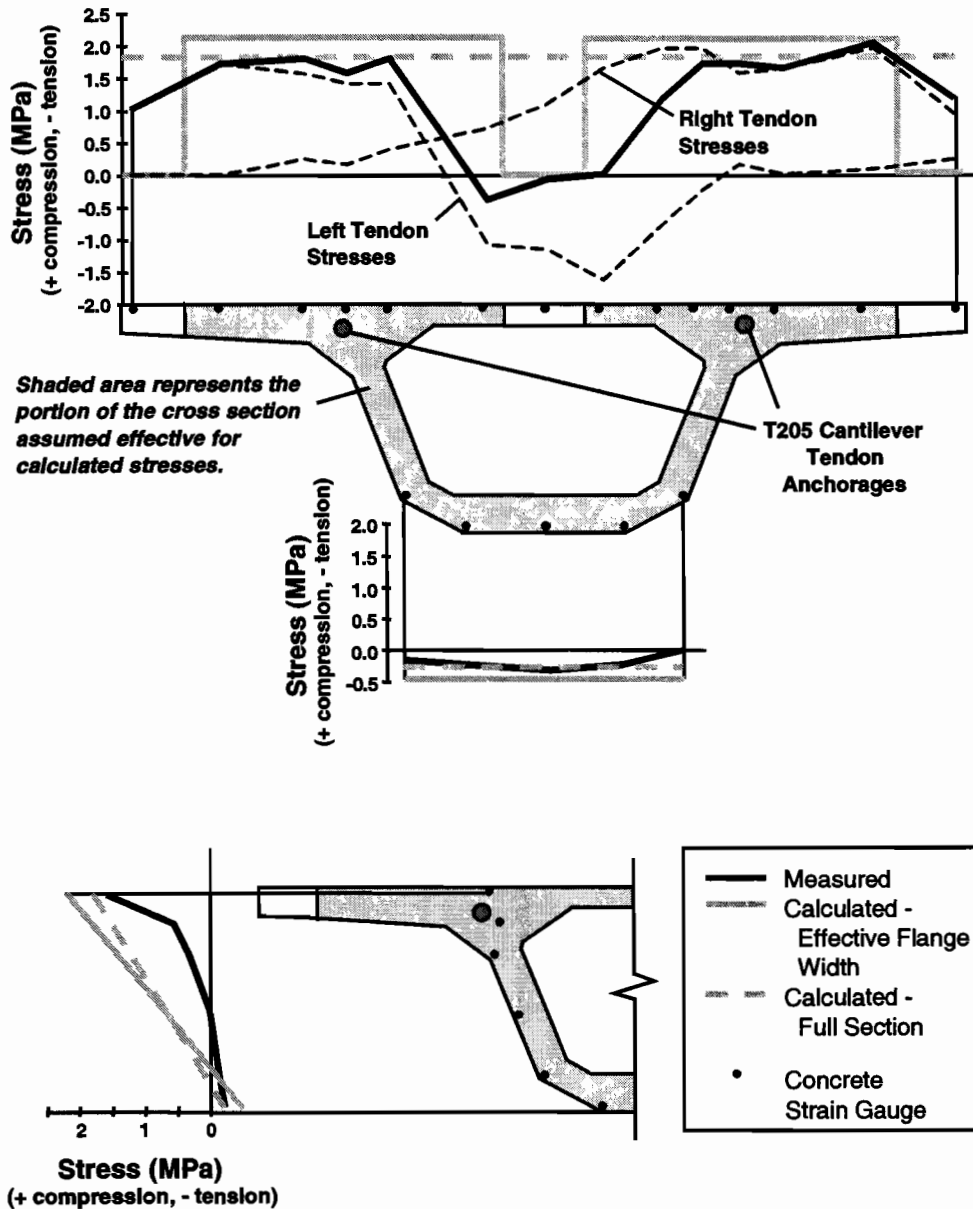


Figure 5.35 Diffusion of post-tensioning force from the cantilever tendons in segment P16-10

Cantilevering Final Stresses

The measured and calculated stresses from all cantilevering dead load and cantilever post-tensioning at the instrumented section in segment P16-2 are shown in Figure 5.36. The instrumented section in segment P16-2 is 450mm from the face of the heavy diaphragm in the pier segment. Full section properties were used to calculate the stresses at this section. From inspection of the plots of measured stresses in the top and bottom flanges, no tension existed in the cross section at the completion of the cantilever construction. Measured stress distribution was nearly linear from both dead loads and post-tensioning forces. The calculated stresses were somewhat unconservative since top flange compression from post-tensioning was overestimated, and bottom flange compression from dead load was overestimated.

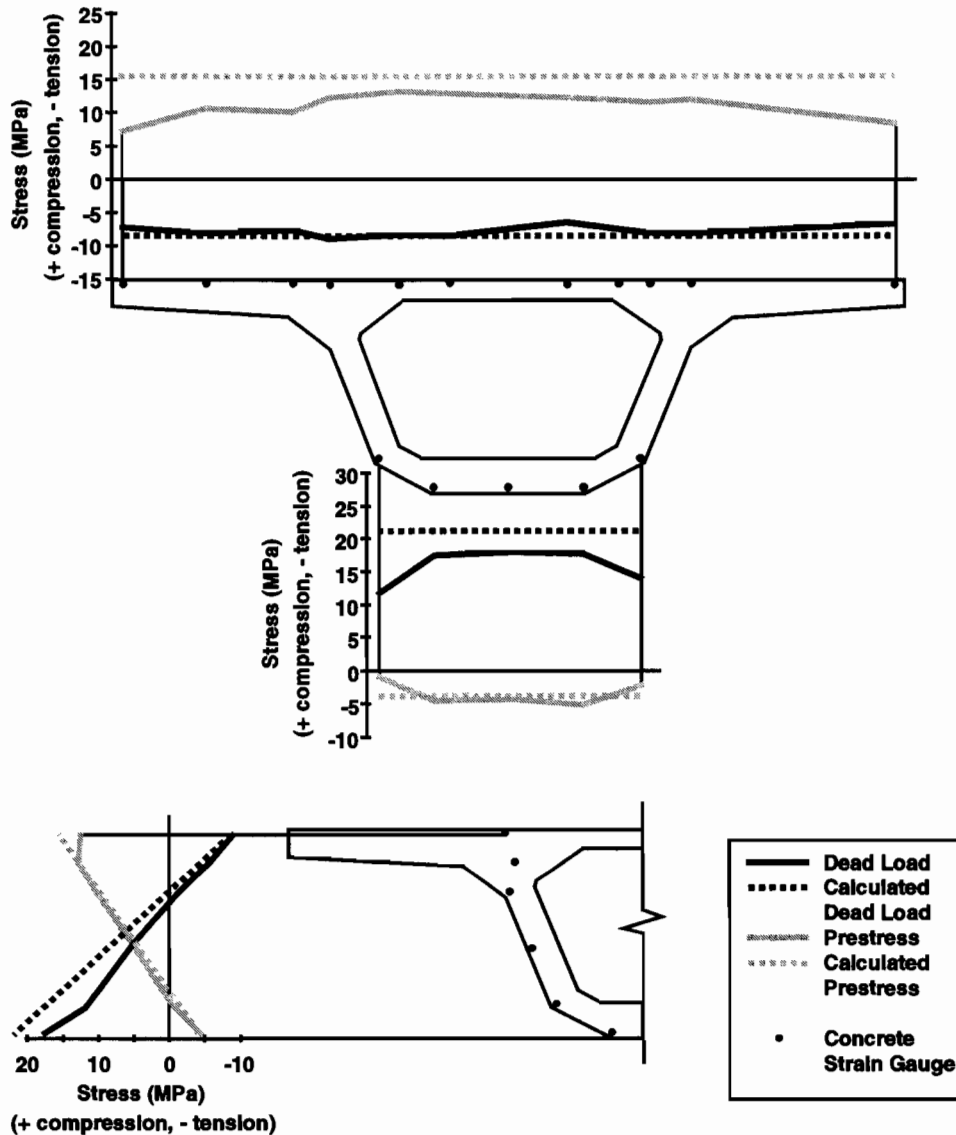


Figure 5.36 Longitudinal stresses in segment P16-2 after completion of the P16 upstation cantilever

The cumulative stress changes from three gauges in segment P16-2 are plotted in Figure 5.37 as a function of construction sequence. A small amount of tension was present in the bottom flange at gauge C638 during the early part of the construction sequence. Tension in the bottom flange over the pier was of little consequence since this section would be in substantial compression by the end of construction. Top flange tensile stresses were not measured at any time at gauge locations C604 or C607. The balance between tensile stress changes from dead load and compressive stress changes from cantilever post-tensioning was achieved during

construction, with a nearly constant residual compressive stress present during most of the construction sequence.

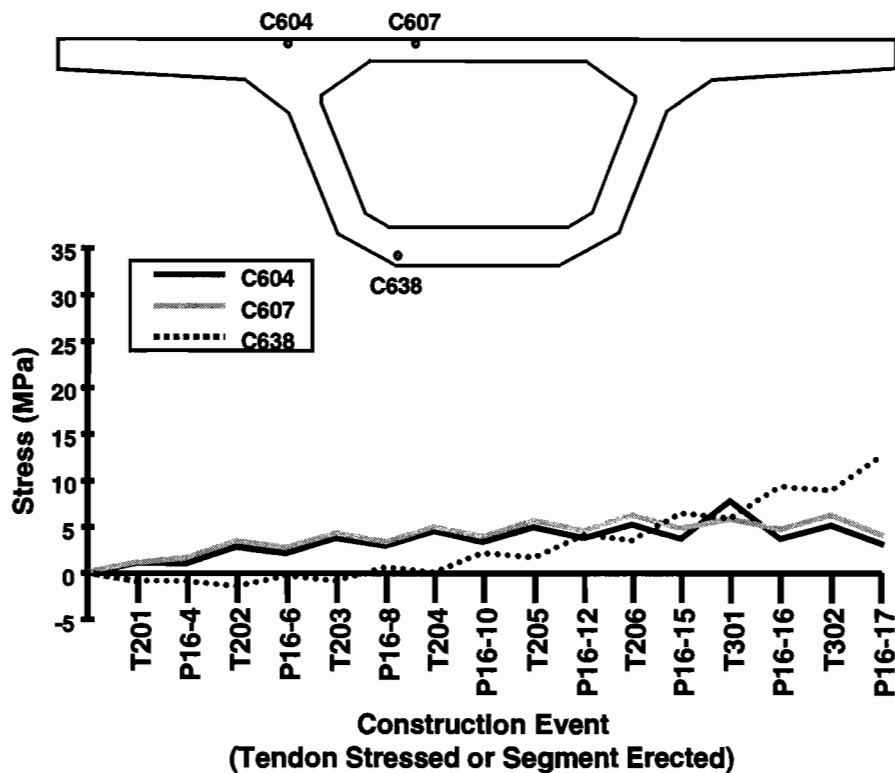


Figure 5.37 Longitudinal stresses from selected strain gauges in segment P16-2 over the course of the cantilever construction sequence

Continuity Post-Tensioning Stresses

The stresses in Ramp P following balanced cantilever construction were altered to those needed for a continuous structure with internal and external continuity post-tensioning. The location of these tendons is shown in Figure 5.38. Bottom slab internal continuity tendons T21 and T22 were stressed in span P16 following the casting of the closure at midspan. The pair of tendons T21 and the pair of tendons T22 were 9-strand 15mm diameter tendons. External deviated tendons T1, T2 and T3 were then stressed, providing an increase in both positive moment capacity at midspan and negative moment capacity over the piers. These tendons were 19-strand 15mm diameter tendons, the same size tendons used on the mainlane girders.

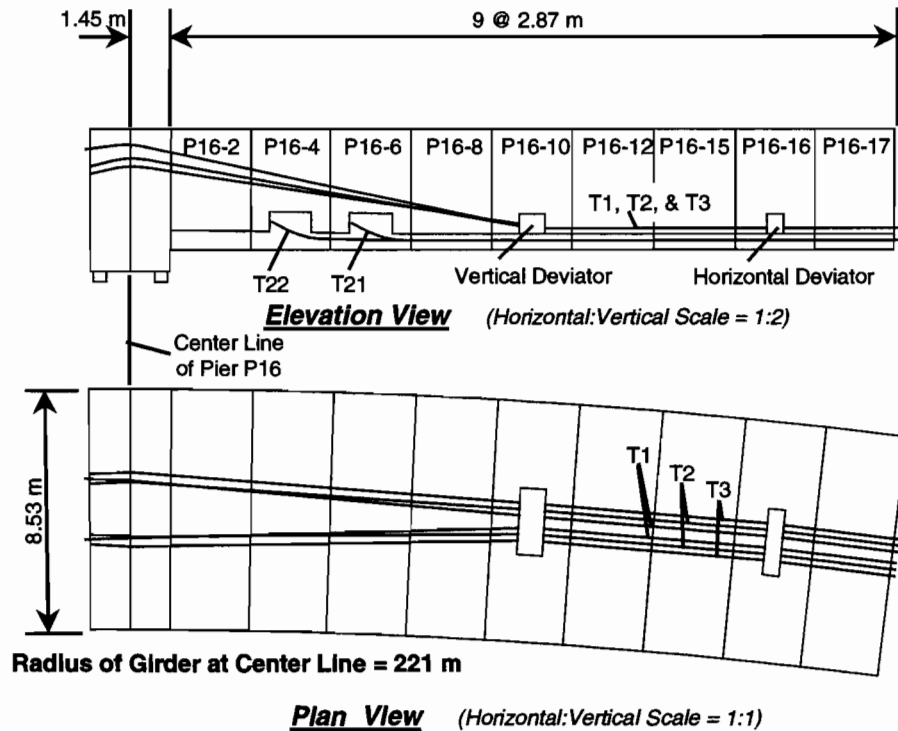


Figure 5.38 *Layout of internal and external continuity tendons in span P16*

Figures 5.39 through 5.41 show plots of the measured and calculated cross-sectional stresses produced by stressing the continuity tendons, and the final measured stresses at the completion of construction. The measured stresses from the continuity tendons in segment P16-2 near the pier segment (shown in Figure 5.39) indicate that the location of the anchorages for tendons T1 and T2 had influence on the distribution of stresses in the top flange. The anchorages for these tendons were located on the other side of the heavy pier segment diaphragm from the instrumented section. The forces in these anchorages did not diffuse into the wings over this short distance of 3350mm. Shear lag response of the continuous girder to the stressing of tendon pair T3 may also have had influence in the distribution of stresses in the top flange. The measured stresses were linear down the depth of the girder webs, as can be seen in the bottom plot of Figure 5.39. The stresses calculated using the AASHTO effective flange width method and 30° diffusion method overestimated the stresses in both the top and bottom flanges of the girder in segment P16-2. The final cross-sectional stresses in segment P16-2 are all compressive, with a minimum of 7MPa residual compression in the top flange for withstanding live load and thermal gradient tensile stresses.

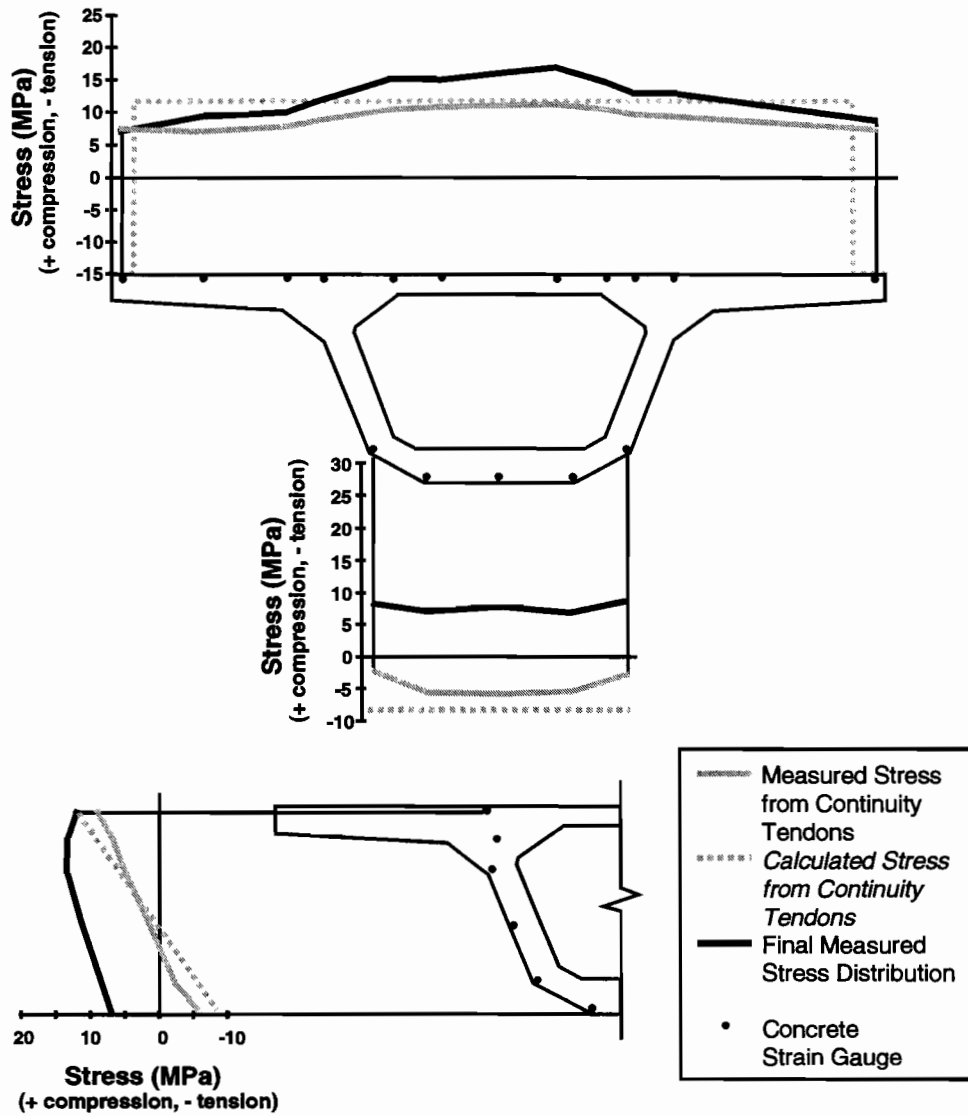


Figure 5.39 Longitudinal stresses in segment P16-2 after stressing of the continuity tendons for span P16

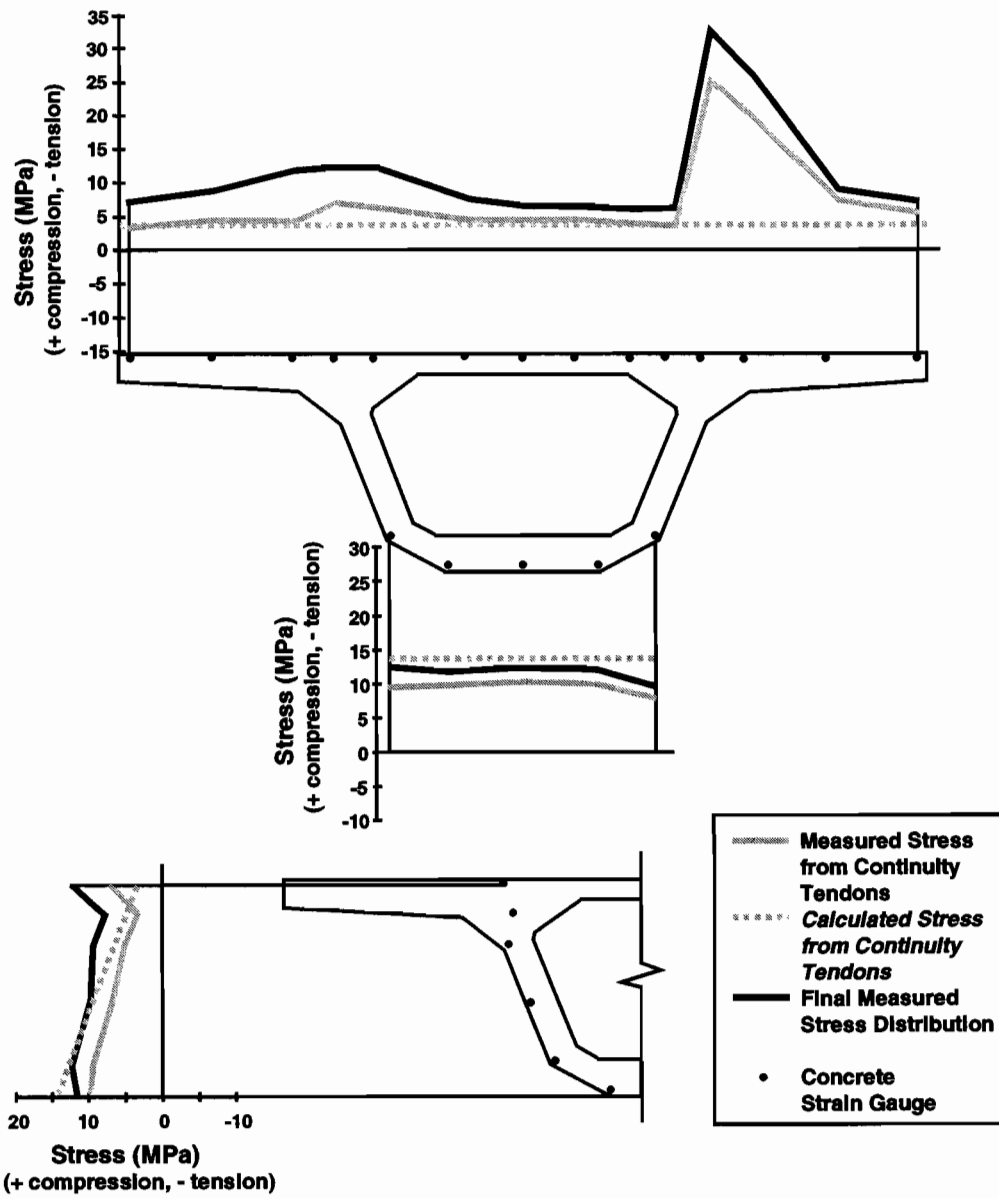


Figure 5.40 Longitudinal stresses in segment P16-10 after stressing of the continuity tendons for span P16

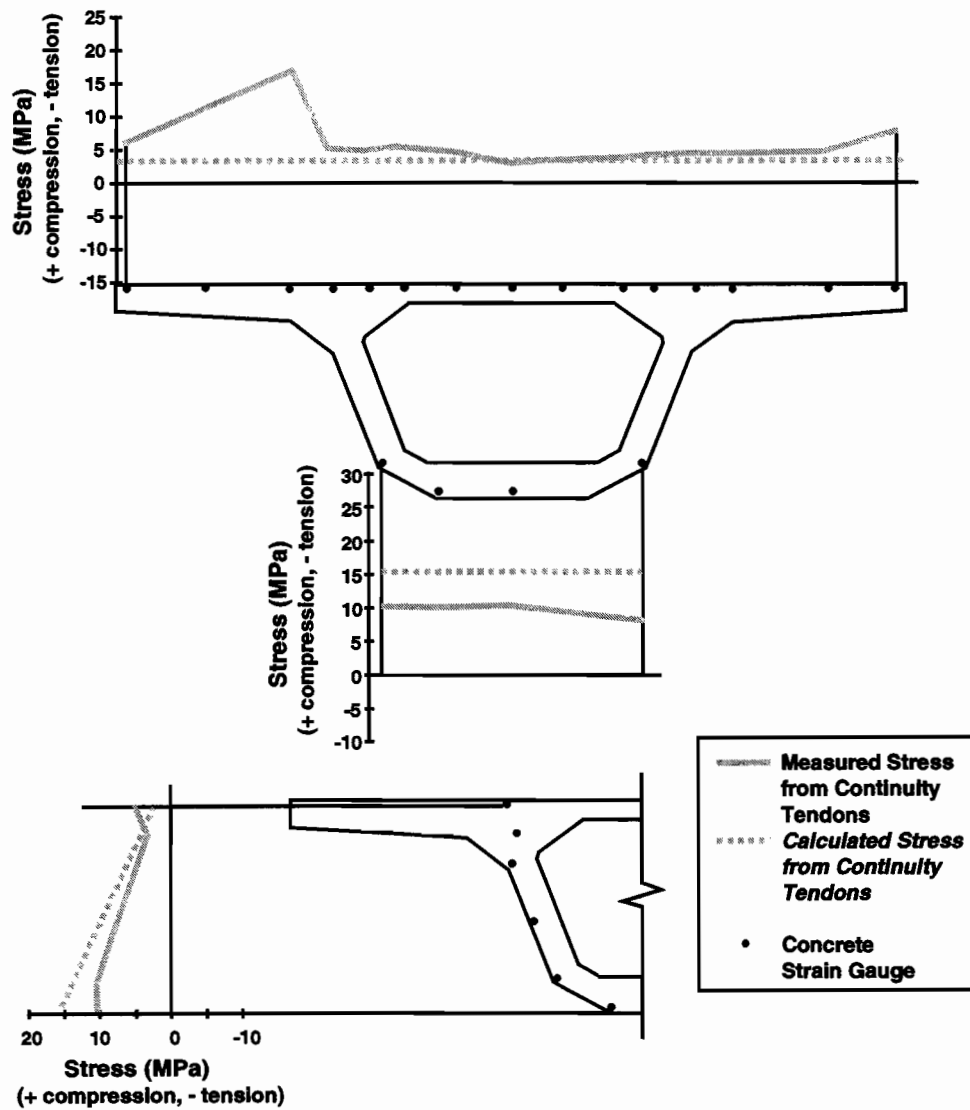


Figure 5.41 Longitudinal stresses in segment P16-17 after stressing of the continuity tendons for span P16

Measured and calculated stresses from the continuity tendons in segment P16-10 are shown in Figure 5.40. The calculated values accurately predicted the measured stresses from post-tensioning in the top flange except over the right girder web in the top flange. The high measured strains from the gauges located over the webs would indicate plastic behavior in the girder concrete. This behavior may have been the case since the strain gauges were located in the most congested location in the segment. The gauges giving the high strain readings were located very close to the large stirrup bars and the cantilever post-tensioning ducts. Segment P16-10 was also a deviator segment with its associated vertical load at the base of the web diffusing into the segment. Bottom flange stresses were overestimated by the calculation. Measured stresses appear to be linear down the depth of the webs except near the gauge near the top fiber of the girder. The final measured stress distribution in segment P16-10 plotted in Figure 5.40 did not reveal tension stresses at any location in the cross section. Segment P16-10 was located at the quarter point of the span, so both small negative moments from live load and somewhat larger positive moments from live loads and thermal loads could be expected. The final stress distribution in the segment had slightly more residual compressive stress in the bottom flange than the top flange to resist tensile stresses from the design live and thermal loads.

The measured and calculated stress distribution from the continuity post-tensioning forces in segment P16-17 (shown in Figure 5.41) was very similar to that in segment P16-10. Once again, several strain gauges in the top flange over the girder web indicated higher than expected strains. Also, the calculated stress was too large in the bottom flange by 50%, which may have led to tensile stresses under live load in an unconservative design. At 10MPa, the bottom flange residual compressive stress was high when compared to stress changes during the live-load tests.

Figures 5.42, 5.43 and 5.44 show plots of the actual concrete stress at various gauge location in segments P16-2, P16-10 and P16-17 respectively. In general, the continuity tendons produced higher stresses in the top flanges at points over the webs, as can be seen by comparing gauges C604 and C607 in Figure 5.42 or C704 and C707 in Figure 5.43. The output from gauge C717 in Figure 5.43 is similar to that of gauge C704, but much larger in magnitude. This may indicate that the gauge was working correctly. The stress changes at all the gauge locations shown in Figures 5.42 through 5.44 were gradual and predictable as tensioning of each of the tendons proceeded.

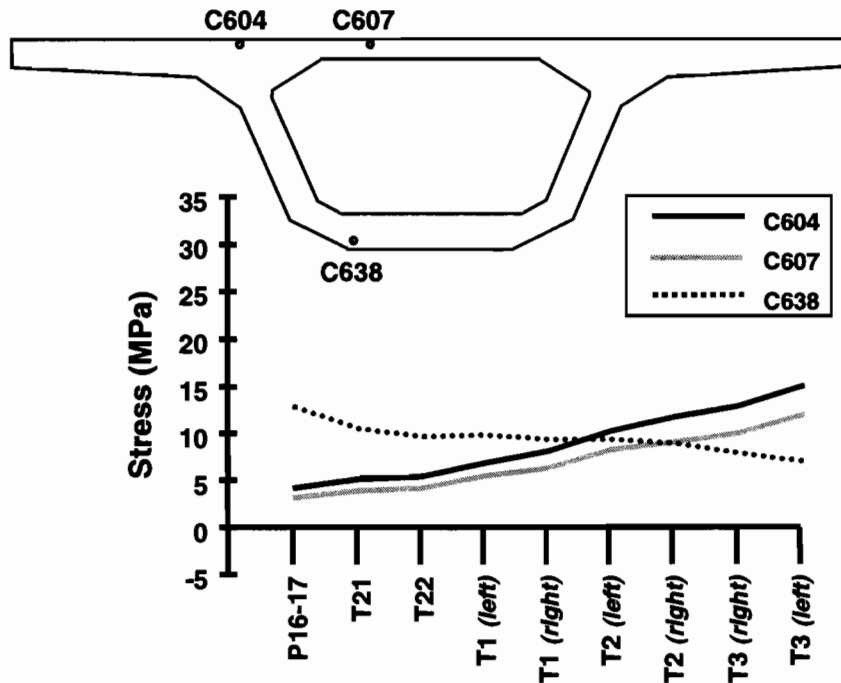


Figure 5.42 Stresses from selected strain gauges from segment P16-2 over the course of the continuity stressing sequence

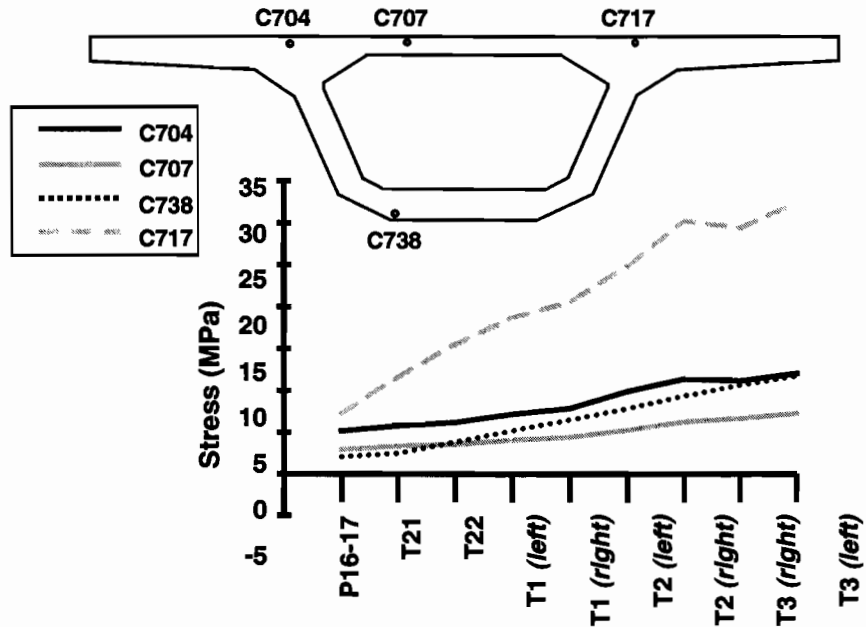


Figure 5.43 Stresses from selected strain gauges from segment P16-10 over the course of the continuity stressing sequence

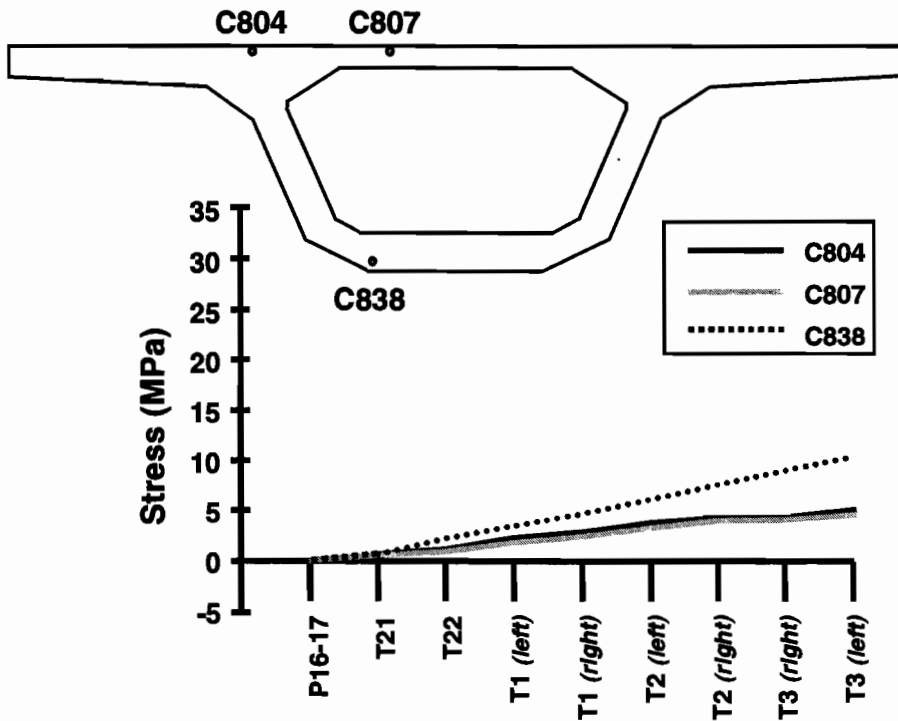


Figure 5.44 Stresses from selected strain gauges from segment P16-17 over the course of the continuity stressing sequence

Live-Load Test

A live-load test was performed on Ramp P shortly after the completion of construction, but before the 50mm of blacktop was placed. Four dump trucks were placed in pairs back to back to simulate positive moments produced by two lanes of HS20-44 truck live loading. The weights and dimensions of each truck are given in

Table 5.2. The five load cases shown in Figure 5.45 produced positive and negative bending moments in the continuous structure, as well as torsional moments. Load cases 1, 3 and 5 were intended to produce maximum positive moments in spans P14, P15 and P16 respectively. Since all strain measurements were taken in span P16, loads were placed on other spans of the five-span continuous unit to study moment distribution.

Table 5.2 Axle weights and spacing for live-load test trucks on Ramp P

Truck	Weight of Rear Axles (kN)	Weight of Front Axles (kN)	Total Weight (kN)	Axle Spacing (mm)
1	121.1	52.5	173.6	4720
2	113.2	47.2	160.4	4700
3	139.5	52.5	192.0	5210
4	120.9	52.6	173.5	5000

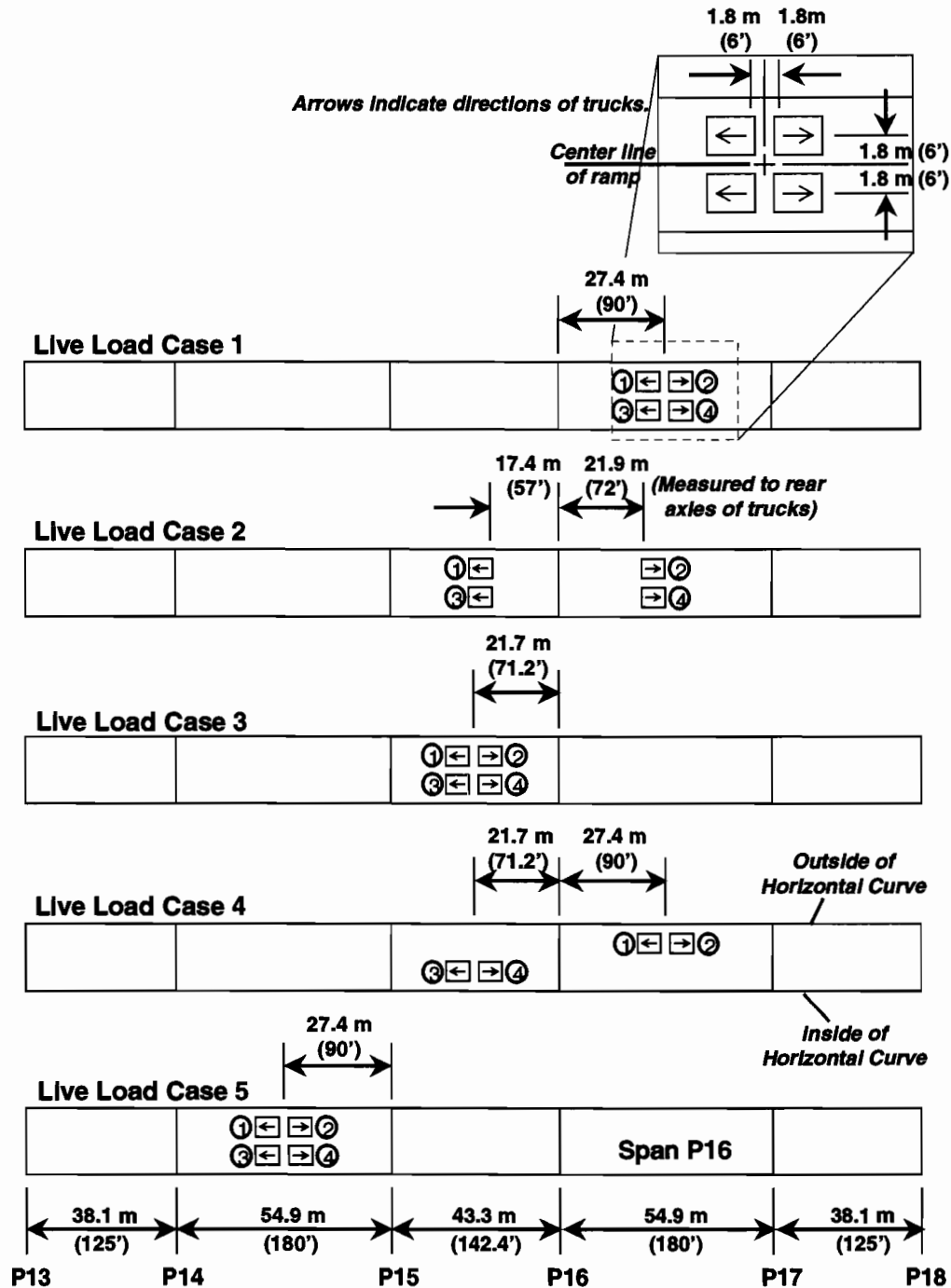


Figure 5.45 Live-load test cases for the Ramp P girder

The measured stresses in segment P16-2 from all load cases are shown in Figure 5.46. The gauges in segment P16-2 were located 1900mm upstation from the centerline of pier P16. Load cases 1 through 4 produced a negative bending moment at segment P16-2, and load case 5 produced a small positive moment. Load case 1 caused the greatest bending moment at P16-2, but the measured stress changes were small with a maximum stress change in the bottom flange of only 1.75MPa or 9% of the allowable service level compressive stress. Load case 3 was similar to load case 1 except the trucks were placed on span P15. Negative moment from load case 3 was distributed both to pier P16 and span P16. The measured stresses at segment P16-2 were less than half those measured during load case 1. The moment connection of the superstructure to the pier appears to

have been working as a monolithic connection. The stress changes in segment P16-2 from load case 5 were very small, even though the load was only one and a half spans away from the instruments. The moments produced by the truckloads from case 5 were distributed both to the downstation portion of the superstructure and to piers P15 and P16.

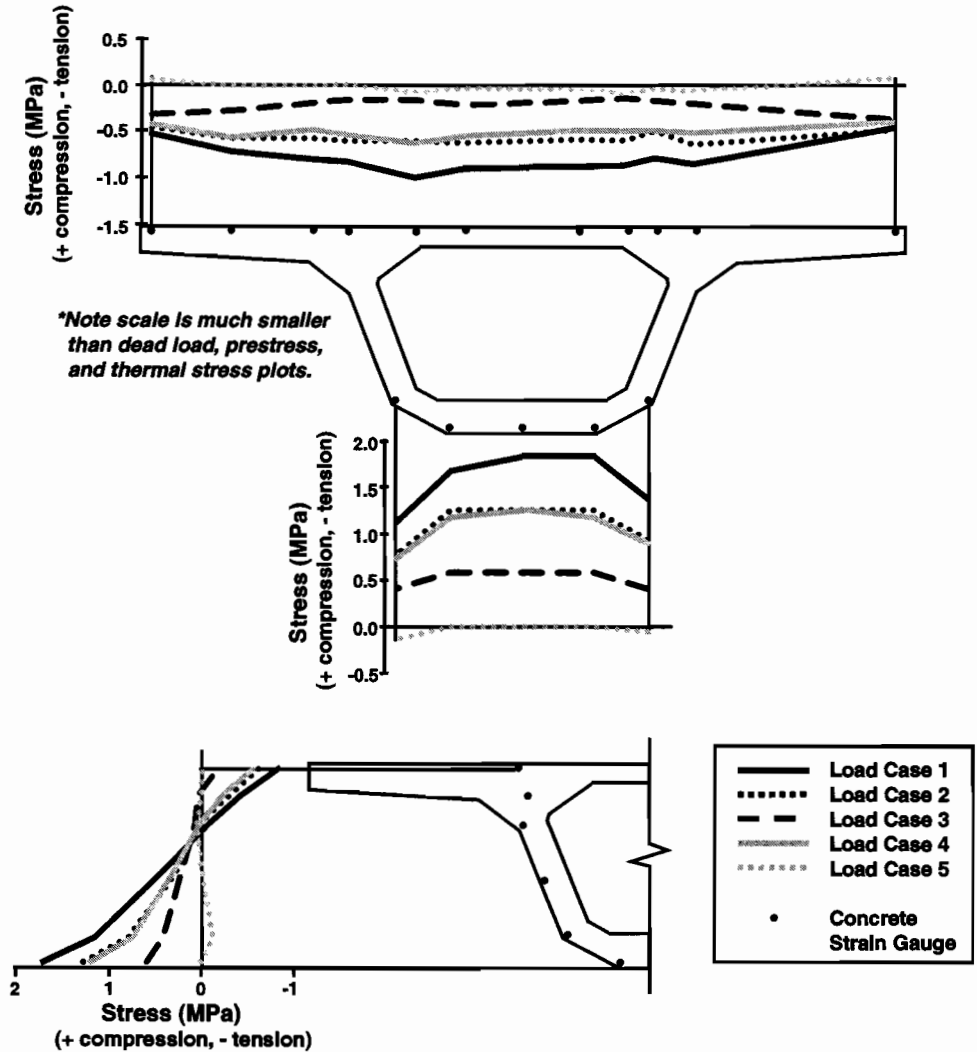


Figure 5.46 Measured live-load longitudinal stresses in segment P16-2

Measured and calculated stresses for load cases 1 and 2 at segment P16-2 are shown in Figure 5.47. The AASHTO effective flange method was used in the calculations and required a small reduction in wing tip length at segment P16-2. Peak stresses in the top flange were conservatively estimated in the calculation, although the measured stresses were probably lower than the actual stresses because of the low assumed modulus of elasticity of the concrete. Shear lag is evident in the measured stresses in the girder wings. At other locations in the cross section the measured stress distributions appear to be uniform, with a nearly linear stress gradient down the depth of the web.

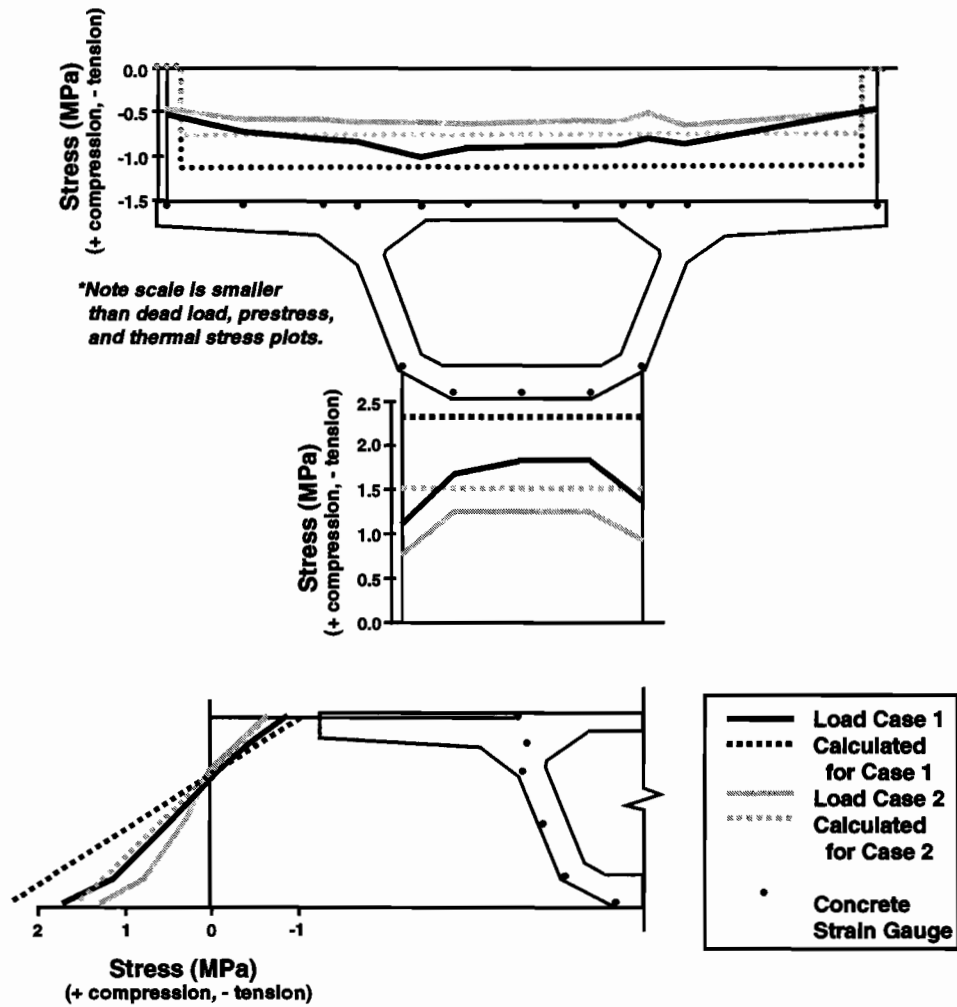


Figure 5.47 Measured and calculated live-load longitudinal stresses in segment P16-2

Measured and calculated stresses for load cases 1 and 2 at segment P16-10 are shown in Figure 5.48. The measured stress changes at this cross section were very small, since this section is close to the inflection point of the span for both load cases. Maximum stress change in the bottom flange for load case 1 was only 0.5MPa in tension. The calculated stresses for the bottom flange predicted the measured stresses well on average. Much more significant stress changes were measured in the midspan segment P16-17. Measured and calculated stresses for load cases 1 and 2 at segment P16-17 are shown in Figure 5.49. Once again, the calculated stresses exceeded the measured stresses in the bottom flange by about 40% in the bottom flange and 20% in the top flange. The peak measured stress change in the bottom flange from load case 1 was 2.2MPa in tension at midspan. The final girder stress in the bottom flange at midspan following continuity post-tensioning was about 10MPa in compression, so the live-load stresses change did not threaten to put the bottom flange in tension. In general, the stress changes from the live loads were small in all test cases.

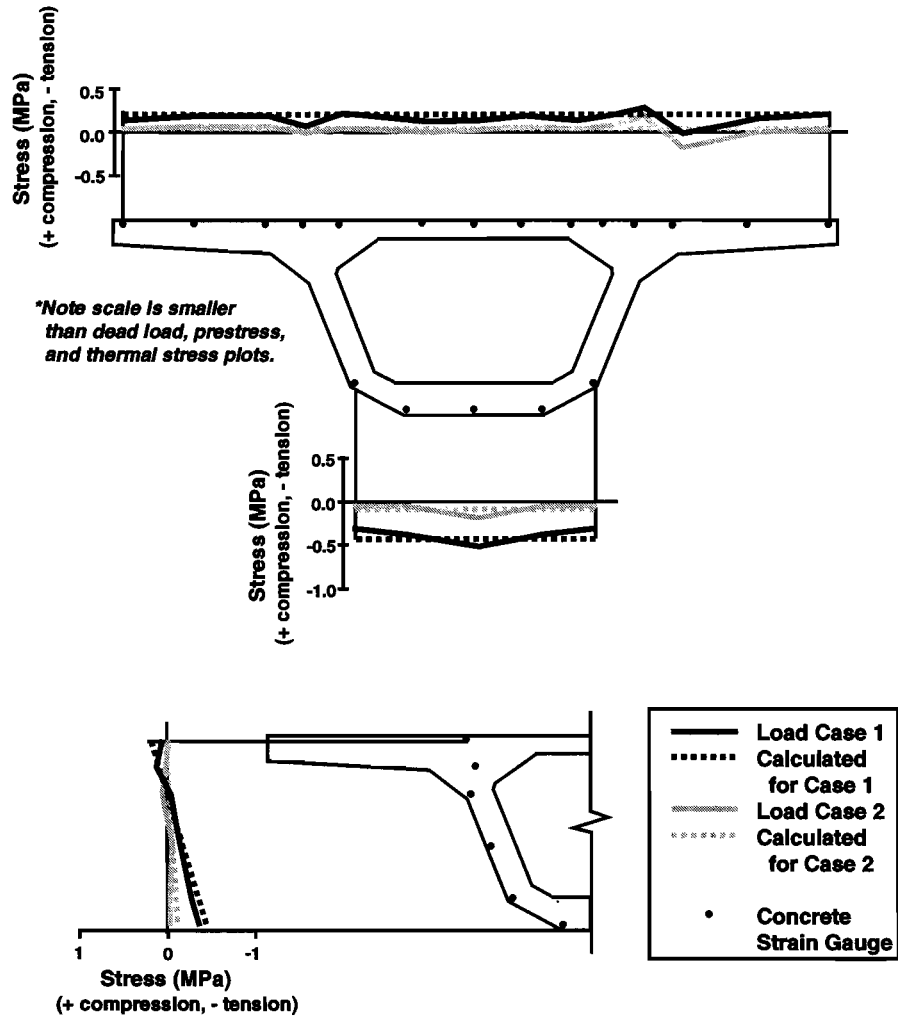


Figure 5.48 Measured and calculated live-load longitudinal stresses in segment P16-10

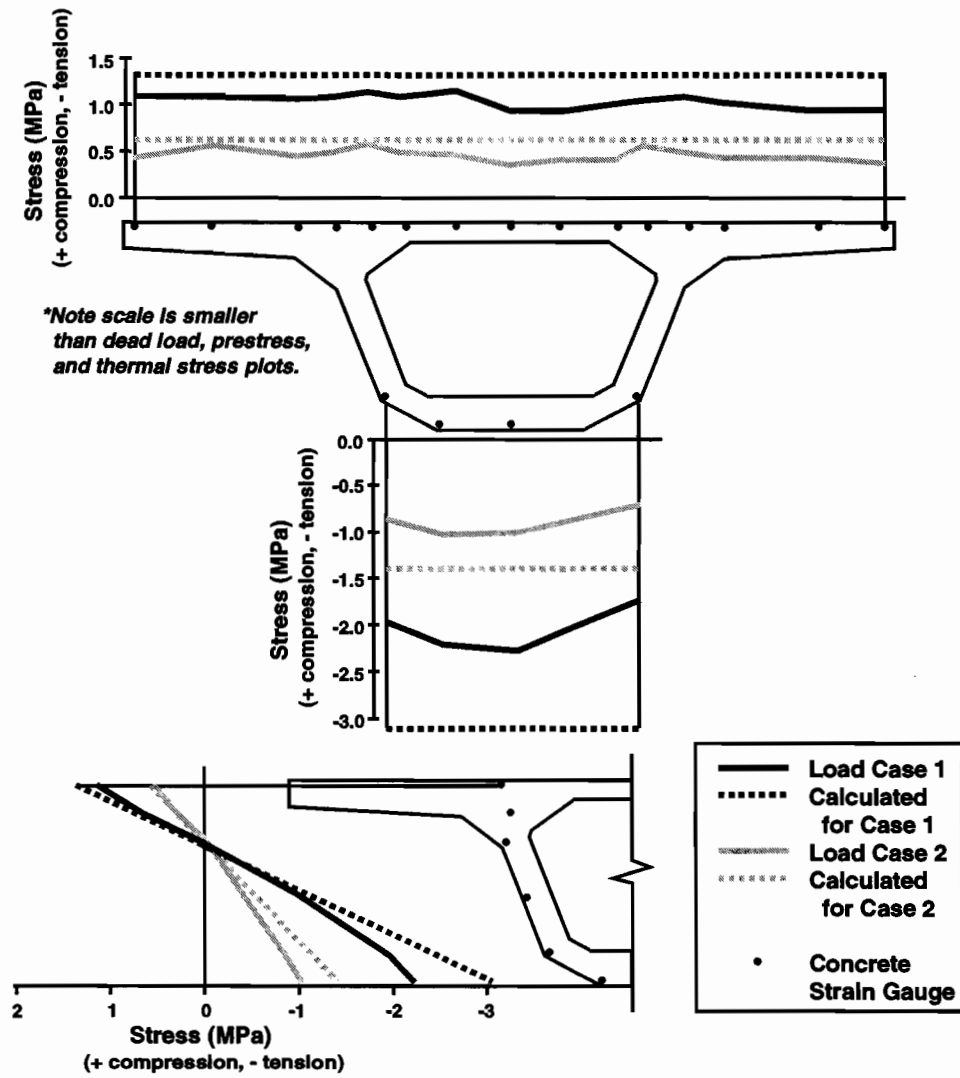
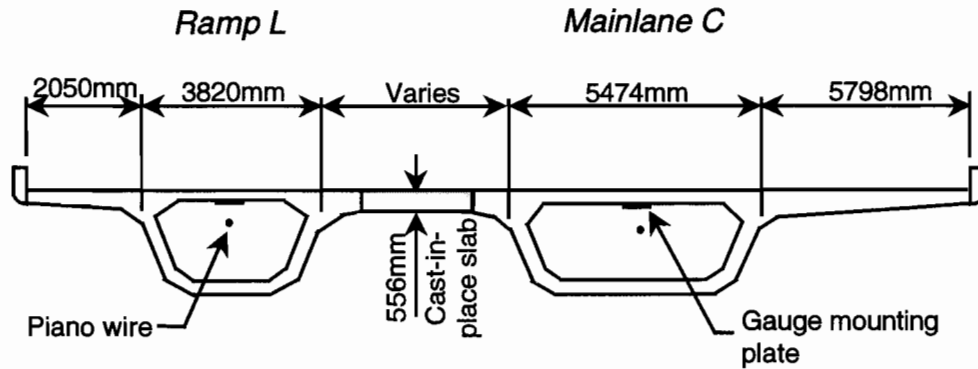


Figure 5.49 Measured and calculated live-load longitudinal stresses in segment P16-17

5.4.3 Two-Cell Girder-Unit C15, L2

Ramp L and mainlane girder C were joined by a cast-in-place closure pour as shown in Figure 5.50. The width of the gore closure varied from 4390mm in span C41 to 6680mm in span C42. The slab was post-tensioned transversely for live loads. Both the ramp L and the mainlane C girders had two bearings at the individual piers that supported the girders. The girders were constructed as simple spans with continuity to the adjacent spans consisting only of the cast-in-place deck joint between top flanges of adjacent girders. These girders were only tested under live load, and deflections were the only measurements taken. The purpose of the measurements was to determine the degree of live-load bending moment sharing between the two transversely connected girders.



Cross Section
Unit C15, L2

Figure 5.50 Cross section of Unit C15, L2

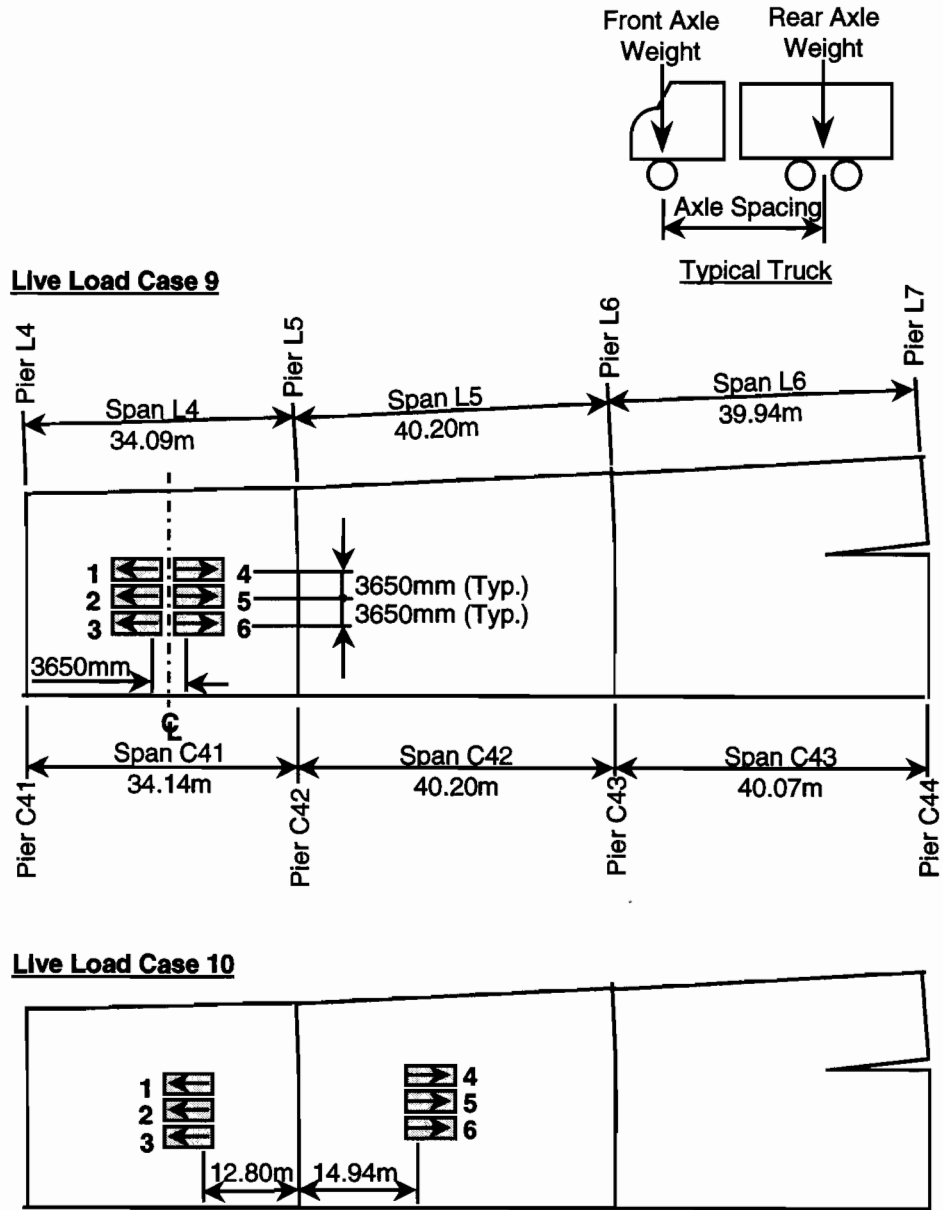
Live-Load Test

The six dump trucks used in the live-load test were loaded similarly to the trucks used in the other live-load tests. The trucks were placed back to back to produce a bending moment equal to that produced by three lanes of HS20-44 trucks. The trucks were also separated to try to produce a negative bending moment in the semicontinuous girder connection over the piers. The weights and dimensions of the trucks used in the test are given in Table 5.3.

Table 5.3 Axle weights and spacing for live-load test trucks on Units C15 and L2

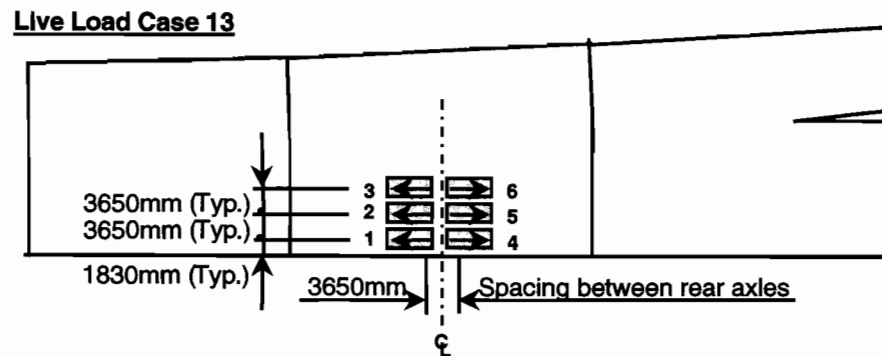
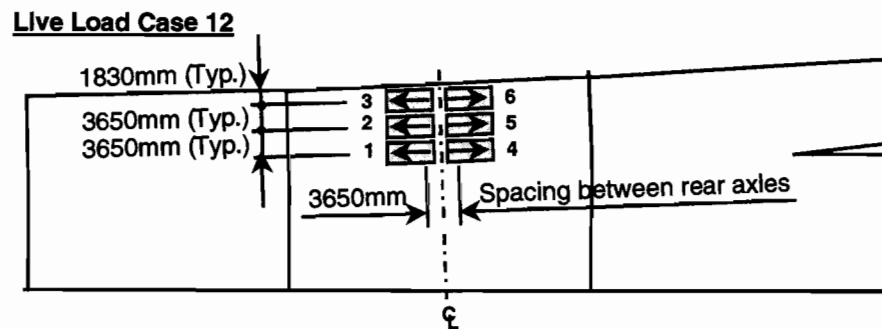
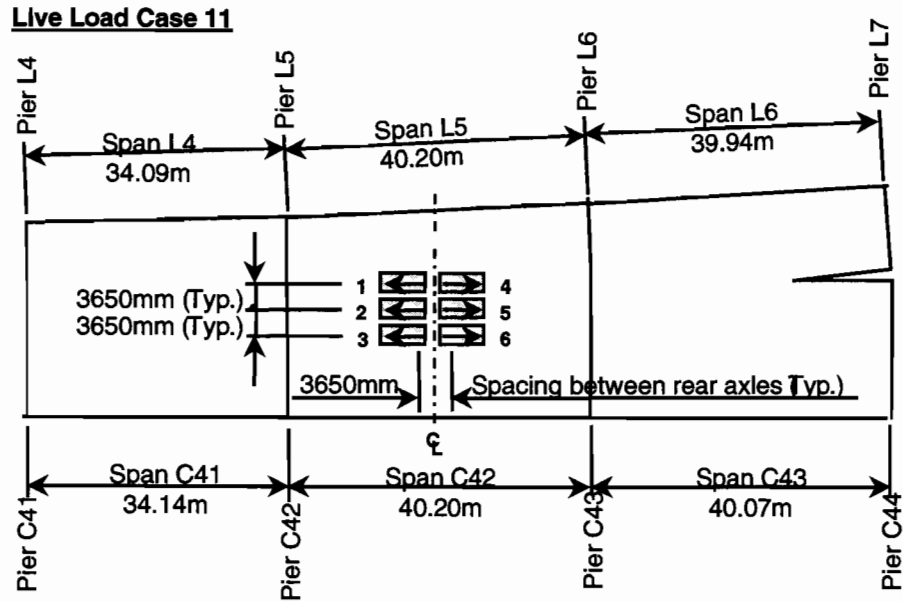
Truck	Weight of Rear Axles (kN)	Weight of Front Axles (kN)	Total Weight (kN)	Axle Spacing (mm)
1	133.9	55.9	189.8	5030
2	128.7	44.0	172.7	4090
3	109.5	41.5	151.0	4100
4	121.3	55.8	177.1	5000
5	137.6	42.5	180.1	5000
6	127.4	34.4	161.8	4700

Unit C15, L2 was a twin three-span semicontinuous unit with expansion bearings at piers C41, L4, C44 and L7. A plan view of the three-span unit is shown in Figure 5.51. The gore closure was terminated within span C43, L6, so the live-load test cases were all located in the other spans. The live-load cases are shown in Figures 5.51a and 5.51b. All load cases except case 10 were designed to determine the degree of moment sharing between the two girders of unequal section properties. Load cases 12 and 13 were drastically unsymmetrical with respect to the longitudinal centerline of the bridge deck.



(a) Live-load cases for Unit C15, L2

Figure 5.51 (a) and (b) Live-load cases for Unit C15, L2 (continued)



(b) Live-load cases for Unit C15, L2

Figure 5.51 (a) and (b) Live-load cases for Unit C15, L2

The deflections measured during load case 9 are shown in Figure 5.52. The trucks for load case 9 were placed symmetrically with respect to the longitudinal and transverse centerline of the bridge deck of span C41, L4. The measured deflections reveal that the mainlane girder took more of total bending moment than did the ramp girder. Assuming that the cast-in-place top flange was shared equally by both the mainlane C girder and the ramp L girder, the ramp L girder was calculated to be only 56% as stiff in bending as the mainlane C girder. Since the mainlane girder deflection was 3.0mm and the ramp girder deflection was 2.2mm, calculations reveal that 71% of the total live-load bending moment was taken by the mainlane girder. The deflection of the

mainlane C girder was only 1/11000 of the span length. The calculated deflections in Figure 5.52 assumed that no transverse continuity existed between the mainlane side of the bridge and the ramp side of the bridge. A fictitious longitudinal cut was taken down the center of the cast-in-place top slab. Wheel loads placed on the mainlane side of the cut were assumed to be taken entirely by the mainlane girder, and wheel loads placed on the ramp side of the cut were assumed to be taken entirely by the ramp girder. This way, the results from the calculated deflections could be easily interpreted and compared to the measured results. The AASHTO effective flange width method was used in all calculations. The calculations for load case 9 assumed that the mainlane carried 2 lanes of the trucks and the ramp girder carried 1 lane of trucks. This assumption obviously means that the mainlane girder would carry 67% of the live-load moment. The measurements revealed that the mainlane girder carried slightly more at 71% of the total live-load moment. The significantly stiffer mainlane girder was only able to attract 4% of additional live-load moment for the symmetrical load case 9.

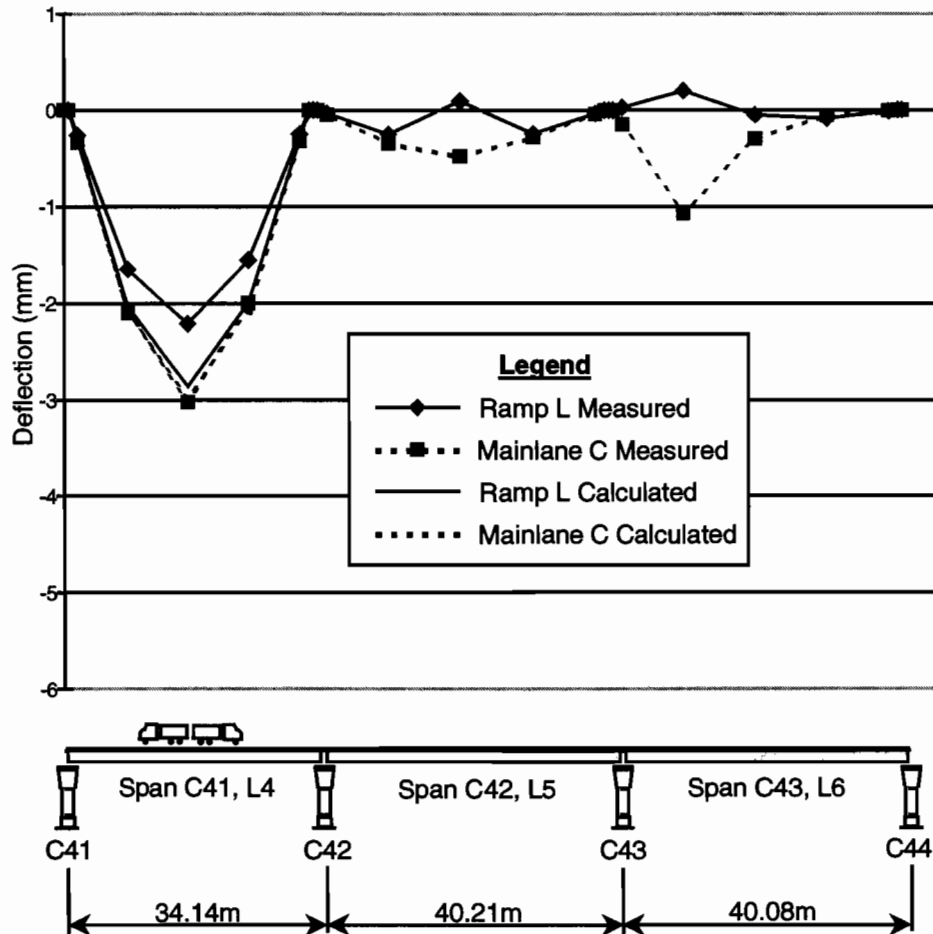


Figure 5.52 Deflections from load case 9

Load case 10 was similar to load case 9 in that the trucks were placed symmetrically with respect to the longitudinal centerline of the bridge deck, but both spans C41, L4 and C42, L5 were loaded. The measured and calculated deflections for load case 10 are plotted in Figure 5.53. The calculations assumed that the mainlane girder carried 2 lanes of trucks and the ramp girder carried 1 lane of trucks. The measured deflection in span C41, the mainlane girder, was 1.9mm, and the deflection in span L4 was 0.9mm. Taking into account the relative stiffnesses of the mainlane and ramp girders, the mainlane girder carried 80% of the total live-load moment. This percentage was a higher percentage of the live-load moment than seen in load case 9. The measured deflection for load case 10 in span C42 was 2.4mm, and the deflection in span L5 was 1.3mm. From calculation the mainlane girder carried 77% of the total live-load moment for span C42, L5.

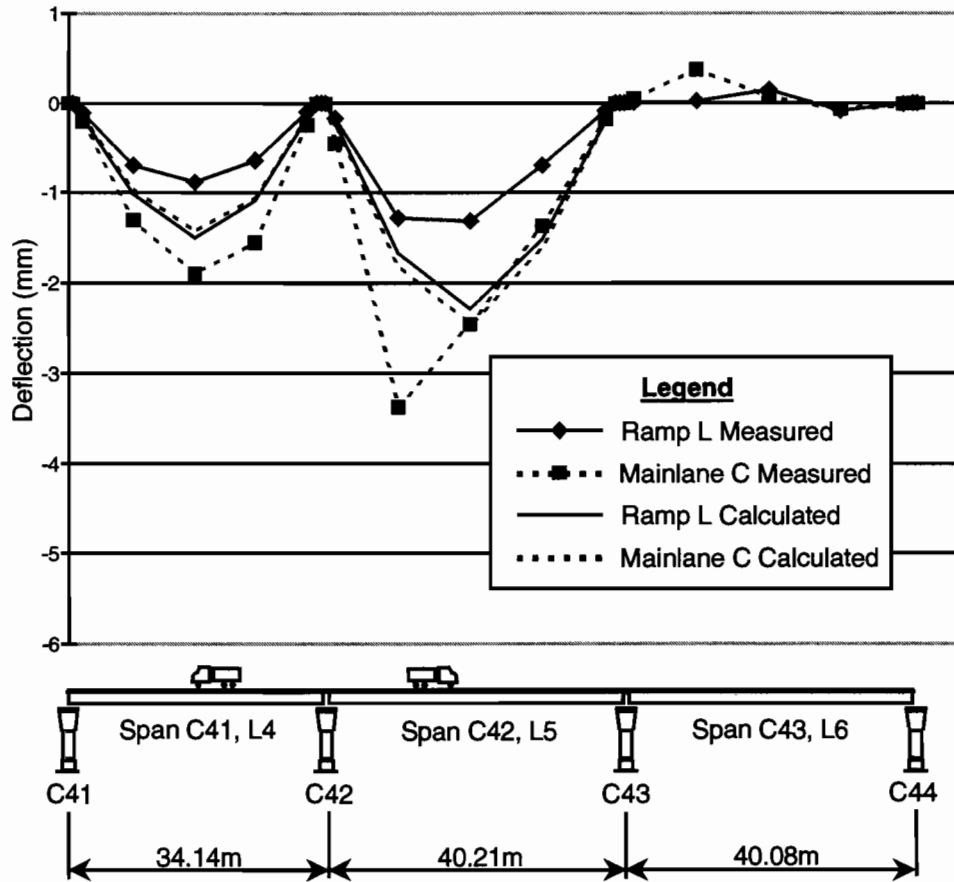


Figure 5.53 Deflections from load case 10

Load case 11 was identical to load case 9, except the trucks were placed on span C42, L5. The measured and calculated deflections for load case 11 are shown in Figure 5.54. The deflection calculation assumed that the mainlane girder carried 2 lanes of trucks, and the ramp girder carried 1 lane of trucks. The measured deflection of mainlane girder C42 was 4.9mm, and the measured deflection of the ramp girder L5 was 3.6mm. The deflection of the mainlane girder was 1/8000 of the span length, which was larger than the deflection of mainlane girder C41 in load case 9. The span length of mainlane girder C42 was significantly longer than C41. From calculation, the mainlane girder carried 71% of the total live-load moment, identical to the percentage taken by the mainlane girder in load case 9.

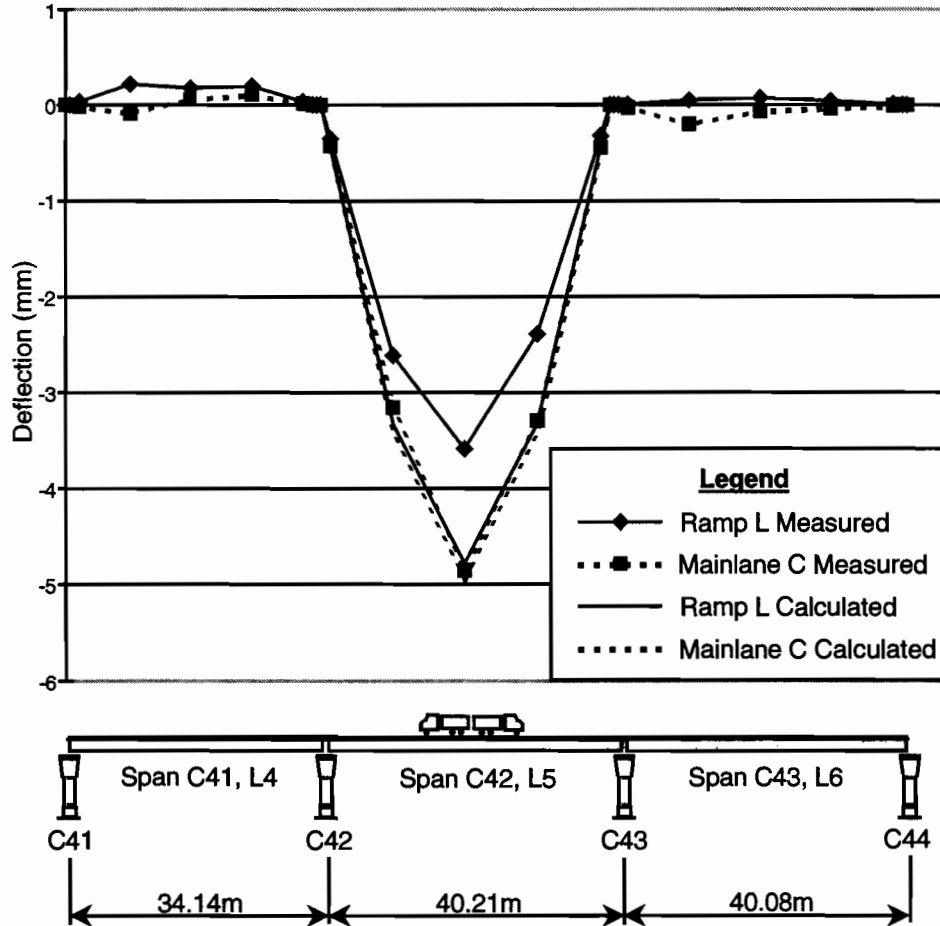


Figure 5.54 Deflections from load case 11

The truck placement for load case 12 placed 2.5 lanes of trucks on the ramp girder and 0.5 lanes of trucks on the mainlane girder for deflection calculation purposes. The ramp girder would carry 83% of the total live-load moment if the girders had no longitudinal connection. The measured deflections in Figure 5.55 indicate that the mainlane girder carried significantly more load than 17% of the total moment. The measured deflection of the mainlane girder was 3.3mm, and the measured deflection in the ramp girder was 6.4mm or 1/6100 of the span length. From calculation the mainlane girder carried 48% of the total live-load moment for load case 12, almost three times the moment predicted by the simple calculation method. The measured and calculated deflections for load case 13 are plotted in Figure 5.56. The truck locations for load case 13 placed all 3 lanes of trucks on the mainlane girder for deflection calculation purposes. The measured deflection for mainlane girder C42 was 5.4mm or 1/7200 of the span length, and the measured deflection for the ramp girder L5 was 2.4mm. From calculation, the mainlane girder carried 80% of the total live-load moment, and the ramp carried 20% of the moment even though no truck wheel loads were located beyond the webline of the mainlane girder.

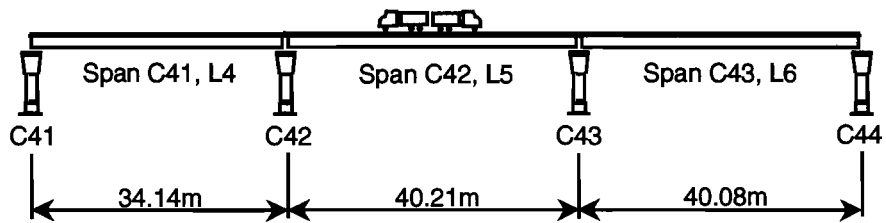
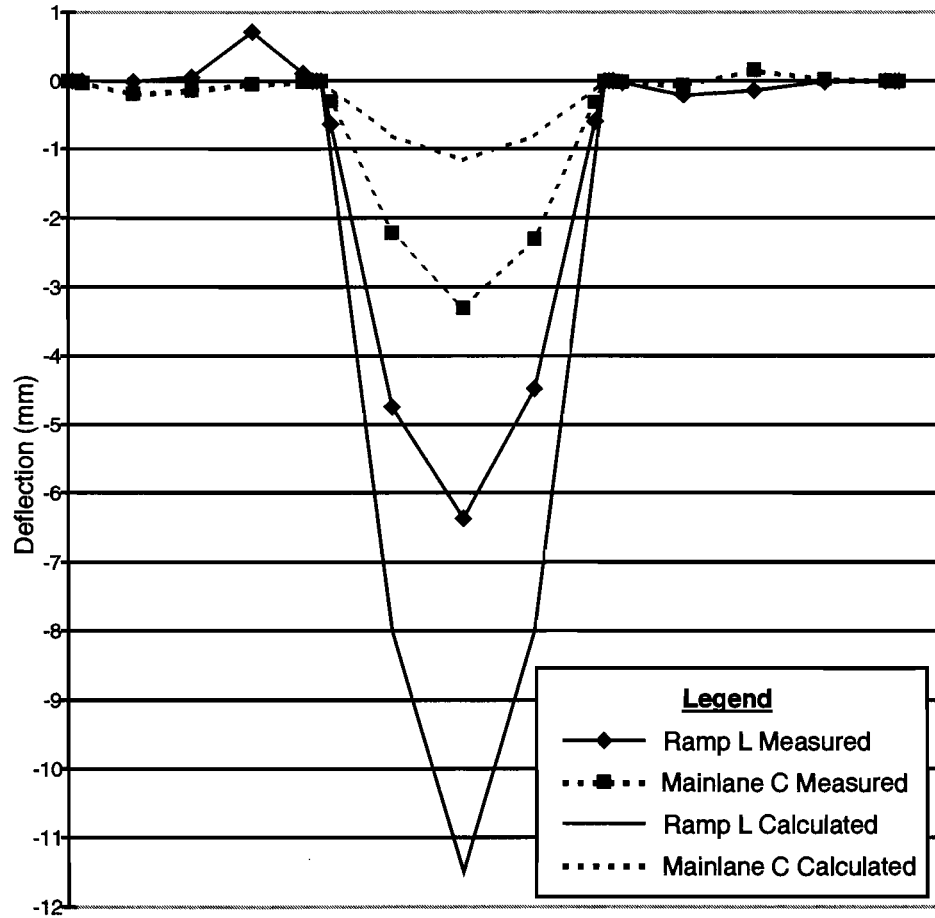


Figure 5.55 Deflections from load case 12

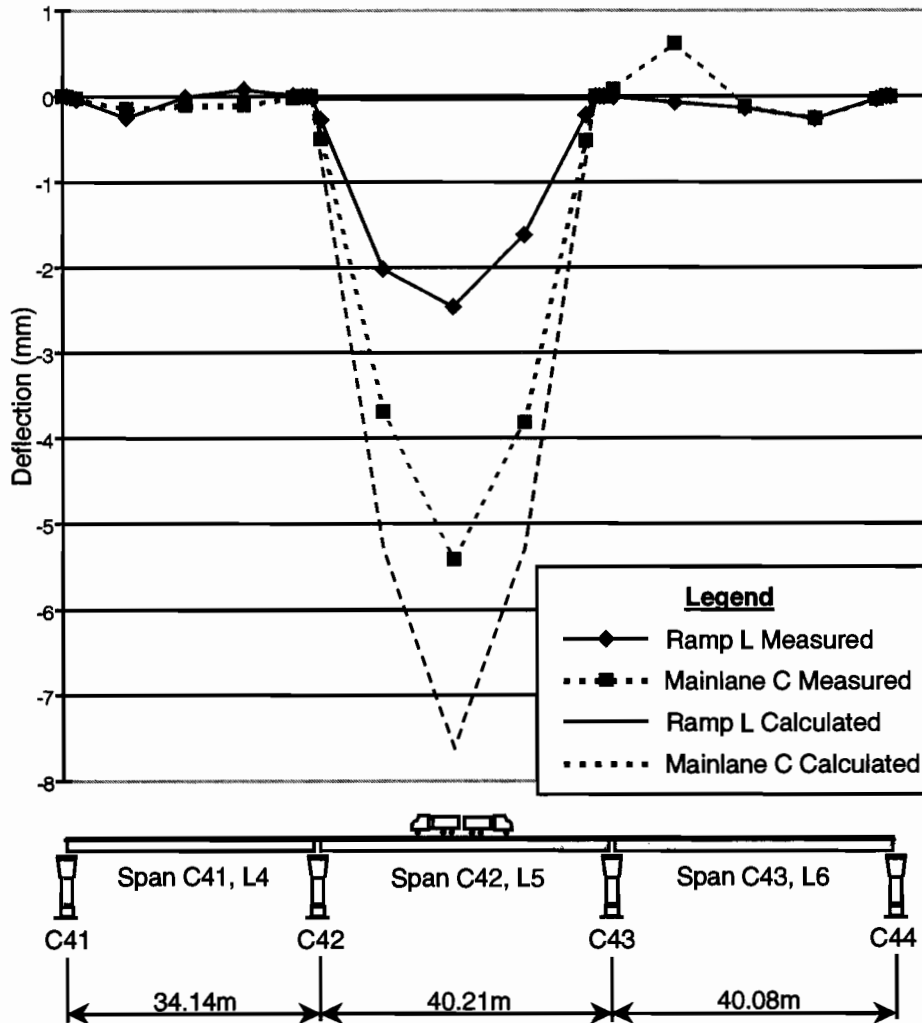


Figure 5.56 Deflections from load case 13

5.4.4 Three-Cell Girder – Unit C13

The three-cell girders of two-span unit C13 were cast-in-place as simple spans. A cross section of the unit C13 girder is shown in Figure 5.57. Since the outer two cells and wings were originally designed to be precast, all the longitudinal post-tensioning was located in these two cells. Also, the bearings supporting the entire span were located only beneath these two cells, with two bearings at each pier. The central top and bottom flanges varied in width from 4800mm in span C36 to 5300mm in span C37. The top flange was post-tensioned transversely. Deflections were measured at the center of each of the three cells. The live-load response of these girders would be expected to differ from that of the twin single-cell girders of Unit C15, L2 because two slabs connect the outer two cells in unit C13, increasing the transverse bending stiffness and substantially increasing torsional stiffness of the central cell.

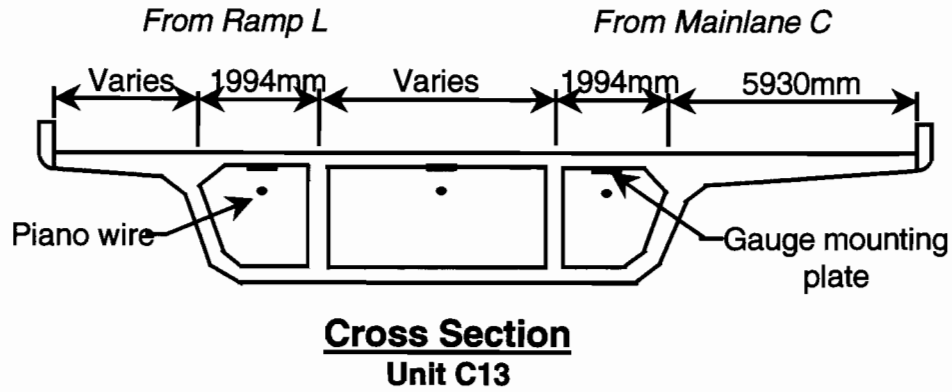


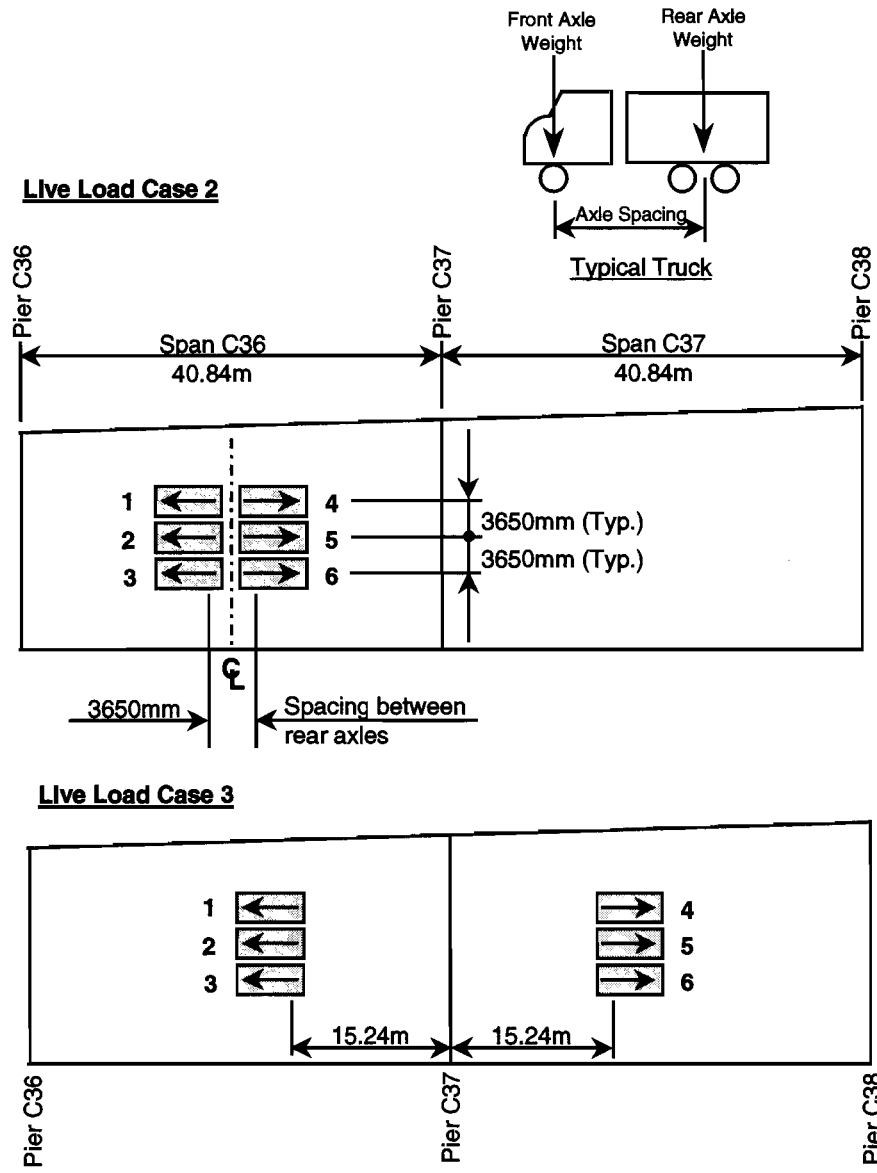
Figure 5.57 Cross section of Unit C13

Live-Load Test

The live-load test was the only test on unit C13. Six dump trucks were placed back to back as in the other live-load tests. The dimensions and weights of the dump trucks are shown in Table 5.4. The five load cases shown in Figures 5.58a and 5.58b are similar to the five load cases tested on unit C15, L2. These load cases were intended to reveal the amount of sharing of bending moments between the two halves of the girders. The three-cell girders were treated as two half girders, or twin single-cell girders, for calculation purposes because bearing reactions were only located under the outer two cells, and the outer two cells were much more compact than the central cell.

Table 5.4 Axle weights and spacing for live-load test trucks on Unit C13

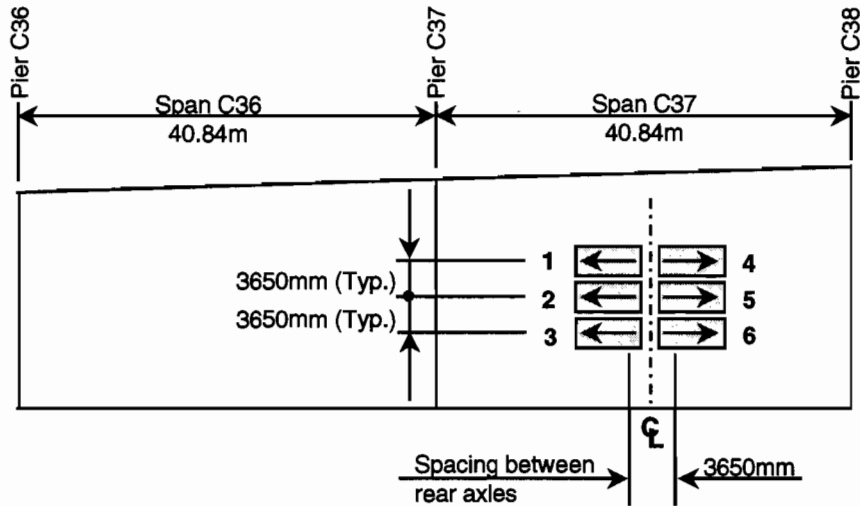
Truck	Weight of Rear Axles (kN)	Weight of Front Axles (kN)	Total Weight (kN)	Axle Spacing (mm)
1	119.2	36.7	155.9	4900
2	117.5	43.9	161.4	4720
3	112.0	45.4	157.4	4900
4	119.0	35.1	154.1	4700
5	113.6	30.6	144.2	4700
6	122.7	41.0	163.7	4090



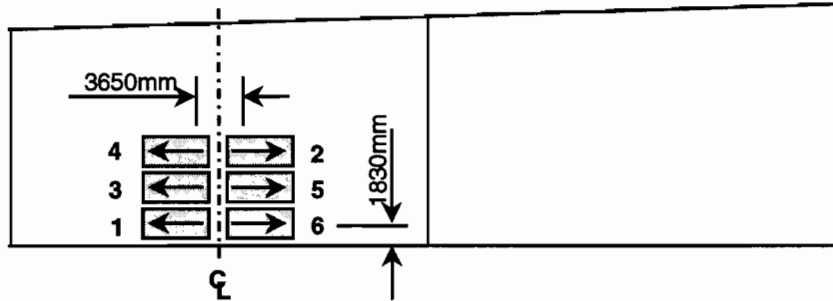
(a) Live-load cases for Unit C13

Figure 5.58 (a) and (b) Live-load cases for Unit C13 (continued)

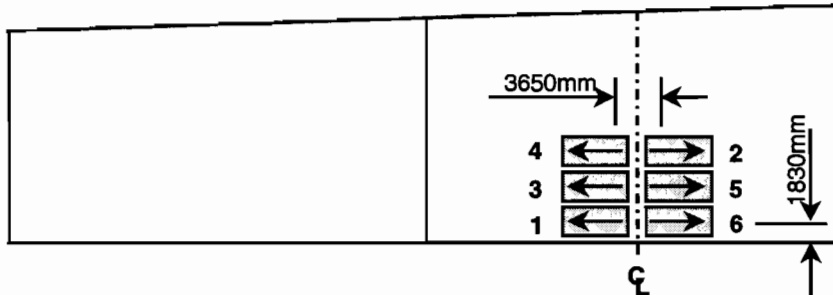
Live Load Case 4



Live Load Case 5



Live Load Case 6



(b) Live-load cases for Unit C13

Figure 5.58 (a) and (b) Live-load cases for Unit C13

Deflection calculations for the load cases to follow were performed using the same assumptions as for the deflection calculation for unit C15, L2, including the AASHTO effective flange width method. A longitudinal cut was taken down the center of both the top and bottom central flanges, and wheel loads falling on each side of the cut were carried by the half girder on that particular side of the cut. The calculated girder stiffnesses used to determine the percentage of live-load moment taken by each half of the girder were also calculated by assuming a longitudinal cut down the centerline of the central top and bottom slabs. This way, the measured deflections could be compared to calculated deflections with well-defined boundary conditions and easily calculated bending stiffnesses.

The measured and calculated deflections from load case 2 are plotted in Figure 5.59. The maximum measured deflection was in the center cell of the girder because of the deflection of the central top slab, and to a lesser extent the torsional rotation of the outer two cells. The calculated deflections assumed that 1.75 lanes of trucks

were carried by the right side of the girder, and 1.25 lanes of trucks were carried by the left side of the girder. The cross section of span C36 was not symmetric with respect with the centerline of the bridge deck, so the symmetrically placed load case 2 was carried more by the right side of the girder that had the longer wing. One line of truck wheels fell exactly on the fictitious longitudinal cut between girder halves. Therefore, calculated deflections assumed that the right side of the girder carried 58% of the total live-load moment, and the left side of the girder carried 42% of the moment. The measured deflection of the right cell was 4.6mm or 1/8900 of the span length, and the measured deflection of the left cell was 4.2mm. The bending stiffness of the left half of the girder was 96% of the bending stiffness of the right half of the girder. Using these values in a calculation, the right half of the girder carried 53% of the load and the left half of the girder carried 47% of the load. These percentages indicate that some of the live-load moment was shared between girders, as would be expected.

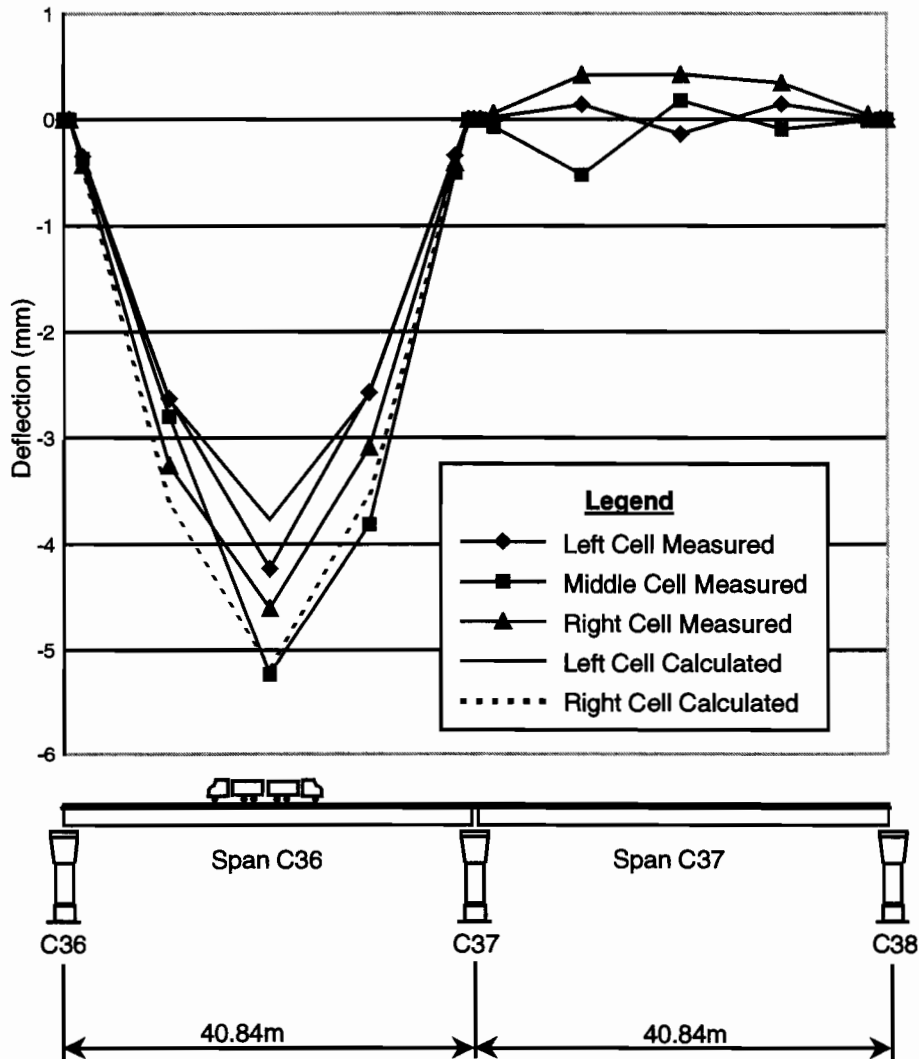


Figure 5.59 Deflections from load case 2

Load case 3 was designed to produce a negative moment over the pier, if possible, but also provided a load case on two spans where the center of gravity of the load was not at midspan. The measured and calculated deflections for load case 3 are shown in Figure 5.60. The calculated deflections assumed that the right and left sides of the girder shared one line of wheels, so the right girder carried 1.75 lanes and the left carried 1.25 lanes as in case 2. The measured deflections in span C36 appear to be effected by the presence of wheel loads near the gauge mounting plates so no conclusions can be drawn from that span. The measured deflections in span C37 from load case 3 indicate a midspan deflection of 1.7mm in the right cell and 1.4mm in the left cell. The bending stiffness of the left cell was 92% of the bending stiffness of the right cell in span C37. From a calculation using the measured deflections and the stiffness ratio, the right side of the girder carried 56% of the

total bending moment and the left side of the girder carried 44% of the total moment. The calculated percentages assuming the longitudinal flange cuts down the centerline of the top and bottom flange were 58% for the right side of the girder and 42% for the left side of the girder.

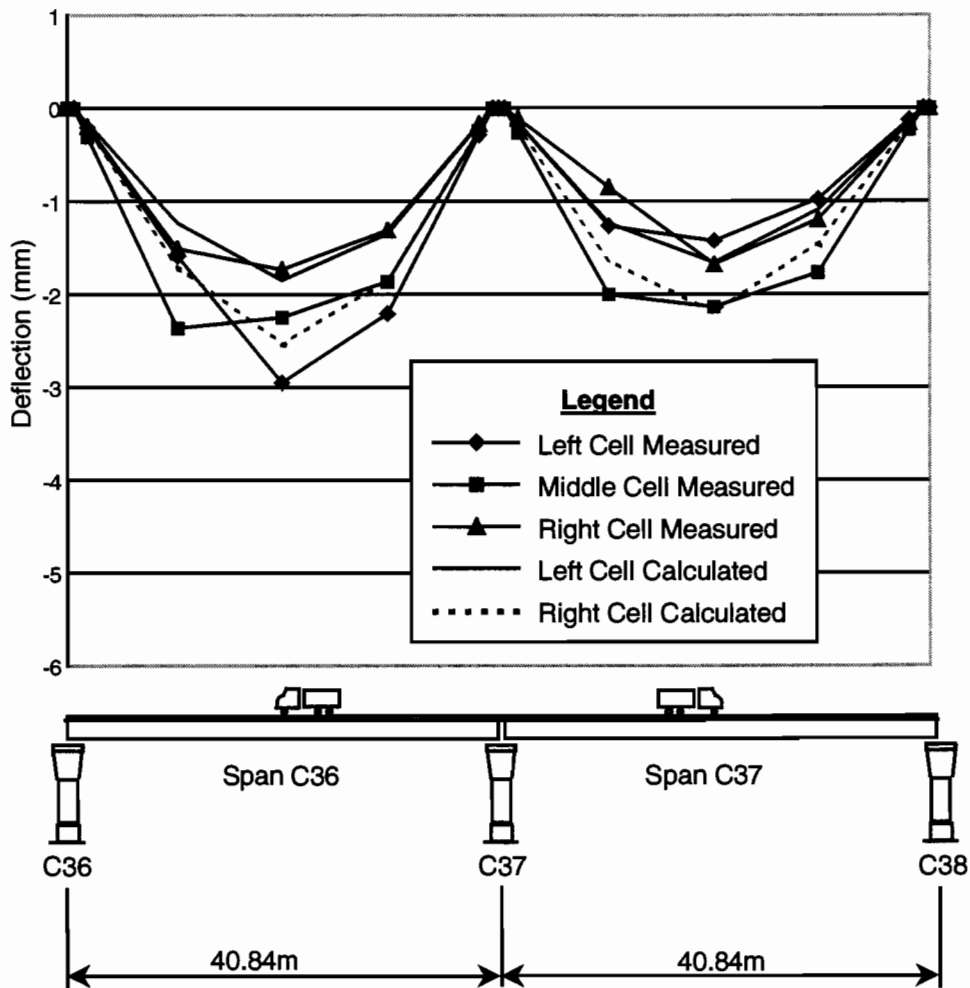


Figure 5.60 Deflections from load case 3

Load case 4 was nearly identical to load case 2, except the live load was placed on span C37. The measured and calculated deflection for load case 4 is plotted in Figure 5.61. The measured deflection of the right side of the girder was 4.2mm, and the measured deflection of the left side was 4.0mm. The right side deflection was only 1/9700 of the span length, which was smaller than the deflection in span C36 from load case 2. From calculation, the right side of the girder carried 53% of the total live-load moment, and the left side of the girder carried 47% of the moment. These are identical to the results from load case 2, even though the relative stiffnesses of the girder halves were different. The calculated deflection calculations assumed that 58% of the total live-load moment was carried by the right girder.

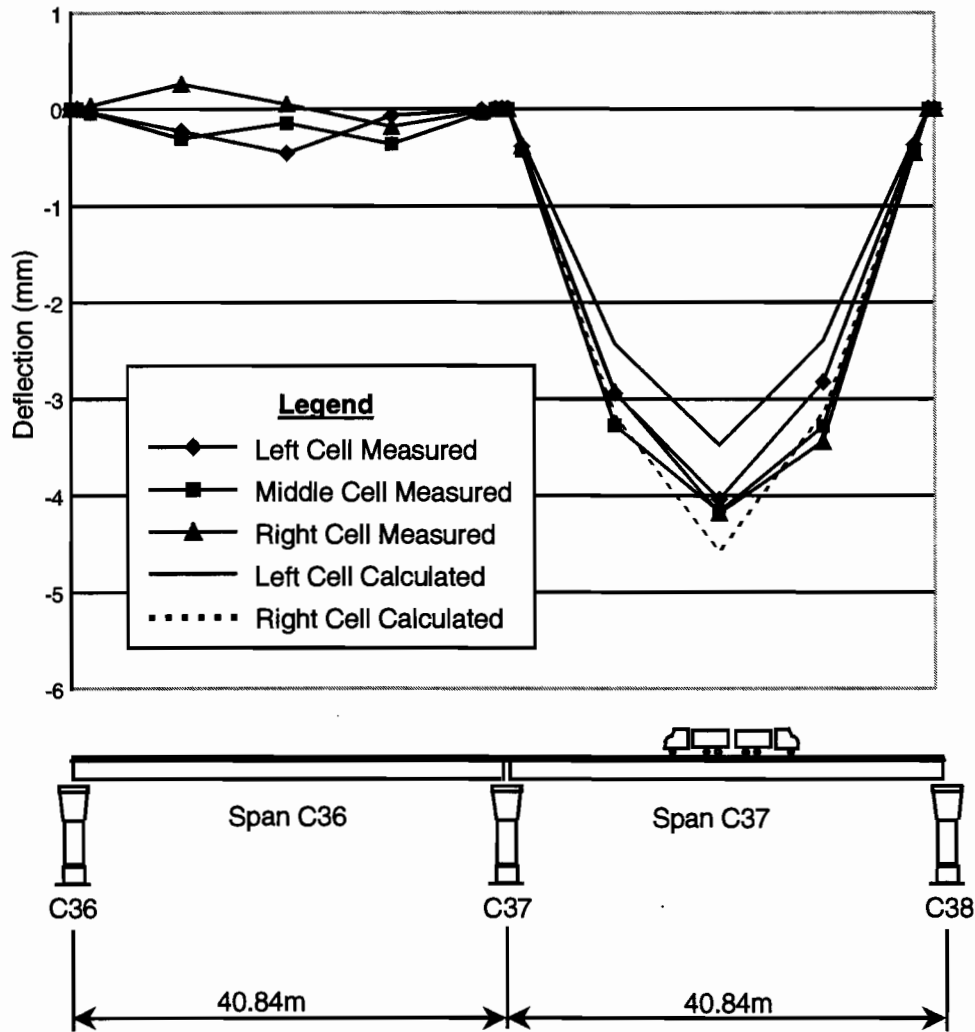


Figure 5.61 Deflections from load case 4

Load case 5 was highly unsymmetrical with all three-load lanes placed on the right girder in span C36. The measured and calculated deflections for load case 5 are plotted in Figure 5.62. The calculated deflection for the right cell is almost twice the measured deflections, indicating significant sharing of the total live-load moment. The measured deflection of the right cell was 5.3mm, and the measured deflection of the left cell was 4.1mm. From calculation, the right cell was carrying only 57% of the total live-load moment, so the left cell was able to share a high percentage of the total live-load bending moment on the girder.

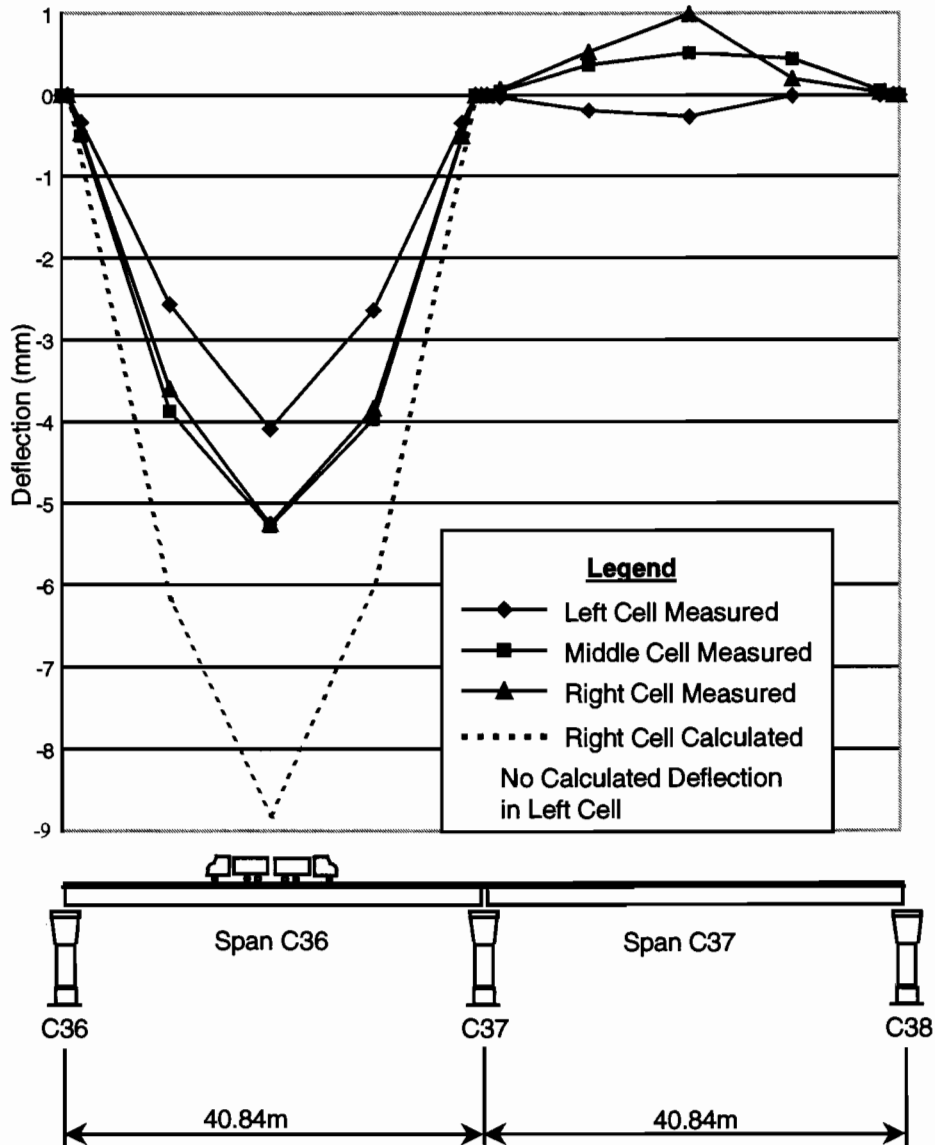


Figure 5.62 Deflections from load case 5

Load case 6 was similar to load case 5 but the load trucks were placed on span C37. All three load lanes were located on the right half of the girder. The measured and calculated deflections for load case 6 are plotted in Figure 5.63. The measured deflection of the right cell was 5.0mm, and the measured deflection of the left cell was 4.1mm. Using the proper ratio of bending stiffnesses for span C37, calculations reveal that just under 57% of the total live-load moment was carried by the right cell. This case was nearly identical to the results from load case 5. The results from load cases 5 and 6 show that the design truck live load for the span produces nearly the same bending moments in two outer cells, regardless of the location of the trucks on the deck. The maximum measured deflections from load cases 5 and 6 were only 1/7700 of the span length.

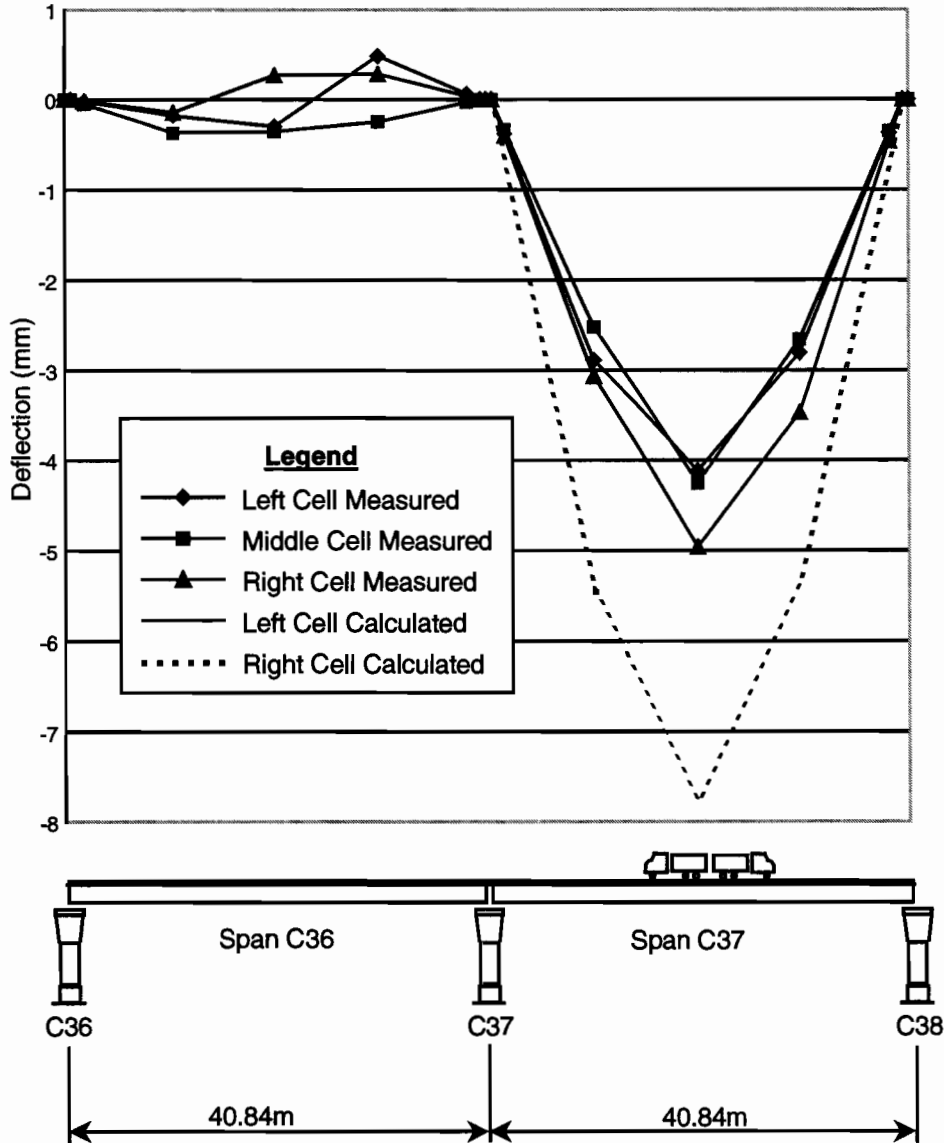


Figure 5.63 Deflections from load case 6

5.4.5 Large Ramp Pier

The large ramp pier P16 was a bending and compression member with the greatest moments occurring during the unbalanced condition from the superstructure construction. Live-load moments on the Ramp P superstructure created bending moments in the pier P16 because the moment connection to the superstructure was not released after superstructure construction was completed. The live-load moments in the pier were smaller than the construction load moments. Strain measurements were taken during all construction stages and during all live-load tests, but the performance of the pier could best be evaluated by studying the load cases providing the largest strain changes.

Response of Large Ramp Pier P16 to Superstructure Construction Loads

The Ramp P superstructure was constructed in balanced cantilever with an unbalanced moment on the piers no larger than that from the weight of one superstructure segment. Since the contractor had trouble adequately stressing the superstructure to pier tie down bars on pier P16, this unbalanced moment was taken partially or completely by the crane used to lift the segment into place. This action was possible since two ground-based

cranes were used to construct the five-span continuous girder on Ramp P. The complicated construction sequence and limited ground access dictated the use of two cranes. Unfortunately, the maximum unbalanced moment on pier P16, as predicted in the pier's design, never occurred. Instead, the maximum moment in the pier from the superstructure construction occurred when segment P16-17 was placed. This segment was the final one placed in cantilever near the midspan of span P16. Most importantly, this segment was placed after continuity had been made in the superstructure span P15. The cantilevering moment from segment PC16-17 was distributed to both pier P16 and to the superstructure span P15 and pier P15. The response of pier P16 was measured for this load case.

Measurements were taken by strain gauges oriented vertically at several locations along the height of pier P16. The bending moment in the pier would have been essentially constant along the height of the pier during balanced cantilevering, but since the pier was part of an indeterminate frame when segment PC16-17 was placed, the moment in the pier changed over its height. Four planes of gauges were selected for study. The first plane of gauges was in segment PC16-1 located 2.057m above the top of the footing. The second set of gauges was in segment PC16-5 located 12.167m above the top of the footing. The third set of gauges was in segment PC16-7 located 16.085m above the top of the footing. The fourth set of gauges was located on the 16 vertical tie down bars located near the top of the pier capital segment PC16-8, 19.810m above the top of the footing. The length from the top of the footing to the center of gravity of the superstructure box girder was 21.886m. The 285kN load from the placement of superstructure segment P16-17 had a cantilever arm of 25.845m to the center of gravity of the pier, yielding a bending moment of -7366kN-m to be distributed to the structure. Because of the horizontal curvature of the superstructure, a torque of 435kN-m also had to be distributed to the structure.

Figures 5.64 through 5.67 show the measured concrete stresses at the gauge locations and calculated stresses along the north-south axis. The superstructure centerline geometry was exactly parallel to the pier's north-south axis at pier P16, as well as the other ramp piers. For the purpose of comparison, a plane frame analysis was performed, ignoring torque effects, and is plotted in Figures 5.64 through 5.67. The solid line assumed fixity at the top of the footing. The dashed line assumed the point of fixity was 4.2m below the top of the footing to account for flexibility of the footing and four 1.070m drilled shafts. The 4.2m pier height increase was chosen to calibrate the model to the measured results of gauges C400, C402, C410 and C412 in Figure 5.64 along the north-south axis of the pier. These gauges in segment PC16-1 were located near the point of inflection in the pier. Distribution of the cantilever moment of -7366kN-m was -3263kN-m to pier P16 and -4103kN-m to span P15 when fixity was assumed at the top of the footing. Distribution was -3041kN-m to pier P16 and -4324kN-m to span P15 when the point of fixity was moved down 4.2m.

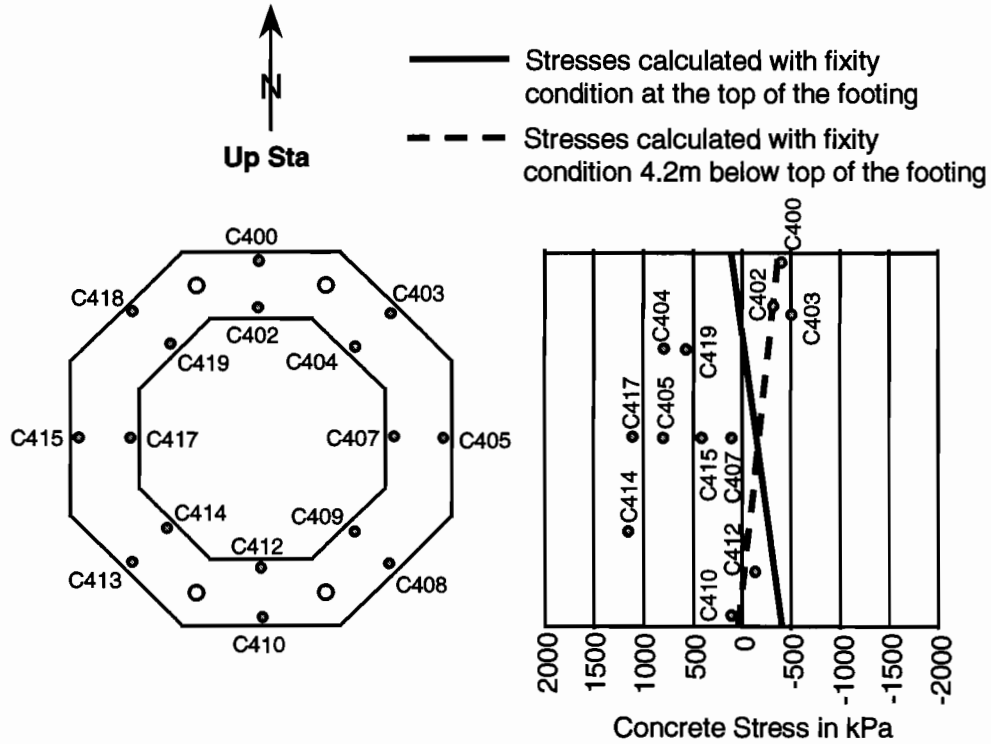


Figure 5.64 Stresses in pier segment PC16-1 from placement of superstructure segment P16-17

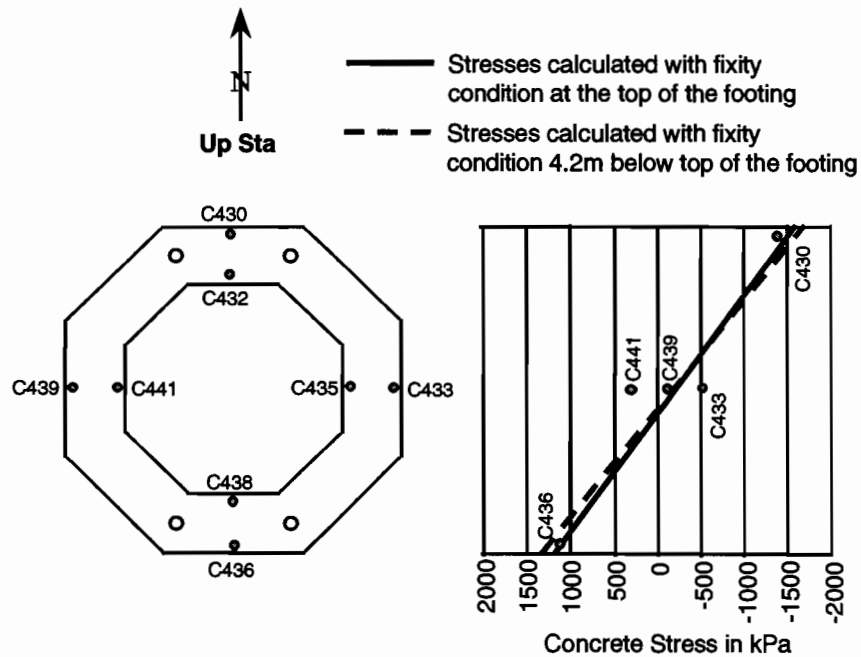


Figure 5.65 Stresses in pier segment PC16-5 from placement of superstructure segment P16-17

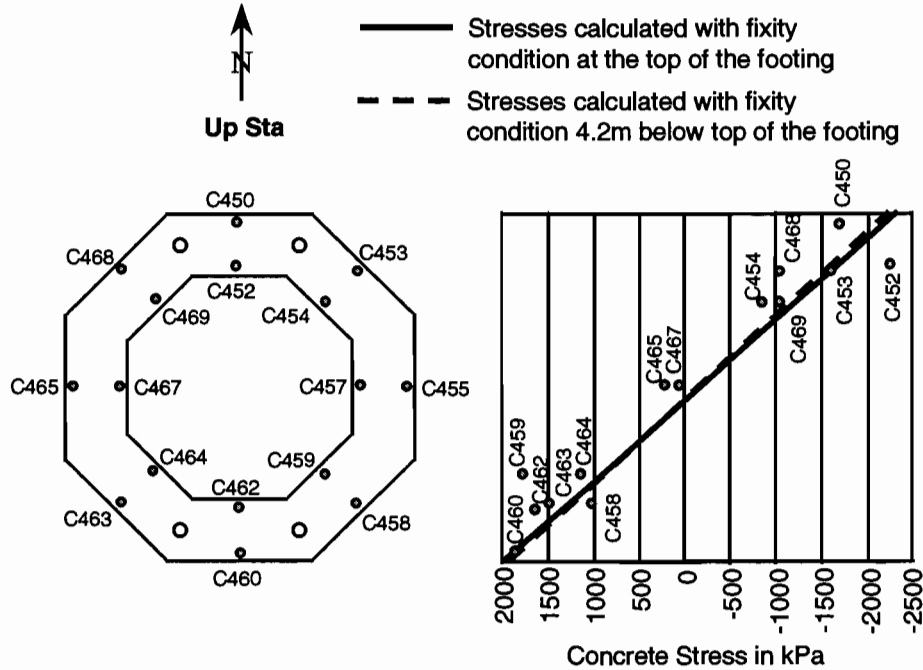


Figure 5.66 Stresses in pier segment PC16-7 from placement of superstructure segment P16-17

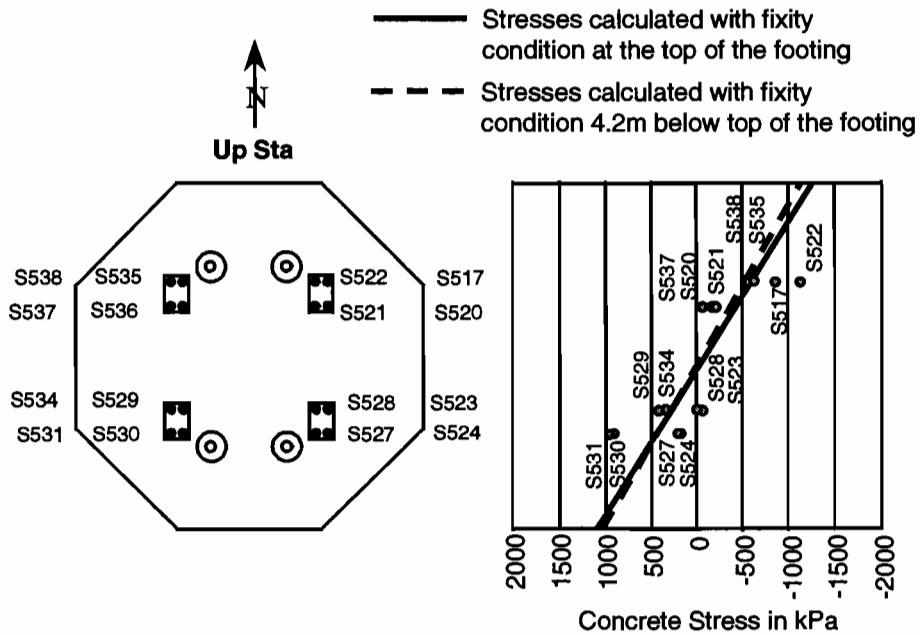


Figure 5.67 Stresses in pier segment PC16-8 tie-down bars from placement of superstructure segment P16-17

In plan view, the torque from the superstructure would tend to cause tension in the west face of the pier. This situation is poorly reflected by the gauges in segment PC16-1 in Figure 5.64. This trend is consistently evident as indicated by the gauge measurements in Figures 5.65 through 5.67. If the entire torque were taken by pier P16, the change in the calculated stresses in the extreme fibers along the east-west axis, plotted in Figures 5.64 through 5.67, would be about 400kPa. The horizontal radius of the superstructure was only 218.3m, so torsional effects were included in the design of this pier.

Pier P16 was compact and regular in shape over much of its height and appears to have behaved in a very predictable way, with stress change linear across the section. The accuracy of the design of this pier would rely more on the accuracy of the analysis, not on the sectional behavior of the pier. Accurate modeling of the foundation stiffness would be part of a good design of this pier. The post-tensioned connection of the superstructure to the pier also behaved in a predictable manner. The calculated stresses plotted in Figure 5.67 assumed that plane sections remained plane in the grout pad on top of the pier capital, and therefore the full moment of inertia of the grout pad could be used. This assumption appears to have been valid, since the measured stresses plotted in Figure 5.67 fall on either side of the calculated stresses. No tension in the connection was evident.

5.5 DISCUSSION OF RESULTS

The following discussion compares the measured results for the different structural elements that were instrumented. The results calculated using the design code methods are also evaluated.

5.5.1 *Diffusion of Post-Tensioning*

The first post-tensioning force to be diffused into a segmental concrete bridge is often the temporary force required to squeeze the segment joints during epoxying. The AASHTO Segmental Guide Specification requires that a minimum of 0.28MPa of stress must exist at all points on the segment joint during epoxying to squeeze the epoxy out of the joint so that concrete surfaces are in contact and presumably to close any geometrical inconsistencies between match-cast joint faces. From visual inspection, this temporary force was not sufficient to close the gap that existed between the center of the top flanges of the mainlane segments in all instances. Epoxy was able to slide down the joint after the temporary force had been fully applied. Additional force should be applied to close these gaps in segmental bridges wide enough to be susceptible to significant thermal-induced warping during casting and curing.

The temporary epoxying stresses measured in the Ramp P segment (shown in Figure 5.33) were just adequate to squeeze the epoxy at all points of the segment joint, but the measured stresses did not meet the code specification at the wing tips and at one point of the bottom flange. The stress plot shows that the temporary joint force was poorly diffused into the section. Designers should give some consideration to the diffusion of the temporary joint forces from the temporary anchorage blisters or other anchorage location. The Ramp P segments had most of the temporary joint force anchored at two blisters located at the tops of the webs inside the core of the box girder. This location was an excellent one for the blisters from a construction standpoint, but the force was too low or too remote to squeeze the wing tips. Also, because of the lack of diffusion of the temporary force into the wings, the bottom flange was put into tension from the stressing of the top four temporary force post-tensioning bars. The contractor had to stress the bottom bar first in order to close the joint across the bottom flange. As the top bars were stressed, the force in the bottom bar changed little because its elastic modulus was much larger than the modulus of elasticity of the concrete, and strain changes were small.

Indications from strain measurements in the mainlane girder anchor segment were that the post-tensioning force from the 6 deviated tendons and 14 bottom slab tendons was diffused to a greater extent than would be found using the AASHTO 30° diffusion method. The shape of the diffused stresses was predicted poorly by the calculation. These tendons were located within or immediately next to the heavy end diaphragm in the anchor segment. The AASHTO 30° diffusion method predicted slightly more diffusion than was measured to occur for the cantilever tendons in segment P16-10, shown in Figure 5.35. The girder wings took more stress than predicted by the calculation, and the webs took less stress. Given the simplicity of the 30° diffusion method, stresses were adequately predicted at the instrumented section in segment P16-10. No diaphragm existed at this location.

Strain measurements at the midspan section of the mainlane girder indicated that the post-tensioning forces had diffused to a nearly uniform distribution (see Figure 5.21), even though the AASHTO effective flange width method would predict otherwise by a small amount. Using the 30° diffusion method, post-tensioning stresses should have been uniform at this cross section of the girder. The cantilever post-tensioning tendon forces did not diffuse to a uniform distribution in segment P16-2 (see Figure 5.36) because the anchorage locations were spaced along the span at each segment joint. Therefore, some of the anchorages were located quite close to the instrumented section in segment P16-2. The prestressing forces and bending moments from the continuity tendons in Ramp P generated well-distributed stresses across the girder cross sections with the exception of the

instrumented section in P16-2 (see Figure 5.39). The anchorages for two sets of the deviated external tendons were too close to that section to be fully diffused.

In general, at cross sections where the AASHTO 30° diffusion method would predict full diffusion of a post-tensioning force, the measurements revealed a nearly uniform distribution of stresses from that prestressing force. Since neither the Ramp P girder nor the mainlane girder required a significant reduction in wing or flange length for the AASHTO effective flange length calculation, the effect of shear lag from primary prestressing moments may not have been seen in the measurements. The b_f curve in Figure 5.10 should be used for the entire girder to account for shear lag effects from primary prestressing moments. For secondary prestressing moments, the appropriate curve b_s or b_f should be selected depending on the location on the span, as specified by AASHTO, since the secondary moments are generated by the pier reactions. If the exact diffusion of post-tensioning forces must be known at points close the anchorages, the AASHTO 30° diffusion method is not sufficiently accurate for the calculation.

5.5.2 Response to Dead Loads and Live Loads

Use of the cross-section properties calculated using the AASHTO effective flange width method adequately predicted the dead load plus prestress final stress distribution for the mainlane girder (shown in Figure 5.21), although an insufficient number of measured data points existed to determine the exact shape of the stress distribution in the flanges. The live-load stresses calculated for mainlane live-load cases 2 and 8 predicted the location of the neutral axis of the girder quite accurately, as seen in Figures 5.25 and 5.26, when the AASHTO effective flange width method was used. The location of the neutral axis was also predicted very accurately for live-load cases 1 and 2 in Ramp P (shown in Figures 5.47, 5.48 and 5.49), although the effective flange for these cases was nearly the actual length. The differences between the measured and calculated stresses in the flanges were mostly due to an underestimation of the modulus of elasticity of the concrete. The maximum measured live-load stress changes for these girders were only 15% of the maximum allowable service level stress. Deflections measured during the live-load cases were similarly small at 1/6500 of the span length or less for the simulated HS20-44 truckloads. Dead-load deflection for the mainlane girder was 1/1050 of the span length, so the live-load moments were about 16% of the dead-load moments.

The AASHTO effective flange width method provided section properties that gave realistic calculated stresses. The major problem with the method is that the moment of inertia of the girder must be calculated at several sections on every span. Using a stepped transition for the flange widths near the piers to the flange widths near midspan would only simplify the calculation in some instances. In a continuous structure, the bottom slab thickness is often modified to provide some extra moment of inertia near the interior piers, so section properties would be varying anyway. The moment of inertia at random sections within the AASHTO tapered transition can be found with sufficient accuracy by interpolation, so little time is saved by using a stepped transition. The greatest realization of time lost is when standard box girder sections are being used with tabulated section properties. Cutting the flanges to their effective width potentially requires minor recalculation of the moment of inertia and neutral axis location for many cross section locations.

A faster method would modify the moments or stresses found from a normal analysis with the full section properties. For example, the moment diagram could be modified by a function of the absolute value of the shear diagram and the girder shape. Peak stresses would be calculated based on the modified moment diagram. The function could be calibrated to results using the AASHTO effective flange width method over a range of b/l_i (from Figures 5.8 and 5.9) of 0.05 to 0.20. This range would cover the flange widths most used in segmental box girder bridges.

5.5.3 Behavior of Multiple-Cell Box Girders

Deflections measured during the live-load tests revealed that significant sharing of live-load moments was occurring in the multiple-cell girders, especially for the highly unsymmetrical load cases. A summary of the test results for these girders is given in Table 5.5. Column (3) in the table is a record of the measured deflections at midspan. Column (4) in the table contains the percentage of total bending stiffness for each girder or girder half assuming the shared central flanges were cut longitudinally down the center. Column (5) gives the calculated percentage of the total live-load moment carried by each girder or girder half based on the data in columns (3) and (4). Column (6) gives the percentage of the live load applied to the girder deck, assuming a longitudinal cut down the centerline of the central girder flanges. The percentage of the total

moment carried by the mainlane C girders in load cases 9, 10, 11 and 12 indicates that the mainlane girders carried more than their expected share of the total moment. This is attributable to the higher torsional stiffness of the mainlane girders. Both the mainlane girders and the ramp girders were set on relatively soft elastomeric bearings. The distance between bearings at each pier for the mainlane girders was 3350mm, and the distance between bearings for the ramp girders was 1830mm.

Table 5.5 Summary of live-load test results for multiple-cell girders

(1) Load Case	(2) Girder	(3) Measured Deflection (mm)	(4) % of Total Bending Stiffness	(5) % of Total Live Load Moment Carried	(6) % of Live Load Applied To Girder Deck
9	C41	3.0	64%	71%	67%
9	L4	2.2	36%	29%	33%
10	C41	1.9	64%	80%	67%
10	L4	0.9	36%	20%	33%
10	C42	2.4	64%	77%	67%
10	L5	1.3	36%	23%	33%
11	C42	4.9	64%	71%	67%
11	L5	3.6	36%	29%	33%
12	C42	3.3	64%	48%	17%
12	L5	6.4	36%	52%	83%
13	C42	5.4	64%	80%	100%
13	L5	2.4	36%	20%	0%
2	C36 Right	4.6	51%	53%	58%
2	C36 Left	4.2	49%	47%	42%
3	C37 Right	1.7	52%	56%	58%
3	C37 Left	1.4	48%	44%	42%
4	C37 Right	4.2	52%	53%	58%
4	C37 Left	4.0	48%	47%	42%
5	C36 Right	5.3	51%	57%	100%
5	C36 Left	4.1	49%	43%	0%
6	C37 Right	5.0	52%	57%	100%
6	C37 Left	4.1	48%	43%	0%

Similar behavior was seen in unsymmetrical load cases 12 and 13. In load case 12, 83% of the truckload was placed on the ramp girder L5, yet the mainlane girder C42 carried 48% of the total live-load bending moment. When 100% of the total live load was placed on the mainlane girder C42 in load case 13, only 20% of the total live-load moment was carried by the ramp girder. Therefore, the ramp girder can more easily distribute its live-load moments to the more torsionally rigid mainlane girder. The stiffness of the bearings must be included in

an analysis calculating the load sharing between these two single-cell girders. The maximum measured live-load deflection for the ramp L girder was very small at only 1/6300 of the span length.

The behavior of the three-cell unit C13 was quite different from that of unit C15, L2. A heavy diaphragm was cast the full width of the three-cell girders over the centerline of bearing, so the torsional rigidity of the individual cells was unaffected by the bearing stiffnesses. In symmetrical live-load cases 2, 3 and 4 the slightly right-of-center live load (58% on the right girder half) was carried by both girders almost evenly (53% to 56% of the total live-load moment carried by the right girder half). For the highly unsymmetrical load cases 5 and 6, where the entire load was placed on one girder half, only 57% of the total live-load moment was carried by the loaded girder half, and 43% of the moment was distributed to the other girder half. The presence of the heavy pier diaphragm would have great influence on live-load moment and stress calculations for this girder, simplifying the calculation. Maximum live-load deflections of unit C13 were similar to the maximum deflections measured during the other live-load tests at only 1/7800 of the span length.

5.6 CONCLUSIONS

The following conclusions have been made based on comparisons of the measured data with the calculated results:

5.6.1 *Temporary Post-Tensioning for Epoxying Segments*

1. An engineer should determine if the segments under design will take a "banana" shape during casting and curing, estimate the warping deflection that will occur, and include the deflection in the design of the temporary post-tensioning to ensure full closure of the gap.
2. The diffusion of the temporary post-tensioning force from the anchorages or blisters should be estimated and stresses calculated at the extremities of the cross section away from the anchorage points. Assuming that plane sections will remain plane, and that a linear stress gradient will pass through the center of gravity of the section may lead to an inaccurate estimate of the actual stress distribution. The temporary post-tensioning forces and locations should be designed to adequately stress the entire cross section considering diffusion. Furthermore, the dead load of the segment constructed in balanced cantilever will not produce a predictable stress distribution during the epoxying and temporary post-tensioning process and should not be relied upon as a source of bottom flange squeezing stress.
3. The sequence of temporary post-tensioning should be considered, especially if anchorages are not well distributed throughout the cross section.

5.6.2 *Diffusion of Post-Tensioning Forces*

1. The AASHTO 30° diffusion method tended to underestimate the amount of diffusion of post-tensioning forces from anchorages in or immediately adjacent to anchorage diaphragms.
2. The AASHTO 30° diffusion method is not sufficiently accurate for calculating stresses in the vicinity of post-tensioning anchorages.
3. The AASHTO 30° diffusion method was sufficiently accurate for predicting the distance from an anchorage to the point of full diffusion into the cross section.
4. At sections where the post-tensioning force is calculated to be fully diffused, shear lag in the cross section from primary post-tensioning moments can be compensated for by using the AASHTO effective flange width method. Only the b_f width should be calculated and used over the entire span since the pier reactions are not included in the calculation of primary moments or the stresses resulting from these moments.
5. Use the AASHTO effective flange width method for predicting cross-sectional stresses from secondary moments.

5.6.3 *Girder Response to Dead Loads and Live Loads*

1. The measured stresses and deflections from the simulated HS20-44 truckload (no impact) were quite small when compared to girder dead load. Live loads on the mainlane girder produced deflections only 1/6500 of the span length, while calculated dead-load deflection was 1/1050 of the span length.

2. The AASHTO effective flange width method gave sufficiently accurate results for the calculation of stresses and deflections from dead loads and live loads, although the girders tested did not experience significant shear lag at sections of high moment and stress gradient.
3. The AASHTO effective flange width method requires considerable section property calculation for girders that may only experience a small amount of shear lag, such as most common segmental girders and nearly all simple-span segmental girders. Another method should be developed for these girders that uses unmodified section properties.

5.6.4 Performance of Multiple-Cell Girders under Live Load

1. The twin single-cell girders tested shared as much as 30% of the applied live-load moment.
2. The amount of live-load moment sharing between the twin single-cell girders was sensitive to the torsional stiffness of each girder. The stiffness of the bearings must be included in the design of these girders.
3. The three-cell girders tested consistently shared as much as 43% of the applied live-load moment.
4. The amount of live-load moment sharing between sides of the three-cell girders was not sensitive to the stiffness of the bearings because of the presence of the pier diaphragm that was cast full width of the three girder cells.
5. Live-load deflections were quite small in the multiple-cell girders with a maximum measured deflection of only 1/6300 of the span length or smaller.

5.6.5 Performance of the Segmental Pier under Bending

1. The cross-sectional behavior of the segmental pier was entirely predictable, but the stiffness of the drilled shaft foundation had to be included in the analysis.
2. The moment connection of the pier to the balanced cantilever ramp superstructure using a cast-in-place grout pad and 16 post-tensioning bars performed as would a monolithic connection.

CHAPTER 6

BEHAVIOR OF DISCONTINUITY (OR D-) ZONES

6.1 PROBLEM AND TECHNICAL BACKGROUND

The design of a post-tensioned segmental box girder or pier must include the design of several discontinuity or D-zones. A D-zone can be described as a region of the structure in the immediate vicinity of an applied concentrated force or drastic change in structural geometry. In such regions, a plane section before loading generally does not remain plane after loading. Since the design of the structure in regions of constant or gradually changing cross-sectional properties (B-zones where plane sections remain plane) is relatively straight forward, many of the problems encountered in post-tensioned segmental structures occur because of design deficiencies or uncertainties in the D-zones. The improper or unconservative design of D-zones may create serviceability problems that overshadow the basic structural soundness of the entire bridge and lead to skepticism regarding the safety of post-tensioned segmental bridges by engineers and the public sector alike.

Because of its basic nature, a post-tensioned structure has very large applied concentrated forces at post-tensioning tendon anchorages. Thus, the design of several anchorage zones is inevitable. The locations of the anchorage plates frequently do not lie within the confines of the typical cross section, requiring anchorage diaphragms or blisters. Furthermore, external tendons require deviators at points along the superstructure that must transfer large vertical forces to the girder. Another source of concentrated force is the reaction of the pier on the superstructure. Segmental box girders generally have one and occasionally two cells. Therefore, the girder webs carry large shear forces that are usually eccentric to the pier or bearing reactions because of the inclination of the webs or bearing locations. The segments located over the piers must be designed to carry the superstructure loads to the bearing reactions, as well as to provide anchorage zones for many of the post-tensioning tendons.

The design of a post-tensioned box girder or pier generally includes two distinct design limit states. The first case is the service load state. The cross section of the girder or pier is usually post-tensioned in such a manner that little or no tension occurs in the concrete, so cracking is not expected and elastic analysis is usually valid. The second design limit state is the factored load limit state, in which the ultimate strength of the girder is checked. Plastic analysis is used for determining resistance at the factored load limit state, as cracking of the concrete and yielding of the tendons and of the mild steel reinforcement may be expected. The design of D-zones must also include these two limit states, but the proper method of analysis may not be readily evident to the engineer. For example, in the design of anchorage zones and deviators, the difference between the applied service level forces and the ultimate forces from the tendons is small, since at service load conditions the tendons are generally stressed to 70% or 80% of their ultimate strength. If the D-zone is designed to be post-tensioned, an elastic analysis may often be valid for the service level limit state and possibly the ultimate limit state. The more common design approach uses plastic methods to design the D-zone at the ultimate limit state as a reinforced concrete structural element. Then the proper distribution of mild reinforcement and sometimes the addition of post-tensioning are chosen to ensure adequate performance at the service limit state.

Strut-and-tie modeling (STM) is increasingly becoming the most common method for plastic analysis of D-zones. The method allows the engineer to visualize the flow of forces in the D-zone, as well as providing a conservative equilibrium model of the D-zone. Strut-and-tie modeling can trace its origin to 1899 with William Ritter's [46] introduction of the truss model for shear design of reinforced concrete beams and Mörsch's [47] introduction of the truss analogy for design of web reinforcement in 1902. Strut-and-tie modeling is a generalized application of the truss analogy. Marti [48] and Mueller[49] created the strut-and-tie model's scientific basis for a rational application, working with Thürliman [50] at the Swiss Federal Institute of Technology, using the theory of plasticity. Leonhardt had advanced the practical use of STM at the University of Stuttgart and in his consulting practice [51]. Schlaich et al further developed STM as a consistent method by which structural concrete can be designed. Their landmark PCI Journal paper was the first major introduction of STM into US literature [52]. A thorough history of strut-and-tie modeling can be found in Bergmeister [53].

Schlaich et al give numerous useful examples of strut-and-tie models in the PCI Journal paper [52], such as the basic models in Figure 6.1. These models can be used to represent the diffusion of concentrated forces. Some

of the strut-and-tie models presented in the PCI Journal paper [52] were intended for box girder structures, such as the models shown in Figure 6.2. Many of these models were reproduced with permission and included in the *AASHTO Guide Specification for the Design and Construction of Segmental Concrete Bridges* [8]. The models shown in Figure 6.2 can be used to calculate the tension forces generated by the transfer of the web shear forces to the single bearing. A possible arrangement for post-tensioning bars is shown in part c) of the figure. In the PCI Journal paper, Schlaich et al give the guidelines and criteria needed to develop an efficient model that will provide good service level performance. Proper assembly of a model requires an understanding of the basic components (struts, ties, and nodes). The elements of the model occupy much of the physical space of the structural element under design, which differs substantially from the design of an actual truss with essentially one-dimensional members. Schlaich et al recommend three types of struts, shown in Figure 6.3, that differ in failure criterion because of their differences in transverse tensile stresses. The determination of tie forces may also require careful consideration since the tie force may be shared by an array of bars and uncracked concrete instead of one or several larger bars. Nodes are defined as singular or smeared nodes. Of paramount importance in nodes with discontinuous or deviated tension ties is adequate anchorage of the tie. Several models of nodal regions are given in Figure 6.4.

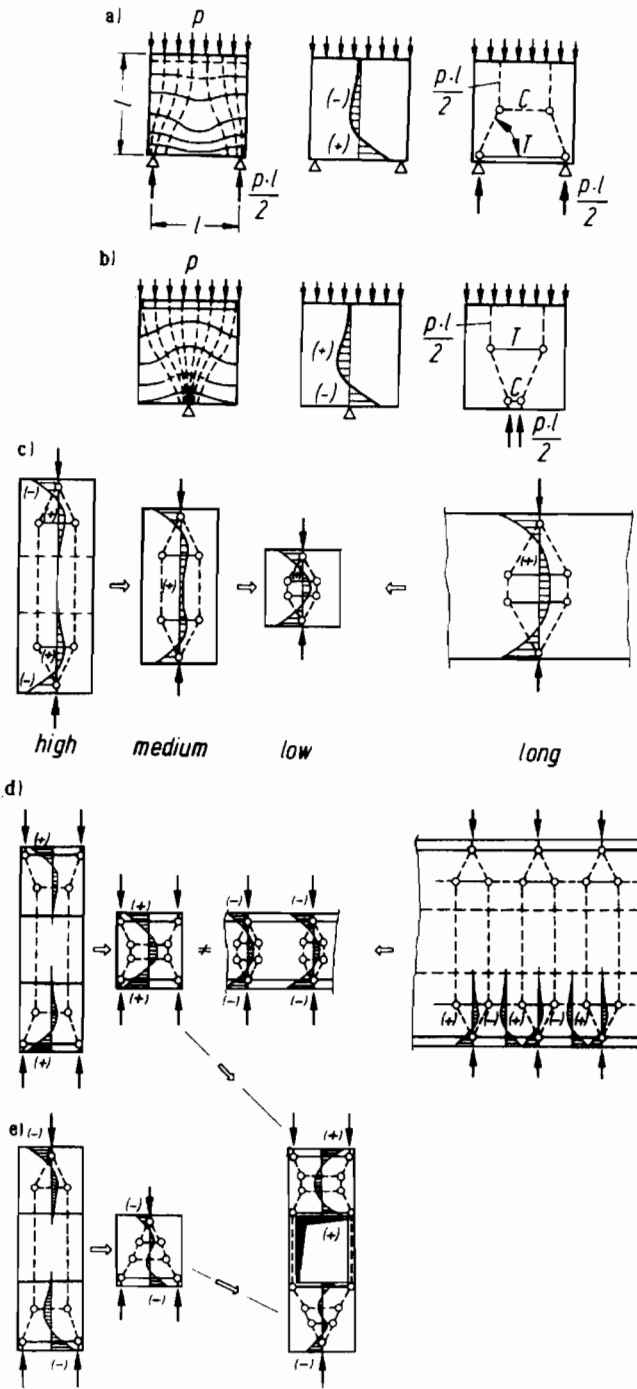


Figure 6.1 Typical strut-and-tie models [52]

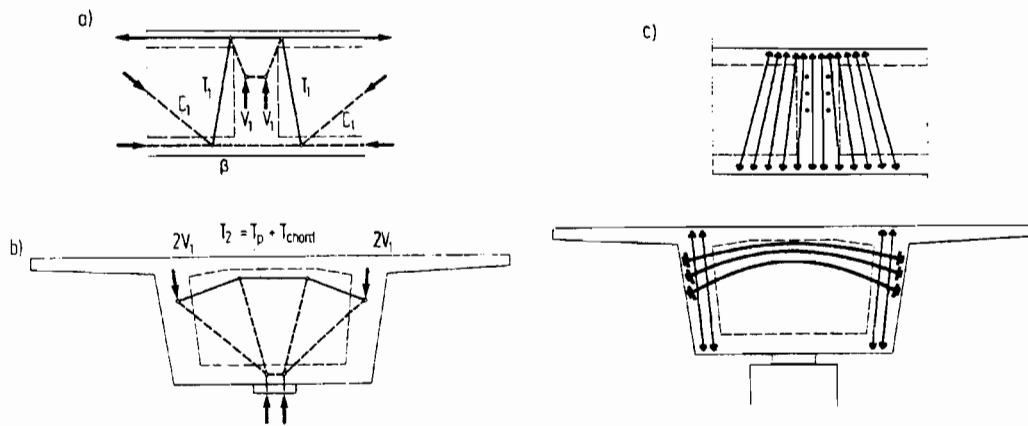


Figure 6.2 Typical strut-and-tie models for segmental box girder design [52]

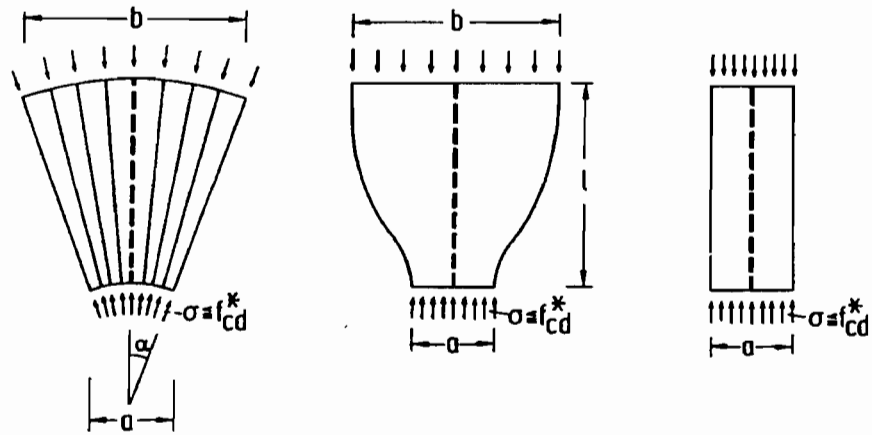


Figure 6.3 Strut types [52]

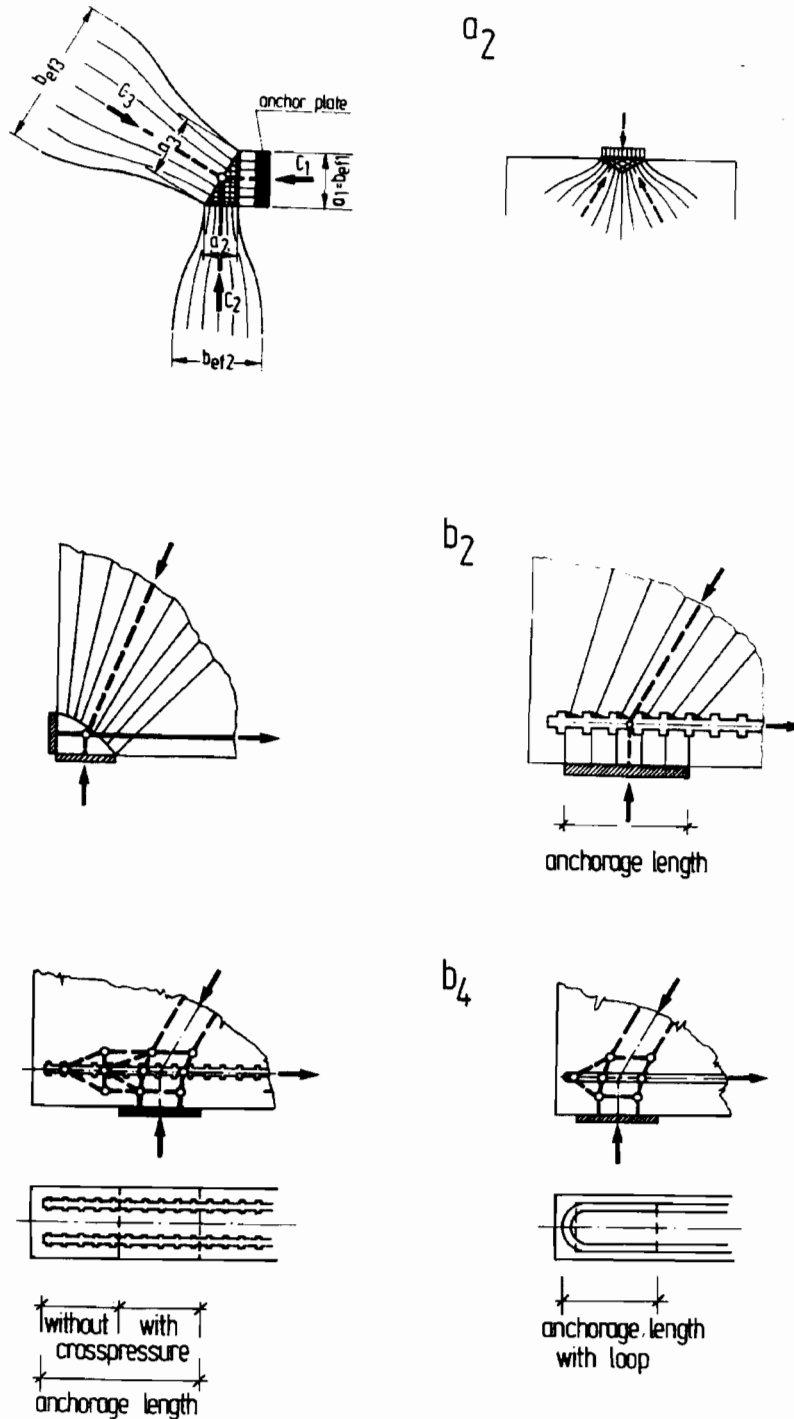


Figure 6.4 Anchorage details at nodes [52]

Strut-and-tie modeling is widely used by engineers to design D-zones for the ultimate limit state, but the effectiveness or accuracy of the design at the ultimate design load level has been tested only in a few laboratory tests. On the other hand, all D-zones designed by the strut-and-tie method are subjected to service limit state loads. Therefore, the adequacy of the design of the D-zone at the service load level is evaluated in every structure, if only visually, providing engineers with broad experience base. This experience is important because strut-and-tie models and reinforcing details that do not perform well at the service load level must not

be used in the future. Also, without a past performance record of various types of D-zones, it is often suggested that elastic analysis be used to locate struts and ties for the ultimate design model. This dual method of analysis takes great time and effort by an engineer and eliminates most practical advantage of the use of strut-and-tie modeling. Strut-and-tie modeling is intended to allow the engineer to visualize the flow of forces at ultimate load. Adequate service level load performance is achieved by following proper detailing guidelines based largely on studying the performance of similar D-zones designed and constructed in the past.

Seven D-zones were instrumented on U. S. 183. The instrumentation was intended to provide strain measurements in the tension and compression fields of the D-zones. Combined with the locations of cracks found in the D-zones, the strain measurements provided an indication of the flow of forces at service load. The instrumented D-zones included two pier capitals, two pier segments with anchorage diaphragms, two deviators, and one anchorage blister.

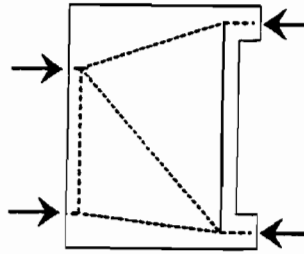
6.2 PREVIOUS STUDIES

Few relevant studies have been performed on full-scale pier capitals, but many studies have been performed on superstructure D-zones such as anchorage diaphragms, blisters and deviators. NCHRP Report 356 [54] titled *Anchorage Zone Reinforcement for Post-tensioned Concrete Girders* summarizes a large number of anchorage zone tests and includes suitable strut-and-tie models for various anchorage geometries. The NCHRP Report 356 [54] and the Schlaich et al paper in the PCI Journal [52] should be studied by engineers before designing anchorage zones by the strut-and-tie method.

Anchorage diaphragms and deviators were instrumented and analyzed by Roberts et al [7] at the San Antonio Y. The anchorage diaphragm and deviator designs were similar in some cases to the anchorage diaphragms and deviators on U. S. 183. The D-zones for both projects were designed by TxDOT engineers. Design improvements were utilized on U. S. 183 based on the knowledge gained at the San Antonio Y. The strut-and-tie models for a San Antonio Y anchorage diaphragm segment shown in Figure 6.5 give an indication of the numerous possible locations of struts and ties in a complex D-zone. The strut and tie locations have great influence on the variability of the total vertical and horizontal tension forces. Model IV at the bottom of Figure 6.5 was selected as the best model of the four. Model IV assumes a 30° diffusion angle of the tendon forces to the far face of the anchorage diaphragm from the anchorage plate. The model also tries to achieve statical determinacy so that the stiffnesses of the struts and ties have little influence on the forces in the struts and ties. The design of the diaphragm proved to be adequate, except for localized spalling of the deck concrete in the anchor segment above and in front of the top tendon anchorages. Reinforcing ties were added in this area on the U. S. 183 anchorage segments and successfully prevented this type of spalling.

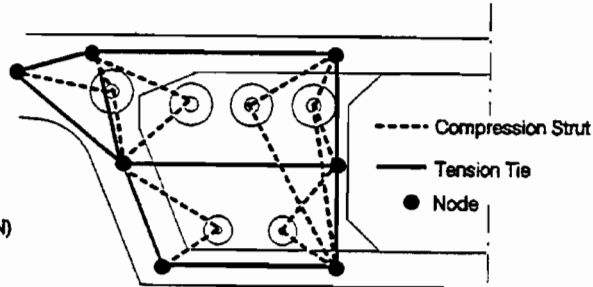
Model I

Vertical Tension = 786 kips (3496 kN)



Model II

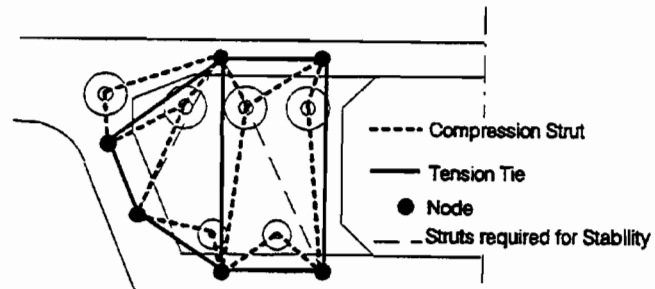
Vertical Tension = 753 kips (3349 kN)
Horizontal Tension = 1224 kips (5444 kN)



Struts between Anchors not Shown for Clarity

Model III

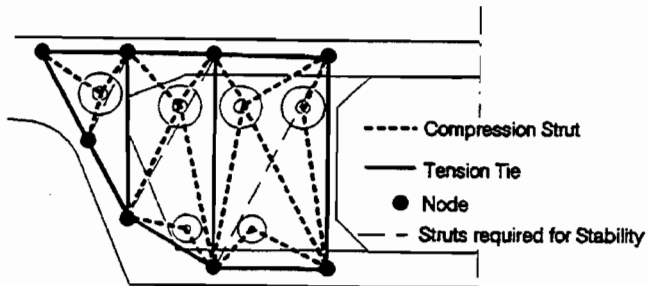
Vertical Tension = 1051 kips (4675 kN)
Horizontal Tension = 374 kips (1664 kN)



Struts between Anchors not Shown for Clarity

Model IV

Vertical Tension = 724 kips (3220 kN)
Horizontal Tension = 360 kips (1601 kN)



Struts between Anchors not Shown for Clarity

Figure 6.5 Strut-and-tie model of a diaphragm from the San Antonio Y [7]

Deviators were also studied by Roberts [7] for the San Antonio Y. Of the various deviators studied, a beam-type deviator shown in Figure 6.6 was instrumented at the San Antonio Y. This one was the same type of deviator used at U. S. 183. Because a large vertical component of force is applied by the external tendons at a deviator, the optimal type of deviator from a design standpoint would be a diaphragm-type deviator connected full-height to the girder web. This type of deviator provides a nearly direct compressive load path from the tendon deviations to the girder web. However, from a constructibility standpoint, the full-height deviator

requires that the core form for the segment be substantially modified from that used for a typical segment. For this reason, a partial-height blister or beam-type deviator is preferable to constructors and will perform adequately if designed correctly. The instrumented deviators at San Antonio performed well with little cracking. A strut-and-tie model was developed for the beam-type deviator, shown in Figure 6.6, that verified the low measured tensile and compressive stresses. The D-zone forces were diffused into the girder cross section by web and beam bending.

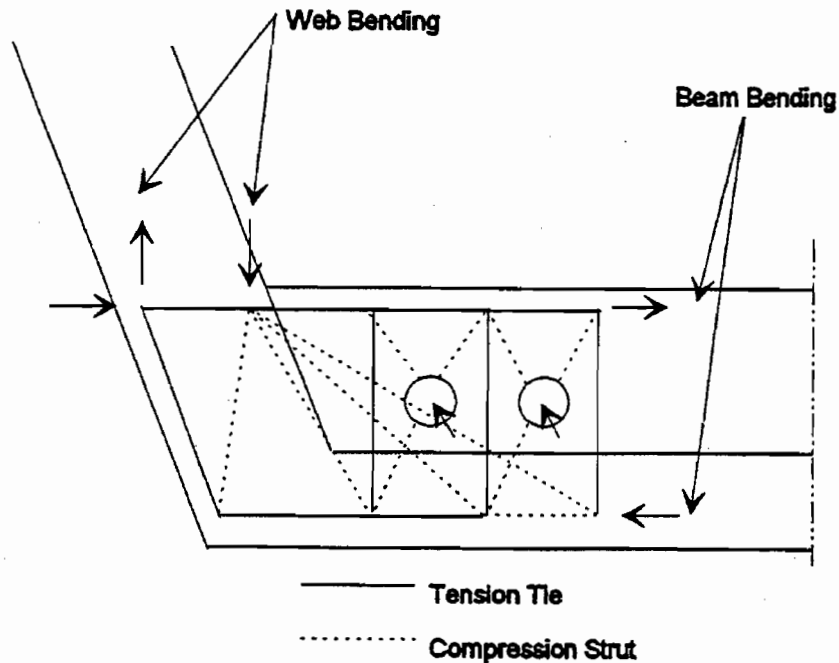


Figure 6.6 *Strut-and-tie model of a deviator from the San Antonio Y (after Roberts et al [7])*

The NCHRP Report 356 [54] presents the results of eight half-scale intermediate anchorages or blisters of the types shown in Figure 6.7. The blister in d) of Figure 6.7 most closely represents the instrumented blister on US 183. The specimens were tested to failure using an oversized tendon. Cracking generally occurred perpendicular to the centerline of the tendon near the anchor plate and parallel to the tendon in front of the blister. Compressive failure occurred immediately in front of the spiral confinement and was explosive in nature.

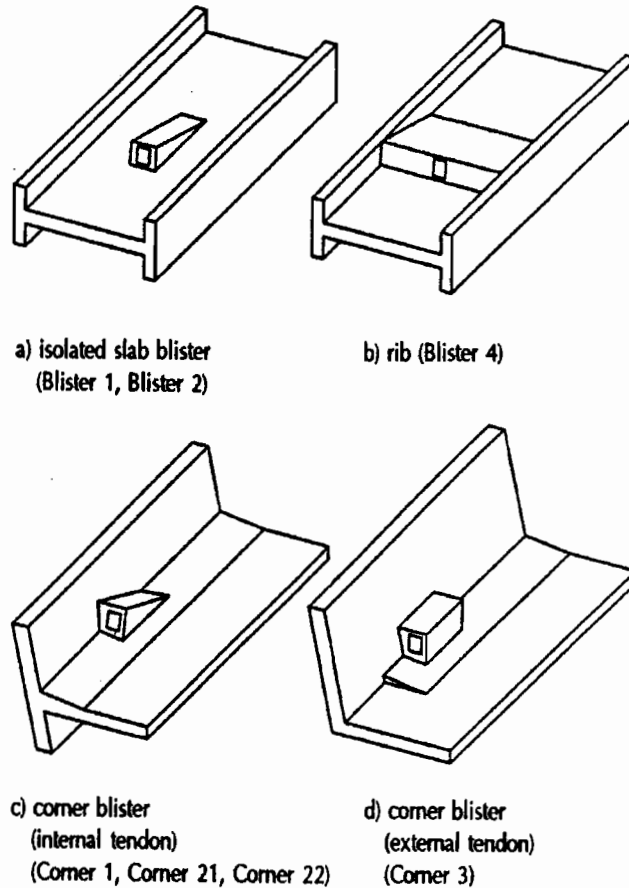


Figure 6.7 Types of anchorage blisters [54]

The design and performance of blister-type deviators were studied by Beaupre et al [55]. Various reinforcement details were used in the deviators. The deviators had either two or three tendons that were deviated vertically as well as horizontally. The measured limit states are shown in Table 6.1. The tendon force D is divided by the nominal design jacking force D_0 (80% of tendon ultimate tensile strength) to give the ratios shown in Table 6.1. Oversize tendons were used to develop the forces needed to test the deviators to the ultimate limit state. The test results revealed that visible cracking generally occurred when the sum of the tendon forces D were close to the total design jacking force D_0 , but varied from this in some test cases because of poor or unnecessarily conservative reinforcement details. Yielding of the reinforcement occurred at about 1.3 times the tendon force needed to crack the concrete on average. The ultimate limit state of deviators was exceeded when the tendon force was greater than twice the design jacking force in most cases. Ultimate strengths were lower for the deviators with tendons deviated vertically as well as horizontally away from the girder web.

Table 6.1 Summary of tendon forces at various limit states for deviators tested by Beaupre *et al.* [55]

Test	D/D ₀ at Each Limit State				Type of Deviator
	Microcracking	Visible Cracking	First Yield	Ultimate	
1A		1.30	1.60	2.33	3 Tendon*
1B	1.23	1.82	2.05	2.41	2 Tendon**
2A	0.87	0.87	1.05	1.45	2 Tendon**
2B	0.96	0.96	1.03	1.27	2 Tendon**
3A		1.03	1.73	2.79	3 Tendon*
3B	1.12	1.33	2.08	3.16	2 Tendon**
4A	0.98	0.98	1.33	2.24	2 Tendon**
4B	1.66	2.03	2.03	2.40	2 Tendon*
5A	0.78	0.78	1.06	2.53	2 Tendon**
5B	1.32	1.49	1.93	2.64	2 Tendon*
Average	1.12	1.26	1.59	2.32	

* Tendons deviated vertically and toward web

** Tendons deviated vertically and away from web

6.3 DATA COLLECTION, ANALYSIS, AND DISCUSSION OF RESULTS

The most important instrumentation in the D-zones under study in the US 183 project were strain gauges. Strain gauges were installed directly on reinforcing bars, as well as on post-tensioning bars and on the steel pipe ties of the mainlane Y-pier. Concrete gauges (C-gauges) were also installed to measure strain changes in uncracked concrete. Cracking of the concrete could be expected at a tensile strain of about $170\mu\epsilon$, assuming $f_c=83\text{Mpa}$. The mild steel reinforcement could be expected to yield at about $2070\mu\epsilon$, assuming $f_y=414\text{Mpa}$. The measured strains were compared to these two limit state strains, that is the cracking and yielding limit states. For the anchorage zones and deviators, the measured strains were used to calculate D/D_0 at the cracking limit state. This measurement was done so that the test results could be compared to the results of the tests by Beaupre et al [55]. D is the sum of the forces from all tendons, and D_0 is the sum of the forces from all tendons if stressed to 80% of ultimate.

6.3.1 Mainlane Pier

The mainlane pier, shown in elevation in Figure 6.8, was designed to visually reveal the flow of forces from the superstructure bearing reactions through the pier capital and into the foundation. A solid pier capital with conventional reinforcement was replaced with a Y-shaped capital and transverse structural steel pipe tension ties across the top of the pier to enhance this visual effect. The removal of the unessential concrete created the appearance of a strut-and-tie model bridge pier. Actually, the pier was designed using a frame model, although the proportions of the capital make such an analysis questionable. The initial intent of the designers was to control cracking in the pier capital by using post-tensioning. However, the post-tensioning was later eliminated. Bending in the top concrete elements of the capital was controlled by increasing the cross-sectional area of the steel pipes over that needed for strength. The design was successful as no cracks were noted anywhere on the pier.

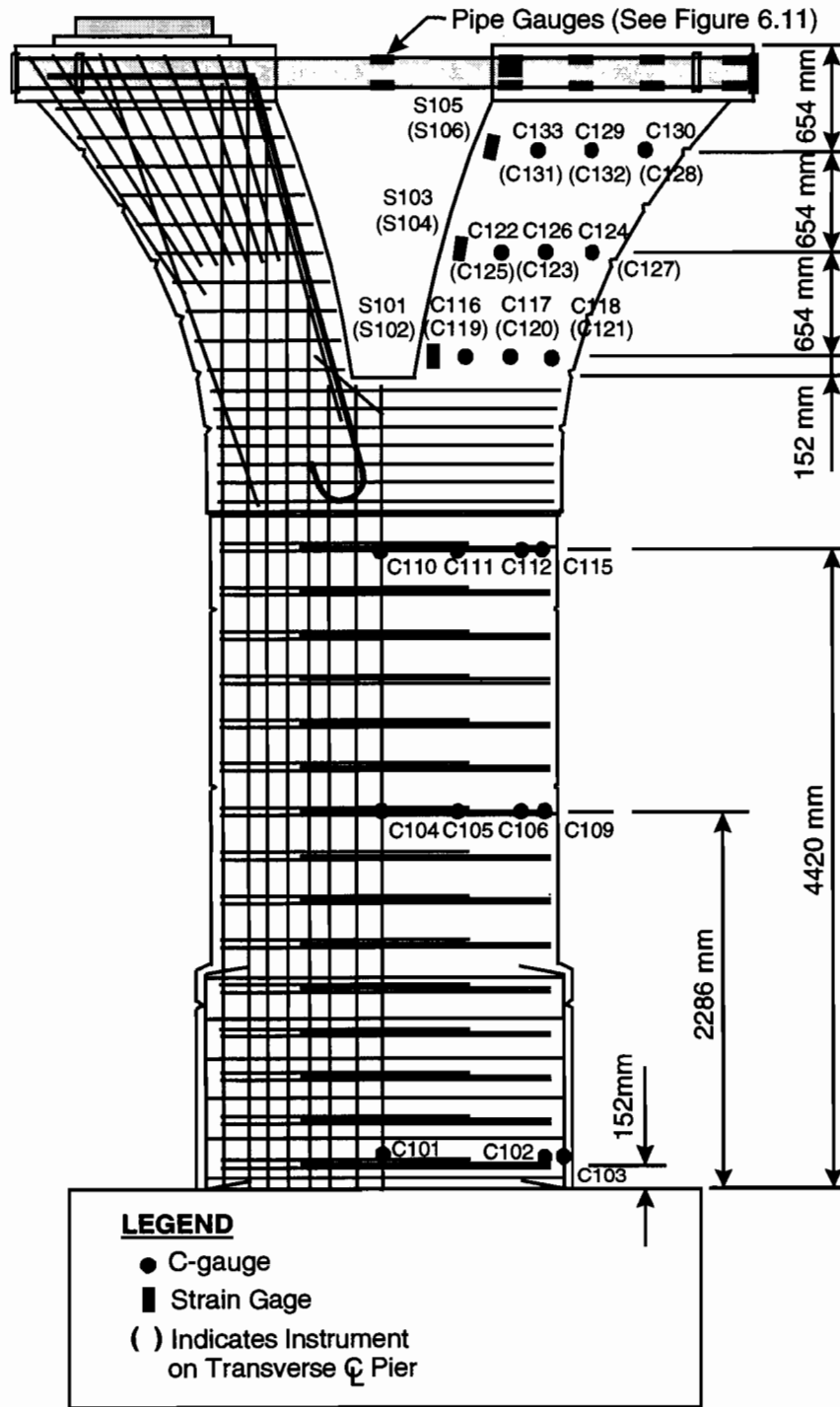


Figure 6.8 Mainlane pier D6 details

Instrumentation was placed in one quadrant of the pier, as shown in Figure 6.8, as well as on the structural steel pipe ties. A simple strut-and-tie model of the pier capital was developed, with the location of the vertical struts made to coincide with the resultant measured compressive force from loads on the bearings. This model is shown in Figure 6.9. A frame model similar to the one used by the designers was also developed and is shown in Figure 6.10. The results calculated from these two models could then be compared to the measured results, especially the tension in the pipes, to check the accuracy of the design models. For the STM model in Figure 6.9, the total tie force is 36% of the total bearing load on one side of the pier. For the frame model in Figure

6.10, the total tie force is 31% of the total bearing load on one side of the pier. The frame model predicts one-sixth less force in the pipe ties because the bending stiffness of the concrete members is included in the analysis. This stiffness is not significantly less than the STM prediction because the pipe ties were very stiff and hence lowly stressed. For the measured results, a $1\mu\epsilon$ strain change in a pipe indicates a force change in each pipe of 1.71kN.

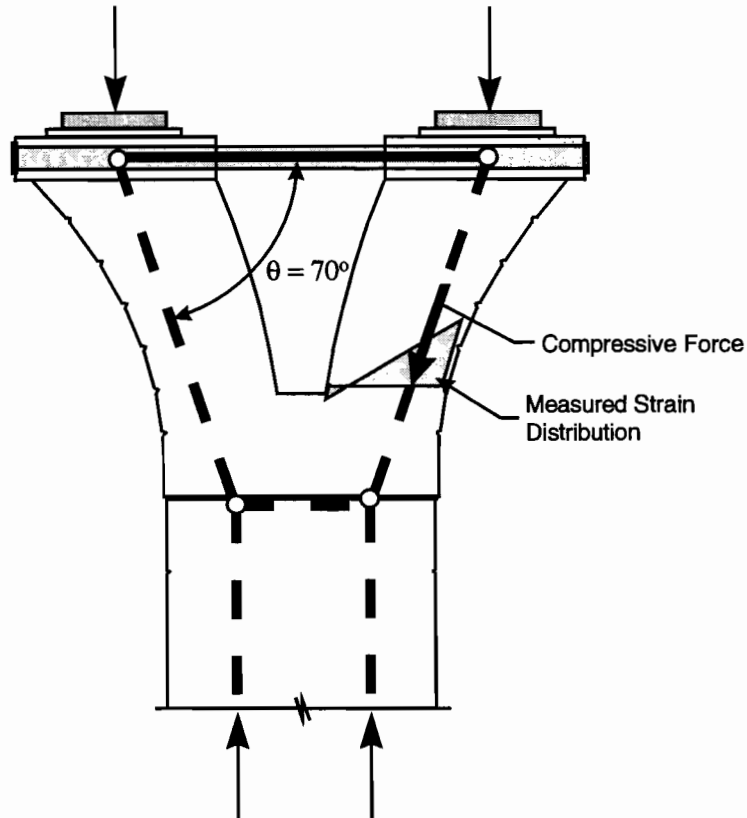


Figure 6.9 Simple strut-and-tie model for mainlane pier D6

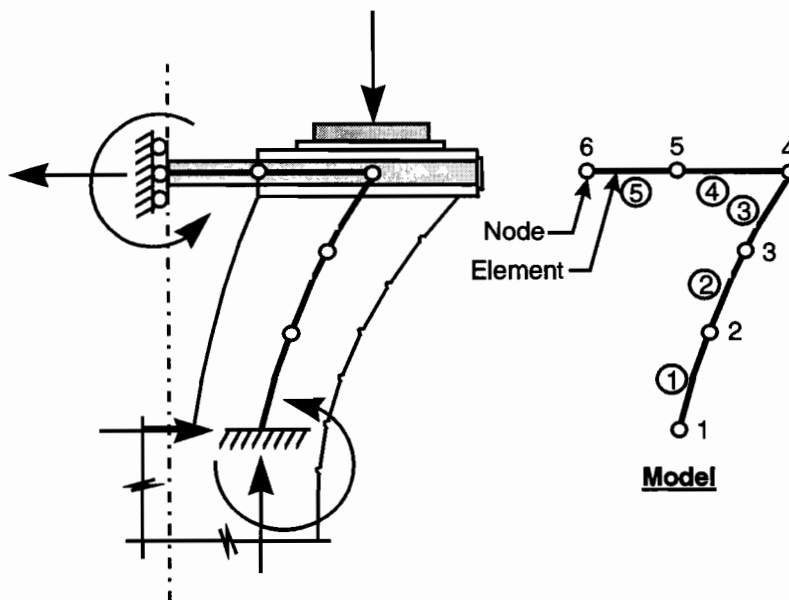


Figure 6.10 Frame model for mainlane pier D6

The greatest application of load on the pier capital occurred when the superstructure was set on its bearings. The dead load from span D5 was placed eccentrically on the pier capital. This load case and the strains measured in the pier capital are shown in Figure 6.11. The measured concrete strains indicated that the stresses from the superstructure dead load were not uniform, even near the base of the capital, as would be expected because of the bending moment with respect to the transverse centerline of the pier. For instance, gauges C133 and C129 located on the exterior face of the concrete showed compressive strains of -72 and -80 $\mu\epsilon$, while the adjacent gauges C131 and C132 located on the transverse centerline of the pier showed compressive strains of only -15 and -27 $\mu\epsilon$. Similarly, the average of the strains measured at the base of the capital by gauges C116, C117 and C118 was $-81\mu\epsilon$, while the average of C119, C120, and C121 located on the centerline of the pier was only $-29\mu\epsilon$. The strain measurements in the concrete also indicated that bending moment was present, with respect to the longitudinal centerline of the bridge, in the capital concrete where it met the column concrete. For example, gauges C119, C120 and C121 gave strains of $-17\mu\epsilon$, $-29\mu\epsilon$ and $-40\mu\epsilon$, indicating a nearly linear strain gradient across the width of the member. No tension was measured anywhere in the concrete by the gauges.

Strain measurements taken by the gauges on the structural steel pipes indicated that the pipes, with their rough galvanized surface and intermediate plates, bonded well to the concrete. Gauges S113 to S116 gave a tension strain measurement of only $94\mu\epsilon$, $36\mu\epsilon$ less than gauges S117 and S118, even though they were located only about 50mm from the exterior face of the concrete. This strain was a reduction in force of 28%. Similar behavior was measured by gauges S125 to S130, but with a reduction in force of only 14%. In order to directly compare the forces measured in the pipes from the unsymmetrical dead-load case in Figure 6.11 to the results predicted by the two-dimensional models, it is assumed that the strain changes in the four pipes varied linearly along the longitudinal centerline of the bridge. Therefore, since the strain measured in the exterior pipe by gauges S117 and S118 was $130\mu\epsilon$, and the strain measured in the interior pipe by gauges S129 and S130 was $116\mu\epsilon$, the strain changes in the other two pipes are assumed to have been $102\mu\epsilon$ and $88\mu\epsilon$. Using these assumed strains and applying additional 2215kN loads to the remaining two bearings, the strain in all the pipes would be $218\mu\epsilon$. The total measured force in the four pipes would then be 1491kN under the dead load of spans D5 and D6, or 34% of the applied bearing forces on one side of the pier. This measured pipe force was close to the mid range average of the forces calculated using the two models from Figures 6.9 and 6.10. The lower bound strut-and-tie model prediction of 36% was shown to be slightly conservative as would be expected. The actual load would be about 10% greater than the elastic analysis prediction. The largest measured concrete strain of $-86\mu\epsilon$ at gauges C117 and C118 was well below the $610\mu\epsilon$ strain that would exist at the usual service level maximum allowable stress of $0.4f_c'$.

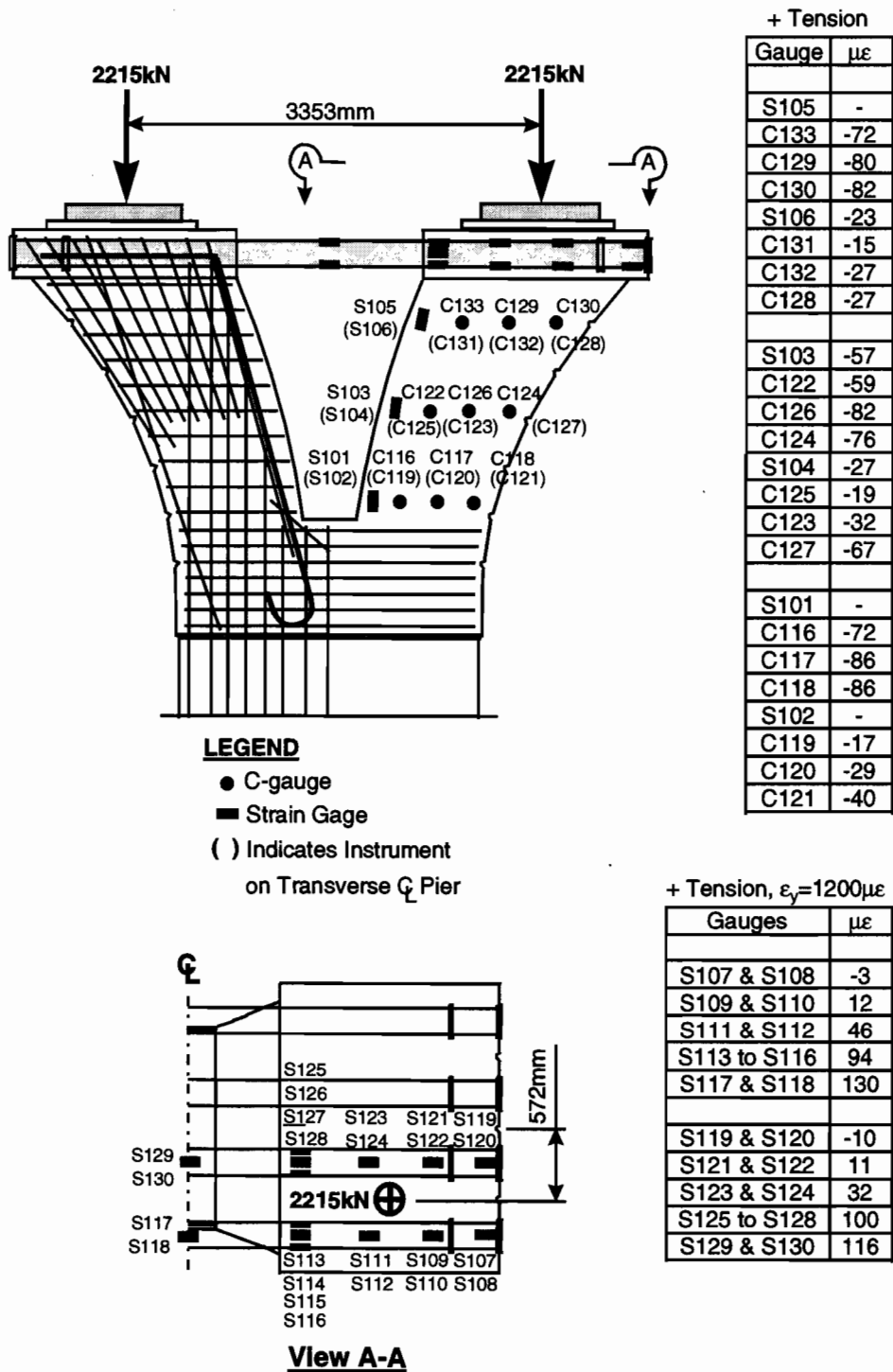


Figure 6.11 Measured strains in pier D6 capital from the superstructure dead load

Strain measurements were also taken during a symmetrically placed live-load case and are given in Figure 6.12. The measured strain in gauges S129 and S130 was $17\mu\epsilon$. Using this strain for all four pipes, the total pipe force is calculated to have been 116kN, or 40% of the bearing load on one side of the pier. This force in the pipes exceeded even that predicted by the strut-and-tie model by around 10%, although strain measurements from gauges S117 and S118 might have had an influence on this result if they had been working. The strain gauges located within the concrete on the pipes continued to show that the pipes were adhering to the concrete, and that

tension stresses from the pipes were diffused over a short length. In general, the pier behaved as designed, with excellent service level behavior in every respect. The frame model was suitable for determining bending moments in the capital for the design of reinforcement, but the strut-and-tie model was more accurate for determining the forces in the pipes and would be improved if concrete tension and concrete creep were considered.

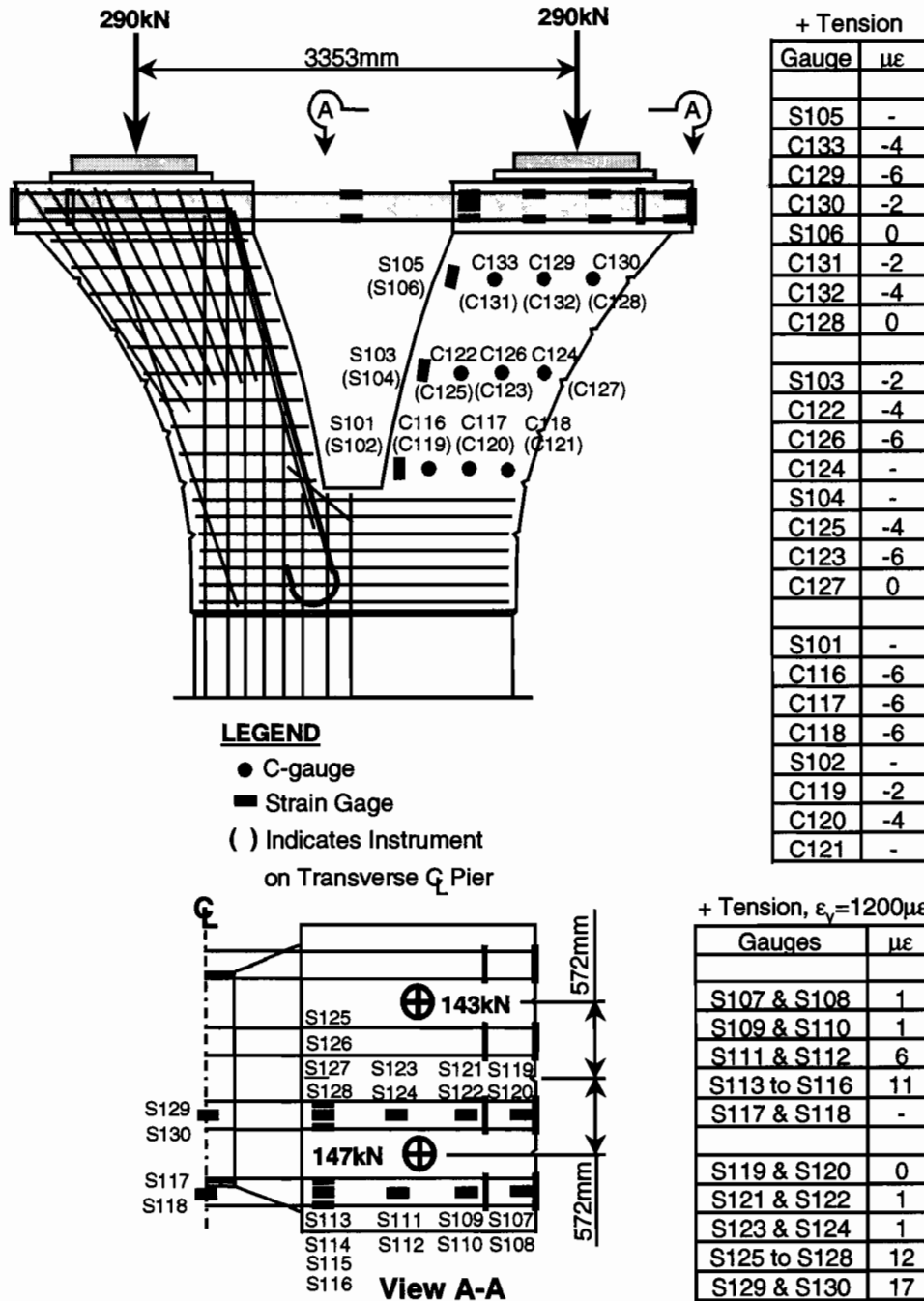


Figure 6.12 Measured strains in pier D6 capital from live-load case 5

6.3.2 Mainlane Deviator Segment

The mainlane deviator was instrumented with 18 strain gauges installed directly on the mild reinforcing bars in the deviator itself. The location of the gauges is shown in Figure 6.13. The instrumentation consisted of three identical planes of six gauges shown in Section A-A of Figure 6.13. The 19 - 15mm diameter strand tendons each produced a vertical deviation force of about 447kN and a horizontal friction force of 145kN. The deviator pipes used were bent on a radius of only 2m, much smaller than the 7.5m radius drawn in the plans, which concentrated the deviation forces from the tendon over a very short length of the deviator. This concentration is evident in the measurements, since gauges S7 to S12 gave strain measurements much larger than the other gauges located more toward the ends of the pipes. Because of the small radius bend, this deviator should not be considered typical of deviators in general. The deviator did have significantly large cracks, and the mild reinforcement did undergo large elastic strains in some cases approaching half the yield point strain. Ideally, the deviator pipes would be smoothly bent with constant radius over the full length of the deviator. Even with the proper radius bend, the deviation force may not be uniform along the length of the deviator because of misalignment between duct and tendon.

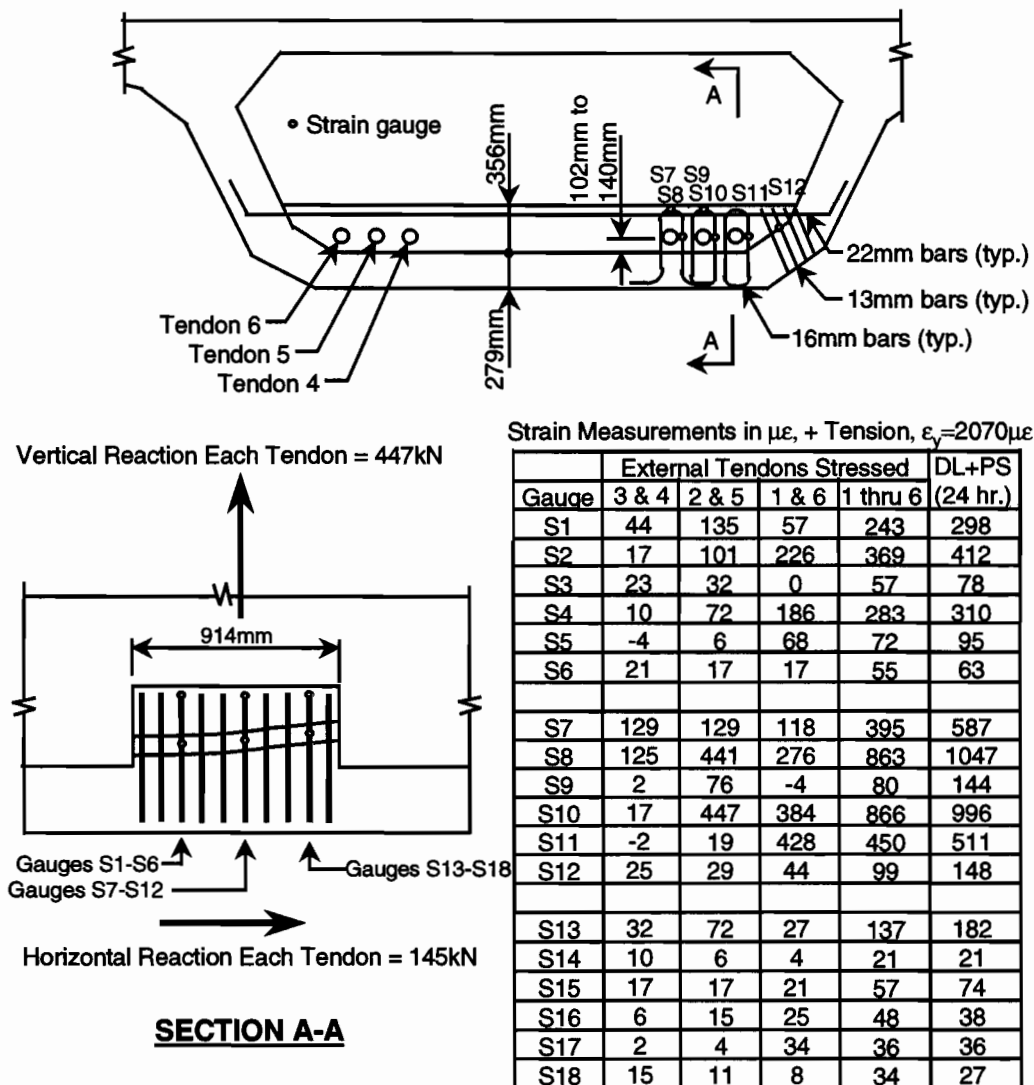


Figure 6.13 Measured strains in the deviator reinforcing bars from superstructure post-tensioning forces and dead load

Cracking of the segment D5-12 deviator most likely began following the stressing of tendons 3 and 4. Gauges S7 and S8, located on the top and side of the deviator pipe for tendon 3, indicated fairly large strain changes, given in Figure 6.13, that could be associated with the formation of cracks close to the tendon ducts. Cracking in the concrete could be expected at strains of about $170\mu\epsilon$, which would be realized during stressing of tendons 2 and 5. As the remaining tendons were stressed, gauges S7 and S8 continued to show large strain changes, with the final stress in gauge S8 being halfway to the yield point. Using simple linear interpolation, D/D_0 at the yielding limit state can be calculated to be 1.72, which is slightly more conservative than the average D/D_0 at yielding of 1.59 measured by Beaupre et al [55]. Large strain changes in gauges S10 and S11 after the stressing of tendons 3 and 4 indicated that an unseen horizontal cracked plane probably existed between deviator pipes, and between the deviator pipe for tendon 1 and the girder web main stirrup bars. D/D_0 for the D5-12 deviator is calculated to be 0.58 at the cracking limit state. This figure is well below the average D/D_0 at cracking of 1.26 measured in the tests by Beaupre et al. The inclined stirrup bars at the interface of the deviator and the web did not undergo appreciable tensile strain changes, as indicated by strain changes in gauges S6, S12 and S18, because of the lack of cracks in the concrete near the web. Strain measured at gauge S12 was $99\mu\epsilon$ at the end of stressing tendons 1 through 6. This strain was below the strain needed to crack the surrounding concrete in tension. The strain measured at gauge S12, 24 hours after the conclusion of prestressing and after the girder had been lowered from the truss onto its bearings, is given in the last column of the table in Figure 6.13 titled DL+PS (24 hr.). This strain was somewhat higher, at $148\mu\epsilon$, than the strain measured on the previous day, but still below the strain needed to crack the concrete. The fine distribution of inclined bars may have limited cracking in the concrete between tendon 1 and the web. The 24-hour strains at all gauge locations were larger in general than the strains measured during the stressing operation.

The location of cracks on the mainlane segment D5-9 deviator are shown in Figure 6.14. Since tendons 3 and 4 were stressed first, the predominant longitudinal cracks occurred over these ducts and tendons. These cracks were wide open and effectively reduced the bending stiffness of the deviator beam. The largest cracks were the transverse cracks over the deviator pipes, probably caused by the concentration of vertical force over the short radius bend in the pipes. This concentrated force at the bend caused a splitting force that could not be restrained by the few longitudinal bars on the top of the deviator beam. Large transverse cracks of this type usually do not occur in deviators with properly bent deviator pipes. Because of the large internal horizontal crack and the large transverse crack, most of the vertical force from the deviation of the tendons had to be transferred by the hoop bars to the bottom slab of the girder section and then diffused through the bottom slab to the web. The average force measured in the three 16mm bars instrumented by gauges S8, S10 and S11 was 35kN, so the 18 legs of hoop bars immediately adjacent to the sharp bend radius of the ducts carried about 634kN of the total 1341kN vertical force. This force put high demand on these nine bars, considering that 30 of these bars were included in the design of the deviator for this purpose.

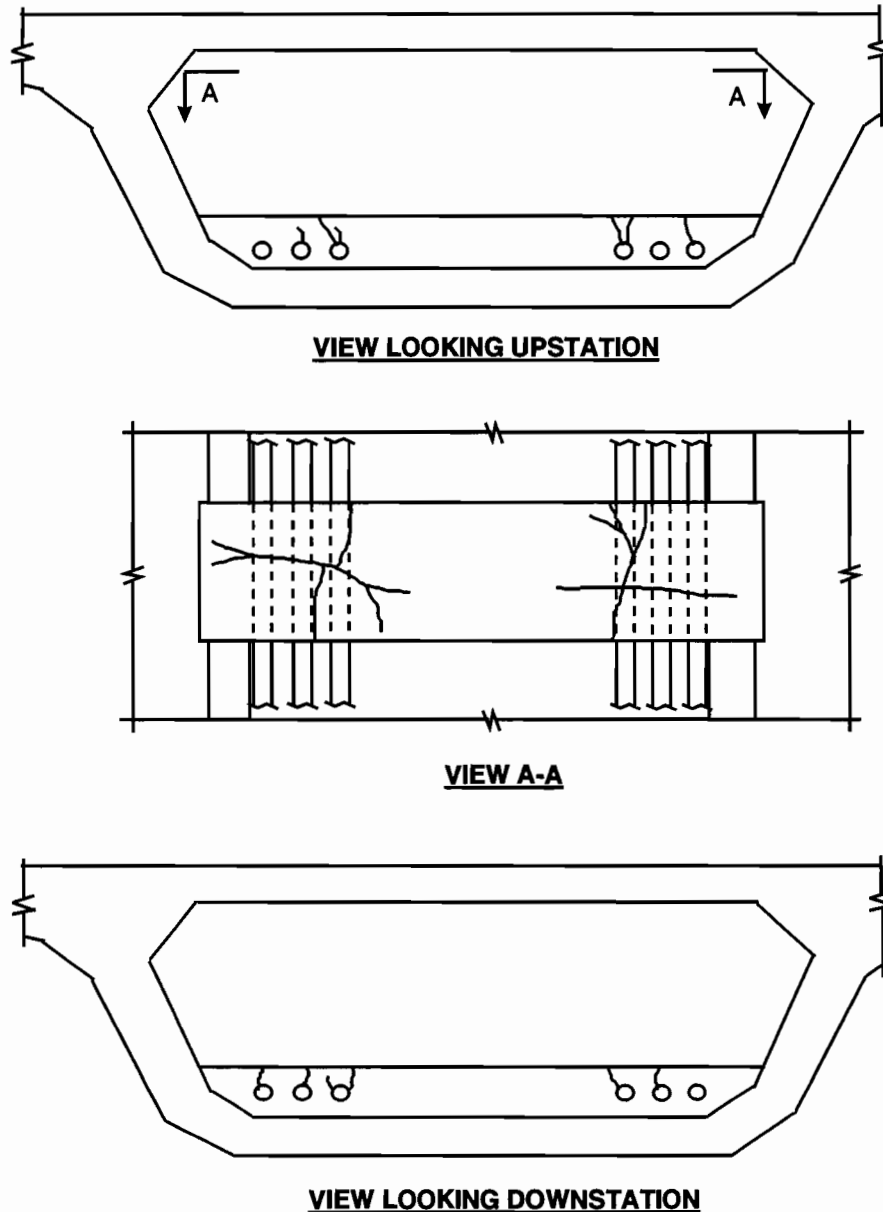


Figure 6.14 Crack patterns in the segment D5-12 deviator

With some of the mainlane deviator bars at one-half yield stress, and considering that 18 legs of bars were taking one-half of the vertical thrust from the deviated tendons, the change in stress in these bars from a simulated HS20-44 live load at midspan was of interest. The strain measurements and forces on the deviator from the live load are presented in Figure 6.15. Given the end rotation of the girder, the deviated portion of the tendons did not undergo any significant force change from the live-load case. For this reason, the vertical reaction from the tendon was very small at only 0.3kN and produced insignificant strain changes in the deviator bars. From a fatigue standpoint, the highly stressed deviator bars should not degrade. The large cracks in the deviator were filled with an epoxy to protect these bars from corrosion, although the integrity of the epoxy was questionable as it never appeared to fully harden.

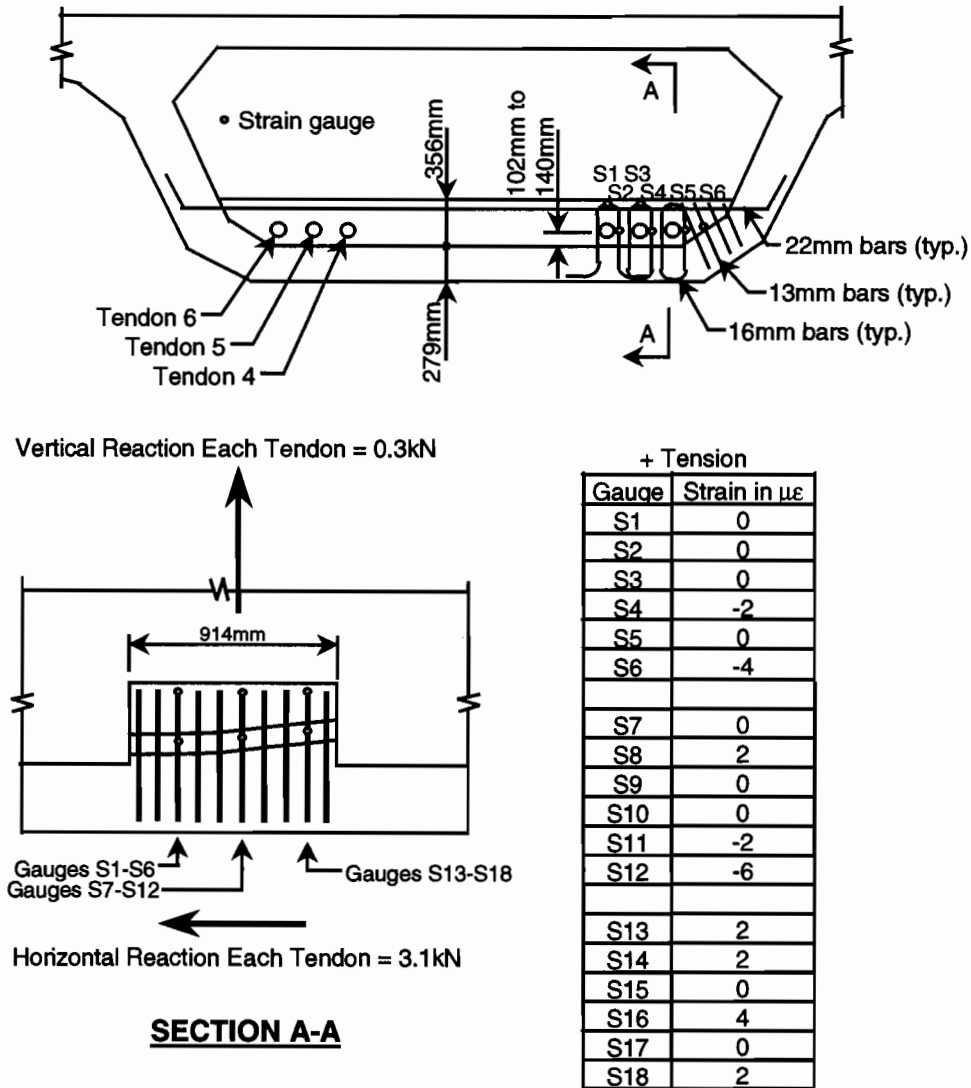


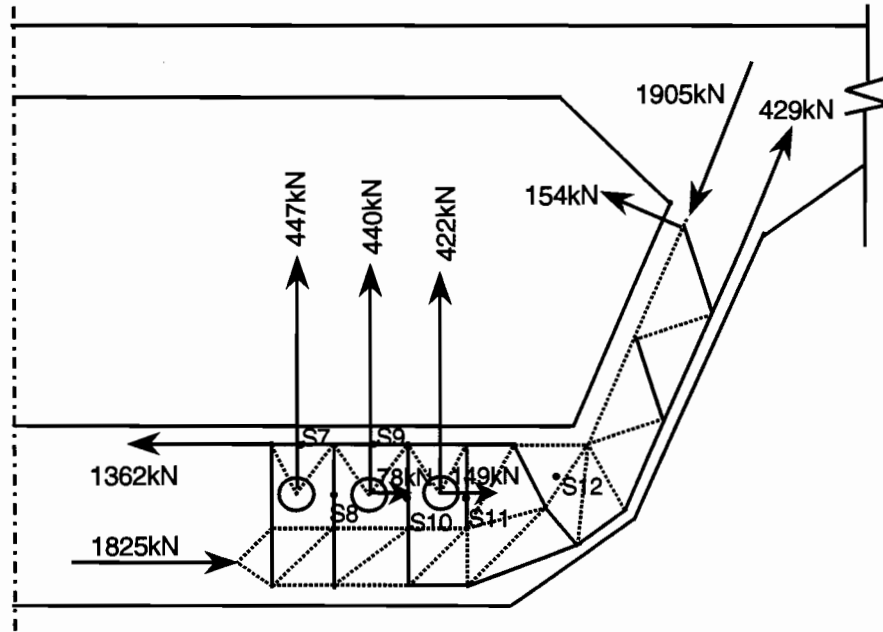
Figure 6.15 Measured strains in the deviator reinforcing bars from live-load case 2

To improve analysis and design of future deviators, general observations about the structural system and loading need to be made. First, if tendons are stressed in symmetry, the transverse loading on the girder from the deviator forces is symmetrical. Therefore, no shear will be present in the central portion of the deviator beam or in the top slab. Shear forces from the deviator will diffuse only toward the girder web. Second, the compressive stiffness of the girder web will predominately dictate the flow of forces from the deviator, so a two-dimensional analysis of the deviator and surrounding girder can be used to determine moments, shears and axial forces at points away from the deviator. Section properties of the deviator beam, girder web and top slab can be calculated assuming the forces from the deviator diffuse longitudinally into the girder at a 30° angle with respect to the transverse section through the centerline of the deviator. The reaction to the vertical components of the deviated tendon forces can be assumed to be located at the center of gravity of the girder in the web.

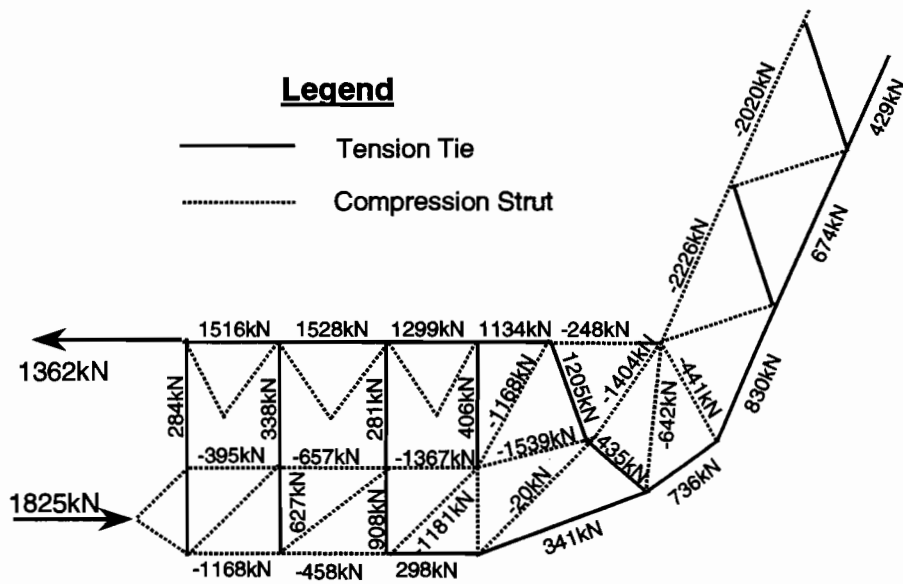
The moment couple created between the deviator forces and the web reaction will be resisted by an axial force couple between the top slab and deviator beam, and transverse bending of the girder. The amount of transverse bending calculated in the deviator beam is somewhat dependent on whether cracked or uncracked section properties are used in the analysis. Cracks will most likely be present near the deviator pipes even at service load, so a reduction in cross-sectional stiffness may be warranted in this area. The results of an analysis for service level forces from the D5-12 deviator are shown as applied loads in Figure 6.16. The deviation forces from the tendons were easily calculated since the deviation angles were known and changed little during the stressing of the tendons. When calculating the deviation forces for the girder at ultimate, the forces in the

tendons and the deviation angles are not as easily calculated. It is unlikely that the external tendons will ever reach their ultimate stress because of the partially bonded nature of external tendons and the imposed limits on the girder's sectional ductility at ultimate moment.

To be very conservative, the ultimate force for the tendon can be used, but the deviation force depends largely on the deviation angle at the ultimate load level. Plastic rotations can be calculated and the deviation angles at ultimate can be determined. Also of utmost importance is the calculation of horizontal force on the deviator from changes in tendon force at ultimate. The force changes in the inclined and horizontal legs of the tendon on either side of the deviator will not be equal and depend greatly on whether the tendon is assumed to be fully bonded to the deviator, or more realistically allowed to slip. For this reason, a longitudinal strut-and-tie model should be developed for the ultimate load design of the deviator, bottom flange, and web.



HALF SECTION THROUGH CENTERLINE OF DEVIATOR



CALCULATED MAJOR STRUT AND TIE FORCES

Figure 6.16 Strut-and-tie model for the segment D5-12 deviator

The service level analysis results for the D5-12 deviator, shown in Figure 6.16, revealed that about half of the moment from the deviator force and web reaction was taken by transverse bending of the girder. The axial force in the deviator beam and top slab must have been 1037kN to resist the entire moment. From Figure 6.16, the axial force in the deviator beam was calculated to be 1825kN compression minus 1362kN tension, or 463kN in compression. Full elastic section properties were used in the analysis, so the moment calculated in the deviator beam would be conservative, and shear and bending in the web would be unconservative. Because of the high shear in the deviator between the deviator pipes and the web, the negative moment in the deviator beam becomes a positive moment at the juncture of the deviator with the web. This change places a point of contraflexure between the deviator pipes for tendons 1 and 6 and the girder web. This contraflexure should be considered when selecting struts and ties during the deviator design. Since the forces and moments near the deviator have been determined for the service load case, a strut-and-tie design can proceed once the limits of the D-zone have been determined. Since only horizontal struts and ties can be used in the central portion of the deviator beam because of the lack of shear forces, the exact limit of the D-zone within the central portion of the deviator beam is unimportant to the design. The limit of the D-zone within the girder web has been selected as one deviator length, or 914mm, up the web from the web to deviator beam juncture.

The strut-and-tie model shown in Figure 6.16 was developed based on the calculated forces and moments and on the assumption that horizontal cracks were present between deviator pipes near the sharp radius bend and at the locations shown in Figure 6.14. The model assumed that shear forces in the deviator beam near the pipes were taken to the web only in the portion of the deviator beam beneath the deviator pipes because of the extensive cracking. For this reason, the model would also be suitable under ultimate load condition. The vertical tendon forces are transferred to the deviator only through the vertical reinforcing. Because of shear forces beneath the pipes, the tensile forces in the vertical ties are largest below the pipes. The flow of transverse tensile force above the pipes is deviated to the bottom of the girder by compression struts near the point of inflection. The main tension tie and the main compression struts intersect orthogonally near the point of inflection, indicating high shear and low moment. The locations of tension ties in the model were chosen such that reinforcement could be designed directly from the calculated tensile values. Failure criteria for the struts and ties must be checked during the ultimate load design, as well as the proper anchorage of reinforcement. The D5-12 deviator had heavy congestion of bars because of the web stirrups and web to bottom flange fillet reinforcement. Modification of the typical web and fillet reinforcement details would have been advisable over the length of the deviator so that the designed tie reinforcement could be placed. The 13mm C-shaped bars placed on an angle, seen in Figure 6.13 at the junction of the deviator and the web, were difficult to install because of the heavy web and fillet reinforcement running perpendicular to the direction of the actual tensile stress field. The short 90° bend of the 13mm angled bars was also inadequate to develop the forces calculated in the strut-and-tie model and could not be relied upon to develop the forces the model would predict at an ultimate load state. Forces would redistribute as anchorage failure of the 13mm bars proceeded.

Forces in the instrumented reinforcing bars could be calculated based on the strain measurements and estimated for the adjacent reinforcement. Reinforcing bar forces were most accurately calculated at crack locations, for example, at gauge S8 shown in the top section of Figure 6.16. Using the average of the 24 hour strains measured by the gauges S2, S8 and S14 and multiplying this average strain by the total reinforcing bar area (20 legs of 16mm bars) and the modulus of elasticity of the steel, the tie force was calculated to be 408kN. This force was about 20% higher than the result of 338kN predicted by the STM. The correlation between these calculated and measured values is good, considering the crudeness of the calculation of measured force in the reinforcement. A similar calculation of the tie force at gauge location S10, shown in the top section of Figure 6.16, gives a measured force of 371kN. This value is 32% higher than the 281kN tie force predicted by the STM. The same calculation of measured force at the tie with S11 proved to be inaccurate because of the lack of cracking at gauge location S5 and S17. The force was calculated to be only 89kN. This calculation assumed that no tension was taken by the concrete. The STM predicted 406kN in the tie at gauge S11. The actual state of stress in the concrete at gauges S5, S11 and S17 was more complex than at the other vertical bar gauges because of their close proximity to the intersection of several major struts and ties. This proximity apparently resulted in fewer cracks at the gauge locations.

Calculation of the tie forces at gauges S7 and S9, shown at the top of Figure 6.16, proved to be inaccurate because the strain gauges were actually placed on the 180° bends of the vertical tie reinforcement. Measurements would have been more easily interpreted if gauges had been placed on the heavy transverse bars as well. Even with the presence of a large crack at S7, the estimated reinforcing bar force based on the average

of gauges S1, S7 and S13 was only 318kN. The STM predicted 1516kN. The STM force was conservative because the bending moment in the deviator calculated in the preliminary analysis used full uncracked section properties for the deviator. The large crack at S7 would have reduced the bending moment and increased the axial compressive force in the deviator, effectively reducing the tension at S7. Tension strains measured at gauge S12 and at the adjacent gauges S6 and S18 were less than the strain required to crack the concrete. Therefore, the tension force in the major inclined tension tie, calculated to be 1205kN by the STM at the bottom of Figure 6.16, was not accurately calculated based on the measured strains since the tensile contribution of the concrete was neglected. Also, because of the poor placement of the inclined bars, gauges S6, S12 and S18 were actually located within the web and very close to the heavy web stirrup reinforcement.

The lack of cracking at some gauge locations made the comparison between the measured strains and calculated forces, and the STM forces difficult except at the vertical ties gauged by S8 and S10. At these two locations the STM was unconservative, at least in the upper portion of these vertical ties. As seen at the bottom of Figure 6.16, the forces in the vertical tie bars are drastically different in their top and bottom halves because of the shear carried in the lower portion of the deviator. Such a drastic force change predicted by the STM in the short tie bars was probably unrealistic. The actual force distribution in the vertical tie bars was probably more constant, resulting in less force in the bottom of the bars and more at the top. The vertical bars should be sized based on the forces calculated in the bottom of these ties using the STM, giving a conservative design.

6.3.3 Mainlane Anchor Segment

The mainlane anchor segment D5-16 was instrumented with strain gauges on the reinforcing bars in the heavy end diaphragm. The location of these gauges is shown in Figure 6.17. Gauges were placed on bars at locations where cracks were expected to occur. The measurement of strain at a crack location allows the total tensile force present to be calculated accurately in the instrumented bar. The reinforcement in the diaphragm was designed to resist tensile forces caused by the post-tensioning that act adjacent to the far face of the diaphragm and away from the tendon anchorages. The gauges were located on bars on this face of the diaphragm, as is indicated in Section A-A of Figure 6.17. Tensile strains expected to occur in the top flange were measured by gauges S25, S26 and S27. Tensile strains expected to occur in the bottom flange were measured by gauges S22, S23 and S24, with gauge S22 actually placed on the lower horizontal leg of a closed tie bar. The remainder of the gauges were placed to measure tensile strains in the vertical direction.

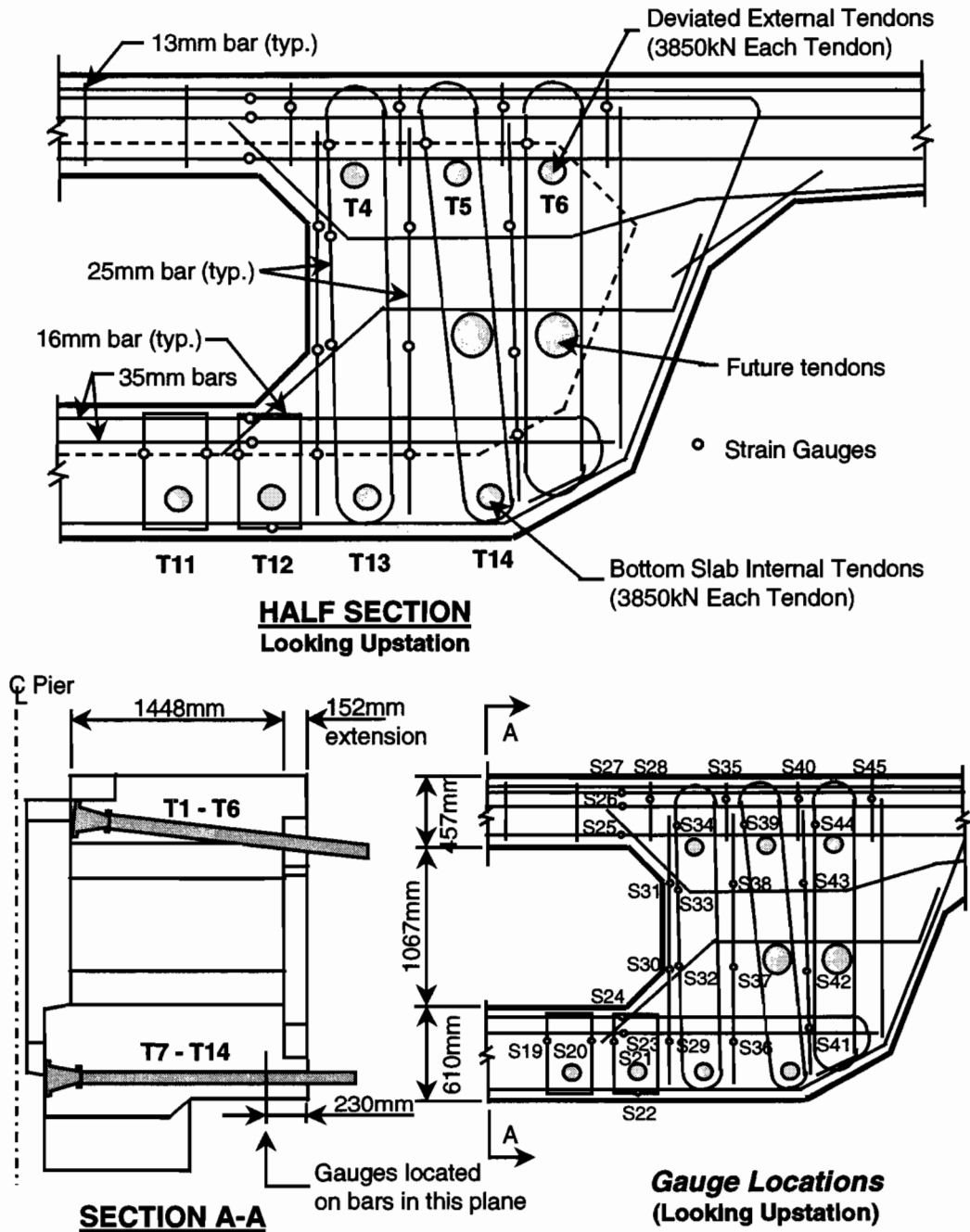


Figure 6.17 Mainlane anchor segment D5-16 details

Visual inspection of the crack patterns in the anchor segment shown in Figure 6.18 indicated that tensile forces were present on most of the downstation face of the diaphragm. Cracks did not propagate into the top flange because of residual compression from the transverse prestressing. From Section A-A of Figure 6.18, it can be seen that vertical tensile forces were present over most of the length of the segment in the top of the diaphragm. Cracks from tensile forces in the bottom of the diaphragm propagated only about 250mm along the length of the segment. The bearing reactions from girder dead load were not present when these cracks were formed. The girder was supported by jacks under the wings near the webs until all tendons were stressed. Additional cracks were noted in the bottom flange of segments D5-15 and D5-14, as shown in Figure 6.19. These cracks were located directly beneath the internal bottom slab tendon ducts and did not propagate to the top surface of the bottom slab.

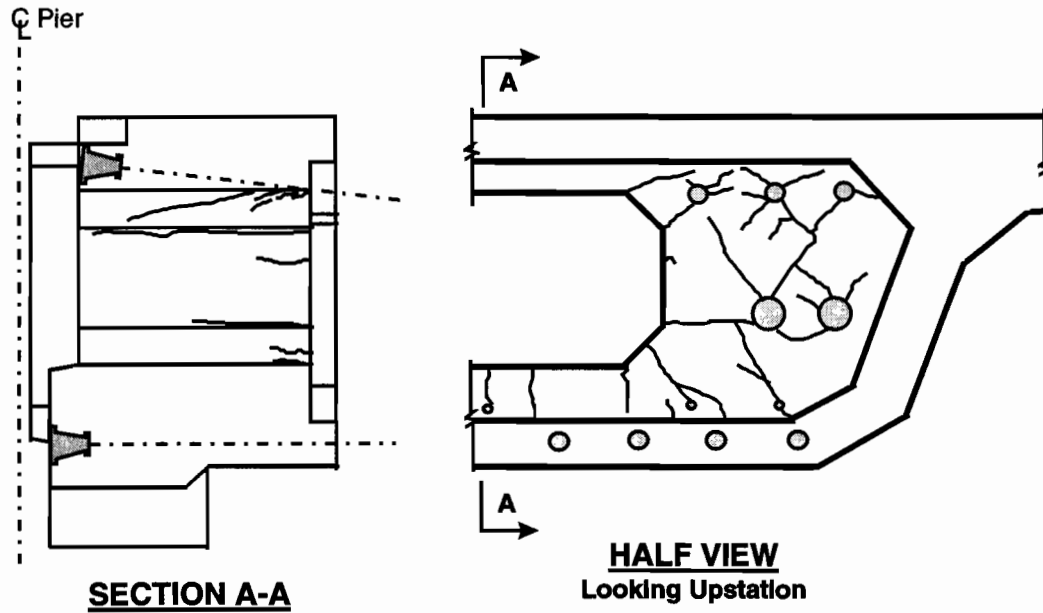


Figure 6.18 Crack patterns in segment D5-16 diaphragm

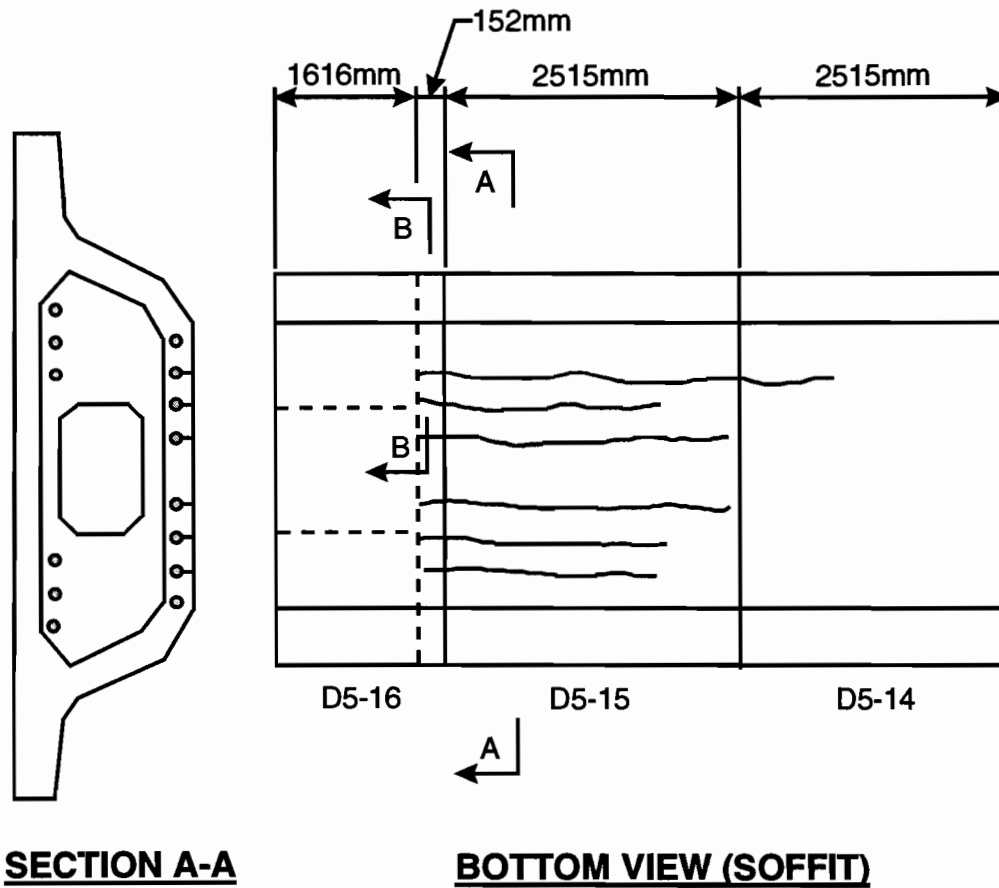


Figure 6.19 Crack patterns in the bottom flange of segments D5-16, D5-15 and D5-14

Table 6.2 contains the strains measured during the post-tensioning of the six deviated external tendons and the wing tendons. Since the stressing operation occurred over several hours, the column titled "Sum T1 to T6" includes strain changes measured over the entire period and does not always match the sum of the strains from the three columns of data to the left. The deviated external tendons were stressed in pairs beginning with tendons T3 and T4. The most significant tensile strain changes during the post-tensioning of tendons T1-T6 were measured by gauges S31 and S33, although the strains were only 36% and 17% of the nominal yield point strain of the bars at $2070\mu\epsilon$. D/D_0 at cracking was quite small since cracking initiated during the stressing of Tendon T3 and T4. The strain at S31 was $219\mu\epsilon$ following the stressing of T3 and T4, which exceeded the approximate cracking strain of $170\mu\epsilon$. The tensile strains measured by gauges S30 and S32 toward the bottom of the diaphragm were much less in magnitude, even though a crack existed at this location. The strain changes measured by gauges S30 to S32 for each pair of deviated external tendons were generally similar, regardless of the location of the tendon pair.

Table 6.2 Measured strains in anchor segment D5-16 reinforcing bars from stressing post-tensioning tendons in microstrain

Strains in microstrain, + Tension					
	Deviated External Tendon Stressed				Wing Tendons
Gauge	T3, T4	T2, T5	T1, T6	Sum T1 to T6	T15 - T18
S19	8	2	6	11	-2
S20	8	11	8	27	2
S21	10	4	6	23	-2
S22	21	17	13	67	4
S23	27	19	8	80	42
S24	29	17	4	68	29
S25	36	13	-8	51	13
S26	6	-6	-10	2	13
S27	13	0	-15	4	-11
S28	23	19	10	53	6
S29	2	8	6	15	2
S30	44	55	27	125	-6
S31	219	276	264	745	-11
S32	15	34	15	67	-4
S33	67	112	152	342	6
S34	17	17	13	48	-4
S36	-4	-10	-6	-11	-2
S37	4	-21	-4	-23	0
S39	13	13	2	23	-10
S40	-49	15	17	-10	-8
S41	-8	-6	-11	-25	2
S42	2	68	19	114	-8
S43	25	21	27	70	-8
S44	17	11	11	38	0
S45	11	13	17	44	8

This similarity may be due in part to the propagation of cracks at these locations as stressing progressed. Strains measured by the horizontal line of gauges S31, S33, S38 and S43 indicated that vertical tensile strains in the diaphragm decreased toward the web. The strain measured by gauge S31 was $745\mu\epsilon$ from the stressing of tendons T1 to T6, while the strain measured by gauge S43 was only $70\mu\epsilon$. A similar decrease across the width of the diaphragm was measured by the horizontal line of gauges S30, S32 and S37 with measured strains of $125\mu\epsilon$, $67\mu\epsilon$ and $-23\mu\epsilon$ (compression) respectively, with gauge S42 located near a crack between the two empty future post-tensioning ducts measuring $114\mu\epsilon$. The line of gauges S29, S36 and S41 did not measure significant tensile strains, with gauge S41 measuring compression. Gauges S34, S39 and S44, located directly in front of the anchorage plates but on the opposite face of the diaphragm, measured about $14\mu\epsilon$ each from the stressing of

each pair of tendons regardless of the pair. Gauges S28, S35, S40 and S45 recorded tensile strains of about $18\mu\epsilon$ when the tendon nearest each gauge was stressed and less strain when other tendons were stressed.

In general, the vertical strains measured at each corresponding gauge location were similar, regardless of the pair of deviated external tendons stressed. Once again, this similarity may be due to the propagation of cracks as stressing progressed, which would relieve tension in the concrete and increase tension in the gauged steel bars.

Gauges S25, S26 and S27 measured transverse strains in the top flange from the tensioning of external deviated tendons T1 to T6. Strains in these three gauges averaged $18\mu\epsilon$ when T3 and T4 were stressed, $2\mu\epsilon$ when T2 and T5 were stressed, and $-11\mu\epsilon$ when T1 and T6 were stressed. The strains in these gauges also indicated that small values of transverse positive bending moment were present. Horizontal strains measured in the bottom flange by gauges S22, S23 and S24 averaged $26\mu\epsilon$ from tendons T3 and T4, $18\mu\epsilon$ from tendons T2 and T5, and $8\mu\epsilon$ from tendons T1 and T6. The strains from these gauges clearly indicated that the response of the girder near the diaphragm was different for each pair of deviated external tendons. Strain changes in the diaphragm from the tensioning of the four internal wing tendons were small, but the horizontal strain changes in the top and bottom flanges were larger. The average strain change in gauges S25, S26 and S27 from the wing tendons was $5\mu\epsilon$, which is very small, but with positive bending indicated in the top flange. The average strain change in gauges S22, S23 and S24 was $25\mu\epsilon$ from the wing tendons, with negative bending indicated in the bottom flange.

The strains measured in all gauges from the stressing of the eight bottom slab internal tendons T7 to T14 are given in Table 6.3. In general, the change in strain at each gauge location was highly dependent on which pair of bottom slab tendons was stressed. Gauges S19, S20, S21, S22, S29, S36 and S41 were located directly in front of the anchor plates for the deviated external bottom slab tendons, and all measured similar tensile strains averaging $130\mu\epsilon$ for all eight tendons. The gauges on the vertical bars near the top of the diaphragm and in the top flange measured very little strain change.

Gauges S31 and S33 measured more substantial tensile strain changes from the stressing of tendons T10 and T11, at $51\mu\epsilon$ and $112\mu\epsilon$ respectively, but measured progressively more compressive strain changes as the other tendon pairs were stressed. Strains measured by S31 and S33 were $-44\mu\epsilon$ and $-30\mu\epsilon$ from the post-tensioning of tendons T7 and T14. These strain changes in S31 and S33 were small, considering the gauges were located at a crack created during the stressing of the external tendons. Gauge S43 gave similar results to S31 and S33, but with smaller magnitude. Gauges S30 and S32 measured strain changes from each pair of tendons that were not easily interpreted, but appear to be influenced by the proximity of the tendon anchorage to the strain gauge. S37 gave progressively more compressive strain changes as the tendons closer to the webs were stressed, while S42 gave progressively more tensile strain changes as the tendons closer to the webs were stressed.

Strains in gauges S25, S26 and S27 were quite small for all stressed bottom slab tendons, averaging near zero. Horizontal strains measured in the bottom flange by gauges S22, S23 and S24 were relatively large and averaged $47\mu\epsilon$ from tendons T10 and T11, $68\mu\epsilon$ from tendons T9 and T12, $38\mu\epsilon$ from tendons T8 and T13, and $-16\mu\epsilon$ from tendons T7 and T14. The trend for transverse strains in the bottom flange was toward compression as tendons closer to the webs were stressed. The strain response to all eight bottom flange tendons as a group was only notable in the bars located in or near the bottom flange, with the exception of the bar gauged by S33.

Table 6.3 Measured strains in anchor segment D5-16 reinforcing bars from stressing post-tensioning tendons (continued) in microstrain

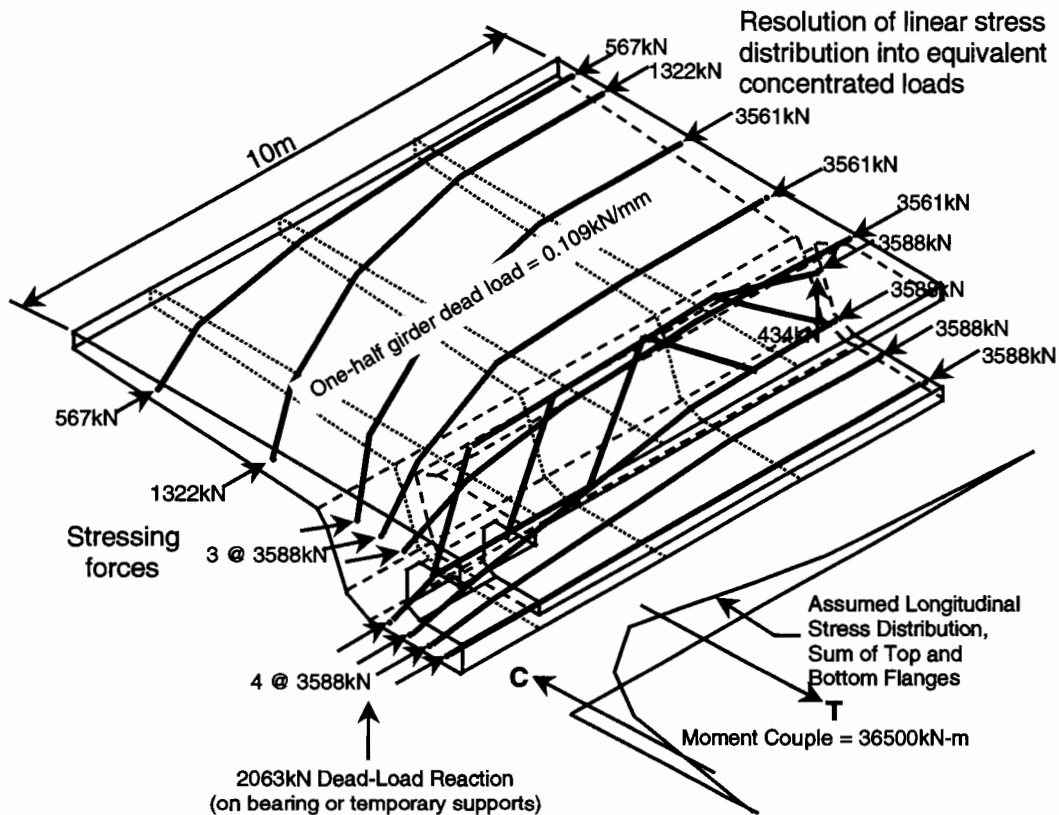
Gauge	Strains in microstrain, + Tension						
	Internal Bottom Slab Tendon Stressed					All Tendons	Dead Load & Prestress
	T10, T11	T9, T12	T8, T13	T7, T14	Sum T7 to T14		
S19	68	34	27	15	143	150	143
S20	59	32	25	13	133	163	156
S21	46	32	25	15	120	141	122
S22	32	42	34	-13	101	182	114
S23	57	91	46	-21	186	317	258
S24	53	72	34	-15	154	258	201
S25	2	4	4	0	4	74	-2
S26	-2	0	-2	-2	-11	8	70
S27	8	4	2	-2	10	-6	-27
S28	0	0	0	-2	-4	57	67
S29	53	68	40	19	182	198	181
S30	0	-6	-6	29	15	129	133
S31	51	11	8	-44	15	730	842
S32	11	8	17	8	2	65	68
S33	112	108	25	-30	230	578	642
S34	-105	-2	2	-2	-106	-63	-25
S36	23	25	36	27	125	112	116
S37	28	29	19	-10	65	38	63
S39	15	13	4	-4	30	38	53
S40	-6	15	-8	-10	-30	-48	-57
S41	27	29	30	25	108	84	87
S42	-13	-10	4	6	-8	108	65
S43	10	8	0	-13	0	55	68
S44	4	0	0	-6	0	36	46
S45	0	0	-2	-4	-4	53	46

From the column titled "All Tendons" in Table 6.3, most of the gauges recorded tensile strains at the end of stressing. As would be expected, the measured strains were larger at the gauge locations where cracks were present and smaller where few or no cracks were present, such as near the webs and in the horizontal bars in the top flange. When the girder was set on its bearings, the strains in the last column of Table 6.3 were recorded. These strains do not differ greatly from those measured at the completion of stressing, except in the vertical bars close to the bearing reaction and in the transverse bars in the bottom flange.

When developing a strut-and-tie model for the anchor segment, the limits of the D-zone and the forces on the D-zone must be determined. The D-zone for the anchor segment ends in the girder at point where plane sections remain plane from the applied prestressing forces. Using the assumption of a 30° diffusion, the force from tendon group T7 to T10 or T11 to T14 diffuses fully to the edge of the wing tip defined by the effective flange width method at a section 11.4m from the anchor plates. This distance may be reduced for the service load case after inspection of the compressive force paths emanating from the anchor plates, including those for the wing tendons, through sections approaching the B-zone boundary. At the chosen section, the linear service load stress distribution from dead load and prestress can be resolved into numerous concentrated loads to be applied to the strut-and-tie model, as shown in Figure 6.20.

The D-zone boundary for the service-load case in Figure 6.20 was selected to be at the centerline of the deviator to simplify calculations. Other loads on the D-zone include the prestress loads at the anchor plates, dead load, and bearing reactions. If symmetry is used and the girder is split down its longitudinal centerline, the transverse axial force distribution and bending moments from the top and bottom flanges must be included as self-

equilibrating reactions. The transverse forces in the top and bottom flanges must provide a moment to balance the eccentricity between the longitudinal post-tensioning forces at the anchor segment and the diffused cross-sectional post-tensioning and dead-load forces. This moment has been calculated and is given in Figure 6.20 for the service-load case. The distribution of the transverse forces and moments in the top and bottom flange must be determined by using equilibrium of the girder in cross section and by assuming a transverse stress distribution along the length of the girder, as shown in Figure 6.20. A shorter assumed diffusion length will result in larger calculated transverse forces. A longer assumed diffusion length will result in smaller calculated transverse tensile forces at sections away from the anchor segment.



Approximate Compressive Force Paths (Dead load and Prestress)

Top and bottom slab forces to be determined by equilibrium using actual support conditions

Figure 6.20 Post-tensioning and dead-load compressive force paths during construction of span D5

A strut-and-tie model can be used to conveniently solve for these transverse diffusion forces, but the model should make provision for dead-load forces since post-tensioning and dead load were applied simultaneously. Assuming symmetrical stressing of tendons during jacking is required, all prestressing should be assumed to be applied simultaneously to reduce calculation effort.

The distribution of dead-load force to the support jacks under the girder wings was difficult to determine during post-tensioning of the girder. The girder was initially supported uniformly along its length by the truss jacks under the girder wings, as shown at the top of Figure 6.21. As the girder was post-tensioned, some of the girder dead load was carried by the girder itself in bending, loading the wing support jacks near the piers and unloading the wing support jacks near midspan. This case is shown in the middle view of Figure 6.21. The deflection measurements taken during post-tensioning and thereafter indicated that the full dead load of the girder was not transferred entirely to the few wing jacks near the girder ends at the completion of post-tensioning. The support reactions during post-tensioning could not be accurately calculated.

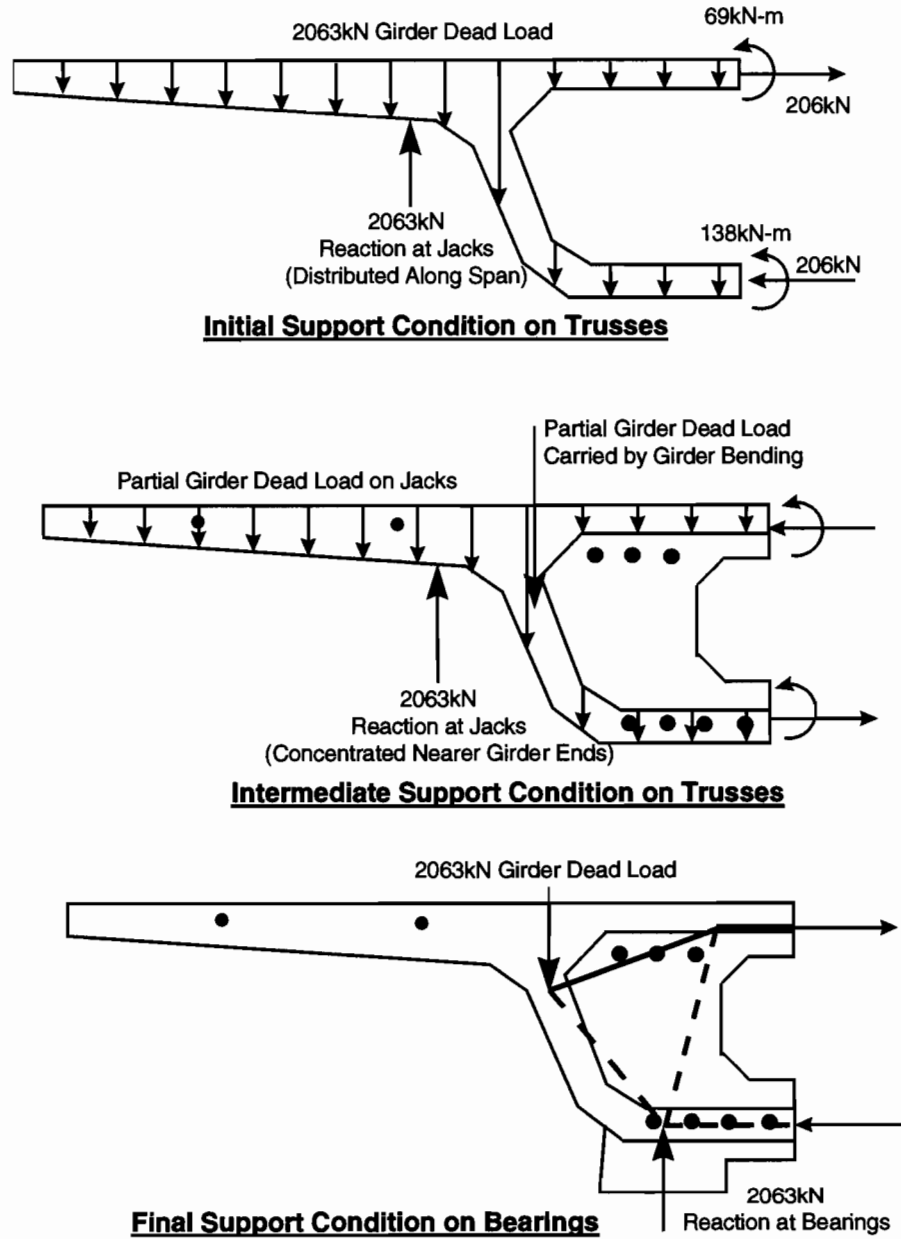


Figure 6.21 *Dead-load support conditions during construction of span D5*

One of the difficulties in comparing measured girder behavior and reinforcement strains with STM calculations is that the STM is a lower bound plasticity model most suitable for the ultimate limit state. Measurements are obtained on the bridge for the service limit state and are not directly comparable. For the calculated ultimate limit state, where the bottom slab internal tendons and perhaps the deviated external tendons are assumed to be at ultimate stress, the location of the boundary of the D-zone could be chosen from service-load stresses to reduce calculation effort. Since the STM is a lower bound calculation procedure, considerable freedom is given to model selection. If the limit of the D-zone is chosen too close to the anchor segment, reinforcement needed to control tensile stresses in the actual D-zone may not be included in the design.

To illustrate the process, the full plastic moment capacity of the section has been assumed to develop at a section near the deviator, as shown in Figure 6.22. Therefore, the ultimate tendon forces are balanced by compression across the full width of the top flange. The forces from the tendons in Figure 6.22 are treated as

external loads on the concrete girder. The compressive force paths from the tendon loads are shown as heavy lines in the figure. The compressive force paths are deviated from the top flange to the web by shear forces. A transverse moment couple of 97,400kN-m is required to offset the moment from diffusion forces.

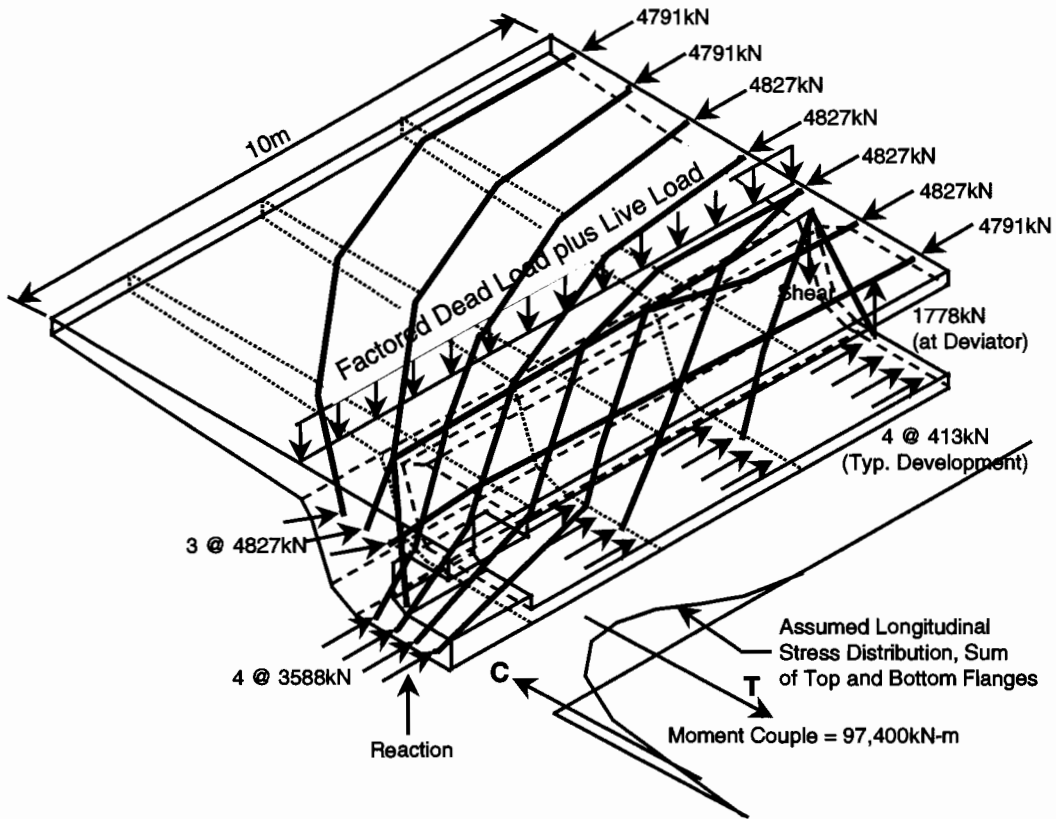


Figure 6.22 Span D5 compressive force paths at ultimate load

A strut-and-tie model can be used to calculate the transverse forces and vertical forces in the girder and diaphragm. Struts and ties for the model should be located on each face of the diaphragm. A STM of forces on the diaphragm interior face is shown in Figure 6.23(a). Struts and ties should also accommodate bearing reaction forces, as shown in Figure 6.23(b). The strut-and-tie model for the D5-16 anchor segment is complex, so strut locations should be limited to those along the compression force paths and those required for equilibrium. Ties should be located and oriented where reinforcement can be effectively placed. Transverse stresses caused by internal spreading within the compressive struts must also be considered, especially near anchorage plates and in the highly stressed bottom flange.

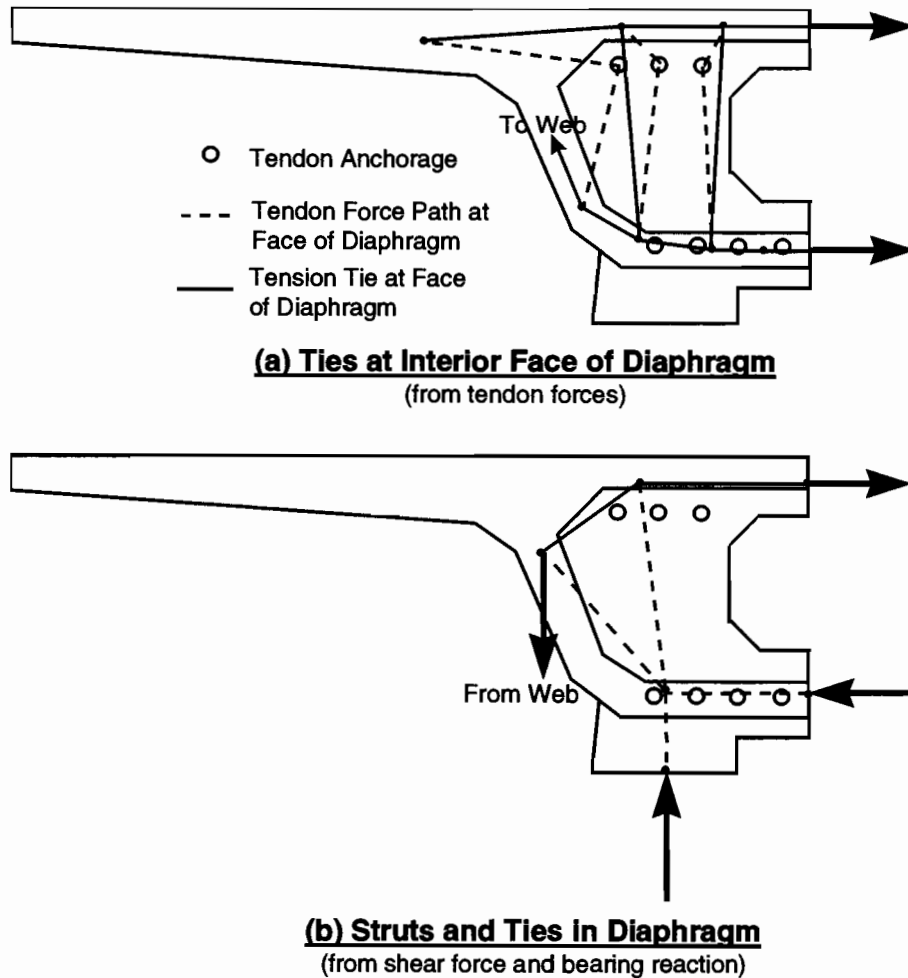


Figure 6.23 Segment D5-16 diaphragm tie locations at ultimate load

The bottom flange cracks shown in Figure 6.19 extended 5.3m along the span indicating that the assumed 1.6m length for the design D-zone for the ultimate-load case was unrealistically short for the service-load case. The nonuniform distribution of bottom flange stresses from post-tensioning forces shown in Figure 6.24 also indicated that significant transverse tensile may have existed well beyond the designed D-zone. Transverse tensile strains in the bottom flange, at the section shown in Figure 6.24, could have been as high as $100\mu\epsilon$ from the Poisson effect alone. Transverse tensile diffusion strains from the bottom flange tendons and the deviated external tendons would add to the Poisson's strains.

From inspection of the compression strut locations in the bottom flange at service load, shown in Figure 6.20, compressive stress in the bottom flange was high at locations between the anchor segment and the deviator. In fact at the instrumented section 1700mm from the anchor plates, shown in Figure 6.24, maximum measured bottom flange strains converted to stresses exceeded the allowable compressive service level stress of 15.2 MPa by 30%. The combination of high longitudinal compressive stress and transverse tensile stress resulted in longitudinal cracking of the bottom flange. The tensile strains measured in the anchor segment diaphragm itself indicated that the diaphragm design was quite conservative, with the highest measured strain of $842\mu\epsilon$ at gauge S31 being only 41% of the yield strain of the bar. Based on this steel strain, first yield would be realized at D/D_0 of 2.44, which is high.

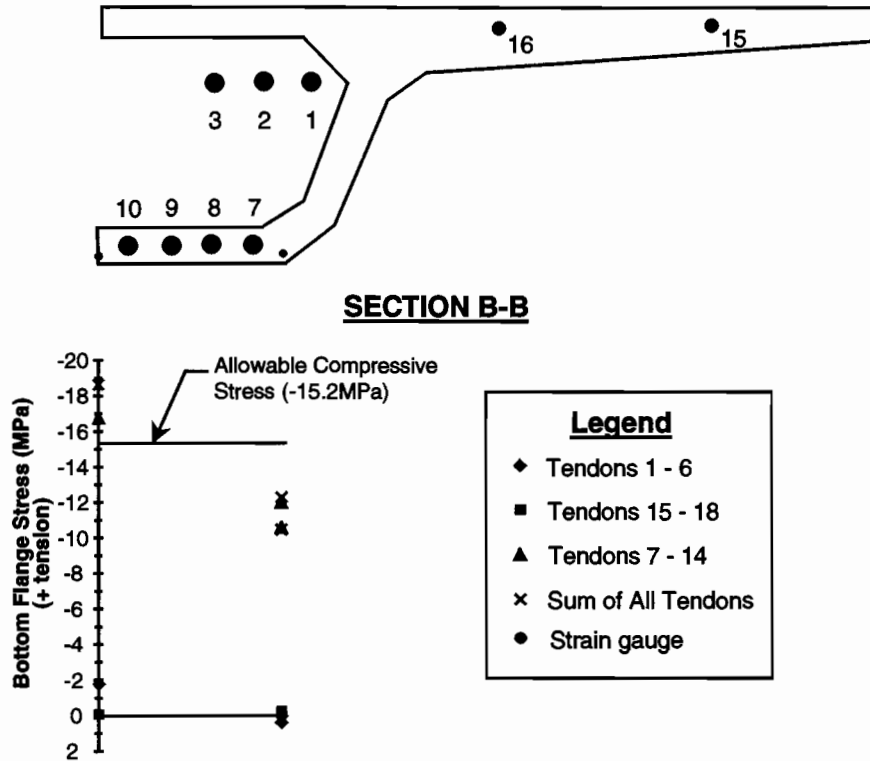
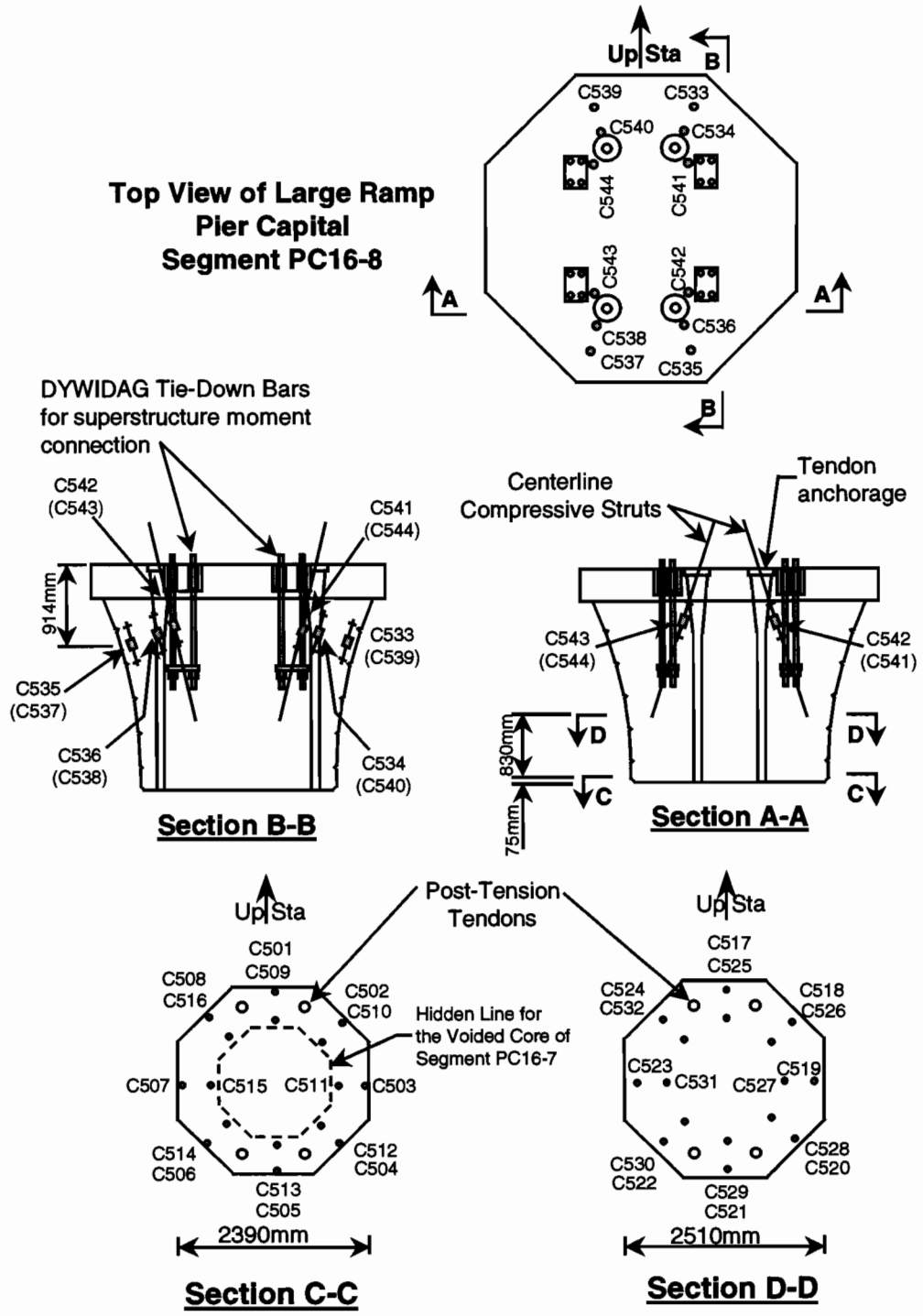


Figure 6.24 Measured bottom flange longitudinal stresses from post-tensioning forces

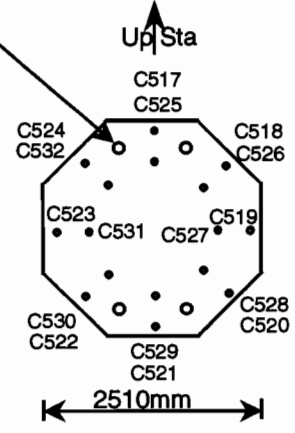
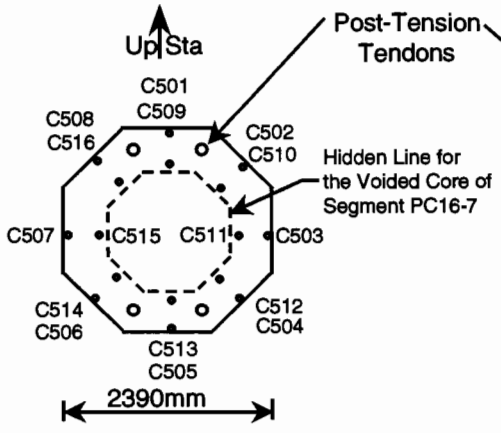
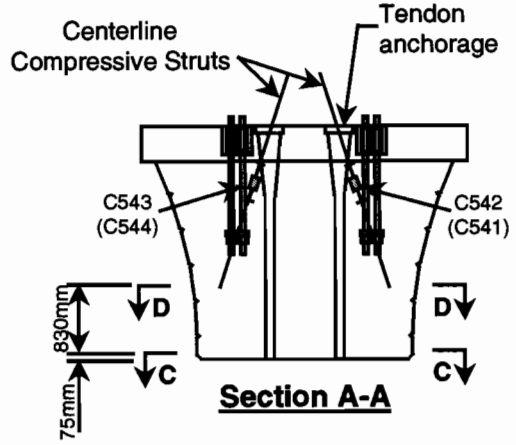
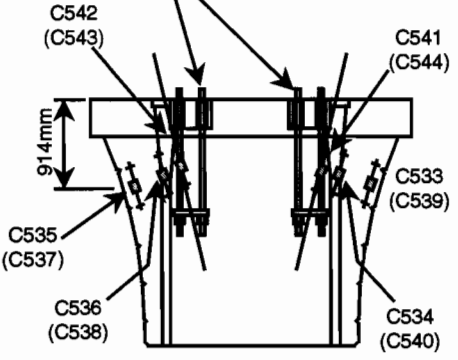
6.3.4 Large Ramp Pier Capital

The large ramp pier capital segment PC16-8 was designed as an anchorage zone for the pair of U-shaped vertical pier post-tensioning tendons, and as the anchorage zone for the 16 threadbars that were used to create a moment connection with the superstructure. In addition, the solid pier capital had to transfer moments from balanced cantilever construction to the voided typical pier segments beneath it. Concrete strain gauges were located as shown in Figure 6.25 to measure the distribution of vertical strain changes throughout the pier capital. Gauges C541 to C544 were installed to measure strains between the anchorage plates for the groups of threadbars and the main pier post-tensioning tendons. Gauges at Sections C-C and D-D were placed to measure the diffusion of vertical forces near the interface of the capital and top pier segment. Strain gauges were also installed directly on the reinforcing bars and threadbars in the capital. The locations of these gauges are shown in Figure 6.26. The gauged bars in Sections B-B and C-C in Figure 6.26 were designed as tie bars to resist tensile forces in the capital from the various applied loads.



DYWIDAG Tie-Down Bars for superstructure moment connection

Centerline Compressive Struts
Tendon anchorage



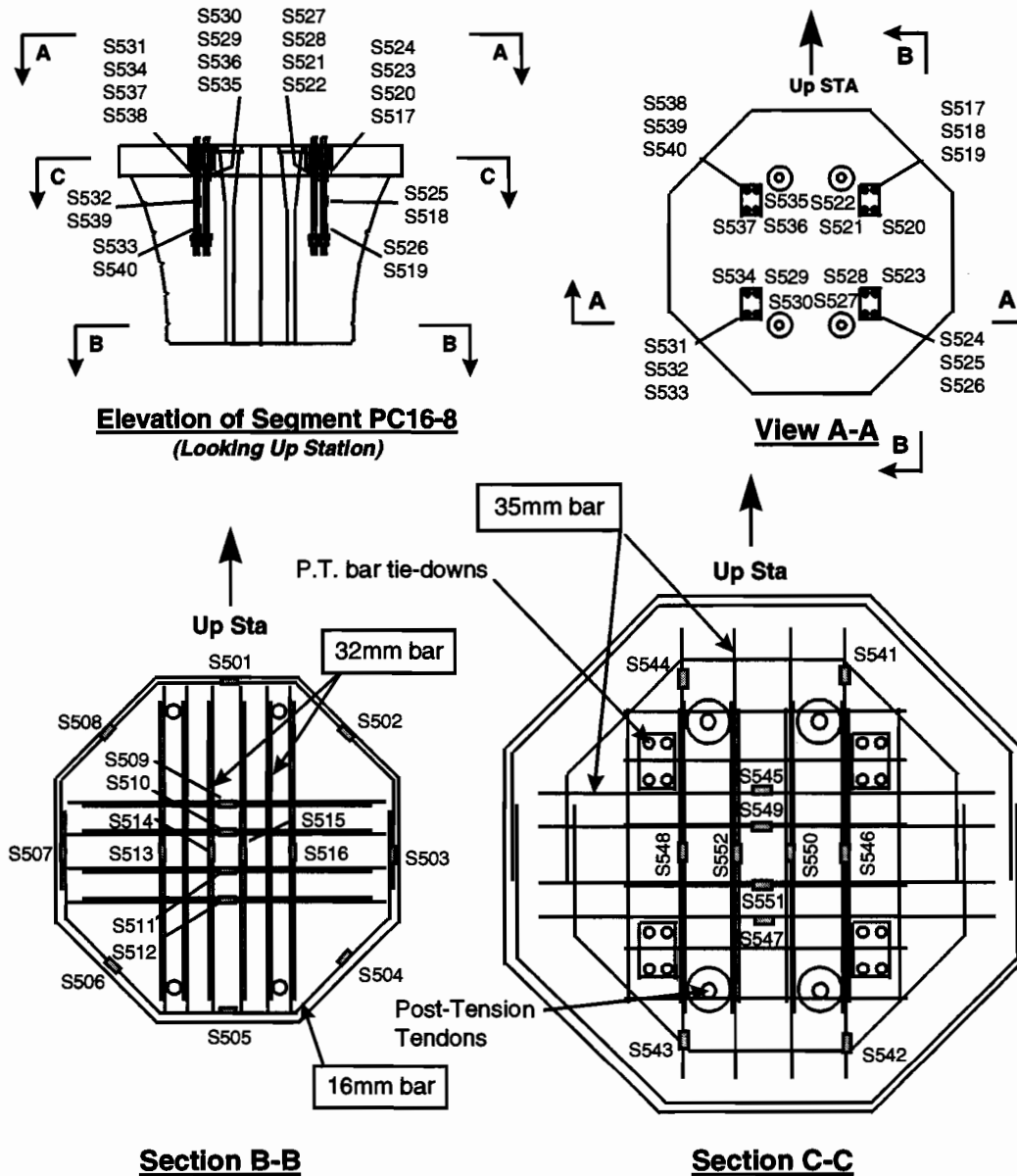


Figure 6.26 Large ramp pier capital segment PC16-8 tie gauges

The measured strain changes from post-tensioning of the main pier tendons are shown in Table 6.4. The strains measured by gauges C541 to C544 between anchor plates and strains measured at the bottom of the threadbars were similar at $-92\mu\epsilon$ and $-86\mu\epsilon$ respectively. This measurement would correspond to a maximum compressive stress of 3.9MPa or 8% f_c' . Compressive vertical strains decreased rapidly toward the outer edge of the pier capital, with strains at gauges C533, C535, C537 and C539 averaging only $-11\mu\epsilon$. Compressive vertical strains also decreased rapidly toward the top of the capital, as seen by the strain measurements on the threadbars, even though these gauges were located very close to the main pier tendon anchor plates. Vertical concrete strains measured at the base of the capital were difficult to interpret because of the large number of damaged gauges. Gauges C501 and C505 at the bottom of the capital measured $-76\mu\epsilon$, while gauges C503 and C507 measured $-51\mu\epsilon$, indicating that the post-tensioning force had not fully diffused. The tendon anchorages were located more toward the longitudinal centerline of the bridge, as can be seen in the Top View in Figure 6.25.

Many of the gauges located on the tie reinforcing carried appreciable tension, such as S548, S552, S550 and S546 located on longitudinal bars at the top of the pier at $159\mu\epsilon$. This strain approaches the $170\mu\epsilon$ required to

crack the concrete, but is well below the $2070\mu\epsilon$ yield point of the reinforcement. Gauges S541 to S544 located near the anchorage hook for these same bars did not go into appreciable tension. The transverse bars gauged by S545, S549, S551 and S547 at the top of the capital were actually within a compression strut and measured $-15\mu\epsilon$. At the bottom of the capital, both the longitudinal and transverse bars gauged by S509 to S516 were in tension.

The transverse bars averaged twice the tensile strain of the longitudinal bars, at $66\mu\epsilon$ versus $31\mu\epsilon$ respectively. Tension was present in the circumferential bars gauged by S501, S505, S503 and S507, with the longitudinally oriented gauges measuring twice the strain of the transverse gauges at $100\mu\epsilon$ and $52\mu\epsilon$ respectively. These strains were well below the $170\mu\epsilon$ required to crack the concrete, and no cracking was noticed beyond those cracks that formed during curing of the segment.

Table 6.4 Measured strain changes in segment PC16-8 gauges from post-tensioning forces

+ Tension		+ Tension	
Strut Gauges	Microstrain	Tie Gauges	Microstrain
C501,5	-76	S501,5	52
C503,7	-51	S503,7	100
C502,4,6,8	6	S502,4,6,8	40
C509,13	-	S509,10,11,12	66
C511,15	-34	S513,14,15,16	31
C510,12,14,16	-78	Threadbar Top	-5
C517,21	-	Threadbar Mid.	-49
C519,23	-11	Threadbar Bot.	-86
C518,20,22,24	-56	S541,42,43,44	7
C525,29	-	S545,49,51,47	-15
C527,31	-29	S548,52,50,46	159
C526,28,30,32	-34		
C533,35,37,39	-11		
C534,36,38,40	-78		
C541,42,43,44	-92		

The measured strain changes from the unbalanced placement of the farthest superstructure segment P16-17 are given in Table 6.5. Segment P16-17 was placed on the upstation side of the pier and produced a substantial moment of $7366\text{kN}\cdot\text{m}$ and compressive force of 285kN . Stresses at the top of the capital were nearly linear, as can be seen in Figure 5.67, and also at a section in the pier 610mm below the bottom of the capital, as seen in Figure 5.66. Strains in each group of threadbars were nearly uniform along their height, but with the gauges at the tops of the threadbars taking less strain than those at the middle or bottom, be it tensile or compressive. For example, gauges S517, S520, S521 and S522 averaged $-17\mu\epsilon$ change at the top of the threadbar group, while gauges S518 and S519 measured $-21\mu\epsilon$ and $-19\mu\epsilon$ at the middle and bottom respectively. A simple $P/A+Mc/I$ type stress calculation predicted that the strain change at the top of the threadbars should have been about $-33\mu\epsilon$, indicating that the threadbars were not yet grouted.

The tie bars, both longitudinal and transverse, located at the top of the capital did not measure significant strain changes. Gauges S545, S549, S551 and S547 on the transverse bars measured tension at $4\mu\epsilon$, while gauges S548, S552, S550 and S546 measured compression at $-6\mu\epsilon$. Strain changes at the bottom of the capital in the tie bars gauged by S509 to S515 measured essentially no strain change. The circumferential bars gauged by S501 to S508 did measure strain changes with a trend toward tension on the compression side of the pier, the upstation side, and compression on the tensile side of the pier. These measured strains were as high as $17\mu\epsilon$ at gauge location S502. These values compare to the calculated Poisson's strain of $14\mu\epsilon$ expansion at S502 that would have occurred at the edge of the grout pad on top of the capital. A strut-and-tie model for this pier capital should include the superstructure anchor segment and the ultimate forces and moments carried to the

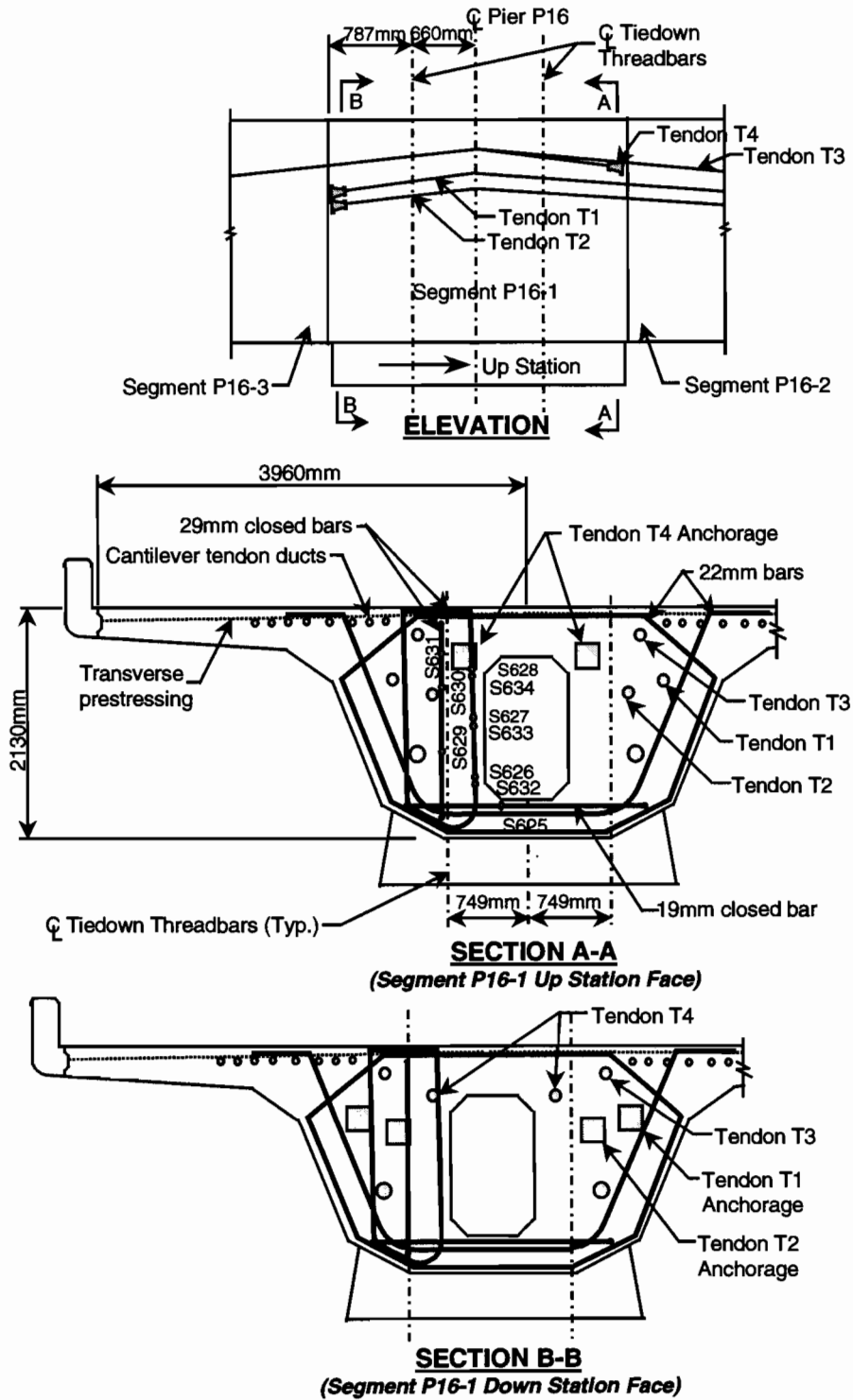
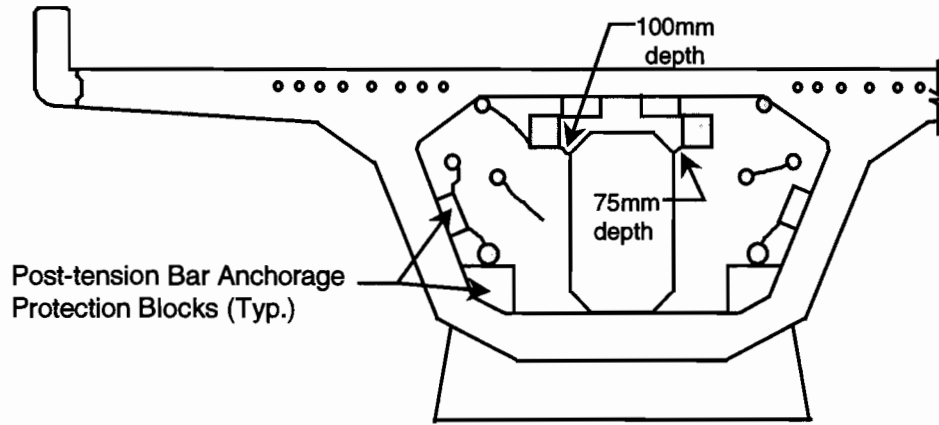
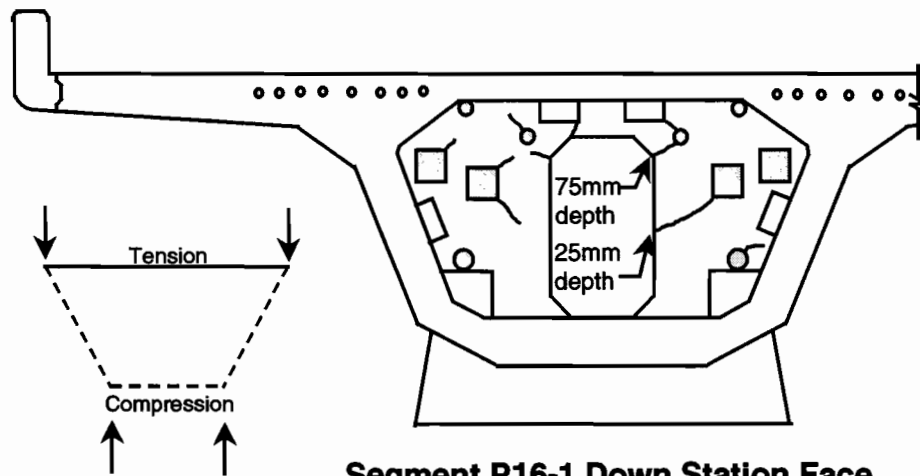


Figure 6.27 Ramp P girder anchor segment P16-1 details



Segment P16-1 Up Station Face



Segment P16-1 Down Station Face

Figure 6.28 Crack patterns in segment P16-1

Strain changes measured in the anchor segment from the unbalanced placement of the most distant superstructure segment P16-17 are given in Table 6.6. Strain changes in the vertical bars were compressive, as shear forces were transferred to the bearing surface. The anchor segment was made monolithic with the pier capital with a grout pad that extended nearly the full width and length of the anchor segment bearing plinth. The flow of shear force from the webs to the single-bearing surface caused tension in gauge S625 of $11\mu\epsilon$. Compression would normally be expected at this location, with tension in the top flange, as demonstrated by the simple STM at the bottom of Figure 6.28. Compression may have existed across the bottom of the diaphragm at locations more toward the centerline of the pier. The gauge S625 measurement may have been influenced by Poisson's-type strains from the vertical compression on the upstation face of the anchor segment. The Poisson's strain is calculated to be about $11\mu\epsilon$ (expansion) at a point halfway between the bottom of the access opening and the bottom of the bearing plinth, using a simple $P/A+Mc/I$ calculation with a Poisson's ratio of 0.2.

Measured compressive strains on the vertical bars tended to increase toward the bottom of the diaphragm, with the highest compressive strain measured by gauge S632 at $-44\mu\epsilon$. This strain at S632 calculated using $P/A+Mc/I$, assuming the entire diaphragm was an effective part of the cross section, would give a strain of $-71\mu\epsilon$. The $P/A+Mc/I$ calculated stress is inaccurate because the state of stress is actually quite complicated within the diaphragm at the junction of the superstructure and the pier capital. The strain measured at S632 was lower because S632 was essentially outside the compression field between the girder web and the pier capital, thus plane sections through the diaphragm were not plane after the loading.

Table 6.6 Measured strain changes in segment P16-1 gauges from placement of superstructure segment P16-17

+ Tension	
Gauge	Microstrain
S625	11
S627	-2
S628	-13
S629	-23
S630	-17
S631	-15
S632	-44
S633	-23

After completion of the superstructure closure pours, continuity post-tensioning was stressed, including external tendons T1, T2, T3 and T4. Tendons T1, T2 and T4 were anchored on the segment P16-1 diaphragm, as shown in Figure 6.27, while tendon T3 passed continuously through the anchor segment. The strain changes measured by the gauges in segment P16-1 from the post-tensioning of these tendons is given in Table 6.7. Gauge S625 measured tension from the stressing of the tendons anchored on the downstation face of the diaphragm and measured compression when T4 was stressed and anchored on the upstation face of the diaphragm. Greater tensile stress was recorded by S625 when T2 was stressed than when T1 was stressed. T1 was located closer to the web. The response of the vertical gauges was very similar from the stressing of tendons T1 and T2, with somewhat higher strain changes caused by the stressing of T2. Tendon T3 caused tension in most of the instrumented vertical bars, even though this tendon passed continuously through the segment producing a downward deviation force.

The instrumented face of the diaphragm and the interior of the diaphragm may have had different responses from the T3 deviation force, especially if the tendon did not contact its duct near the face of the diaphragm. Tendon T4 was anchored very near the plane of strain gauges, with compression indicated by the gauges closest to the anchor plate. Gauge S628 and S631 measured $-11\mu\epsilon$ and $-29\mu\epsilon$ respectively. All other gauges measured a small amount of tension from the stressing of T4, with the exception of S625 on the bottom flange transverse bar. The greatest tensile change from the stressing of all continuity tendons was measured by S630 at $71\mu\epsilon$. With an assumed cracking strain of $170\mu\epsilon$, D/D_0 at first cracking from the longitudinal external post-tensioning alone would be high at 2.7.

Table 6.7 Measured strain changes in segment P16-1 gauges from superstructure post-tensioning forces in microstrain

Gauge	Strain in microstrain, + Tension				
	Tendons Stressed				
	T1	T2	T3	T4	All Tendons
S625	6	10	4	-6	14
S627	10	8	13	11	42
S628	23	19	-13	-11	18
S629	10	15	10	8	43
S630	23	25	13	10	71
S631	19	25	11	-29	26
S632	13	15	10	2	40
S633	13	11	2	11	37

An elevation of a strut-and-tie model for the Ramp P girder under ultimate load in span P16 is shown in Figure 6.29. AASHTO [23] factored dead load and live loads have been placed to maximize the moment at the top of

the capital. The superstructure moments, shears, and axial forces from dead load, live load and prestress have been resolved into concentrated forces and applied to the model. The discontinuous post-tensioning in the girder and pier from both multistrand tendons and post-tensioning bars makes this model quite complicated. Ties have been placed at locations of primary reinforcement, including at three levels in the pier capital. The vertical tie-down bars are the only reinforcement passing through the horizontal plane between the bottom of the anchor segment plinth and the top of the capital. The selected struts and ties crossing this plane reflect this limitation. The vertical tie down bars on the tension side of the capital have reached ultimate tensile capacity at 7922kN. Another important tie location was member 8 located within the anchor segment. High moment from span P16 must be distributed to the pier, requiring a continuous flow of tension force from the top of the P16 girder near the pier, through the diaphragm, and down the upstation side of pier P16. Other important tie locations were at the top of the capital at members 21 and 22, between tiedown bar anchorages at members 28 and 36, and at the bottom of the capital. Based on the strain measurements, the circumferential bars at the base of the capital were at important strut and tie locations, depending on the load applied. This situation would be expected since the voided pier can only react on the capital along its top perimeter. Also, to maintain the integrity of the voided pier section, all diffusion of forces from the superstructure and post-tensioning tendons and bars should be designed to occur within the limits of the capital without excessive strains or large cracks at the base of the capital. Additional transverse reinforcement could have been added in the voided pier segments where drastic changes in pier cross-sectional geometry occurred, such as at the top and bottom of the voided section, to resist diffusion forces occurring outside the designed D-zones. No cracks were noted at the top or bottom of the voided pier section from service level forces.

A strut-and-tie model taken through a section of the compression face of the anchor segment and pier capital is shown in Figure 6.30. The eccentricity of the web shear forces to the anchor segment plinth reaction causes a tensile force to occur in the top flange. This transverse tensile force was partially resisted by the transverse deck post-tensioning. Other important tie locations were at members 3 and 4 and between tiedown bar anchorages at member 11. The three-directional prestressing of the anchor segment resulted in excellent service load level performance. The factored loads applied to the STM in Figures 6.29 and 6.30 were AASHTO HS25-44 factored live loads and factored dead load placed in the pattern needed to produce a maximum ultimate moment on the span P16 face of the P16-1 anchor segment. These loads were much lower than the loads required to cause a plastic moment in the superstructure, or even cause top fiber tension in the anchor segment. The ultimate factored load was nearly enough to cause an ultimate moment at the top of the capital and was assumed to do so in the STM in Figure 6.29 to create the largest possible forces in the D-zone. Based on the results of the STM in Figure 6.29 and 6.30, minimal plasticity would be expected in the anchor segment at factored ultimate load because of the effectiveness of the three-dimensional prestressing. The mild steel in the anchor segment diaphragm was many times more than necessary for taking the calculated tension tie forces.

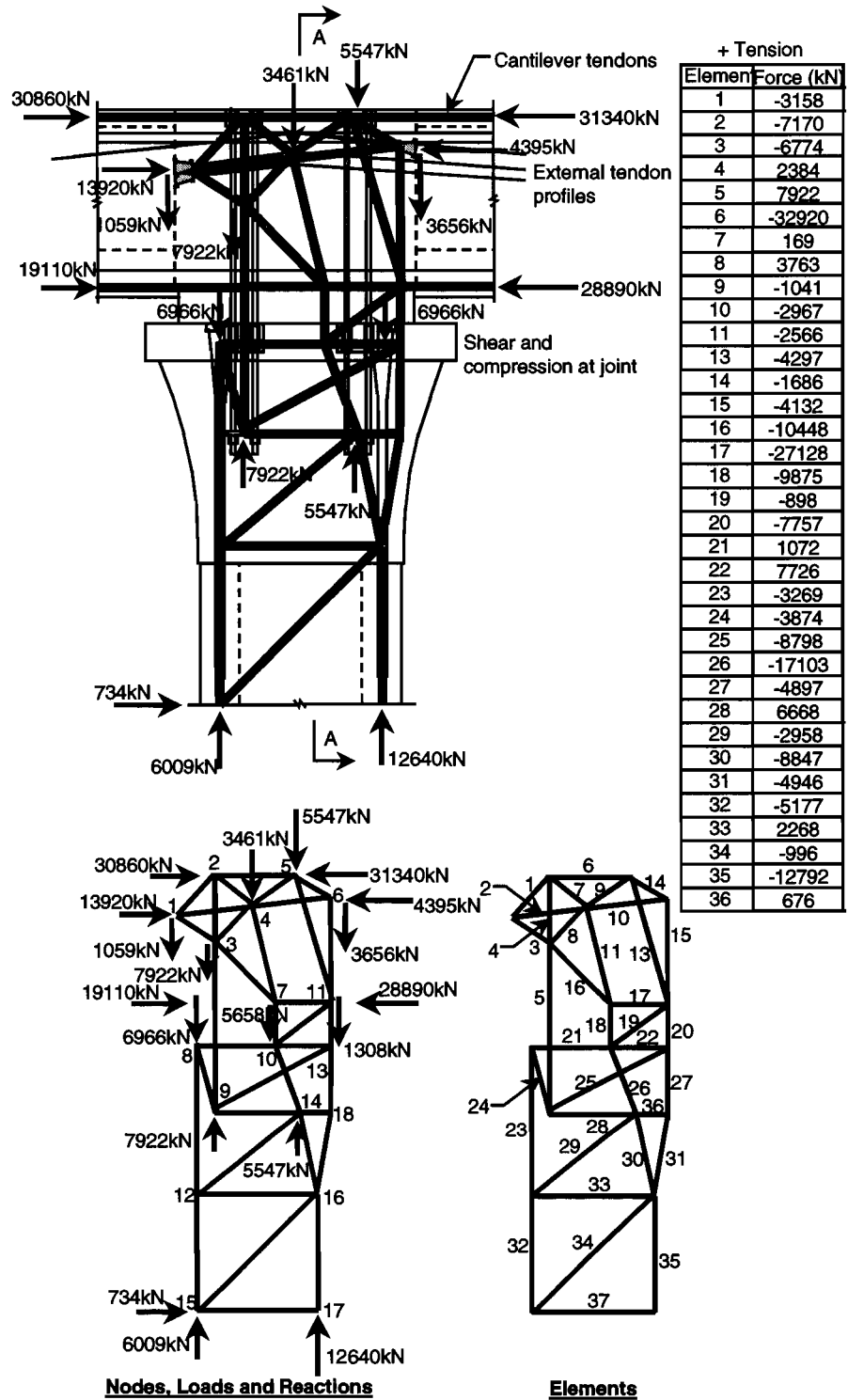


Figure 6.29 Strut-and-tie model at pier P16 - Side view

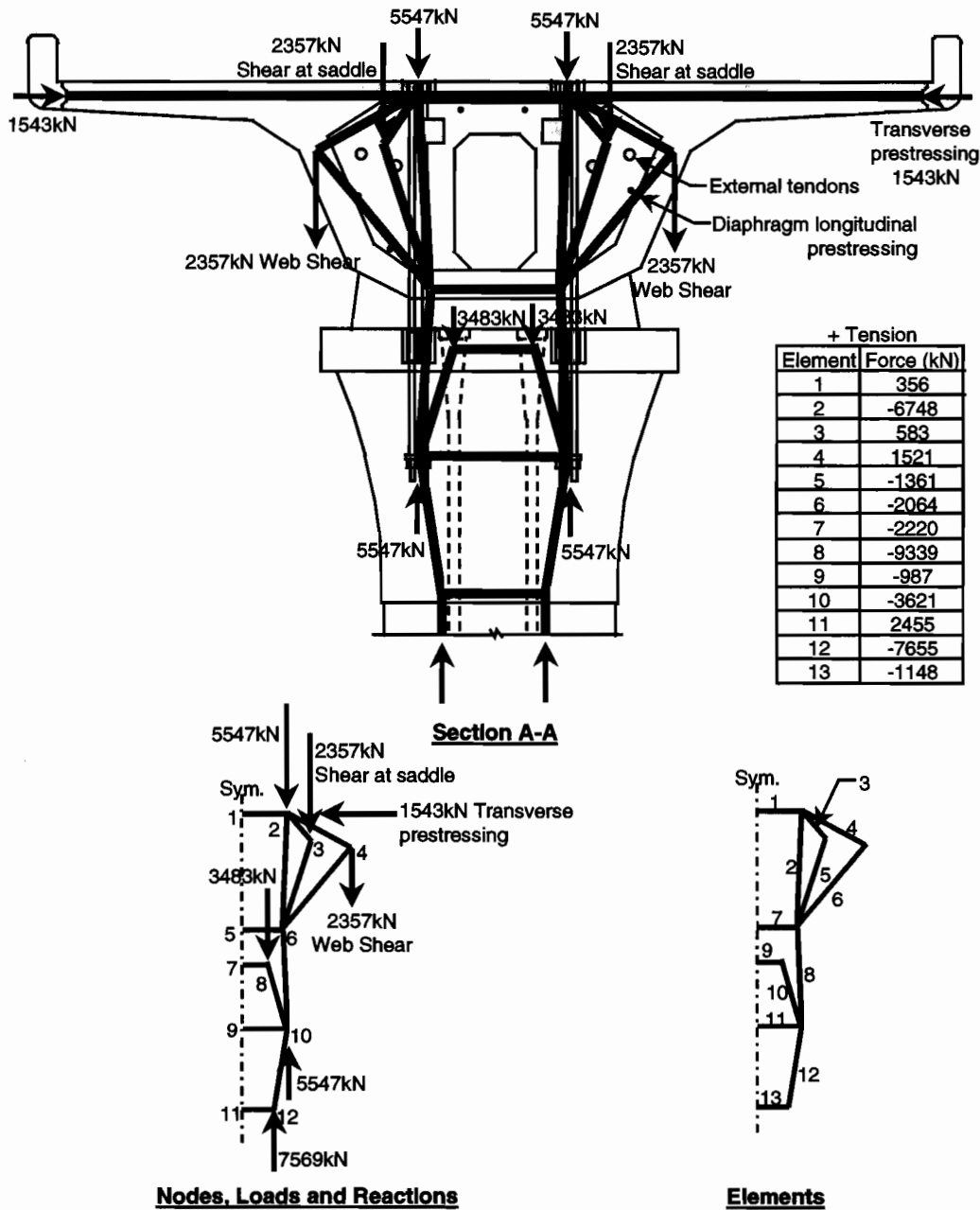


Figure 6.30 Strut-and-tie model at pier P16 - Looking down station

6.3.6 Ramp Deviator Segment

The deviator in segment P16-10 of Ramp P, shown in Figure 6.31, was designed as an inverted T-beam type deviator similar to those in the mainlane girders. The primary difference between the Ramp P deviator and the mainlane deviators was the width. The six 19-15mm diameter strand tendons passing through the Ramp P deviator occupied nearly the full width of the deviator. The primary reinforcement in the Ramp P deviator is shown in Figure 6.31. The instrumentation in the Ramp P deviator is also shown in Figure 6.31. The instrumentation locations were similar to those in the mainlane deviator, but additional gauges were added to measure strains at points away from the deviator pipes. Gauges S719, S720 and S721 were added to measure tensile strains at the top center of the deviator beam, but unfortunately none of the gauges survived the casting process of the segment.

Gauges S722 and S723 were installed on the bottom flange longitudinal reinforcement near the bottom flange to web fillet juncture. Also, gauges S724 and S725 were installed on the bottom flange longitudinal reinforcement at the centerline of the segment. Concrete strain gauges C749 to C755 were installed 40mm from the interior surface of the web at the locations shown in Figure 6.31. Tendons T1 to T3 produced both horizontal and vertical deviation forces that were not symmetrical on both sides of the deviator because of the horizontal curvature of the bridge. The deviation forces are given in Figure 6.32. The instrumentation was located on the left side of the deviator looking upstation, and therefore was close to tendons T1 left, T2 left and T3 left.

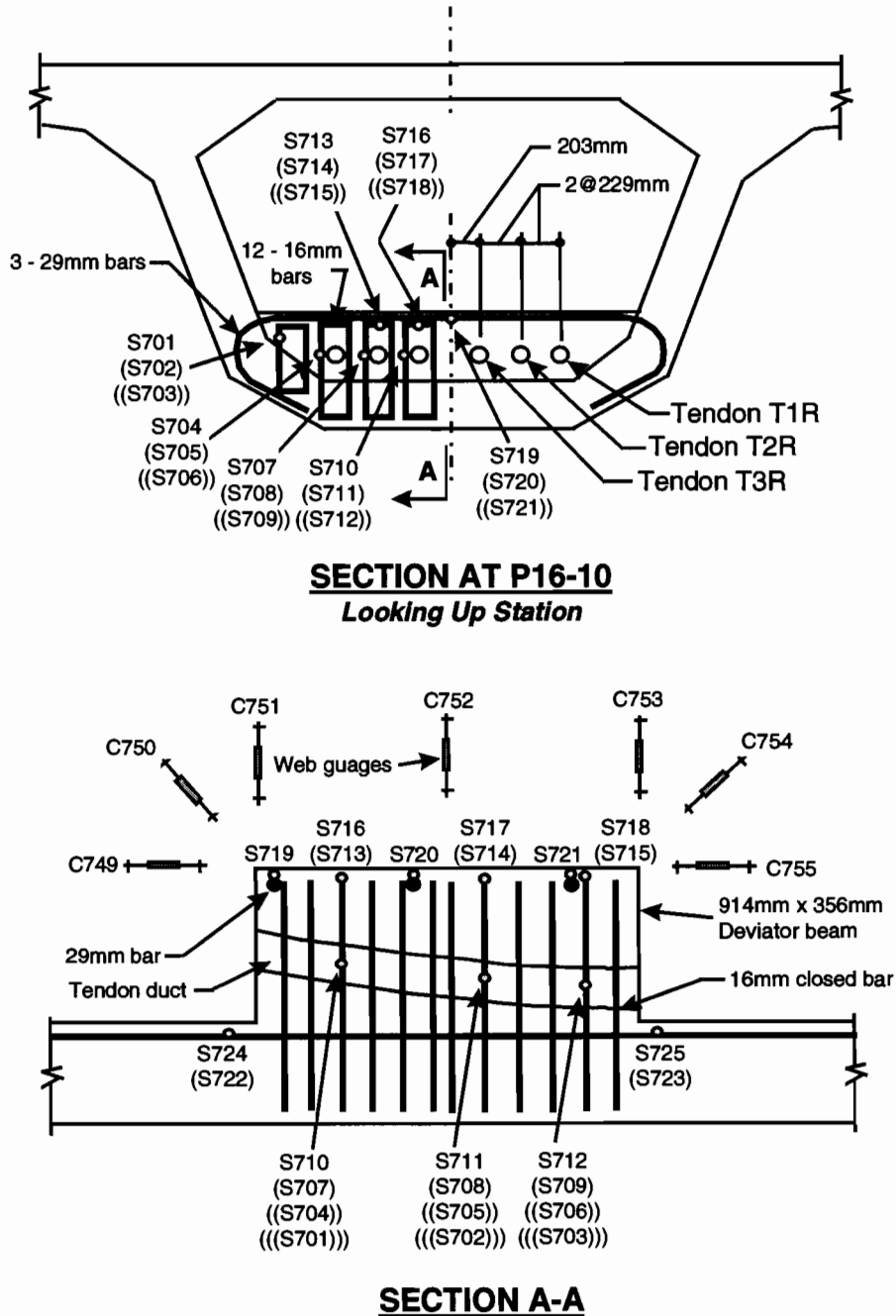


Figure 6.31 Ramp P girder segment P16-10 deviator details

Vertical Reactions from Post-tensioning	Horizontal Reactions from Post-tensioning
Tendon T1 Left = 305kN Tendon T1 Right = 469kN Tendon T2 Left = 275kN Tendon T2 Right = 426kN Tendon T3 Left = 299kN Tendon T3 Right = 465kN	Tendon T1 Left = 107kN Tendon T1 Right = 165kN Tendon T2 Left = 93kN Tendon T2 Right = 151kN Tendon T3 Left = 102kN Tendon T3 Right = 165kN

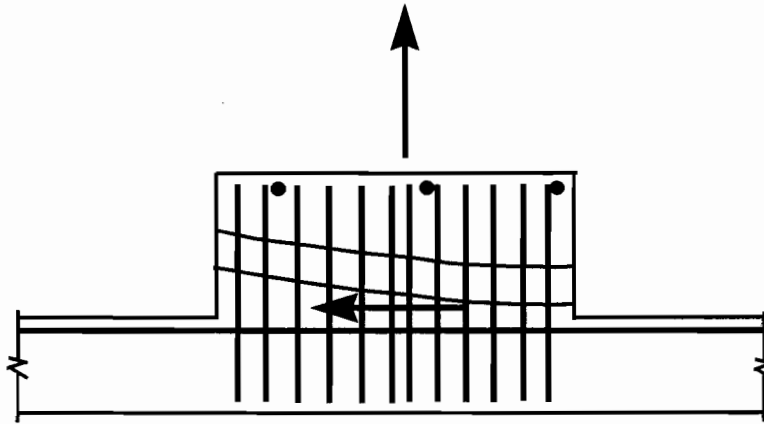


Figure 6.32 Vertical and horizontal forces from tendons T1, T2 and T3

The tendons were not stressed in pairs, and because of the balanced cantilever construction sequence they were not stressed on the same day or even during the same week. The strains presented in Table 6.8 were the strain changes that occurred during the actual stressing operation of the tendon indicated. The last column of Table 6.8 titled "Final" includes strain changes measured over the entire construction period, and therefore include time-dependent strains. Gauges S701 to S703 were located on the closed bars intended to act as shear reinforcement for the deviator beam. These gauges were located on the plane at the top surface of the web fillet, as shown in Figure 6.31. From Table 6.8 it can be seen that the measured strain changes in these bars were similar and very small, regardless of whether tendons on the right side or left side were stressed, at about an average of $9\mu\epsilon$ for tendons T1 and an average of $4\mu\epsilon$ for tendons T3. The total average instantaneous strain in gauges S701 to S703 was $38\mu\epsilon$ from the stressing of all tendons T1, T2 and T3. Longitudinally oriented gauges C749 and C755 measured a total instantaneous strain change from the stressing of all tendons of $-152\mu\epsilon$ and $-159\mu\epsilon$ respectively at an elevation in the girder slightly closer to the neutral axis of the section than that of gauges S701 to S703. Gauges S722 and S723 measured instantaneous strains from all tendons of $-182\mu\epsilon$ and $-205\mu\epsilon$ at an elevation lower than gauges S701 to S703. Using a linear interpolation of these measured compressive strains, the longitudinal strain near S701 to S703 would be about $-170\mu\epsilon$. Using a Poisson's ratio of 0.2 gives a vertical strain at gauges S701 to S703 of about $34\mu\epsilon$. This value is only slightly less than the measured total instantaneous strain of $38\mu\epsilon$, indicating that most of the measured strain change was not due to tensile forces from the tendon deviations. Gauges S701, S702 and S703 may have been located too close to the girder web to measure appreciable tensile strains from the shear force.

Table 6.8 Measured strain changes in segment P16-10 gauges from post-tensioning forces in microstrain

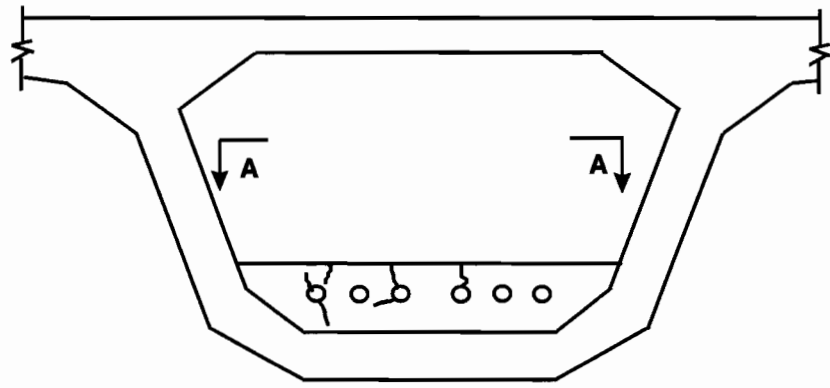
Gauge	Strain in microstrain, + Tension							Sum of Instant.	Final
	Tendon stressed								
	T1L	T1R	T2L	T2R	T3L	T3R			
S701	10	10	8	10	0	6	42	78	
S702	8	8	6	6	4	8	38	80	
S703	8	8	6	6	4	4	34	46	
S704	0	-2	-4	4	0	0	-2	93	
S705	11	2	11	2	2	4	32	163	
S707	6	0	4	0	6	2	17	61	
S708	10	0	10	8	2	0	29	84	
S709	8	0	34	-6	0	-2	34	84	
S710	-2	-4	0	8	40	23	65	239	
S711	2	0	8	11	19	4	44	106	
S713	8	6	19	10	-2	8	47	84	
S714	8	4	23	-2	6	6	44	0	
S716	8	8	19	21	53	8	116	13	
S722	-32	-34	-32	-40	-11	-32	-182	-287	
S723	-36	-32	-34	-40	-27	-36	-205	-300	
S724	-32	-34	-32	-40	-10	-25	-173	-243	
C749	-30	-23	-29	-30	-13	-27	-152	-172	
C750	-27	-15	-27	-25	-19	-25	-137	-203	
C751	0	4	0	-2	-6	-4	-8	4	
C752	-4	2	-4	-2	-6	-6	-19	-13	
C753	0	4	-2	-2	-2	-2	-4	-2	
C754	-2	-13	-19	-17	-11	-17	-97	-101	
C755	-30	-25	-27	-29	-19	-29	-159	-201	

Gauges S704, S705 and S706 were located on the vertical reinforcing immediately adjacent to the duct for tendon T1 left, as seen in Figure 6.31. From Table 6.8 it can be seen that the strain changes from the stressing of T1 left were quite different at gauges S704 and S705, at $0\mu\epsilon$ and $11\mu\epsilon$ respectively. Gauge S706 was not working. This difference in strain indicates that the tendon was not bearing evenly on the entire surface of the duct. Gauges S704 and S705 also recorded different strains when T2 left was stressed, at $-4\mu\epsilon$ and $11\mu\epsilon$. The sum of the total instantaneous strains for gauge S704 was essentially zero, while the sum of total instantaneous strains for gauge S705 was $32\mu\epsilon$. The final long-term strain at gauges S704 and S705 indicated much more substantial tension, at $93\mu\epsilon$ and $163\mu\epsilon$ respectively. Continued cracking of the deviator over time probably was the cause of the increase in tensile strain at these gauge locations. The strain at S705 was close to the cracking strain of $170\mu\epsilon$. Gauges S707, S708 and S709, located adjacent to the tendon duct for T2 left, also measured quite different strain changes from each other as each tendon was stressed. This difference was especially apparent when tendon T2 left was stressed. Gauges S707, S708 and S709 measured $4\mu\epsilon$, $10\mu\epsilon$ and $34\mu\epsilon$ respectively, indicating that the tendon was bearing more on the upstation side of the deviation duct.

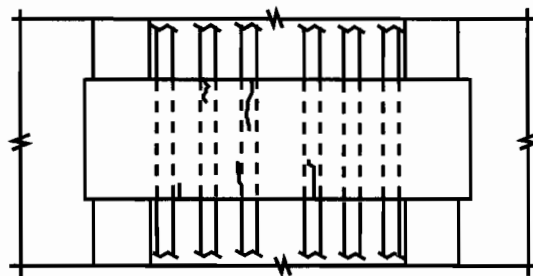
The long-term final strains for gauges S707, S708 and S709 were somewhat more uniform than the sum of instantaneous strain measurements, at $61\mu\epsilon$, $84\mu\epsilon$ and $84\mu\epsilon$. The long-term strain measurements at gauges S710 and S711, located adjacent to the tendon duct for T3 left, differed quite a bit at $239\mu\epsilon$ and $106\mu\epsilon$ respectively. Gauge S710 was located at a horizontal crack, as seen in Figure 6.33. Gauge S716, located above tendon T3 left, was also located at a crack and indicated a tensile strain of $53\mu\epsilon$ when T3 left was stressed. The sum of the instantaneous measured strain changes at gauge S716 was $116\mu\epsilon$, but had declined to only $13\mu\epsilon$ over the long term as seen in Table 6.8. The strain behavior at gauge S714 above tendon T2 left was similar, with a sum of the instantaneous strains of $44\mu\epsilon$ declining to zero strain over the long term. Gauges S714 and S716 were located on the very short length top leg of the vertical stirrup bars. The tensile stress in this short leg may

have decreased because of concrete cracking or creep near the top of these bars. This stress would have been taken by the 29mm full-width top bars, shown in Figure 6.31. Unfortunately, gauges S719 to S721 were damaged and could not measure the strain in these top bars.

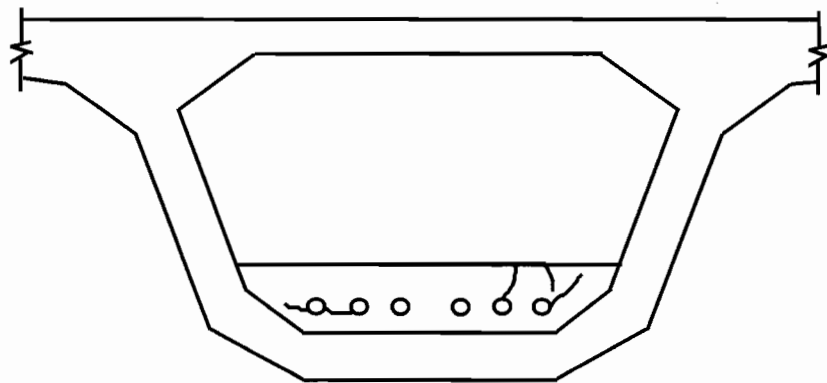
As seen in the mainlane deviator, the largest strain readings were taken on the vertical bars adjacent to the tendons closest to the centerline of the girder, even though the stressing order was reversed. Cracking was much less substantial in the Ramp P deviator, initiating during the stressing of the T3 tendons. This behavior relates to a D/D_0 at cracking of about 0.88. Deviator reinforcing bars were stressed to 12% of the yield stress or less. An estimated D/D_0 at first yield would be unrealistically large at 7.6. In actuality yielding would occur earlier than this, since the concrete in tension would rupture, placing more force on the steel reinforcement.



VIEW LOOKING UPSTATION



VIEW A-A



VIEW LOOKING DOWNSTATION

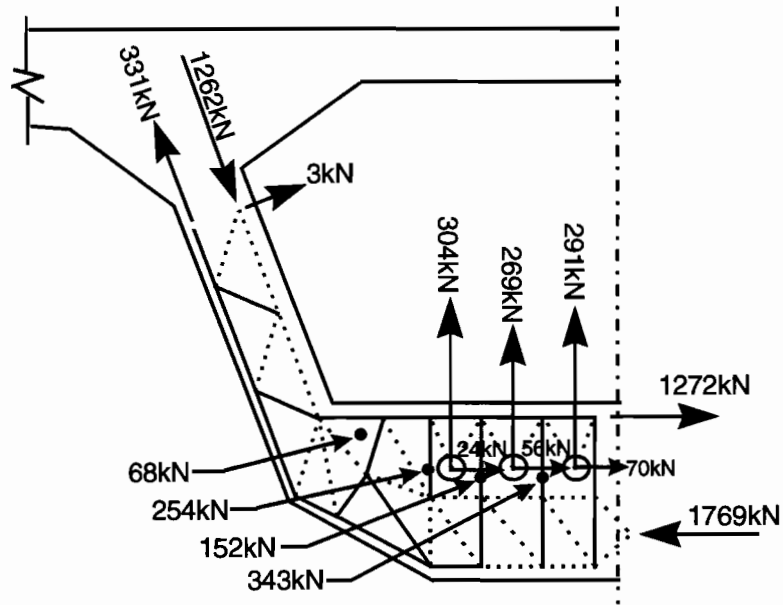
Figure 6.33 Crack patterns in segment P16-10

Gauges S722, S723 and S724 gave similar strain changes from the stressing of each of the tendons, except when T3L was stressed. The strain changes at gauge S723 were higher than the strain changes at S722 and S724 during the stressing of tendons T3 left and T3 right. This case is opposite of what would be expected because the horizontal friction force acted toward gauges S722 and S724. A greater number of gauges at this location may have shown otherwise, but gauges C749 and C755 gave a similar result. The total instantaneous strain change was $-152\mu\epsilon$ at C749 and $-159\mu\epsilon$ at C755, very close to the cracking strain. The strain measurements at diagonally placed gauges C750 and C754 included the local compressive strain from the tendon deviation forces, the Poisson's strain from longitudinal prestressing forces, and the shear strain from the reaction at the deviator. Gauge C750 measured a higher total instantaneous strain change than gauge C754, at $-137\mu\epsilon$ and $-97\mu\epsilon$ respectively, because of the difference in shear strain on each side of the deviator and the orientation of the gauges. Gauges C751, C752 and C753 measured very little compressive strain change, but may have been located near the neutral bending and compression axis of the web.

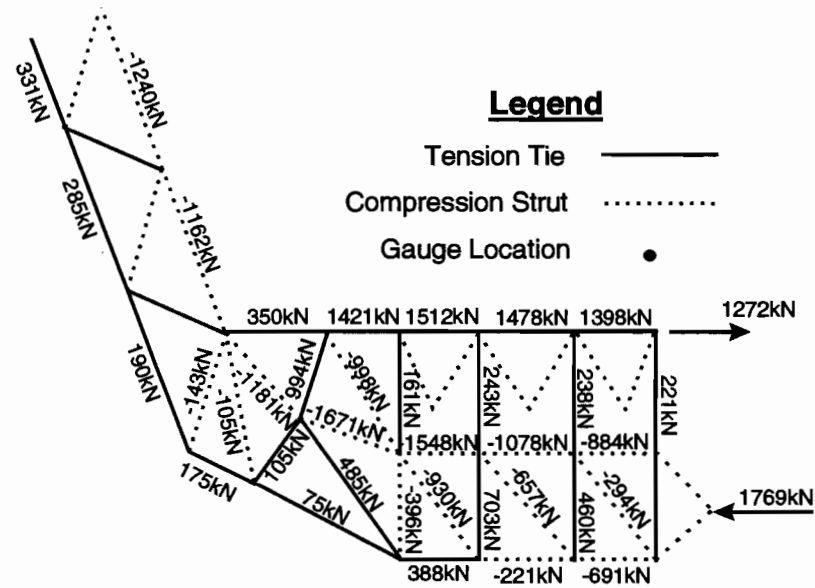
Development of a transverse strut-and-tie model for service or ultimate strand forces for the Ramp P deviator used the same method as in the mainlane deviator. The service-load forces on the tendon ducts within the deviator are given in Figure 6.32. A strut-and-tie model for the deviator is shown in Figure 6.34. The model assumes that significant cracking between deviator pipes would occur at ultimate load. Therefore vertical forces from the tendons are assumed to be transferred to the concrete below the ducts and then carried in shear to the web. The location of the tension ties was chosen to directly allow selection of reinforcement for the region of the tie. The service level live-load forces on the deviator had little influence on the reinforcement in the deviator. The strain changes on the bars in the deviator for the maximum positive live-load moment in span P16, given in Table 6.9, were less than 1% of ϵ_r , showing negligible live-load changes.

For the ultimate-load case, tendon force changes and deviation angle changes might result in 35% or larger vertical force changes on the deviator and substantial horizontal force changes on the deviator when compared to the service-load case. Assumptions made about the slippage or lack of slippage of the tendons within the deviator will have an influence on the horizontal force changes. The service level performance of the P16-10 deviator was far superior to that of the mainlane deviator, with no extensive cracking seen or anticipated based on the measurements. Measured strains were only marginally higher than the strains necessary to crack the concrete at a few locations. The distribution of force from the tendons to the deviator was not uniform along the length of the ducts.

An approximate calculation of tie forces based on the measured strains gave the forces shown in the top section of Figure 6.34. The STM assumed that a horizontal cracked plane existed between deviator pipes, as might be the case at ultimate load. Judging by the measured strains, this cracking was not the case at the service-load level except near the T3 deviator pipe. The calculated tie force based on the measured strains from gauges S710 and S711 was 343kN. The STM predicted 238kN at this location. The estimated tie force at S704 and S705 based on the measured strains was also higher than the force predicted by the STM at 254kN versus 161kN. The estimated tie force, based on the measured strains at S707, S708 and S709, was lower than predicted by the STM at 152kN versus 243kN. As was the case for the mainlane deviator, the forces in these ties in the top portion of the deviator were probably different from the STM prediction because the actual flow of forces in the deviator differed somewhat from the STM. The forces would differ because of cracking at some location and not others, and also because of the crude method used to calculate forces from the measured strains. Vertical ties designed by using the STM tie forces from the lower half of the deviator would be conservative for a fully cracked deviator at ultimate-load levels. This deviator must also be designed for longitudinal forces from the tendons at ultimate load.



HALF SECTION THROUGH CENTERLINE OF DEVIATOR



CALCULATED MAJOR STRUT AND TIE FORCES

Figure 6.34 Strut-and-tie model for the segment P16-10 deviator

Table 6.9 Measured strain changes in segment P16-10 gauges from live-load case 2

Gauge	Microstrain, + Tension
S701	-2
S702	-2
S703	-2
S704	0
S705	0
S707	0
S708	0
S709	0
S710	-2
S711	-2
S713	0
S714	0
S716	-2
S722	13
S723	17
S724	15
C749	8
C750	15
C751	0
C752	0
C753	-2
C754	-4
C755	8

6.3.7 Ramp Anchorage Blister Segment

The anchorage blister in segment P16-4 was instrumented with both strain gauges installed directly on the mild reinforcing bars and with concrete strain gauges. The location of these gauges and details of the blister are given in Figure 6.35. Tendon T22, anchored in the blister, was a bottom slab continuity tendon located within the length of span P16, passing through the cast-in-place closure near the center of the span. Two 9 - 15mm diameter strand tendons T22 were anchored in blisters in segment P16-4, one located on each side of the girder. The measurements presented in this section were taken only during the stressing of tendon T22 left. The main reinforcement in the blister consisted of 16mm closed bars, located around the tendon duct and extending into the bottom flange of the girder, and 90° bend 16mm bars anchored in the web and bottom flange of the girder. This reinforcing, shown in Figure 6.35, was distributed over the full length of the blister, but only the bars near the anchor plate were instrumented. Additional confinement reinforcing was placed within the larger 16mm closed bars shown in Figure 6.35. Longitudinal 13mm bars located in the bottom flange and web were instrumented with gauges S618 to S622. Concrete strain gauges C649 to C655 were placed in the bottom flange and web, but were oriented both longitudinally and transversely. Tendon T22 was only deviated in the vertical plane within segment P16-4, so the tendon applied a distributed vertical force on the top of its duct as well as a compressive force of 1800kN on the anchor plate.

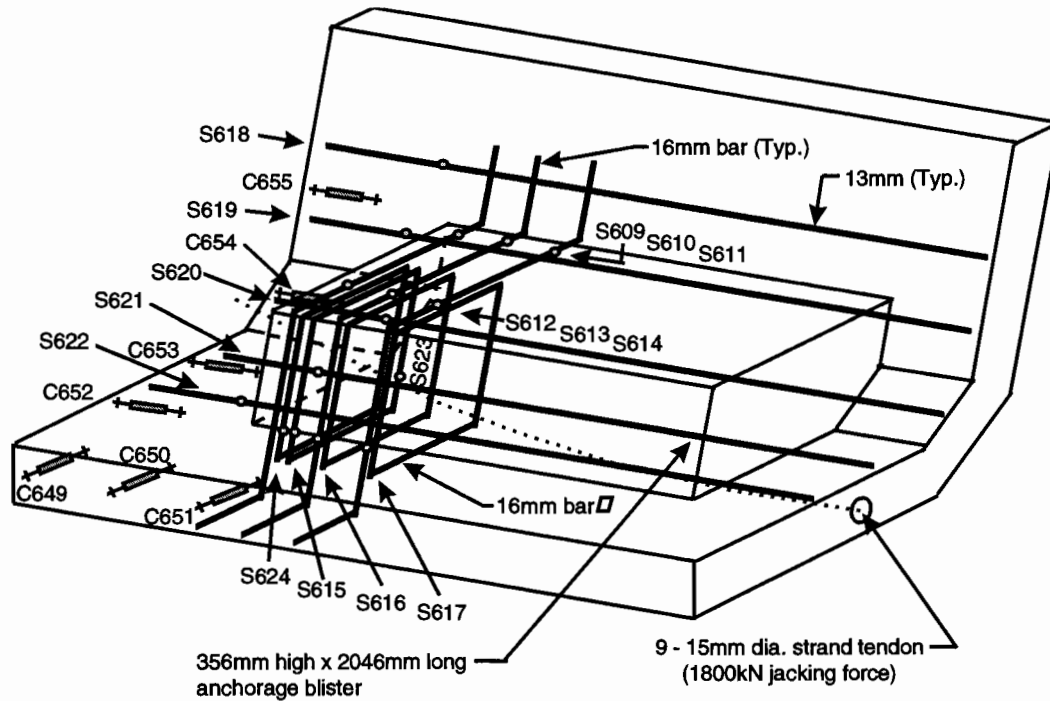


Figure 6.35 Ramp P girder segment P16-4 anchorage blister details

During the cantilever erection process this segment experienced substantial negative moment so that the lower flange had high compressive stresses. Measured strains in the blister from the stressing of tendon T2 left are given in Table 6.10. No cracks were seen on the blister, and all values of measured strain were well below the cracking strain for the concrete of $170\mu\epsilon$. Thus, the concrete can be assumed uncracked so that the measured strains in the reinforcing bars can be assumed to exist in the concrete surrounding the bars. This uncracked state greatly increased the area of material available to take tensile stresses over that of a cracked blister and reduced the magnitude of the measurements from those for cracked concrete. Based on the maximum measured tensile strain of $40\mu\epsilon$ in the blister, D/D_0 at first cracking would be large at about 4.3. In plan view, the blister can be visualized as a corbel extending from the girder web. The measurements from gauges S609, S610 and S611 substantiate the corbel action, with strain changes of $11\mu\epsilon$, $-2\mu\epsilon$ and $-4\mu\epsilon$ respectively. The tensile strain at gauge S609 quickly changes to a compressive strain at gauges S610 and S611. The distance between gauges S609 and S611 was only 400mm, and the distance from S609 to the edge of the blister was 75mm.

Viewing the blister in elevation, corbel action may also be anticipated, but the measurements by gauges S624, S615, S616 and S617 did not indicate corbel-type behavior. The measured strain changes at gauges S624 and S615 averaged $-37\mu\epsilon$, the strain at S616 was $-30\mu\epsilon$, and at S617 was $-6\mu\epsilon$. These measurements indicated a trend of compression changing to tension along the length of the blister from the applied loads. In elevation, the tendon anchorage applied force to the blister at an angle of 14° with respect to the horizontal. The horizontal component of the anchorage force was, therefore, 1750kN, and the vertical component was 435kN downward. Also, the deviation of the tendon within the blister along the 6m radius duct provided an upward distributed force totaling 427kN and a horizontal frictional force totaling 107kN.

Table 6.10 Measured strain changes in segment P16-4 anchorage blister gauges from post-tensioning of tendon T22

Gauge	Microstrain, + Tension
S609	11
S610	-2
S611	-4
S612	40
S614	25
S615	-44
S616	-30
S617	-6
S618	8
S619	21
S620	38
S621	38
S622	40
S623	0
S624	-30
C649	-4
C650	-2
C651	-6
C652	34
C653	38
C655	13

Gauges S612 and S614, located above the anchorage plate, measured strain changes of $40\mu\epsilon$ and $25\mu\epsilon$ respectively, indicating that transverse tension was present in the immediate vicinity of the concentrated load from the anchor plate. This tension should be considered a local zone force from the anchorage. Gauge S623, located on a closed 16mm bar near the face of the blister and the bottom flange to web fillet, indicated no strain change. Gauges S618 to S622 measured tensile strains behind the blister in the bottom flange and web.

Wollman [54] recommended that 25% of the unfactored stressing force on an intermediate anchorage be tied back by mild reinforcing steel stressed no greater than 60% of its yield strength. Gauges S620 to S622 were located most directly behind the anchorage and measured nearly equal strain changes at $39\mu\epsilon$. This tensile strain was insufficient to crack the concrete and produced negligible tensile stress changes in the longitudinal bottom flange mild reinforcement. This tension decreased quickly further up the web, with gauge S619 measuring a strain of $21\mu\epsilon$, and gauge S618 measuring a strain of only $8\mu\epsilon$. The concrete strain gauges C652, C653 and C655 measured nearly the same strain changes as the S-gauges located behind the blister at $34\mu\epsilon$, $38\mu\epsilon$ and $13\mu\epsilon$ respectively. The longitudinal tensile stresses behind the anchorage would be balanced by compression stresses at other points in the cross section. Transversely oriented concrete strain gauges C649, C650 and C651 indicated a small amount of compressive strain, averaging $-4\mu\epsilon$. A strut-and-tie model for the anchorage blister must include ties to deviate the compression force from the anchor plate and curved duct to the bottom slab and web, as well as to control splitting forces from the concentrated load within the blister. Tensile forces behind the blister will also result in diffusion of some of the compressive force from the tendon. Calculation of general zone stresses in front of and behind the blister from the stressing of the tendon anchored in the blister will help define the flow of compressive forces.

The response of the girder from force changes in tendon T22 is different for the service-load case and the ultimate-load case. For the service-load case, the tensioning of partial span length tendon T22 produces compression and negative bending in the central portion of span P16. The side spans P15 and P17 and the

portion of the girder over the piers are put in positive bending from the secondary or boundary condition effects of stressing T22. This bending changes the moment diagram from that of simple post-tensioned cantilevers to that more closely resembling a post-tensioned continuous girder. The shear diagram changes little in span P16 from the stressing of T22. Therefore, the diffusion of the compression force in front of the T22 anchorage and the tension force immediately behind the blister are affected only by forces in the local zone. The compression in the bottom flange continues to be large on average at the blister location after T22 is stressed, but decreases when the external tendons are stressed. Tension may exist in the concrete behind a blister at the service-load level, so it is not advisable to locate the anchorage end of a blister on the same transverse plane as a segment joint. A strut-and-tie model for the anchorage blister is shown in Figure 6.36 at the service-load level.

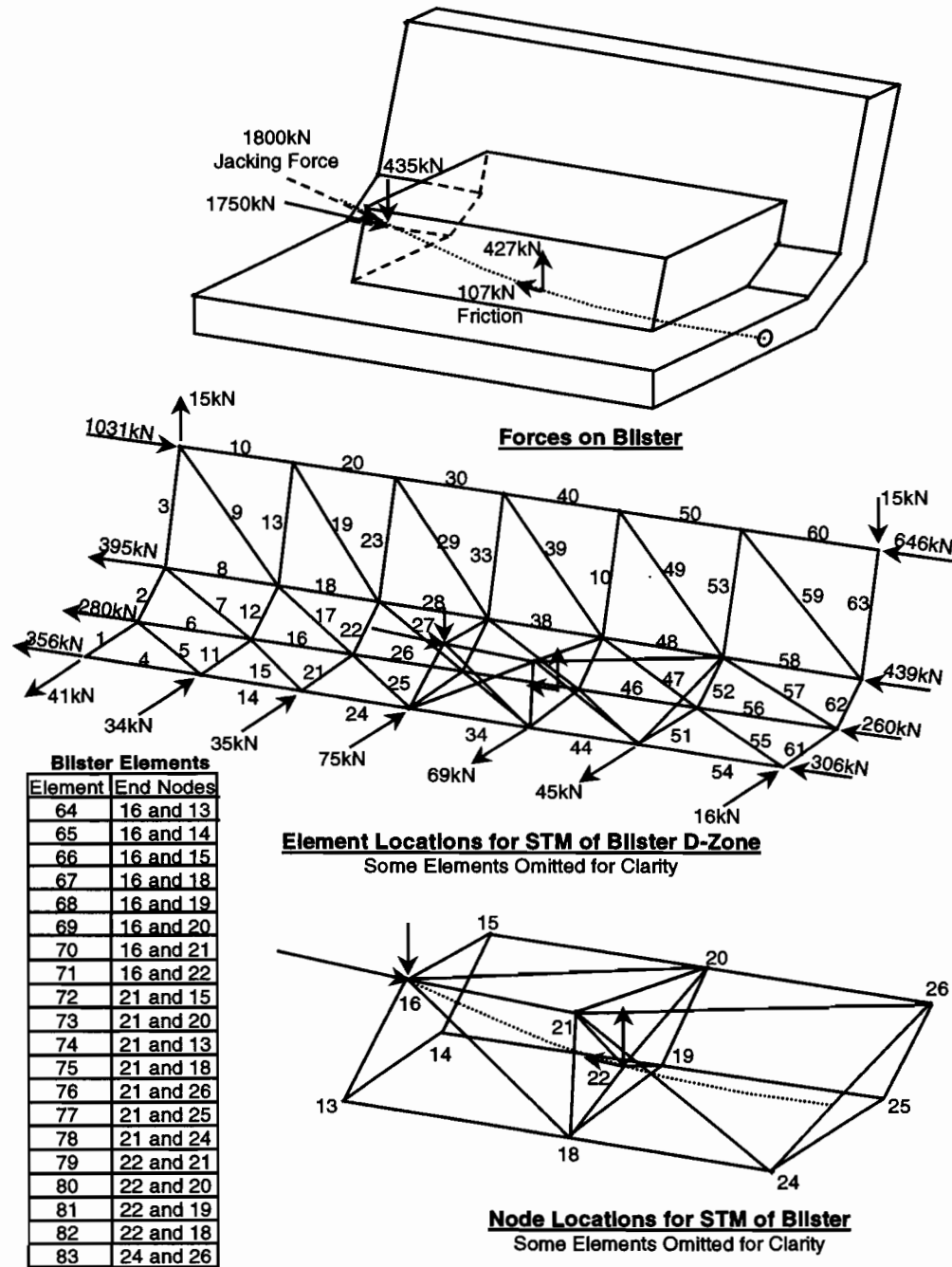


Figure 6.36 Strut-and-Tie model for segment P16-4 anchorage blister for service-load forces from Tendon T22

The STM was subjected only to the force from the tendon anchored in the blister and the resultant reactions. Cantilevering dead-load and prestressing stresses were present, but not included in the model. The cantilevering stresses were easily calculated within the D-zone near the blister and should be added to the stresses found from the STM. The STM in Figure 6.36 was designed to predict tensile forces in the blister at points away from the local zone, as well as to predict the tension in the bottom flange behind the anchorage. Boundary conditions were carefully applied so that the bottom flange and web could be modeled as plates, since the flow of axial forces was of primary interest. The limits for the D-zone were chosen using the 30° diffusion method. Full diffusion was assumed to occur when the full-height of the girder web was included in the 60° diffusion cone. Moments, axial forces and shears were calculated at the limits of the D-zone and resolved into and applied as concentrated forces on the STM. Positive bending of the girder created tension in the bottom slab between the pier and the blister.

Using an analysis based upon the assumption that plane sections before loading remain plane after loading and including no local effects from the anchorage, a tensile stress of 1.83MPa was calculated to exist at gauge location S622. Using the measured strain at S622 of 40 $\mu\epsilon$, the actual stress was calculated to be about 1.60MPa in tension, or within 12% of that predicted by the simple analysis. Tie forces in members 24, 26 and 28 calculated using the STM were 396kN, 198kN and 144kN, as shown in Table 6.11. This predicted the trend measured by gauges S622, S621, S620 and S619, with decreasing strains of 40 $\mu\epsilon$, 38 $\mu\epsilon$, 21 $\mu\epsilon$ and 8 $\mu\epsilon$. The stress at gauge S622 predicted using the STM would be about 1.92MPa, which is 20% larger than the measured strain converted to stress of 1.60MPa.

Comparison of the measured and calculated tension behind the anchor plate indicated that the bottom flange longitudinal stress distribution was not substantially influenced by the presence of the point load. The recommended 25% of the point load, at 99kN, would not need to have been added to the bottom flange force calculated using the plane sections analysis in order to get sufficiently accurate bottom flange stresses. The positive bending moment, caused by continuity of the span, essentially produced the proper tensile stress distribution behind the blister.

Table 6.11 Element forces from P16-4 blister STM

Tension (+)					
Element	Force in kN	Element	Force in kN	Element	Force in kN
1	42	29	-44	57	-19
2	98	30	-783	58	-431
3	107	31	52	59	-10
4	356	32	77	60	-646
5	18	33	140	61	1
6	264	34	304	62	11
7	-3	35	91	63	18
8	397	36	125	64	-287
9	-182	37	38	65	-78
10	-898	38	32	66	-26
11	-42	39	-190	67	-535
12	-62	40	-653	68	-542
13	79	41	-109	69	-332
14	372	42	-46	70	-391
15	26	43	-1	71	-108
16	238	44	-105	72	65
17	35	45	-82	73	152
18	236	46	-282	74	177
19	-115	47	71	75	158
20	-814	48	-420	76	-36
21	-46	49	1	77	-70
22	-51	50	-654	78	-94
23	30	51	58	79	-66
24	396	52	-9	80	-81
25	75	53	6	81	290
26	198	54	-262	82	287
27	10	55	-47	83	45
28	144	56	-244		

Blister member 64 was in compression, at 287kN, confirming the measured compressive strain at gauges S615 and S624 that averaged $37\mu\epsilon$ compression. Reactions at nodes 9 and 13 indicated slight compression, averaging about 0.15MPa or $4\mu\epsilon$ compression. This value compared well to measured strains at gauges C649, C650 and C651 that averaged $4\mu\epsilon$ compression. Slight compression was calculated using the STM in member 66, which indicated that significant corbel action was not occurring. The small measured strains at gauges S609, S610 and S611 would tend to verify this calculation. Significant tension ties within the blister were the members that tied node 21 to the bottom flange and web, namely members 72, 73, 74 and 75. The greatest tensile forces were associated with the upward thrust of the tendon on the curved section of duct inside the blister. Since all this thrust was concentrated at node 22 in the STM, all the tension force was taken by members 81 and 82. Steel designed to take this tensile force would need to be distributed along the length of the duct curvature, as was done in the actual design of this blister.

Forces within the blister changed little with the application of live loads since the blister was located near the point of inflection. At the ultimate-load level, large shear force changes in span P16 and plastic behavior of the girder will deviate the compressive force in front of the T22 anchorage, as well as development forces from the tendon, to the top flange of the girder as shown in the strut-and-tie model in Figure 6.37. Forces in the blister change because of longitudinal stress changes in the bottom flange and webs although transverse and vertical forces within the blister itself change little, since the ultimate force in the tendon within the blister can only be moderately larger than the force after jacking. Since the service-load level performance of the T22 blister was excellent, the ultimate-load level performance can also be expected to be good, since the forces within the blister will change little.

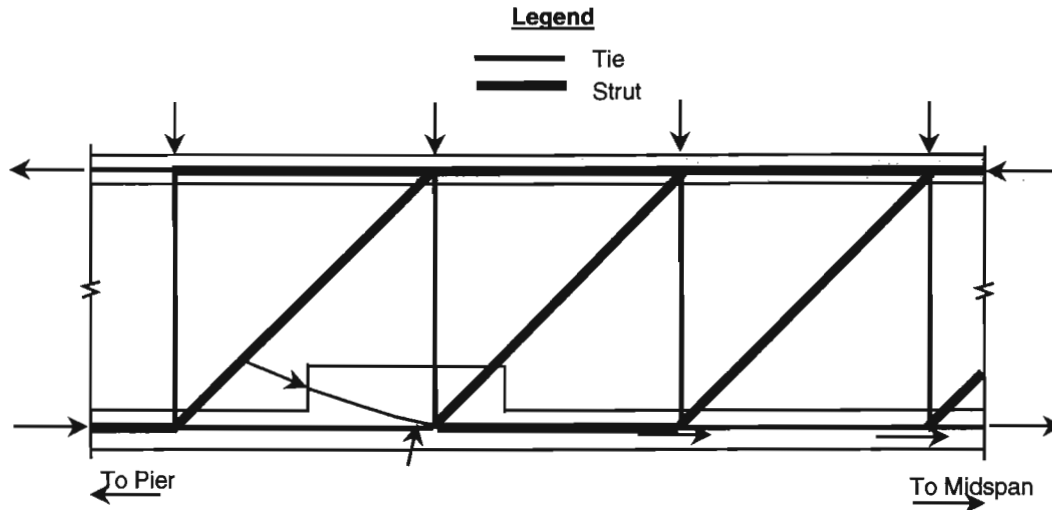


Figure 6.37 Struts and ties near anchorage blister at ultimate

6.4 RECOMMENDATIONS AND CONCLUSIONS

The service level performance of the D-zones under study ranged from inadequate when unanticipated details like sharply bent deviator pipes were used, to excellent when designs were very conservative. The following recommendations and conclusions were drawn from observations of the measured data, visual inspections, and review of the designs and details.

6.4.1 Pier Capitals

The mainlane Y-pier was designed as a concrete-steel composite structure. The force in the transverse steel pipe ties was reasonably predicted using either a frame analysis, at 31% of the vertical applied vertical force, or a simple strut-and-tie model, at 36% of the applied vertical force. As would be expected the STM was more conservative compared to the measured pipe force of 34% of the applied vertical force. The anchorage of the pipe ties in the concrete was excellent, with a fully bonded condition existing at the time of testing under full superstructure dead load. The stiffness of the pipe ties limited the bending moment in the concrete Y compression struts such that no cracking occurred at the service-load level. Given the low stress levels in the pipes and in the concrete, the pier should behave very well with an ultimate load placed on the superstructure.

The pier P16 capital segment also essentially remained uncracked from service-load level forces although the capital was initially cracked from thermal gradient forces during curing. These cracks had little impact on the service level performance of the capital, based on visual inspection. Most measured tensile strain changes were small during the monitored live-load test cases, at less than 5% of the yield strain for the instrumented reinforcement. Heavy bars placed longitudinally and transversely at the top and bottom of the pier capital carried tensile force as expected in most cases, but measured strain changes in the circumferential gauged bars at the bottom of the pier were equal to or larger than the magnitude of the strain changes in the designed heavy tie bars. At the ultimate-load condition, a strut-and-tie model for this solid section should include circumferential ties at the bottom to maintain similar geometry to the voided section below.

6.4.2 Deviators

The instrumented mainlane and ramp deviators were beam-type deviators similar in dimension and reinforcement, with the exception of the width. The vertical tendon loads on the ramp deviator were only about 85% of those on the mainlane deviator. The deviation force on the tendon ducts did not appear to be well distributed along the length of the ducts in the ramp deviator. Bar strains near the center and end of the deviator pipes varied by as much as 200%. However, no large cracks developed and no exceptionally large strains were measured in the bars. The ramp deviator had good service level performance with small crack widths and maximum reinforcement tensile strains of only 10% the yield strain. The mainlane deviator ducts did not

follow the design drawing and were sharply bent, concentrating the entire deviation force near the center of the deviator. This concentration of force caused extensive open cracks, and high stresses (50% of f_y) in the reinforcing bars adjacent to the sharp bend in the duct.

Deviation ducts should be smoothly radiused over the full length of the deviator to improve service level performance. A sharp bend may also increase friction between tendon, grout and duct, increasing horizontal loads on the deviator at ultimate. The reinforcement details for both deviators were easily constructed at points away from the girder webs. Near the web to deviator intersection, the heavy web stirrup bars and other bars transitioning the web to the bottom flange remained unchanged from that for a typical section. This left little room for the deviator top bars or shear reinforcement.

Priority should be given to the placement and development of the bars connecting the deviator to the webs, since this is the critical force path for developing the ultimate moment capacity of the girder. Figure 6.38 is a photograph of the actual reinforcement connecting the deviator to the web of the Ramp P girder. This picture demonstrates that the heavy concentration of web to bottom slab fillet typical reinforcement, as well as the main web reinforcement, makes it difficult to include properly located and anchored inclined reinforcement. The excellent performance ($\epsilon_{smax} < 10\% \epsilon_y$) dictates that some reinforcement might be removed. Prime candidates for removal would be those bars placed parallel to the compression field. Further model tests could confirm the result of reducing such reinforcement.

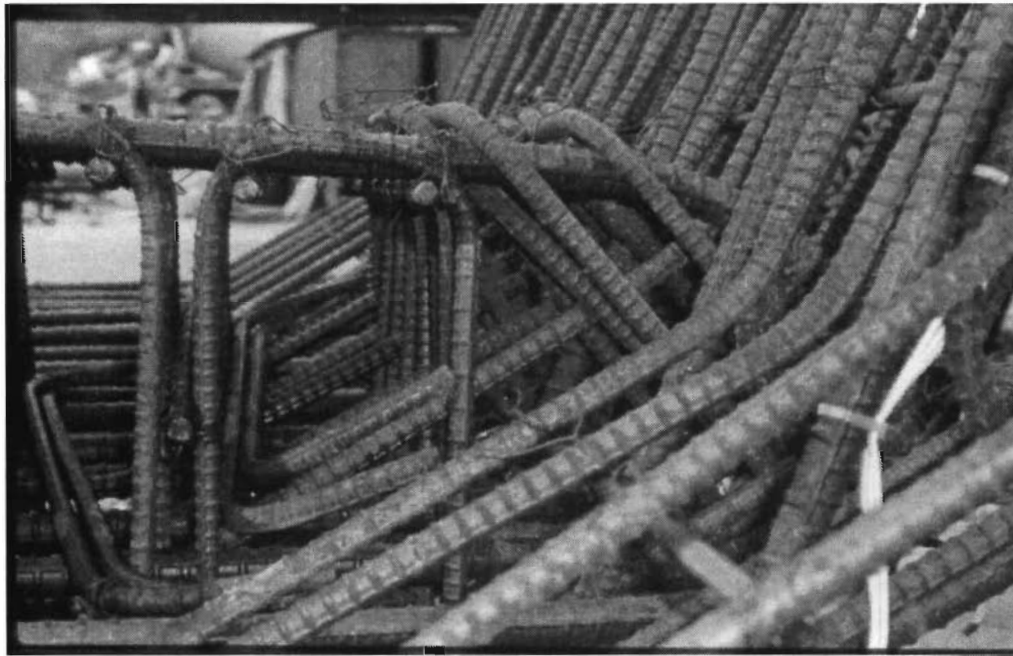


Figure 6.38 Ramp P girder segment P16-10 deviator to web detail

6.4.3 Pier Segments

The mainline pier segment, with heavy anchorage diaphragm, was not post-tensioned vertically to control tensile stresses from the diffusion of post-tensioning forces. Regardless of this, the mainline pier segment performed well at service-load levels. The highest measured reinforcing bar stress was 35% of the yield stress and occurred in the heavy vertical bar immediately adjacent to the access passage through the diaphragm at a crack location. The heavy end diaphragm was designed to take all the transverse and vertical tensile stresses from the anchorage zone at the ultimate-load condition. The transverse stiffness of the anchorage diaphragm was insufficient to attract all the transverse tension in the bottom flange of the girder at the service level-load condition, since the post-tensioning forces were poorly diffused over the short length of the anchor segment.

The bottom flange cracked longitudinally directly beneath the bottom flange internal tendon ducts. The designed D-zone should have included a length of typical section beyond the anchorage diaphragm, since the bottom flange was highly stressed over this length by the bottom flange internal post-tensioning tendons. The

area of transverse bottom flange steel could then have been calculated and included in the design to control cracking. The pier segment instrumented on Ramp P was post-tensioned vertically to make a moment connection with the pier. As a result, little cracking occurred in the heavy anchorage diaphragm and strain measurements were small.

6.4.4 Anchorage Blister

The instrumented anchorage blister was uncracked following post-tensioning and thereafter. A small amount of induced tension was measured behind the anchorage, but since the bottom flange of the girder was in significant compression from cantilevering dead load, no cracks were found. Very small tension was also measured in the bars that connected the blister to the web, indicating some corbel action. No corbel action was indicated between the blister and the bottom slab. Instead, compression was measured in the vertical bars adjacent to the anchor plate where the blister joined the bottom slab. Tension was measured in the vertical bars further along the blister because of the vertical force generated by the radial deviation of the tendon over the length of the blister. The design of this blister was very conservative. Tension forces behind the blister were predicted conservatively using a STM.

CHAPTER 7

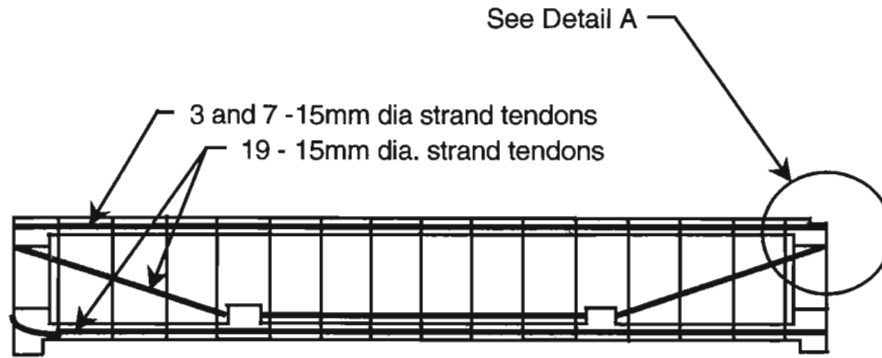
BEHAVIOR OF A SEMICONTINUOUS UNIT

7.1 INTRODUCTION

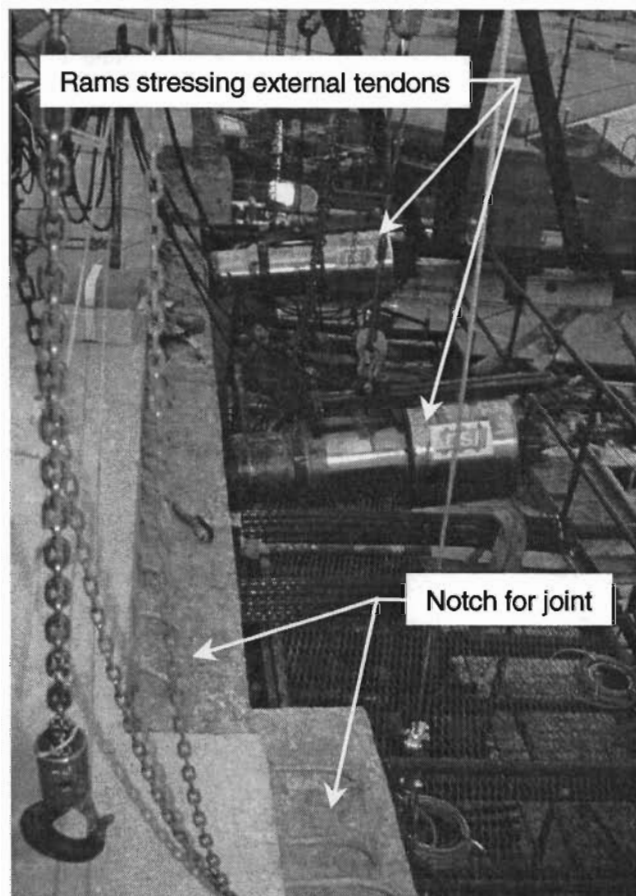
The mainlane and ramp girders on US 183 constructed by the span-by-span method were designed as three-span semicontinuous units. The box girders were constructed as isolated simple spans and then lowered off the erection trusses onto four independent elastomeric bearings. At a later stage in construction, the individual simple spans were linked into semicontinuous units by cast-in-place deck slab closures. Construction in simple spans allowed the erection sequence to advance more quickly than for continuous girders with multiple span tendons and possible closure pours. TxDOT engineers decided to design the structure in simple spans based on the construction experiences on the San Antonio Y.

The San Antonio Y had multiple span fully continuous units requiring complex tendon layouts, involved stressing sequences, and difficult to build pier segments with deviated ducts and varying anchorage locations. Even though the final girder configuration was continuous, the maximum moments in the girder were the positive moments from self weight during construction, either as a simple span for the first unit erected after an expansion joint, or as a span with one end continuous with the preceding span for subsequent units erected. Economy dictates that span-by-span erected segmental bridges be constructed using a single-span erection truss. Thus, a continuous structure erected span by span does not have the moment diagram for dead load of a continuous girder constructed and tensioned entirely on falsework.

In addition, continuous spans must be designed for thermal-gradient-induced moments over interior piers that often are opposite in sign to the live-load moments. Post-tensioning provided to prevent tension from thermal gradients would act opposite to that provided for live load. This fact results in a substantial amount of prestressing in continuous girders across the pier, with little eccentricity to the centroid of the girder cross section. In order to avoid such contradictory conditions, the US 183 girders, except for the five-span continuous girder built by the balanced cantilever method on Ramp P, were all designed and constructed as simple spans. The external tendon profiles had no curvatures at the anchor segments (Figure 7.1), and the internal tendons only had substantial curvature near the dead-end anchorage.



Elevation - Girder D5

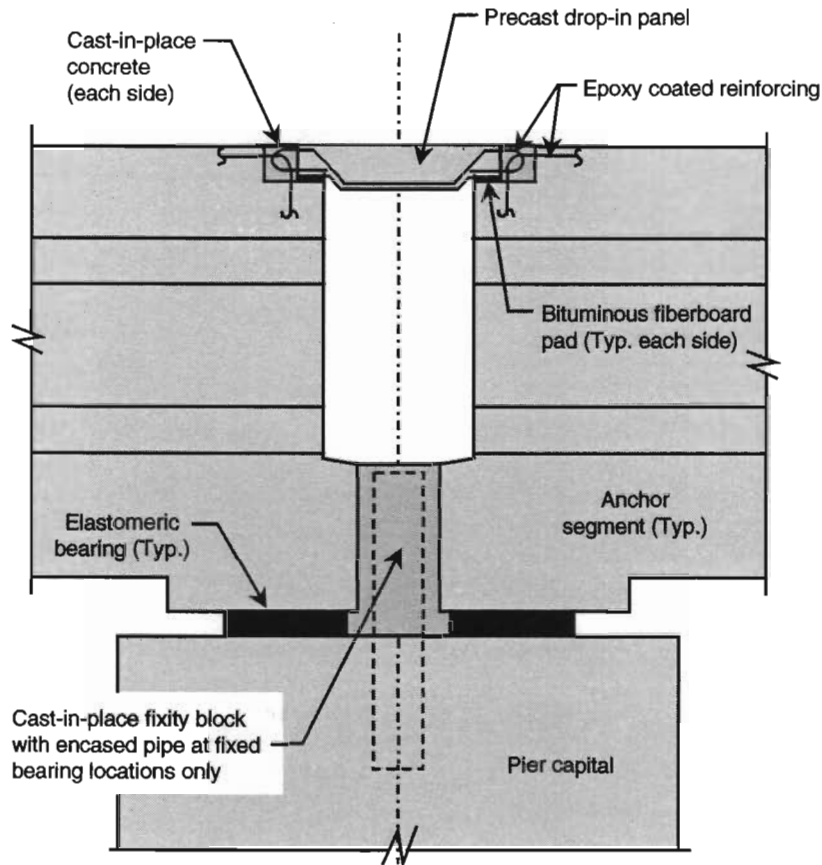


Detail A

Figure 7.1 Post-tensioning tendons on the mainlane girder

Since providing an expansion joint at every pier would have proven to be costly, would have increased maintenance, and potentially would have given a poor ride quality, most spans were connected longitudinally at the deck into three-span units. Longitudinal expansions and contractions from temperature changes required that deck finger joints be provided at least at every third span since the girders were supported on elastomeric bearings. TxDOT has been designing deck slabs to be cast continuously over simple-span I-girders for many years. The durability and ride quality of these slabs has proven to be excellent when properly detailed. Since

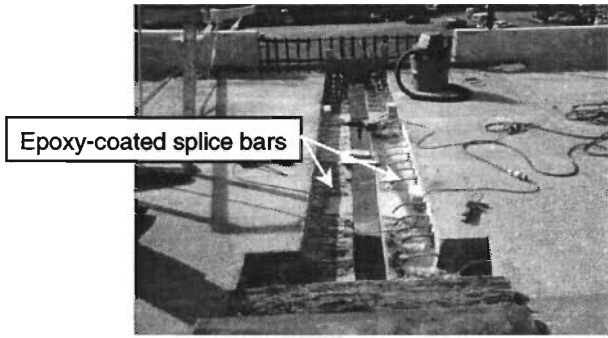
the deck of the box girder was precast monolithic with the girder webs and bottom flange, the closure at the deck between the ends of each simple span was cast-in-place on US 183. The original details in the contract plans provided for a concrete drop-in panel that would later be connected to the box girders with a closure pour (Figure 7.2).



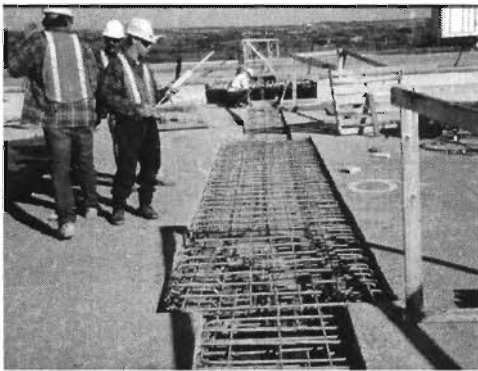
Longitudinal Section

Figure 7.2 Original joint details from contract plans for U. S. 183

The contractor decided to provide temporary construction access along the length of the bridge deck by spanning the gaps between spans with heavy timbers covered by steel plates instead of using the concrete drop-in panel. The joints were then fully cast-in-place three at a time well after construction of the main spans. The construction sequence of the joints is shown in Figure 7.3. All reinforcing was epoxy coated, including the 90° splice bars in the anchor segment.



a). Notch provided for deck joint



b). Epoxy-coated reinforcing steel in place



c). Deck joint concreting

Figure 7.3 Actual cast-in-place joint construction

The primary design case for the joint slab was to withstand wheel loads placed directly on the joint. A secondary design consideration was to maintain the bridge alignment, since guided bearings and fixity blocks were provided at the minimum required number of locations. One guided bearing was provided at each pier, and one fixity block was provided for each bridge unit. Because of this secondary design consideration, the joint-to-anchor segment connection would have to be capable of carrying tension and compression caused by thermal strain changes in the girders. Deterioration of the deck-to-girder connection would be detrimental to the performance of the bridge unit and would require the replacement of the joint.

The ride quality of these cast-in-place deck joints, topped with 5mm of asphalt placed continuously over the entire unit, is exceptional. The only indication to the motorist that the joint exists occurs on those few spans where the camber from prestress and dead load differed from the design vertical alignment because of creep or casting geometry errors. Even the worst spans on the project have very good ride quality.

7.2 PROBLEM AND TECHNICAL BACKGROUND

Once the closures had been cast, the length of joint slab had the potential to carry tension, compression, and bending forces. The overlap of hooked reinforcement from the anchor segment and the joint slab could possibly carry moment caused by girder end rotations, although the girder end rotations from live load were extremely small. TxDOT design engineers were interested in the magnitude and effects of negative moment developed in the box girders, not the joint itself, over the piers from live loads. Potentially, a live-load-induced moment couple could develop between the joint slab in tension and the restraint from the bearings and pier capital as a compression force. TxDOT engineers did not intend or desire this moment couple as a performance characteristic. The closure slab was designed as a bending member for wheel loads and girder end rotations, seen in Figure 7.4, with two layers of reinforcement. The slab bars were spliced to 90° bars in the notch of the girder, providing a moment connection even if the closure concrete did not totally bond to the girder concrete. Some of the 90° bars in the anchor segment notch, shown in Detail A of Figure 7.1, were of insufficient length and were supplemented with additional straight bars drilled and epoxied into the anchor segment. TxDOT designers controlled the effective longitudinal length of the slab between girder wings with bituminous fiberboard pads, shown in the bottom section of Figure 7.4. The actual 150mm gap between the wings was effectively lengthened to 380mm by the bituminous pads. The angle change at the end of one box girder from positive girder bending, as well as differential wing tip deflection from live load, otherwise would have induced large bending moments in the closure slab with high shear forces because of the short slab span lengths. The fiberboard pads reduced the effective bending stiffness of the slab and therefore reduced the shear forces for a given angle change at the end of the box girder. An additional reduction in bending stiffness was caused by shrinkage cracks at the cold joint.

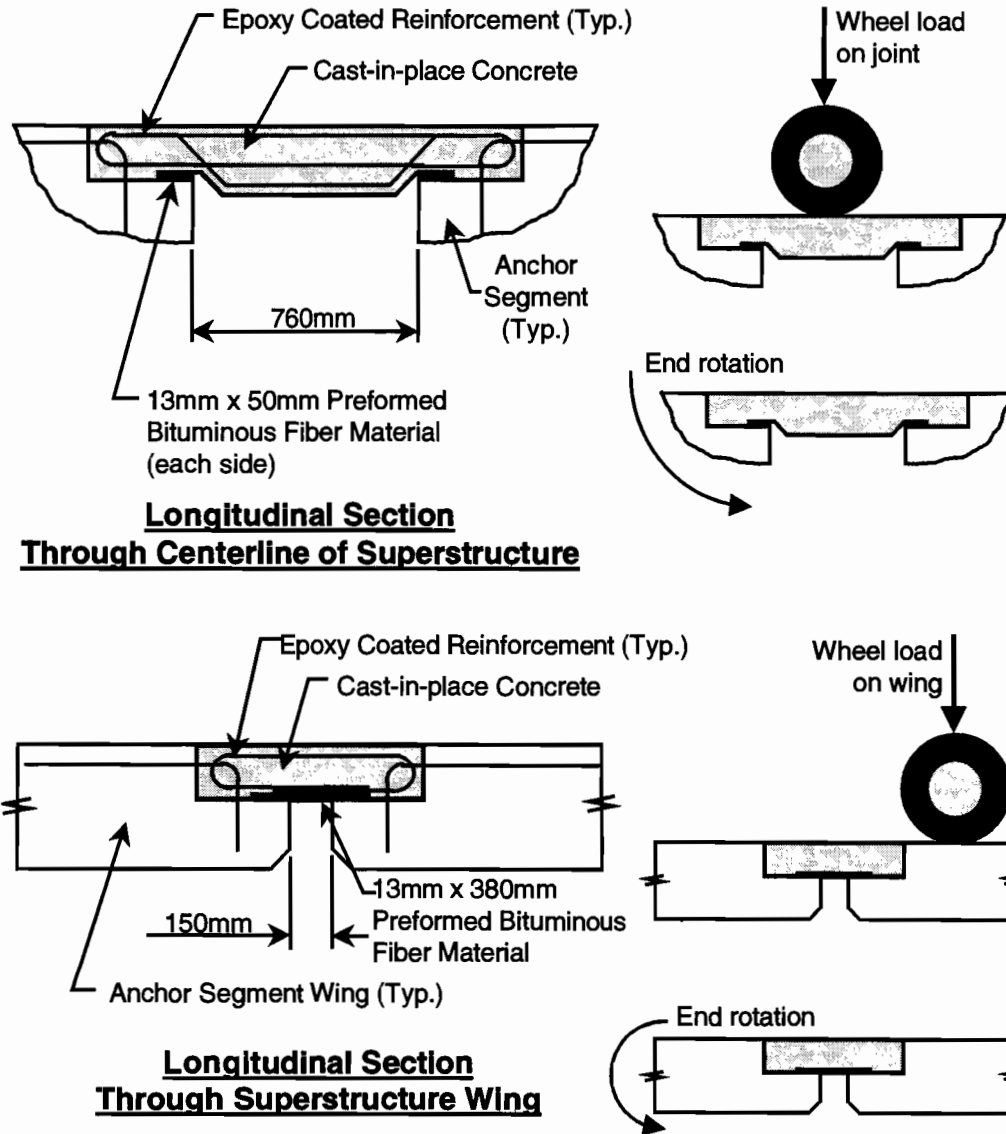


Figure 7.4 Longitudinal sections—cast-in-place joint

Another source of force in the slab comes from thermal loading, both from uniform temperature changes and from thermal gradients in the box girders. A uniform temperature change causes the length of the box girders to change, with the finger joints accommodating this deflection. The three-span semicontinuous unit has one longitudinally fixed set of elastomeric bearings, fixity being provided by a fixity block, at an interior pier and three other sets of longitudinal expansion elastomeric bearings at the remaining piers of the unit. Expansion of the central span had to be carried across one end span and two sets of elastomeric bearings. The shear force required to longitudinally deflect these bearings is taken by the closure slab and changes on both a daily basis and on a seasonal basis. To provide some residual compression in the slab concrete, the adjacent spans were jacked apart slightly using threadbars and held in place until the joint concrete had cured. Regardless of this procedure, shrinkage cracks formed at the cold joints. The overlap of the 180° joint bars and the 90° anchor segment bars, shown in Figure 7.4, must be strong enough to carry any tensile forces developed across the joint. An initial assessment of the strength of this detail, based on inspection of Figure 7.4, is that the longitudinal tensile capacity would be minimal.

Thermal gradients in the box girder also produce forces in the continuity slab. The thermal gradient causes a rotation at the girder end, producing resultant bending and axial forces in the slab. Also, since the box girders under study have some shear lag in the top flange in response to thermal gradients, the continuity slab acts to

stiffen the top flange and change the behavior of the box girders to some extent. Stress changes in the slab give an indication of the validity of assumptions made during the thermal gradient analysis of the girder, such as plane sections remaining plane.

7.3 PREVIOUS STUDIES

Extensive research was conducted and reported by Roberts, *et al.* [7] on a cast-in-place continuity joint similar to that in use on the US 183 segmental box girders. Details of the joint studied by Roberts, *et al.* [7] on the San Antonio Y are shown in Figure 7.5. One difference between the dimensions of this joint and the joints used on US 183 was the distance between anchor segments. The length of the slab between girder webs was 970mm (seen in the top section of Figure 7.5), compared to 760mm on US 183 (seen in the top section of Figure 7.4). The gap between wings of the San Antonio Y girders was only 50mm, effectively lengthened to 250mm by a bituminous pad, as seen in the bottom section of Figure 7.5. This length was somewhat shorter than the 380mm bituminous pad length on US 183 (see the bottom section of Figure 7.4). Another difference was that the reinforcement detail connecting the joint to the anchor segments was far more substantial on the San Antonio Y and would be expected to provide greater moment fixity and tensile capacity between anchor segment and joint slab than the detail used at U. S. 183.

The most important difference between the joint details of the San Antonio Y and US 183 was the type of bearing used on each project. The San Antonio Y girders were supported on 50mm thick fabric-reinforced pads with a Teflon sliding surface at expansion joints. In order for the bearing to allow longitudinal movement from girder expansion, contraction and end rotation, the friction between the Teflon pad and the steel plate attached to the fabric reinforced pad must be overcome. The bearings on US 183 were 70mm thick steel-shim-reinforced 50 durometer elastomeric pads at the locations of the continuity joints. Longitudinal movement of the girders was accommodated by horizontal shear deformation of the elastomeric pads.

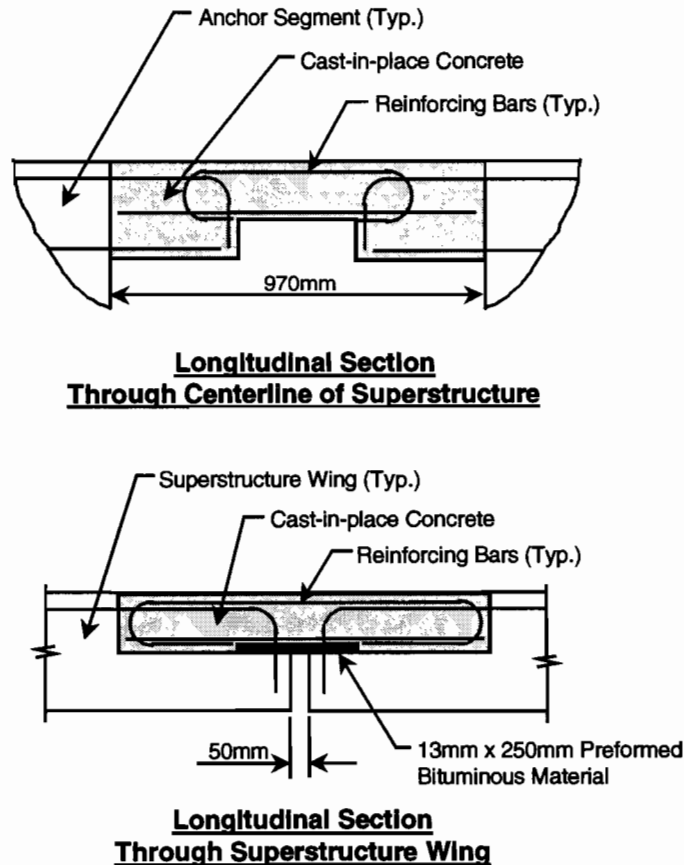


Figure 7.5 Joint details on the San Antonio Y

Figure 7.6 shows a typical live-load test result from Roberts, *et al.* [7]. Significant continuity was developed across the joint as evidenced by the deflection of the adjacent span. Roberts was able to accurately predict this deflection using a frame model that treated the bearings as bending and compression members. Figure 7.6 shows the large degree of continuity that was developed, even though the bearings at pier A44 were expansion bearings with a Teflon-stainless steel sliding surface. The rotational or bending stiffness of the 50mm fiber reinforced pads and friction between the Teflon and stainless steel plates contributed greatly to the negative moment capacity of the system. This moment continuity was not a desired performance characteristic. Roberts predicted that elastomeric pads, with their lower shear stiffness, would develop substantially less negative moment continuity across the joint.

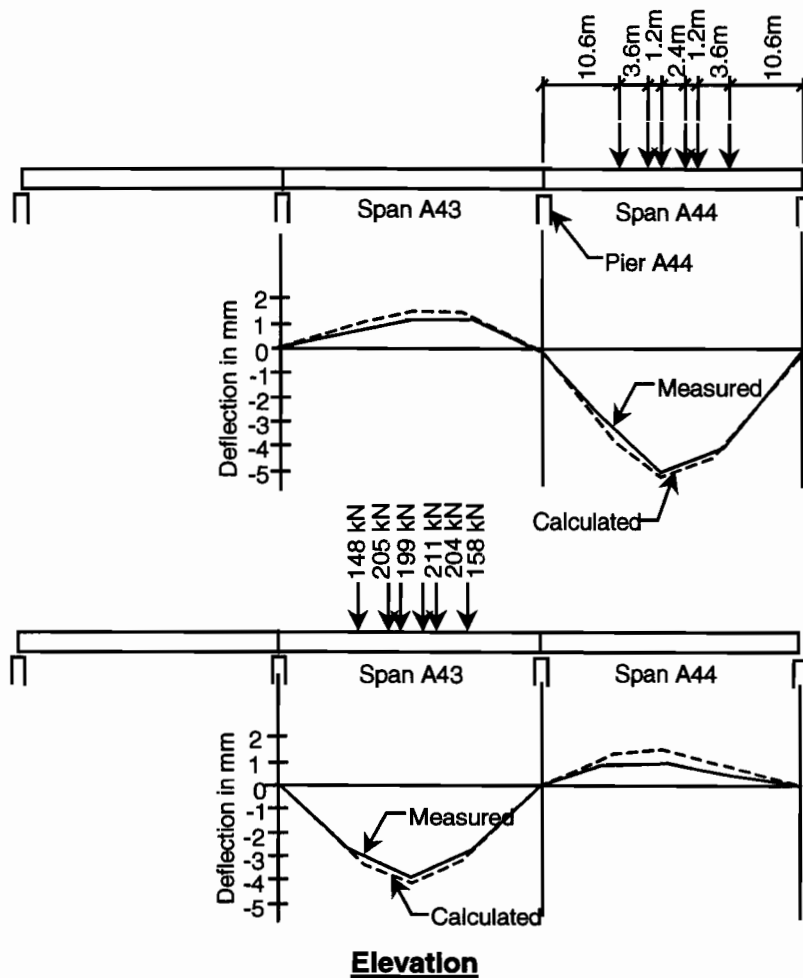
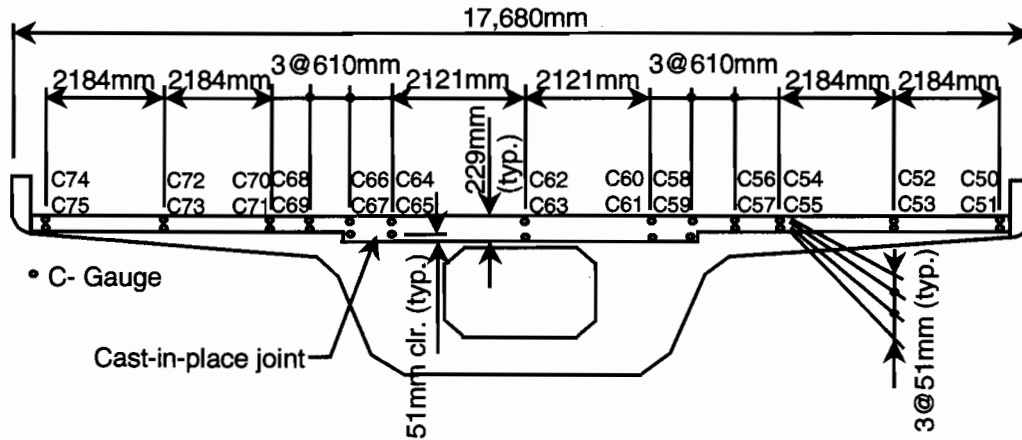


Figure 7.6 Deflections during live-load test, from Roberts, *et al.* [7]

7.4 DATA COLLECTION AND ANALYSIS

Strain gauges were cast within the cast-in-situ joint concrete between spans D5 and D6 of bridge unit D2 and located as shown in Figure 7.7. Gauges were placed in two layers to measure bending strains in the slab, as well as tension and compression strains. The transverse location of the strain gauges was identical to gauges located in the box girder anchor segment. The continuity slab on bridge unit D2 was the only slab to be instrumented with strain gauges.



**Section Through Anchor Segment
Near Centerline of Bearing**

Figure 7.7 Strain gauge locations in cast-in-place joint—Unit D2

7.4.1 Live-Load Tests

Live-load tests were conducted on three different bridge units that had the cast-in-place continuity slabs. Load cases were selected to maximize the negative moment carried by the joint-bearing couple, using the trucks available during the test. The trucks used in the test were actually designed to produce a positive moment, when placed back to back at midspan, similar to an HS20 design truckload.

The first live-load test of a joint was conducted on bridge unit D2. Strains in the joint and girder concrete were recorded electronically, and deflections were measured in all three spans of the unit. The second test of the continuity slab detail was conducted on Unit C13, a three-cell cast-in-place two-span unit, providing the transition in roadway width from the mainlane girder to both a ramp and mainlane girder. The third live-load test of the joint detail was conducted on two three-span girder units, C13 and L2, connected longitudinally at their wing tips by a gore closure.

Live-Load Test on Mainlane Unit D2

The live-load cases of interest and the span geometry for Unit D2 are shown in Figure 7.8. The truck weights are shown in Table 7.1.

Table 7.1 Axle weights and spacing for live-load test trucks on Unit D2

Truck	Weight of Rear Axles (kN)	Weight of Front Axles (kN)	Total Weight (kN)	Axle Spacing (mm)
1	122.5	43.1	165.6	5030
2	132.0	39.6	171.6	4850
3	119.6	44.4	164.0	4890
4	119.1	40.8	159.9	4090
5	135.1	39.0	174.1	4720
6	119.7	44.1	163.8	4360

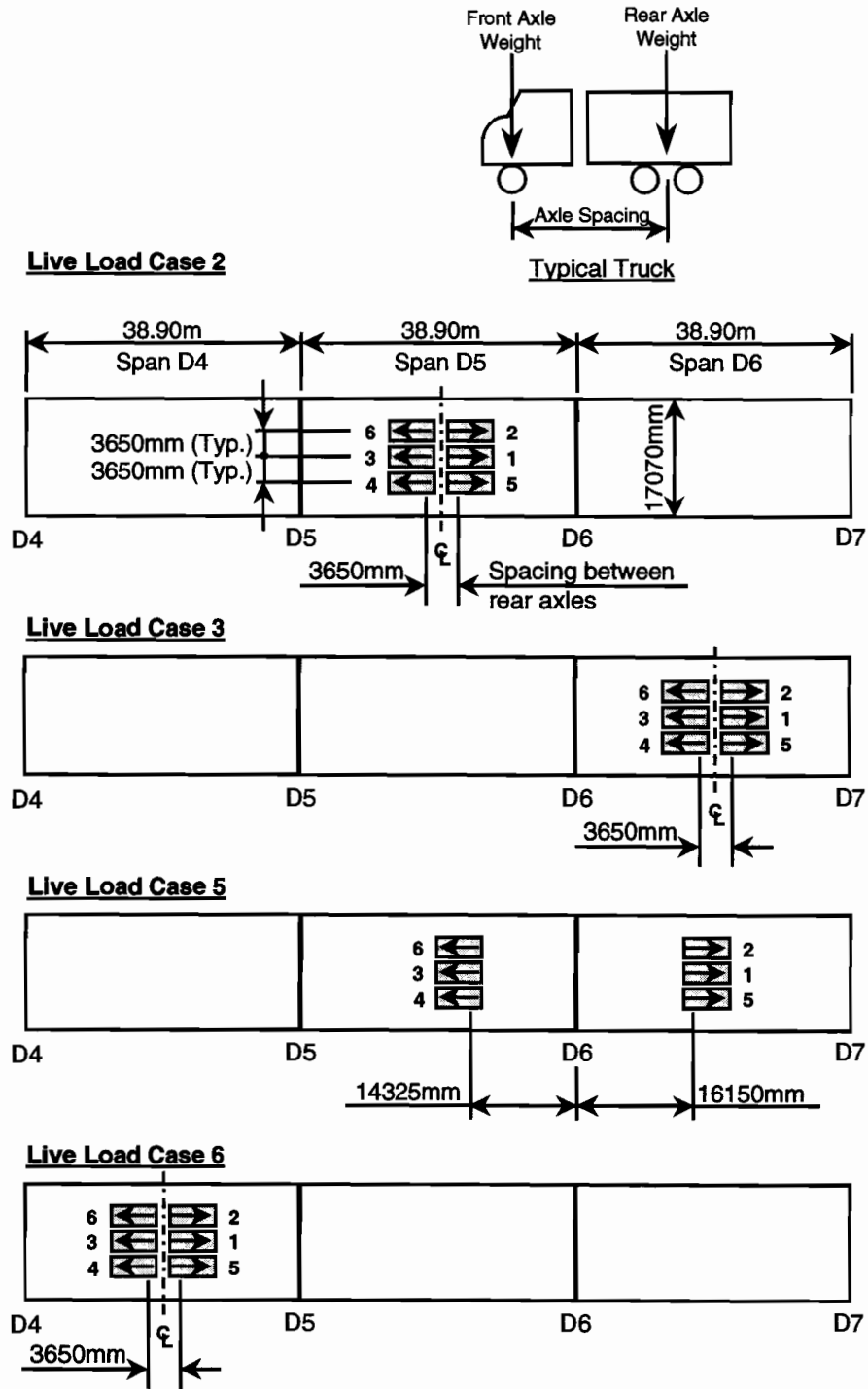
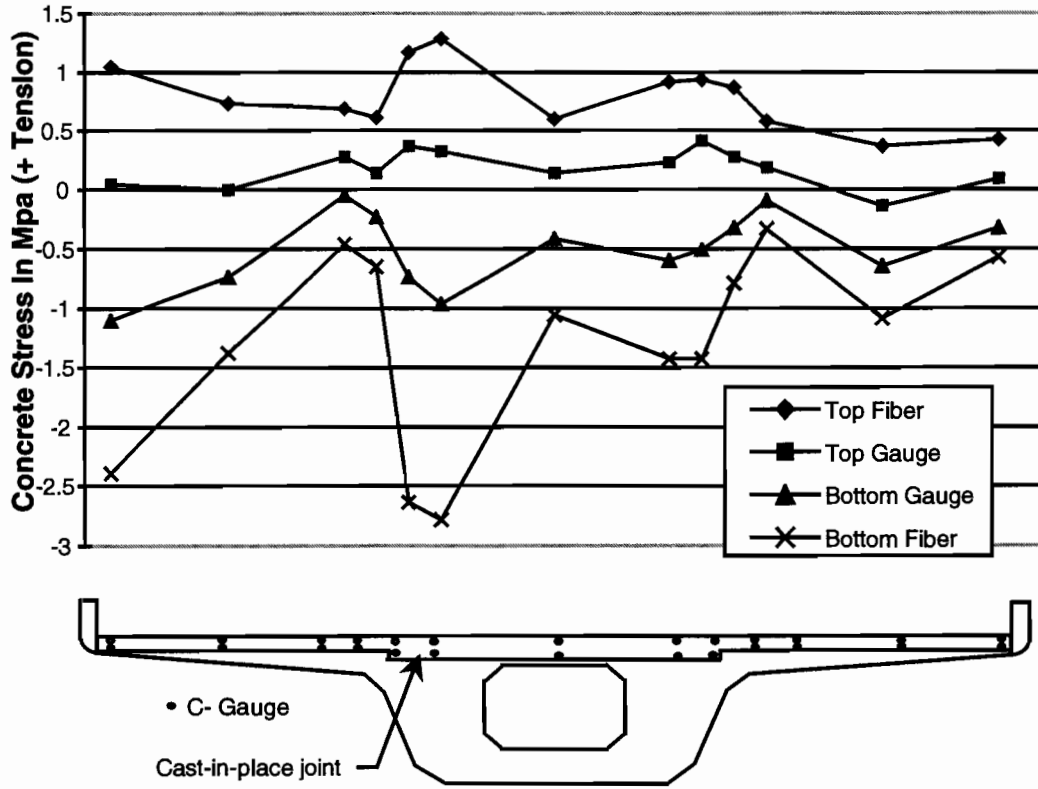


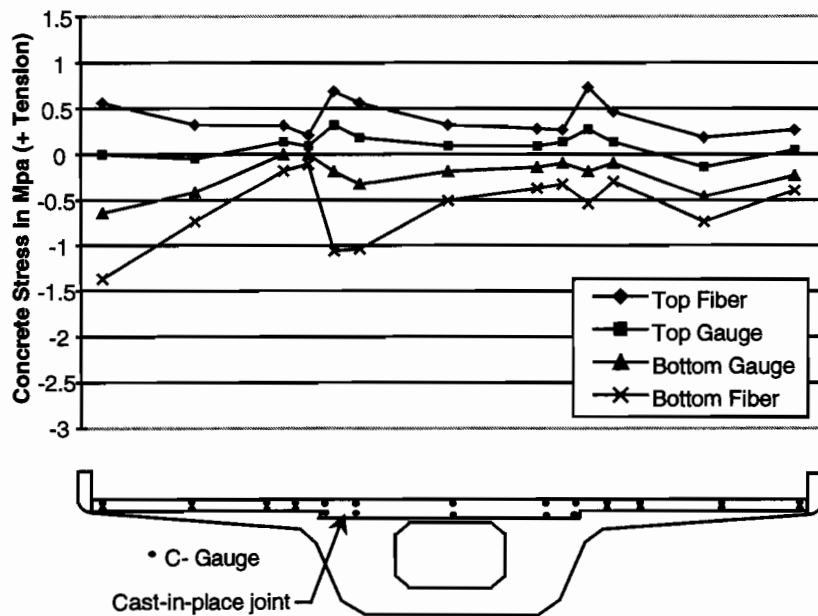
Figure 7.8 Live-load cases for Unit D2

The measured strains in the instrumented joint between spans D5 and D6 for the various load cases have been converted to concrete stresses and are shown in Figures 7.9 through 7.12. The top and bottom fiber stresses have been linearly extrapolated from the concrete strains measured by the two gauges at a given transverse location in the slab.



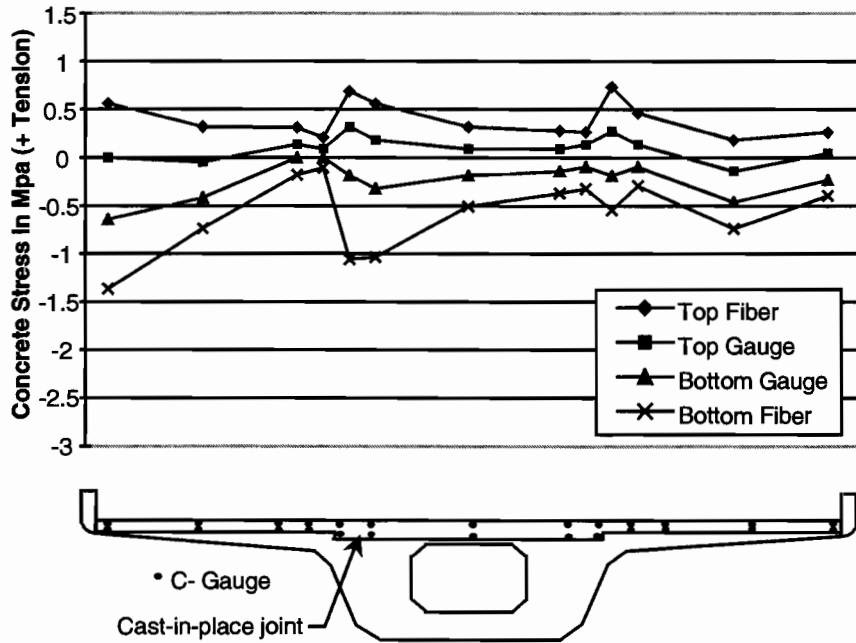
**Section Through Cast-in-place Joint
at Pier D6**

Figure 7.9 Cast-in-place joint stresses-load case 2



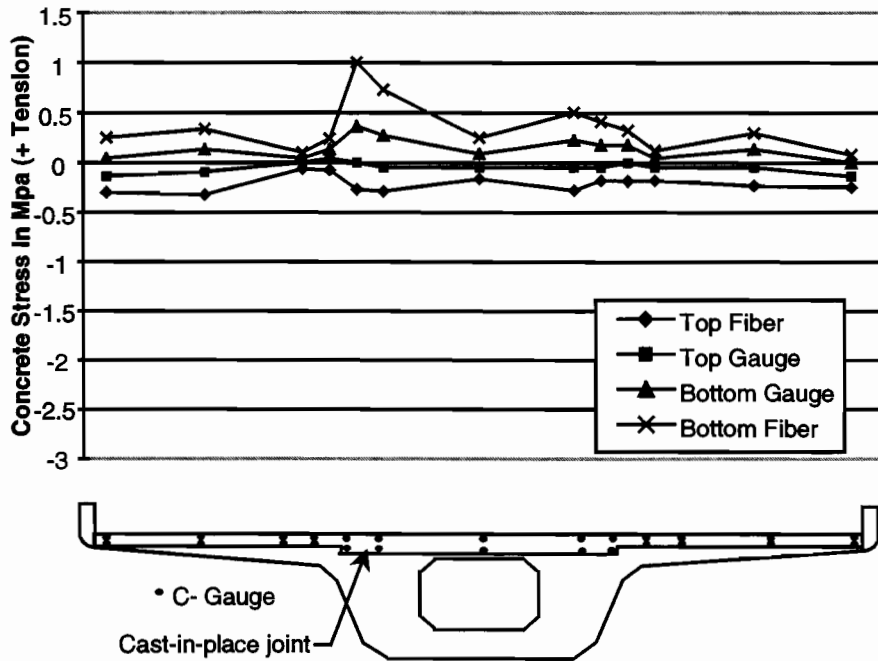
Section Through Cast-in-place Joint at Pier D6

Figure 7.10 Cast-in-place joint stresses-load case 3



Section Through Cast-in-place Joint at Pier D6

Figure 7.11 Cast-in-place joint stresses-load case 5



Section Through Cast-in-place Joint at Pier D6

Figure 7.12 Cast-in-place joint stresses-load case 6

Integrating the slab stresses over the slab area for the load cases shown in Figures 7.9 through 7.12, the net axial force in the slab was close to zero. Therefore, moment carried by the slab-bearing couple should have been close to zero. Figure 7.9 shows that the stresses in the joint were not uniform. The measured stresses tended to peak just inside of the girder webs where the continuity slab changed width. The continuity slab had a longer bearing area at this location because of the geometry of the notch in the anchor segment, as can be seen at the

very bottom of Figure 7.1. This longer bearing area caused greater fixity at the anchor segments where the slab changed width, and therefore increased the bending stiffness of the slab. The stresses shown in Figure 7.9 were primarily slab bending stresses. Also interesting to note was the apparent difference in bending stiffness of the slab near the wingtips. The left portion of the slab had greater bending stresses than the right portion of the slab because of the difference in location of the vertical expansion cuts in the adjacent parapets. The right parapet had an expansion cut very near the centerline of the joint which reduced the bending stiffness of the joint and parapet. In load cases 2, 3 and 5, the average stress at the joint in the wing was compressive. This condition was due to tensile stresses in the parapets.

Also interesting to note was the difference in the magnitudes of the joint stresses between load case 2 (see Figure 7.9) and case 3 (see Figure 7.10). The measured stresses were much higher in load case 2. The moment connection of the slab to the anchor segment for span D6 must have been less effective than the connection to the span D5 anchor segment. Shrinkage cracks between the slab and the precast concrete anchor segments were noted along the entire length of the interface and may have been different on each side of the slab. The stresses measured in load case 6 (see Figure 7.12) indicated that the slab was in positive bending. Therefore, the joint over pier D5 must have been capable of carrying some negative moment in the joint slab itself. The reinforcement detail connecting the joint to the notch in the anchor segment would allow a moment to be developed in the joint because of end rotations of the box girder. The joint was specifically designed to carry small amounts of moment caused by end rotations of the girders. The presence of shrinkage cracks at the cold joint would tend to reduce moments in the joint caused by end rotations of the girders. This reduction would have negligible influence on the behavior of the box girders and no influence on the intended function of the joint itself.

The deflection plots shown in Figures 7.13 through 7.16 show that little continuity was developed across the joint at Pier D6. The magnitudes of the maximum deflections from load cases 2 and 3, shown in Figures 7.13 and 7.14, were nearly identical at 6mm, or only 1/6500 of the span length. They were both substantially different from the 4mm maximum deflection in span D4 from load case 6, shown in Figure 7.16, indicating some continuity of the joint over pier D5. A negative moment was developed at the down station joint of the three span unit at pier D5 during load case 6, based on the measured upward deflection of span D5 shown in Figure 7.16. The cast-in-place fixity block (see Figure 7.2), located between the bottom flanges of the box girders at pier D5, provided a substantially stiffer compression strut when compared to the elastomeric bearings alone at pier D6.

The negative moment developed was still small and unpredictable because of gaps between the bottom flanges and the fixity block caused by temperature changes in the girders, and possibly by shrinkage of the block itself. Very small negative moment was developed by the joint at pier D5 during load case 2, as seen from the very small deflections in span D4 shown in Figure 7.13. The fixity block was also eccentric to the longitudinal centerline of the girder. The joint at pier D6 was selected for instrumentation because this fixity block, cast around a heavy steel pipe emanating from the pier capital, was not present.

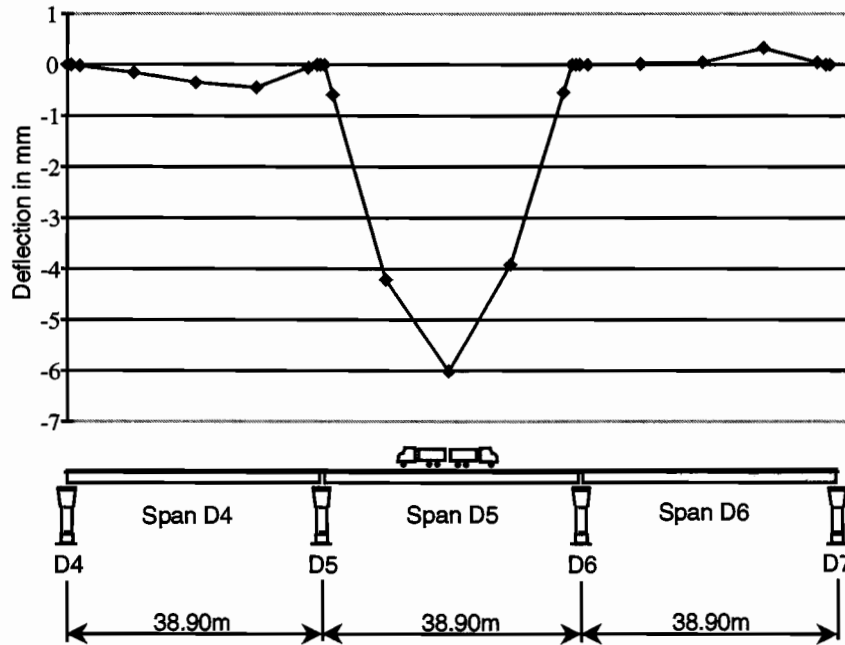


Figure 7.13 Deflections from live-load test on Unit D2-load case 2

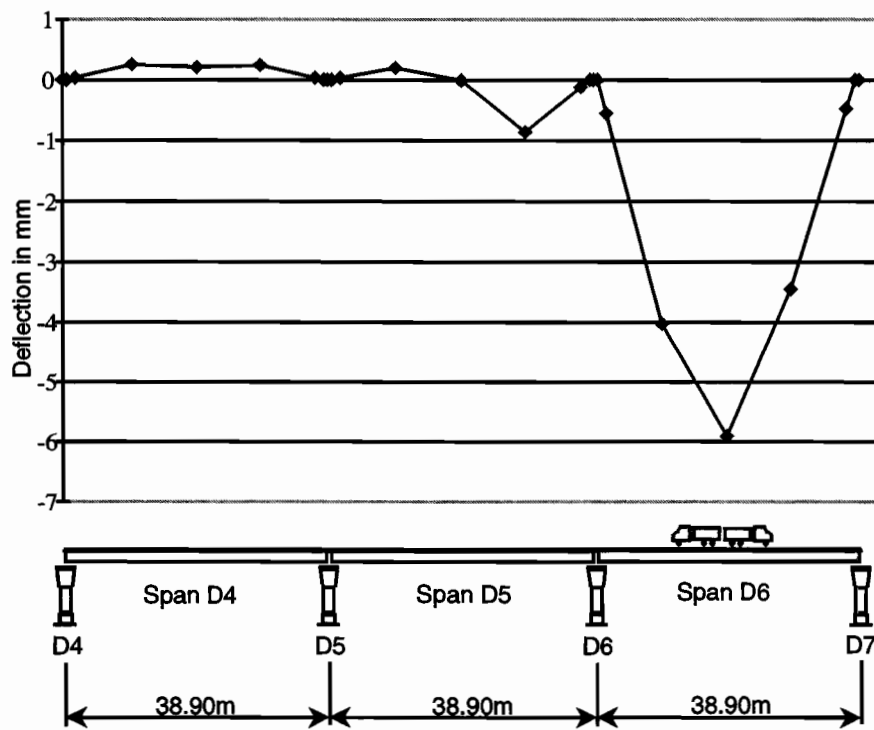


Figure 7.14 Deflections from live-load test on Unit D2-load case 3

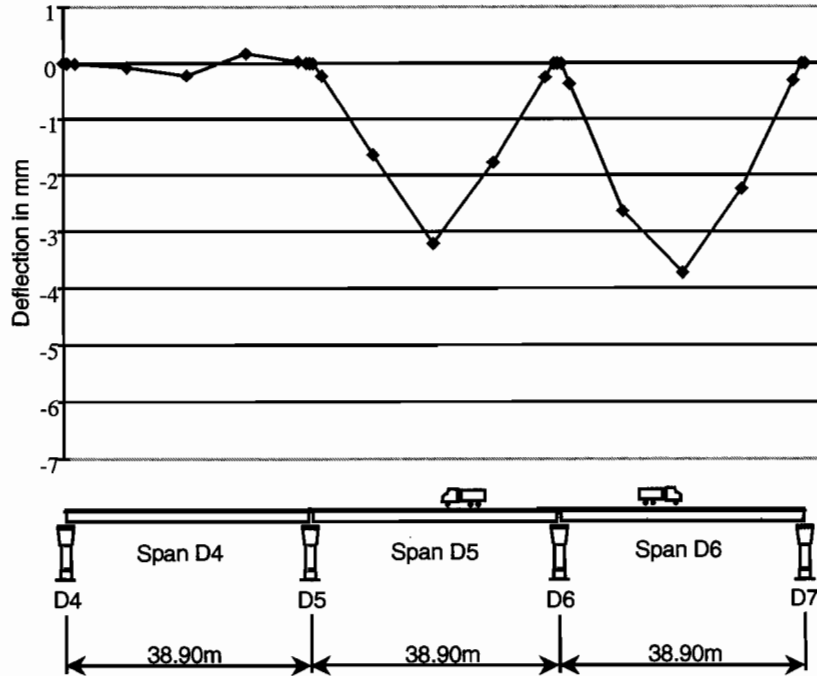


Figure 7.15 Deflections from live-load test on Unit D2-load case 5

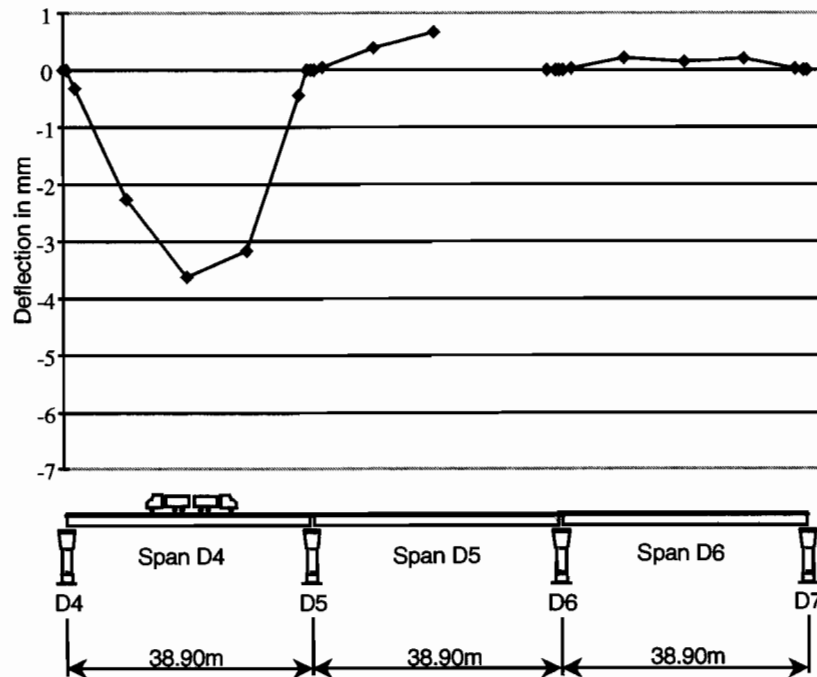


Figure 7.16 Deflections from live-load test on Unit D2-load case 6

Live-Load Test on Unit C13

The span geometry for Unit C13 and the load cases of interest are shown in Figure 7.17. The axle weights for the trucks used are given in Table 7.2. The girder on Unit C13 was originally designed to be precast and erected as two single-celled girders, with cast-in-place top and bottom slabs between the two girders. Since these girders would have required a special casting machine and erection equipment, the contractor decided to

cast these spans in place. The original girder shape was retained, as was the cast-in-place continuity slab between spans. Details for the continuity slab were similar to those for Unit D2.

Table 7.2 Axle weights and spacing for live-load test trucks on Unit C13

Truck	Weight of Rear Axles (kN)	Weight of Front Axles (kN)	Total Weight (kN)	Axle Spacing (mm)
1	119.2	36.7	155.9	4900
2	117.5	43.9	161.4	4720
3	112.0	45.4	157.4	4900
4	119.0	35.1	154.1	4700
5	113.6	30.6	144.2	4700
6	122.7	41.0	163.7	4090

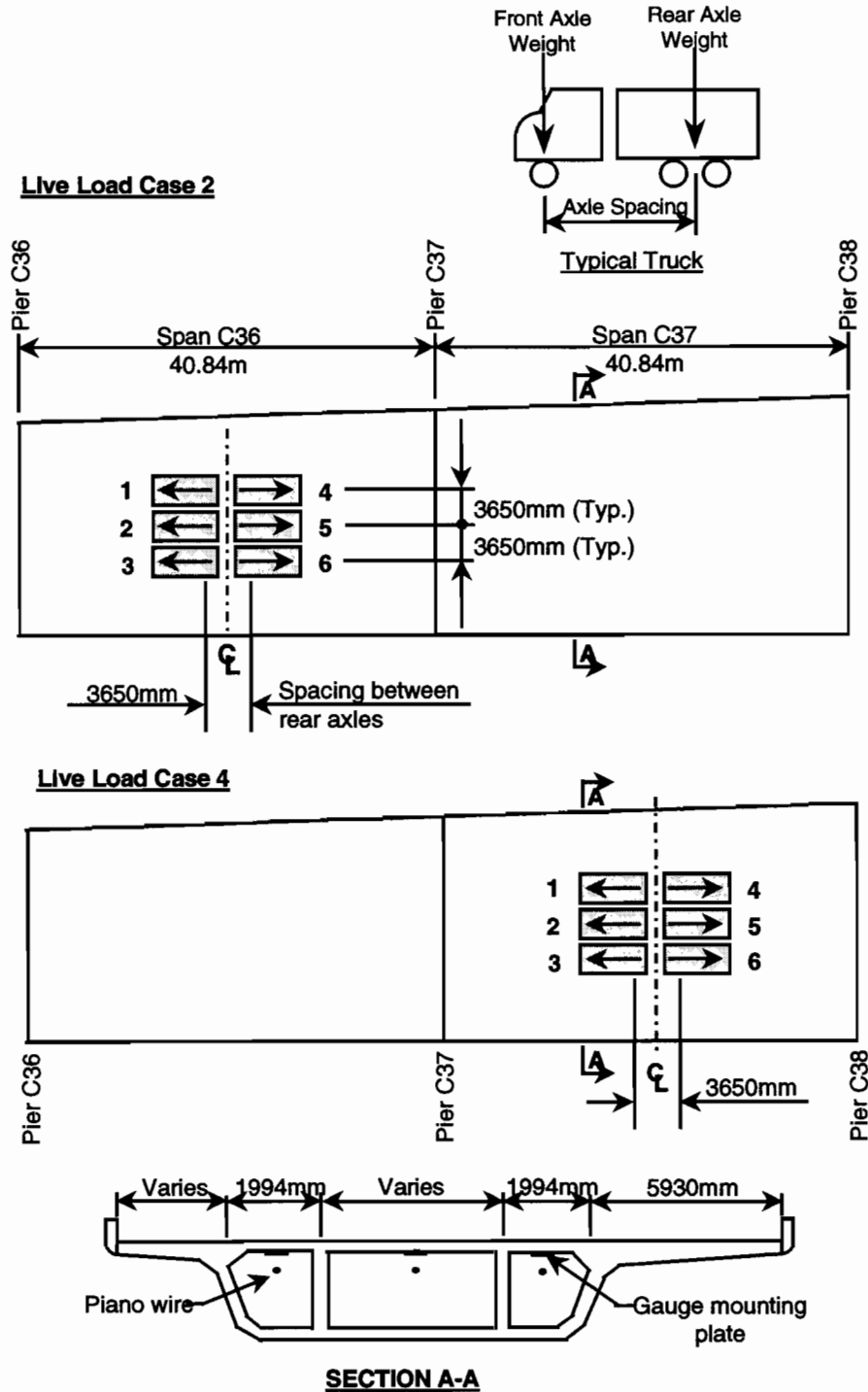


Figure 7.17 Live-load cases—Unit C13

Span deflections were the only measurements taken during the live-load test on Unit C13. Deflections were measured at the quarter points of each cell in each span. Continuity provided by the joint for live load was small, as shown in Figures 7.18 and 7.19, even with fixity blocks on each of the two piers at C37. Maximum deflections were approximately 20% smaller in span C37 than in span C36 because the C37 girder was the wider of the two. The maximum deflection in span C36 was very small at 1/7900 of the span length. Deflections in the unloaded span in Figures 7.18 and 7.19 averaged to about zero.

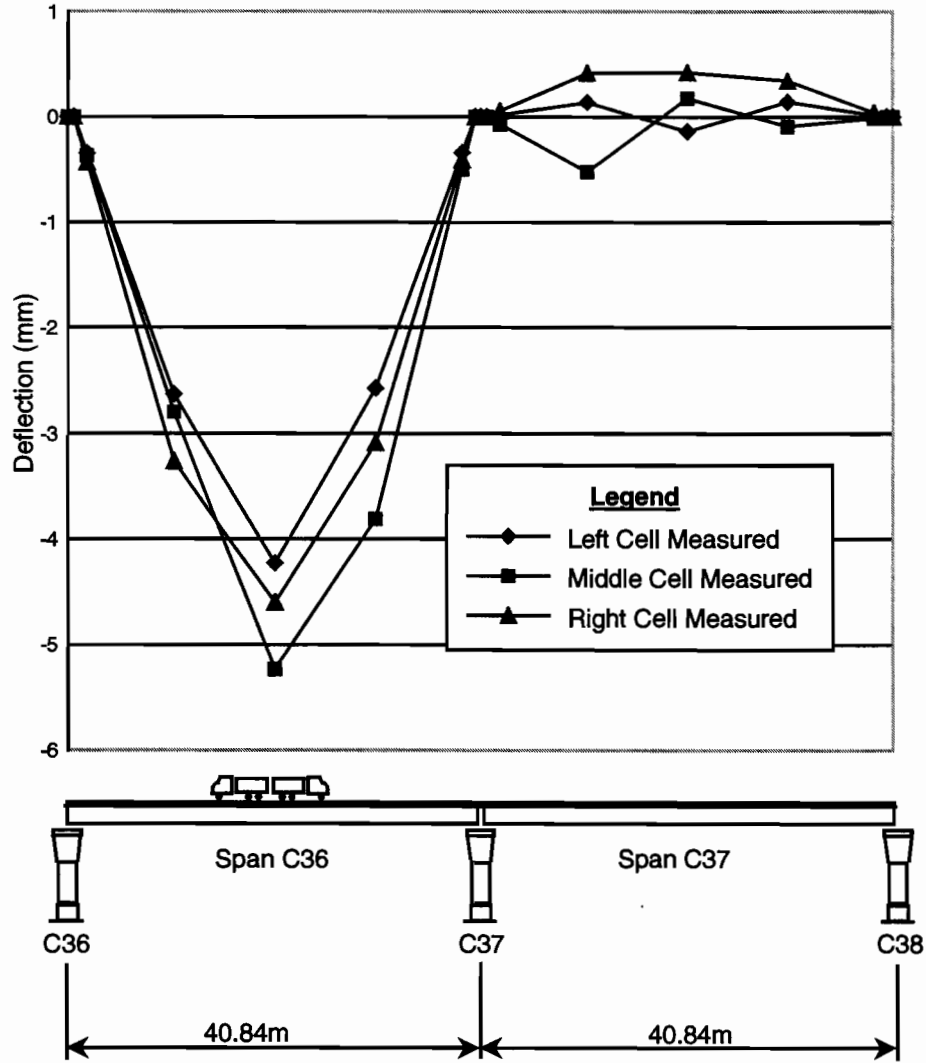


Figure 7.18 Deflections from live-load test on Unit C13-load case 2

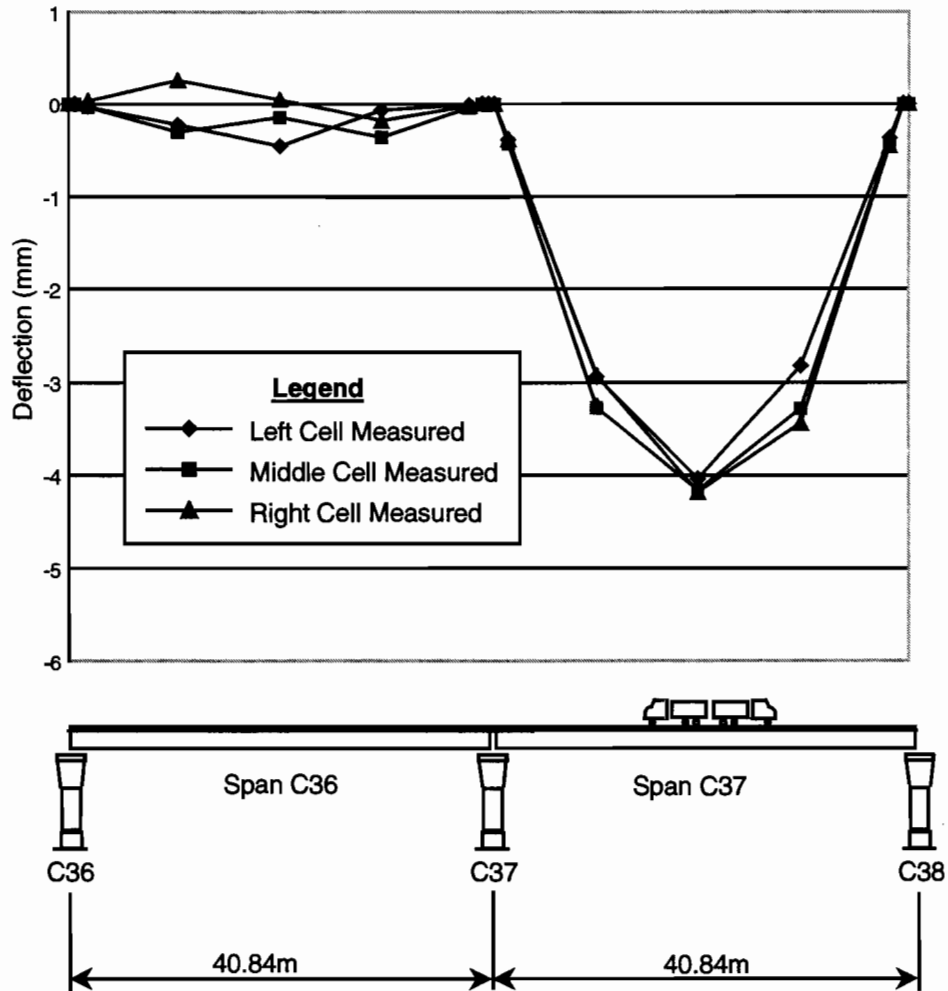
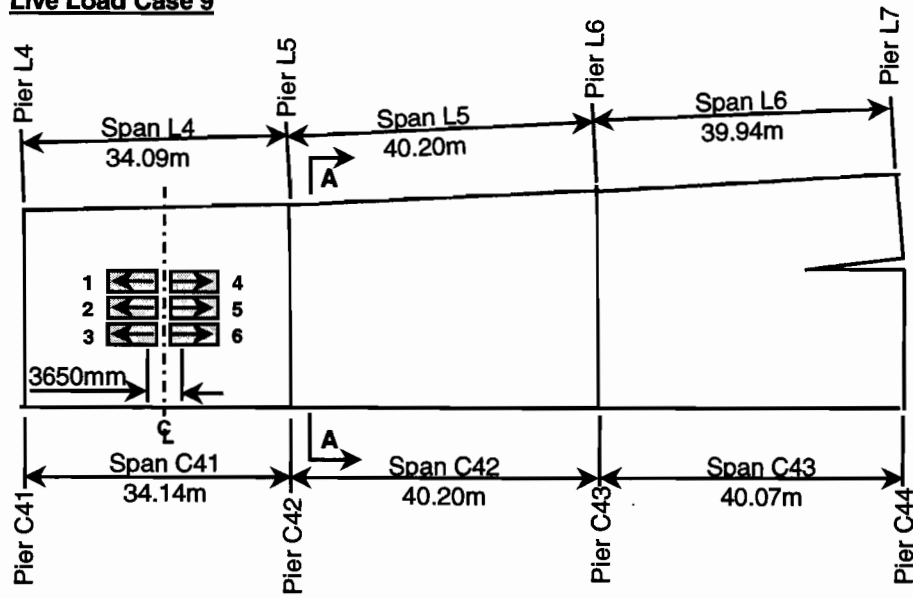


Figure 7.19 Deflections from live-load test on Unit C13-load case 4

Live-Load Test on Units C15 and L2

The span geometry for the twin single-celled girders and the live-load cases of interest are shown in Figure 7.20. The girders were constructed using the span-by-span method on erection trusses. The mainlane girder on line C and the ramp girder on line L both had one variable width wing. The wing tips were joined with a cast-in-place closure strip. The axle weights for the trucks used in this live-load test are shown in Table 7.3. A fixity block was located only at pier C42.

Live Load Case 9



Live Load Case 11

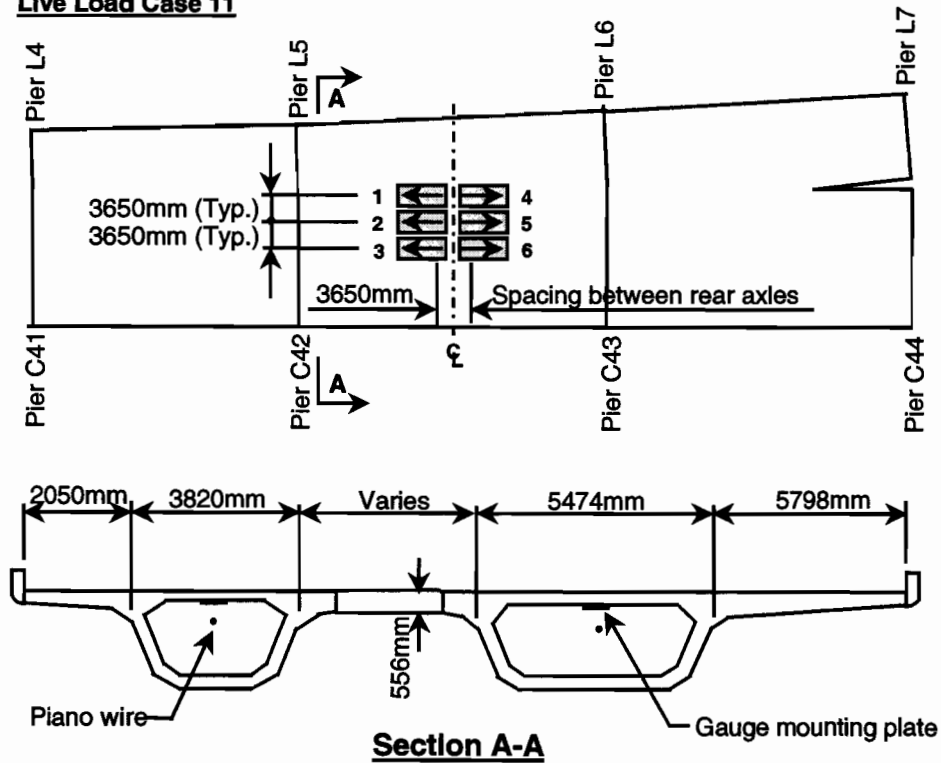


Figure 7.20 Live-load cases—Units C15 and L2

Table 7.3 Axle weights and spacing for live-load test trucks on Units C15 and L2

Truck	Weight of Rear Axles (kN)	Weight of Front Axles (kN)	Total Weight (kN)	Axle Spacing (mm)
1	133.9	55.9	189.8	5030
2	128.7	44.0	172.7	4090
3	109.5	41.5	151.0	4100
4	121.3	55.8	177.1	5000
5	137.6	42.5	180.1	5000
6	127.4	34.4	161.8	4700

Deflections were measured down the center of each of the two girder cells for each load case and are shown in Figures 7.21 and 7.22. The live load in the side span C41 in load case 9 actually caused the middle span C42 to deflect downward, as seen in Figure 7.21. The end rotation of the anchor segment for span C41 probably caused uplift forces to be carried through the joint to the anchor segment for span C42. This uplift force would have been eccentric to the span C42 bearing reactions, resulting in a positive moment applied to the end of span C42. Figure 7.22 indicates that a negative moment was carried by the joint over pier C42, with the fixity block, from live loads in the central span, although the moment was probably quite small based on the small measured upward deflections of spans C41 and L4. Maximum downward deflections in the loaded spans were quite small at 3mm for span C41 during load case 9 (1/11400 of the span length), and 4.9mm for span C42 during load case 11 (1/8200 of the span length). The deflection in span C42 was larger than the deflection in span C41 because span C42 was the longer of the two spans.

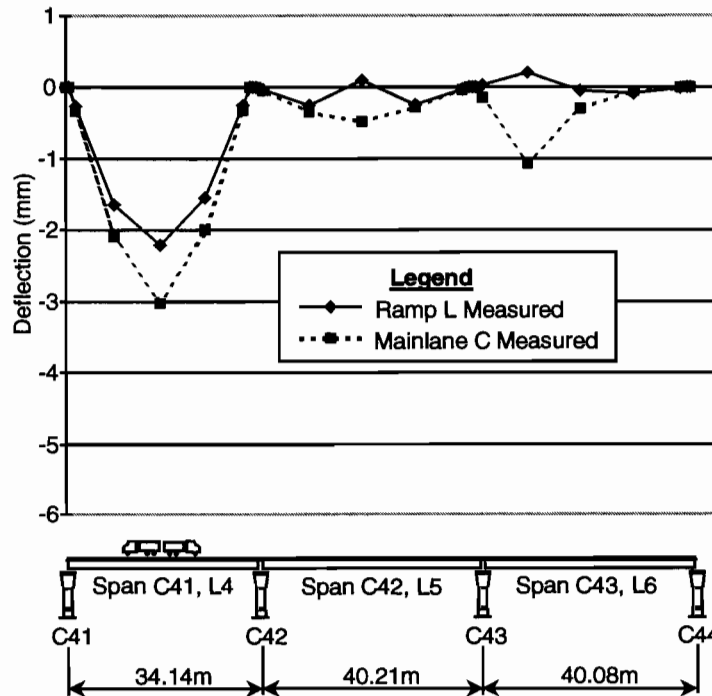


Figure 7.21 Deflections from live-load test on Units C15, L2-load case 9

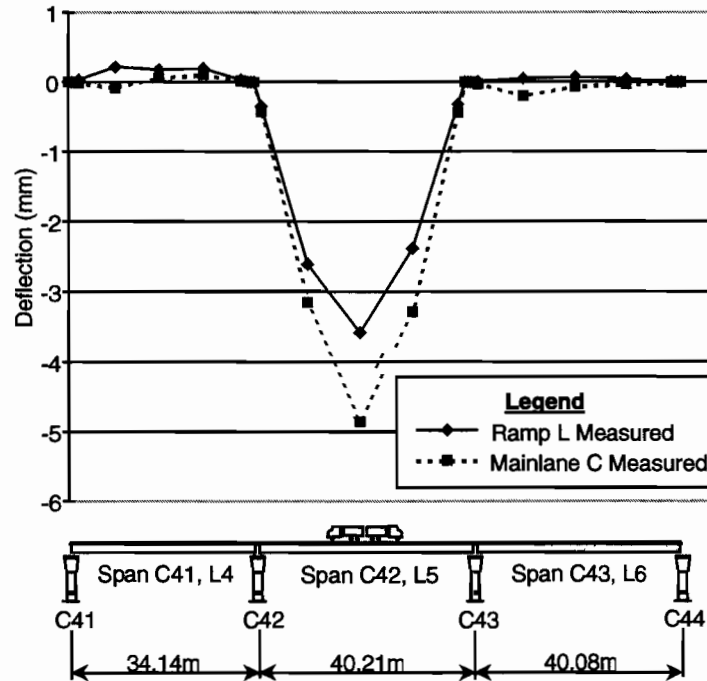


Figure 7.22 Deflections from live-load test on Units C15, L2-load case 11

7.4.2 Temperature Gradient Effects

To study the effects of temperature gradients in the girders on the joints, two positive temperature gradient cases were selected. The first gradient occurred on June 4, 1995, before the continuity joint had been cast, and the second gradient occurred on August 20, 1996, after the joint and blacktop were in place. These positive gradient cases were selected for their similarity. The temperature changes measured by the thermocouples in mainlane segment D5-9 are shown in Figure 7.23 for each case. The magnitude of the August 20, 1996, case was slightly larger than the June 4, 1995, case, but the two gradient shapes were almost exactly alike.

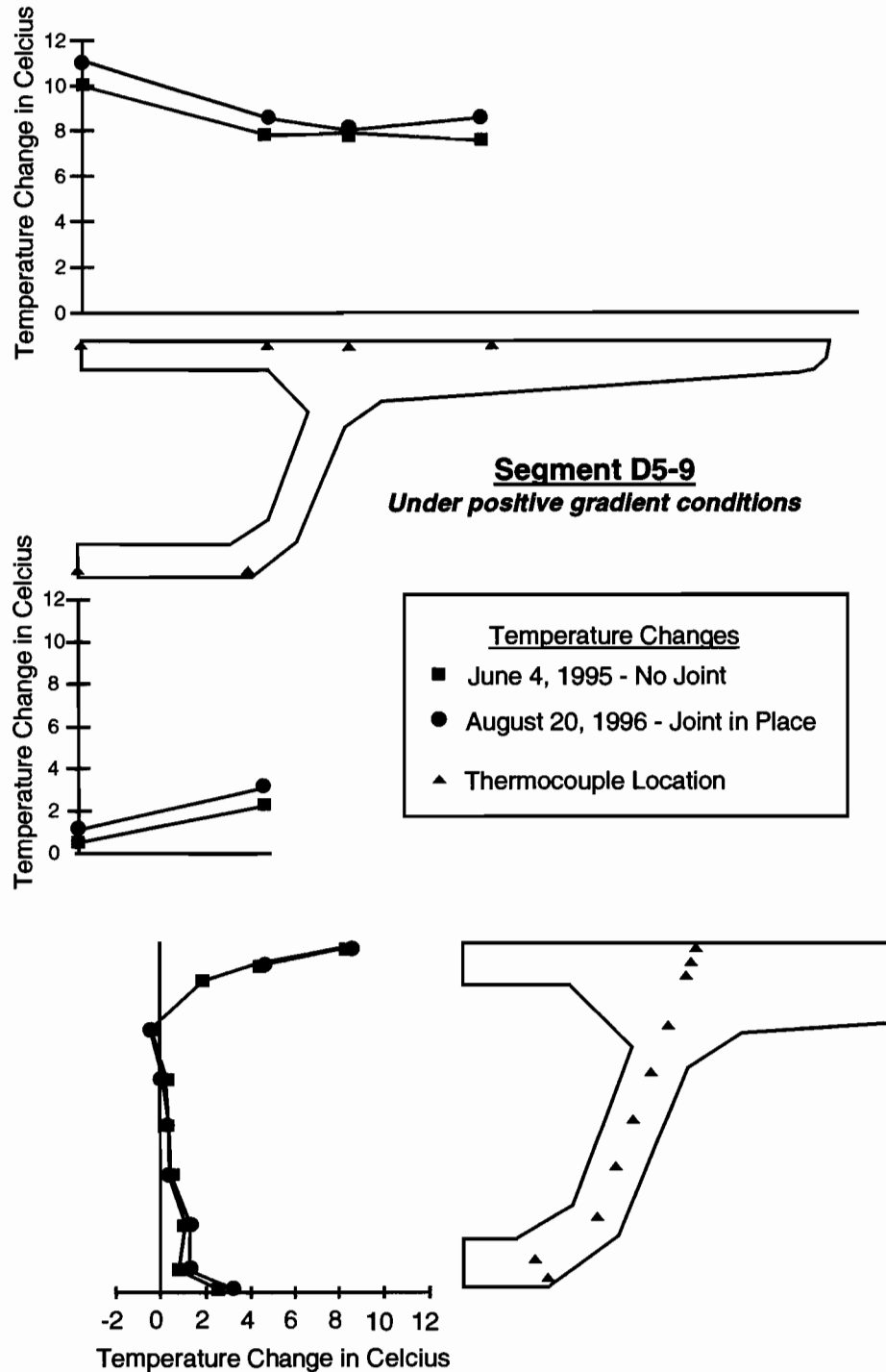


Figure 7.23 Measured temperatures for thermal gradient load case

Longitudinal cross-sectional strains caused by the thermal gradients were measured in segment D5-9 near midspan, and in segment D5-16 immediately adjacent to the heavy end diaphragm. The measured strains in segment D5-9 are shown in Figure 7.24. Because of the large number of damaged gauges in the top flange, no conclusions could be made by comparing the strain changes from the two gradient cases in this part of the girder. The temperature change in the wingtip thermocouple was larger in the August 20, 1996, case, and therefore produced higher strain changes, as shown at the top of Figure 7.24. Strain changes in the web and

bottom flange gauges were similar for each gradient case, making it difficult to identify any influence that the joint may have had on the girder's structural response to thermal gradients.

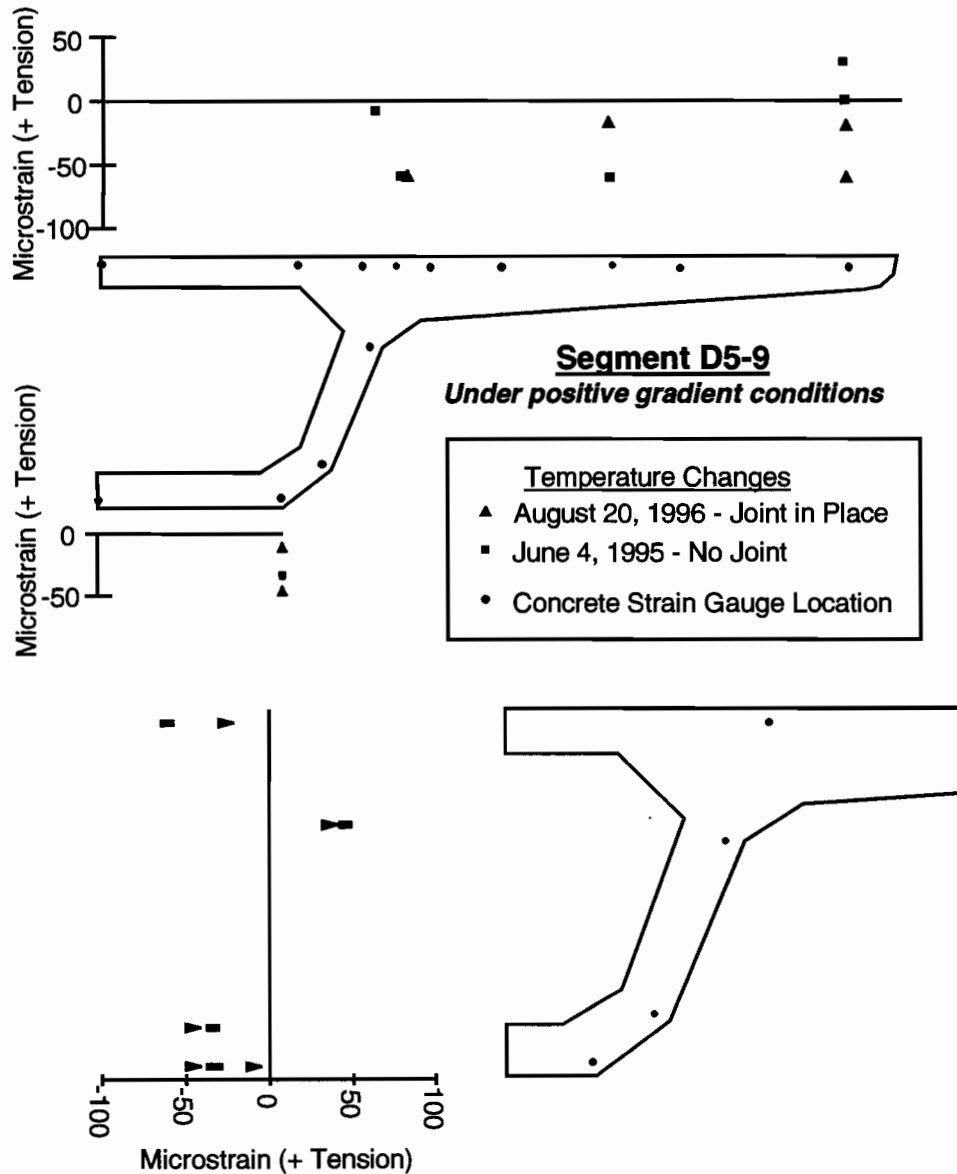


Figure 7.24 Measured strains in segment D5-9 from thermal gradient load case

The measured strains in segment D5-16 and the cast-in-place continuity joint are shown in Figure 7.25. The measured strains from the segment D5-16 gauges in the top flange, webs and bottom flange were nearly identical for both thermal load cases. The stiffening effect of the joint on the top flange was apparently small and did not significantly change the girder's response to the thermal gradient loading. The positive thermal gradients in the girders did produce bending and axial strains in the continuity slab. The rotation at the girder ends produced positive bending in the slab, as can be seen by comparing the top and bottom slab gauge strains at the top of Figure 7.25. These strains tended to peak where the slab changed width, as in the live-load cases. The transverse distribution of joint strains also revealed that the joint was acting to stiffen the top flange of the girders. The joint strains were more compressive in the wings and tensile between webs of the box girders, indicating that self-equilibrating stresses were acting across the joint width because of warping of the girder flanges.

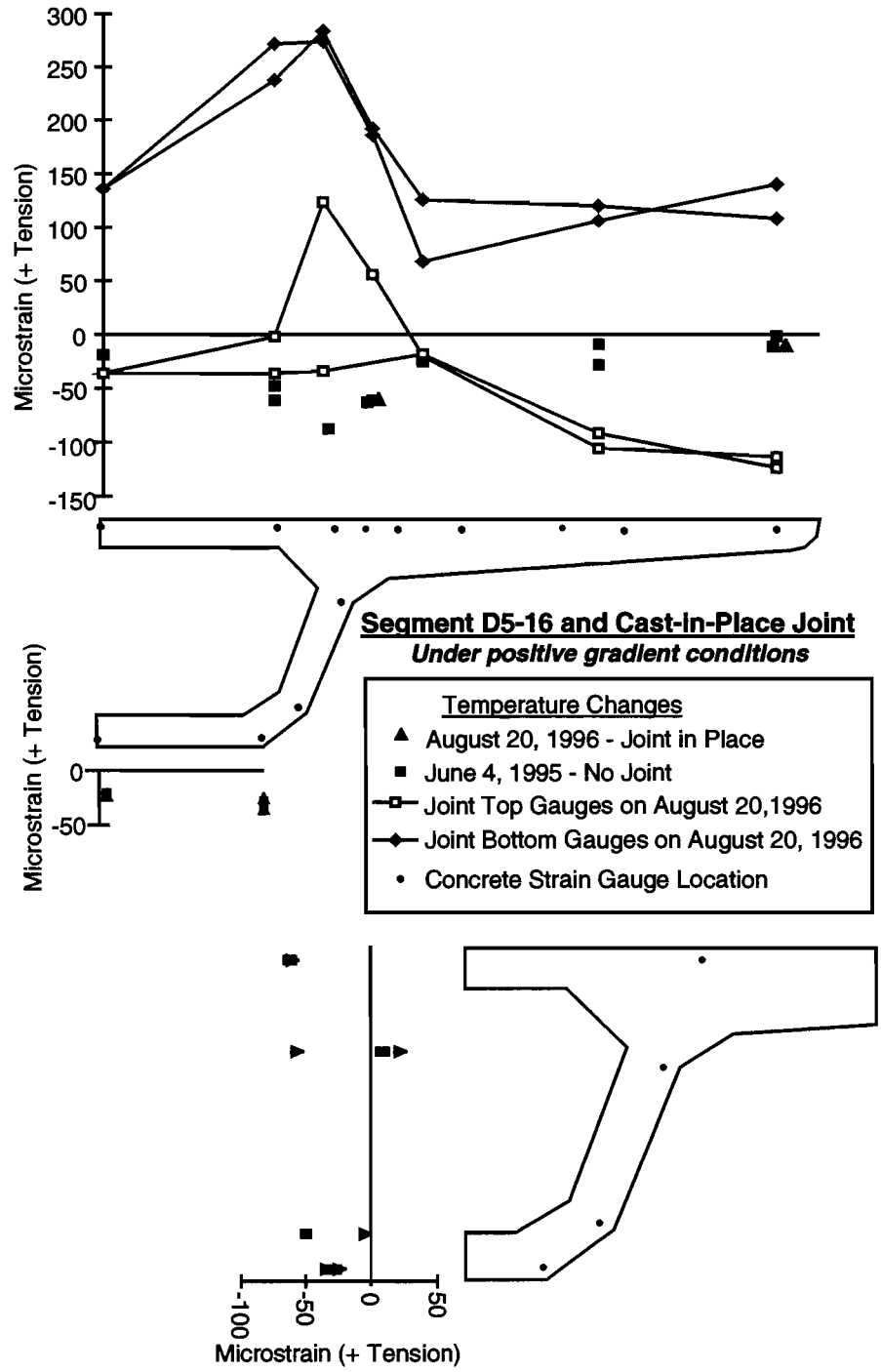


Figure 7.25 Measured strains in segment D5-16 and cast-in-place joint from thermal gradient load case

7.5 CONCLUSIONS AND RECOMMENDATIONS

The cast-in-place continuity joints on the US 183 Elevated, in most respects, performed as designed. The joints were intended to provide a low-cost riding surface between simple-span box girders. The joints were not designed to carry superstructure moments across the joint, but were designed to carry axial loads produced by shear forces in the elastomeric bearings from thermal expansion of the box girders. The joints had a semirigid

moment connection to the anchor segments of the box girders and were designed for moments from truck wheels and shear forces from the end rotation of the box girders.

7.5.1 Construction Procedures

The reinforcing bars for the cast-in-place continuity joints were spliced to 90° bend bars in the anchor segments, seen in Figure 7.1, that passed through the construction joint seat for the cast-in-place slab. The 90° bend bars were difficult to properly locate when the anchor segments were cast, resulting in the addition of many extra bars that were drilled into and bonded to the anchor segment. Also, these 90° bend bars often intruded into the horizontal surface intended for the fiberboard material used to tune the effective length of the joint. Widening the notch for the cast-in-place joint would have reduced the potential for inadequate splice lengths in the 90° bend anchor segment bars and provided more room for the fiberboards and stay-in-place forms. The short overlap of the 180° bars in the joint and 90° anchor segment notch bars provided adequate tensile strength across the deck joint during the test period, but long-term strength of this splice detail is questionable and was not tested in this study.

The fiberboards used under the joint between girder wings were also used as the stay-in-place form for the joint itself. A steel stay-in-place form was eventually used in the wider portion of the joint between girder webs. The use of these stay-in-place forms was ideal because of the lack of access to the underside of the joint once it was cast and the speed at which the forms could be placed.

In order to control the movement of the end of the box girders from thermal expansion while the joint concrete hardened, adjacent box girders were locked together with the used of post-tensioning bars. These bars passed through the future post-tensioning ducts located in the anchor segment diaphragms. Only one joint of a span was locked at any one time. The joint was locked at a time when the girders were cool so that some residual compression would be applied to the joint after the joint was unlocked. The system seemed to work quite well, although the shrinkage of the joint concrete eventually caused a crack to open along the entire length of the cold joint, reducing the fixity of the joint to the girders. Shrinkage cracks were also noted to propagate from the reentrant corner of the joint where the joint slab changed width. Softening the reentrant corner of the joint with a 45° angle would be nearly as easy to form in the surface of the anchor segment and would lessen the stress concentration effect of the 90° corner. Fiberboards with a 45° cut could be used under the joint slab in this area if the 90° corner is retained beneath the joint.

7.5.2 Cast-in-Place Joint Behavior under Live Loads and Thermal Loads

The continuity joint did not substantially alter the structural performance of the adjacent box girders. The large negative moment couple that was measured on the San Antonio Y [7] did not develop in the US 183 semicontinuous three-span or two-span units. The relatively stiff fabric reinforced pads with Teflon-stainless steel sliding surface developed a substantial negative moment in the San Antonio Y girders. Such a couple should be avoided unless this effect is specifically included in the design of the girders and the joint. The elastomeric bearings used on the US 183 girders were very weak in shear, as this type of bearing is intended to be, and did not allow the formation of any appreciable negative moment in the live-load tests. The joint itself experienced local bending moment from the rotation of the ends of the girders from both live loads and thermal loads. The bending strains in the joint were much increased at the reentrant corner of the joint where the joint suddenly changed width. The joint width change was provided between girder webs to allow access to the tendon ducts. A 45° transition where the joint changed width would have lessened the stresses in the joint, while not influencing access to the tendon ducts or the interior of the box girder.

The cast-in-place fixity block between box girder bottom flanges was responsible for the development of some moment continuity across joints where the blocks were located. The negative moments developed ranged from insignificant to large. They did not develop in every case, depending on the fit of the block to the girder flanges. The fixity blocks were also eccentric to the centerline of the girder. In order to eliminate the formation of this negative moment, the fixity block should be moved or redesigned to eliminate a moment couple with the continuity joint.

CHAPTER 8

SUMMARY, RECOMMENDATIONS AND CONCLUSIONS

8.1 PROJECT SUMMARY

The US 183 Segmental Bridge is an urban viaduct constructed with both precast and cast-in-place structural elements. The mainlane girders were precast segmentally and constructed using the span-by-span method. One three-span semicontinuous (top slab continuity only) mainlane unit was selected as one of the units for study during precasting, erection and under live load. The mainlane girders rested on innovative Y-shaped piers with a steel pipe tension tie across the top of the "Y". One Y-pier was instrumented in conjunction with the mainlane three-span unit under study. Most of the ramp girders were also constructed using the span-by-span method. However, five of the spans of Ramp P were constructed in balanced cantilever. This five-span girder constructed in balanced cantilever was also selected for detailed study, along with one precast segmental pier located beneath the most heavily instrumented ramp span. A limited study, only for live-load behavior, was carried out on a two-span semicontinuous three-cell girder that was cast in-place, as well as on three spans of twin single-cell girders with gore closures at the wing tips. These single-cell girders were constructed by the span-by-span method and provided the transition in cross section needed where the ramp girders merged into the mainlane girders.

One of the topics studied in detail on the project was post-tensioning tendon force losses, which included friction losses, elastic shortening losses, and long-term losses. Several different post-tensioning tendon profiles were studied on both the mainlane and ramp girders, along with a U-shaped tendon in the segmental pier. Another topic studied was thermal gradients and their effects. Thermal gradients were measured in the mainlane and ramp girder, and in the segmental voided pier. Temperatures were measured every hour beginning immediately after construction, and measurements continued for years. The measured gradients and measured thermal-induced strains and related stresses were compared to design code recommended gradients, and stresses calculated using common analysis methods. The third topic studied was the general response of the girders and piers to applied loads, including dead loads, prestressing loads, and live loads. Measured strain distributions, related stress profiles, and deflections were compared to results calculated using methods recommended in design specifications, such as the AASHTO effective flange width method. Another topic under study was the performance of post-tensioned anchorage zones and other D-zones (discontinuity zones). The service-level performances of seven D-zones were evaluated using strain measurements and visual inspections. The D-zones studied included two tendon deviators, two anchor segments with heavy anchorage diaphragms, two pier capitals, and one anchorage blister. The final topic under study was the performance of the cast-in-place deck slab joint that provided the riding surface between simple-span girders. Live-load tests were performed to determine if a moment couple developed between this deck joint and the bearings.

8.2 GENERAL CONCLUSIONS

The implementation of sound and proven design and construction practices resulted in a highly successful TxDOT bridge project for the City of Austin. High quality piers and superstructure were constructed. The design proved to be stiff and amply strong, as well as attractive. The project was completed on schedule with few problems. The bridge design was performed by the TxDOT Design Division staff. These engineers drew on their experiences from the construction of the San Antonio Y segmental viaduct when designing the U. S. 183 segmental project. The primary contractor was Martin K. Eby Construction Company in a joint venture with Flatiron Structures Company. The experienced construction team produced high quality precast segments with few rejections. The erection scheme for the piers and superstructure was straightforward, resulting in few delays once initial spans were successfully erected. The designer allowed the constructor to use flexible and consistent construction cycles.

8.2.1 *Post-Tensioning Losses*

The post-tensioning tendons used on the project were of common design and provided an opportunity for routine friction and elongation tests. The friction losses were found to be higher than expected in the deviated

external tendons, and lower than expected in the internal straight tendons. The elongation measurements could not always be counted on to accurately predict the measured friction losses because of small differences in tendon stiffness.

8.2.2 Thermal Gradients

The positive design thermal gradients recommended for central Texas by NCHRP 276 [39] were found to be excessive and temperature measurements indicated the magnitudes at deck level could be reduced from 26°C to 16°C for the no blacktop case, and from 20°C to 15°C with 50mm of blacktop. However, from comparison of measured stresses with the results of the conventional analysis procedure indicated that further development of this unproved analytical technique is urgently required. In the interim, the NCHRP values and the current analysis procedure give results close to the measured structural response.

The negative design thermal gradient recommended by NCHRP 276 was found to be excessive and temperature measurements indicated the magnitudes at deck level could be reduced from peak values of -12.8°C to -7°C without blacktop and -10°C to -5°C with 50mm of blacktop. However, they were found to produce calculated strains less than those actually measured that occurred with less severe measured negative thermal gradients. Again, improved calculation methods are urgently needed. The *AASHTO LRFD* [9] design negative gradient shape was found to be inaccurate when compared with measured gradients. The magnitude of positive and negative thermal gradients through the thicknesses of the girder webs and flanges indicated that the thermal gradient design case should also be considered during transverse design of the cross section. The transverse thermal design gradients should be linear. Significant positive and negative thermal gradients were measured in the voided segmental pier, yet produced tensile stresses important only during certain construction load cases.

8.2.3 Load Response of Box Girders

The structural response of the various elements under study to dead load, prestressing, and live loads was found to be predictable using common design methods. The diffusion of post-tensioning forces assuming the spread of force within a 60° cone, and the prediction of shear lag by the effective flange width method were found to be adequate, with some limitations. The diffusion of temporary post-tensioning forces needs to be carefully considered when determining the compressive stresses actually present during curing of epoxy joints. The measured deflections of the box girders under live loads indicated high stiffness, with the multi-cell girders able to significantly distribute or share moments from unsymmetrically placed live loads.

8.2.4 Behavior of D-Zones

The discontinuity zones studied all proved to be very conservatively designed, but had different service-level performances. One D-zone had large cracks with bars stressed half way to the yield point because of sharply bent deviator pipes, while others had no service-level cracking. Strut-and-tie modeling, with due consideration for the load paths to the boundaries of the D-zones, is encouraged.

8.2.5 Cast-in-Place Joint Behavior

The instrumented cast-in-place joint, providing the riding surface between simple spans of the three-span semicontinuous bridge units, generally performed as designed. No live-load moment was carried across the joint because of the lack of shear stiffness in the elastomeric bearings. The details of the joint could be modified to improve constructibility, especially where the cast-in-place joint splices to the precast anchor segment.

8.3 SPECIFIC CONCLUSIONS AND RECOMMENDATIONS

The following specific conclusions and recommendations are based on the evaluation of the measurements, review of other field and laboratory data, and visual observations made over the course of the project.

8.3.1 Post-Tensioning Losses

1. Measurements of live-end anchorage zone friction losses in the laboratory bench test and in-place friction test indicated that an assumed design loss of 2% would be sufficient, unless actual live-end losses are

known from previous measurements. This measurement includes the friction losses within the trumpet, through the anchorage hardware, and from the stressing equipment.

2. Measured wedge seating losses were slightly less than the design value of 6mm. The current design value is adequate.
3. The bench test proved to be of little value to all parties except the researchers, other than as a basic calibration trial of the various pieces of the stressing system. The modulus of elasticity determined in the bench test did not prove to be representative of most of the tendons used in the structure, presumably because of slight variations in strand area. The in-place friction test was much more useful for providing information to the engineers and constructors. Accurate elongation calculations must be based on the results of an in-place friction test, otherwise the measured elongation tolerance may not be easily met.
4. Wobble friction in the straight internal ducts of the structure was quite small. These ducts were effectively held in position during concrete placement by inflatable mandrels. Friction coefficients for internal tendons in ducts constructed using inflatable or rigid mandrels can conservatively be selected as $\mu=0.16$ and $K=0.0007\text{m}^{-1}$. For draped internal ducts, friction coefficients are $\mu=0.16$ and $K=0.0013\text{m}^{-1}$ for monolithic girders and $K=0.0016\text{m}^{-1}$ for segmental girders, based on other studies [19] [22].
5. The friction coefficient for external tendons in smoothly bent deviator pipes with consistent radius can be chosen as $\mu=0.25$. The friction coefficient in the sharply bent deviator pipes used in some of the U. S. 183 girders, at about a 2m radius, generated a coefficient of friction of about $\mu=0.35$. The sharp radius bend also caused large cracks in the deviator concrete and should be avoided.
6. The additional wobble angle $\beta=0.04$ radians suggested by Roberts [7] was found to be sufficient when applied at each deviator of the mainlane girders, if the proper coefficient of friction was used in the calculation. The additional wobble angle $\beta=0.04$ radians was recommended based on studies of girders constructed span-by-span with straight or large radius horizontal geometry. The additional β angles measured in Ramp P, with a horizontal curvature of 221m, were higher at $\beta=0.11$ radians when using an assumed friction coefficient of $\mu=0.25$. The horizontal curvature of the girder makes accurate deviator pipe placement more difficult, thereby warranting a higher design β angle. The β angle should be applied at all deviators and saddles. The use of a diablo, or double trumpet-bell-shaped deviator pipe, would help reduce the β angles on curved structures. The diablo-style deviator pipe was not necessary for the mainlane girders, based on the friction tests.

Table 10-2 in the *AASHTO Segmental Guide Specification* [8] should be modified as follows:

	Friction Coefficient (μ)	Wobble Coefficient
1. For draped-strand tendons in galvanized metal sheathing (segmental construction)	0.16-0.25*	0.0016m^{-1}
2. For straight-strand tendons in galvanized metal sheathing (segmental construction using mandrels)	0.16	0.0007m^{-1}
6. For strand tendons in rigid steel pipe deviators	0.25-0.35**	0.04rad***

* A friction coefficient of 0.25 is appropriate for duct curvatures with radii between 6m and 15m.

** A friction coefficient of 0.35 is appropriate for duct curvatures with radii of 2m or less.

*** This additional wobble angle is applied at each deviator and saddle and may be higher for girders with horizontal curvature. It can be reduced to 0.02rad if a diablo-type deviator pipe is provided.

7. Anchorage details for the long 150m (three-span) external tendons in Ramp P adjacent to a deviation saddle proved to be unacceptable. The large elongations caused entangled tendons to be drawn close to the back of the anchor head where they broke. Straight anchorage geometry would have allowed the 19-strand tendons to untangle to some extent in the long distance between the anchorage and the deviator. No strand breakages of this type occurred in any of the 14 tendons in each of 162 spans of mainlane girders. If deviation saddles are required adjacent to a live-end anchorage where a first pull must be made, the length of elongation may need to be limited, requiring stressing from both ends of the tendon. Proper support of

unstressed tendons over their deviated length would help reduce the total elongation substantially by reducing the slack length.

8. Elastic shortening loss calculations for the external deviated tendons were found to be inaccurate if slippage was not assumed to occur at the deviators. The measured values fell between the cases calculated using a deviator with infinite friction and zero friction. The more conservative loss from these two cases should be used for design unless an extremely complex calculation is performed.
9. Long-term losses were found to be small when compared to other losses for the girders under study. The segments were well aged before they were erected and prestressed.

8.3.2 Thermal Gradients

The following recommendations and conclusions have been made based on the measured gradients in the various structural elements under study, as well as the measured response of the structure both to these gradients and to the current AASHTO LRFD design thermal gradients. The recommended gradients based on this study apply specifically to central Texas.

8.3.2.1 Superstructure Gradients for Longitudinal Design

Positive Thermal Gradients

1. The 95% fractile values for measured deck-level magnitudes of the positive gradients were similar for both the cases without and with 50mm of blacktop, at 16°C without blacktop and 15°C with blacktop, although thermal data without blacktop were limited.
2. The NCHRP 276 or AASHTO LRFD recommended design positive gradients for girders with 50mm of blacktop at $T_1=20^\circ\text{C}$, and $T_1=25.6^\circ\text{C}$ without blacktop, were unrealistically high when compared to the 95% fractile $T_{1,\text{meas}}$ values and also considerably larger than the absolute maximum $T_{1,\text{meas}}$ values. The distribution of positive gradient magnitudes over time indicated that the thermal gradient case without blacktop deserves a higher design gradient magnitude than the case with 50mm of blacktop. Measured peak positive gradient magnitudes at deck-level decreased when the instrumented bridge units were opened to traffic, presumably because of cooling from the increased airflow (see Figure A.1).
3. The AASHTO LRFD recommended positive gradient shape more accurately represented the measured positive gradient shape of the Ramp P girder, and the NCHRP 276 recommended positive gradient shape better represented the shape measured on the mainlane, with the exception of the deck-level temperature. In either case, the temperature gradient in the bottom slab should be considered, with the soffit-level temperature at 3°C for central Texas.
4. Calculated stresses using the AASHTO LRFD recommended design positive thermal gradient compared well to stresses measured on the mainlane girder, but compared poorly and unconservatively to stresses measured on the Ramp P girder, even though the design gradient was larger than the measured gradient. Evidence of sectional distortion or warping was measured in every thermal gradient case. Also, soon into the life of the girders, high strains were measured in response to thermal gradients in the top slab over the webs. These high strains were measured in both the mainlane girder and the Ramp P girder and would indicate plastic behavior in the concrete. Improved analysis techniques for thermal gradients are urgently required.
5. Based on the measured positive gradients alone, a reduction in the magnitude of the design positive thermal gradient T_1 values would be warranted. However, analytical study of the structural response to thermal loads of a wide variety of girder cross sections needs to be performed before any reduction in the design positive thermal gradients can be implemented. The effects of cross-sectional shape, diaphragms, continuity, and potential plasticity should be considered in this study.

Negative Thermal Gradients

1. The shape of the AASHTO LRFD recommended negative thermal gradient did not compare well to measured negative thermal gradient shapes in either the mainlane girder or the Ramp P girder. The

negative gradient shape recommended by NCHRP 276 better represented the actual shape of the negative gradient, especially in the lower part of the cross section.

2. Based on the measured negative thermal gradients, the peak top fiber gradient temperatures recommended by AASHTO LRFD or NCHRP 276 were too extreme for central Texas. The maximum $T_{1,meas}$ values were closer to -0.3 times the NCHRP 276 recommended positive gradient temperatures. Measured 95% fractile $T_{1,meas}$ values were -7°C without blacktop and -5°C with 50mm of blacktop at deck-level. These 95% fractile values are substantially below the AASHTO LRFD recommended peak negative design gradient temperatures of $T_1=-13^{\circ}\text{C}$ and $T_1=-10^{\circ}\text{C}$ without and with blacktop respectively. All points of the negative gradient other than the top fiber temperature would be represented fairly accurately with the NCHRP 276 negative gradient shape.
3. Based on the unconservative calculated stresses in the Ramp P girder when compared to the measured stresses, no change to the current recommended design negative gradient from NCHRP 276 can be recommended, pending further study of box girder response to thermal gradients.

8.3.2.2 Thermal Gradients for Transverse Design

1. Measured stresses from both positive and negative thermal gradients through the thicknesses of the top slab, webs and bottom slab were large enough to warrant a design thermal gradient for transverse design.
2. Based on the measured temperatures, a positive thermal gradient should only be applied to the top flange, and the gradient shape should be linear. For Central Texas, a positive thermal gradient for no blacktop should have a peak deck-level temperature of 18°C and decrease at $-0.072^{\circ}\text{C}/\text{mm}$ for top slabs less than 250mm thick. For thicker top slabs the 18°C gradient can be assumed to decrease linearly through the thickness of the slab to 0°C at the bottom fiber. Similarly, a positive thermal gradient for 50mm blacktop should have a peak deck-level temperature of 17°C and decrease at $-0.068^{\circ}\text{C}/\text{mm}$ for top slabs less than 250mm thick. For thicker top slabs the 17°C gradient can be assumed to decrease linearly through the thickness of the slab to 0°C at the bottom fiber.
3. Based on the measured temperatures, significant negative thermal gradients occurred simultaneously in the top flange, webs, and bottom flange. For central Texas, a negative thermal gradient for a top flange with no blacktop should have a peak deck-level temperature of -10°C and increase at $0.040^{\circ}\text{C}/\text{mm}$ for top slabs less than 250mm thick. For thicker top slabs the -10°C gradient magnitude can be assumed to increase linearly through the thickness of the slab to 0°C at the bottom fiber. Similarly, a thermal gradient for 50mm blacktop should have a peak deck-level temperature of -5°C and increase at $0.020^{\circ}\text{C}/\text{mm}$ for top slabs less than 250mm thick. For thicker top slabs the -5°C gradient can be assumed to decrease linearly through the thickness of the slab to 0°C at the bottom fiber. The negative gradients occurring in the webs and bottom flange should also be assumed to be linear and can be obtained by multiplying the recommended top flange negative gradient peak temperature and slope for no blacktop by 0.75. This assumption gives a peak surface temperature of -7.5°C increasing at $0.030^{\circ}\text{C}/\text{mm}$.

8.3.2.3 Thermal Gradients for the Design of Piers

1. Significant thermal gradients and thermal-induced stresses were measured in the voided segmental pier P16 and the solid mainlane pier D5.
2. A positive thermal gradient for the design of voided piers based on the measurements can be derived by multiplying recommended positive gradient shape for box girders from Section 8.3.2.1 with no blacktop by 0.75. The peak magnitude of the gradient is 12°C . The far fiber temperature should remain at 3°C .
3. A negative thermal gradient for the design of voided piers based on the measurements is identical to that in Section 8.3.2.1 for superstructures, with a peak gradient value of -7°C .
4. Given the inaccuracy of the analysis method commonly used, the proposed gradients should not be used until better analysis methods have been developed. Pending further research into a better analysis method, the NCHRP 276 recommended positive thermal gradient shape with no blacktop multiplied by 75% can be used for the design of voided piers. The extreme fiber temperature should remain at 3°C . The NCHRP 276 recommended negative thermal gradient shape with no blacktop can also be used for the design of voided piers. The peak negative gradient temperature at the extreme fiber should be reduced to -0.3 times the

recommended positive gradient temperature with no blacktop, and the rest of the gradient shape should be used unmodified.

5. Although little data were taken to define the shape of thermal gradients in solid pier sections, the magnitude of the thermal gradients were measured to be similar to those of the voided pier. The recommended thermal gradients for the design of voided piers in point 4 above are recommended for the design of solid piers until further studies can be done.
6. The significant stresses produced by the thermal gradients in the piers were mostly inconsequential for pier design because the dead-load axial stresses prevented tension, except for one construction load case during the construction of the balanced cantilever superstructure of Ramp P. The decision to use a thermal gradient load case for the design of piers should be made by the engineer.
7. The following text should be added to Section 7.4.4 in the AASHTO Segmental Guide Specification: At the discretion of the Engineer, voided segmental piers may be designed for thermal gradients. A positive thermal gradient for the design of voided piers can be derived by multiplying the NCHRP 276 recommended positive gradient shape for box girders with no blacktop by 0.75, with the exception of the far fiber temperature which should remain at 3°C. The NCHRP 276 recommended negative thermal gradient shape with no blacktop can be used for the design of voided piers. The peak negative gradient temperature at the extreme fiber should be reduced to -0.3 times the recommended positive gradient temperature with no blacktop.
8. Daily thermal-induced stress changes in the piers were measured to be of the same magnitude as those produced by the superstructure dead load. In order to control surface stresses and concrete fatigue cracking, a nominal amount of transverse steel should be selected for a pier based on both the concrete volume and surface area, such as by the AASHTO LRFD equation 5.10.8.2-1.
9. Negative thermal gradients that occurred during curing of the pier P16 segments were large enough to crack the concrete segments while in the form. Negative thermal gradient magnitudes were measured as high as -35°C shortly after removal from the form. An area of transverse steel calculated by the AASHTO LRFD Equation 5.10.8.2-1 would not have been enough to prevent the cracking, since the transverse area of steel actually in the pier segments exceeded the amount found by this equation. A designer should consider the negative gradient produced in higher strength concrete elements during curing. Transverse steel should be increased to handle the thermal stresses, or provisions should be made to reduce the heat of hydration.

8.3.3 Load Response of Box Girders

The following conclusions have been made based on comparisons of the measured data with the calculated results:

8.3.3.1 Temporary Post-Tensioning for Epoxying Segments

1. An engineer should determine whether or not the segments under design will take a "banana" shape during casting and curing, estimate the warping deflection that will occur, and include the deflection in the design of the temporary post-tensioning to ensure full closure of the gap.
2. The diffusion of the temporary post-tensioning force from the anchorages or blisters should be estimated using a 30° diffusion angle, and stresses calculated at the extremities of the cross section away from the anchorage points. Assuming that plane sections will remain plane and that a linear stress gradient will pass through the center of gravity of the section may lead to an inaccurate estimate of the actual stress distribution. The temporary post-tensioning forces and locations should be designed to adequately stress the entire cross section considering diffusion. Furthermore, depending on temporary support methods, the dead load of the segment constructed in balanced cantilever may not produce a predictable stress distribution during the epoxying and temporary post-tensioning process and should not be relied upon as a source of bottom flange epoxy-squeezing stress.
3. The sequence of temporary post-tensioning should be considered, especially if anchorages are not well distributed throughout the cross section.

8.3.3.2 Diffusion of Post-Tensioning Forces

1. The AASHTO 30° diffusion method assumes a post-tensioning force or other point load is fully diffused in a concrete member within a 60° cone emanating from the point of force application. This method tended to underestimate the amount of diffusion of post-tensioning forces from anchorages in or immediately adjacent to anchorage diaphragms. The strut-and-tie method or other continuum method should be used to predict stresses near these diaphragms.
2. The AASHTO 30° diffusion method is not sufficiently accurate for calculating stresses in the vicinity of post-tensioning anchorages. These local zone stresses can be designed based on the recommendations from other studies such as NCHRP Report 356 [54].
3. The AASHTO 30° diffusion method was sufficiently accurate for predicting the distance from an anchorage to the point of full diffusion into the cross section.
4. At sections where the post-tensioning force is calculated to be fully diffused, shear lag in the cross section from primary post-tensioning moments can be compensated for by using the AASHTO effective flange width method. Only the b_f width should be calculated and used over the entire span since the pier reactions are not included in the calculation of primary moments or the stresses resulting from these moments.
5. Use the AASHTO effective flange width method for predicting cross-sectional stresses from secondary moments.

8.3.3.3 Girder Response to Dead Loads and Live Loads

1. The measured stresses and deflections from the simulated HS20-44 truck load (no impact) were small when compared to girder dead load. Live loads on the mainlane girder produced deflections only 1/6500 of the span length, while calculated dead-load deflection was 1/1050 of the span length.
2. The AASHTO effective flange width method gave sufficiently accurate results for the calculation of stresses and deflections from dead loads and live loads, although the girders tested did not experience significant shear lag at sections of high moment and stress gradient.
3. The AASHTO effective flange width method requires considerable section property calculation for girders that may only experience a small amount of shear lag, such as most common segmental girders and nearly all simple-span segmental girders. Another method should be developed for such girders that uses unmodified section properties.

8.3.3.4 Performance of Multiple-Cell Girders under Live Load

1. The twin single-cell girders tested shared as much as 30% of the applied live-load moment.
2. The amount of live-load moment sharing between the twin single-cell girders was sensitive to the torsional stiffness of each girder. The stiffness of the bearings must be included in the design of these girders.
3. The three-cell girders tested consistently shared as much as 43% of the applied live-load moment.
4. The amount of live-load moment sharing between sides of the three-cell girders was not sensitive to the stiffness of the bearings because of the presence of the pier diaphragm that was cast full width of the three girder cells.
5. Live-load deflections were small in the multiple-cell girders with a maximum measured deflection of only 1/6300 of the span length or smaller.

8.3.3.5 Performance of the Segmental Pier under Bending

1. The cross-sectional behavior of the segmental pier was entirely predictable, but the stiffness of the drilled shaft foundation had to be included in the analysis.
2. The moment connection of the pier to the balanced cantilever ramp superstructure using a cast-in-place grout pad and 16 post-tensioning bars performed as would a monolithic connection.

8.3.4 Behavior of D-Zones

The service-level performance of the D-zones under study ranged from inadequate when unanticipated details were used, like sharply bent deviator pipes, to excellent when designs were conservative. The following recommendations and conclusions were drawn from observations of the measured data, visual inspections, and review of the designs and details.

8.3.4.1 Mainlane Y-Pier

1. The mainlane Y-pier was designed as a concrete-steel composite structure. The force in the transverse steel pipe ties was reasonably, but unconservatively, predicted using a frame analysis, but was more conservatively predicted by a simple strut-and-tie model.
2. The anchorage of the mainlane Y-pier pipe tension ties in the concrete was excellent, with a fully bonded condition existing at the time of testing under full superstructure dead load.
3. The stiffness of the pipe ties limited the bending moment in the concrete Y compression and bending struts such that no cracking occurred at the service load level. Given the low stress levels, the pier should behave adequately with an ultimate load placed on the superstructure.

8.3.4.2 Segmental Pier P16 Capital

1. The pier P16 capital segment essentially remained uncracked from service load level forces, although the capital was initially cracked from thermal gradient forces during curing. These cracks had little impact on the service-level performance of the capital, based on visual inspection. Measured strains from service loads were small when compared to the strains needed to crack the concrete.
2. The heavy bars placed longitudinally and transversely at the top and bottom of the pier capital carried tensile force as expected in most cases, but the circumferential gauged bars at the bottom of the pier measured strains of equal or larger magnitude to the designed heavy tie bars. A strut-and-tie model for this solid section should include circumferential ties at the bottom to maintain similar geometry to the voided section beneath at the ultimate load condition.

8.3.4.3 Deviators

1. The instrumented mainlane and ramp deviators were beam-type deviators similar in dimension and reinforcement, with the exception of the width. The vertical tendon loads on the ramp deviator were only about 85% of those on the mainlane deviator. The deviation force on the tendon ducts did not appear to be well distributed along the length of the duct in the ramp deviator, but no large cracks developed and no exceptionally large strains were measured in the bars. The ramp deviator had good service-level performance. The mainlane deviator ducts did not meet the design requirement for smoothly bent pipes. The actual pipes used were sharply bent, concentrating the entire deviation force at the center of the deviator. This concentration of force caused extensive open cracks, and high stresses in the reinforcing bars adjacent to the sharp bend in the duct. Deviator ducts should be smoothly bent over the full length of the deviator to improve service-level performance. A sharp bend also increases friction between tendon, grout and duct, increasing horizontal loads on the deviator at ultimate. Such sharp bends should not be permitted.
2. The reinforcement details for both deviators were easily constructed at points away from the girder webs. Near the web to deviator intersection, the heavy web stirrup bars and other bars transitioning the web to the bottom flange remained unchanged from that for a typical section. This reinforcement left little room for the deviator top bars or shear reinforcement. Priority should be given to the placement and development of the bars connecting the deviator to the webs, since this is critical force path for developing the ultimate moment capacity of the girder.

8.3.4.4 Mainlane Anchor Segment D5-16

1. The mainlane pier segment with heavy anchorage diaphragm was not post-tensioned vertically to control tensile stresses from the diffusion of post-tensioning forces. Regardless of this fact, the mainlane pier

segment performed well at service load levels. The highest measured reinforcing bar stress was 35% of the yield stress and occurred in the heavy vertical bar immediately adjacent to the access passage through the diaphragm at a crack location.

2. The heavy end diaphragm was designed to take all the transverse and vertical tensile stresses from the anchorage zone at the ultimate load condition. At the service load level, the bottom flange of the girder near the anchor segment remained under high compression from the internal bottom slab tendons. The bottom flange cracked longitudinally directly beneath the bottom flange internal tendon ducts. The designed D-zone should have included a length of typical section, or a distribution of transverse service-level stresses should have been estimated, and additional steel provided to control cracking.

8.3.4.5 Ramp P Anchor Segment P16-1

The pier segment instrumented on Ramp P was post-tensioned vertically to make a moment connection with the pier. The top flange of the girder was also post-tensioned transversely. As a result little cracking occurred in the heavy anchorage diaphragm, and strain measurements were small.

8.3.4.6 Anchorage Blister

1. The instrumented anchorage blister was uncracked following post-tensioning and thereafter, indicating a very conservative design. A significant tensile stress change was measured behind the anchorage, at 1.7MPa, primarily from secondary prestressing moment. The tensile force change in the bottom flange was about 70% of the force from the post-tensioning tendon in the blister, based on the measured strains. Since the bottom flange of the girder was in significant compression from cantilevering dead load, no cracks were found. Very minor tension was also measured in the bars in front of the anchor plate that connected the blister to the web, indicating little corbel action. No corbel action was indicated between the blister and the bottom slab. Instead, compression was measured in the vertical bars adjacent to the anchor plate where the blister joined the bottom slab.
2. Tension was measured in the vertical bars along the length of the blister because of the vertical force generated by the radial deviation of the tendon over the length of the blister, and from diffusion of the tendon force into the blister.

8.3.5 *Cast-in-Place Joint Behavior*

8.3.5.1 Construction Procedures

1. The reinforcing bars for the cast-in-place continuity joints were spliced to 90° bend bars in the anchor segments that passed through the construction joint seat for the cast-in-place slab. The 90° bend bars were difficult to properly locate when the anchor segments were cast, resulting in the addition of many extra bars that were drilled into and bonded to the anchor segment. Also, these 90° bend bars often intruded into the horizontal surface intended for the fiberboard material used to tune the effective length of the joint. Widening the notch for the cast-in-place joint would have reduced the potential for inadequate splice lengths in the 90° bend anchor segment bars and provided more room for the fiberboards and stay-in-place forms.
2. The fiberboards used under the joint between girder wings were also used as the stay-in-place form for the joint itself. A steel stay-in-place form was eventually used in the wider portion of the joint between girder webs. The use of these stay-in-place forms was ideal because of the lack of access to the underside of the joint once it was cast and the speed at which the forms could be placed.
3. In order to control the movement of the end of the box girders from thermal expansion while the joint concrete hardened, adjacent box girders were locked together with the used of post-tensioning bars. These bars passed through the future post-tensioning ducts located in the anchor segment diaphragms. Only one joint of a span was locked at any one time. The joint was locked at a time when the girders were cool so that some residual compression would be applied to the joint after the joint was unlocked. The system seemed to work quite well, although the shrinkage of the joint concrete eventually caused a crack to open along the entire length of the cold joint, reducing the fixity of the joint to the girders. Shrinkage cracks were also noted to propagate from the reentrant corner of the joint where the joint slab changed width.

Softening the reentrant corner of the joint with a 45° angle would be nearly as easy to form in the surface of the anchor segment and would lessen the stress concentration effect of the 90° corner. Fiberboards with a 45° cut could be used under the joint slab in this area if the 90° corner is retained beneath the joint in the anchor segment.

8.3.5.2 Cast-in-Place Joint Behavior under Live Loads and Thermal Loads

1. The continuity joint did not substantially alter the structural performance of the adjacent box girders. The large negative moment couple that was measured on the San Antonio Y [7] did not develop in the U. S. 183 semicontinuous three-span or two-span units. The relatively stiff fabric reinforced pads with Teflon-stainless steel sliding surface developed a substantial negative moment in the San Antonio Y girders. Such a couple should be avoided unless this effect is specifically included in the design of the girders and the joint. The elastomeric bearings used on the U. S. 183 girders were very weak in shear, as this type of bearing is intended to be, and did not allow the formation of any appreciable negative moment in the live-load tests.
2. The cast-in-place continuity joint experienced local bending moment from the rotation of the ends of the girders from both live loads and thermal loads. The bending strains in the joint were much increased at the reentrant corner of the joint where the joint suddenly changed width. The joint width change was provided between girder webs to allow access to the tendon ducts. A 45° transition where the joint changed width would have lessened the stresses in the joint, while not influencing access to the tendon ducts or the interior of the box girder.
3. The cast-in-place fixity block between box girder bottom flanges was responsible for the development of some moment continuity across joints where the blocks were located. The negative moments developed ranged from insignificant to large. They did not develop in every case, depending on the fit of the block to the girder flanges. The fixity blocks were also eccentric to the centerline of the girder. In order to eliminate the formation of this negative moment, the fixity block should be moved or redesigned to eliminate a moment couple with the continuity joint.

8.4 OBSERVATIONS ON CONSTRUCTIBILITY AND DESIGN

The following observations are intended to point out the elements of design and methods of construction that proved to be excellent, as well as those that were less than optimal.

8.4.1 *Mainlane Y-Pier*

1. Since most of the superstructure was to be precast, creating the necessity for a large precasting facility, all the piers on the project were initially designed to be precast and post-tensioned. Considering the construction timeline, the time required to construct the precasting facility and bring casting machines into operation, and the availability of space at the site, the contractor elected to cast most of the piers in place. Designers should have considered including a cast-in-place substructure option in the contract plans as a means of potentially reducing bid prices and reducing the amount of design engineering to be performed during the course of the construction period.
2. The cast-in-place construction of the mainlane piers proceeded without difficulty, with the exception of the fabrication of the capital reinforcement bar cage. The complex shape of the capital formwork, the configuration of the bars, and the exact fit of the tension tie pipes to the forms made it desirable that the capital bar cages be tied in the form. The contractor in electing to cast-in-place should have designed the cage to be tied on a jig, thus speeding construction of the cage and eliminating bar cage fabrication time from the capital construction time. Based on observation, this fabrication would also have greatly improved the working condition for the ironworkers.
3. The wires intended to deter roosting of pigeons on the flat surfaces of the pier have proved to be ineffective.

8.4.2 Mainlane Girder

1. The simple-span design of the mainlane girders allowed the superstructure construction to proceed uninterrupted on a pace of a span every two days for each set of trusses. Reducing the number of critical construction steps was important since many of the time consuming tasks could only be performed at night. The simple-span construction also eliminated continuity-induced thermal gradient stresses.
2. The proportions chosen for the mainlane girder cross section could have been more efficient structurally if soffit width was increased. However the light, soaring appearance was a more important consideration for project acceptance by the public.
3. The twin triangular erection trusses designed for U. S. 183 worked well at all locations, except near the straddle bents. The trusses selected by the contractor could not fit in the space below the girder wing and above the top surface of the straddle bents. This problem should have been considered in the construction engineering.
4. The casting procedure for the typical mainlane segments was quickly refined and perfected, producing very high quality segments. The complicated shape of the anchor segments, combined with the congestion of heavy bars with their lap splices initially made construction of these segments difficult. To reduce congestion designers should consider using post-tensioning bars or T-headed bars to replace heavy mild reinforcement bars with conventional anchorage hooks and lap splices.
5. Many of the casting machines had bulkheads for transverse pretensioning of the top flange of the segments. This arrangement was very efficient given the number of segments cast in each of these machines. In general, the foundation conditions were suitable for rock anchors that tied the heel of the bulkheads to the ground.
6. The ride quality on the three-span semicontinuous bridge units was excellent. The asphalt topping was placed continuously across the cast-in-place deck joints and the ballasted future location of the finger joints. The asphalt was later cut, and the finger joint and surrounding cast-in-place concrete installed flush with the top of the asphalt.
7. The duct boot clamps that provided the water tight seal between the steel deviator and diaphragm pipes and the polyethylene ducts were removed immediately following grouting. This removal eliminated the air tight seal for the grout. Grout allowed to dry out readily shrinks and cracks. These clamps should be left in place.
8. The bottom slab tendon anchorages were deviated at one end of the girder to facilitate tendon feeding. Tendons were prefabricated and installed by pulling through from the girder dead end. The deviation was not necessary and required that the anchor segments on the live and dead end of the girder have different blockout locations.
9. The temporary post-tensioning blisters proved very effective and efficient during span construction, although forming and reinforcing these external blisters added some complexity to the precasting process.
10. The 25mm drain holes through the bottom slab and deviator beams were too small in diameter and immediately became clogged with debris and eventually grout. Rain frequently entered the girders through the storm drains and other openings before all the storm drain piping was installed, flooding the girders.
11. The access holes located in the bottom flange near one anchor segment in each span were frequently blocked by the storm drain pipes.
12. Storm drains should be located only near pier segments, in the first adjacent segment, to minimize the length of pipe located inside the core of the box girder. Also, routing the storm drain pipes through the center of the anchor segment access passage destroys the usefulness of the access passage. The storm drain pipe should be routed against the side of large size access passages, or routed through the diaphragm of anchor segments with small access passages.

8.4.3 Segmental Pier P16

1. The precasting and erection procedures for the segmental piers were very efficient.

2. Casting the voided typical column segments was very simple compared to the casting procedure and complexity for some of the segments on the project, but a systematic twist was cast in. Fortunately this twist was accommodated at the ramp anchor segments that were cast later. Otherwise, the ducts for the tie down bars would not have aligned.
3. Vertical thermal cracks formed in the voided pier segments during curing. These cracks were located adjacent to the large drain pipes cast within the cross section. Also, drain pipes were installed where they were not necessary in some piers used for cantilever construction of the superstructure. This probably weakened these piers torsionally.
4. The capital segment reinforcement was tied in two separate pieces because the heavy bars at the top of the cage could not be supported by the lower portion of the cage, requiring additional time for ironwork inside the form. A one-piece cage would have reduced production time
5. The capital segment generated too much heat during curing and cracked in many places from tensile stresses caused by the huge negative thermal gradient.
6. The tie down bars and anchorage plates were difficult to locate at the required compound angle within the central portion of the pier capital segment. The tie down bars were also difficult to stress at deck level because of close spacing and a small recess. A U-shaped strand tendon with oversize duct would have allowed for more alignment error and been easier to stress within the recess at deck level.
7. The cast-in-place base around and under the first pier segment above the footing, placed on a stay-in-place steel stand, appears to have been an effective method of connecting the precast elements to the footing. Unfortunately, it was impossible to check for voids and collection of bleed water on the underside of the first segment.
8. The small amount of transverse steel originally designed for the pier was doubled for actual construction. Shear capacity of the pier should be sufficient to develop a ductile failure mode for the entire five-span frame.
9. Fabrication of the reinforcement cage for the typical voided pier segments was simple. A segmental post-tensioned cage is lightweight with small size vertical bars. The effectiveness of the short bars, with a 180° bend on one end and 90° bend on the other end, placed on a grid through the thickness of the pier segment walls should be evaluated. These bars were intended to provide a restraining force on the small vertical bars to prevent their buckling when the local concrete became plastic under an ultimate load and to restrain the transverse reinforcement so it could act as concrete confinement. The grid spacing was much too great to prevent buckling of the small size vertical bars, or provide confinement, especially in light of the fact that these short bars had an ineffective 90° bend on one end. In a post-tensioned pier, the vertical bars are intended to reinforce the concrete against tensile stresses from thermal forces, shrinkage forces and other forces not associated with the develop of a plastic moment. These vertical bars are not the main tension bars, nor are they significant compression reinforcement or confinement reinforcement.
10. Four internal post-tension bars were used to construct the segmental pier. Two of these bars were terminated at the top of the last typical voided pier segment. The blockout for the anchorage created two substantial voids beneath the pier capital that were not filled with epoxy or grout. The contract plans should specify that the voids be filled at the time the capital is set in place.

8.4.4 Ramp P Constructed in Balanced Cantilever

1. The quality of the precast segments was excellent. They were constructed similarly to the mainlane segments using the short-line method.
2. The overall construction scheme of the Ramp P five-span continuous girder was excellent and allowed construction to proceed from one or both ends of the five-span girder. Efficient construction required two ground-based cranes.
3. The web bar detail at the top slab, with 90° bends for development, created significant congestion. The ducts for the cantilevering tendons had to be deviated from outside the plane of web bars to the anchorage plate at the centerline of the web. Closed stirrup-type web bars should be used where possible.

4. The two-piece anchor segment was difficult to assemble and move into final surveyed position on top of the pier capital. This type of assembly would have been greatly simplified if the halves were epoxied together on the ground then lifted into place, weight permitting. The anchor segment should have been designed to be of similar weight to the other segments on the project so that it could have been cast and erected in one piece.
5. Final positioning on top of the pier may have been simplified with the use of a precision match-cast concrete or high strength grout template at the locations with permanent fixity. The use of fiber reinforced elastomeric pads as temporary bearings worked well once the anchor segment halves were assembled.
6. Small adjustments of the ramp geometry were easily accomplished because of the flexibility of the piers. Substantial adjustments up to 150mm were easily made when the permanent expansion bearings were installed on piers P14 and P17.
7. Access to the core of the box girder was poor until the girder was essentially completed. The access passage through the top flange should have been located near the anchor segments for use during balanced cantilever construction and post-tensioning of the continuity tendons.
8. The external temporary post-tensioning anchorage blisters were easy to use, although the location of bottom flange blisters interfered with movement of workers and with the alignment of the external tendons. The use of the top flange cantilever tendon ducts for temporary post-tensioning of the first two typical segments to the anchor segments worked poorly. The post-tension bars were nearly impossible to remove because the size of the bar couplers was only marginally smaller than the size of the duct, and because of the horizontal curvature of the bridge. The temporary post-tensioning bars should have passed through the anchor segment diaphragm, regardless of the congestion.
9. The 19-strand external continuity tendons used in the ramp girder were the same size as most of the tendons used on the rest of the project, but unfortunately required the use of a very large ram inside the completed box girder. Clearance problems were immediately evident. A combination of the large amount of slack from the lack of support of the unstressed external tendons, the large number of strands in the tendons, the long lengths of the tendons and resultant long elongations, the location of a saddle immediately adjacent to the stressing end anchorage, and the eventual entanglement of the strands resulted in several broken tendons. It can be assumed that some similar entanglement also existed behind the anchor heads of the tendons that did not break.
10. The complex three-dimensional geometry of Ramp P made proper alignment of the deviator and saddle pipes very difficult in the short-line casting machine. Pipes with bell-shaped ends, or "diabolos," would have greatly reduced the impact of a misalignment.
11. The drain holes were too small, as in the mainlane girder and immediately became clogged.

8.4.5 Transition Spans

1. The contractor elected to cast the three-cell transition spans in place because of two reasons. First, there were relatively few transition spans so the cost of two additional casting machines was not warranted. Second, the erection trusses used on the project could not be used to erect the precast single-wing, single-cell girders without major modification. The decision to cast these girders in place was later regretted. The merger of a ramp girder into the main girder is a problem often encountered in precast segmental construction. Provisions should be made in the design so that the standard casting machines can construct the special segments required at the transition locations. Also, construction methods should be conceived, considering pier and superstructure shapes, so that the standard erection trusses can be used to erect the special segments. For example, on the U. S. 183 transition spans, the full-width anchor segment diaphragm could have been cast between precast anchor segments, and the girders constructed as torsional cantilevers using only one erection truss under each of the single wings.
2. The location of the drain pipes was poor, as for the mainlane girder. The combination of the three external tendons and the drain pipes in the small outer two cells of the three-cell girder made passage in these cells nearly impossible.

8.4.6 Modified Spans

1. Construction of the modified spans proceeded without major incident, and the gore closures between the two girder wings were easily formed and cast from deck level.
2. The drain pipes were poorly located and blocked the bottom flange access openings.

8.5 RECOMMENDATIONS FOR FUTURE STUDIES

8.5.1 Instrumentation

The Campbell 21X dataloggers and AM416 Multiplexers used on the project worked exceptionally well without error. The greatest limitation of this datalogger system was the maximum time interval of one hour. Current Campbell dataloggers may have overcome this limitation. When using the AM416 multiplexers, it is important not to switch power to the instruments because damage to the precision low resistance switches can be the result. Future use of a multiplexer used for such a purpose could cause errant readings because of the increased resistance of the switches. The quarter bridge wiring scheme used on this project with the strain gauges worked very well for the short-term measurements and allowed a maximum number of channels to be read for each multiplexer. The long-term use of this wiring system is questionable. Since switching occurs within the bridge, changes in resistance anywhere in the system are interpreted as strain changes when the output voltage is read.

If this system is to be used for long-term readings, eliminating the task of rewiring the system after the short-term measurements have been completed, multiple dummy gauges should be read by the system to help calibrate the strain gauges in the structure over time. Also, the interval used for the short-term measurements should not exceed 30 seconds, unless preliminary tests prove otherwise, so that temperature-induced resistance changes do not occur. For the same reason, the system should be allowed to run at the minimum time interval for a time to let the system reach a stable temperature before testing begins. A better wiring scheme for long-term strain gauge measurements with the 21X or similar datalogger would use an independent full bridge for each strain gauge, switching only the output voltage. Excitation voltage could be provided directly by the datalogger either intermittently or continuously. Battery life would be reduced if the gauges are excited continuously. No problems should be expected from the wiring schemes used for other gauges used on this project.

The strain gauges used on this project, whether C-type or S-type, performed well over the short-term unless damaged during construction. Damage usually occurred from vibration or direct impact. The gauges also tended to fail rapidly after traffic was allowed on the bridge. To limit damage to the C-type gauges, installed on short steel rods and embedded in the concrete, larger rods should be used than the 5mm rods used on this project. The necessary increase in length of the larger rods would also speed field installation. The 5mm rods used on this project for the C-gauges worked exceptionally well in the laboratory, but were easily bent in the field. For long-term measurements weld-on-type strain gauges should be used when steel elements are instrumented, especially if field installation does not allow temperature and humidity control, or if vibration is expected. Some vibrating wire gauges should be used for long-term concrete strain measurements. High redundancy of strain gauges is recommended, since some are bound to fail and all gauges do not have to be used. The shielded and Teflon-coated thermocouples used on this project worked extremely well.

Gauges for each instrumented segment should be wired to an independent datalogger system that can be tested and calibrated to temperature changes, well before erection of the segment begins. Demec strain measurements can only be relied upon for very short test periods on an actual structure, since temperatures and temperature gradients change continuously throughout the day. A substantial number of temperature measurements, combined with time consuming analysis, is required to eliminate thermal strains from the Demec strain data. The speed at which Demec strains can be read almost precludes their use in any number during short-term tests. The use of more internal or external thermally compensated strain gauges is preferable to the use of the Demec for all but backup duty, unless actual strain changes are required. Reliable strain gauge data from the instrumented tendons proved the most difficult of measurements. These gauges were field installed with the glue least sensitive to temperature, yet often did not stay bonded to the tendons after they were stressed, given the large strain-change-induced shear force in the glue. Other methods should be considered for instrumentation of tendons. However, weld-on strain gauges do not seem feasible.

The number of gauges of all types used on this project was formidable, but denser grids of strain gauges should have been used in the cross sections of the girders to measure, for example, strain changes across the width of the webs. More cross sections along the length of the girders should also have been instrumented to evaluate the effects of the D-zone forces.

8.5.2 Future Research Topics

Friction losses were not entirely predictable on this project. A large database of friction data must exist, particularly with the proprietary prestress hardware suppliers and state agencies. This data should be evaluated, and future research needs recommended, if necessary. Friction between tendon and deviator duct following stressing should be studied for both ungrouted and grouted tendons. This friction has important design implications on elastic shortening loss calculations, ungrouted tendon force changes from construction loads, and tendon force changes at the ultimate load state for various allowed plastic rotations.

An extensive thermal record was obtained for various structural elements on U. S. 183. The thermal record was largely limited to the years after the application of asphalt, but the thermal gradients from NCHRP 276 appear to be much larger than actually occur. The commonly used design method for calculating thermal gradient stresses does not appear to be accurate, based on the measured strains. The common design method assumes plane sections remain plane, and this assumption was definitely not the case. An analytical study needs to be performed to evaluate the current design method. The study should consider different box girder shapes and girder continuity, as well as the influence of changes in the design gradient shape on calculated stresses. The effect of local concrete plasticity in areas of the cross section that have heavy reinforcement should also be considered. The analysis results could be tabulated as a design aid for standard box girder sections. The reinforcing steel in the pier segments, especially the solid capital, was inadequate for controlling thermal-induced tensile stresses during curing. Given the importance of high one-day concrete strengths for precast segments, with the resultant high heat of hydration, a study should be performed to determine an adequate percentage of surface reinforcement for control of thermal stresses for segmental elements of different shapes, thicknesses, and concrete mixtures.

The box girders studied at U. S. 183 behaved in a predictable manner to dead loads, live load, and prestressing forces. Shear lag in the box girders did not have great influence on the design. Using the *AASHTO Effective Flange Width Method* [8] resulted in substantial cross-sectional reduction of the mainlane simple-span girder only near the supports, where moment was low. Also, the Ramp P girder was compact and did not suffer greatly from shear-lag-induced stiffness reduction. Nevertheless, the stress calculations for these girders were as complex as for girders with substantial shear lag. A new method for calculating shear-lag-induced stress increases in box girders of common proportion should be developed and tabulated for standard box girder cross sections.

APPENDIX

SUMMARY OF MEASURED THERMAL GRADIENTS

The following Figures A.1, A.2 and A.3 were prepared by M. Keith Thompson for CTR Report 1820-S [56]. The report presents a summary of all the long term thermal data taken by University of Texas researchers at both the U. S. 183 Segmental in Austin, and at the San Antonio Y Project. Report 1820-S also gives a statistical analysis of the data beyond that performed for this dissertation. From Figures A.1 and A.2, it can be seen that the daily maximum negative thermal gradients decreased markedly after the blacktop was applied to these superstructure box girders. Also from Figure A.1, the maximum daily positive gradient appears to have decreased somewhat after the bridge was opened to traffic. Little change in the maximum daily positive or negative thermal gradients occurred in the segmental pier column as a result of the construction of the superstructure, judging by the regularity of the data over time in Figure A.3.

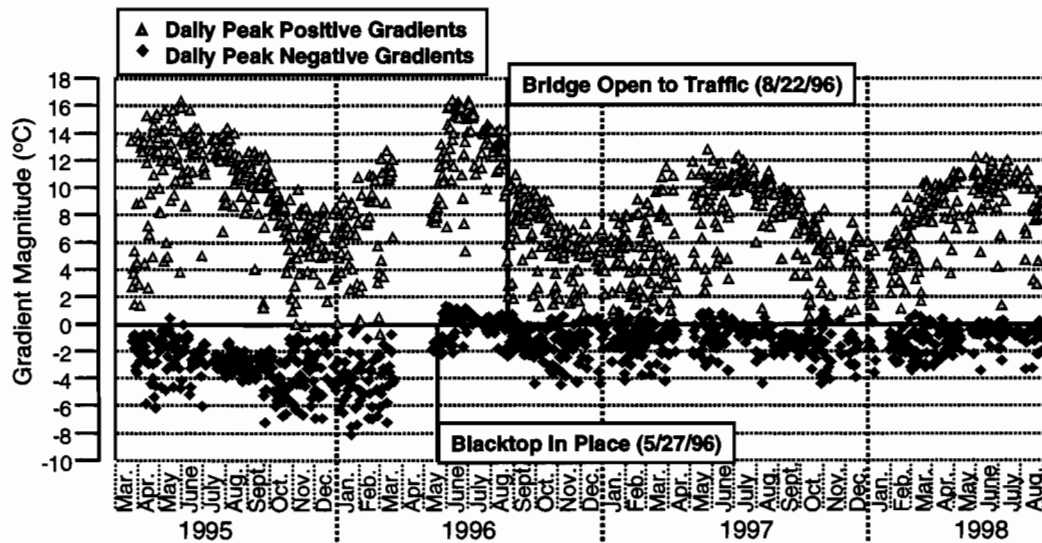


Figure A.1 US 183 Mainlane box girder daily maximum thermal gradients

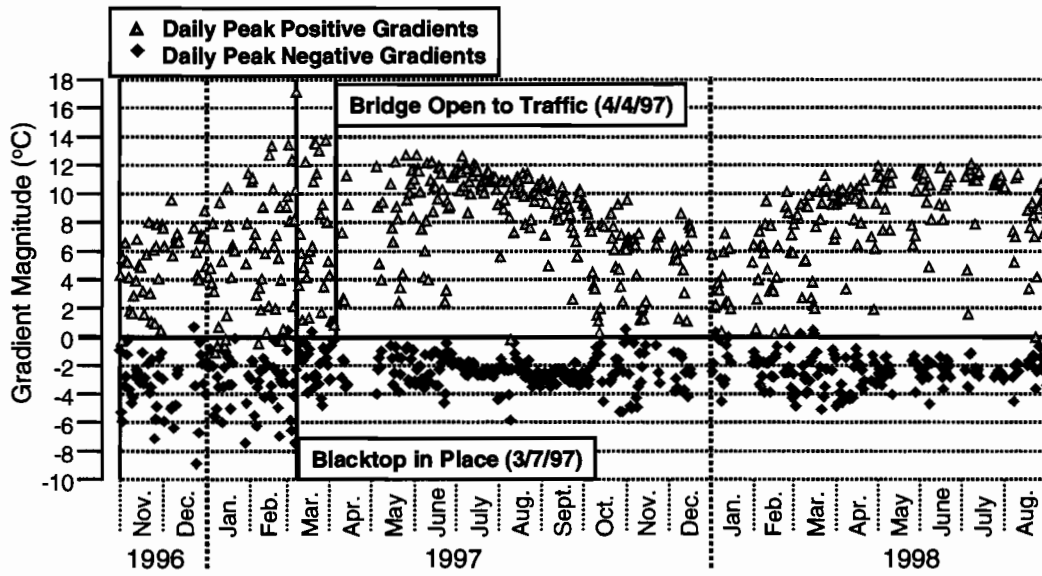


Figure A.2 US 183 Ramp P box girder daily maximum thermal gradients

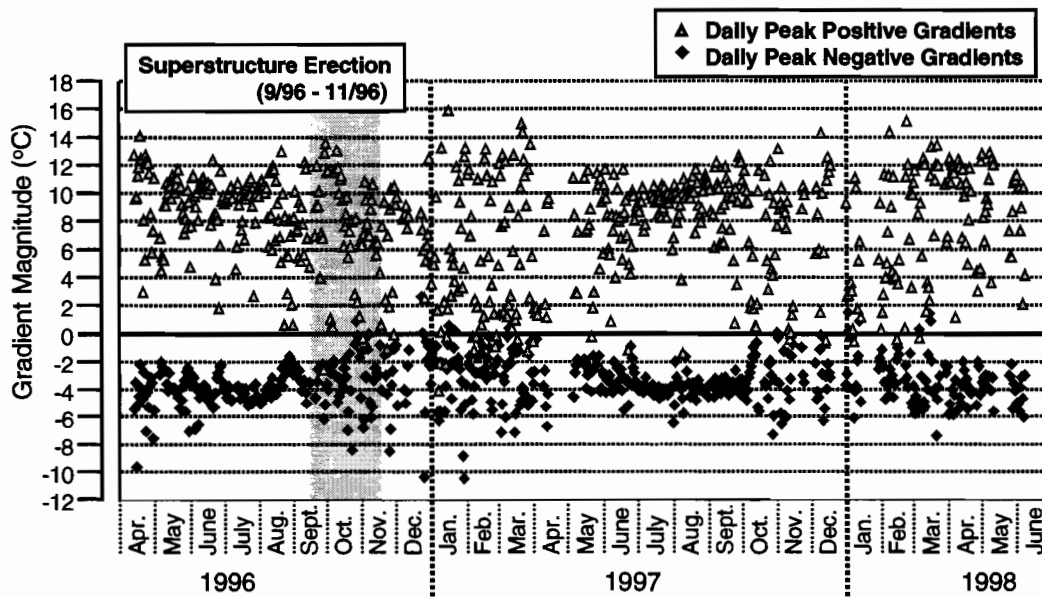


Figure A.3 US 183 segmental box pier P16 daily peak thermal gradients

REFERENCES

1. Billington, Sarah L., "Improving Standard Bridges Through Aesthetic Guidelines and Attractive, Efficient Concrete Substructures," Ph.D. Dissertation, The University of Texas at Austin, December 1997.
2. Koseki, K., Breen, J. E., "Exploratory Study of Shear Strength of Joints for Precast Segmental Bridges," Center for Transportation Research Report No. 248-1, Austin, Texas, September 1983.
3. MacGregor, R. J. G., Kreger, M. E., Breen, J. E., "Strength and Ductility of a Three-Span Externally Post-Tensioned Segmental Box Girder Bridge Model," Center for Transportation Research Report No. 365-3F, Austin, Texas, January 1989.
4. Taylor, A. W., Rowell, R. B., Breen, J. E., "Design and Behavior of Thin Walls in Hollow Concrete Bridge Piers and Pylons," Center for Transportation Research Report No. 1180-1F, Austin, Texas, November 1990.
5. Beaupre, R. J., Powell, L. C., Breen, J. E., "Deviation Saddle Behavior and Design for Externally Post-Tensioned Bridges," Center for Transportation Research Report No. 365-2, Austin, Texas, July 1988.
6. Wollman, G. P., Yates, D. L., Breen, J. E., "Deviation Saddle Behavior and Design for Externally Post-Tensioned Bridges," Center for Transportation Research Report No. 465-2F, Austin, Texas, November 1988.
7. Roberts, C. L., Breen, J. E., Kreger, M. E., "Measurement Based Revisions for Segmental Bridge Design and Construction Criteria," Center for Transportation Research Report No. 1234-3F, Austin, Texas, August 1993.
8. *Guide Specifications for Design and Construction of Segmental Concrete Bridges*, American Association of State Highway and Transportation Officials, Washington, D. C., 1989.
9. *AASHTO LRFD Bridge Design Specifications, 1st Edition*, American Association of State Highway and Transportation Officials, Washington, D.C., 1994.
10. Roberts, Carin L., "Measurement Based Revisions for Segmental Bridge Design and Construction Criteria," Ph.D. Dissertation, The University of Texas at Austin, December 1993.
11. Arrellaga A., J. A., "Instrumentation Systems for Post-Tensioned Segmental Box Girder Bridges," Master's Thesis, The University of Texas at Austin, 1991.
12. Stone, W. C., "Design Criteria for Post-Tensioned Anchorage Zone Tensile Stresses," Ph.D. Dissertation, The University of Texas at Austin, May 1980.
13. Andres, Valerie A., "Verification of Force Distribution in an Innovative Bridge Pier," Master's Thesis, The University of Texas at Austin, 1995.
14. Chang, W. R., Etsion, I., Bogy, D. B., "Static Friction Coefficient Model for Metallic Rough Surfaces," *Journal of Tribology*, Transactions of the American Society of Mechanical Engineers, Vol. 110, January 1988.
15. Mindess, Young, *Concrete*, Prentice-Hall, Englewood Cliffs, New Jersey, 1981.
16. Bezouska, T. J., "Friction Loss in Post-Tensioned Prestressing Steel Units," Report SSR-3-66, Division of Highways, Department of Public Works, California, September 1966.
17. Bezouska, T. J., "Friction Losses in Rigid Post-Tensioning Ducts," Division of Highways, California Department of Public Works, California, February 1971.
18. Dywidag Systems International, USA, Inc., "Methods for Reducing Friction in Post-Tensioning Tendons," Dywidag Report, Lincoln Park, New Jersey, February 1988.

19. Tran, T. T., "Reducing Friction Loss for Post-Tensioning Tendons in Monolithic Girders," Master's Thesis, The University of Texas at Austin, December 1992.
20. Harstead, G. A., Kummerle, E. R., Archer, J. C., Porat, M. M., "Testing Large Curved Prestressing Tendons," Journal of the Power Division, Proceedings of the American Society of Civil Engineers, March 1971.
21. Yasuno, H., Kondo, S., Tadano, N., Mogami, T., Sotomura, K., "Friction Problems with Multi-Strand Tendons," Proceedings of the 9th Congress of the Federation Internationale de la Precontrainte, Volume 2, Wexham Springs, England June 1982.
22. Davis, R. T., Tran, T. T., Breen, J. E., Frank, K. H., "Reducing Friction Losses in Monolithic and Segmental Bridge Tendons," Center for Transportation Research Report No. 1264-2, Austin, Texas, October 1993.
23. *Standard Specifications for Highway Bridges*, Sixteenth Edition, American Association of State Highway and Transportation Officials, Washington, D.C., 1996.
24. Comite Euro-International du Beton-Federation Internationale de la Precontrainte, *CEB-FIP Model Code for Concrete Structures*, Switzerland, 1990.
25. ACI Committee 318, *Building Code Requirements for Reinforced Concrete (ACI-318-95)*, American Concrete Institute, Detroit, 1995.
26. PTI, *Precast Segmental Box Girder Bridge Manual*, Prestressed Concrete Institute and Post-Tensioning Institute, 1977.
27. ACI-ASCE Committee 323, "Tentative Recommendations for Prestressed Concrete," *Journal of the American Concrete Institute*, Proceedings V. 54, January 1958.
28. Zia, P., Preston, H. K., Scott, N. L., and Workman, E. B., "Estimating Prestress Losses," *Concrete International: Design and Construction*, V. 1, June 1979, pp. 32-38.
29. ACI Committee 209, "Prediction of Creep, Shrinkage, and Temperature Effects in Concrete Structures," ACI-209R-82, American Concrete Institute, Detroit, Michigan, 1982.
30. ASTM A416-74, from *Post-Tensioning Manual*, Third Edition, Post-Tensioning Institute, Phoenix, Arizona, 1982.
31. Tassin, D., Dodson, B., Takebayashi, T., Deeprasertwong, K., Leung, Y. W., "Computer Analysis and Full Scale Test of the Ultimate Capacity of a Precast Segmental Box Girder Bridge," The American Segmental Bridge Institute.
32. Hoffman, P. C., McClure, R. M., and West, H. H., "Temperature Studies for an Experimental Bridge," Research Project 75-3 Interim Report, Pennsylvania State University, June 1980.
33. Hirst, M. J. S. and Dilger, W. H., "Prediction of Bridge Temperatures," *IABSE Proceedings* P138/89, August 1989.
34. Shiu, K. N., "Seasonal and Diurnal Behavior of Concrete Box-Girder Bridges," *Transportation Research Record* 982.
35. Priestly, M. J. N., "Design of Concrete Bridges for Thermal Gradients," *ACI Journal*, May 1978, pp. 209-217.
36. Arockiasamy, M., and Reddy, D. V., "Thermal Response of Florida Bridges," Florida Atlantic University, Boca Raton, Florida, June 1992.
37. Pentas, H. A., Avent, R. R., Gopu, K. A., and Rebello, K. J., "Field Study of Bridge Temperatures in Composite Bridges," *Transportation Research Record No. 1460*, pp. 45-52.

38. Potgieter, I. C., and Gamble, W. L., "Response of Highway Bridges to Nonlinear Temperature Distributions," Report No. FHWA/IL/UI-201, University of Illinois at Urbana-Champaign, April 1983.
39. Imbsen, R. A., Vandershof, D. E., Schamber, R. A., and Nutt, R. V., "Thermal Effects in Concrete Bridge Superstructures," NCHRP 276, Transportation Research Board, Washington, D. C., September 1985.
40. British Standards Institution, "Steel, Concrete and Composite Bridges, Part I, General Statement," *British Standard BS 5400*, Crowthorne, Berkshire, England 1978, pp. 43.
41. Ryals, K. K., "Fretting Fatigue of Tendons in Deviator Ducts of Externally Post-Tensioned Segmental Box Girders," Master's Thesis, The University of Texas at Austin, 1992.
42. Beer, F. P., Johnson, E. R., *Mechanics of Materials*, McGraw-Hill, New York, 1981.
43. *1983 Ontario Highway Bridge Design Code*, Highway Engineering Division, Toronto, Ontario, 1983.
44. Kristek, V., *Theory of Box Girders*, John Wiley and Sons, New York, 1979.
45. Song, Q., "Shear Lag Analysis of Simple and Continuous T, I, and Box Beams," Report No. UCB/SESM-84/10, University of California at Berkeley, June 1984.
46. Ritter, W., "Die Bauweise Hennebique (The Hennebique System)," *Schweizerische Bauzeitung*, Bd. XXXIII, No. 7, Zurich, 1899.
47. Morsch, E., *Der Eisenbetonbau, Seine Theorie und Anwendung (Reinforced Concrete, Theory and Application)*, Stuttgart, 1902.
48. Marti, P., "Truss Models in Detailing," *Concrete International*, V. 7, No. 12, 1985, pp. 66-73.
49. Muller, P., "Plastic Analysis of Reinforced Walls and Beams," *Report No. 83*, Institute of Structural Engineering, ETH Zurich, 1978, 160pp.
50. Thurlimann, B., "Plastic Analysis of Reinforced Concrete Beams," *Introductory Report*, IABSE Colloquium on Plasticity in Reinforced Concrete (Copenhagen, 1979), International Association for Bridge and Structural Engineering, Zurich, V. 28, 1978, pp. 71-90.
51. Leonhardt, F., Monnig, E., "Lectures on Reinforced Concrete Structures, Part 2: Special Cases of Calculations for Reinforced Concrete Construction," 3rd edition, Springer Verlag Publishers, Berlin, 1986.
52. Schlaich, J. *et al.*, "Toward a Consistent Design of Structural Concrete," *PCI Journal*, Volume 32, No. 3, Prestressed Concrete Institute, May/June 1987.
53. Bergmeister, K. *et al.*, "Detailing for Structural Concrete," Center for Transportation Research Report 1127-3F, Austin, Texas, May 1993.
54. Breen, J.E., Burdet, O., Roberts, C., Sanders, D., Wollman, G., "Anchorage Zone Reinforcement for Post-Tensioned Concrete Girders," NCHRP Report 356, Transportation Research Board, National Academy Press, Washington, D. C., 1994.
55. Beaupre, R. J., Powell, L. C., Breen, J. E., Kreger, M. E., "Deviation Saddle Behavior and Design for Externally Post-tensioned Bridges," Center for Transportation Research Report 365-2, Austin, Texas, July 1988.
56. Thompson, M. K., Breen, J. E., Kreger, M. E., "Indications About Thermal Gradient Magnitudes From Studies of Concrete Box Girder Bridges," Center for Transportation Research Report 1820-S, Austin, Texas, October 1998.
57. Davis, Rodney T., "Measurement Based Performance Evaluation of a Segmental Concrete Bridge," Ph.D. Dissertation, The University of Texas at Austin, May 1999.

